MVP Deployment #4 (May 1997) Tracer Gas Atmospheric Dispersion Measurements at Vandenberg Air Force Base

15 June 2000

Prepared by

R. N. ABERNATHY
Space Science Applications Laboratory
Laboratory Operations

Prepared for

SPACE AND MISSILE SYSTEMS CENTER
AIR FORCE MATERIEL COMMAND
2430 E. El Segundo Boulevard
Los Angeles Air Force Base, CA 90245

20000808 007

Space Systems Group
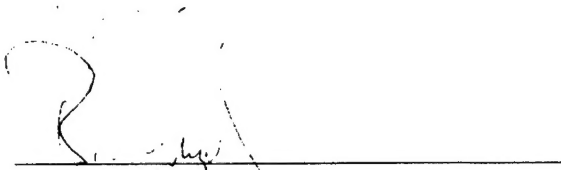
THE AEROSPACE CORPORATION
El Segundo, California

DTIC QUALITY INSPECTED 4

Capt. William Kempf
SMC/CLTE

REPORT DOCUMENTATION PAGE

Form Approved
OMB No. 0704-0188

Public reporting burden for this collection of information is estimated to average 1 hour per response, including the time for reviewing instructions, searching existing data sources, gathering and maintaining the data needed, and completing and reviewing the collection of information. Send comments regarding this burden estimate or any other aspect of this collection of information, including suggestions for reducing this burden to Washington Headquarters Services, Directorate for Information Operations and Reports, 1215 Jefferson Davis Highway, Suite 1204, Arlington, VA 22202-4302, and to the Office of Management and Budget, Paperwork Reduction Project (0704-0188), Washington, DC 20503.

1. AGENCY USE ONLY (*Leave blank*)	2. REPORT DATE 15 June 2000	3. REPORT TYPE AND DATES COVERED

4. TITLE AND SUBTITLE
MVP Deployment #4 (May 1997) Tracer Gas Atmospheric Dispersion Measurements at Vandenberg Air Force Base

5. FUNDING NUMBERS
F04701-93-C-0094

6. AUTHOR(S)
R. N. Abernathy

7. PERFORMING ORGANIZATION NAME(S) AND ADDRESS(ES)
The Aerospace Corporation
Laboratory Operations
El Segundo, CA 90245-4691

8. PERFORMING ORGANIZATION REPORT NUMBER
TR-2000(1490)-2

9. SPONSORING/MONITORING AGENCY NAME(S) AND ADDRESS(ES)
Space and Missile Systems Center
Air Force Materiel Command
2430 E. El Segundo Boulevard
Los Angeles Air Force Base, CA 90245

10. SPONSORING/MONITORING AGENCY REPORT NUMBER
SMC-TR-00-15

11. SUPPLEMENTARY NOTES

12a. DISTRIBUTION/AVAILABILITY STATEMENT
Approved for public release; distribution unlimited

12b. DISTRIBUTION CODE

13. ABSTRACT (*Maximum 200 words*)

As part of the USAF Atmospheric Dispersion Model Validation Program (MVP), puffs of tracer gas were released from an airship (i.e., free-flying blimp) over the eastern and western rocket launch ranges (Cape Canaveral Air Force Station, MVP deployments 1-3, and Vandenberg Air Force Base, MVP deployment 4, respectively). Infrared cameras, located at multiple locations, simultaneously imaged the transport and dispersion of the sulfur hexafluoride (SF_6) tracer from various perspectives. The imagery is being quantitatively analyzed to follow the movement and the dispersion of the puffs with time. Analysis of the simultaneous multi-perspective imagery quantifies the absolute dispersion of individual puffs as well as the relative dispersion and motion of groups of puffs. Expansion rates are reported separately for the various axes (alongwind, crosswind, etc...) relative to the puff trajectory (effective wind bearing). The infrared imagery revealed the puff extent to a threshold of 1-5 ppm-m column density, which included the bulk of the SF_6 tracer. The objective of the activity is to correlate the imagery-derived atmospheric expansion rates with other measurements of atmospheric turbulence. Results of the activity will be used to evaluate and improve the models that are used at the launch ranges to predict the dispersion of toxic clouds generated by launch operations. This is the first time that tracer gases have been released from a free-flying blimp and imaged simultaneously by infrared cameras at multiple ground locations. This report provides a summary of the imagery-derived results from the MVP #4 puff releases at Vandenberg Air Force Base.

14. SUBJECT TERMS
Atmospheric Dispersion Model Validation Program, MVP, Sulfur Hexafluoride, SF6 tracer, Turbulence, Alongwind and crosswind expansion rates, Blimp, Airship, Rocket launch ranges, Vandenberg Air Force Base, Cape Canaveral Air Force Station, VAFB, CCAFS

15. NUMBER OF PAGES
216

16. PRICE CODE

17. SECURITY CLASSIFICATION OF REPORT UNCLASSIFIED	18. SECURITY CLASSIFICATION OF THIS PAGE UNCLASSIFIED	19. SECURITY CLASSIFICATION OF ABSTRACT UNCLASSIFIED	20. LIMITATION OF ABSTRACT

NSN 7540-01-280-5500

Standard Form 298 (Rev. 2-89)
Prescribed by ANSI Std. Z39-18
298-102

Acknowledgements

Contents

Figures

Tables

1. Introduction

1.1   Executive Summary

This report describes a series of atmospheric tracer gas releases conducted at Cape Canaveral Air Force Station (CCAFS) and Vandenberg Air Force Base (VAFB) to characterize local dispersion parameters. An airship (i.e., free-flying blimp) released puffs of sulfur hexafluoride (SF_6) tracer while a series of ground-based infrared (IR) cameras simultaneously imaged the puffs' motion and dispersion. Analysis of the simultaneous multi-perspective imagery quantifies the absolute dispersion of individual puffs as well as the relative dispersion and motion of groups of puffs. Expansion rates are reported separately for the various axes (i.e., alongwind, crosswind, etc...) relative to the puff trajectory (effective wind bearing). The IR imagery revealed the puff extent to a threshold of 1–5 ppm-m column density, which included the bulk of the SF_6 tracer. The imagery-derived expansion rates document dramatic differences (i.e., a factor of 3 to 4) in the along- and crosswind dispersion rates under certain release conditions. These imagery-derived dispersion data can be used to calculate values for the turbulence fluctuations. Comparison of these imagery-derived turbulent fluctuations to values derived by other methods (i.e., from meteorological data) and to model predictions will provide one basis for tuning the atmospheric dispersion models in use at the launch sites. This report is available electronically as a PDF document (viewable in color using the free Acrobat viewer). Many of the details contained in the figures are more easily seen in color.

1.2   Model Validation Program

Range safety offices at CCAFS and VAFB use atmospheric dispersion models to predict toxic hazard corridors (THCs) for space launches. The safety offices may recommend a launch hold when predicted THCs extend into public areas. The Launch Programs Office at the Air Force Space and Missile Systems Center (SMC/CL) is conducting the Atmospheric Dispersion Model Validation Program (MVP) to review and improve model predictions. MVP activities are coordinated by an integrated product team, which is funded primarily by SMC/CL and the USAF Research Laboratory. Other key MVP participants include the range safety offices at CCAFS and VAFB, NOAA, NASA, ACTA Inc., Kamada Science & Design, and SRS Technologies. The MVP involved two field efforts: (1) collection and analysis of Titan launch cloud data (see references 1–15) and (2) collection and analysis of tracer release data.[16,17] This report discusses the collection and quantitative analysis of the tracer release imagery during the MVP #4 deployment at Vandenberg AFB in May 1997.

MVP conducted four three-week tracer dispersion sessions to simulate the dispersion of toxic launch gases under a variety of meteorological conditions. Three of the sessions were conducted at CCAFS (July 1995, November 1995, and April/May 1996), and one of the sessions was conducted at VAFB (May 1997). Continuous plumes and intermittent puffs of an inert, invisible tracer gas (sulfur hexafluoride) were released in small quantities from an elevated blimp (i.e., 500 to 3300 ft or 150 to 1000 m AGL). A total of 92 plumes (each about two hours in duration) and 256 puffs were released during different times of the day and night. Aircraft and ground vehicles equipped with tracer

1

detectors tracked the dispersing plumes and quantified plume profiles and concentrations. Infrared cameras located at multiple ground sites simultaneously recorded imagery of the movement and dispersion of the puffs. The IR threshold for edge detection ranged from 1–5 ppm-m column density and depended upon several random factors that included operator bias, atmospheric background, and low-altitude fog. Quantitative analysis of the simultaneous multi-perspective imagery quantifies the absolute dispersion of individual puffs as well as the relative dispersion and motion of groups of puffs. Dispersion rates are reported separately for the various axes (i.e., alongwind, crosswind, etc...) relative to the puff trajectory (effective wind bearing).

A comprehensive meteorological dataset was collected to compliment the tracer dataset. Data collected from the extensive range of meteorological systems were supplemented by data from NOAA aircraft, sodars, and surface energy flux stations. All of the tracer dispersion and meteorological data collected during the four tracer sessions are being processed and posted on a NOAA FTP site.

2. Field-Deployable Quantitative Infrared Imagery

The Surveillance Technologies Department of The Aerospace Corporation's Space Science Applications Laboratory developed the visible and IR imaging systems (VIRIS) to support the MVP. Each VIRIS contains a co-aligned Hitachi visible CCD video camera and an AGEMA Thermovision 900 IR scanner. The visible CCD camera enables the tracking of a rocket's exhaust cloud using scattered visible solar radiation (i.e., during daylight hours). The long-wavelength IR scanners (sensitive over 8–12 μm band) enable the tracking of clouds and chemicals using their thermal signature (i.e., during daylight and at night). For the sulfur hexafluoride (SF_6) tracer releases discussed in this report, a narrow-band filter provided improved sensitivity (1–5 ppm-m column densities) for the SF_6 absorption near 10.6 μm (940 cm^{-1}). The VIRIS provides not only co-aligned and simultaneous visible and IR imagery but also collects GPS data (time and VIRIS position) along with angular data (azimuth and elevation of the VIRIS tripod). The VIRIS imagery can be interpreted quantitatively by using the encoded time, camera position, tripod azimuth, and tripod elevation to calibrate not only the field of view (FOV) of the cameras but also the pointing angles relative to absolute references.

2.1   Long-Wavelength Infrared Scanners

The AGEMA Thermovision 900 LW scanner downloads a 12-bit digital image to the controller. The 20° by 10° lens provides a spatial resolution of 1.5 mrad (0.09°) at 50 % modulation while the 40° by 20° lens provides a spatial resolution of 3.0 mrad (0.17°) at 50 % modulation. Without filters, the scanner's thermal range is –25°F to +2700°F Fahrenheit (–30°C to +1500°C). The scanner has a 6-position filter cassette to allow targeting narrower bands (i.e., chemical-specific detection) or hotter temperatures. The scanner supports a 15-Hz data rate with a 230 by 136 line resolution. However, the image is interpreted to 272 pixels per line (i.e., square pixels). The Mercury Cadmium Telluride (MCT) detector is cooled using a Stirling cycle system.

2.2   Quantitative Analysis of Infrared Imagery

The analysis of the IR imagery involves field-of-view (FOV) calibration, angular calibration (both azimuth and elevation), and quantitative analysis of simultaneous imagery from multiple perspectives. During MVP #4 tracer releases, the AGEMA IR cameras collected synchronized imagery from four sites once every 15 s. Pair-wise analysis of simultaneous imagery of a puff from multiple sites provides the triangulated position and extent of the puff. The PLMTRACK program was developed and is maintained by Brian P. Kasper of Aerospace for the MVP program. Robert N. Abernathy used PLMTRACK to triangulate each puff's position as a function of time using all of the available imagery (i.e., 6 pair-wise combinations from 4 imagery sites). The PLMTRACK analysis has been described in detail in an earlier report[12] and in Appendix A.

Plotting the PLMTRACK-derived position data documented the puff's speed, direction, and altitude during the time that it was observed. Linear regression fits to plots of these data provided the "best" value for the puff's position as a function of time. This provided the slant range from the camera site

to the middle of the puff and allowed the analyst to convert the angular extent of the puff observed in any image to physical extent. The IR threshold for detecting the edge of the puff ranged from 1 to 5 ppm-m column density and depended upon several random factors. The analyst assessed the accuracy of the imagery-derived puff data using various analysis schemes and multiple perspectives. Appendix A illustrates the various angles and dimensions involved in our analysis.

3. Results and Discussion

3.1   Accuracy of Imagery-Derived Values

We documented the accuracy of our analysis in several ways. We used PLMTRACK to triangulate the blimp's position and compared the imagery-derived position to the blimp's GPS-derived position. We analyzed trends in the tracer puff data to illustrate that the expansion rates were insensitive to resolution, slant range, and elevation angle. We documented that the maximum tracer concentrations within the puff always remained over an order of magnitude higher than our threshold for detecting the puff. In a separate series of reports, Inki Min documents that the imaged extent corresponds to 4 to 6 sigma levels on the Gaussian fit to the puff's column density profiles.

Appendix B provides a series of plots that document the difference between the blimp's GPS position (1–3 m accuracy) and the PLMTRACK-derived (i.e., imagery-derived) blimp position. The blimp's onboard differentially corrected GPS provided 1-m resolution for latitude (y) and longitude (x) while providing 3-m resolution for altitude (z). The plots in Appendix B document that the differences between the GPS position and the imagery-derived position fall within 100-m resolution (2-sigma value) for horizontal and within 30-m resolution (2-sigma value) for vertical position. Based upon these data, we can conclude that the PLMTRACK analyses provide positional information with accuracy comparable to, or better than, that of regular GPS.

Appendix C contains a series of expansion rate plots for two example puffs. The two puffs are the first puff from 21 May and the first puff from 23 May 1997. A filter is adjusted to peel successive layers of the data to illustrate any sensitivity of the data to the experimental parameter(s). The filter is area per pixel (i.e., APP). Since the FOV of the scanners remained constant, APP is related to slant range (SR), to elevation (EL), and to background radiance. The plots in Appendix C reveal that the expansion rate (i.e., slope) remains constant as the APP filter was tuned to remove successive layers of data. For each puff, the largest setting for the APP filter allows all of the available data to be viewed. The smallest APP filter setting is the last value that provides enough points to establish a line and reveals the best data (i.e., shortest slant range, steepest elevation angle, lowest background radiance (i.e., contrast), and highest resolution). For 21 May, the APP filter is changed by factors of 2 from 48 to 6 m^2 per pixel without affecting the measured expansion rate (i.e., slope). For 23 May, the APP filter was set to 102, 60, 40, and 20 without affecting the expansion rate. These APP filter settings include a reasonable operational range for slant range, for elevation, and background radiance. Hence, the expansion rates (i.e., the observed extent of the cloud) are not sensitive to resolution, slant range, elevation angle, or background radiance over an operational range of their values. These results document that there was a reproducible threshold for edge detection.

Appendix D provides a series of plots to illustrate that the imagery-derived SF$_6$ column densities remained well above our 1–5 ppm-m threshold level. Unfortunately, the column density (i.e., product of concentration times path length) remained too concentrated to accurately quantify the mass. M. L. Polak developed the PLMMASS approach as a variation of the special ratio approach that was

previously describe in reference 18. His analysis uses a filter-corrected transmission function to correlate column density to apparent transmission. The apparent transmission of the puff is estimated using the background radiance, the puff radiance, and the radiance from a blackbody emitter at the puff's temperature. R. N. Abernathy applied PLMMASS to the MVP #4 imagery with the hopes of calibrating the pixel intensity as column density and, thereby, revealing the distribution of tracer within the puff images. Unfortunately, the systematic errors are greatest at the high column densities observed during the MVP #4 deployment. In addition to the underestimation of mass (i.e., column density) for concentrated puffs, there were random errors due to the variable backgrounds (i.e., broken clouds) observed on 23 May 1997. Appendix D documents an inverse linear correlation between the APP (i.e., slant range, resolution, elevation, and background radiance) and the total imagery-derived puff mass. The data in Appendix D document that there are significant errors (factor of 2 to 3) in estimating the mass within the puff from narrow-band imagery. The plots in Appendix D document that the imagery-derived mass of the puff improves as the puff is diluted (i.e., better for lower column densities) and as the APP decreases (i.e., better resolution, smaller slant range, steeper viewing elevation, and lower background radiance). As discussed above, Appendix C documented that the expansion rate (i.e., observed puff extent) is independent of APP. Based upon the combined data in Appendices C and D, one can infer that the measured extent (and expansion rate) includes the bulk of the SF_6 and is insensitive to dilution, resolution, slant range, and elevation. Hence, there was a reproducible threshold for edge detection, but we cannot quantify the peak column density.

Inki Min of the Space Architecture Department is processing our puff imagery data in an attempt to extract turbulent fluctuations. His analyses involve various approaches to extracting sigma (i.e., for Gaussian fits to the puff extent and distributions). The results document less than a 30% error in using a fixed 1 ppm-m threshold for edge detection and automating the puff analysis by using PLMTRACK-derived puff characteristics (i.e., x and y dimensions within the image). An alternative approach involves quantitative measurements on individual puff images that have been processed by PLMMASS. Robert Abernathy of Surveillance Technologies Department provides the PLMTRACK-derived puff characteristics and the PLMMASS-calibrated puff imagery for Inki Min's analyses. Inki Min is documenting the analysis methods and their results in a separate report.[19] The results of the analyses document that the observed puff extent (i.e., diameters) correspond to 4 to 6 sigma levels on the Gaussian fits. The threshold is further out (~6 sigma) on the Gaussian distribution for the most concentrated puffs at early times. The threshold remains fairly sensitive (~4 sigma) on the Gaussian distribution for the most dilute puffs at later times. Therefore, the analysis indicates that the observed extent corresponds roughly to 6 sigma at early times and to 4 sigma at later times. Dr Min's analyses document that the observed expansion rates (slope of full extent versus time) are 3 to 4 times steeper than for sigma's increase with time for 21 May 1997 and are 4 to 5 times steeper than for sigma's increase with time for 23 May 1997. The PLMTRACK data and the PLMMASS calibrated images are available for further analysis by other analysts.

3.2   Imagery and Tracer Release Information

3.2.1   Imagery Site Locations

Figure 1 is a map of south Vandenberg AFB documenting the imagery sites used on 21 and 23 May 1997. All four sites used on 21 May 1997 were along the ridge of Santa Ynez road. For 21 May 1997, Site 1 (NASA) was near the NASA radar dome, Site 2 (VHF) was at the intersection of VHF
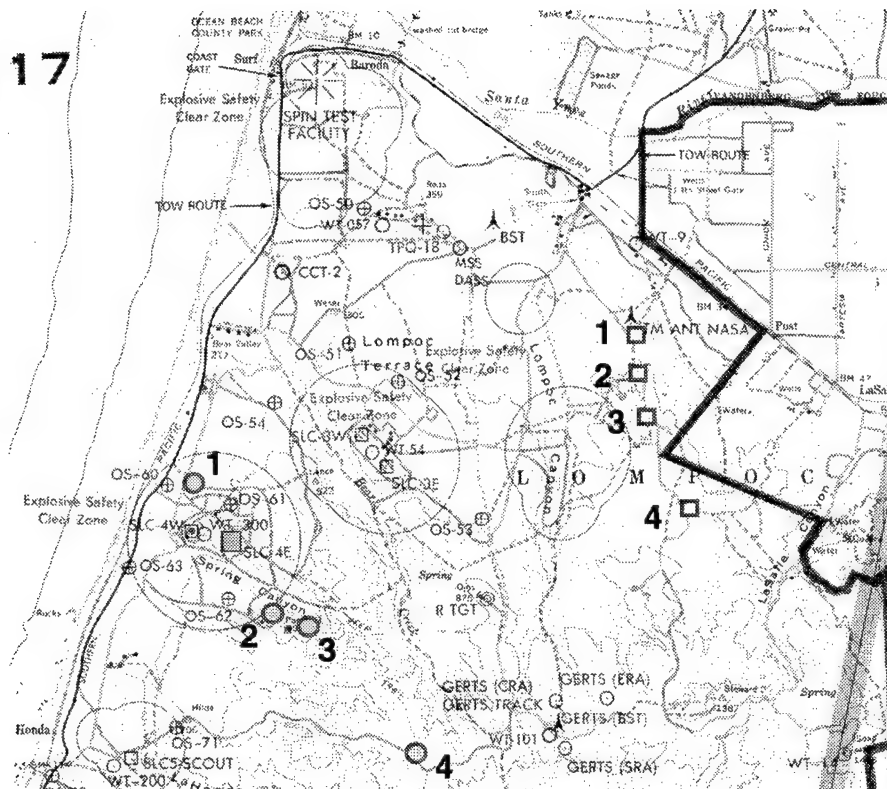
Figure 1. Map of South VAFB showing imagery sites used on 21 and 23 May 1997.

road and Santa Ynez road, Site 3 (MOTU) was near the MOTU 4 geodetic marker, and Site 4 (SY Site 4) was on a dirt road off of Santa Ynez road. The airship tracer releases originated to the northeast and northwest of Site 1 (NASA) on 21 May 1997, and the wind carried the puffs to the southeast. For 23 May 1997, Site 1 (DIX) was on Dix road, Site 2 (CEMT) was 30 ft southeast of a cement marker above the water tower on Tank road, Site 3 (SMT2) was on the second summit along Tank road past the water tower, and Site 4 (Avery) was along Avery road. The airship tracer releases were as close as possible to SLC-4E (i.e., the Titan IV launch pad) on 23 May 1997, and the wind carried the puffs to the southeast. Due to the cloudy conditions along the coast and restrictions in airspace over the launch pad, the releases on 23 May 1997 were not always optimal.

Table 1 documents the differentially corrected GPS-derived latitude, longitude, and altitude for each imagery site used to track tracer puff releases during MVP #4. The table provides the site number for each day. The site number refers to the order of the sites along the path of the puff trajectories or wind bearing. The site name and the location file name (LOC column) refer to the location of the site relative to landmarks. The GPS data was acquired using a PathFinder Pro-Beacon differentially corrected GPS receiver. The accuracy should be within 23 ft (i.e., 7 m) for latitude and longitude and 45–69 ft (i.e., 14–21 m) for altitude. Appendix B documents that the OmniSTAR GPS on the Blimp had better accuracy than the PathFinder Pro-Beacon used to survey the camera sites. The Pro-Beacon's accuracy was adequate for surveying the camera sites.

Table 1. MVP #4 Imagery Site Locations for 21 and 23 May 1997

Day May 97	Site (#)	Name	Loc	Latitude	Longitude	Alt. (M MSL)	Alt. (Ft MSL)
21	1	NASA	nasasite	34:39:17.008	120:33:19.773	99	326
21	2	VHF	syvhf	34:39:02.728	120:33:17.915	129	423
21	3	MOTU	motuhill	34:38:44.717	120:33:15.186	152	499
21	4	Site4	sysite4	34:38:08.579	120:32:53.235	202	662
23	1	DIX	dix23pol	34:38:17.250	120:36:56.427	78	257
23	2	CEMT	cemt30se	34:37:25.873	120:36:17.813	265	869
23	3	SMT2	tanksmt2	34:37:20.260	120:35:58.794	301	988
23	4	AVERY	avery523	34:36:29.813	120:35:9.475	329	1079

3.2.2 Release Information for 21 May 1997

Table 2 documents the release information for each puff on 21 May 1997. Table 2 provides the GMT for the release of the first puff in each series, the duration (length in seconds) of the liquid SF_6 release for each puff, the gap between the start of successive puffs in each series, and the mass of SF_6 in each puff. The "note" column documents the approximate release position relative to the position of Site 1 (NASA). Table 2 documents that there were 5 series containing 3 puffs each on 21 May 1997. On 21 May 1997, the five series (three puffs per series) were separated by 8 to 15 min. For 21 May 1997, all puffs were 5-s releases of liquid SF_6 with gaps of 1 min separating the start of successive puffs in each series.

The imagery documented that the liquid vaporized within seconds of its' release. The IR scanner acquired one image every 15 s and, so, could not record the expansion of the liquid SF_6 to form the initial vapor cloud (i.e., source). The imagery documented no significant altitude change for times longer than 15 s after the release. This observation suggests that the SF_6 puff quickly reached equilibrium (i.e., thermal and density) with the surrounding air.

Table 2. SF_6 Release Information for 21 May 1997 Puffs

Day May 97	Series (#)	Puff (#-#)	GMT (Start)	Length (s)	Gap (s)	Mass (g)	Note (Release Info)
21	1	1-3	21:00:00	5	60	910	NW of NASA Site
21	2	4-6	21:15:00	5	60	910	NE of NASA Site
21	3	7-9	21:27:00	5	60	910	NE of NASA Site
21	4	10-12	21:38:32	5	60	910	NE of NASA Site
21	5	13-15	21:46:51	5	60	910	NE of NASA Site

The puffs can be numbered 1–15 as in Table 2. We prefer numbering the puffs as 1–3 for each series. Using this approach, each puff can be referenced as S#P#, where the S# refers to the series while the P# refers to the puff in each series. Therefore, S1P1 is series 1 puff 1 while S3P2 is series 3 puff 2. This scheme will be used throughout this report. Typically, the three puffs of each series are within the FOV of each imagery site, and their analysis is based upon the same set of images.

Figure 2 is a Cartesian plot that documents not only the locations of the imagery sites (the triangles) but also the imagery-derived puff tracks (the lines) for the 21 May 1997 SF_6 releases on south Vandenberg AFB. It is apparent from this plot that the airship releases originated to the northeast and northwest of Site 1 (NASA). The legend identifies each puff as S#P#, where the S# refers to the series while the P# refers to the puff in each series. Figure 2 documents that the puffs moved to the southeast with little variation in direction (i.e., the lines are almost parallel). During this same period, Figure 3 documents that the imagery-derived puff speed increased from 7.8 to 10.7 knots (4 to 5.5 m/s) while the imagery-derived puff bearings shifted from 145° to 135° clockwise from north. The puff bearing is the direction that the puff moved, and, therefore, a 135° bearing documents that the puff's movement was toward the southeast. Figure 4 documents that imagery-derived altitudes of the puffs were between 2460 and 2820 ft (750 to 860 m) above mean sea level (MSL).

3.2.3   Release Information for 23 May 1997

Table 3 documents the release information for each puff on 23 May 1997. Table 3 provides the GMT for the release of the first puff in each series, the duration (length in seconds) of the liquid SF_6 release for each puff, the gap between the start of successive puffs in each series, and the mass of SF_6 in each puff. The "note" column documents the approximate release position relative to the position
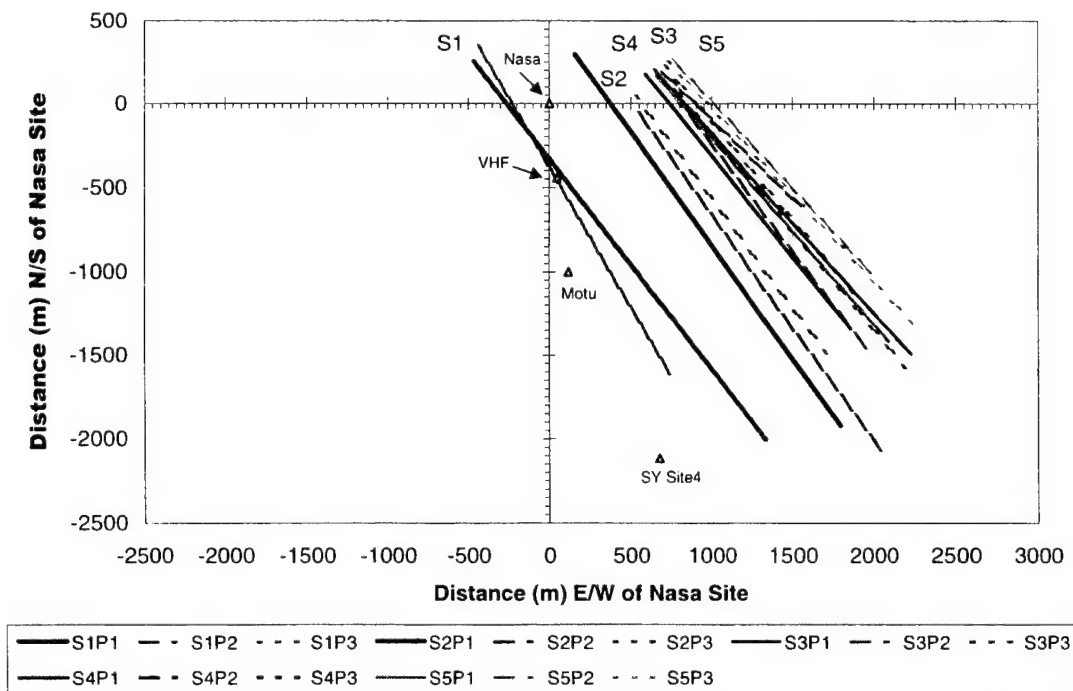
Figure 2. Puff trajectories derived from imagery of 21 May 1997 SF_6 releases.

9
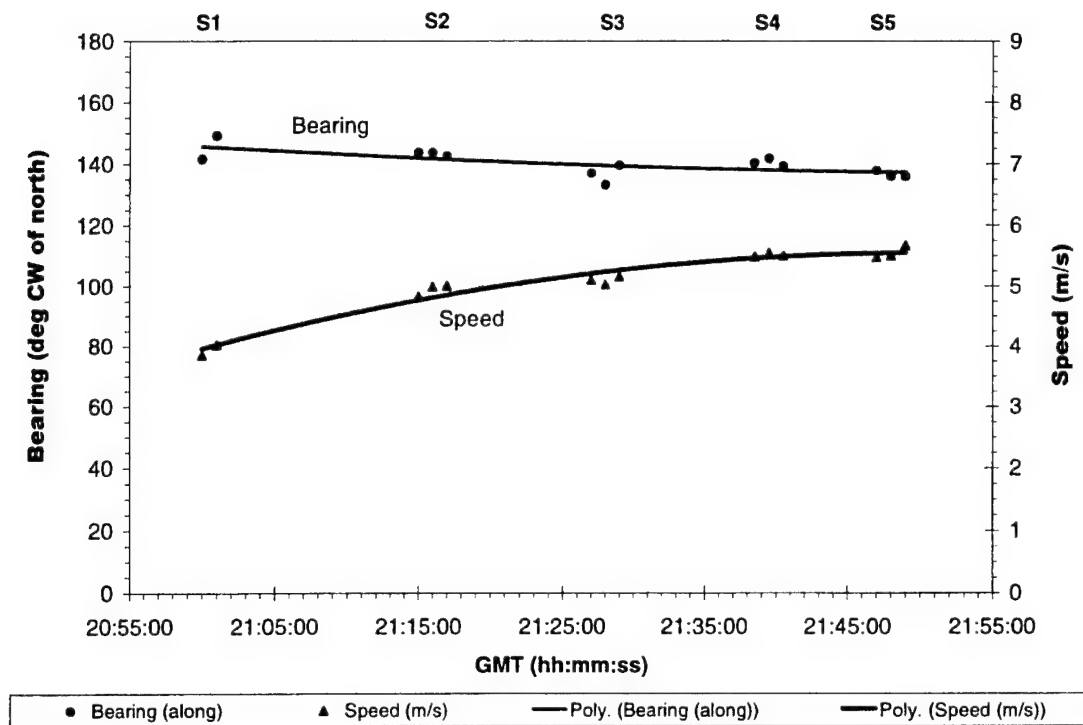
Figure 3. Puff bearing and speed derived from imagery of 21 May 1997 SF_6 releases.
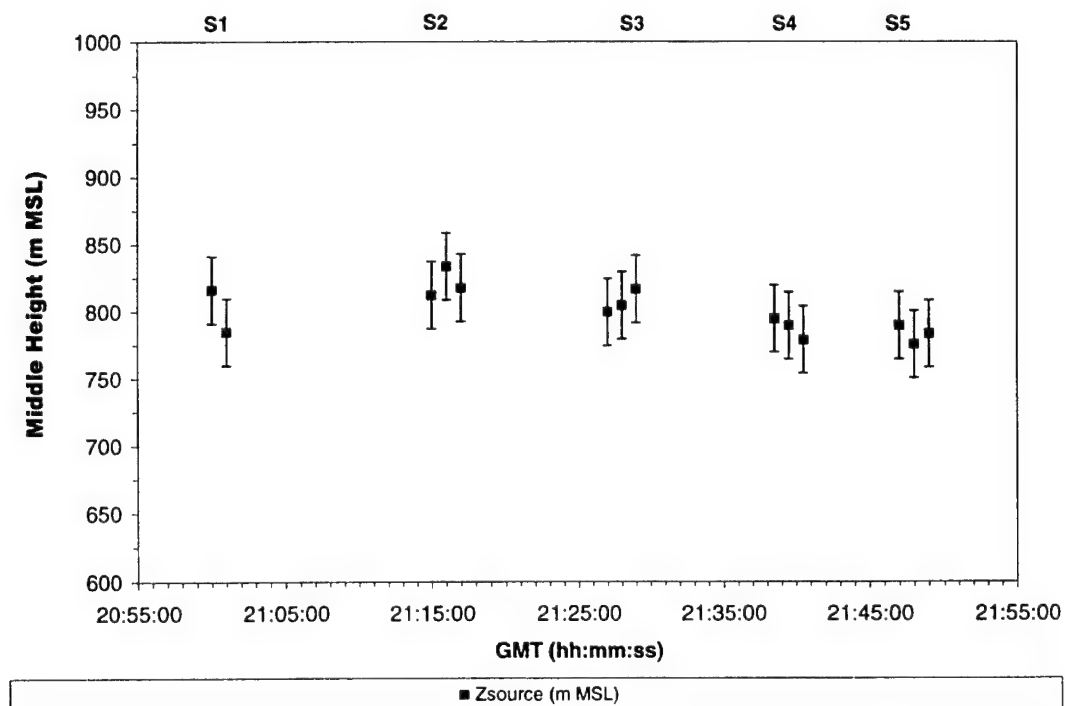
Figure 4. Puff altitude derived from imagery of 21 May 1997 SF_6 releases.

Table 3. SF$_6$ Release Information for 23 May 1997 Puffs

Day May 97	Series (#)	Puffs (#-#)	GMT (Start)	Length (s)	Gap (s)	Mass (g)	Note
23	1	1-3	19:00:00	10	60	1750	NE of SLC-4E
23	2	4-6	19:10:00	10	60	1750	NE of SLC-4E
23	3	7-9	19:17:00	10	60	1750	NE of SLC-4E
23	4	10-12	19:36:00	10	50	1750	Poor S/N
23	5	13-15	19:44:00	10	50	1750	Poor S/N
23	6	16-18	19:54:30	10	50	1750	Poor S/N
23	7	19-21	20:10:45	10	50	1750	SW of SLC-4E
23	8	22-24	20:17:45	10	50	1750	SW of SLC-4E
23	9	25-27	20:22:45	10	50	1750	Poor S/N
23	A(10)	28-30	20:27:25	10	50	1750	Only Sites 1&3
23	B(11)	31-33	20:41:05	10	50	1750	SW of SLC-4E
23	C(12)	34-36	20:46:35	10	40	1750	Poor S/N
23	D(13)	37-39	20:50:25	10	40	1750	Poor S/N
23	E(14)	40-42	20:57:45	10	30	1750	Poor S/N
23	L(LINE)	LINE	21:24:45	N/A	N/A	N/A	Cloudy & Hazy
23	F(15)	43-45	21:37:50	10	40	1750	SE of SLC-4E
23	G(16)	46-48	21:41:50	10	40	1750	SE of SLC-4E
23	H(17)	49-51	21:45:10	10	40	1750	SE of SLC-4E
23	I(18)	52-54	21:48:30	10	40	1750	Too Cloudy
23	J(19)	55-57	21:51:40	10	40	1750	Too Cloudy
23	K(20)	58-60	21:55:20	10	40	1750	Poor S/N

of Site 1 (NASA) or comments on the quality of the data (i.e., for puffs not processed due to poor signal-to-noise ratios). Table 3 documents that there were 20 series of 3 puffs each on 23 May 1997. On 23 May 1997, the series were separated by 3 to 26 min. For 23 May 1997, all puffs were 10-s releases of liquid SF$_6$ with gaps ranging from 30 s to 60 s separating the start of successive puffs in each series. The gaps between successive puffs were constant within each series.

The imagery documented that the liquid vaporized within seconds of its release. The IR scanner acquired one image every 15 s and, so, could not record the expansion of the liquid SF$_6$ to form the initial vapor cloud (i.e., source). The imagery documented no significant altitude change for times longer than 15 s after the release. This observation suggests that the SF$_6$ puff quickly reached equilibrium (i.e., thermal and density) with the surrounding air.

The puffs can be numbered 1–60 as in Table 3. We prefer numbering the puffs as 1–3 for each series. Using this approach each puff can be referenced as S#P#, where the S# refers to the series while the P# refers to the puff in each series. On 23 May 1997, the first 9 series were numbered 1–9. As indicated in Table 3, the subsequent series were labeled a–k (for 10–20) so that one character could be used to represent each series. Typically, the three puffs of each series are within the FOV of each imagery site, and their analysis is based upon the same set of images.

Table 3 also references a "line" release between puff series E and F. The line release was a continuous release of liquid SF$_6$ from the blimp as it flew crosswind. The cloudy background provided a poor signal-to-noise ratio for measuring the variations in alongwind motion and dispersion as the "line" moved successively over each of the camera sites. Therefore, we did not process any line release data.

Figures 5 and 6 are Cartesian plots that document not only the locations of the imagery sites (the triangles), but also the imagery-derived puff tracks (the lines) for the 23 May 1997 SF$_6$ puff releases on south Vandenberg AFB. On 23 May 1997, the airship releases originated near space launch complex 4 east (SLC-4E) with the puffs moving toward the southeast. The legend identifies each puff as S#P#, where the S# refers to the series while the P# refers to the puff in each series. On 23 May 1997, the first 9 series were numbered 1–9. As indicated in Table 3, the subsequent series were labeled a–k (for 10–20) so that one character could be used to represent each series. For the puffs that were tracked, Figures 5 and 6 document that the puffs moved to the southeast with little variation in direction (i.e., the lines are nearly parallel). During this same period, Figures 7 and 8 document that the imagery-derived puff speed decreased from 16.1 to 11.4 knots (8.3 to 5.9 m/s) while the imagery-derived puff bearings shifted from 141° to 131° (i.e., clockwise from north and the direction of motion). During this same period, Figures 9 and 10 document that the puff altitudes were between 2625 to 3120 ft MSL (800 to 950 m MSL).
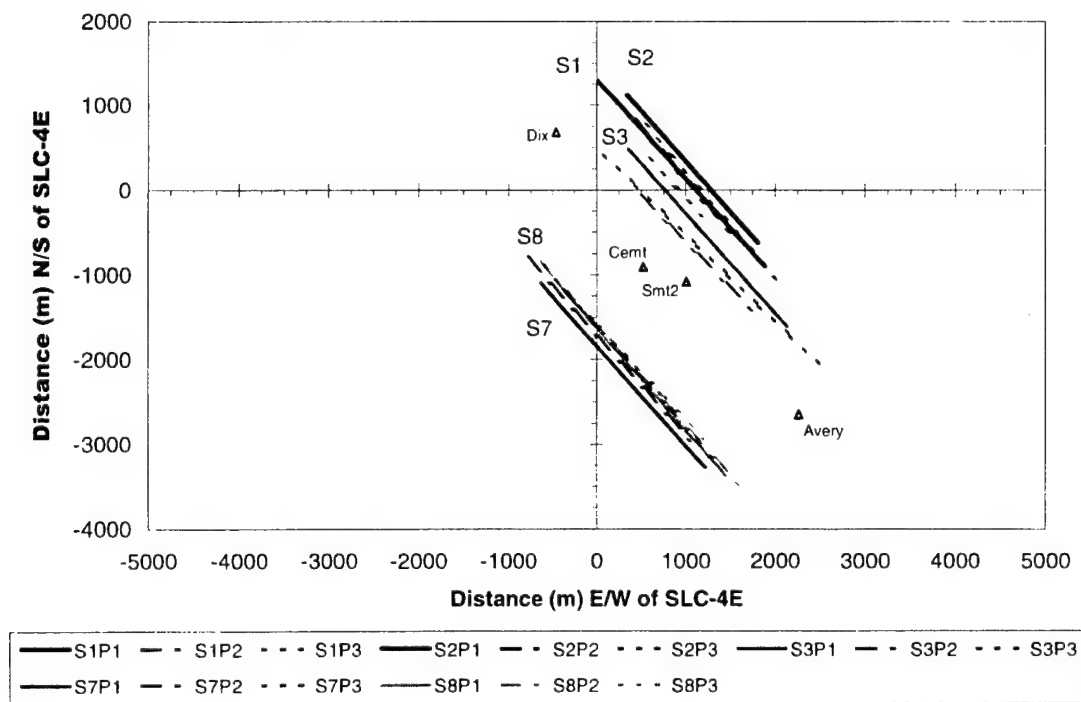
Figure 5. Puff trajectories derived from imagery of the earlier SF$_6$ releases on 23 May 1997.

12
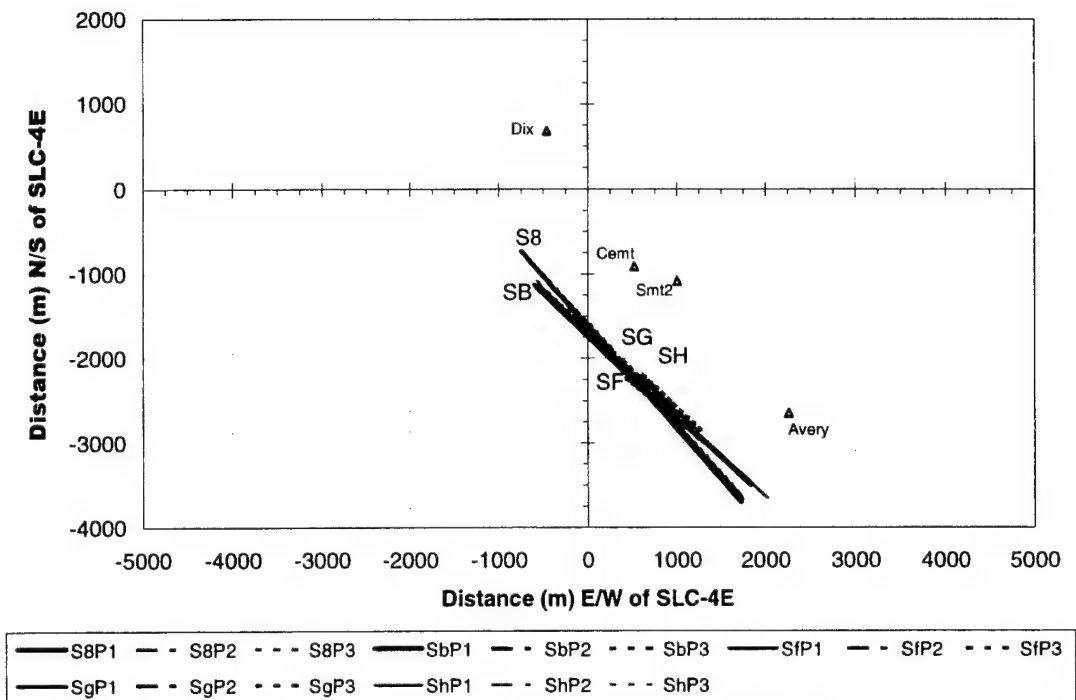
Figure 6. Puff trajectories derived from imagery of the later SF$_6$ releases on 23 May 1997.
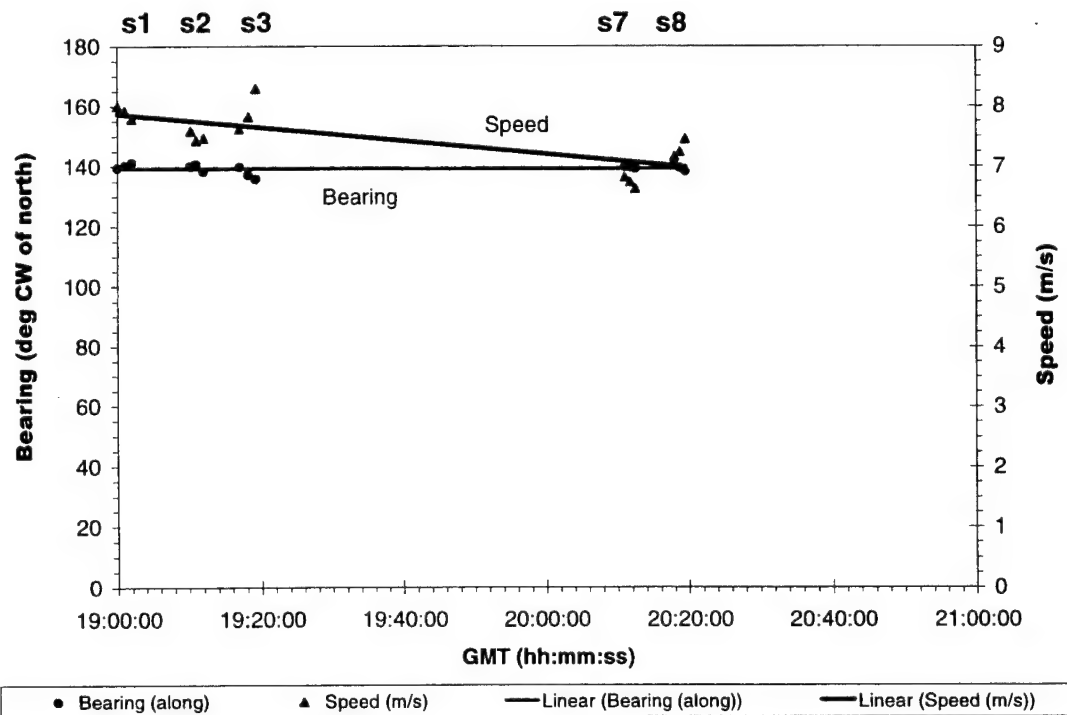
Figure 7. Puff bearing and speed derived from imagery of the earlier SF$_6$ releases on 23 May 1997.

13
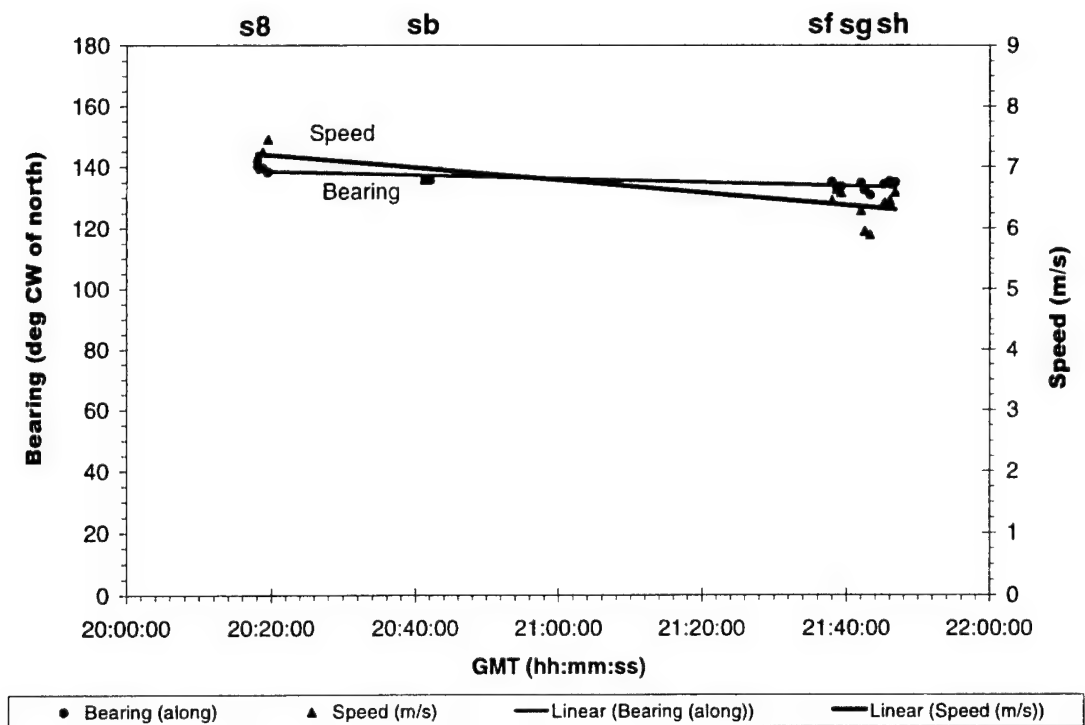
Figure 8. Puff bearing and speed derived from imagery of the later SF$_6$ releases on 23 May 1997.
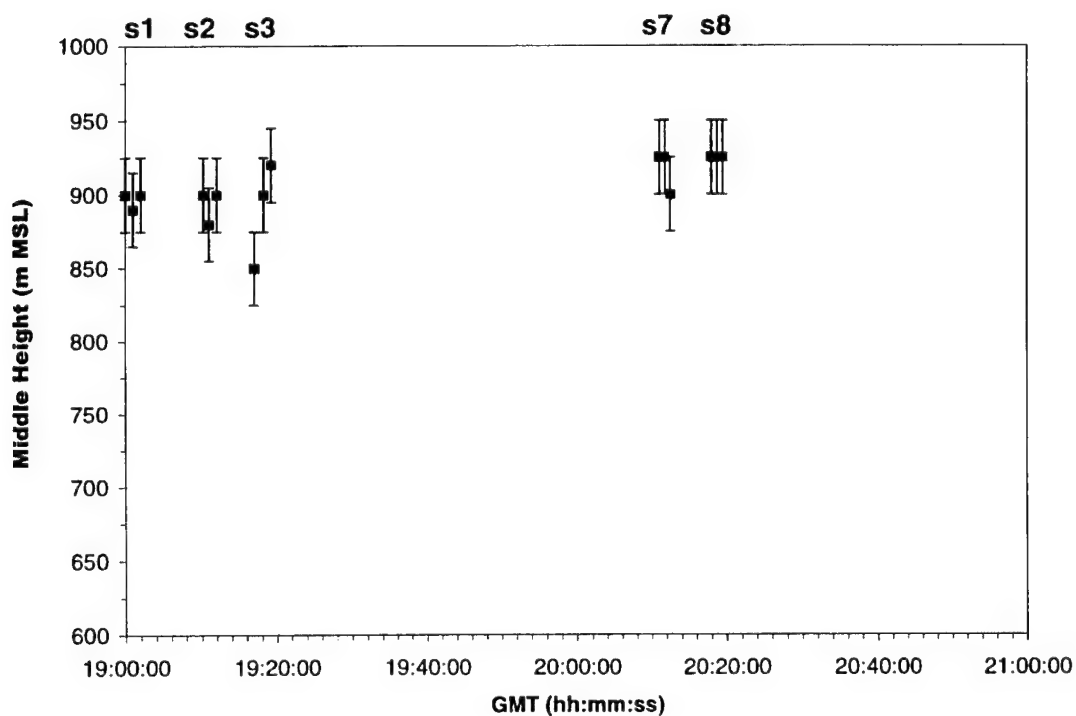
Figure 9. Puff altitude derived from imagery of the earlier SF$_6$ releases on 23 May 1997.

14
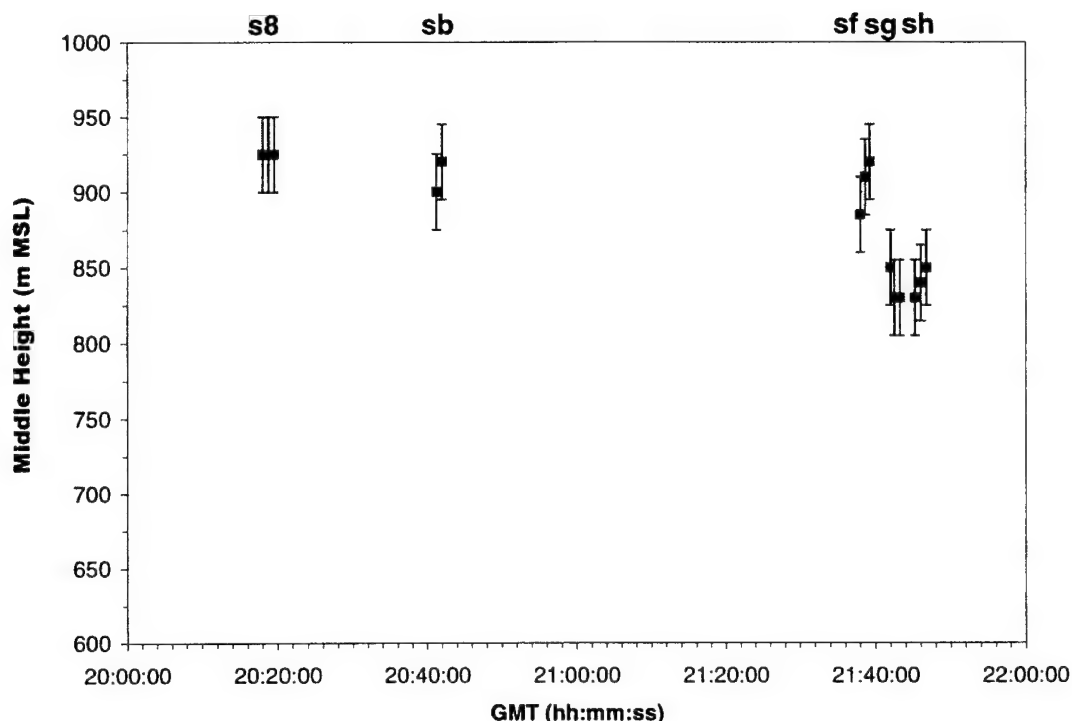
Figure 10. Puff altitude derived from imagery of the later SF_6 releases on 23 May 1997.

The weather conditions were not optimal for tracking the puffs since the sky was cloudy and hazy throughout 23 May 1997. Fog prevented releases close to the coast for much of the day. In spite of these difficulties, we were able to track several of the SF_6 puffs for greater distances than on 21 May 1997. A few puff trajectories extended almost the entire length of the imagery sites on 23 May 1997. However, due to poor release geometry and very cloudy conditions, the later puff tracks on 23 May 1997 were shorter than on 21 May 1997. In addition, it was not always possible to measure true along- or crosswind dispersion since poor visibility combined with releases near the third camera site reduced the number of available perspectives. When available, we also report expansion rates for other axes (i.e., 45° or 135° rather than only for 0°, 180°, or 90°). Appendix D documents lower imagery-derived mass estimates for series B (11), F (15), and G (16). These results suggest that the spotty high-altitude atmospheric clouds interfered with accurate imagery-derived mass measurements. It is interesting to note that the measured expansion rates were not substantially lower for these puffs than for series 1, 2, or 3. The imagery-derived mass estimates were greatest for those early releases that had much better contrast. These results suggest that the expansion rate (i.e., observed extent) is less sensitive to the background than is the imagery-derived mass. This is consistent with the results presented in Appendix C and Appendix D, which document that the imagery-derived extent (at a threshold of 1–5 ppm-m column density) contains the bulk of the SF_6 tracer.

15

3.3   21 May 1997 Results

3.3.1   Infrared Imagery Documenting Puff Shapes for 21 May 1997

Figures 11 through 15 show examples of the IR imagery from 21 May 1997. Each figure contains four images. The four images include various perspectives and various times for a tracer series. It is apparent from review of this imagery that the sky was relatively clear, and the puffs were observed with good contrast against a fairly uniform background. In Figures 11 through 15, the text above each image documents the imagery site, the time after release of the specified puff, and the perspective (i.e., X pixels correspond to alongwind, crosswind, or mixed). The figure caption identifies the puff used as the time reference. An alongwind perspective from the camera site reveals a crosswind dimension (X pixels correspond to crosswind extent) for the observed puff. A crosswind perspective from the camera site reveals an alongwind dimension (X pixels correspond to alongwind extent). Numbers placed within each image identify the three puffs. Puff 1 was the first released in each series and should be the farthest downwind. This is true for all but series 2 where the blimp flew in a figure-8 release pattern.

The following comments should help one interpret the imagery included in Figures 11 through 15. At or shortly after the release, the crosswind perspective from Site 1 (NASA site closest to the release) often documented the alongwind extent of the puff as X (horizontal) pixels. At later times, the alongwind perspective from Site 1 often documented the crosswind extent of the cloud as X (horizontal) pixels.

Review of the imagery contained in Figures 11 through 15 reveals that the crosswind dispersion appeared to be greater than the vertical dispersion, with the exception of puff 1 of series 1. When the crosswind (i.e., X pixel) dispersion is greater than the vertical (i.e., Y pixel) dispersion, the puffs appear as a wide but short shape when viewed at a great distance from the alongwind perspective (from the source, NASA site). It should be noted that the puff's height in Y pixels is not purely vertical diffusion but may include various degrees of alongwind dispersion when viewed from the alongwind perspective. For a viewing elevation of 90°, the Y pixels would correspond only to horizontal dispersion. For a viewing elevation of 0°, the Y pixels would correspond to vertical dispersion. For puff 1 of series 1 (S1P1), Figure 11 reveals that the Y pixels in the alongwind perspective (i.e., lower left image from NASA site) are dominated by the large degree of alongwind dispersion. The large degree of alongwind dispersion for S1P1 is evident as X pixels in the crosswind perspective (i.e., lower right image from SY site 4) in Figure 11.

Review of the imagery contained in Figures 11 through 15 also reveals that the crosswind dispersion appeared to be greater than the alongwind dispersion, with the exception of puff 1 of series one. This is more difficult to substantiate by reviewing the imagery since the crosswind and alongwind puff dimensions are seldom observable within a single image. However, the bottom two images in Figure 12 illustrate wide but short puffs when viewed from the alongwind perspective (NASA site at 8.0 min) at a long distance while simultaneously documenting narrow and tall puffs when viewed from the crosswind perspective (SY Site4 at 8.0 min) from a shorter distance. In the alongwind perspective shown in the bottom left image in Figure 12, the X pixels (width) are crosswind dispersion and the Y pixels (height) are mainly vertical dispersion due to the relatively low viewing angle. In the crosswind perspective shown in the bottom right image in Figure 12, the X pixels (width) are alongwind dispersion and the Y pixels (height) are a mix of crosswind and vertical dispersion due to steep elevation angles.

NASA @ 1.25 min (x ~ alongwind)
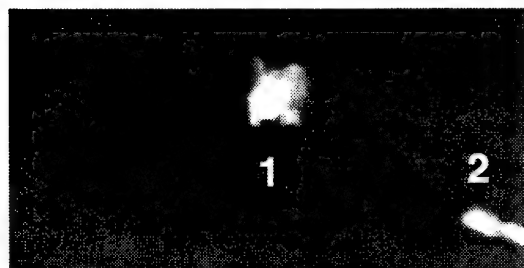
MOTU @ 3.25 min (x ~ crosswind)
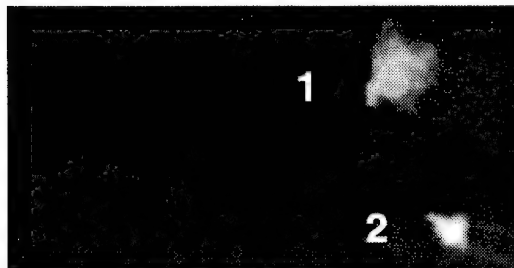
NASA @ 11.50 min (x ~ crosswind)
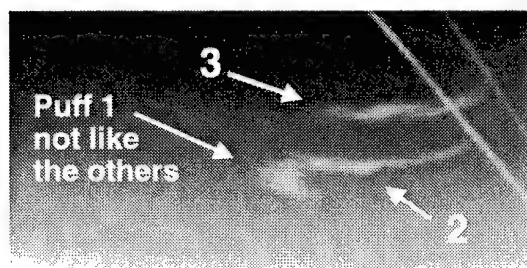
SY Site 4 @ 11.50 min (x ~ alongwind)

Figure 11. 21 May 1997 series 1 puff imagery documenting cross- and alongwind perspectives at various times after the release of series 1 puff 1.

NASA @ 3.25 min (x ~ mixed)
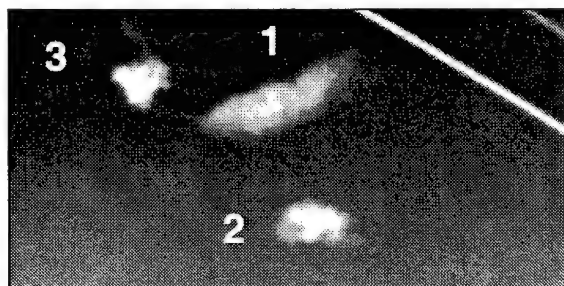
MOTU @ 3.25 min (x ~ crosswind)
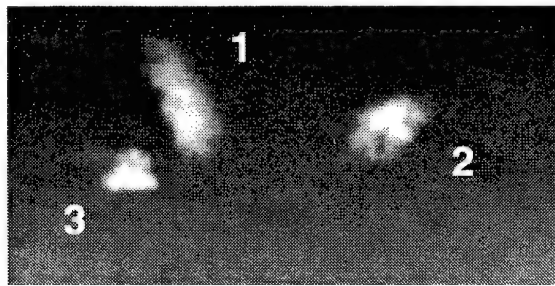
NASA @ 8.00 min (x ~ crosswind)
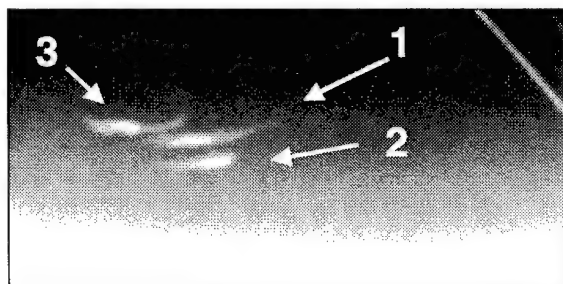
SY Site4 @ 8.00 min (x ~ alongwind)
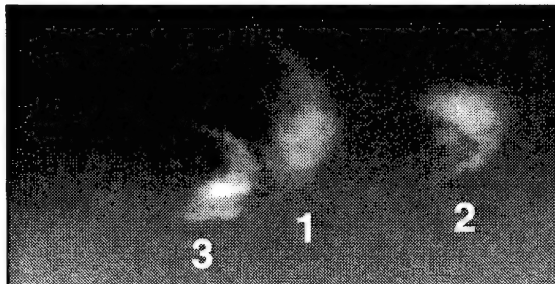
Figure 12. 21 May 1997 series 2 puff imagery documenting cross- and alongwind perspectives at various times after the release of series 2 puff 1.

17

MOTU @ 1.50 min (x ~ alongwind)

NASA @ 5.00 min (x ~ mixed)

SY Site4 @ 5.50 min (x ~ alongwind)

SY Site4 @ 8.00 min (x ~ crosswind)
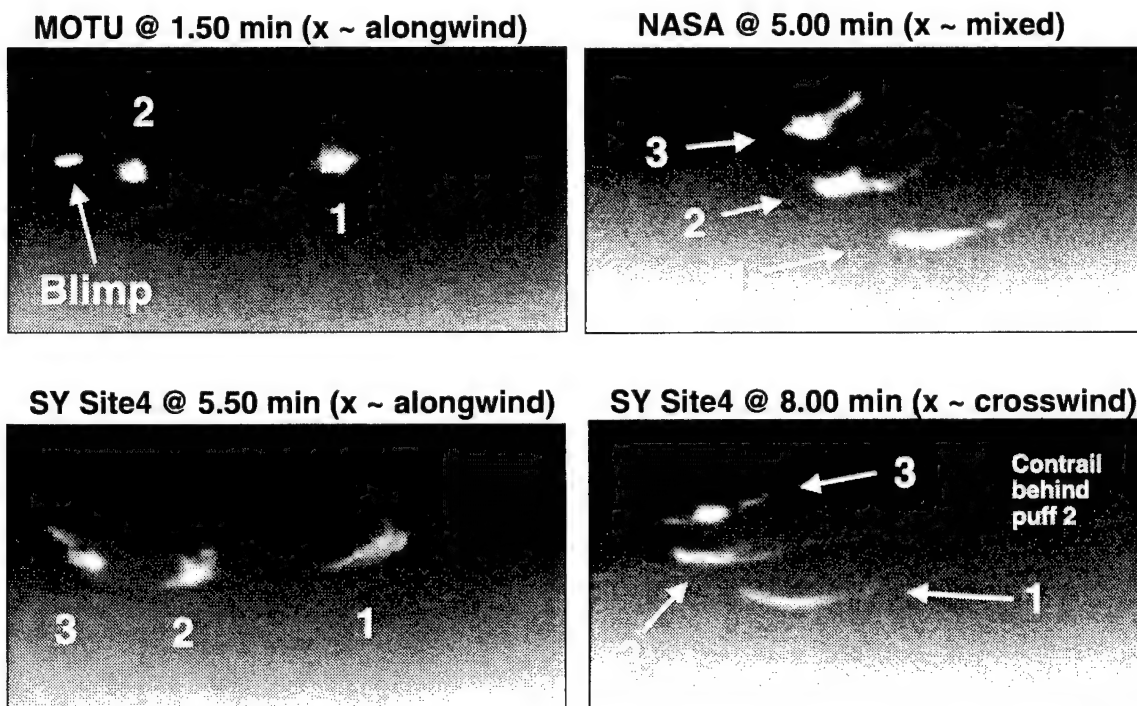
Figure 13.   21 May 1997 series 3 puff imagery documenting cross- and alongwind perspectives at various times after the release of series 3 puff 1.

VHF @ 1.00 min (x ~ alongwind)

MOTU @ 3.25 min (x ~ alongwind)

NASA @ 5.75 min (x ~ mixed)

SY Site4 @ 5.75 min (x ~ alongwind)
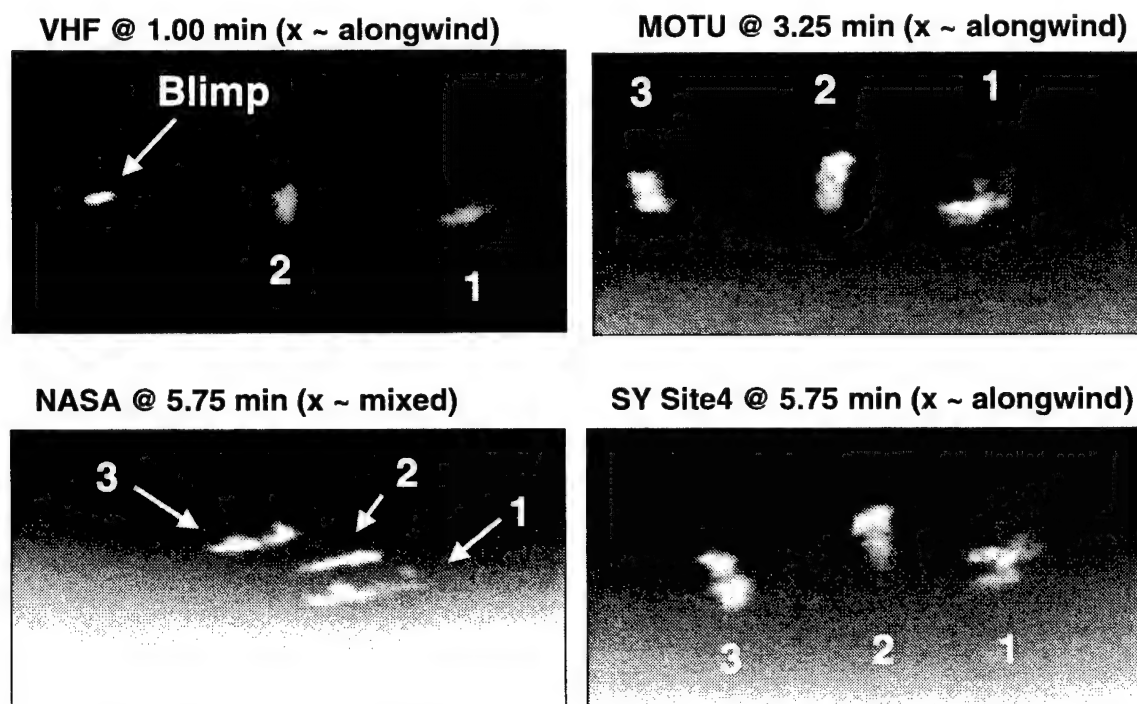
Figure 14.   21 May 1997 series 4 puff imagery documenting cross- and alongwind perspectives at various times after the release of series 4 puff 2.

18

MOTU @ 1.50 min (x ~ alongwind)   **NASA @ 3.00 min (x ~ mixed)**

VHF @ 5.25 min (x ~ mixed)   **SY Site4 @ 5.25 min (x ~ alongwind)**
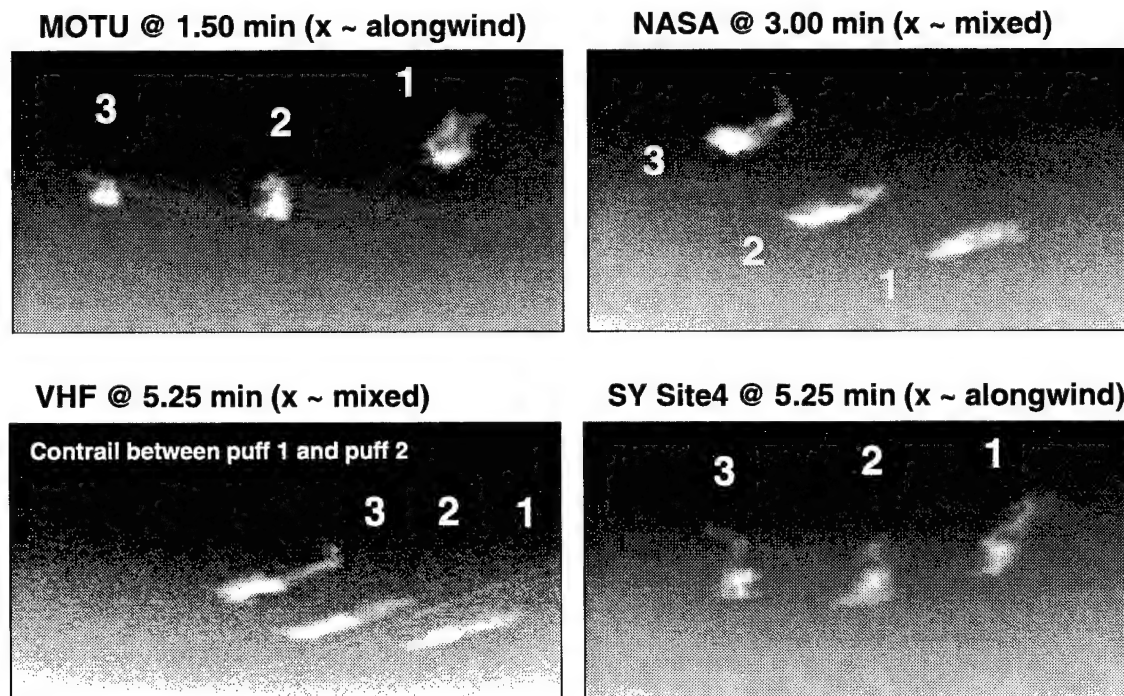
Figure 15.   21 May 1997 series 5 puff imagery documenting cross- and alongwind perspectives at various times after the release of series 5 puff 2.

It is apparent from the above discussion that it is difficult to qualitatively interpret the puff imagery due to the constantly changing perspective. In the next section of this report, the quantitative analysis of the puff imagery documents that the crosswind expansion rate was larger than the alongwind expansion rate for most puffs. Only puff 1 from series 1 had a greater alongwind than crosswind expansion rate on 21 May 1997.

3.3.2   Imagery-Derived Puff Characteristics for 21 May 1997

3.3.2.1   Alongwind and Crosswind Expansion Rates for 21 May 1997

Figure 16 plots the imagery-derived expansion rates (meters growth per meter of travel) as a time series (i.e., release time for each puff) for the 21 May 1997 SF_6 puff releases. These data document a dramatic change in the relative cross- and alongwind expansion rates followed by a slowly varying ratio. For the first puff of the first series (the earliest data points in Figure 16), the alongwind expansion rate was significantly larger than the crosswind expansion rate. This is evident, qualitatively, in the imagery presented in Figure 11. As illustrated by the data in Figure 16, this trend reversed for the next puff and for all subsequent puffs on 21 May 1997. This is evident, qualitatively, in the imagery presented in Figures 11 through 15. For times after 21:15 GMT, the crosswind expansion rate was 3 to 4 times greater than the alongwind expansion rate. These data document the dispersion rates for non-spherical puffs that started out with dimensions of 160 to 490 ft(50 to 150 m) and grew to 490 to 1640 ft (150 to 500 m) over the 5–10 min (1200–3000 m) of tracking. The imagery-derived expansion rates include the full extent of the puff (to a threshold of 1–3 ppm-m column density) that contains the bulk of the SF_6 tracer.
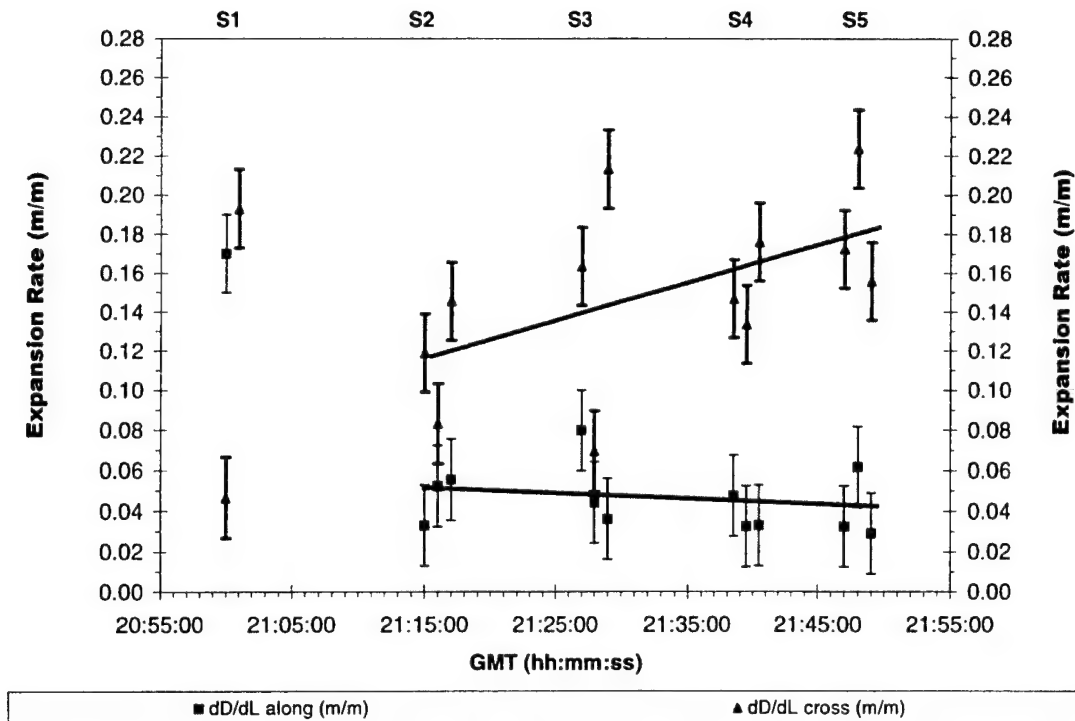
Figure 16. Puff expansion rates (m/m) derived from imagery of 21 May 1997 SF_6 releases.

As illustrated by the imagery presented in Figures 11 through 15, the puffs were released with various aspect ratios and orientations relative to the wind direction. The processed imagery data suggest that the expansion rates were relatively independent of the initial aspect ratio and geometry. The data plotted in Figure 16 suggest a slowly increasing ratio of crosswind to alongwind expansion rates for times after 21:15 GMT. During this same period, the imagery-derived data in Figure 3 document a slow shift in puff bearing and a small increase in puff speed. Figure 4 documents that imagery-derived altitude of the puffs ranged between 2460 to 2820 ft (750 to 860 m) above mean sea level (MSL). In summary, the increasing expansion rates do not appear to correlate with any large changes in release height, puff speed, puff bearing, or release location.

Figure 17 documents the angles (i.e., tilt angle in Appendix A) used to define the along- and crosswind dimensions referenced in Figure 16 (i.e., expansion rates in m/m) and in Figure 18 (i.e., expansion rates in m/min). Due to the variation in release geometry and the fixed camera positions, the available imagery did not always include purely along- and crosswind perspectives. When there was not enough data at the desired perspective, the analyst chose a tilt angle close to the desired perspective or opened the window of acceptance about the tilt angle to include values on both sides of the desired value. Often the analyst had to tune both the tilt angle and the width of the acceptance window about the chosen tilt angle in order to obtain enough data to reveal a trend.

Figure 17 documents the tilt angle as a data point and the acceptance window about that tilt angle as the error bars for the data point. As indicated in Figure 17 and in Appendix A, a tilt angle of 0° or 180° corresponds to a true alongwind dimension while a tilt angle of 90° corresponds to a true crosswind dimension. As illustrated in Appendix A, the tilt angle ranges from 0° to 180° as the left
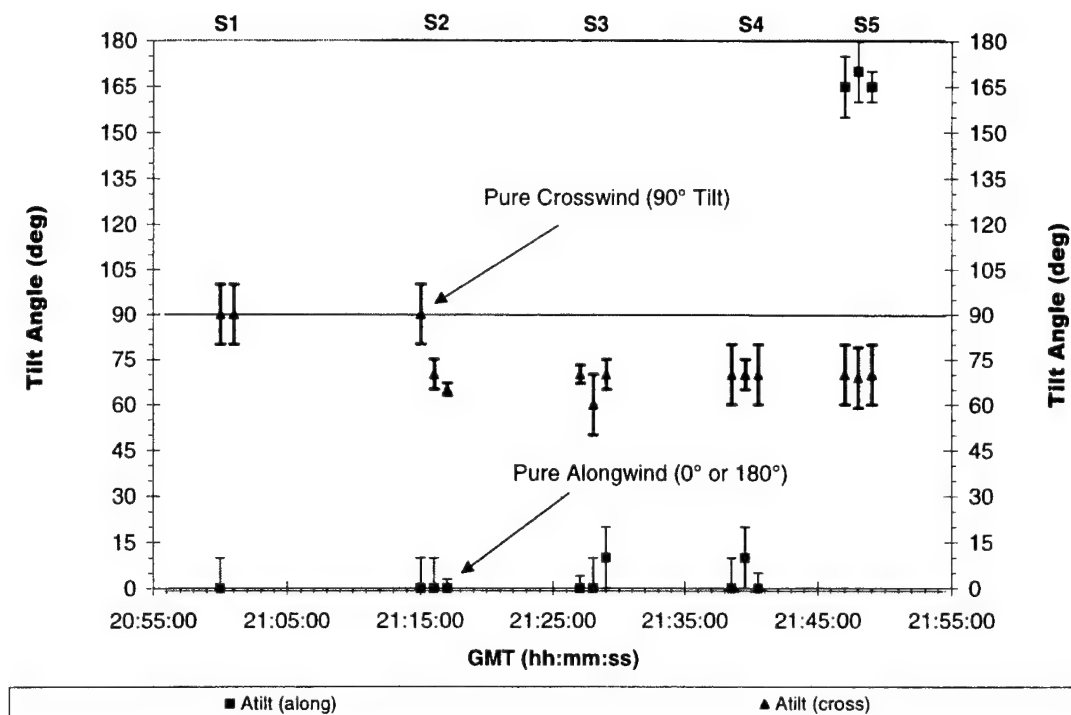
Figure 17. Tilt angles for alongwind and crosswind data on 21 May 1997.
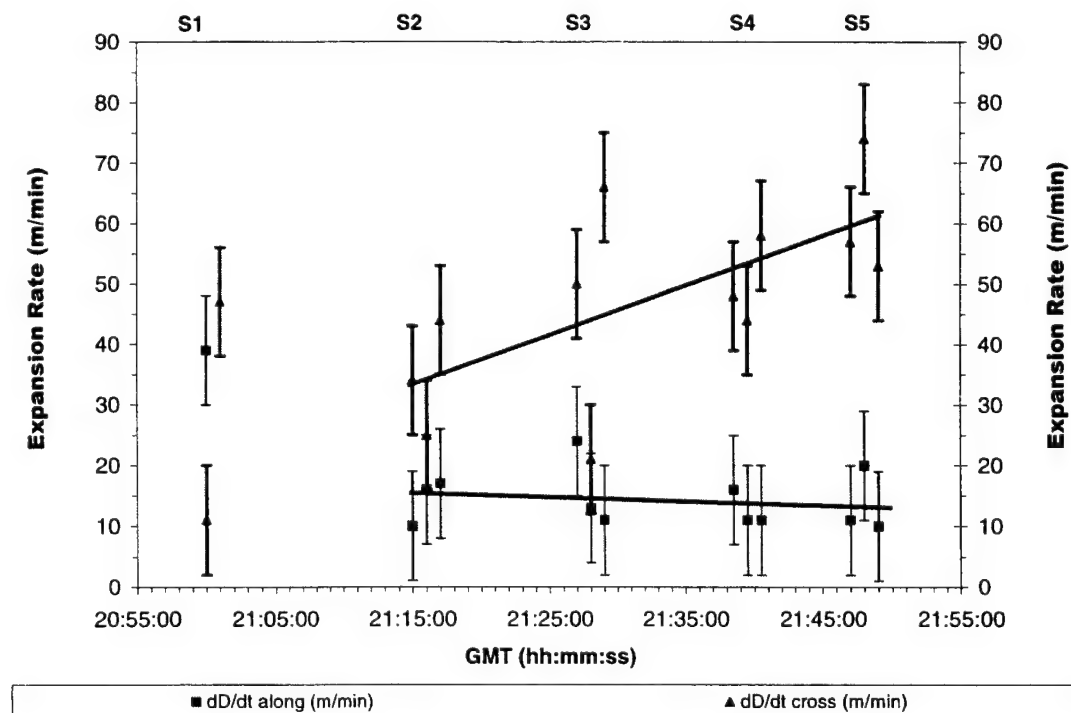
Figure 18. Puff expansion rates (m/min) derived from imagery of 21 May 1997 SF$_6$ releases.

21

end (i.e., as seen from the source) of the puff's diameter rotates from aligned with the wind and closest to the source to aligned with the wind and farthest from the source. A tilt angle of 90° corresponds to the puff's diameter being normal (i.e., crosswind) to the wind (i.e., puff trajectory). Appendix A illustrated that the tilt angle is not aligned with any particular axis of the puff but merely documents the orientation of the reported dimension (determined by the camera's perspective rather than the puff's orientation). In Figure 17, a narrow angle of acceptance (i.e., small error bars) about the tilt angle indicates that the expansion rate was measured from almost identical perspective for the data included in the fit. In contrast, a large window of acceptance (i.e., large error bar) indicates that it was necessary to combine data of similar but varying perspectives in order have enough data for a linear regressive fit. There is more uncertainty in the reported expansion rate when it was necessary to widen the window about the tilt angle. Likewise, the reported expansion rates may vary from the true along- or crosswind values as the tilt angle wanders from the pure along- or crosswind perspective even with a small window of acceptance.

The data in Figure 17 document that Figures 16 and 18 include tilt angles within 25° of true along- or crosswind perspectives with angular windows about the tilt angle of less than 10°. Therefore, the plotted expansion rates should be very close to the values for pure along- and crosswind axes.

Table 4 provides a data summary for each puff on 21 May 1997. The first column provides the variable name, while the other columns provide the value of that variable for each puff of each series. Most of the data presented in this table have been plotted in one or more figures included in this report.

Several times are provided in Table 4. The Greenwich Mean Time (GMT) for the release of each puff (t(0)S#P#) is related to the GMT for the release of the first puff of the day (t(0)S1P1) by reporting the time difference in decimal minutes between these two times (dt(0)S#P#-S1P1). For May 1997, there was a 7-h offset between local time (PDT) and GMT. Another time (dtSOURCE(min)) is the time elapsed in minutes between the first image of the start of the release of a puff and the first measurement of the full extent of that puff (i.e., the source size and position). Since the imagery was collected at 15-s increments, the first dimension (i.e., the source size and position) was typically measured a quarter of a minute after the first sign of the start of release. The length of time in minutes that the puff was tracked is reported by the variable dtEND(min).

Table 4. Imagery-Derived Puff Data for 21 May 1997

Series#Puff#	S1P1	S1P2	S1P3	S2P1	S2P2	S2P3	S3P1	S3P2	S3P3	S4P1	S4P2	S4P3	S5P1	S5P2	S5P3
t(0)S1P1	21:00:00	21:00:00	21:00:00	21:00:00	21:00:00	21:00:00	21:00:00	21:00:00	21:00:00	21:00:00	21:00:00	21:00:00	21:00:00	21:00:00	21:00:00
t(0)S#P#	21:00:00	21:01:00	21:02:00	21:15:00	21:16:00	21:17:00	21:27:00	21:28:00	21:29:00	21:38:30	21:39:30	21:40:30	21:47:00	21:48:00	21:49:00
dt(0)S#P#-S1P1	0.00	1.00	2.00	15.00	16.00	17.00	27.00	28.00	29.00	38.50	39.50	40.50	47.00	48.00	49.00
dtSOURCE (min)	0.25	0.25	#N/A	0.25	0.25	0.25	0.25	0.50	0.50	0.25	0.25	0.25	0.00	0.00	0.00
dtEND (min)	13.00	10.00	#N/A	10.00	9.00	7.00	8.00	5.00	8.50	6.50	7.00	6.25	7.00	6.00	7.00
Xsource (m)	-467	-438	#N/A	156	545	527	659	637	645	590	644	708	601	696	665
Ysource (m)	254	346	#N/A	295	-57	43	182	243	231	175	199	224	227	320	312
Zsource (m MSL)	816	785	#N/A	812	834	818	800	805	817	795	790	779	790	776	784
dH/dt (m/min)	-1	0	#N/A	3	5	0	0	0	0	0	0	0	0	0	0
Slope (dY/dX)	-1.2549	-1.6649	#N/A	-1.3544	-1.345	-1.2966	-1.0649	-0.9335	-1.1646	-1.1968	-1.2662	-1.1585	-1.1001	-1.0316	-1.0276
Bearing (along)	141	149	#N/A	144	143	142	137	133	139	140	142	139	138	136	136
Bearing (cross)	51	59	#N/A	54	53	52	47	43	49	50	52	49	48	46	46
Speed (m/s)	3.9	4.0	#N/A	4.8	5.0	5.0	5.1	5.0	5.2	5.5	5.6	5.5	5.5	5.5	5.7
dD/dt cross (m/min)	11	47	#N/A	34	25	44	50	21	66	48	44	58	57	74	53
dD/dt along (m/min)	39	#N/A	#N/A	10	16	17	24	13	11	16	11	11	11	20	10
error dD/dt	5	5	#N/A	6	6	6	6	6	6	7	7	7	7	7	7
dD/dL cross (m/m)	0.05	0.19	#N/A	0.12	0.08	0.15	0.16	0.07	0.21	0.15	0.13	0.18	0.17	0.22	0.16
dD/dL along (m/m)	0.17	#N/A	#N/A	0.03	0.05	0.06	0.08	0.04	0.04	0.05	0.03	0.03	0.03	0.06	0.03
error dD/dL	0.02	0.02	0.02	0.02	0.02	0.02	0.02	0.02	0.02	0.02	0.02	0.02	0.02	0.02	0.02
Atilt (cross)	90	90	#N/A	90	70	65	70	60	70	70	70	70	70	69	70
dAtilt (cross)	10	10	#N/A	10	5	2	3	10	5	10	5	10	10	10	10
Atilt (along)	0	#N/A	#N/A	0	0	0	0	0	10	0	10	0	165	170	165
dAtilt (along)	10	#N/A	#N/A	10	10	3	4	10	10	10	10	5	10	10	5

The earliest imagery-derived position for each puff is the "source" of the release and is reported in Table 4 as Xsource (m), Ysource (m), and Zsource (m MSL). The imagery-derived position is the "middle" of the puff derived from PLMTRACK analysis. Xsource and Ysource are relative to the position of the first camera site (near the NASA radar dome) for the 21 May 1997 data. Ysource is relative to mean sea level (MSL). Typically, the "best positioned" camera sites provided a direct measure of the source position. However, the analyst sometimes derived the source position using fits to observed trends (i.e., height vs time and Cartesian plots). In Table 4, the change in altitude with time is reported as dH/dt (m/min) and was zero or negligibly small. Appendix B documented that PLMTRACK's positional accuracy (100 m horizontal and 30 m vertical) is comparable to regular GPS (100 m horizontal and 250 m vertical) accuracy.

Based upon PLMTRACK's accuracy, the imagery documented no significant altitude change for any of the puffs after their release. This is consistent with the immediate vaporization of the liquid SF_6 and rapid equilibration (i.e., both in temperature and in density) with the ambient air.

Table 4 also documents the horizontal movement of each puff at elevation. Each puff's trajectory is reported as a "Slope (dX/dY)" for the Cartesian plot and a bearing in degrees clockwise from north. The "Bearing (along)" provides the alongwind bearing (the direction toward which the puff was moving) while the "Bearing (cross)" provides the crosswind bearing (the perpendicular to the puff bearing). The "Speed (m/s)" is the slope of a plot of the puff's horizontal range from the source versus time.

Table 4 uses the dD/dt and dD/dL to denote expansion rates derived by plotting the puff's dimension (along- or crosswind diameter measured to a threshold of 1–3 ppm-m) against either time (t) or horizontal distance (L) from the source. On 23 May 1997, the threshold was slightly higher (2–5 ppm-m) because of the cloudy conditions. Approximate error bars were assigned as ±0.02 m/m and converted to the m/min value using the puff's speed. The tilt angle (Atilt) relates the reported puff dimension (i.e., axis) to the alongwind direction. As illustrated in Appendix A, Atilt values of 0° or 180° correspond to alignment with the wind bearing, while a value of 90° indicates the perpendicular to the wind bearing. Appendix A also illustrated that the tilt angle is not aligned with any particular axis of the puff but merely documents the orientation of the reported dimension (determined by the camera's perspective rather than the puff's orientation). The dAtilt variable is the angular window of acceptance for the tilt angle (i.e., Atilt ±dAtilt). Small values of dAtilt indicate greater similarity in perspective for the fitted data. In contrast, larger values of dAtilt suggest greater variability in perspective for the data included in the fit. As discussed earlier, the analyst adjusted the values of Atilt and dAtilt as needed to obtain enough data near the desired along- or crosswind perspective to warrant a linear regressive fit. The #N/A entries in the table indicate that a number was not available. S1P3 was not tracked because the series 1 puffs were released too close to the imagery sites; only two of the three puffs fit in the FOV for all of the camera sites.

3.3.2.2 Examples of Trends Revealed by Detailed Analyses

Appendices E, F, and G provide detailed data plots for 21 May 1997 puffs S1P1, S1P2, and S2P1, respectively. These plots provide examples of the type and quality of the data available from our analysis of the imagery. These appendices illustrate the sensitivity of the measured expansion rates to the various analysis schemes and to the experimental variables. The results document that the

expansion rate (imagery-derived cloud extent) is not sensitive to the number of pixels occupied by the puff above a threshold value of 8–10 pixels. The appendices also show that the imagery can document complex angular trends for the expansion of the puff along various axes (i.e., tilt angles). Likewise, the plots document that the expansion rate for a specific tilt angle can be quite sensitive to the angular window about that tilt angle. This is consistent with expansion rates that vary with tilt angle (i.e., the axes of the dimension relative to the puff's bearing).

Appendices E, F, and G also document why we do not report the PLMTRACK-derived extent of the puff. Since the PLMTRACK vertices are the closest approach of rays projected from two perspectives, slight angular errors can lead to under- or over-estimates of the extent of the puff. These errors would not be significant for a large launch cloud, but can be significant for the smaller tracer puffs (i.e., at early times). We also do not report the expansion rate derived from separate tracking of the ends of the puff. The plots in the appendices illustrate that it is difficult for the analyst to identify the alongwind or crosswind ends of the puffs. This is due to two facts: (1) there is a constantly changing perspective as the puff moves across the sky, and (2) the longest axis of the puff does not necessarily align with the wind. Finally, the PLMTRACK horizontal accuracy (100 m based upon Appendix B) is comparable to the initial size of the puff.

Appendices E, F, and G document the method that was used to measure the expansion rates reported in Table 4. The results presented in Table 4 are from the "best" method of analysis. Instead of using the extent triangulated from the PLMTRACK analysis, we get a more accurate puff extent by interpreting the angular information from each image with the "best" value for the puff's position. The "best" value is derived from regressive fits to combined data derived from multiple perspectives as well as from various analysis schemes. Appendices E, F, and G include the various plots used to determine the "best" value for the puff's position as well as other plots used to illustrate the points discussed in this section of the report and in the appendices.

3.3.2.3   Puff Dimension Plots for 21 May 1997

Appendix H includes horizontal puff dimension plots for all available data for each puff as well as for selected tilt angles for each puff. The "all tilt angle" plot provides an indication of the amount of available data as well as the angular dependence of the data; in some instances, the imagery-provided data from only one narrow perspective. In other cases, the imagery-derived puff dimensions ramped between the extremes defined by the alongwind and crosswind perspectives. Remember that an alongwind perspective from the camera site reveals the crosswind extent of the puff, while a crosswind perspective is needed to see the alongwind puff extent. Appendix H provides the plots used to determine the along- and crosswind expansion rates reported in Table 4. The plot headings provide the values of the experimental variables used to filter the data. These plots provide the modeler with some indication of the quality and quantity of the horizontal dimension data.

We provide no plots for the vertical puff dimensions since it was impossible to obtain a true horizontal perspective (i.e., camera at same altitude as the puff) that could reveal the true vertical puff extent. The imagery-derived estimates ranged from 50 to 180 m for the vertical puff extent. Plots of apparent vertical dimension against time and distance typically included badly scattered points and revealed no consistent trends. Due to the oblong puff shapes (5-s releases) and inclined camera angles (~20° EL), we could not eliminate a contribution from the horizontal puff dimension to the

observed Y pixel dimension. This difficulty was discussed earlier when referring to the images included in this report.

3.3.2.4 Relative Motion of Puffs within Each Series for 21 May 1997

Figure 19 documents the dispersion affecting a slightly larger scale by tracking the relative distance between puffs within each series of releases. In Figure 19, the distance between puffs is plotted against time, and the rate of change (in meters per minute) is next to each dataset. The distances between puffs ranged from 660 to 2300 ft (200 to 700 m). The data in Figure 19 document that the relative motion between puffs was less than 33 ft/min (10 m/min) for the 21 May 1997 releases. The individual puff data in Figure 18 documented that the alongwind expansion rates were less than 66 ft/min (20 m/min), while the crosswind expansion rates ranged from 80 to 250 ft/min (25 to 75 m/min) after 21:15 GMT.

The data in Figure 20 document the angular information for the pairs of puffs relative to the imagery-derived crosswind (225 ° to 235 °) and alongwind (135 ° to 145 °) bearings. The data in Figure 20 document that the puffs were separated mainly in the alongwind direction. This is qualitatively consistent with the 1 to 2 min differences in their release times (each puff moved downwind until the next puff was released). Series 2 was the exception because of the figure-8 release pattern that scattered the puffs randomly in space. Review of the data presented in Figures 19 and 20 reveals that the relative dispersion between puffs appears to be random (±33 ft/min or ±10 m/min). These data also document that the relative puff dispersion rates were low in magnitude (less than 66 ft/min or 20 m/min), similar to the alongwind dispersion rates measured for the individual puffs.
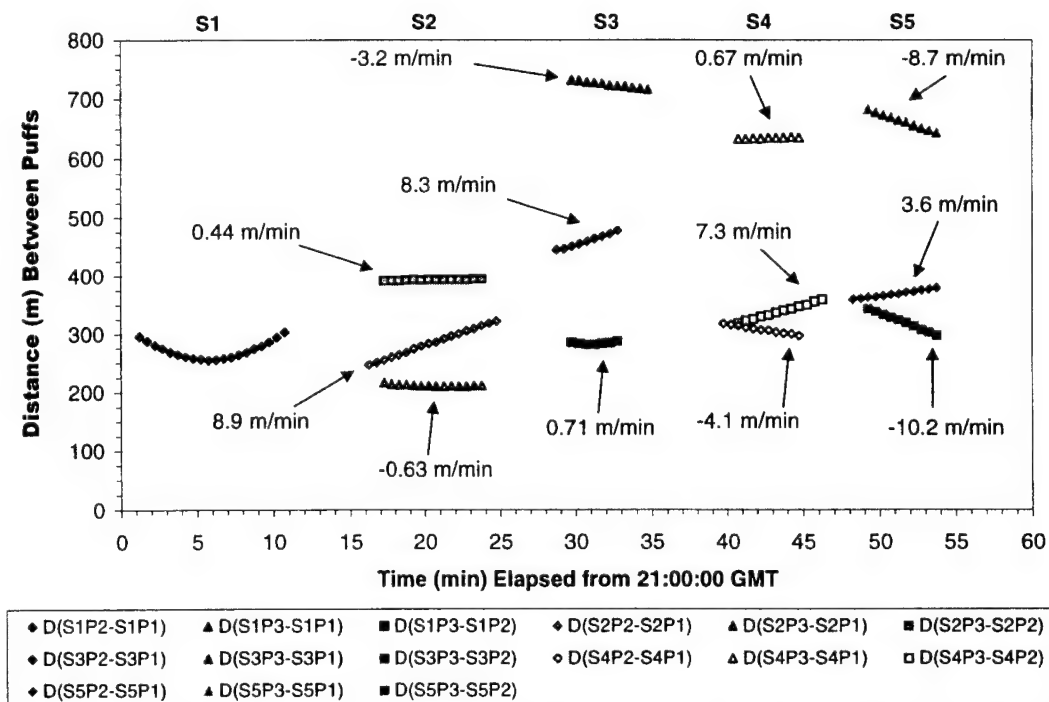
Figure 19. Relative puff spacing derived from imagery of 21 May 1997 SF$_6$ releases.

25
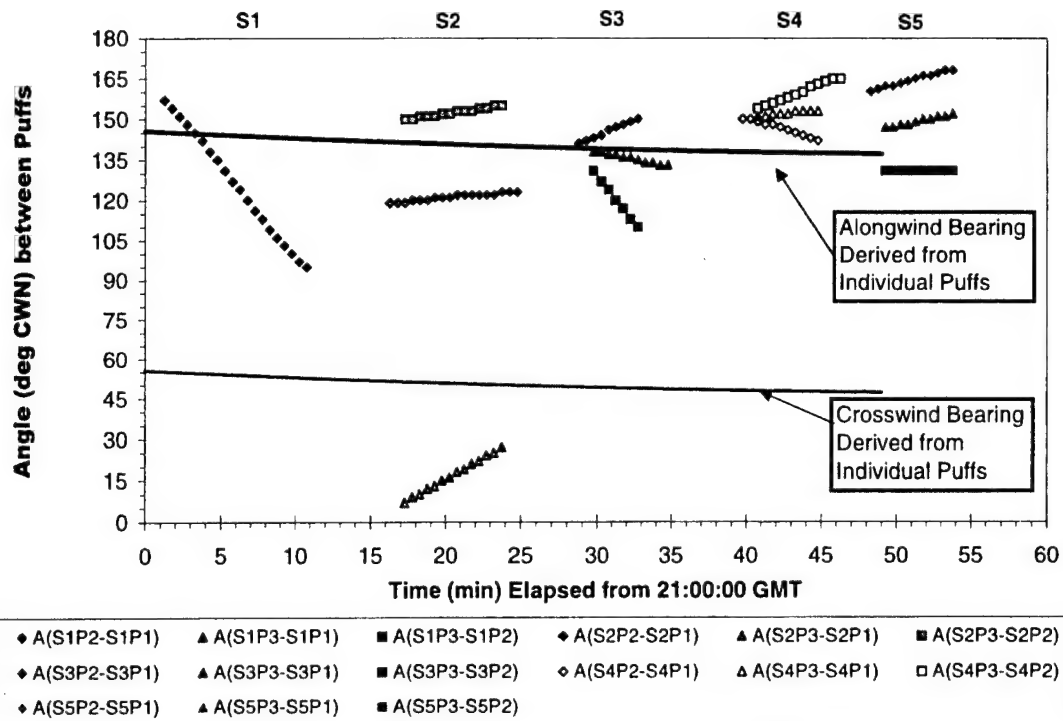
Figure 20. Angles between puffs derived from imagery of 21 May 1997 SF$_6$ releases.

3.4   23 May 1997 Results

3.4.1   Infrared Imagery Documenting Puff Shapes for 23 May 1997

Figures 21 through 29 show examples of the imagery from 23 May 1997. Each figure contains four images. The four images include various perspectives and various times for a tracer series. It is apparent from review of this imagery that the sky was relatively cloudy or hazy on 23 May 1997. Many puffs were observed with good contrast against a background that ranged from fair (uniform haze) to poor (broken clouds). In Figures 21 through 29, the text above each image documents the imagery site, the time after release of the specified puff, and the perspective (i.e., X pixels correspond to alongwind, crosswind, or mixed). The figure caption identifies the puff used as the time reference. An alongwind perspective from the camera site reveals a crosswind dimension (X pixels correspond to crosswind extent) for the observed puff. A crosswind perspective from the camera site reveals an alongwind dimension (X pixels correspond to alongwind extent). Numbers placed within each image identify the three puffs. Puff 1 was the first released in each series and, therefore, was the farthest downwind.

The following comments should help one interpret the imagery documented in Figures 21 through 29. At or shortly after the release, the crosswind perspective from the site (Dix or Cemt) closest to the release often documented the alongwind extent of the cloud as X (horizontal) pixels. At later times, the alongwind perspective from DIX or Cemt sites often documented the crosswind extent of the cloud as X (horizontal) pixels.

26

DIX @ 2.25 min (x ~ mixed)
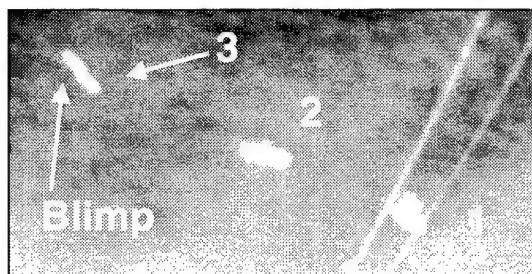
DIX @ 6.75 min (x ~ mixed)
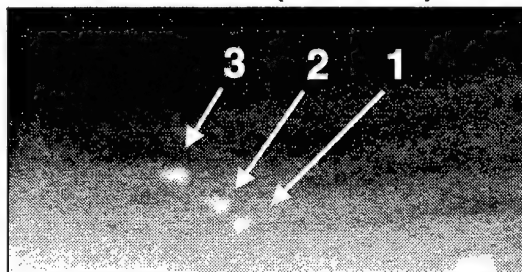
SMT2 @ 5.50 min (x ~ alongwind)
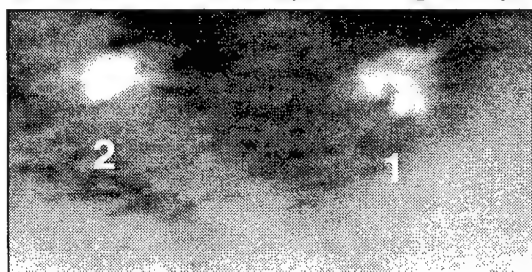
SMT2 @ 7.75 min (x ~ mixed)
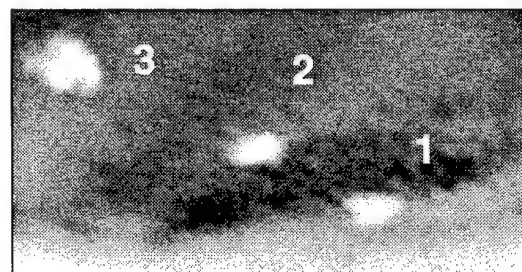
Figure 21.   23 May 1997 series 1 puff imagery documenting cross- and alongwind perspectives at various times after the release of series 1 puff 1.

CEMT @ 1.50 min (x ~ mixed)
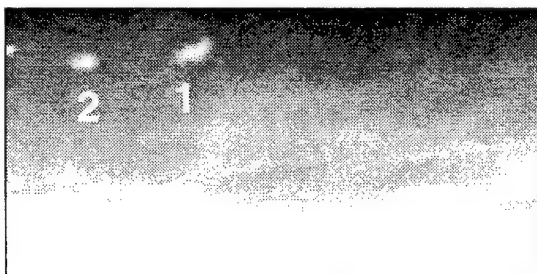
SMT2 @ 2.50 min (x ~ mixed)
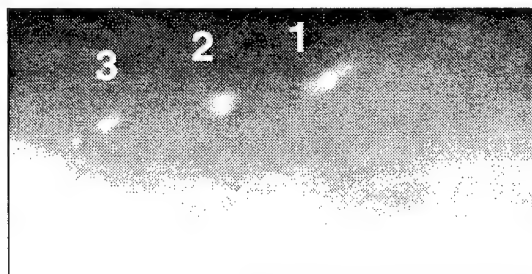
SMT2 @ 3.50 min (x ~ mixed)
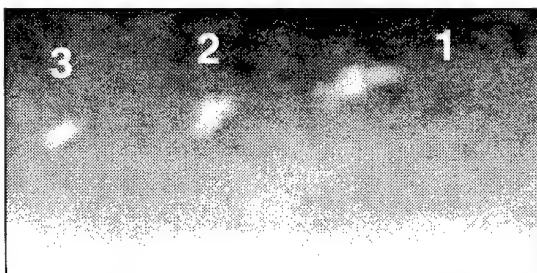
CEMT @ 4.25 min (x ~ alongwind)
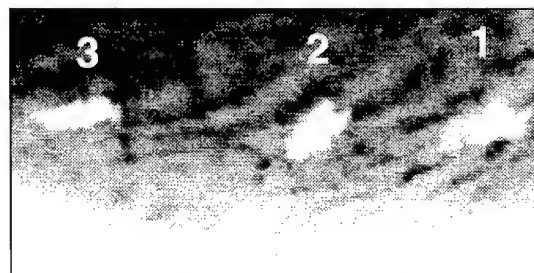
Figure 22.   23 May 1997 series 2 puff imagery documenting cross- and alongwind perspectives at various times after the release of series 2 puff 1.

27

DIX @ 0.75 min (x ~ mixed)
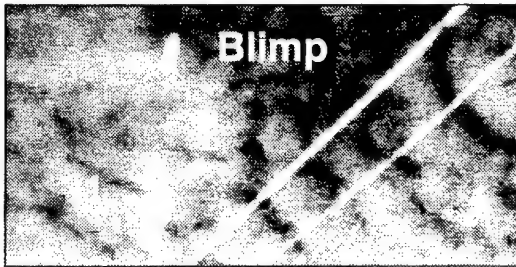
DIX @ 4.00 min (x ~ crosswind)

CEMT @ 5.25 min (x ~ mixed)

SMT2 @ 7.50 min (x ~ crosswind)
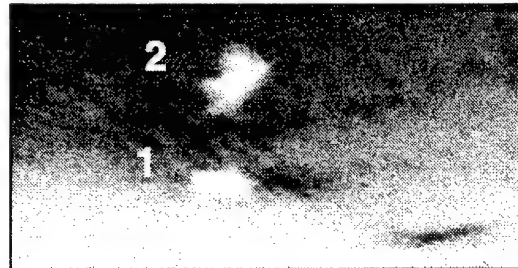
Figure 23.   23 May 1997 series 3 puff imagery documenting cross- and alongwind perspectives at various times after the release of series 3 puff 1.

DIX @ 2.00 min (x ~ crosswind)
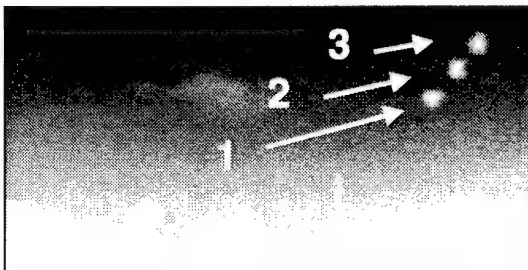
SMT2 @ 2.00 min (x ~ alongwind)
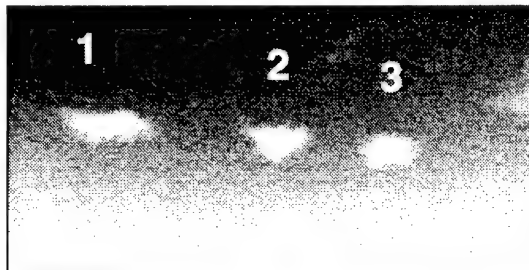
DIX @ 3.00 min (x ~ crosswind)
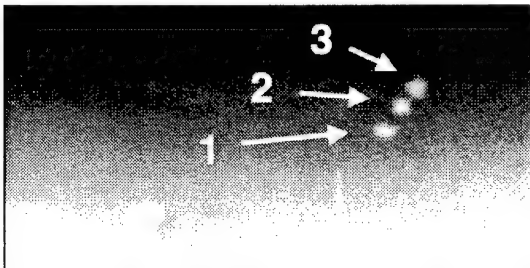
CEMT @ 5.50 min (x ~ crosswind)
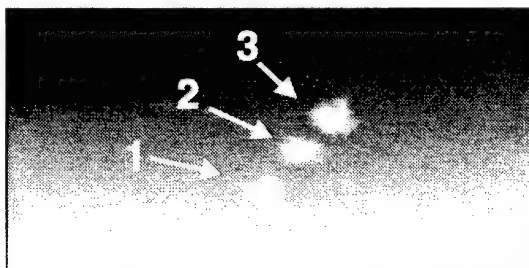
Figure 24.   24 May 1997 series 7 puff imagery documenting cross- and alongwind perspectives at various times after the release of series 7 puff 3.

28
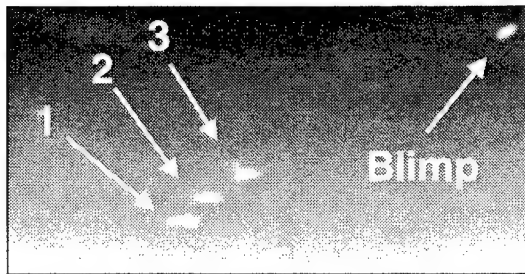
DIX @ 2.50 min (x ~ mixed)

SMT2 @ 2.50 min (x ~ alongwind)
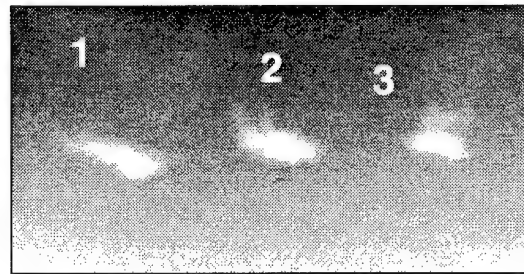
CEMT @ 5.25 min (x ~ mixed)
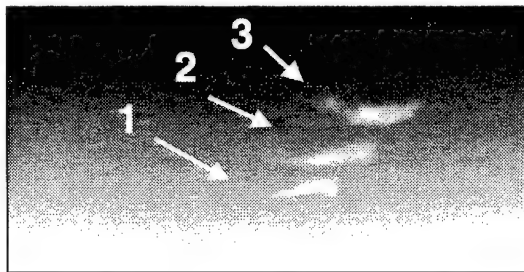
CEMT @ 7.00 min (x ~ crosswind)
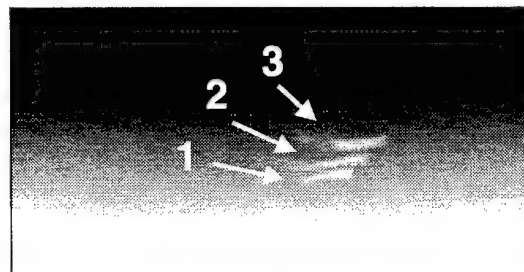
Figure 25.   23 May 1997 series 8 puff imagery documenting cross- and alongwind perspectives at various times after the release of series 8 puff 3.

DIX @ 1.25 min (x ~ mixed)
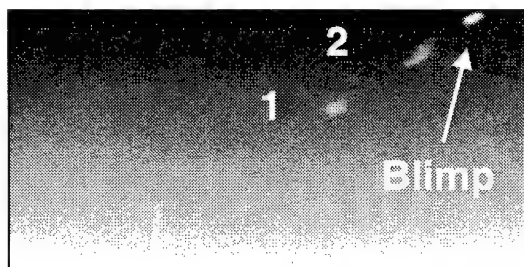
DIX @ 3.75 min (x ~ mixed)
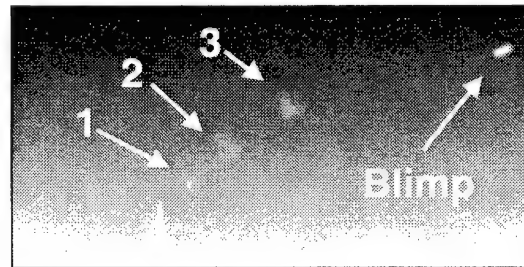
CEMT @ 1.00 min (x ~ alongwind)

SMT2 @ 2.75 min (x ~ alongwind)
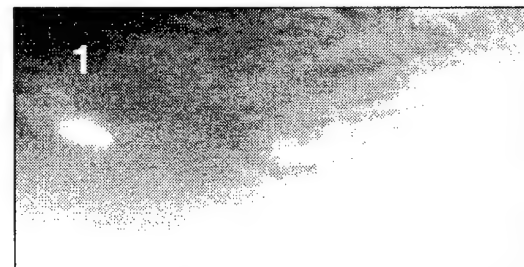
Figure 26.   23 May 1997 series B (11) puff imagery documenting cross- and alongwind perspectives at various times after the release of series B puff 1.

29

SMT2 @ 0.58 min (x ~ alongwind)
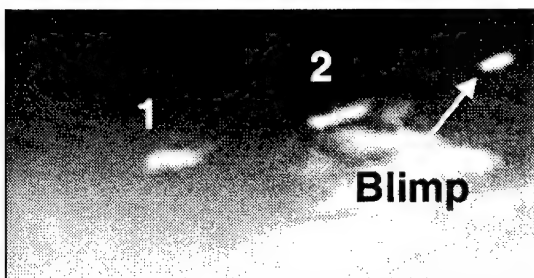
SMT2 @ 1.58 min (x ~ alongwind)
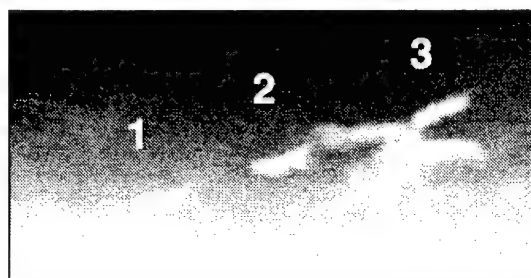
CEMT @ 2.83 min (x ~ mixed)
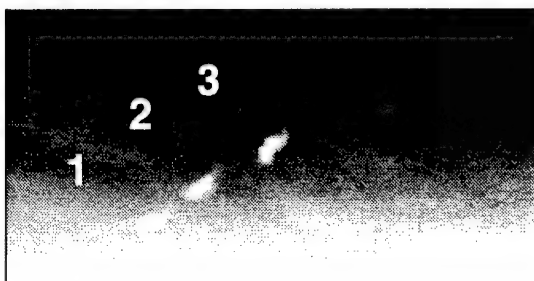
CEMT @ 4.58 min (x ~ mixed)
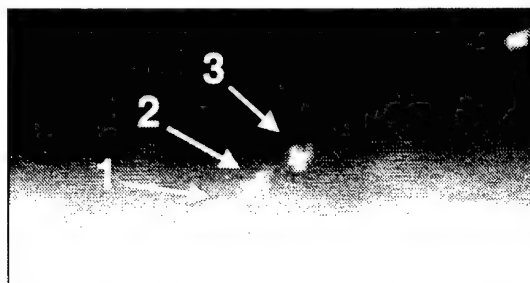
Figure 27.   23 May 1997 series F (15) puff imagery documenting cross- and alongwind perspectives at various times after the release of series F puff 2.

SMT2 @ 1.00 min (x ~ alongwind)
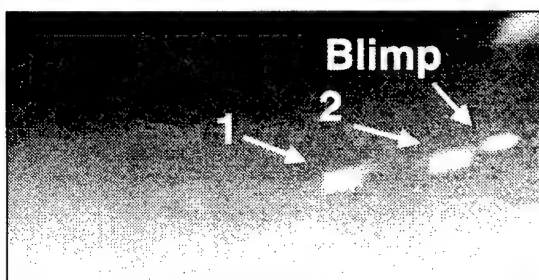
SMT2 @ 2.00 min (x ~ alongwind)
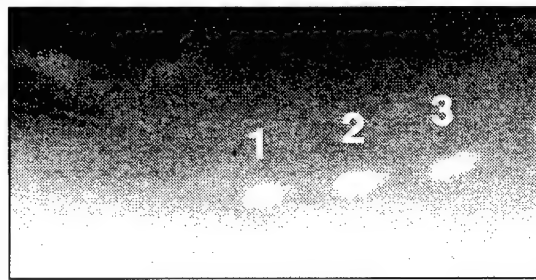
CEMT @ 4.00 min (x ~ mixed)
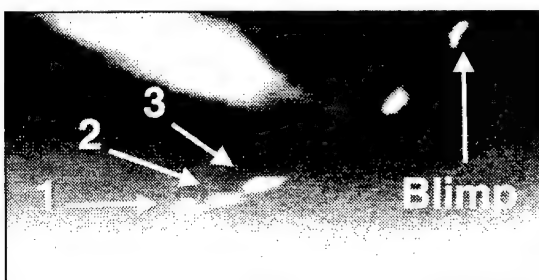
SMT2 @ 5.75 min (x ~ mixed)

Figure 28.   23 May 1997 series G (16) puff imagery documenting cross- and alongwind perspectives at various times after the release of series G puff 1.

30

CEMT @ 1.00 min (x ~ mixed)
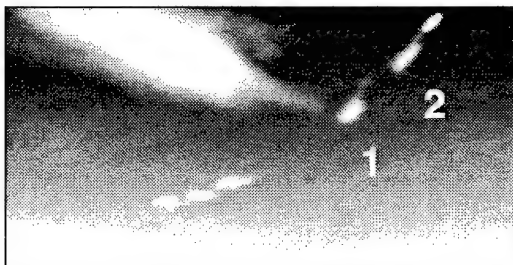
SMT2 @ 1.25 min (x ~ mixed)
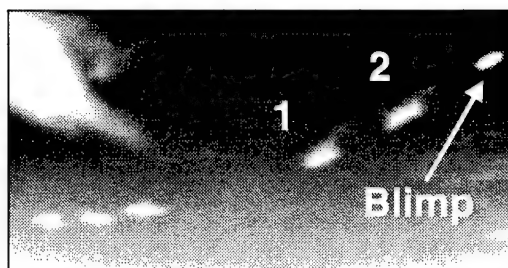
SMT2 @ 3.00 min (x ~ mixed)
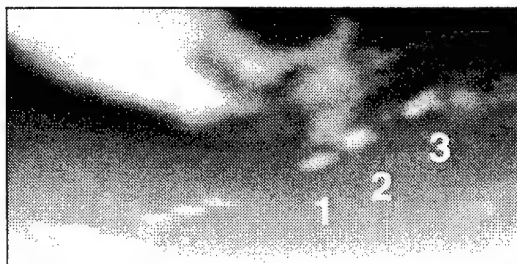
CEMT @ 4.00 min (x ~ crosswind)

Figure 29.   24 May 1997 series H (17) puff imagery documenting cross- and alongwind perspectives at various times after the release of series H puff 1.

Review of the imagery contained in Figures 21 through 29 reveals no consistent difference in the rates of the along- and crosswind dispersion on 23 May 1997. The imagery documents that series 8 showed much larger crosswind than vertical dispersion than the other series. It is apparent from these images, that it is difficult to qualitatively interpret imagery due to the constantly changing perspective. In spite of hazy or cloudy background, the imagery documents good contrast for seeing many of the low-altitude puffs against the cooler upper-altitude clouds. However, it is apparent that many puff series were not included in our analysis. This was due to poor signal-to-noise ratio for seeing the puffs due to broken cloud cover or low-altitude fog. Even for the puffs selected for our analysis, the data in Appendix D documented that the variable background (broken clouds) increased the scatter in the imagery-derived column density estimates. For several puffs (series B, F, and G), the imagery-derived mass estimates were substantially lower than for the other puff series. As illustrated by the examples in Appendix C, the expansion rates (i.e., extent of the puff) were not sensitive to many of the parameters that affect the mass estimates. In the next section of this report, the quantitative analysis of the puff imagery documents the along- and crosswind expansion rates for 23 May 1997.

3.4.2   Imagery-Derived Puff Characteristics for 23 May 1997

3.4.2.1   Alongwind and Crosswind Expansion Rates for 23 May 1997

Figures 30 and 31 are summary plots that document the imagery-derived expansion rates (meters growth per meter traveled) as a function of GMT for the 23 May 1997 SF_6 puff releases. It is interesting to note that the along- and crosswind values are comparable to each other and that the values
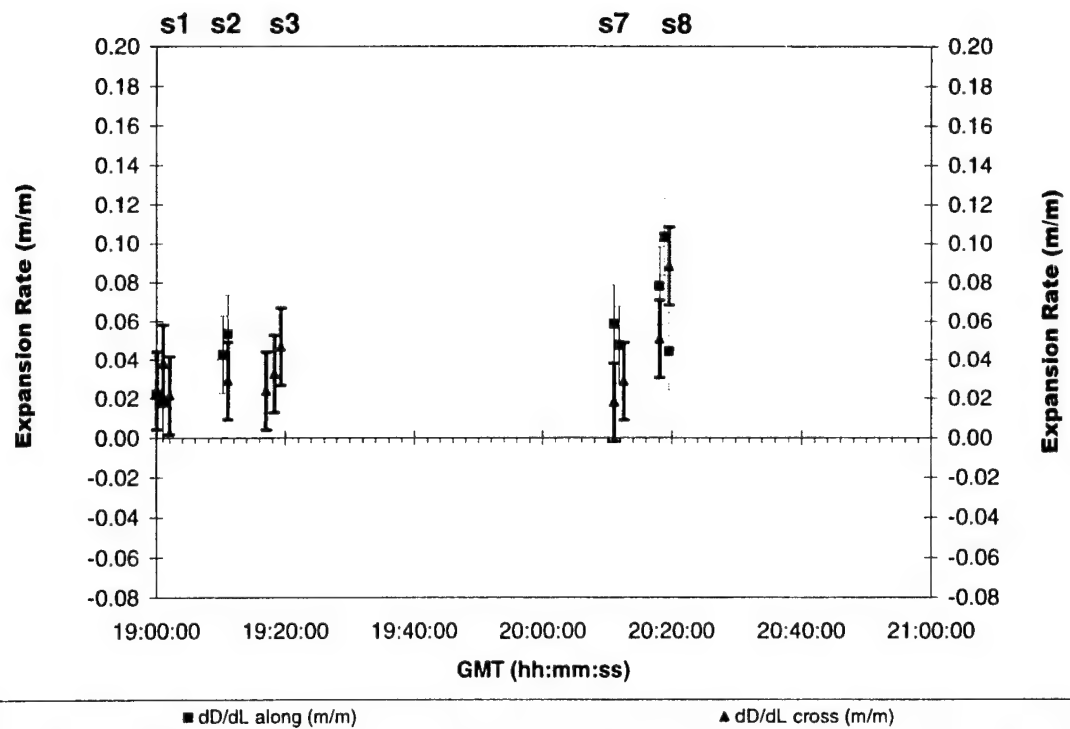
Figure 30. Puff expansion rates (m/m) derived from early imagery of 23 May 1997 SF$_6$ releases.
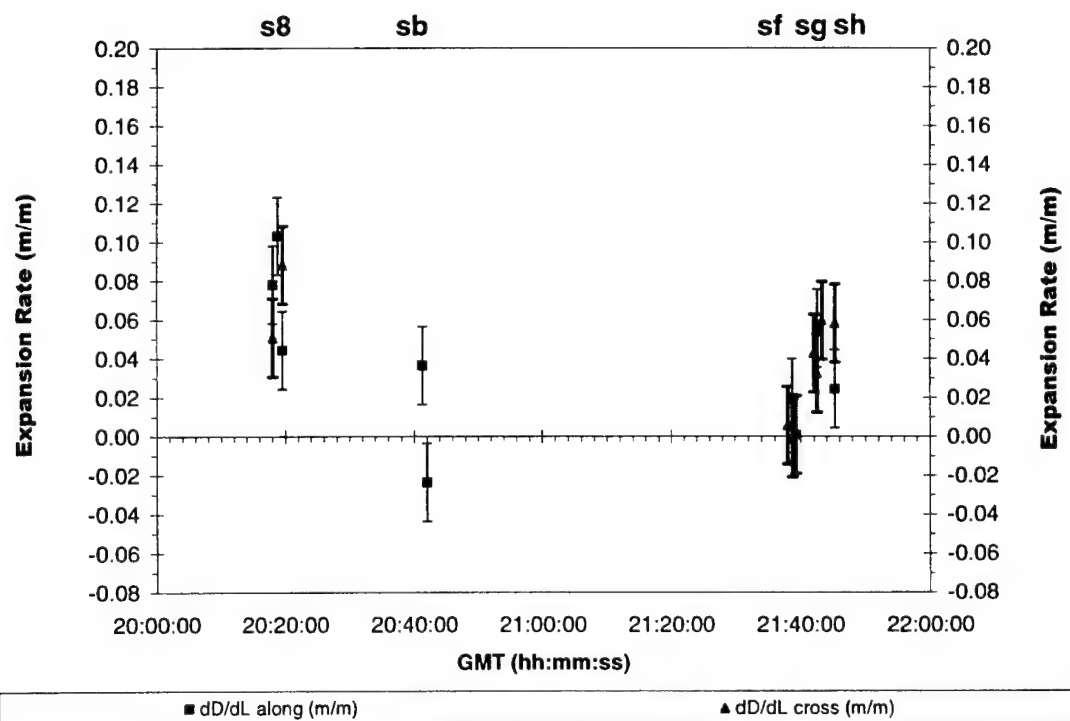
Figure 31. Puff expansion rates (m/m) derived from later imagery of 23 May 1997 SF$_6$ releases.

are comparable to the alongwind expansion rates measured in the afternoon on 21 May 1997. These data document the expansion rates for non-spherical puffs that started out with dimensions of 160 to 490 ft (50 to 150 m) and grew to 250 to 1230 ft (75 to 375 m) over the 3–9 min (800–3500 m) of tracking.

The measured expansion rates were low and even negative for series "B" (i.e., series 11) puffs. Figure 26 documented relatively poor contrast for seeing the series "B" puffs against a non-uniform background. The data in Appendix D documented that the variable background (broken clouds) increased the scatter in the imagery-derived column density and mass estimates. For several puffs (series B, F, and G), the imagery-derived mass estimates were substantially lower than for the other puffs on 23 May 1997. As illustrated by the examples in Appendix C, the expansion rate (i.e., full extent of the puff to 2–5 ppm-m threshold) was not sensitive to many of the parameters that affect the mass estimates. However, for the series "B" puff, there is a correlation between extremely low mass estimates (Appendix D), the poor contrast in the imagery (Figure 26), and the negative expansion rates (Figure 31). This correlation certainly implies the importance of having "good" imagery. The contrast is much better for seeing most of the other series shown in Figures 21 through 29. This is also illustrated by the imagery-derived mass estimates in Appendix D. However, the quality of the imagery was better on 21 May (1–3 ppm-m threshold) than on 23 May (2–5 ppm-m threshold).

As revealed by the imagery presented in Figures 21 through 29, the puffs were released with various aspect ratios and orientations relative to the wind direction. During this same period, Figures 7 and 8 document that the imagery-derived puff speed decreased from 16.1 to 11.4 knots (8.3 to 5.9 m/s), while the imagery-derived puff bearings shifted from 141° to 131° clockwise from north (the direction of puff movement). Figures 9 and 10 document that the puff altitudes were between 2625 and 3120 ft MSL (800 to 950 m MSL).

Figures 32 and 33 document the tilt angles used to define the along- and crosswind dimensions referenced in Figures 30 and 31 (i.e., expansion rates in m/m) and in Figures 34 and 35 (i.e., expansion rates in m/min). Due to coastal fog and range restrictions near the launch pad, the release geometry was not optimal for most releases on 23 May 1997. Therefore, the available imagery did not always include purely along- and crosswind perspectives. When there were not enough data at the desired perspective, the analyst chose a tilt angle close to the desired value or opened the window of acceptance about the tilt angle to include values on both sides of the selected perspective. For the 23 May 1997 imagery, the analyst had to tune both the tilt angle and the tilt window to obtain enough data to reveal a trend.

Figures 32 and 33 document the tilt angle as a data point and the acceptance window about that angle as the error bars for the data point. As illustrated in Appendix A and indicated in Figures 32 and 33, a tilt angle of 0° or 180° corresponds to alongwind data, while a tilt angle of 90° corresponds to crosswind data. Appendix A illustrates that the tilt angle is not aligned with any particular axis of the puff, but merely documents the orientation of the reported dimension (determined by the camera's perspective rather than the puff's orientation). An alongwind perspective from the camera site reveals the crosswind dimension of the puff, while a crosswind perspective is needed to measure the alongwind dimension. A narrow angle of acceptance (i.e., small error bars) indicates that the expansion rate was measured from almost identical perspective for the data included in the fit. In contrast,

33
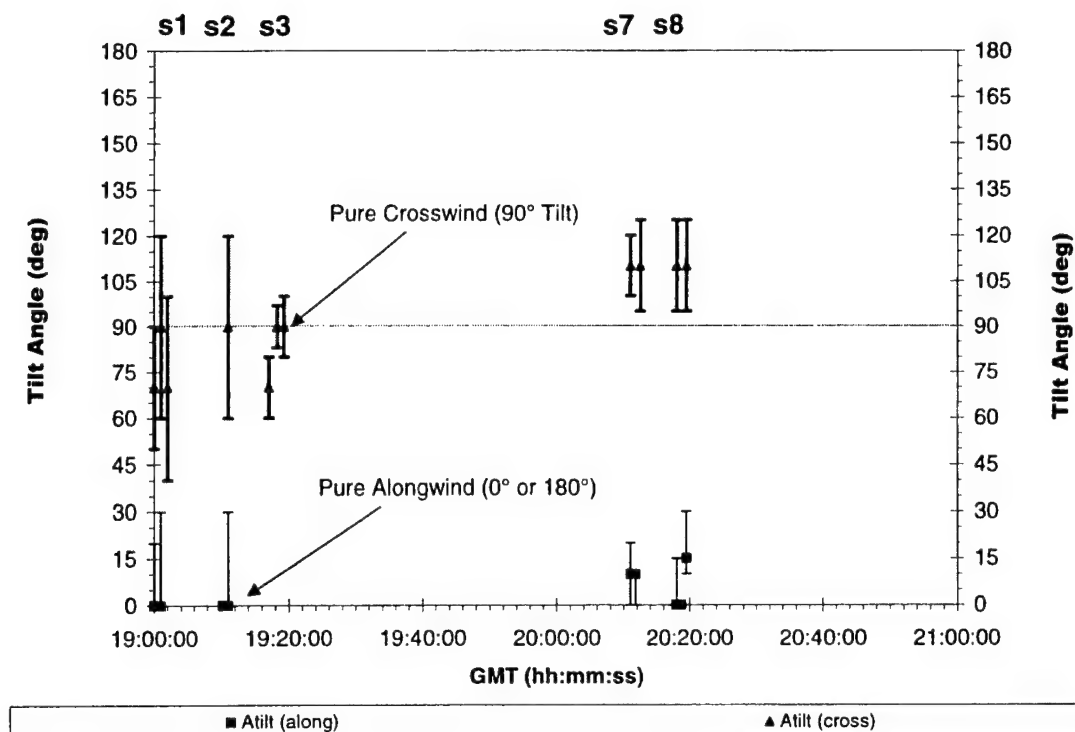
Figure 32. Tilt angles for along- and crosswind data for earlier releases on 23 May 1997.
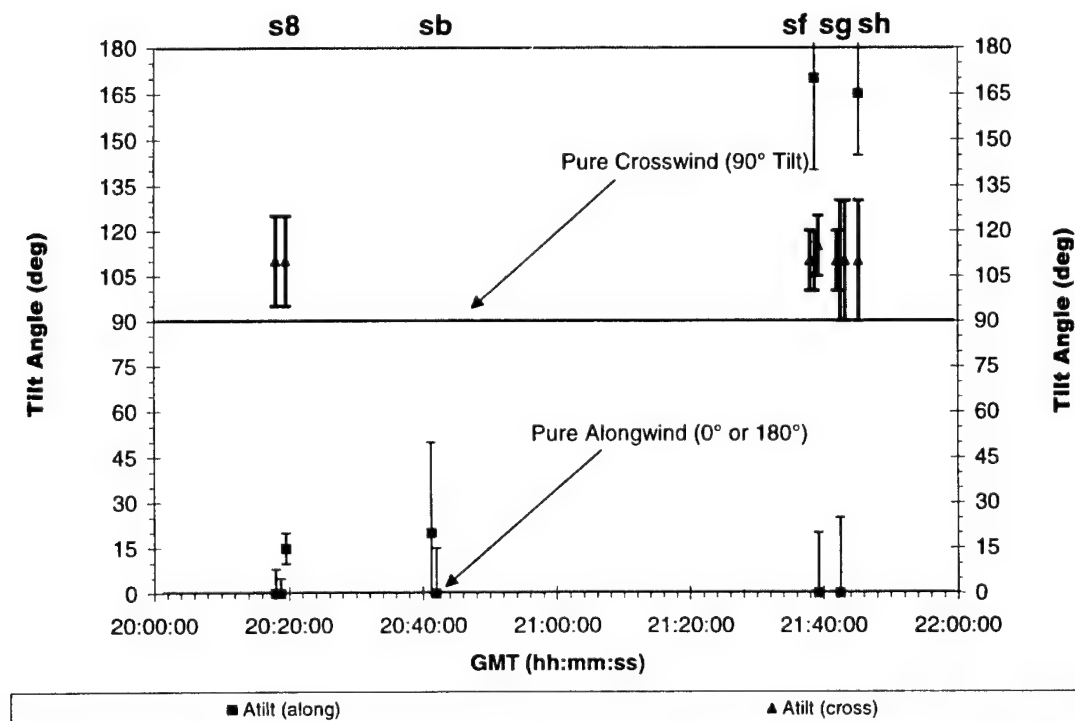
Figure 33. Tilt angles for along- and crosswind data for later releases on 23 May 1997.
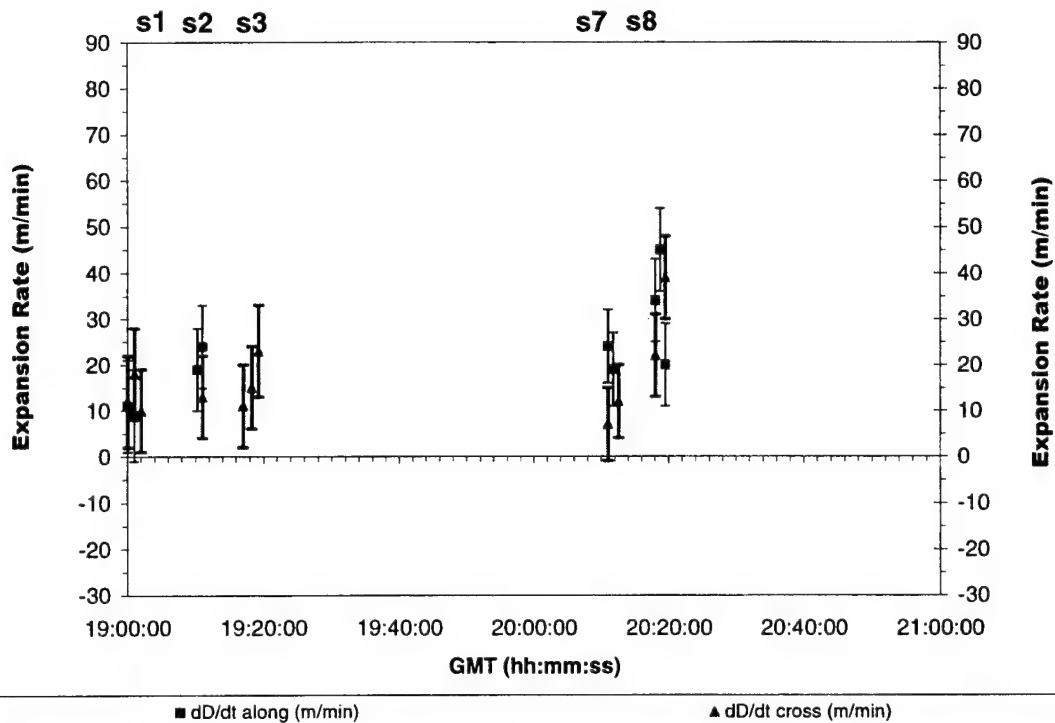
Figure 34. Puff expansion rates (m/min) derived from early imagery of 23 May 1997 SF$_6$ releases.
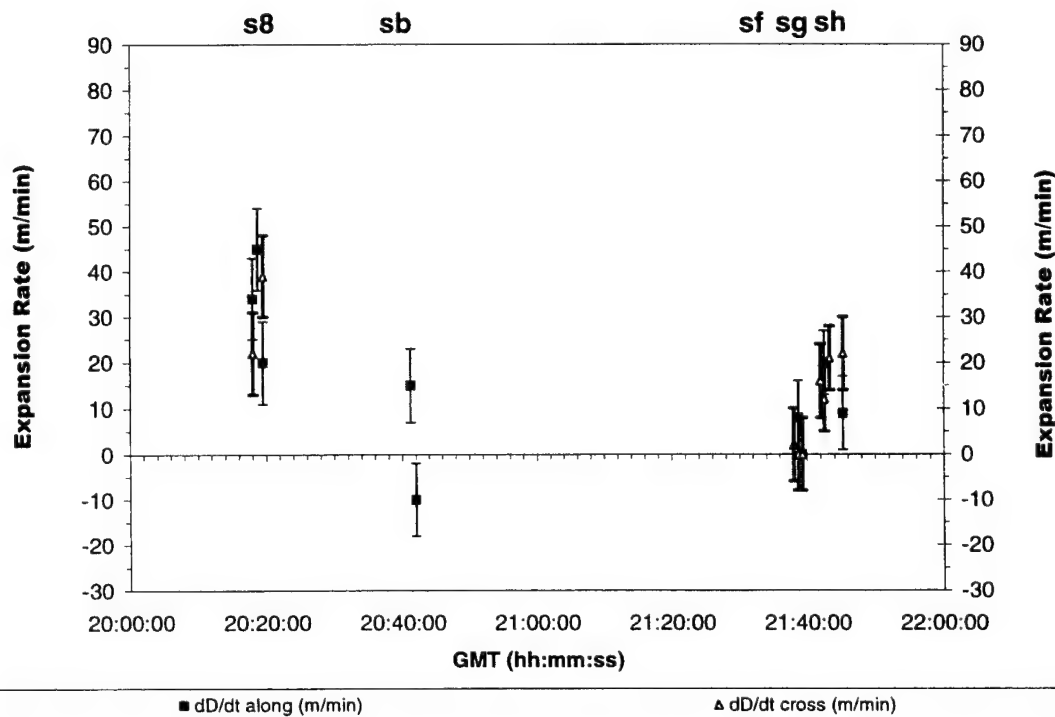
Figure 35. Puff expansion rates (m/min) derived from later imagery of 23 May 1997 SF$_6$ releases.

a large window of acceptance (i.e., large error bar) indicates that it was necessary to combine data of similar but varying perspectives in order have enough data for a linear regressive fit. There is more uncertainty in the reported expansion rate when it was necessary to widen the window about the angle. Likewise, the reported expansion rates may vary from the true along- or crosswind values as the tilt angle wanders from the pure along- or crosswind value. Based upon the angular data in Figures 32 and 33, the expansion rates in m/m (i.e., Figures 30 and 31) and m/min (i.e., Figures 34 and 35) only include data that is relatively close to along- and crosswind in perspective. Therefore, the reported expansion rates should be relatively close to the true along- and crosswind values.

Tables 5 and 6 provide data summaries for each puff on 23 May 1997. The first column provides the variable name, and the other columns provide the value of that variable for each puff of each series. Most of the data presented in these tables have been plotted in one or more figures included in this report.

Table 5. Imagery-Derived Puff Data for Earlier SF$_6$ Releases on 23 May 1997

| Series#Puff#	S1P1	S1P2	S1P3	S2P1	S2P2	S2P3	S3P1	S3P2	S3P3	S7P1	S7P2	S7P3	S8P1	S8P2	S8P3
t(0)S1P1	19:00:00	19:00:00	19:00:00	19:00:00	19:00:00	19:00:00	19:00:00	19:00:00	19:00:00	19:00:00	19:00:00	19:00:00	19:00:00	20:18:00	20:18:00
t(0)S#P#	19:00:00	19:01:00	19:02:00	19:10:15	19:11:00	19:12:00	19:17:00	19:18:15	19:19:15	20:11:00	20:11:45	20:12:30	20:18:00	20:18:45	20:19:30
dt(0)S#P#-S1P1	0.00	1.00	2.00	10.25	11.00	12.00	17.00	18.25	19.25	71.00	71.75	72.50	78.00	78.75	79.50
dtSOURCE (min)	0.50	0.50	0.50	0.25	0.50	1.50	0.50	1.00	0.00	0.25	0.25	0.50	0.50	0.25	0.50
dtEND (min)	6.00	5.25	7.00	6.00	5.75	4.75	8.00	6.00	8.00	8.75	8.00	7.00	9.00	9.00	7.00
Xsource (m)	168	272	397	194	226	438	209	250	-178	-836	-785	-609	-612	-652	-581
Ysource (m)	1101	1015	948	1291	1041	533	651	192	687	-862	-796	-894	-899	-848	-938
Zsource (m MSL)	900	890	900	900	880	900	850	900	920	925	925	900	925	925	925
dH/dt (m/min)	0	0	0	0	0	0	0	0	0	0	0	0	0	0	0
Slope (dY/dX)	-1.1684	-1.2015	-1.2406	-1.1884	-1.2178	-1.1196	-1.1804	-1.0799	-1.0287	-1.1783	-1.175	-1.1573	-1.2015	-1.1709	-1.1184
Bearing (along)	139	140	141	140	141	138	140	137	136	140	140	139	140	140	138
Bearing (cross)	49	50	51	50	51	48	50	47	46	50	50	49	50	50	48
Speed (m/s)	8.0	7.9	7.8	7.6	7.4	7.5	7.6	7.8	8.3	6.8	6.7	6.6	7.2	7.2	7.5
dD/dt cross (m/min)	12	18	10	#N/A	13	#N/A	11	15	23	7	#N/A	12	22	#N/A	39
dD/dt along (m/min)	11	9	#N/A	19	24	#N/A	#N/A	#N/A	#N/A	24	19	#N/A	34	45	20
error dD/dt	10	10	9	9	9	9	9	9	10	8	8	8	9	9	9
dD/dL cross (m/m)	0.02	0.04	0.02	#N/A	0.03	#N/A	0.02	0.03	0.05	0.02	#N/A	0.03	0.05	#N/A	0.09
dD/dL along (m/m)	0.02	0.02	#N/A	0.04	0.05	#N/A	#N/A	#N/A	#N/A	0.06	0.05	#N/A	0.08	0.10	0.04
error dD/dL	0.02	0.02	0.02	0.02	0.02	0.02	0.02	0.02	0.02	0.02	0.02	0.02	0.02	0.02	0.02
Atilt (cross)	70	90	70	#N/A	90	#N/A	70	90	90	110	#N/A	110	110	#N/A	110
dAtilt (cross)	20	30	30	#N/A	30	#N/A	10	7	10	10	#N/A	15	15	#N/A	15
Atilt (along)	0	0	#N/A	0	0	#N/A	#N/A	#N/A	#N/A	10	10	#N/A	0	0	15
dAtilt (along)	20	40	#N/A	5	20	#N/A	#N/A	#N/A	#N/A	10	10	#N/A	8	5	5

Table 6. Imagery-Derived Puff Data for Later SF$_6$ Releases on 23 May 1997

Series#Puff#	S8P1	S8P2	S8P3	SbP1	SbP2	SbP3	SfP1	SfP2	SfP3	SgP1	SgP2	SgP3	ShP1	ShP2	ShP3
t(0)S8P1	20:18:00	20:18:00	20:18:00	20:18:00	20:18:00	20:18:00	20:18:00	20:18:00	20:18:00	20:18:00	20:18:00	20:18:00	20:18:00	20:18:00	20:18:00
t(0)S#P#	20:18:00	20:18:45	20:19:30	20:41:15	20:42:00	20:43:00	21:38:00	21:38:40	21:39:15	21:42:00	21:42:30	21:43:15	21:45:15	21:46:00	21:46:45
dt(0)S#P#-S8P1	0.00	0.75	1.50	23.25	24.00	25.00	80.00	80.67	81.25	84.00	84.50	85.25	87.25	88.00	88.75
dtSOURCE (min)	0.50	0.25	0.50	0.25	0.50	#N/A	0.25	0.33	0.50	0.25	0.50	0.50	0.25	0.25	0.25
dtEND (min)	9.00	9.00	7.00	4.00	3.75	#N/A	4.00	5.00	4.00	6.00	5.50	4.00	6.00	3.00	3.00
Xsource (m)	-612	-652	-581	-602	-571	#N/A	586	505	441	352	375	427	501	571	619
Ysource (m)	-899	-848	-938	-1133	-1100	#N/A	-2267	-2226	-2172	-2048	-2137	-2234	-2173	-2182	-2181
Zsource (m MSL)	925	925	925	900	920	#N/A	885	910	920	850	830	830	830	840	850
dH/dt (m/min)	0	0	0	0	0	#N/A	0	0	0	0	0	0	0	0	0
Slope (dY/dX)	-1.2015	-1.1709	-1.1184	-1.0167	-1.0201	#N/A	-0.9997	-0.9411	-0.9499	-0.9876	-0.9102	-0.8598	-0.9728	-1.0087	-0.994
Bearing (along)	140	140	138	135	136	#N/A	135	133	134	135	132	131	134	135	135
Bearing (cross)	50	50	48	45	46	#N/A	45	43	44	45	42	41	44	45	45
Speed (m/s)	7.2	7.2	7.5	6.8	6.8	#N/A	6.5	6.6	6.6	6.3	6.0	5.9	6.4	6.5	6.6
dD/dt cross (m/min)	22	#N/A	39	#N/A	#N/A	#N/A	2	0	0	16	12	22	22	#N/A	#N/A
dD/dt along (m/min)	34	45	20	15	-10	#N/A	#N/A	8	0	#N/A	20	#N/A	9	#N/A	#N/A
error dD/dt	9	9	9	8	8	#N/A	8	8	8	8	7	7	8	8	8
dD/dL cross (m/m)	0.05	#N/A	0.09	#N/A	#N/A	#N/A	0.01	0.00	0.00	0.04	0.03	0.06	0.06	#N/A	#N/A
dD/dL along (m/m)	0.08	0.10	0.04	0.04	-0.02	#N/A	#N/A	0.02	0.00	#N/A	0.06	#N/A	0.02	#N/A	#N/A
error dD/dL	0.02	0.02	0.02	0.02	0.02	0.02	0.02	0.02	0.02	0.02	0.02	0.02	0.02	0.02	0.02
Atilt (cross)	110	#N/A	110	#N/A	#N/A	#N/A	110	110	115	110	110	110	110	#N/A	#N/A
dAtilt (cross)	15	#N/A	15	#N/A	#N/A	#N/A	10	10	10	10	20	20	20	#N/A	#N/A
Atilt (along)	0	0	15	20	0	#N/A	#N/A	170	0	#N/A	0	#N/A	165	#N/A	#N/A
dAtilt (along)	8	5	5	30	15	#N/A	#N/A	30	20	#N/A	25	#N/A	20	#N/A	#N/A

Several times are provided in Tables 5 and 6. The GMT for the release of each puff (t(0)S#P#) is related to the GMT for the release of the first puff in the table (t(0)S1P1 for Table 5 and t(0)S8P1 for Table 6) by reporting the time difference in decimal minutes between these two times (dt(0)S#P#-S1P1 and dt(0)S#P#-S8P1). For May 1997, there was a 7-h offset between local time (PDT) and GMT. Another time (dtSOURCE(min)) is the time elapsed in minutes between the first image of the start of the release of a puff and the first measurement of the full extent of that puff (i.e., the source size and position). Since the imagery was collected at 15-s increments, the first dimension (i.e., the source size and position) was typically measured a quarter of a minute after the first sign of the start of release. The length of time in minutes that the puff was tracked is reported by the variable dtEND(min).

The earliest measured position for each puff is the "source" of the release and is reported in Tables 5 and 6 as Xsource (m), Ysource (m), and Zsource (m MSL). This imagery-derived position is the "middle" of the puff derived from PLMTRACK analysis. Xsource and Ysource are relative to the position of the space launch complex 4 east (SLC-4E) for the 23 May 1997 data. Ysource is relative to mean sea level (MSL). Typically, the "best-positioned" camera sites provided a direct measure of the source position. However, the analyst sometimes derived the source position using fits to observed trends (i.e., height vs time and Cartesian plots). In Table 5, the change in altitude with time is reported as dH/dt (m/min). Appendix B documented that PLMTRACK's positional accuracy (100 m horizontal and 30 m vertical) is comparable to regular GPS accuracy (100 m horizontal and 250 m vertical). Based upon the PLMTRACK accuracy, the imagery documented no significant altitude change for any of the puffs after their release. This is consistent with the immediate vaporization of the liquid SF_6 and rapid equilibration (i.e., both in temperature and in density) with the ambient air.

Tables 5 and 6 also document the horizontal movement of each puff at elevation. Each puff's trajectory is reported as a "Slope (dX/dY)" for the Cartesian plot and a bearing in degrees clockwise from north. The "Bearing (along)" provides the alongwind bearing (direction of puff movement) while the "Bearing (cross)" provides the crosswind bearing. The "Speed (m/s)" is the slope of a plot of the puff's horizontal range from the source versus time.

Tables 5 and 6 use the dD/dt and dD/dL to denote expansion rates derived by plotting the puff's dimension (along- or crosswind extent to 2–5 ppm-m threshold) against either time (t) or horizontal distance (L) from the source. Due to the clouds and fog on 23 May 1997, the threshold (2–5 ppm-m) was greater than on 21 May 1997 (1–3 ppm-m). Approximate error bars for the expansion rates were assigned as ±0.02 m/m and converted to the m/min value using the puff's speed. The tilt angle (Atilt) relates the reported puff dimension (i.e., axis) to the alongwind direction. As illustrated in Appendix A, Atilt values of 0° or 180° correspond to alignment with the wind bearing, while a value of 90° indicates the perpendicular to the wind bearing. Appendix A also illustrated that the tilt angle is not aligned with any particular axis of the puff but merely documents the orientation of the reported dimension (determined by the camera's perspective rather than the puff's orientation). The dAtilt variable is the angular window of acceptance for the tilt angle (i.e., Atilt ±dAtilt). Small values of dAtilt indicate greater similarity in perspective for the fitted data than larger values of dAtilt. As discussed earlier, the analyst adjusted the values of Atilt and dAtilt to obtain enough data near the desired along- or crosswind perspective to warrant a linear regressive fit. The #N/A entries in the table indicate that a number was not available. Table 3 documented poor contrast for many of the series released on 23 May 1997. This is consistent with the lack of entries for those series in Tables 5 and 6.

3.4.2.2 Puff Dimension Plots for 23 May 1997

Appendix I includes horizontal puff dimension plots for all available data for each puff as well as for selected tilt angles for each puff. The "all tilt angle" plot provides an indication of the amount of available data as well as the angular dependence of the data. In some instances, the imagery provided data from only one narrow perspective. In other cases, the puff dimensions ramped between the extremes defined by the alongwind, crosswind, or diagonal perspectives. Unlike the 21 May data (Appendix H), the 23 May results document that the largest and smallest puff dimensions did not always align with the along- and crosswind perspectives. Indeed, the largest expansion rate (0.16 m/m) was observed for SGP3 on a diagonal (i.e., Atilt = 45°) that was halfway between alongwind and crosswind. Appendix I provides the plots used to determine not only the along- (i.e., Atilt = 0° or 180°) and crosswind (i.e., Atilt = 90°) expansion rates reported in Tables 5 and 6 but also expansion rates along other axes (i.e., 45° and 135° diagonals). The plot titles provide the values of the experimental variables used to filter the data. These plots provide the modeler with some indication of the quality and quantity of the data.

We provide no plots for the vertical puff dimensions since it was impossible to obtain a truly horizontal perspective (i.e., camera at the same height as the puff) that revealed only the vertical puff extent. The imagery-derived estimates ranged from 55 to 165 m for the vertical puff extent. Plots of vertical dimension against time and distance included only scattered points and revealed no consistent trends. Due to the oblong puff shapes (i.e., 10-s release times) and inclined camera angles (~20° EL), we could not eliminate a contribution from the horizontal puff dimension to the observed Y pixel dimension. This difficulty was discussed earlier when referring to the images included in this report.

3.4.2.3 Relative Motion of Puffs within Each Series for 23 May 1997

Figures 36 and 37 document the dispersion affecting a slightly larger scale by tracking the relative distance between puffs within each series of releases. In Figures 36 and 37, the distance between puffs is plotted against time and the rate of change (in meters per minute) is next to each dataset. The distances between puffs ranged from 660 to 3600 ft (i.e., 200 to 1100 m). The data in Figures 36 and 37 document that the relative motion between puffs was less than 144 ft/min (44 m/min) for the 23 May 1997 data. The individual puff data in Figures 34 and 35 documented that both the along- and crosswind dispersion rates were also less than 150 ft/ min (45 m/min).

The data in Figures 38 and 39 document the angular information for the pairs of puffs within each series relative to the imagery-derived crosswind (41° to 51°) and alongwind (131° to 141°) bearings. The alongwind bearing is the direction of movement for the puff expressed as degrees clockwise from north of its source. The data in Figures 38 and 39 document that the puffs were separated mainly in the alongwind direction. This is qualitatively consistent with the 30-s to 60-s difference in their release times (each puff moved downwind until the next puff was released).

Review of the data presented in Figures 36 through 39 reveals that the relative dispersion and motion between puffs appears to be random. These data also document that the relative puff dispersion rates were similar in magnitude (less than 150 ft/min or 45 m/min) to the imagery-derived dispersion rates for the individual puffs.

38
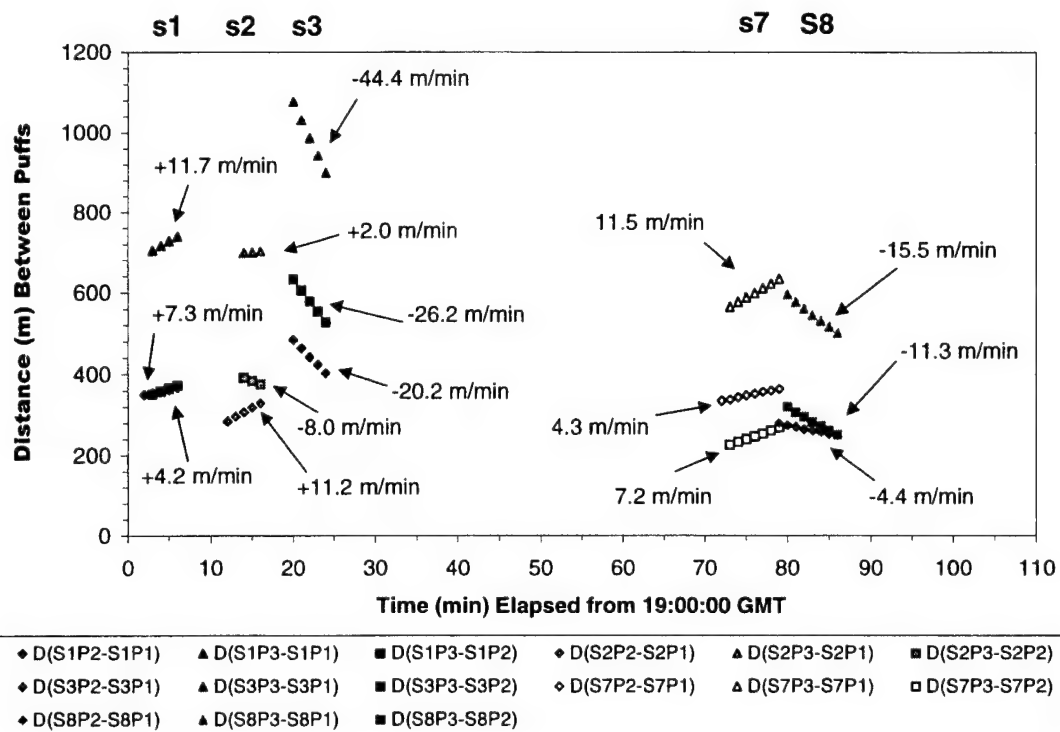
Figure 36. Relative puff spacing derived from imagery of earlier releases on 23 May 1997.
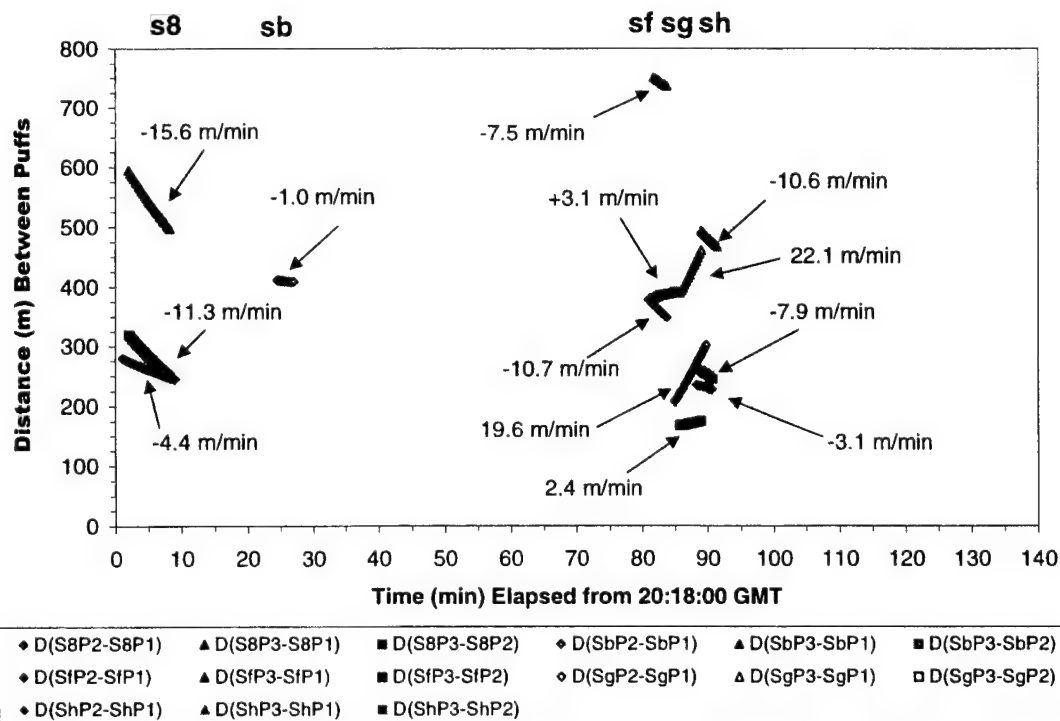
Figure 37. Relative puff spacing derived from imagery of later releases on 23 May 1997.
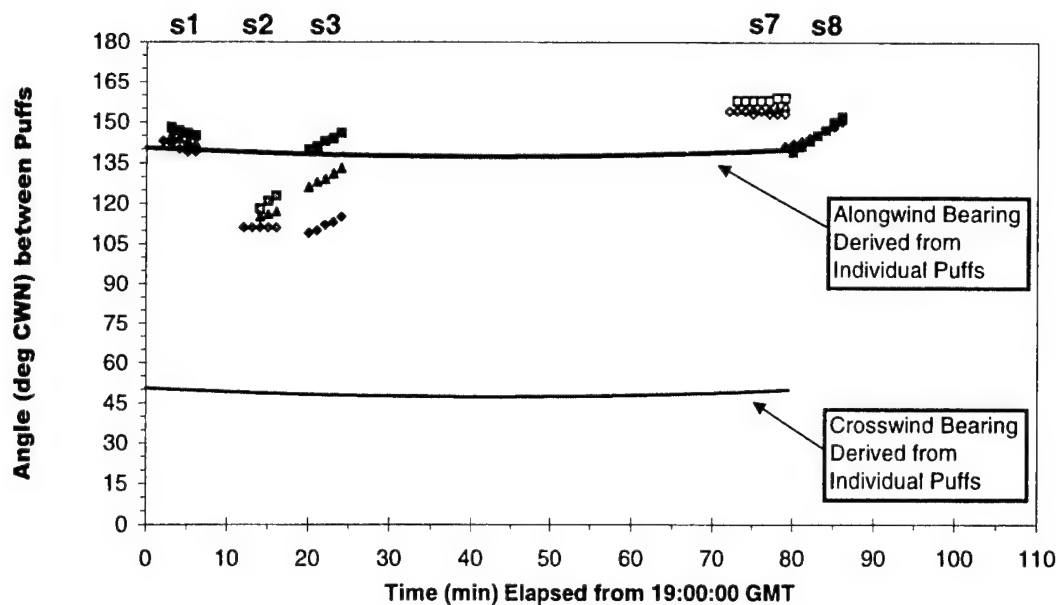
39

Figure 38. Angles between puffs derived from imagery of earlier releases on 23 May 1997.
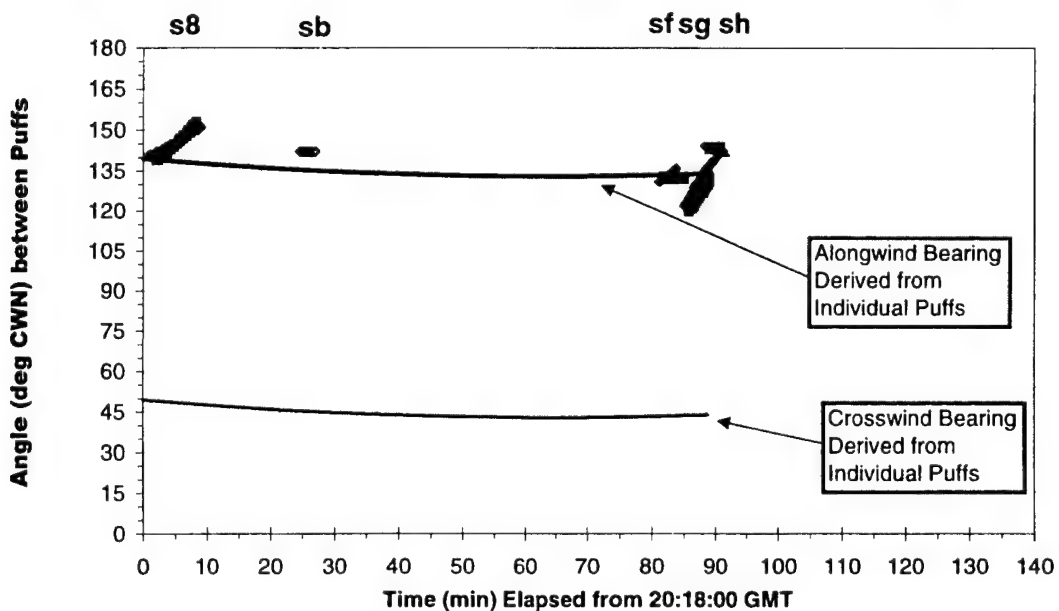
Figure 39. Angles between puffs derived from imagery of later releases on 23 May 1997.

3.5 Extraction of Atmospheric Turbulence Information From Puff Imagery

An estimate of atmospheric turbulence at the altitude of cloud dispersion is a key input to atmospheric dispersion models. Estimates of atmospheric turbulence fluctuations at the altitudes of interest for rocket exhaust clouds (200–900 m AGL) can be extracted directly from the puff imagery data. These values can then be compared to turbulence fluctuation values produced from other meteorological data sources. MVP collected meteorological data from numerous sources during the tracer release sessions, including meteorological towers, rawinsonde soundings, flux towers, radar profilers, sodar profilers, and instrumented aircraft (NOAA Long-EZ). Figure 40 shows how turbulence fluctuations are calculated from these data sources.

In addition, the tracer puff data can be used to evaluate and verify the performance of the REEDM built-in climatological algorithm. REEDM uses σ_u and σ_w values to calculate cloud spread rate and, hence, concentration levels. The REEDM algorithm for calculating σ_u and σ_w is a function of z (altitude). At the surface (z ~ 33 ft or 10 m), the sigma values are based either upon instrumented tower measurements or upon a climatological algorithm. In either case, adjustments are made for surface roughness. For higher altitudes, the sigma values are based upon the stability class and the height. The spread rate is based upon the RMS of the sigma values and the layer wind shear. Inki Min's preliminary analysis[19] of the MVP #4 puff data indicates that the observed puff dimensions correspond to 4 to 6 sigma levels on Gaussian fits to puff data. At early times, 1 ppm-m corresponds to 6 sigma for the concentrated puff while that same threshold corresponds to 4 sigma for a more dilute puff (later times).

The processing and analysis of the tracer puff data will continue in order to reveal the strengths and weaknesses of the various methods used for calculating the turbulence intensity at the altitudes of interest. Inki Min will author several reports that report values for sigma and the turbulent fluctuations from MVP puff data. This work will lead to the development of improved methods for predicting turbulence profiles for use in REEDM and other atmospheric dispersion models used at the space launch ranges.
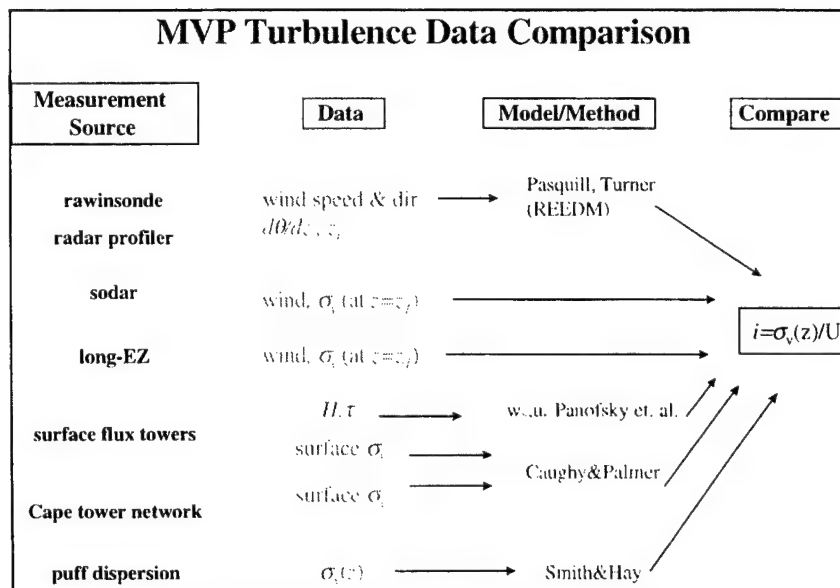
Figure 40. Flow chart for conversion of data to turbulence fluctuations.

4. Summary and Conclusions

We successfully used multiple-perspective synchronized infrared imagery to quantify the dispersion rates (expansion rates) of tracer puffs along various axes relative to the wind direction. These axes included not only the along- and the crosswind perspectives but also expansion rates along various diagonals to the puff's bearing. The imagery-derived expansion rates document dramatic differences (i.e., factors of 3 to 4) between the various dispersion axes under certain conditions. The puff extent was measured to threshold levels of 1–5 ppm-m column densities, depending upon the quality of the imagery. Analysis indicates that 1 ppm-m corresponds to the 6 sigma level for the initial concentrated puff. At later times, the 1 ppm-m threshold includes 4 sigma on the Gaussian fit to the dilute puff's concentration profile. Therefore, the imagery-derived puff extent included the bulk of the tracer. Atmospheric turbulence information can be extracted directly from these imagery-derived puff dimensions. The imagery-derived turbulence fluctuations can be compared with other measured and projected turbulence data. This basis of comparison can be used to evaluate and improve upon the current algorithm used for turbulent dispersion in REEDM and other atmospheric dispersion models.

This completes the analysis of one of four MVP deployments. Since the apparatus and procedures evolved during the four MVP deployments, we processed the MVP #4 data first because it provided the best dataset. The VIRIS hardware, calibration procedures, and camera crews were optimal for this latest deployment. The analysis of the MVP #4 data has demonstrated that the best algorithm for processing the imagery uses the puff's angular extent derived from individual imagery. The angular extent is then converted to physical extent by using the "best" estimate of the puff's position, derived from pair-wise PLMTRACK analysis of all available imagery.

This same approach will be applied to processing the imagery from the other three MVP deployments. By using the "best" estimate for the puff's position, the analysis minimizes any bias introduced by any one imagery site. We are confident that this approach will extract expansion rates from the earlier MVP deployments with accuracy comparable to the MVP #4 analysis. Therefore, the data presented in this report provide an indication of the quantity and quality of data collected during each of the four MVP sessions. These puff data should provide an interesting dataset for challenging current and future dispersion models.

References

1. "Ground Cloud Dispersion Measurements During the Titan IV #K23 (14 May 1995) at Cape Canaveral Air Force Station: Volume 1 – Test Overview and Data Summary," The Aerospace Corporation Report No. TR-96(1410)-1, SMC-TR-96-01, The Aerospace Corporation, El Segundo, CA (27 February 1996).

2. "Ground Cloud Dispersion Measurements During the Titan IV #K19 (10 July 1995) at Cape Canaveral Air Force Station," The Aerospace Corporation Report No. TR-96(1410)-3, SMC-TR-96-18, The Aerospace Corporation, El Segundo, CA (22 March 1996).

3. "Ground Cloud Dispersion Measurements During the Titan IV #K21 (6 November 1995) at Cape Canaveral Air Force Station," The Aerospace Corporation Report No. TR-96(1410)-4, SMC-TR-96-21, The Aerospace Corporation, El Segundo, CA (21 June 1996).

4. R. N. Abernathy, R. F. Heidner III, B. P. Kasper, and J. T. Knudtson, "Visible and Infrared Imagery of the Launch of Titan IV K-23 from Cape Canaveral Air Force Station on 14 May 1995," The Aerospace Corporation Report No. TOR-96(1410)-1, The Aerospace Corporation, El Segundo, CA (15 September 1996).

5. R. N. Abernathy, R. F. Heidner III, and K. L. Foster "Aircraft HCl Sampling of the Titan IV K-23 Launch Effluent Cloud," SMC-TR-96-22, The Aerospace Corporation Report No. TR-96(1410)-2, The Aerospace Corporation, El Segundo, CA (15 September 1996)

6. "Ground Cloud Dispersion Measurements During The Titan IV Mission #K15 (5 December 1995) at Vandenberg Air Force Base, Volume 1 – Test Overview and Data Summary", SMC-TR-97-05, The Aerospace Corporation Report No. TR-97(1410)-3, The Aerospace Corporation, El Segundo, CA (10 February 1997)

7. "Ground Cloud Dispersion Measurements During the Titan IV #K16 (24 April 1996) at Cape Canaveral Air Force Station, Volume 1 – Test Overview and Data Summary," The Aerospace Corporation Report No. TR-97(1410)-4, SMC-TR-97-10, The Aerospace Corporation, El Segundo, CA (31 March 1997)

8. "Ground Cloud Dispersion Measurements During the Titan IV #K22 (12 May 1996) at Vandenberg Air Force Base, Volume 1 – Test Overview and Data Summary," The Aerospace Corporation Report No. TR-97(1410)-5, SMC-TR-97-18, The Aerospace Corporation, El Segundo, CA (30 June 1997).

9. "Ground Cloud Dispersion Measurements During the Titan IV Mission #K2 (3 July 1996) at Cape Canaveral Air Force Station, Volume 1 – Test Overview and Data Summary," The Aerospace Corporation Report No. TR-97(1410)-6, SMC-TR-97-19, The Aerospace Corporation, El Segundo, CA (15 July 1997).

10. "Ground Cloud Dispersion Measurements During the Titan IV Mission #K24 (23 February 1997) at Cape Canaveral Air Force Station, Volume 1 – Test Overview and Data Summary," The Aerospace Corporation Report No. TR-97(1410)-7, SMC-TR-98-01, The Aerospace Corporation, El Segundo, CA (10 October 1997).

11. "Ground Cloud Dispersion Measurements During the Titan IV Mission #K13 (20 December 1996) at Vandenberg Air Force Base, Volume 1 – Test Overview and Data Summary," The Aerospace Corporation Report No. TR-97(1410)-8, SMC-TR-98-02, The Aerospace Corporation, El Segundo, CA (10 October 1997).

12. R. N. Abernathy, "Titan 34D-9 Abort Cloud Measurements — Quantitative Imagery from Two Camera Sites," The Aerospace Corporation Technical Report TR-98(1410)-1, SMC-TR-98-4, The Aerospace Corporation, El Segundo, CA (20 February 1998).

13. R. N. Abernathy and K. L. Foster, "Ground Cloud Dispersion Measurements During The Titan IV Mission #K15 (5 December 1995) at Vandenberg Air Force Base – Volume 2 – Further Analysis of Quantitative Imagery and of Aircraft HCl Data," The Aerospace Corporation Technical Report TR-98(1410)-2, The Aerospace Corporation, El Segundo, CA (12 May 1998).

14. "Ground Cloud Dispersion Measurements During the Titan IV Mission #B33 (15 October 1997) at Cape Canaveral Air Force Station," The Aerospace Corporation Report No. TR-98(1410)-3, SMC-TR-98-31, The Aerospace Corporation, El Segundo, CA (30 June 1998).

15. B. L. Lundblad, R. N. Abernathy, and B. J. Laine, Capt., "Atmospheric Dispersion Model Validation Program," 1998 JANNAF Propellant Development and Characterization Subcommittee (PDCS) and Safety and Environmental Protection Subcommittee Joint (S&EPS) Joint Meeting, Held at NASA Johnson Space Center, *JANNAF PDCS and S&EPS Meeting Proceedings*, CPIA Publication 674, (21-24 April 1998).

16. R. Abernathy, I. Min, and B. Lundblad (The Aerospace Corporation) and B. Kempf (U.S. Air Force Space and Missile System Center), "Tracer Puff Dispersion at Launch Sites," Paper at 28th Propellant Development and Characterization Subcommittee and 17th Safety and Environmental Protection Subcommittee Joint Meeting, Town & Country Hotel/Naval Submarine Base, San Diego, CA (26-30 April 1999), Chemical Propulsion Information Agency (CPIA) Publication 687, April 1999

17. R. N. Abernathy, I. A. Min, B. L. Lundblad, and W. S. Kempf, "Tracer Puff Dispersion at Launch Sites" The Aerospace Corporation Report No. TR-99(1413)-4, SMC-TR-99-25, The Aerospace Corporation, El Segundo, CA (15 July 1999).

18. Mark L. Polak, Jeffrey L. Hall, and Kenneth C. Herr, "Passive Fourier-transform Infrared Spectroscopy of Chemical Plumes: An Algorithm for Quantitative Interpretation and Real-Time Background Removal," *Applied Optics*, Volume 34, Number 24, pages 5406-5412 (20 August 1995)

19. Inki A. Min, "Puff Sigma Values from MVP4," work in progress, The Aerospace Corporation (2000).

Appendix A-Illustrations of Angles and Perspectives

Illustrations within this appendix document the various angles, rays, and dimensions associated with the MVP puff analyses. When the puff diameters are plotted against time after release or distance from the source, the slopes of the trends are the puff expansion rates in m/min and m/m, respectively. The various angles described in this appendix are used to filter the puff data for high quality and for specific perspective (i.e., alongwind, crosswind, or other axes). This appendix documents several approaches to puff analysis. Appendices E, F, and G illustrate the analysis of PLMTRACK-derived puff data for several puffs using the various approaches described in this appendix.

PLMTRACK-Derived Puff Dimensions

Figure A-1 is a sketch that represents a puff as an ellipse at two points in time, at the source and at its' current position. The figure also shows two imagery sites and the various PLMTRACK-derived parameters from a downward looking perspective. PLMTRACK software calculates the nearest approach in three-dimensional space for each pairing of rays, one from each site. The illustrated parameters are derived from one pair of images (i.e., one of six combinations for four camera sites). The numbered vertices represent the nearest approach of the illustrated rays from the two camera sites. The rays are labeled L (left), R (right), and M (middle) for each site. In our analysis scheme, camera 2 of each pairing is typically to the right of camera 1 (as shown in Figure A-1). The nearest
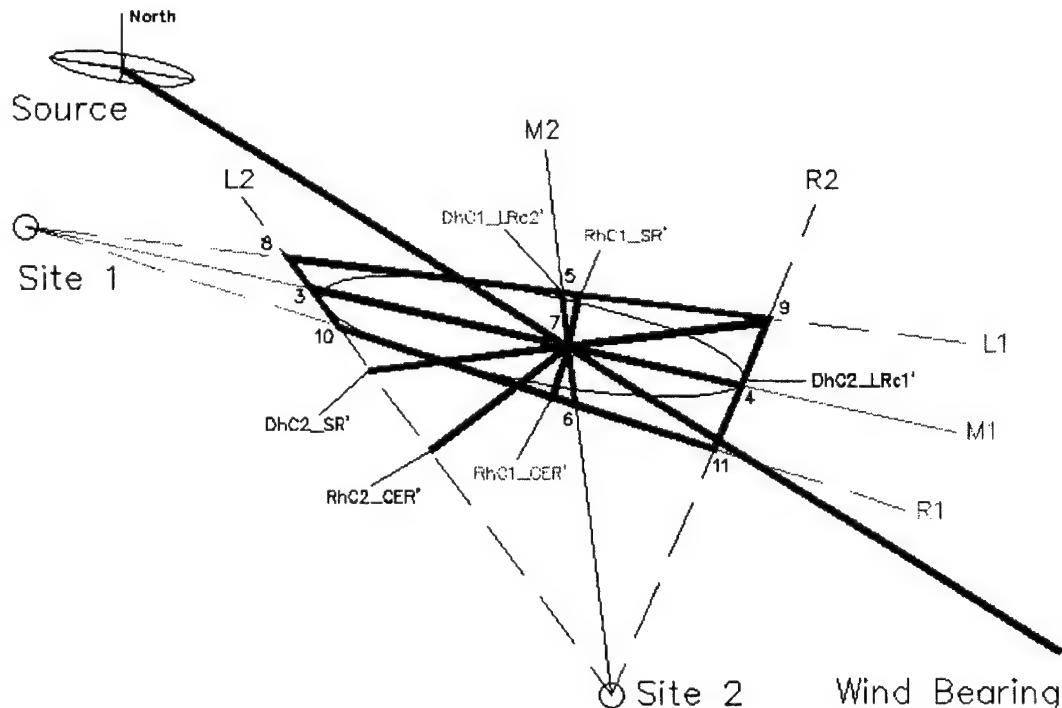
Figure A-1. PLMTRACK-derived rays, vertices, and dimensions for the tracer puff.

47

approach of the two middle rays is the value for the PLMTRACK-derived current position (MID) of the puff. Figure A-1 also indicates various puff dimensions as RhC1_SR', RhC2_SR', DhC1_CER', DhC2_CER', DhC1_LRc2', and DhC2_LRc1'.

We use a variable name that ends in an apostrophe to indicate when the dimensions were derived directly from one set of PLMTRACK vertices. Since the PLMTRACK vertices are the nearest approach of rays projected from two camera sites, they provide a less accurate angular extent for the puff than revealed directly from the puff's angular extent (i.e., width in pixels) within individual images. This alternative approach will be discussed later in this appendix.

The first two characters of our dimension notation refer to horizontal radius (Rh) or horizontal diameter (Dh). Immediately following the dimension identifier is a notation that identifies the camera (C1 or C2) used to view the axis of the radius or diameter. Finally, the notation specifies the method of approximation: (1) SR, (2) LRc#, or (3) CER. Examples of these methods are illustrated in Figure A-1 and discussed in the following paragraphs.

RhC1_SR' and RhC2_SR' are estimates for two horizontal puff radii derived from camera 1 and camera 2, respectively. These radii are based upon the PLMTRACK-derived slant range (SR) to the MID (vertex #7) of the puff and the PLMTRACK-derived polygon (i.e., defined by the extreme vertices: 10, 8, 9, and 11). The SR is the distance from the camera to the intersection of the middle rays. As illustrated in Figure A-1, the radius, RhC#_SR', is determined by the SR from camera # and is the length of a perpendicular to the middle ray that is included within the PLMTRACK-derived polygon and intersects the MID (vertex #7) of the puff.

Figure A-1 also illustrates DhC1_LRc2' and DhC2_LRc1'. These two horizontal diameters are defined by the interception of the left and right rays from one camera with the middle ray of the other camera. DhC1_LRc2' is the extent seen by camera 1 (i.e., camera 1's left and right rays intercepted by camera 2's middle ray). DhC2_LRc1' is the extent seen by camera 2 (i.e., camera 2's left and right rays intercepted with the middle ray of camera 1).

Figure A-1 shows that RhC1_CER' and RhC2_CER' are circle-equivalent radii derived from camera 1's and camera 2's perspective, respectively. The circle-equivalent radius (CER) is the length of the perpendicular from an extreme ray (i.e., L or R) through the MID (vertex #7) of the puff. RhC1_CER' is a PLMTRACK-derived CER seen from camera 1's perspective. RhC2_CER' is a PLMTRACK-derived CER seen from camera 2's perspective.

The apostrophes at the end of the dimension notations indicate that the PLMTRACK-derived polygon is used to define the extent and the position of the puff. The use of the PLMTRACK polygon introduces errors since the vertices are the calculated nearest approach of the rays from the two cameras. The errors result from any inaccuracies in the angular calibration of the camera sites. Therefore, all of the dimensions shown in Figure A-1 would include such errors.

Best Estimate of Puff Dimensions

Instead of triangulating the puff's extent with PLMTRACK, a more accurate angular extent is obtained directly from the image recorded by a single camera. The puff's size in pixels in any image can be converted to an angular extent by using the camera's known FOV. This angular extent can then be converted to a physical dimension by using the "best" estimate of the SR. These "best" estimates of the puff's dimensions are illustrated in Figure A-2 and discussed below. The "best" estimate of the SR is calculated from the camera's known position and from the formula for the puff's position as a function of time. The formula for the puff's position is obtained by fitting trends revealed by all useful puff position data. The available puff position data includes data derived from all pair-wise combinations of imagery from the four sites (i.e., six values for the puff's MID for each set of four images) and from all times (i.e., the entire puff track). As discussed in this appendix and in Appendices E, F, and G, experimental parameters can be used to filter the puff data to include only reasonable results in the fitted trends. The fitted data provides a better estimate for puff position and, subsequently, SR than obtained by any one pair-wise PLMTRACK analysis.

Figure A-2 is similar to the sketch in Figure A-1 except for the addition of the tilt angles (Atilt) and a couple of new puff dimension notations. Again, the puff is seen from above simultaneously at two times (at the source and at its current positions). A tilt angle of 0° or 180° corresponds to an
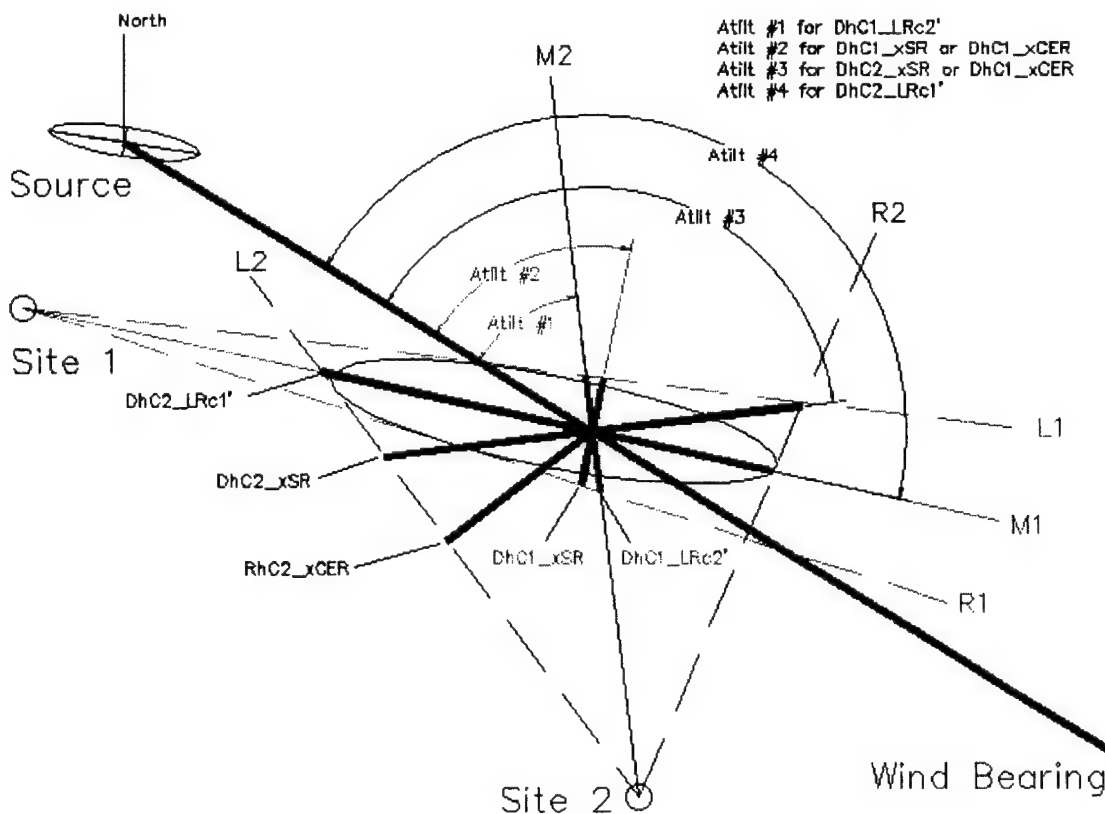
Figure A-2. Tilt angles relative to puff trajectory (wind bearing).

49

alongwind dimension, while a tilt angle of 90° corresponds to a crosswind dimension. As illustrated in Figure A-2, the tilt angle ranges from 0° to 180° as the left end (i.e., as seen from the source) of the measured dimension rotates from aligned with the wind and closest to the source to aligned with the wind and farthest from the source. For our purposes, there is no difference between a 0° and a 180° tilt since we cannot differentiate the ends of the puff dimension (i.e., other than one end is to the left of the middle of the cloud when viewed from the source). It is apparent from Figure A-2 that the measured dimension and, hence, the tilt angle does not necessarily align with any major or minor axis of the puff. The tilt angle is defined by the camera perspectives, by the puff's bearing (i.e., direction of motion), and by the puff's current position.

Two of the dimensions (DhC2_LRc1' and DhC1_LRc2') were included both in Figure A-1 and in Figure A-2. The apostrophes indicate that the extent and position of the puff were derived from PLMTRACK analysis using one pair of camera sites. The three new dimensions included in Figure A-2 are DhC2_xSR, DhC1_xSR and RhC2_xCER. These dimensions lack the apostrophe and, therefore, are derived from the puff's angular extent (i.e., X pixel size as fraction of the FOV) in one image and from the "best" position of the puff (i.e., best slant range from the camera).

DhC1_xSR and DhC2_xSR are estimates of the puff's horizontal diameters as seen from camera 1's and camera 2's perspectives, respectively. These diameters are perpendicular to the camera's perspective, are derived from the X pixels within the camera's image, and are calculated using the "best" SR value to the middle of the puff. DhC1_xSR is based on the angular extent (i.e., seen as X pixels) in camera 1's FOV, while DhC2_xSR is based on the angular extent (i.e., seen as X pixels) in the camera 2's FOV. In both cases, the "best" puff position (i.e., SR) and the field of view (FOV) of the camera are used to convert the angular extent to physical extent.

RhC2_xCER is the circle-equivalent radius based on the angular extent (i.e., seen as X pixels) in camera 2's FOV and the "best" position (i.e., SR) for the puff. The circle-equivalent radius (CER) is the length of a perpendicular from the puff's left or right ray (see Figure A-2) to the middle of the puff. In this case, the middle of the puff is at the center of the angular extent and at SR from the camera site. The lack of the apostrophe on the dimension notation indicates that the SR is based upon the "best" position of the puff at that time. Although it is not shown in Figure A-2, there would also be a CER from camera 1's perspective (i.e., RhC1_xCER). Again, the x in the notation indicates that the angular extent is derived from the X pixels in the image.

Figure A-3 is a sketch that is similar to those used in Figures A-1 and A-2. Figure A-3 documents various angles defined by the camera sites, the current position of the puff, and puff's bearing (direction of travel determined by the effective wind bearing). Asm is the angle clockwise from north of the source to the middle of the puff. When Asm is 90°, the puff is moving toward the east. As illustrated by Figure A-3, Ac1n and Ac2n are the angular offset of camera 1 and camera 2 from the normal to the puff's bearing at the puff's middle. When the absolute value of Ac1n is 90°, camera 1 is looking at the puff along the bearing of the puff and would see the puff's crosswind width as X pixels. When the absolute value of Ac2n is 0°, camera 2 is looking at the puff from a perspective normal to the puff's trajectory and, therefore, would see the puff's alongwind width as X pixels.

50
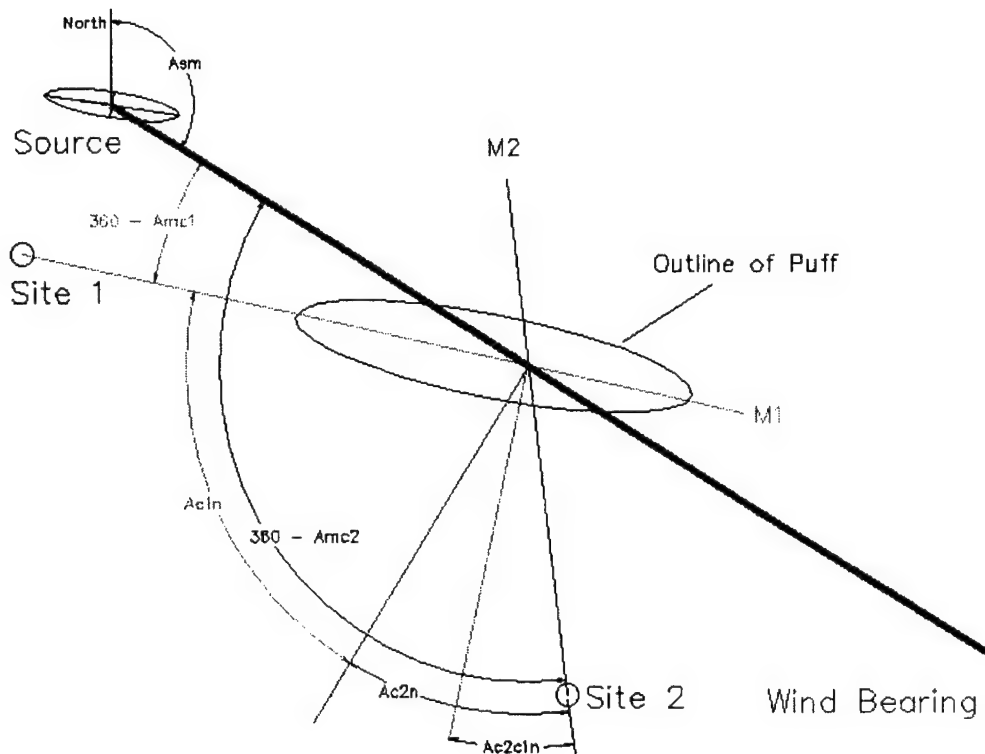
Figure A-3. Camera angles relative to puff position and bearing.

Figure A-3 illustrates that Ac2c1n is the angular offset of camera 2 from normal to camera 1's perspective of the puff. Therefore, when Ac2c1n is 0°, camera 2 and camera 1 have optimal (i.e., normal) perspectives for triangulating the position of the puff. When the absolute value of Ac2c1n is 90°, camera 1 and camera 2 are looking at the puff along the same line (i.e., have parallel perspectives) and are either on the same or on opposite sides of the puff. For low elevation angles, this could be the least accurate situation for triangulating the position of the puff. Figure A-3 shows an almost optimal case for Ac1c1n.

Figure A-3 also illustrates that Amc1 and Amc2 are the clockwise angular rotation of camera 1's and camera 2's perspectives from being at the source side of the middle of the puff. Rather than drawing the large arc in Figure A-3, we show "360° – Amc1" and "360° – Amc2." When Amc1 equals 0° or 360°, camera 1 would be looking downwind at the puff. When Amc1 equals 180°, camera 1 would be looking upwind at the puff. When Amc2 equals 90°, camera 2 would see the alongwind dimension of the puff as X pixels with the leading edge (downwind edge) to the left in its FOV. When Amc2 equals 270°, camera 2 would see the alongwind dimension of the puff as X pixels with the leading edge (downwind edge) to the right in its FOV.

Puff Dimensions from Elevation Angles

Unlike the other figures in this appendix, Figure A-4 is a sketch that shows a side-view of the puff and the elevation angles from only one site. R_yCER (TOP) and R_yCER (BOT) represent the

51
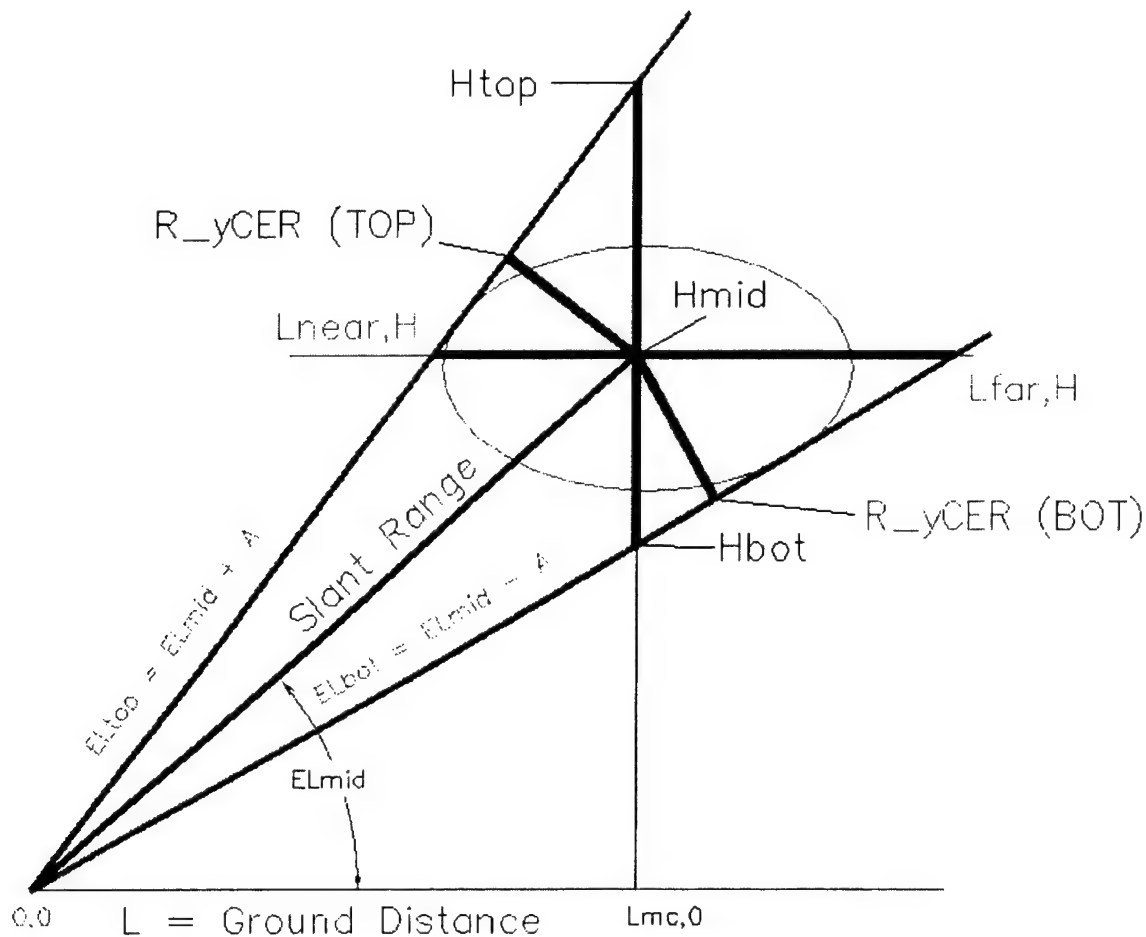
Figure A-4. Elevation angles and puff dimensions.

circle-equivalent radii (CER) derived from the Y pixels in the image and from the "best" value of the puff's position (i.e., SR) at that time. One can see that the top and bottom CER are not equal for the case illustrated in Figure A-4 (i.e., ~45° elevation). The circle-equivalent diameter would be the sum of the CER for the top and bottom. Figure A-4 also illustrates Htop and Hbot, which are based upon the best puff position and the elevation angles to the top and bottom of the puff from the camera site. For shallow elevation angles (i.e., less than 20°) and reasonable slant ranges (i.e., the puff occupying less than 10° of angular extent), the sum of Htop and Hbot is almost identical to the sum of the top and bottom CERs.

Figure A-4 illustrates points "Lnear,H" and "Lfar,H". These points are the near and far extremes of the puff's horizontal extent as defined by the elevation angles to the top and to the bottom of the puff and by the "best" value for the height (H) of the puff. One can see that these two points are not equi-distant from the middle of the puff. Therefore, the horizontal diameter at the height of the puff would be calculated as the sum of Lnear and Lfar. For steep elevation angles (i.e., greater than 70°) and reasonable slant ranges (i.e., the puff occupying less than 10° of angular extent), the sum of Lnear and Lfar is almost identical to the sum of the top and bottom CERs. For steep elevation angles, "top" and "bottom" in the image (i.e., Y pixels) reveal the horizontal extent of the puff.

52

The differences between the various estimates of the puff dimensions are exaggerated in Figure A-4 because of the small SR, intermediate elevation angle, and large puff diameter. Typically, there are small differences between the CER-based horizontal diameter and the near-far diameter when the elevation to the puff's middle is steep (i.e., greater than 70°). Likewise, there are small differences between the CER-based vertical diameter and the TOP-BOT diameter when the elevation to the puff is shallow (i.e., less than 20°).

Using Experimental Parameters to Filter Puff Data

One can see from the figures included in this appendix that "good" values for position and extent can only be derived from imagery that contains "useful" perspectives of the puff. Therefore, we use the various angles illustrated in these figures to filter the puff data for optimum accuracy or desired perspective. Obviously, we would not report horizontal extent derived from vertical pixels (Y pixels) when the elevation angle is shallow. Likewise, we use the Ac2c1n parameter to filter data for different viewing perspectives for each pair of cameras. Another filter is the size (in pixels) of the puff within the image. Obviously, the analysis errors can increase, as the puff becomes very small in the image. Typically, the puff must occupy 8 to 10 pixels before we include the data in our analyses. The tilt angle is used to select the desired puff dimension (i.e., alongwind, crosswind, or diagonal to the wind). The values of the filters are included in the headers for all plots within this report. If the header for a plot does not include a value or range for a variable, then that variable was not used as a filter for that particular plot.

Appendix B-Imagery-Derived Position versus GPS Position

This appendix compares the accuracy of the PLMTRACK-derived blimp position to the Omni-Star differentially corrected GPS position recorded by the airship. Since this comparison was not part of the MVP test plan, the analyst had to find simultaneous blimp imagery from multiple camera sites before triangulating the blimp's position using the PLMTRACK method. Since this was fortuitous data, some pair-wise combinations of camera sites provided little or no useful blimp imagery. Only one camera pair collected simultaneous blimp imagery on 21 May 1997. Every pairing of cameras collected some simultaneous blimp imagery on 23 May 1997.

We use four plots for each pair of cameras to show the difference between the blimp's GPS and PLMTRACK positions. In the first plot, we show the Cartesian positions derived by both methods along with the positions of the imagery-sites. The second plot reports the difference between the two methods for X-, Y-, and Z-axes (i.e., N/S, E/W, and vertical) against time of day (GMT). It is apparent from the first Cartesian plot that the viewing angles must change dramatically as the blimp moves relative to the camera sites. Therefore, the next two plots for each camera pair report the difference between the two methods against two angular criteria. The third plot reports the difference against Ac2c1n (defined in Appendix A). When Ac2c1n is 0°, the second camera of the pair has an orthogonal view of the blimp relative to the first camera. When Ac2c1n is –90°, both cameras are viewing the blimp along the same azimuth but from different distances. When Ac2c1n is +90°, the cameras have opposite azimuths to the blimp. The fourth, and final, plot reports the positional errors against the elevation (EL) difference between the two camera sites. When the EL difference is positive, the first camera of the pair has a steeper elevation angle to the blimp than the second camera. Review of these plots reveals no consistent correlation between the angular perspectives and the accuracy of the PLMTRACK analysis.

The plots in this appendix and the results in Table B-1 document precise calibration of all scanners during MVP #4. We include 2-sigma values (calculated using sample and population statistics) for

Table B-1. Statistics for the Differences Between PLMTRACK and GPS Positions

Date	Camera 1	Camera 2	2s(XY)	2s(X)	2s(Y)	2s(Z)	HDOP
21-May-97	3	4	67	30	96	42	1.1-1.2
23-May-97	1	2	90	98	93	35	1.1-1.6
23-May-97	1	3	86	107	58	19	1.1-2.0
23-May-97	1	4	72	91	64	11	1.0-2.0
23-May-97	2	3	137	116	143	64	0.9-2.0
23-May-97	2	4	91	83	94	18	1.0-2.0
23-May-97	3	4	132	149	63	26	1.3-1.6
Average	All	All	96	96	87	31	#N/A
Stdev	All	All	25	22	29	17	#N/A

55

the differences between the PLMTRACK and GPS data. We report values separately for horizontal (combined XY) and vertical (Z) as well as for X and Y (i.e., N/S and E/W). The last two rows in Table B-1 provide the average and standard deviation for the 2-sigma (2s) values included in the table. We included only the sample variance (i.e., 2s(s) = 2s in the table) due to the small number of data points. Regular GPS accuracy is 100 m for the horizontal axes (i.e., the 2-sigma for combined X,Y) and 250 m for the vertical axis (i.e., the 2-sigma for Z). For the Omni-Star differentially corrected receiver, the 2-sigma values are ~1 m for horizontal and ~3 m for vertical. The approximation signs are included since the horizontal dilution of precision (HDOP) recorded by the GPS ranged from 0.9 to 2.0 (i.e., Table B-1), indicating that the GPS errors could be as much as a factor of 2 worse than nominal. The 2-sigma (2s) values in Table B-1 are comparable to regular GPS accuracy for the horizontal axes and better, by a factor of almost 10, than regular GPS accuracy for the vertical. Since the analyst could not identify the horizontal position of the GPS antennae as well as its' vertical position, the larger PLMTRACK errors for the horizontal position may be due to this experimental uncertainty.
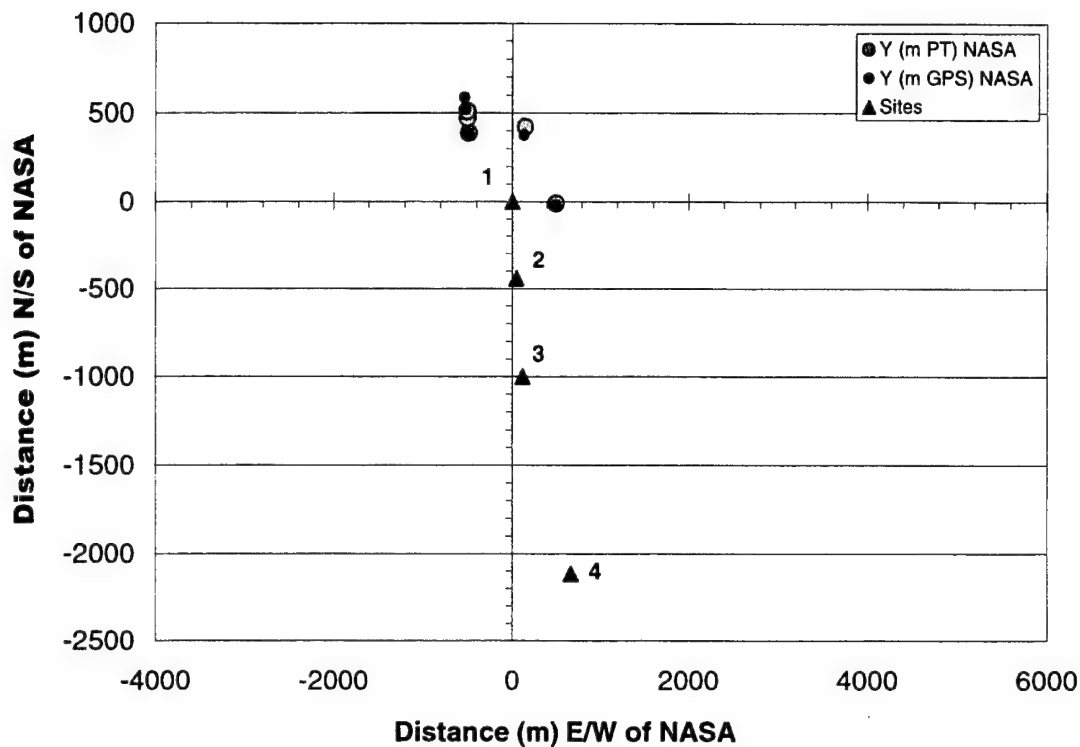
Figure B-1. Cartesian plot for 21 May '97 PLMTRACK accuracy by sites 3 and 4.
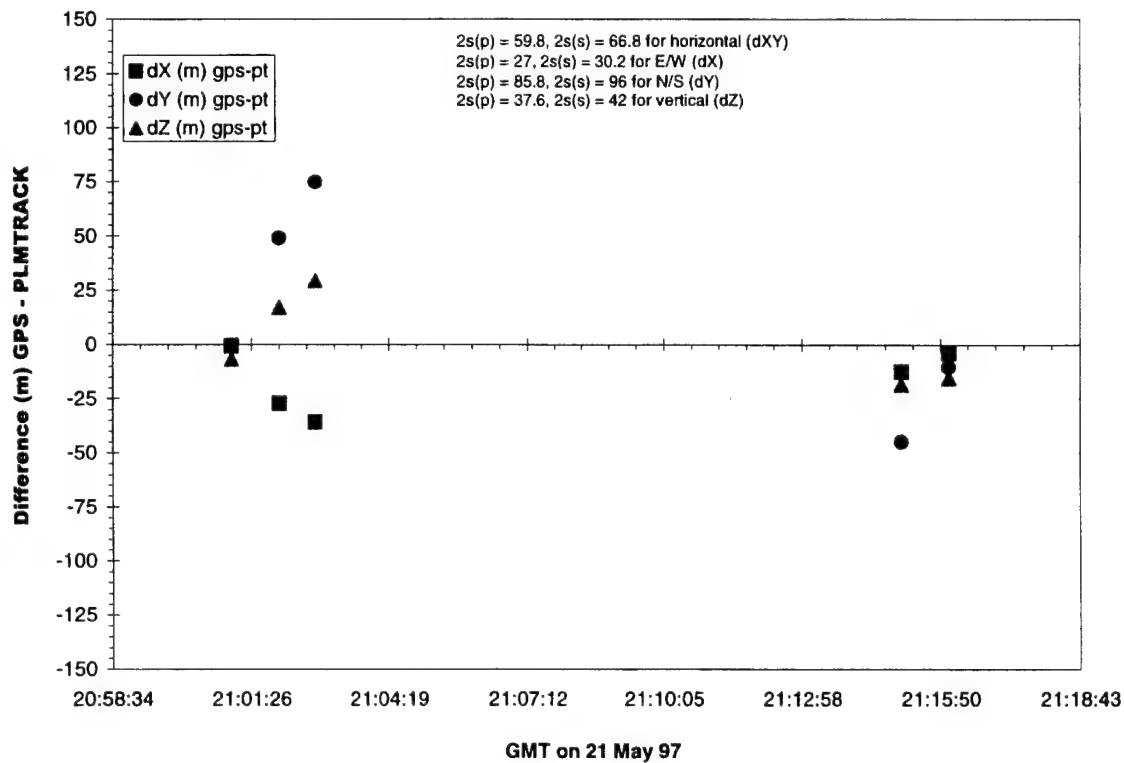
Figure B-2. Time plot for 21 May '97 PLMTRACK accuracy by sites 3 and 4.
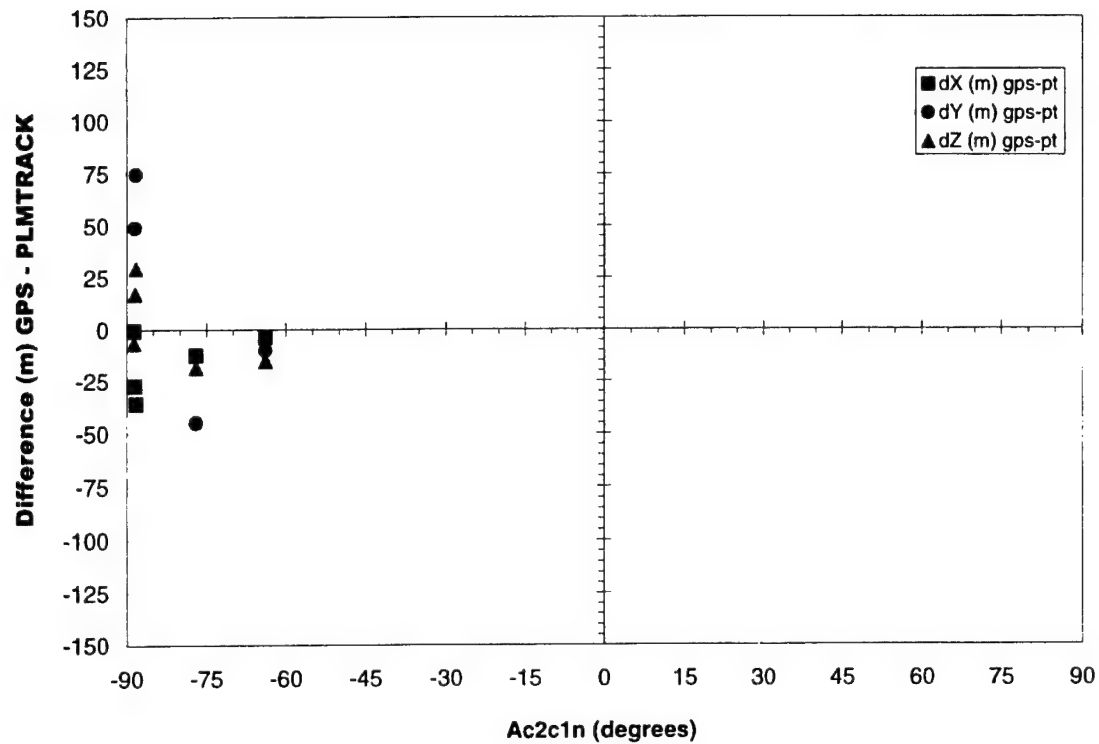
Figure B-3. Ac2c1n plot for 21 May '97 PLMTRACK accuracy by sites 3 and 4.
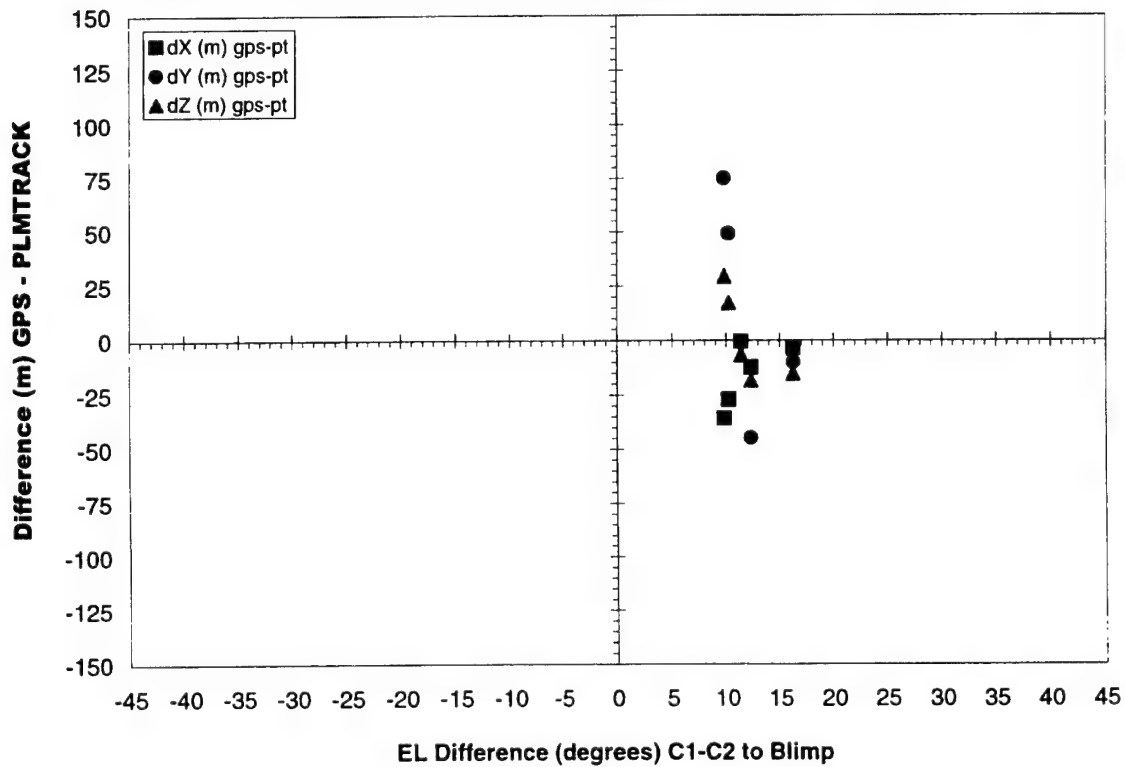
Figure B-4. EL difference plot for 21 May '97 PLMTRACK accuracy by sites 3 and 4.

58
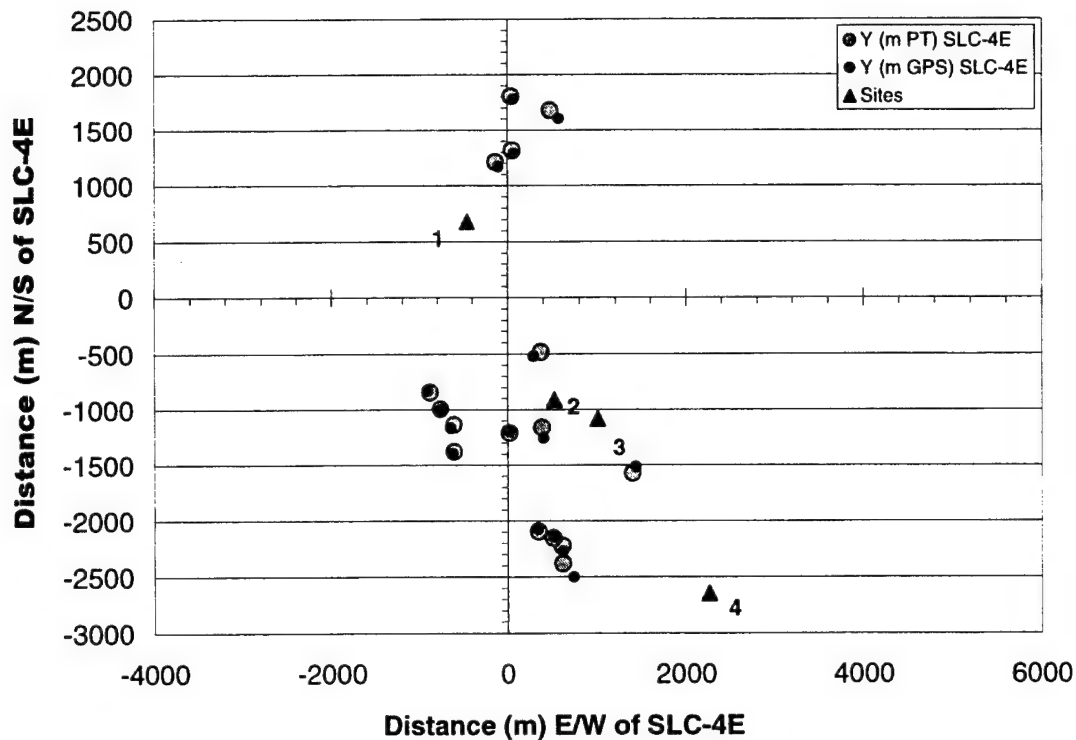
Figure B-5. Cartesian plot for 23 May '97 PLMTRACK accuracy by sites 1 and 2.
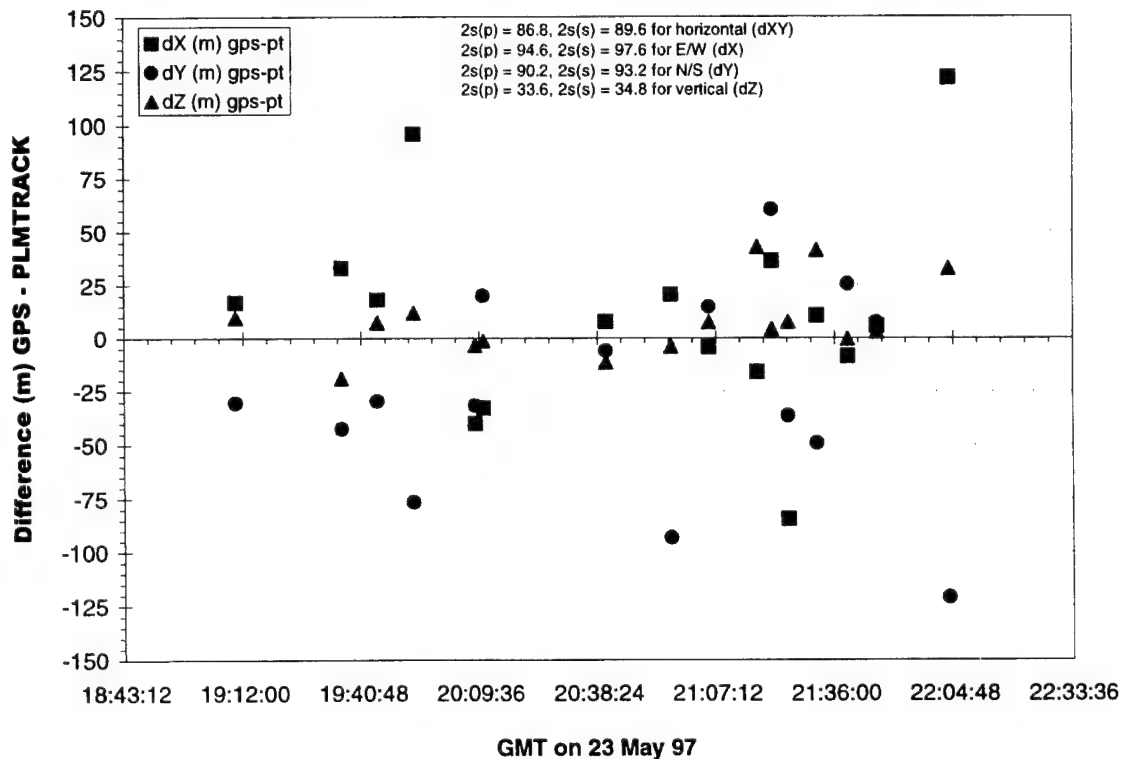
Figure B-6. Time plot for 23 May '97 PLMTRACK accuracy by sites 1 and 2.
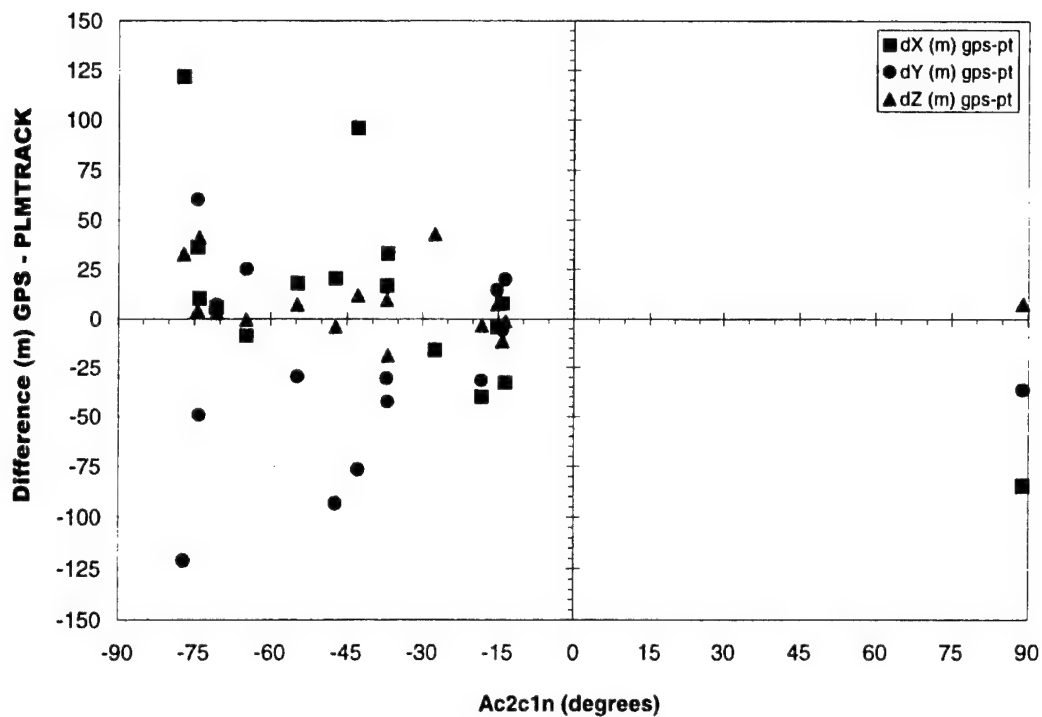
Figure B-7. Ac2c1n plot for 23 May '97 PLMTRACK accuracy by sites 1 and 2.
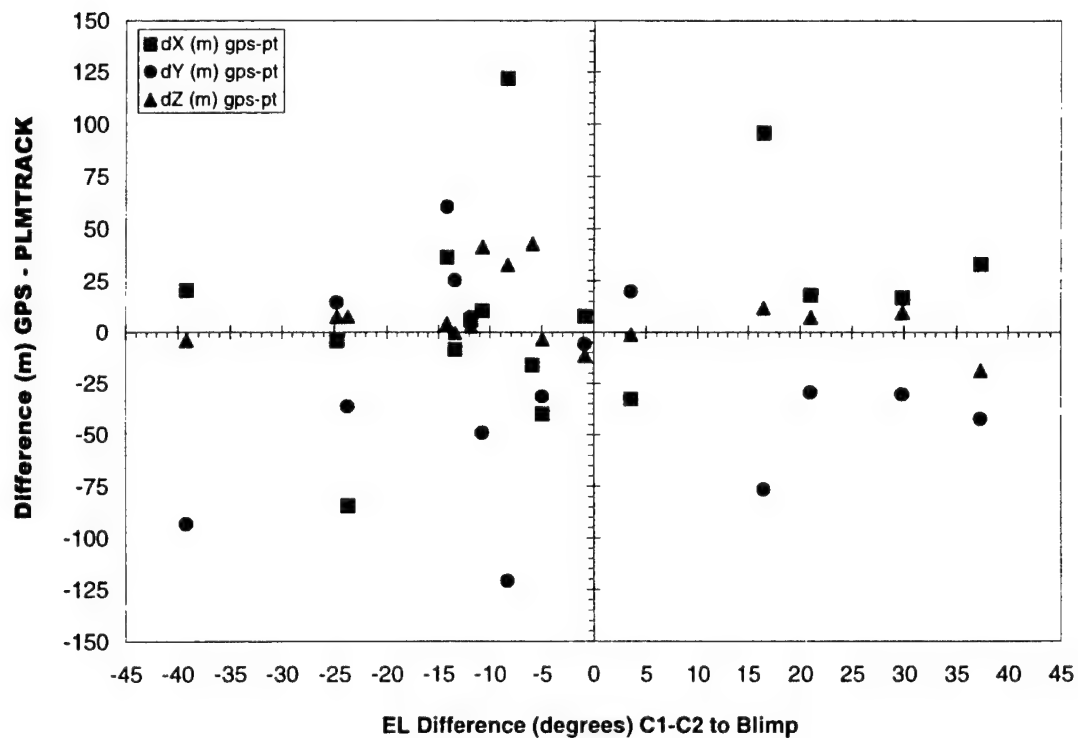
Figure B-8. EL difference plot for 23 May '97 PLMTRACK accuracy by sites 1 and 2.

60
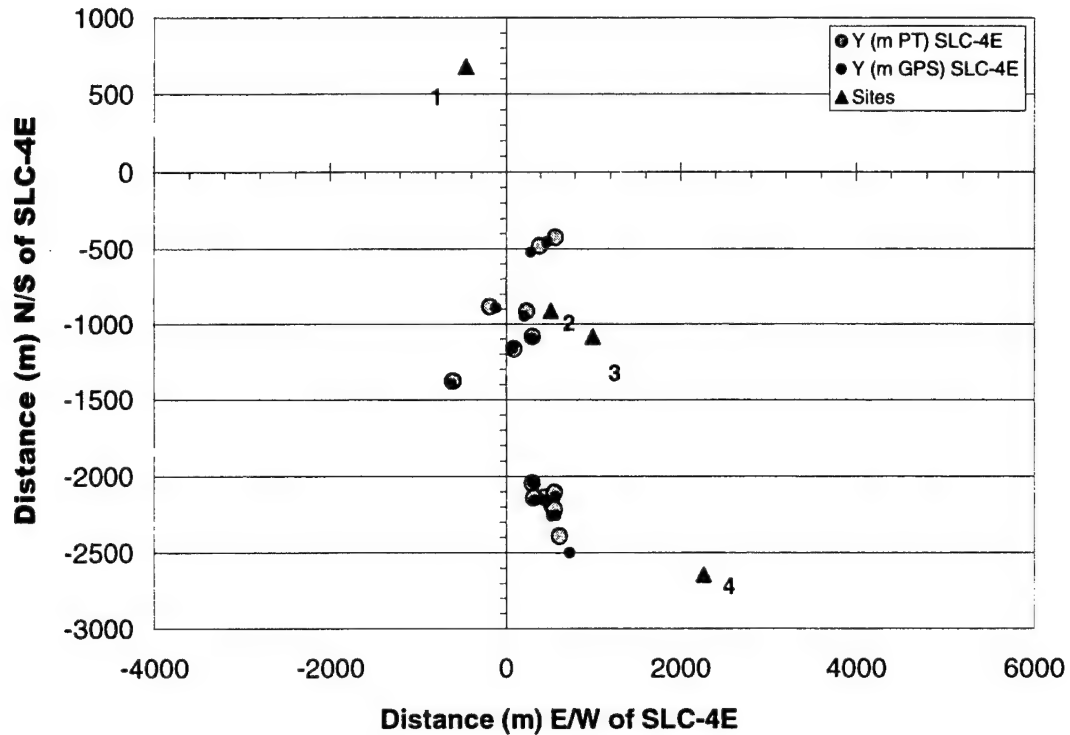
Figure B-9. Cartesian plot for 23 May '97 PLMTRACK accuracy by sites 1 and 3.
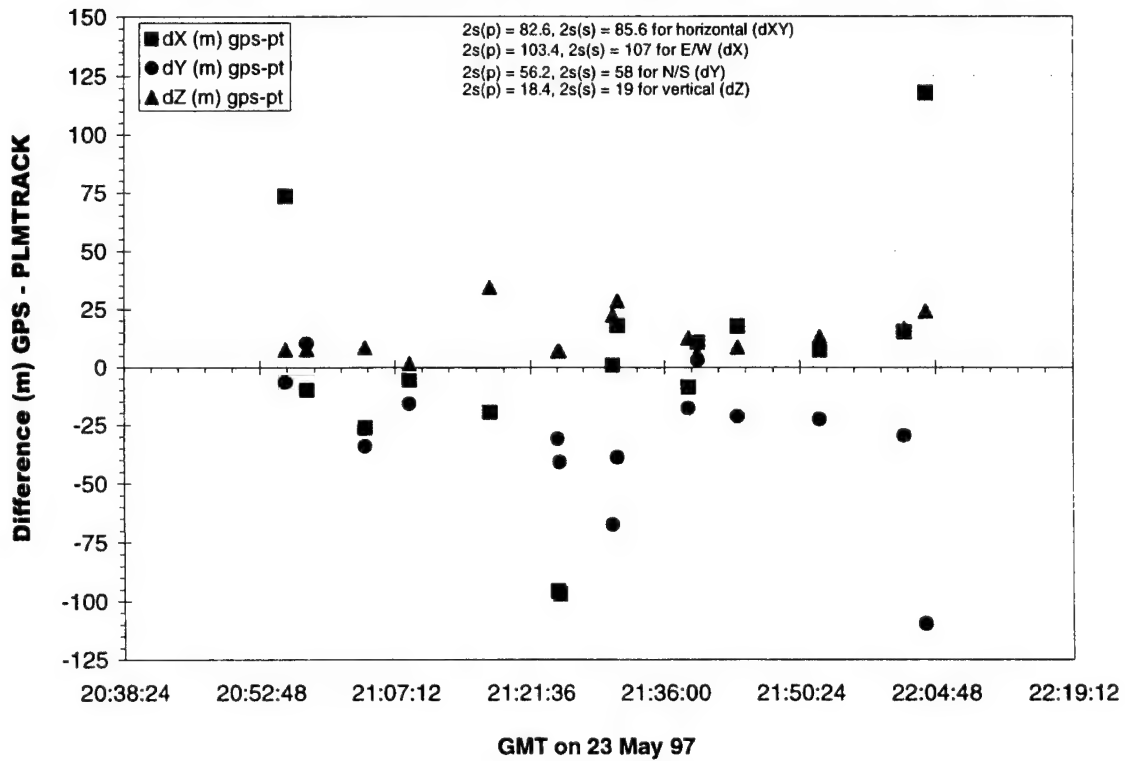
Figure B-10. Time plot for 23 May '97 PLMTRACK accuracy by sites 1 and 3.
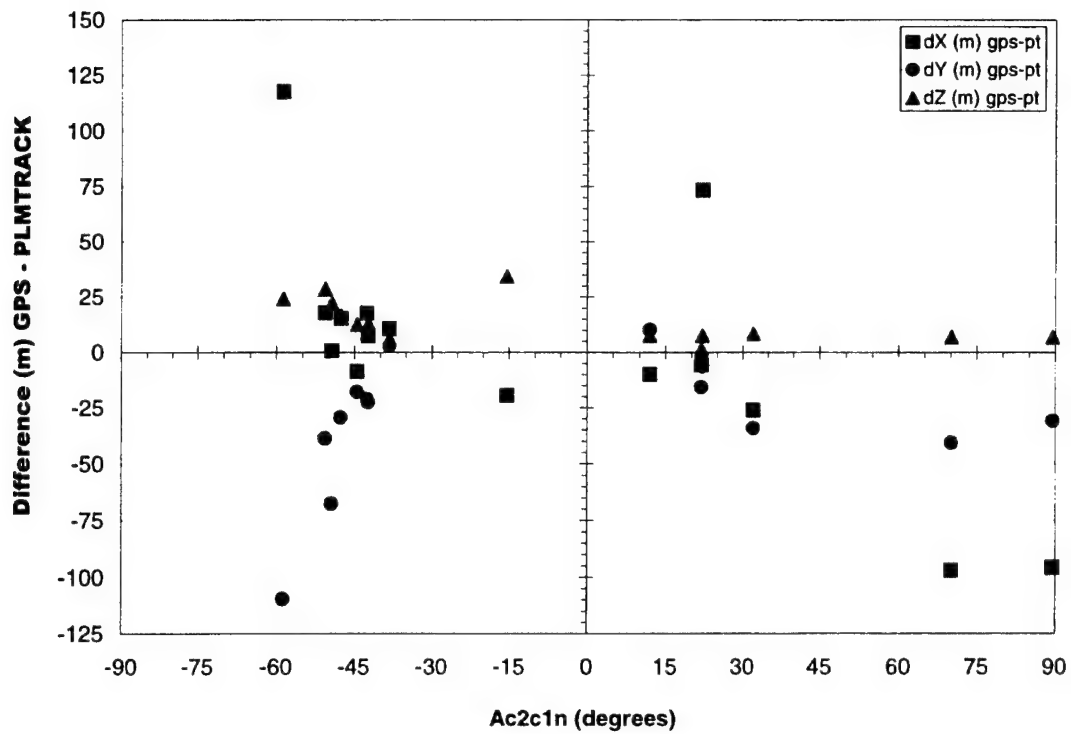
Figure B-11. Ac2c1n plot for 23 May '97 PLMTRACK accuracy by sites 1 and 3.
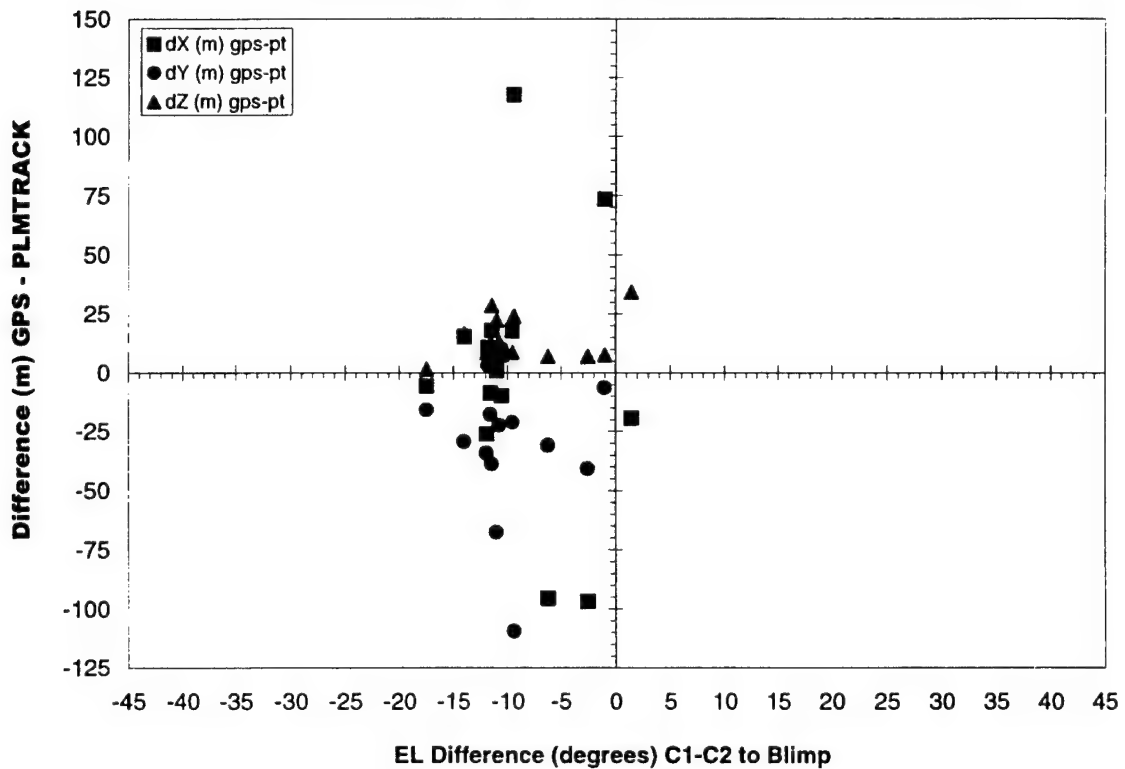
Figure B-12. EL difference plot for 23 May '97 PLMTRACK accuracy by sites 1 and 3.
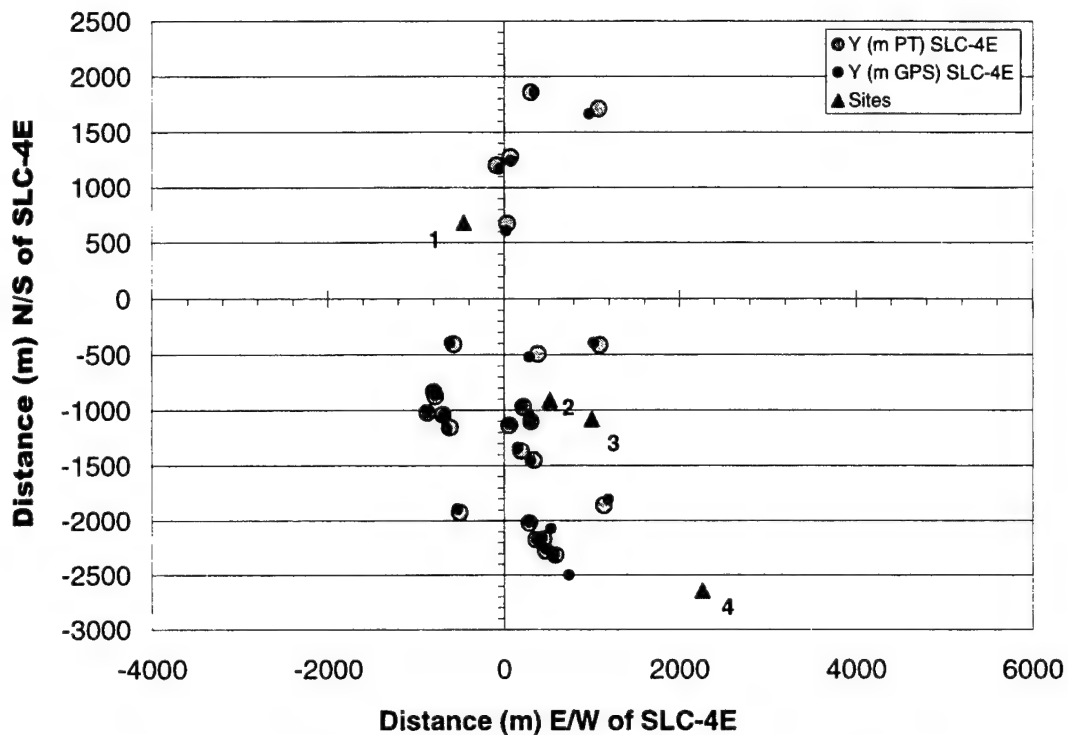
Figure B-13. Cartesian plot for 23 May '97 PLMTRACK accuracy by sites 1 and 4.
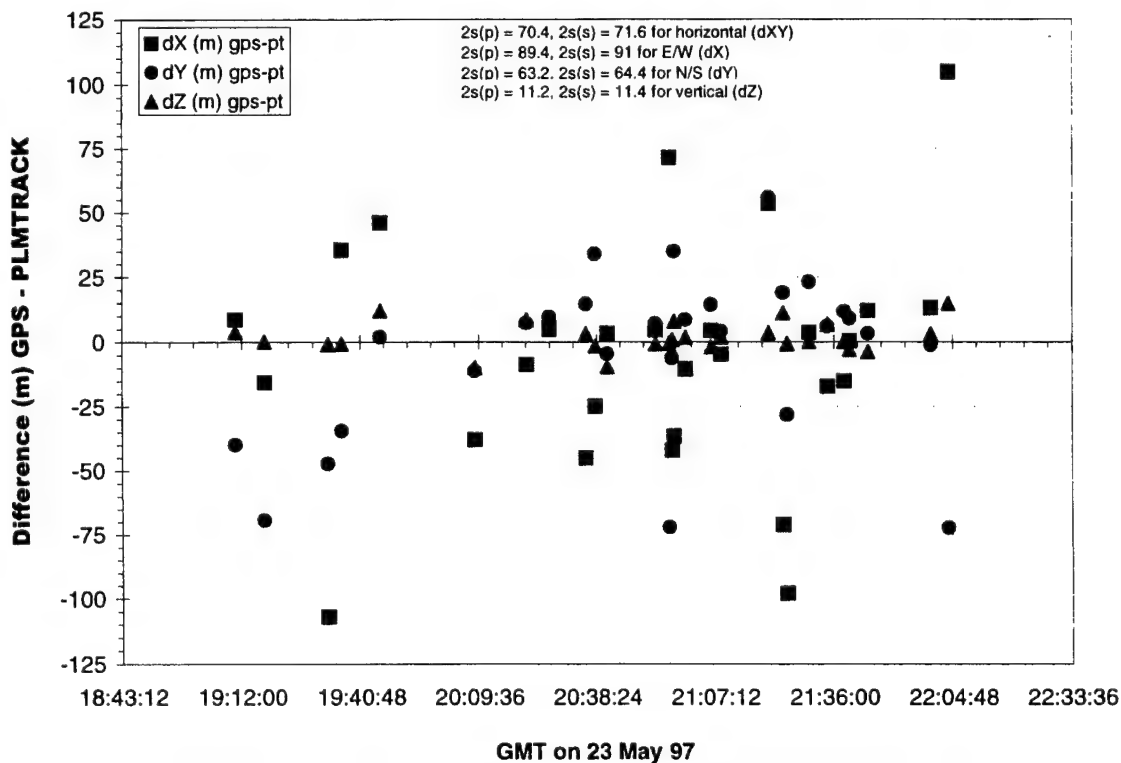
Figure B-14. Time plot for 23 May '97 PLMTRACK accuracy by sites 1 and 4.
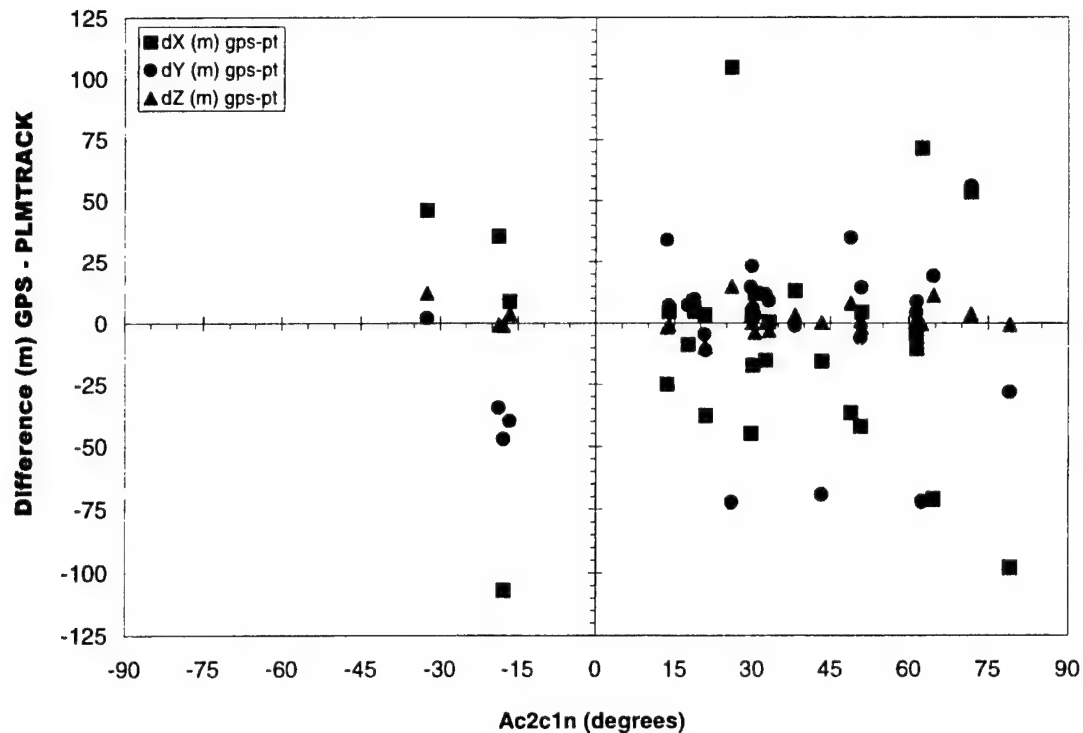
Figure B-15. Ac2c1n plot for 23 May '97 PLMTRACK accuracy by sites 1 and 4.
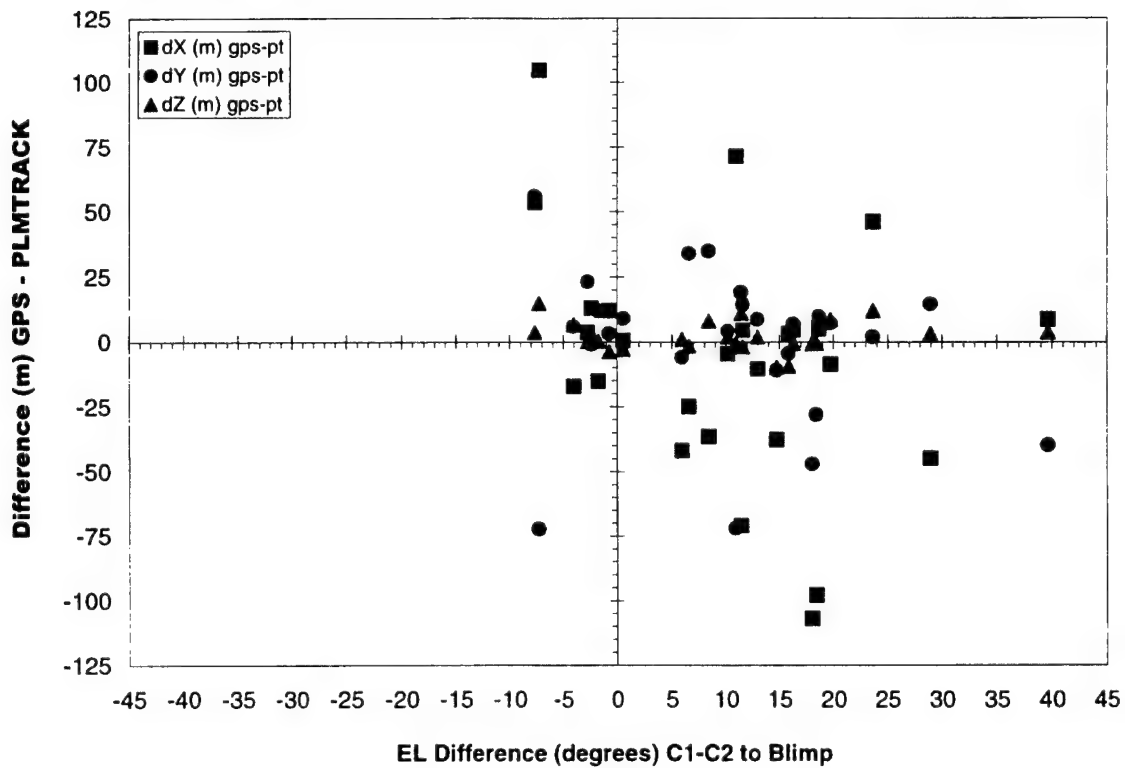
Figure B-16. EL difference plot for 23 May '97 PLMTRACK accuracy by sites 1 and 4.
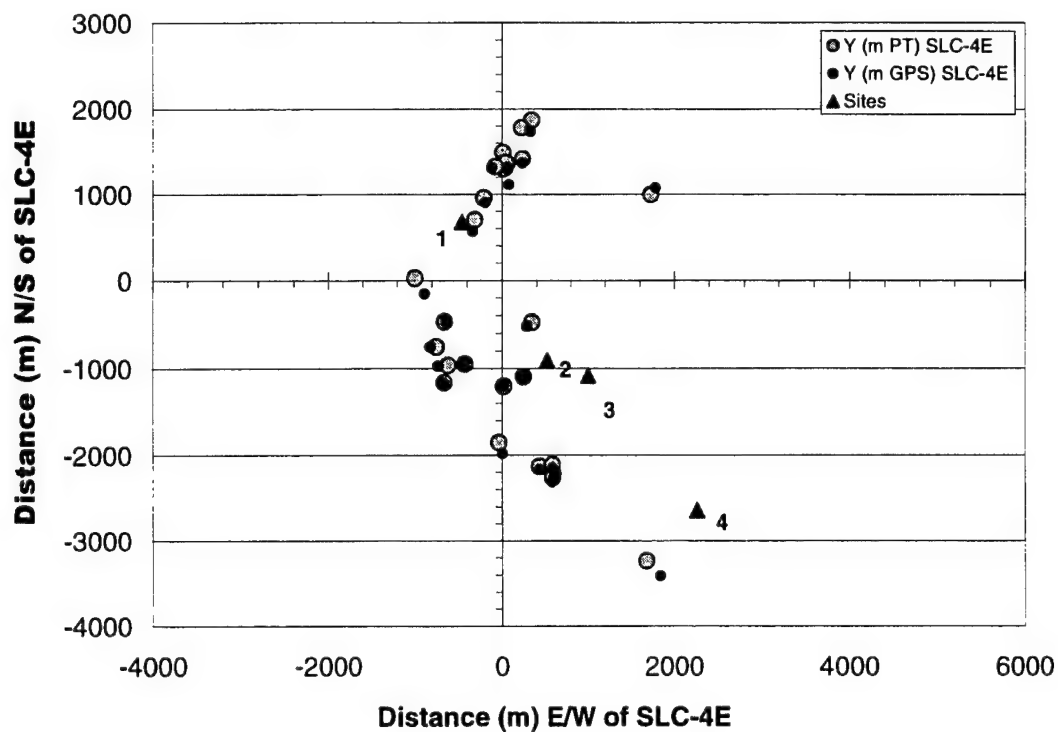
Figure B-17. Cartesian plot for 23 May '97 PLMTRACK accuracy by sites 2 and 3.
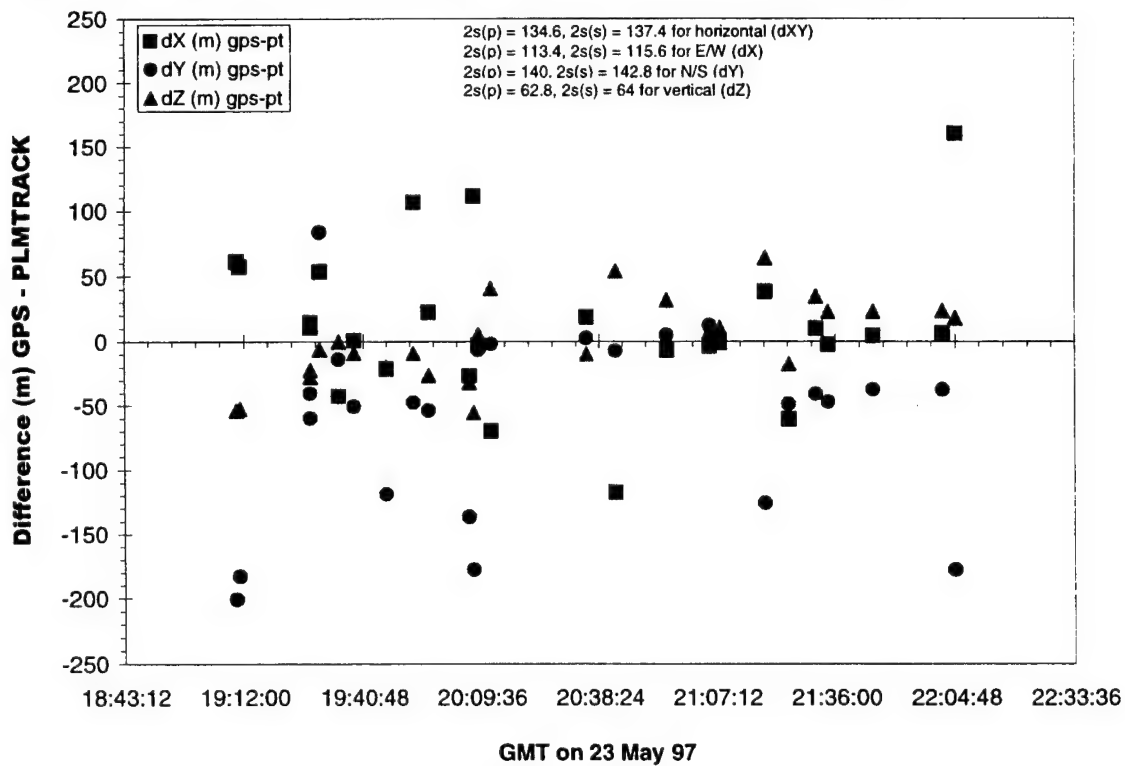
Figure B-18. Time plot for 23 May '97 PLMTRACK accuracy by sites 2 and 3.

65
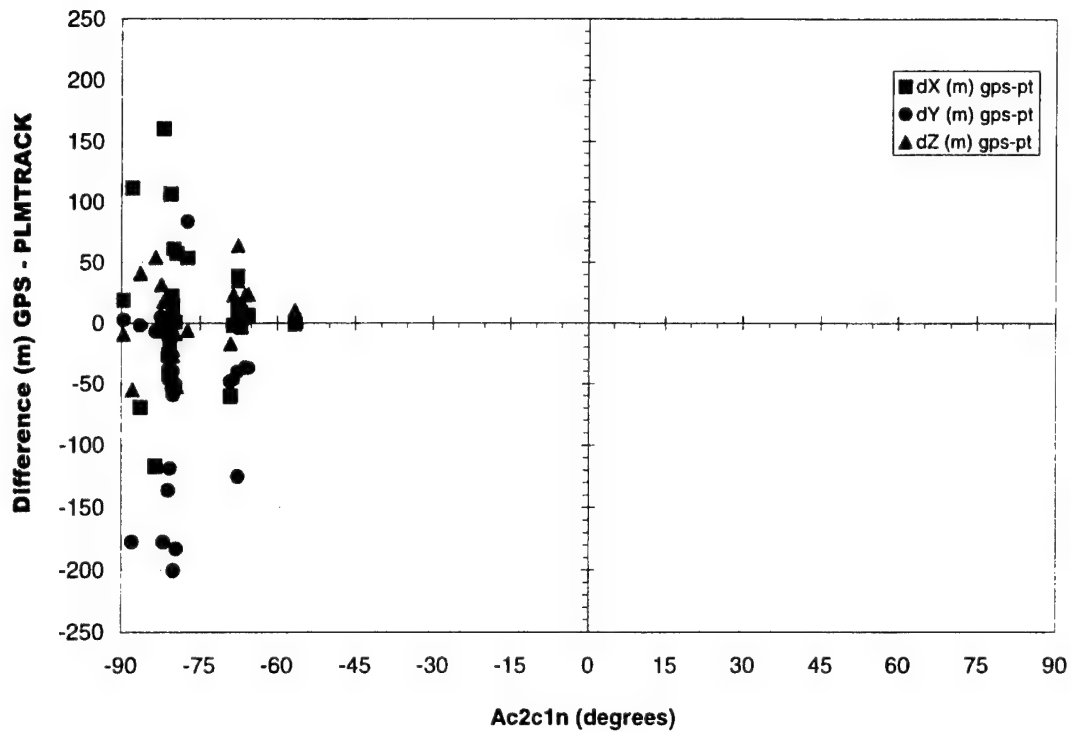
Figure B-19. Ac2c1n plot for 23 May '97 PLMTRACK accuracy by sites 2 and 3.
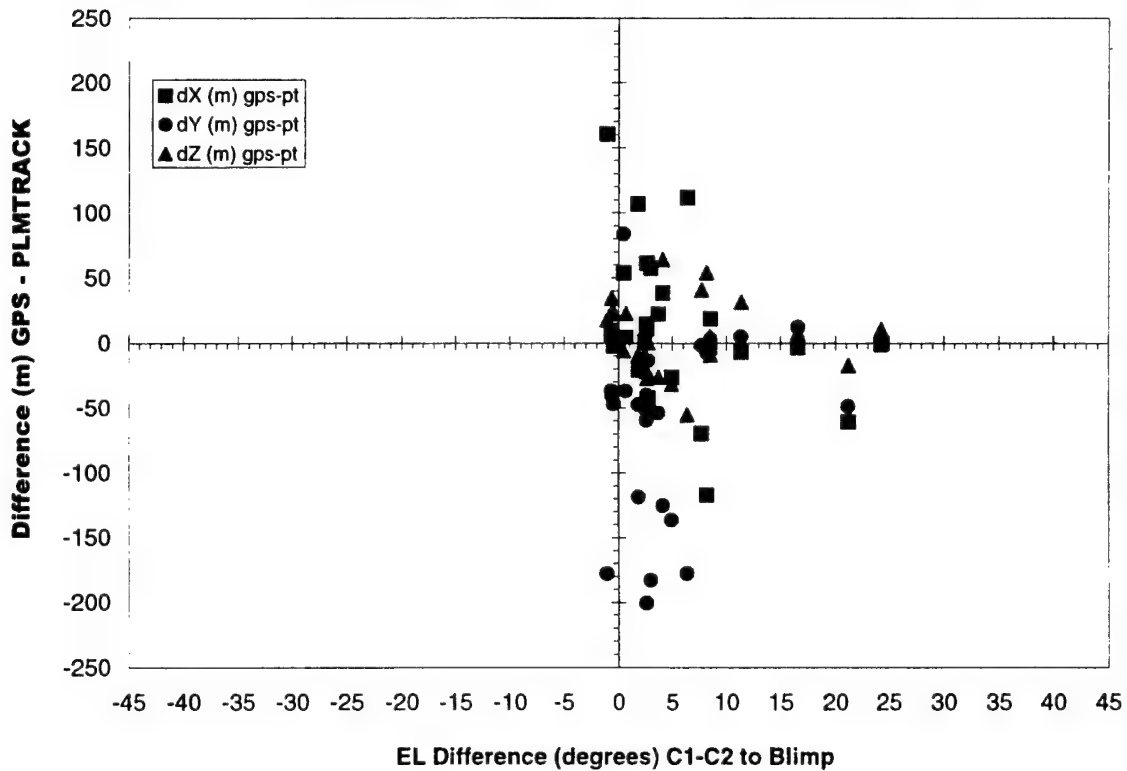
Figure B-20. EL difference plot for 23 May '97 PLMTRACK accuracy by sites 2 and 3.

66
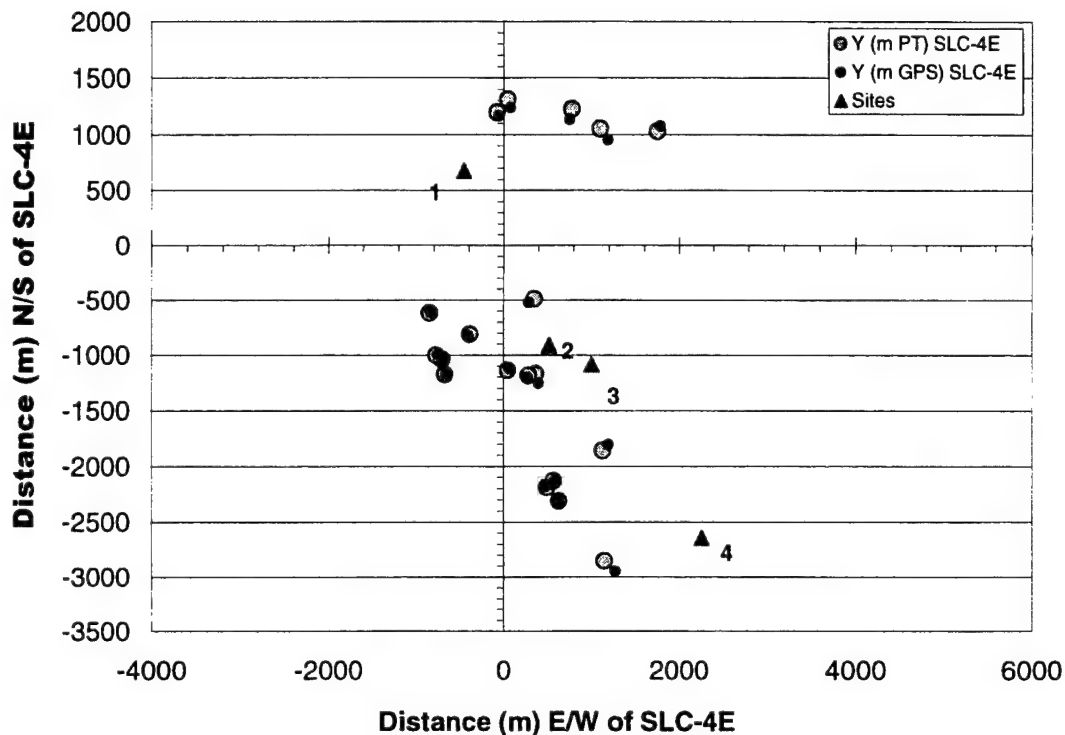
Figure B-21. Cartesian plot for 23 May '97 PLMTRACK accuracy by sites 2 and 4.
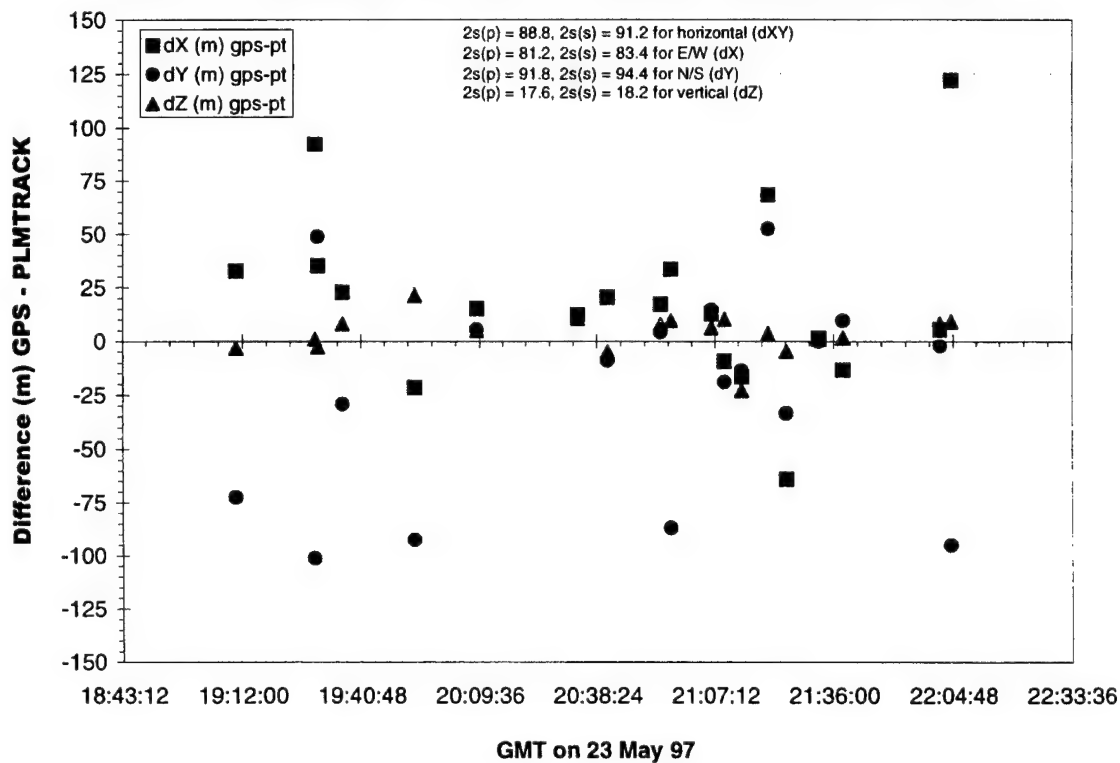
Figure B-22. Time plot for 23 May '97 PLMTRACK accuracy by sites 2 and 4.

67
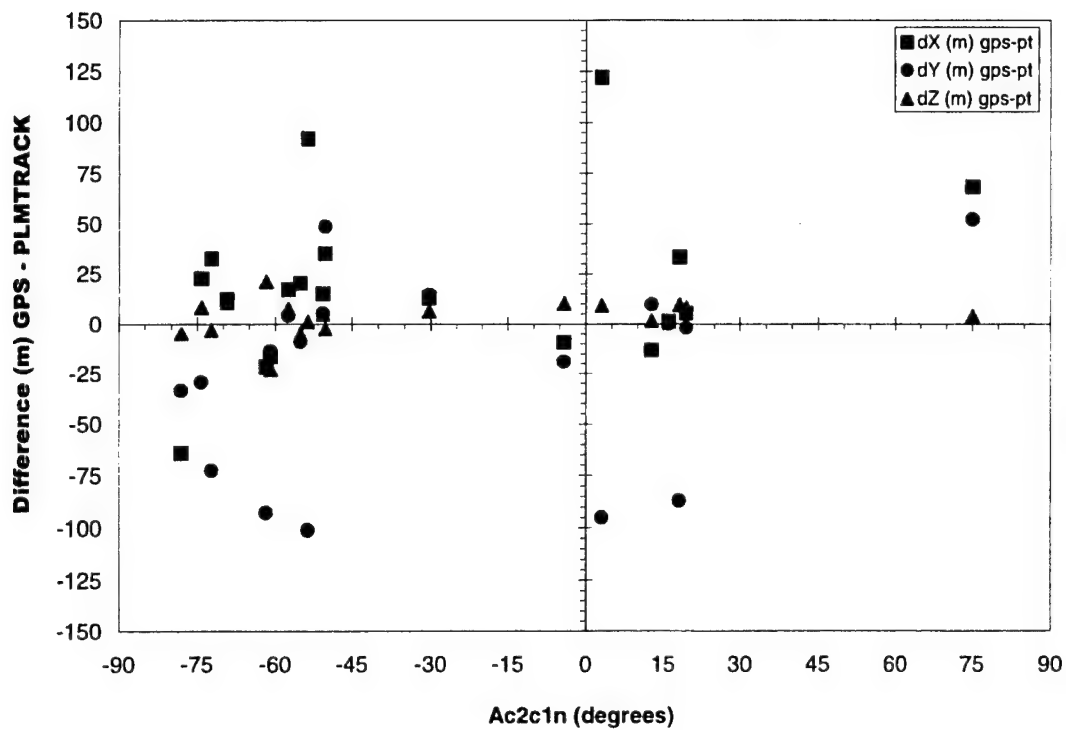
Figure B-23. Ac2c1n plot for 23 May '97 PLMTRACK accuracy by sites 2 and 4.
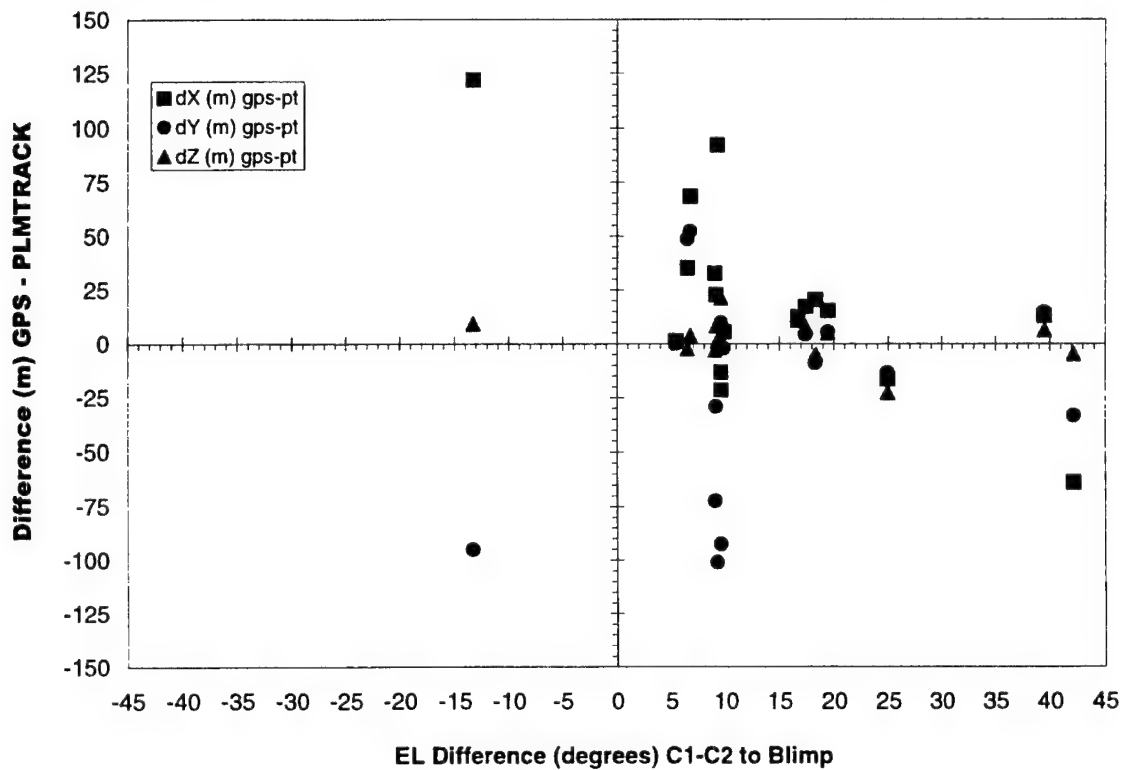
Figure B-24. EL difference plot for 23 May '97 PLMTRACK accuracy by sites 2 and 4.

68
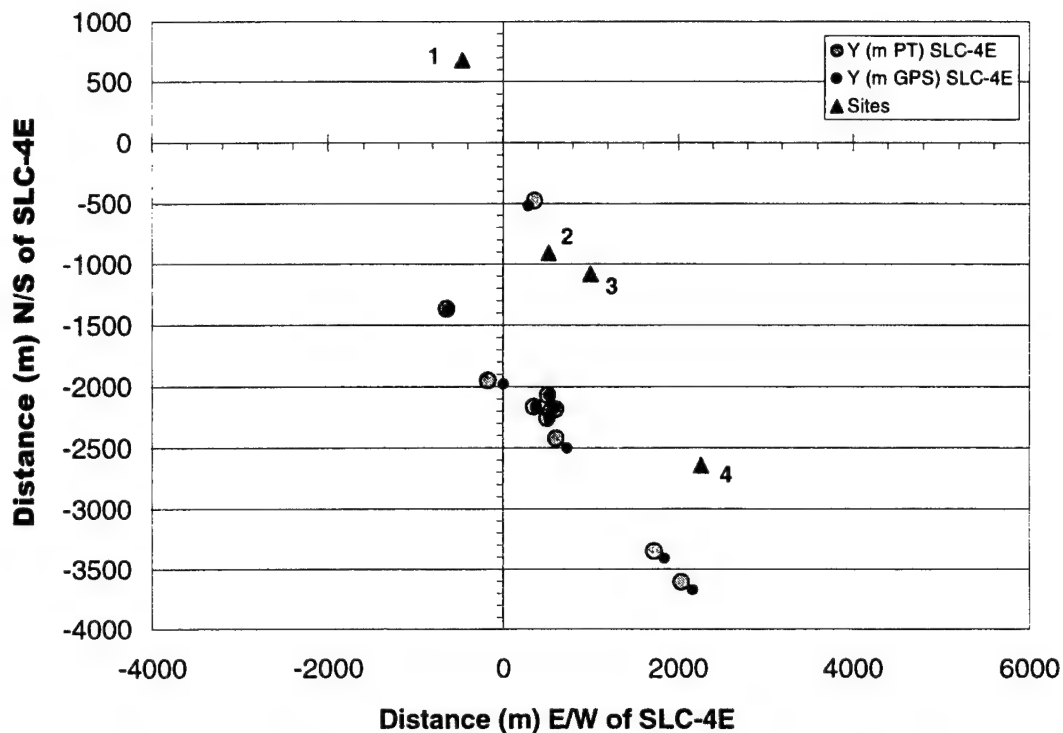
Figure B-25. Cartesian plot for 23 May '97 PLMTRACK accuracy by sites 3 and 4.
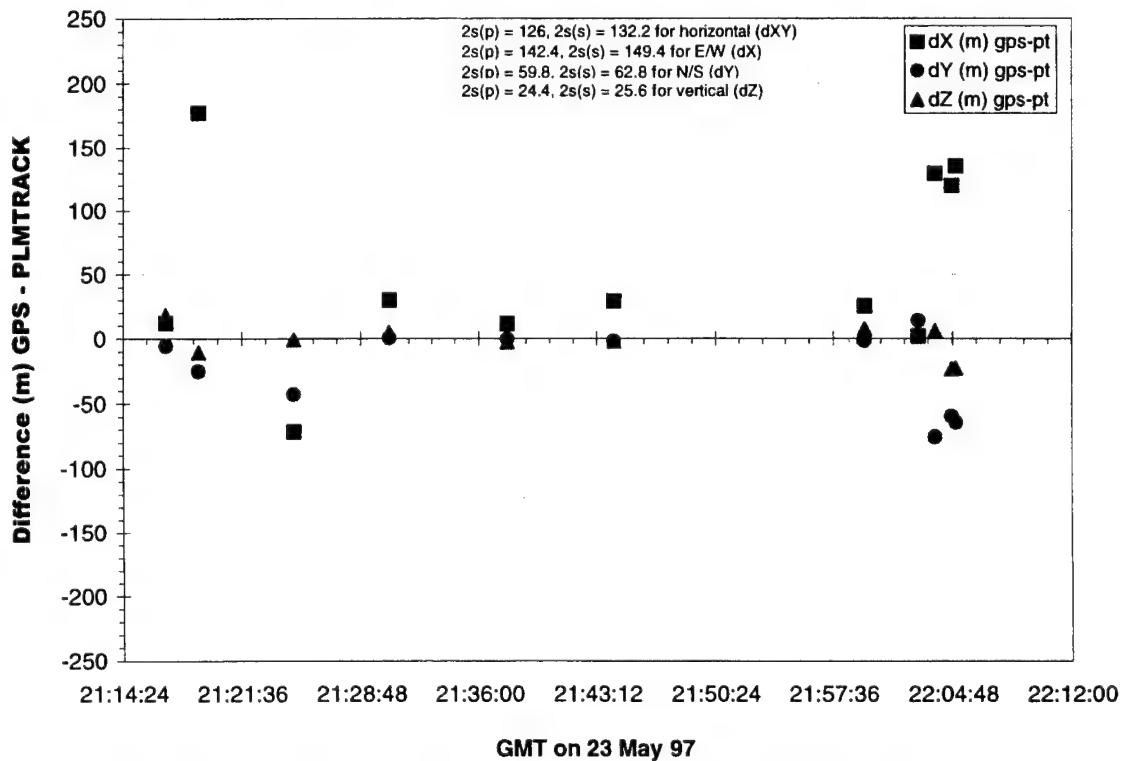
Figure B-26. Time plot for 23 May '97 PLMTRACK accuracy by sites 3 and 4.
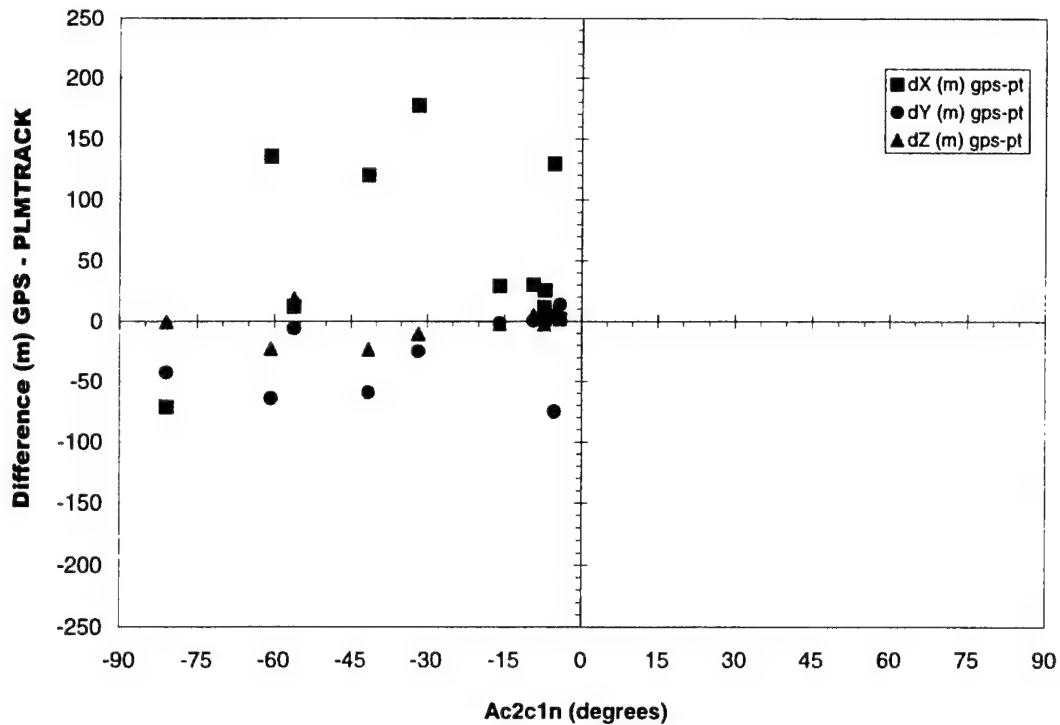
Figure B-27. Ac2c1n plot for 23 May '97 PLMTRACK accuracy by sites 3 and 4.
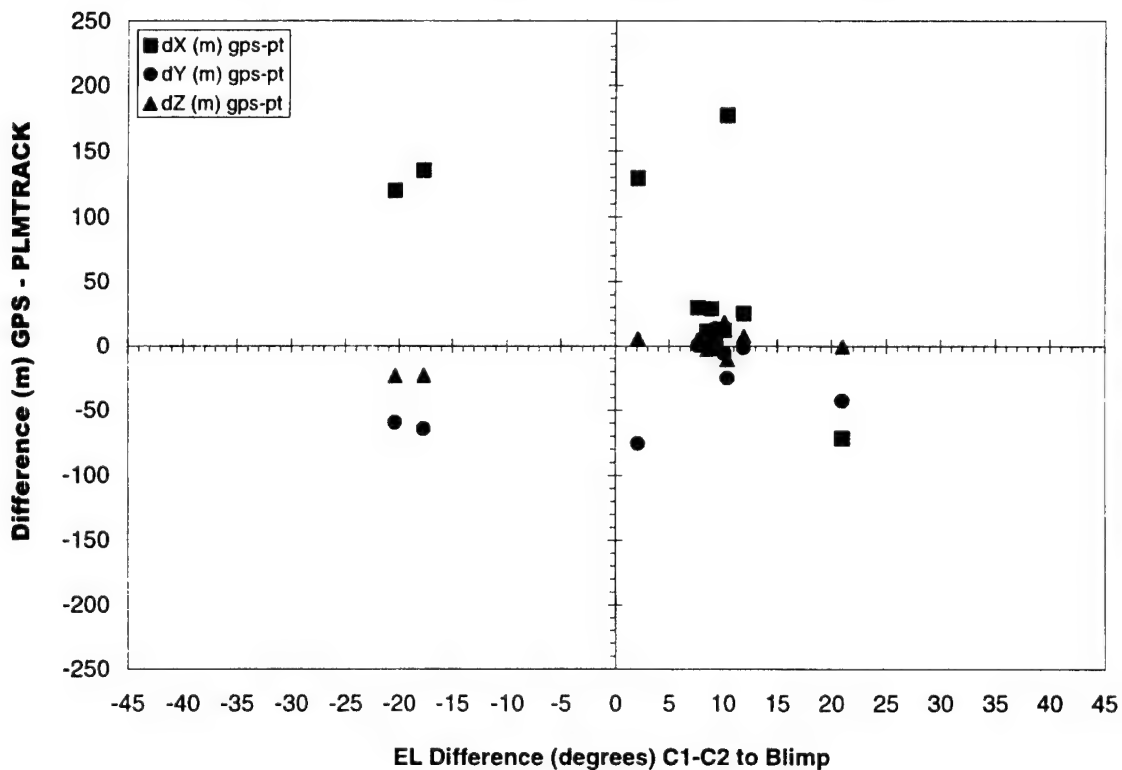
Figure B-28. EL difference plot for 23 May '97 PLMTRACK accuracy by sites 3 and 4.

70

Appendix C-Sensitivity Analysis of Expansion Rate Data

Results plotted within this appendix document that the imagery-derived expansion rates and the observed puff extent are insensitive to most of the experimental variables. We use imagery of two puffs to illustrate this fact. The two puffs are the first puffs from both the 21st and the 23rd of May 1997. Several of the experimental variables are interdependent. These interdependent variables include the slant range (SR) from the camera to the puff's middle, the area per pixel (APP) within the image for the current SR, the elevation (EL) from the camera to the puff's middle, and the background radiance (BR) from the sky at the current EL. Even though the camera's field of view (FOV) remains constant, the APP, SR, EL, and BR change as the puff moves relative to each camera site. All of the imagery-derived puff extent data fall on the same expansion rate curve, even though these linked parameters vary dramatically for the data included in these plots. Since the expansion rate curve is a plot of the puff's extent (i.e., a diameter viewed from a particular perspective) against time (or distance), these plots also show that the imagery-derived extent is not sensitive to these experimental variables over their operational ranges.

Figures C-1 through C-4 are data plots for series 1 puff 1 from 21 May 1997 and document a decrease in the number of plotted data points as the APP filter is reduced by factors of 2, from 48 to 6 m^2 per pixel. The slope of the plot of horizontal diameter against time remains constant even though the value of the APP filter is changed dramatically in this series. This result illustrates that all of the data fall on the same line independent of the values of any of the variables linked to the APP. The slope of the plot of diameter against time is the crosswind expansion rate in these figures since the tilt angle is 90° ±10°.

Figures C-5 through C-8 are data plots for series 1 puff 1 from 23 May 1997 and document a decrease in the number of plotted data points as the APP filter is reduced from 102 to 20 m^2 per pixel. The slope of the plot of horizontal diameter against time remains constant even though the value of the APP filter is changed dramatically in this series. This result also illustrates that all of the data fall on the same line independent of the values of any of the variables linked to the APP. The slope of the plot of diameter against time is nearly the crosswind expansion rate since the tilt angle is 70° ±20°.

The plots in this appendix show trends representative of the MVP #4 imagery-derived puff data. There is typically greater scatter in the data derived from poorer resolution data (i.e., data with larger values of APP); however these data fall along the same expansion rate curve as the less scattered higher resolution data (i.e., data with smaller values of APP). Since the SR increases, the EL decreases, and the BR increases as the resolution degrades (i.e., APP increases), these plots document that the imagery-derived extent of the puff is not sensitive to any of these linked experimental variables over their operational ranges.

71
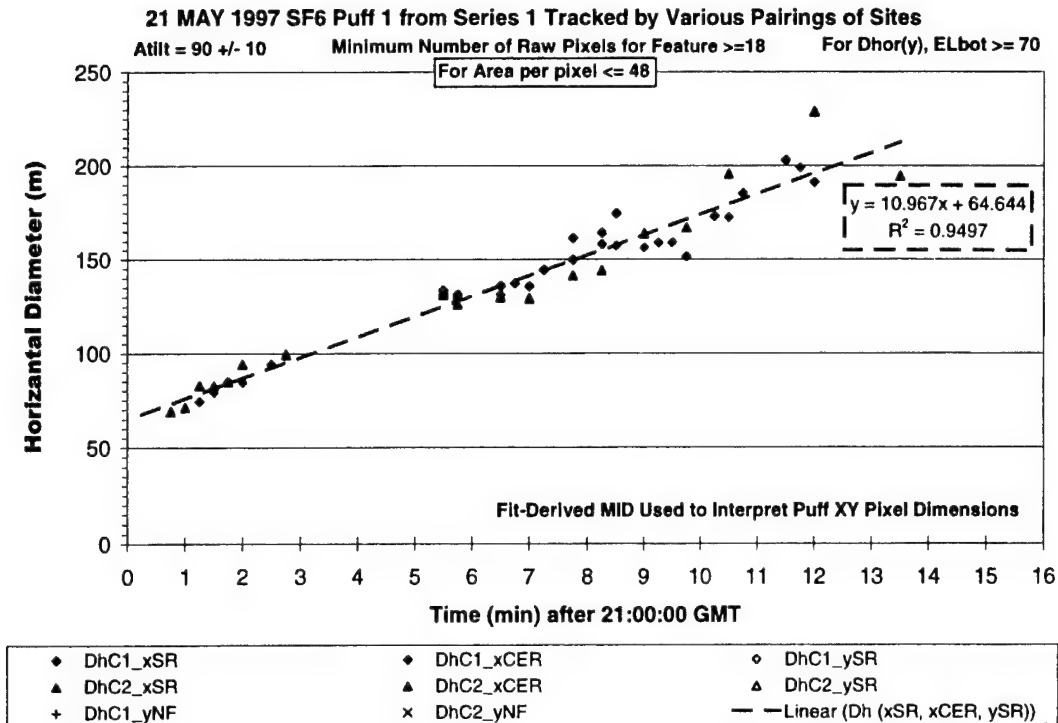
Figure C-1. All data points (APP ≤ 48 m^2 per pixel) for 21 May 1997 S1P1.
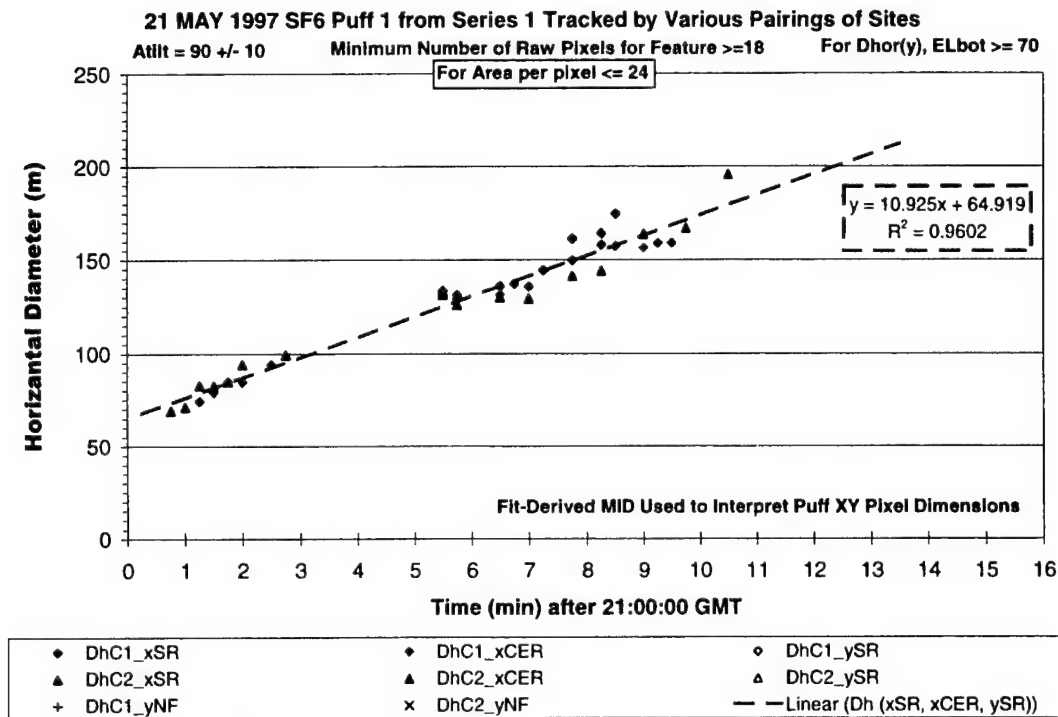
Figure C-2. Fewer data points (APP ≤ 24 m^2 per pixel) for 21 May 1997 S1P1.
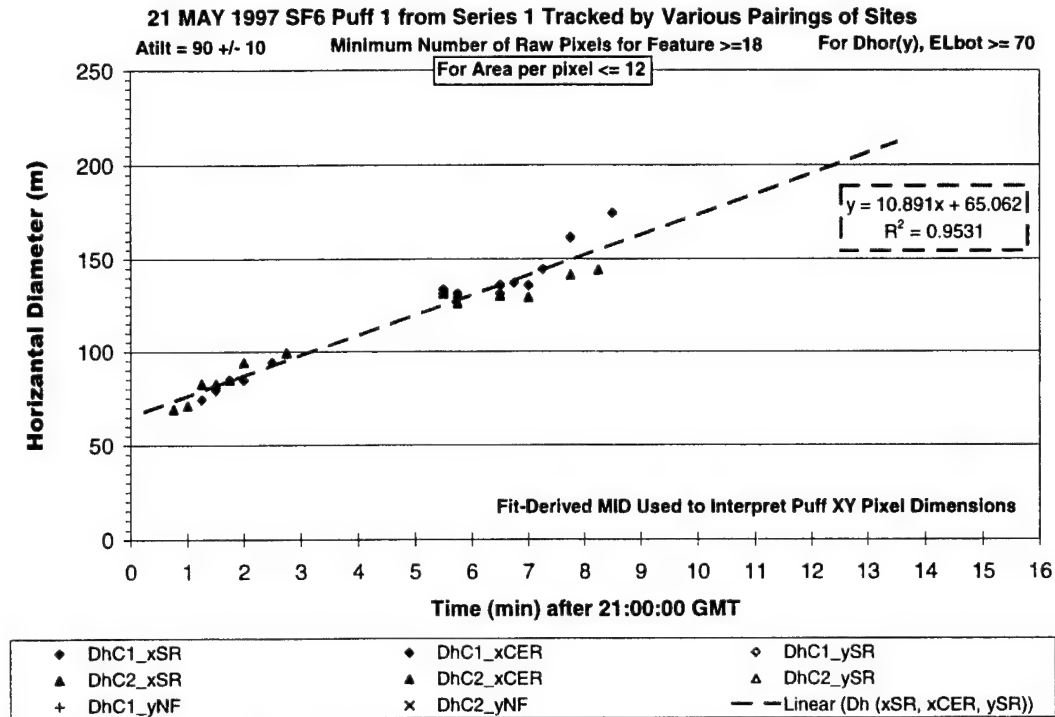
Figure C-3. Even fewer data points (APP $\leq$ 12 m^2 per pixel) for 21 May 1997 S1P1.
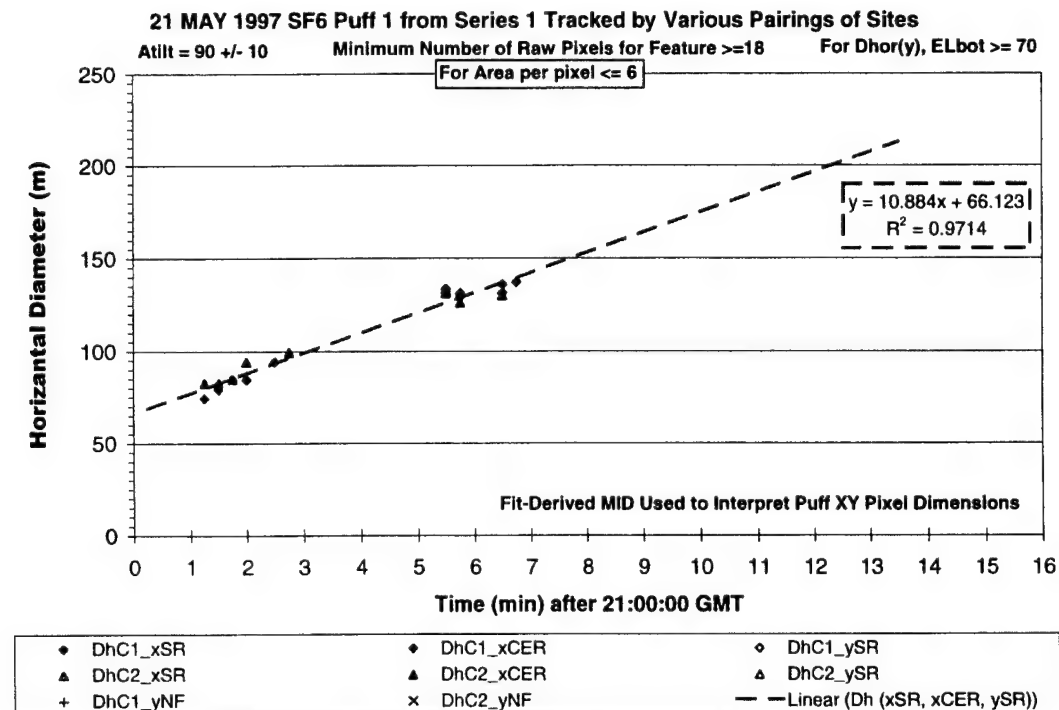
Figure C-4. Fewest data points (APP $\leq$ 6 m^2 per pixel) for 21 May 1997 S1P1.
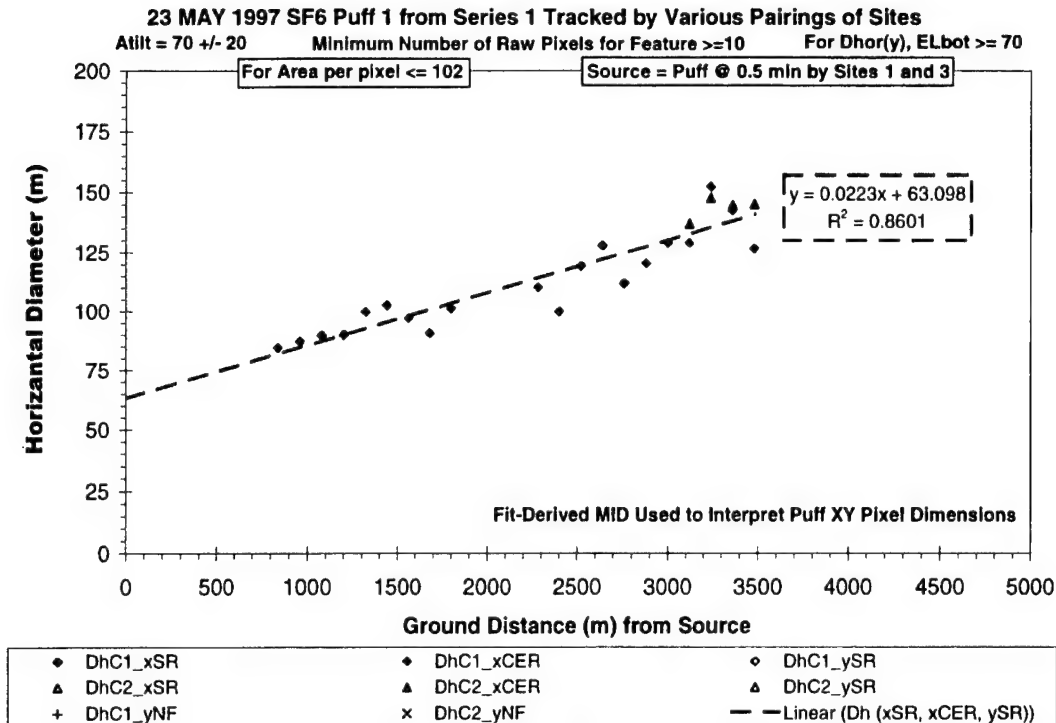
Figure C-5. All data points (APP $\leq$ 102 m^2 per pixel) for 23 May 1997 S1P1.
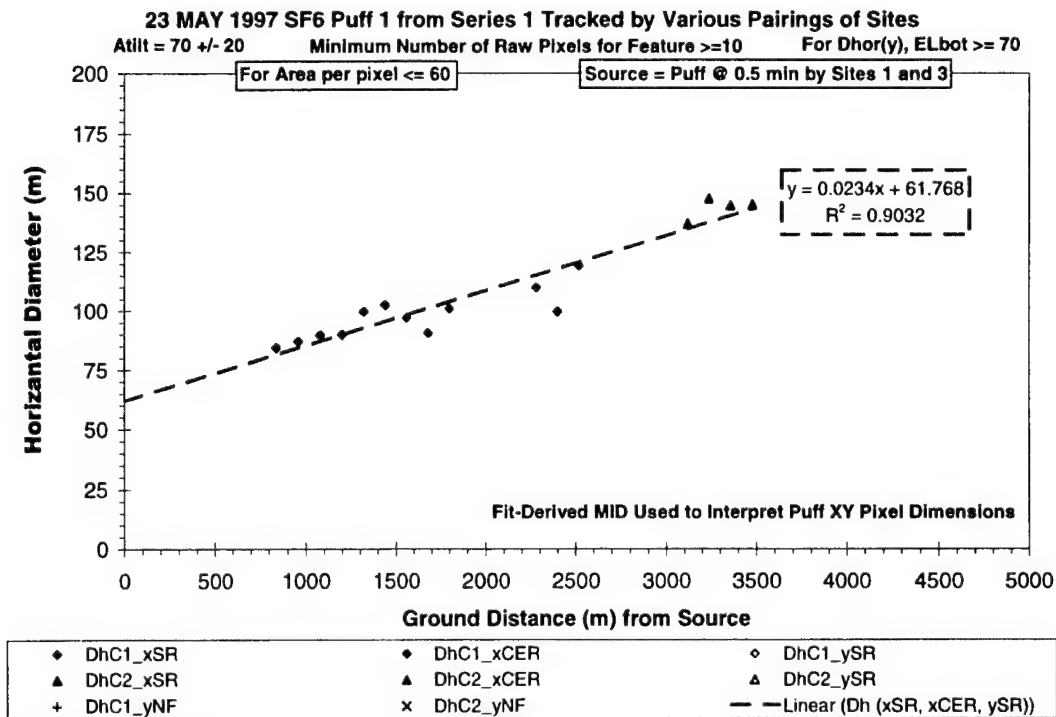
Figure C-6. Fewer data points (APP $\leq$ 60 m^2 per pixel) for 23 May 1997 S1P1.
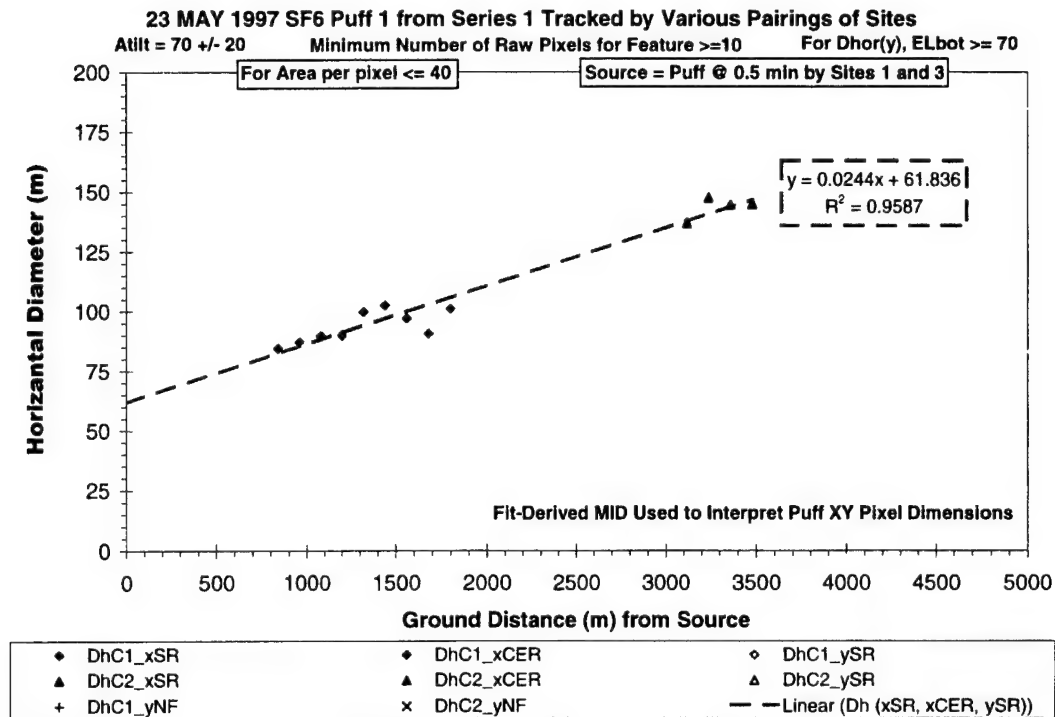
Figure C-7. Even fewer data points (APP $\leq$ 40 m^2 per pixel) for 23 May 1997 S1P1.
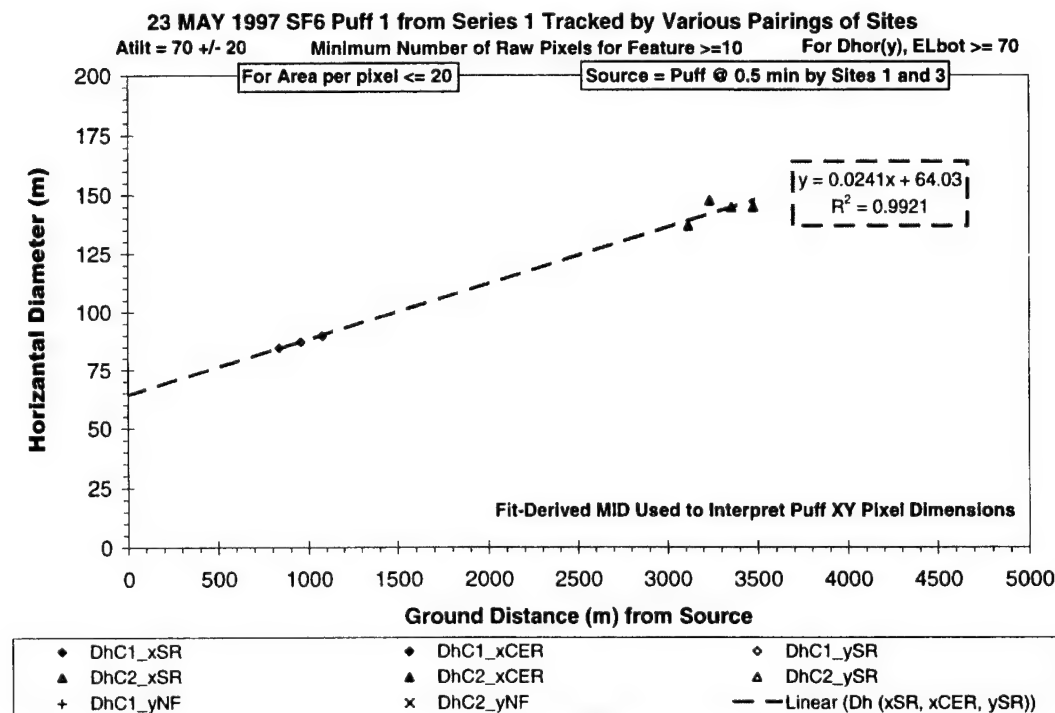
Figure C-8. Fewest data points (APP $\leq$ 20 m^2 per pixel) for 23 May 1997 S1P1.

75

Appendix D-Imagery-Derived Column Density and Puff Mass

Appendix C demonstrated that the observed puff extent was insensitive to most experimental variables. However, Appendix C did not establish that the bulk of the tracer was contained in the observed extent. The Aerospace Corporation developed an algorithm, PLMMASS, which estimates tracer column densities and mass from narrowband IR imagery. For 21 and 23 May 1997, one puff was selected from each series to evaluate the quality of the imagery with the PLMMASS algorithm. This appendix summarizes the results of these analyses.

The results presented in this appendix document that PLMMASS approach works best when there is reasonable contrast for seeing a dilute puff against a fairly uniform background and when the imagery is optimal, having a steep elevation, short slant range, small area per pixel, and low background radiance. PLMMASS underestimates the puff's mass for less than optimal imagery (high values of APP), for broken cloud cover, and for concentrated puffs. The trends included in Appendix C and in this appendix support the assertion that the observed extent of the cloud does include the bulk of the SF_6.

Review of the results from 21 May 1997 reveals that the PLMMASS-derived puff mass increases as the puff dilutes. This result is consistent with underestimation of mass at high column densities and is not consistent with poor edge detection, which should result in worsening mass estimates with further dilution. The PLMMASS-derived results are much more scattered for 23 May than for 21 May 1997. The tracer releases were twice as long (10 s) on 23 May 1997 as on 21 May 1997. If the PLMMASS method is less accurate for higher column densities, the longer releases on 23 May could be responsible, in part, for the reduced accuracy of those mass estimates. For 23 May 1997, the results also document lower mass estimates when detecting puffs against a broken cloud cover than when detecting puffs against a uniform cloud cover or clear sky. This observation documents the deleterious impact of poor-quality imagery upon the mass estimates. As discussed in Appendix C, the resolution, or area per pixel (APP), is linked to slant range (SR), elevation angle (EL), and background radiance (BR). All of these variables also affect the quality of the imagery. The results in this appendix reveal that the PLMMASS-derived puff mass increases as the APP decreases. Therefore, the mass estimates are sensitive to these linked variables, which, on the average, were worse on 23 May than on 21 May 1997. Appendix C established that the observed extent of the puff was insensitive to APP and, hence, to these linked variables. Therefore, the sensitivity of the mass estimates to APP cannot be a result of poor edge detection.

Additional analysis, described in Inki Min's report[19], indicates that the observed puff extent has a threshold at approximately 5 sigma on a Gaussian fit to the puff's column density distribution for the MVP4 imagery. Dr Min's analysis reveals that an edge-detection threshold of 1 ppm-m ranges from 6 sigma (for the concentrated puff at early times) to 4 sigma (for the diluted puff at later times). His results support the conclusion that the bulk of the tracer is included in the observed extent.

The PLMMASS Analysis Scheme

The PLMMASS algorithm uses the radiance from the puff, from the sky (background), and from a blackbody emitter (at the temperature of the puff) to estimate transmission through the puff at each pixel in the image. The transmission of the IR radiation through the puff is related to the column density (CD), which is the product of the concentration of tracer and the path length through the puff. Integration of the column density for all pixels occupied by the puff yields an estimate of the tracer mass within the observable puff extent. In this report, the units for column density are parts-per-million meters (ppm-m), and the units of mass are grams.

Beer's law relates the attenuation (or emission) of light from a vapor to its column density using the wavelength-dependent extinction coefficient. In the limit of low concentrations and short path lengths, there is a linear relationship between the attenuation of light and the column density. The relationship is non-linear at higher column densities. The relationship "saturates" at very high column densities where small errors in the observed radiance can create large errors in the calculated column densities. This appears to be the case for the MVP4 puffs at early times.

Mark L. Polak, Jeffrey L Hall, and Kenneth C. Herr developed a technique to extract column density information from on- and off-puff spectral information.[18] By using a filter-corrected transmission coefficient, they developed a similar technique to extract not only column density but also mass from narrowband imagery. Mark L. Polak encoded this algorithm into the PLMMASS program. We applied this technique to the MVP #4 puff imagery. PLMMASS converts pixel intensity into column density within each puff image. PLMMASS also integrates the column density to estimate the integrated mass contained within the observable puff. The results plotted in this appendix are from the PLMMASS analysis of MVP #4 imagery.

Ideally, the PLMMASS analysis of the MVP4 imagery would have demonstrated conservation of mass in every image of the puff. Instead, the mass estimates ranged from 44% to 88% of the nominal value (910 g) on 21 May and from 23% to 120% of the nominal value (1750 g) on 23 May 1997. The results presented in this appendix document that the PLMMASS method provides better estimates for the diluted, rather than the concentrated, puff and requires high-quality imagery. In spite of these difficulties, the trends in the puff mass data document that the imagery-derived extent of the puff included the bulk of the SF_6 tracer.

We will review the PLMMASS-derived results for the 21st and 23rd of May in separate sections of this appendix. Although the observed trends are similar for both days, there is much more scatter in the data from 23 May 1997. This scatter is attributed to the lower quality of the imagery and the higher puff concentrations on 23 May. The background was variable and less than ideal on the 23 May. In fact, we could not process imagery for several releases on the 23 May because we could not see the puffs from certain sites or over much of their track. The 23 May results are derived from imagery that had fog, high-level clouds, and broken clouds as the backdrop for observing the puffs.

Estimates of Column Density and Mass for the 21 May 1997 Imagery

This section of the appendix provides various plots that reveal trends in the imagery-derived column density and mass estimates for 21 May 1997. The imagery-derived mass ranged from 400 to 800 g

(i.e., 44% to 88% of the nominal mass) for puffs containing an average mass of 910 g. The lowest estimates were due to a combination of long slant range, low viewing elevation, poor resolution, high background radiance, and concentrated puffs.

Figures D-1 and D-2 are plots of the imagery-derived maximum column density against time. In Figure D-1, the time is in minutes after each puff's release. In Figure D-2, the time is in minutes after 21:00:00 GMT (i.e., the release time for the first puff on 21 May 1997). The imagery-derived time of release is accurate to the nearest 15 s (i.e., the data rate of the imagery collection). These plots document a rapid initial decrease in the maximum column density followed by a slower decay. It is apparent that there are not enough data to fully define the decay curves.

Figure D-3 is a plot of the imagery-derived mass against time in minutes after 21:00:00 GMT. The data in this plot are labeled with different symbols for each puff. The estimated mass is highest for puffs from series 1, 2, and 4. These releases were closest to the line of camera sites, and this resulted in better quality imagery. Therefore, the lowest mass estimates correlate with the longer slant range, shallower elevation angles, and lower resolution (i.e., larger area per pixel). Another trend is apparent only in series 1 and series 2 data. That trend is an increase in apparent mass with the initial dilution of the puff and is consistent with a systematic error at high column densities. Figures D-4 and D-5 are plots of imagery-derived mass against the maximum imagery-derived column density. Figure D-4 includes labels to indicate along- or crosswind data. The alongwind data are acquired from imagery with a crosswind perspective, looking at the puff from the side with the shortest distance between the puff and the camera. The crosswind data are acquired from imagery with an alongwind
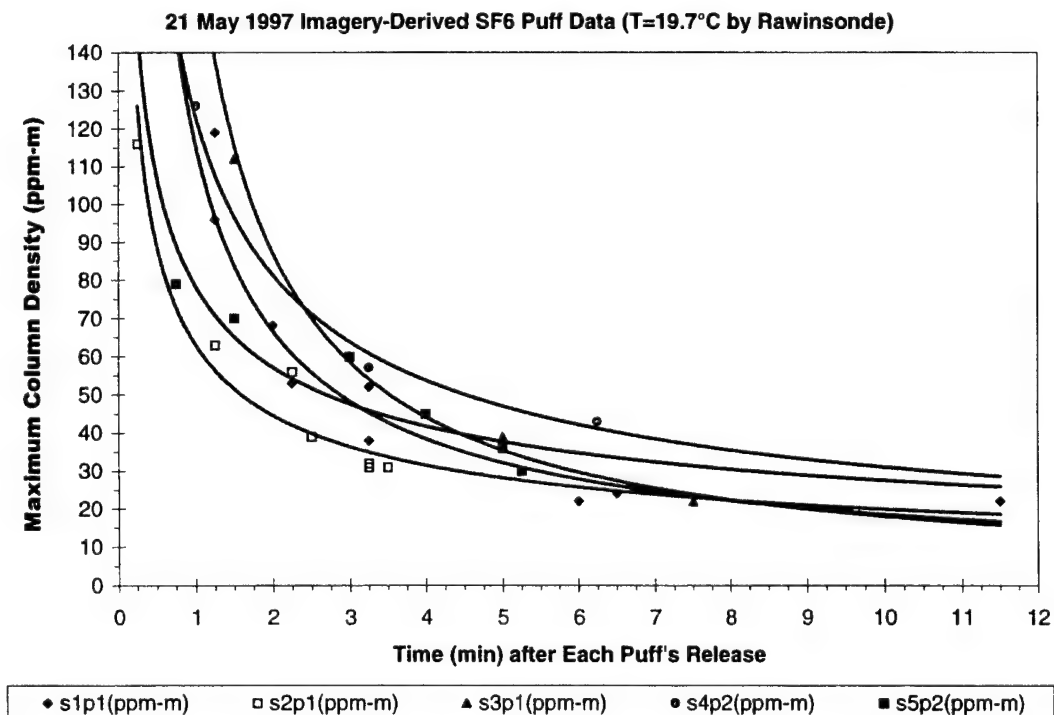
Figure D-1. Max column density versus time after release with puff labels (21 May 1997).

79

21 May 1997 Imagery-Derived SF6 Puff Data (T=19.7°C by Rawinsonde)
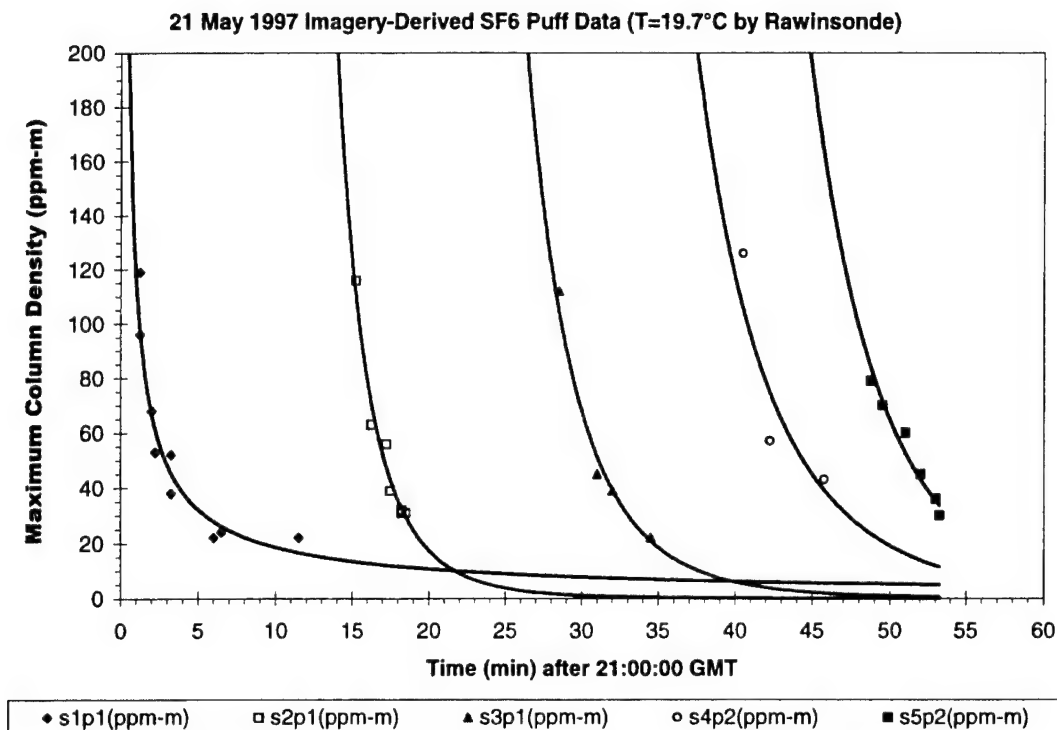
Figure D-2. Max column density versus GMT with puff labels (21 May 1997).

21 May 1997 Imagery-Derived Puff Mass (T=19.7°C by Rawinsonde)
Total Mass per Puff ~ 910 grams
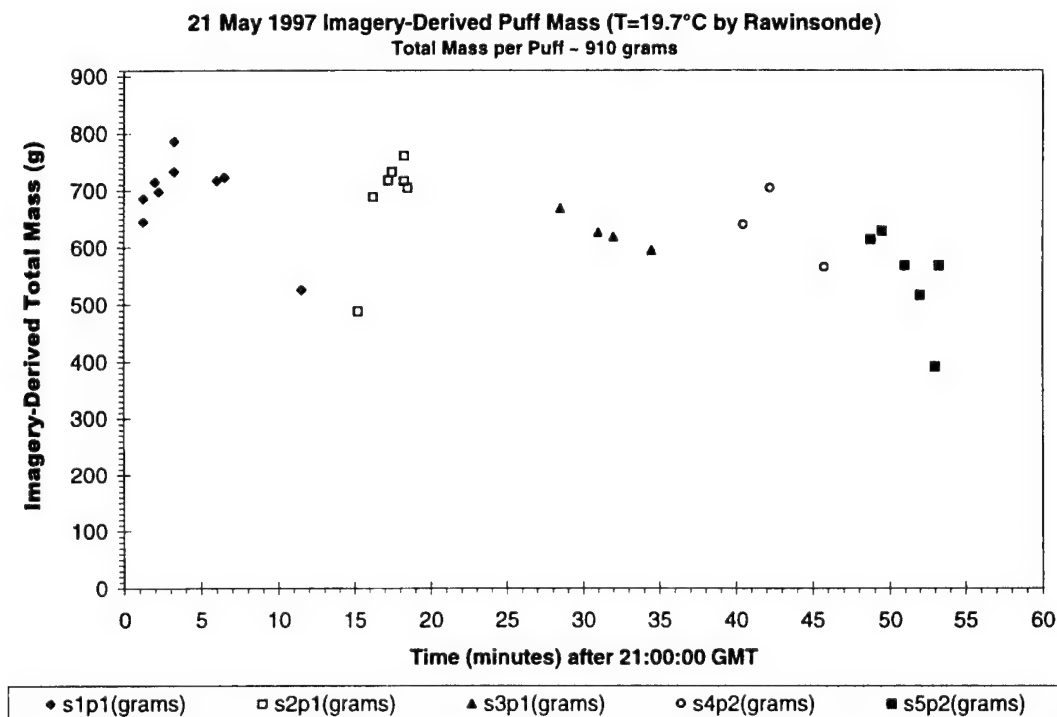
Figure D-3. Mass estimates versus GMT with puff labels (21 May 1997)

80

21 May 1997 Imagery-Derived Puff Data (T=19.7°C by Rawinsonde)
Total Mass per Puff ~ 910 grams

$$y = -0.8201x + 731.32$$
$$R^2 = 0.4754$$

- ♦ Cross(grams) □ Along(grams) — —Linear (Along(grams))
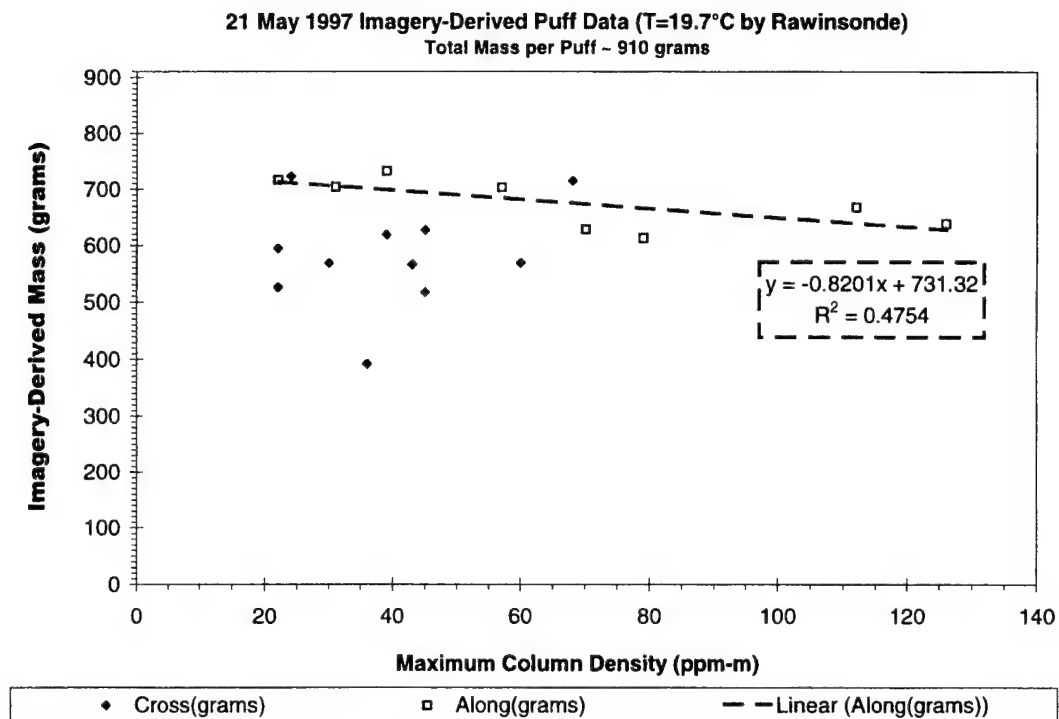
Figure D-4. Mass estimates versus column density with tilt axis labels (21 May 1997).

21 May 1997 Imagery-Derived Puff Data (T=19.7°C by Rawinsonde)
Total Mass per Puff ~ 910 grams

Area per Raw Pixel <= 20 m^2, Max Column Density <= 100 ppm-m

$$y = -1.5698x + 777.84$$
$$R^2 = 0.3515$$
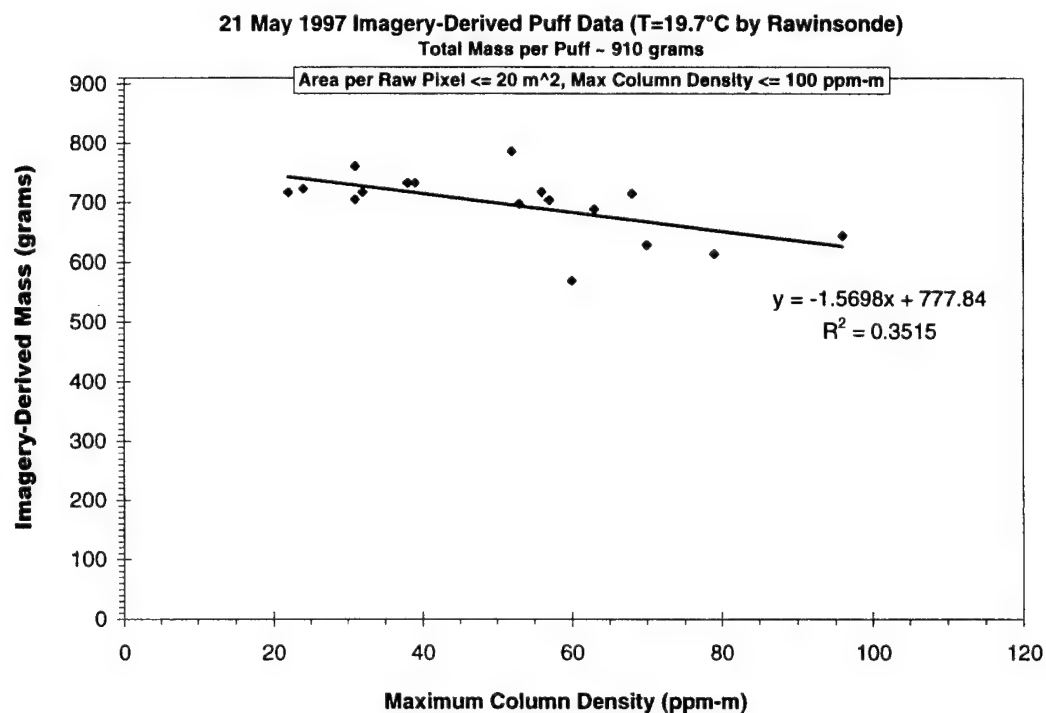
Figure D-5. Filtered estimates of mass versus column density with trend line (21 May 1997).

perspective, looking along the wind bearing at the distant puff as it moved away from or toward the camera. Figure D-4 reveals greater scatter and lower mass estimates for most of the crosswind data than for the alongwind data. The errors reflect the longer slant ranges, shallower elevation angles, and lower resolution associated with the crosswind data. For the alongwind data, Figure D-4 documents increasing accuracy in the mass estimates as the puff dilutes, reducing the maximum column density. These results are consistent with systematic errors at high CD and not with poor edge detection, which would worsen the mass estimates with dilution.

Figure D-5 includes filtered data from all perspectives (i.e., alongwind, crosswind, and other tilt axes). The filters were area per pixel (APP $\leq$ 20 m^2 per pixel) and maximum imagery-derived column density (Max CD $\leq$ 100 ppm-m). The APP filter removes the data with the poorest resolution, longest slant range, shallowest elevation angle, and highest background. The maximum column density filter removed the largest values for the column density, corresponding to imagery of concentrated puff before it dilutes. It is apparent from Figure D-5 that filtered data show an improvement in accuracy as the puff dilutes, which corresponds to decreasing column density. This trend is consistent with larger systematic errors in the estimates at high column densities. One would not expect the mass estimates to improve with dilution if the errors were dominated by poor edge detection, which should worsen with dilution.

Figures D-6 through D-8 are plots of the imagery-derived mass against area per pixel (APP). The field of view (FOV) of the scanners remained constant, but the APP, SR, EL, and BR all changed as the puff moved relative to the camera site. Since the APP is linked to SR, EL, and BR, Figures D-6 through D-8 document sensitivity to all of these linked variables.

21 May 1997 Imagery-Derived Puff Data (T=19.7°C by Rawinsonde)
Total Mass per Puff – 910 grams

$y = 954.43x^{-0.1613}$
$R^2 = 0.5808$
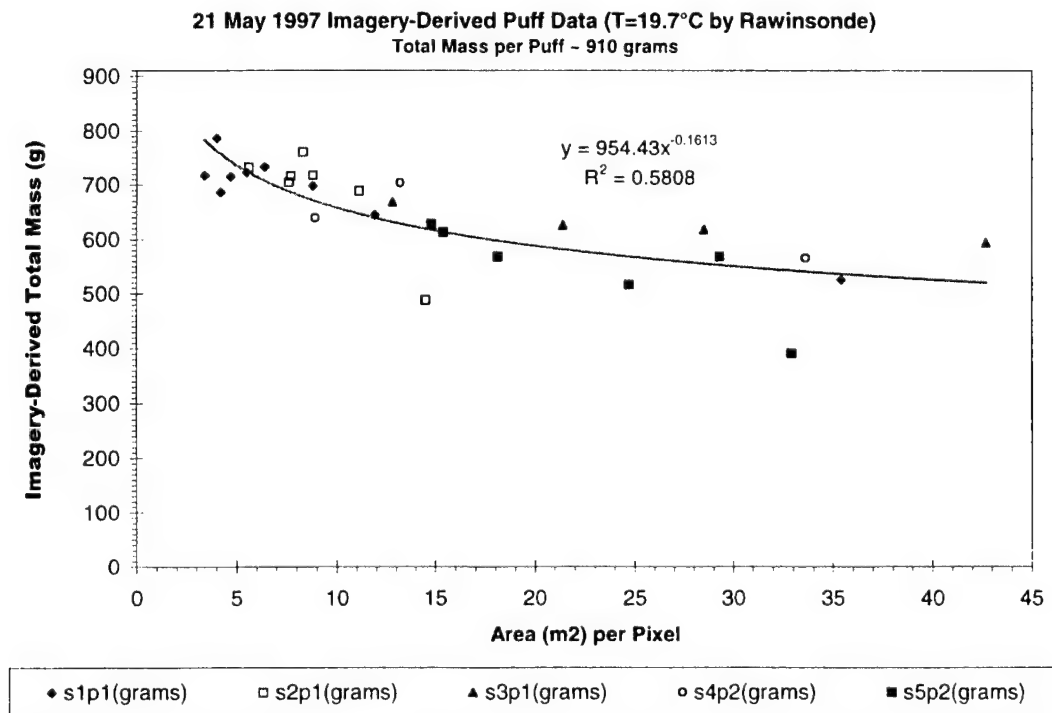
Figure D-6. Mass estimates versus APP with puff labels (21 May 1997).

21 May 1997 Imagery-Derived Puff Data (T=19.7°C by Rawinsonde)
Total Mass per Puff ~ 910 grams

$y = 925.94x^{-0.1512}$
$R^2 = 0.5714$

Imagery-Derived Mass (grams)

Area (m^2) per Pixel

♦ Cross(grams)   □ Along(grams)   —— Power (Both(grams))
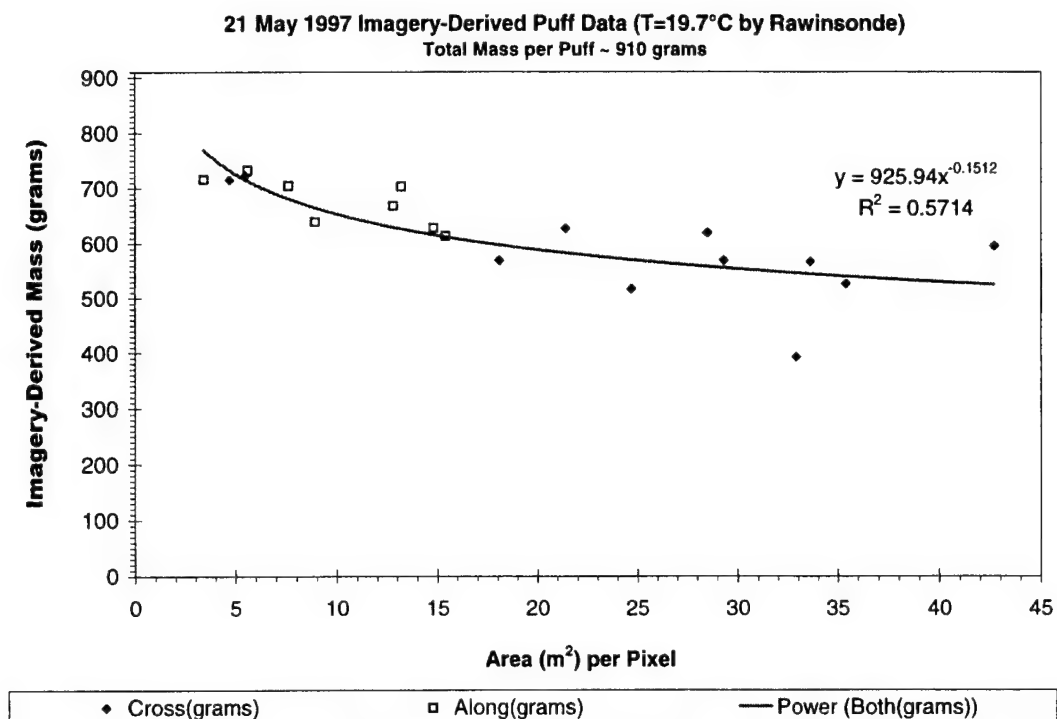
Figure D-7. Mass estimates versus APP with tilt axis labels (21 May 1997).

21 May 1997 Imagery-Derived Puff Data (T=19.7°C by Rawinsonde)
Total Mass per Puff ~ 910 grams

Area per Raw Pixel <= 20 m^2, Max Column Density <= 100 ppm-m

$y = -10.96x + 797.54$
$R^2 = 0.7496$

Imagery-Derived Mass (grams)

Area (m^2) per Pixel
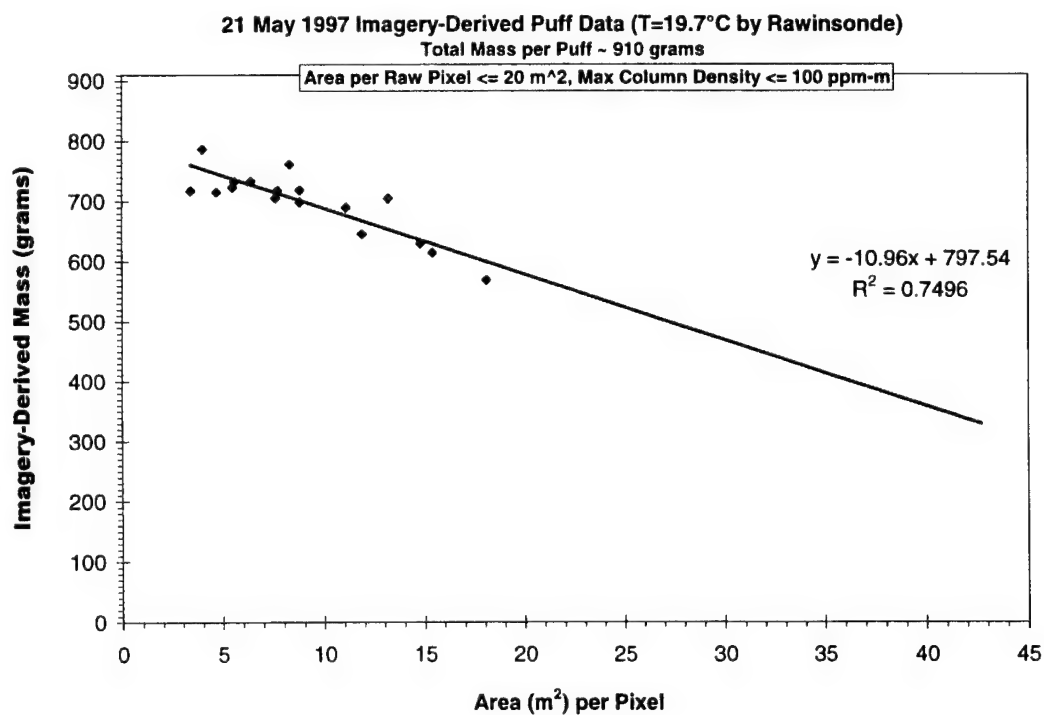
Figure D-8. Filtered estimates of mass versus APP with trend line (21 May 1997).

83

Figure D-6 includes all data, labeled with different symbols for each puff. The plot shows a decrease in the estimated mass with an increase in APP, but also documents greater scatter at large values of APP. Hence, the PLMMASS results are most accurate when the APP is small, SR is short, EL is steep, and BR is low.

Figure D-7 includes only data from alongwind or crosswind perspectives, which is indicated by using different symbols for along- and crosswind data points. The data in Figure D-7 document a trend similar to the data included in Figure D-6, which included all perspectives. In addition, the data in Figure D-7 reveal that the greater scatter in the crosswind data correlates with the fact that most of the data is of poorer quality than the alongwind data. A large value of APP documents poor resolution as well as long slant range, low elevation, and less contrast (i.e., greater background radiance). Therefore, the image quality suffers in all respects as the APP value increases. There is no difference between the alongwind and crosswind results when they are derived from imagery of similar quality, as illustrated by the data near 5 m^2 per pixel.

Figure D-8 is a plot of estimated mass against APP, after filtering the data by area per pixel (APP $\leq$ 20 m^2 per pixel) and maximum column density (CD $\leq$ 100 ppm-m). These filtered data reveal that the estimates of mass improve substantially as the APP decreases. This illustrates that the PLMMASS estimates are most accurate when one has high-quality imagery. A low value of APP documents better resolution as well as shorter slant range, steeper elevation, and better average contrast (i.e., lower average background radiance). Therefore, the image quality is better in all these respects. On a clear day, the background radiance is larger for low elevation and smaller for steep elevation. Since the sky was fairly clear on 21 May 1997, the quality of the imagery is documented fairly well by APP.

Figure D-9 is a plot of imagery-derived mass against background radiance (BR). The plot includes mass estimates based upon the rawinsonde-derived temperature at the release height as well as mass estimates based upon a temperature three degrees cooler than the actual temperature. The purpose of this plot was to demonstrate the sensitivity of the PLMMASS estimates to the assumed temperature of the puff. As with other plots in this report, BR is linked to EL, SR, and APP. Therefore, the decrease in estimated mass with increasing background radiance documents the same sensitivity to image quality as the earlier APP plots. Figure D-9 also includes additional labels for three of the data points. An aircraft contrail within the image interfered with the mass estimates for two out of three of worst data points. Obviously, the presence of the contrail in the image is not revealed by the APP value, and so the APP does not characterize the image quality when the sky is not clear. The contrail did not interfere with the measurement of the extent of the cloud or its expansion rate. Therefore, these points illustrate that the imagery-derived estimation of mass is much more complicated than measuring the extent of the puff and is more sensitive to the quality of the imagery.

The plots in this appendix document that the imagery-derived column densities and masses are underestimated because the PLMMASS method of analysis is strongly dependent upon the image quality and the optical density (i.e., maximum column density) of the puff. The results document that the PLMMASS method only produced accurate mass estimates for very dilute puffs when using the best-quality imagery. The image quality is dependent upon several linked parameters, which included resolution (APP), slant range, elevation, and average background radiance. The image quality is degraded further by fog, broken cloud cover, and aircraft contrails. Since the imagery-

21 May 1997 SF$_6$ Puff Data (910 g each) - VHF (Site 2)
Analyzed using 19.7C vs 16.7C as well as Tight and Wide Shapes

T(rawinsonde) - 3 = 16.7 °C

Contrail far away from Puff

T(rawinsonde) = 19.7 °C

Contrail below Puff

Contrail above Puff

Background Radiance (uW sr-1 cm-2)

Total Mass (g)

| ● g(19.7C)t | □ g(16.7C)t | ▲ g(16.7C)w |
| ——Linear (g(19.7C)t) | — —Linear (g(16.7C)t) | - - - Linear (g(16.7C)w) |

Figure D-9. Mass estimates versus background radiance labeled with assumed puff temperature (21 May 1997).

derived mass becomes more quantitative as the puff dilutes, the systematic errors are not due to poor edge detection, which would worsen with dilution. This hypothesis assumes that edge detection is insensitive to most of the variables that affect the mass estimates. This was shown to be the case in Appendix C where the extent of the cloud was insensitive to APP and, therefore, SR, EL, and BR.

Estimates of Column Density and Mass for the 23 May 1997 Imagery

This section of the appendix provides various plots that reveal trends in the imagery-derived column density and mass estimates for 23 May 1997. The plots document more scattered results for the mass estimates than obtained on 21 May 1997. The imagery-derived mass ranged from 400 to 2100 g (23% to 120% of nominal mass) for puffs containing an average mass of 1750 g. The lowest estimates were due to a combination of long slant range, low viewing elevation, poor resolution, high background radiance, concentrated puffs, and poor viewing conditions, including fog and broken cloud cover.

Figures D-10 through D-13 are plots of the imagery-derived maximum column density against time. In Figures D-10, D-11, and D-13, the time is in minutes after the release of the puff. In Figure D-12, the time is in minutes after 19:00:00 GMT (i.e., the release of the first puff on 23 May 1997).

The same data are plotted in Figures D-10 and D-11, using different labels for the data points (i.e., puff number and site number, respectively). Even though the data are very badly scattered in these

23 May 1997 Imagery-Derived SF6 Puff Data (T=14.4°C by Rawinsonde)

Very low values for sbp1.

(Max Column Density (ppm-m) versus Time (minutes) after Puff's Release)

Legend:
♦ s1p1(ppm-m) ■ s2p1(ppm-m) ▲ s3p1(ppm-m) ● s7p3(ppm-m) ♦ s8p3(ppm-m)
□ sbp1(ppm-m) △ sfp2(ppm-m) ○ sgp1(ppm-m) ✕ shp1(ppm-m)
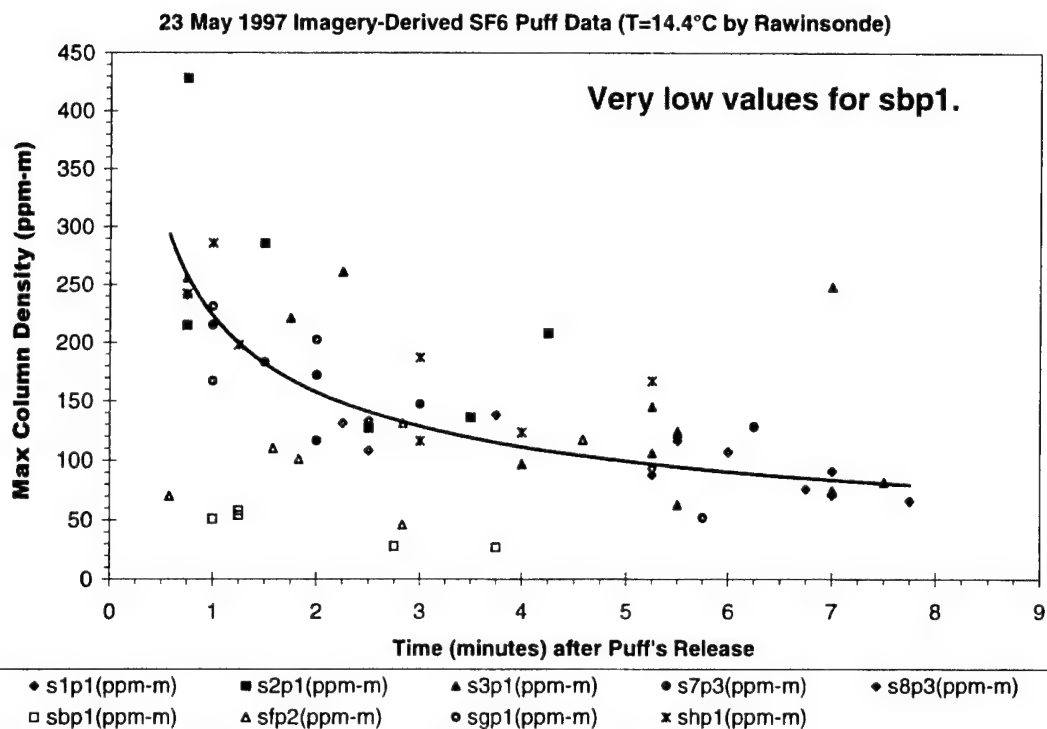
Figure D-10. Max column density versus time after release with puff labels (23 May 1997).

23 May 1997 Imagery-Derived Puff Data (T=14.4°C by Rawinsonde)

Very low values for sbp1.

(Max Column Density (ppm-m) versus Time (minutes) after Puff Release)

Legend:
■ DIX(ppm-m) ♦ CEMT(ppm-m) ▲ SMT2(ppm-m) —— Power (SMT2(ppm-m))
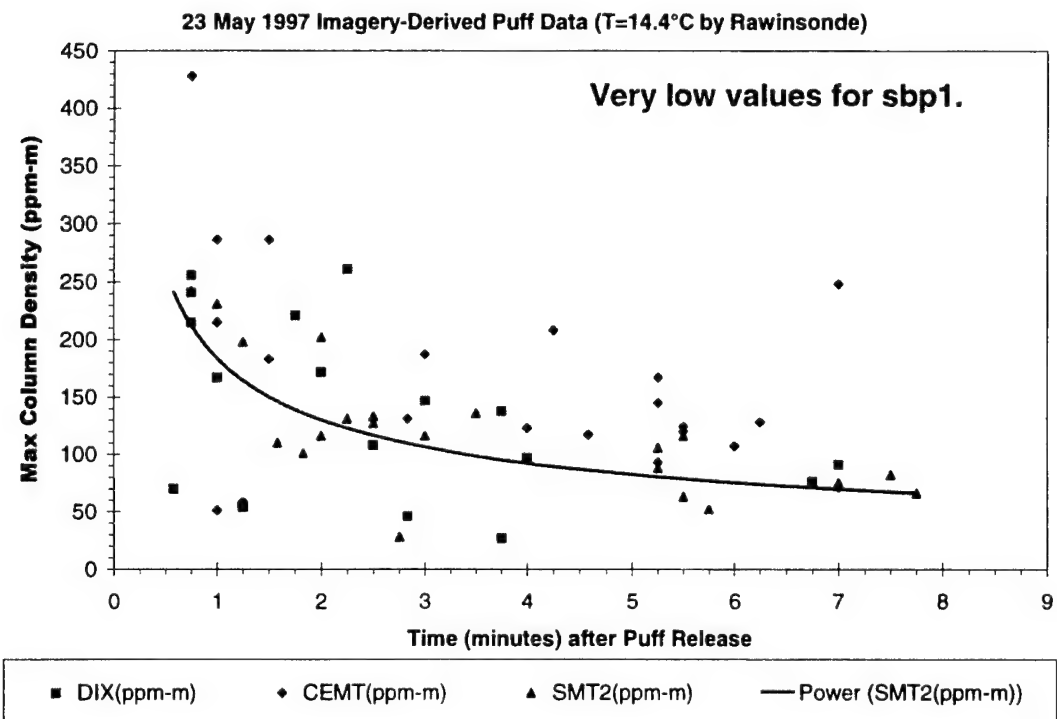
Figure D-11. Max column density versus time after release with site labels (23 May 1997)

86

23 May 1997 Imagery-Derived SF6 Puff Data (T=14.4°C by Rawinsonde)
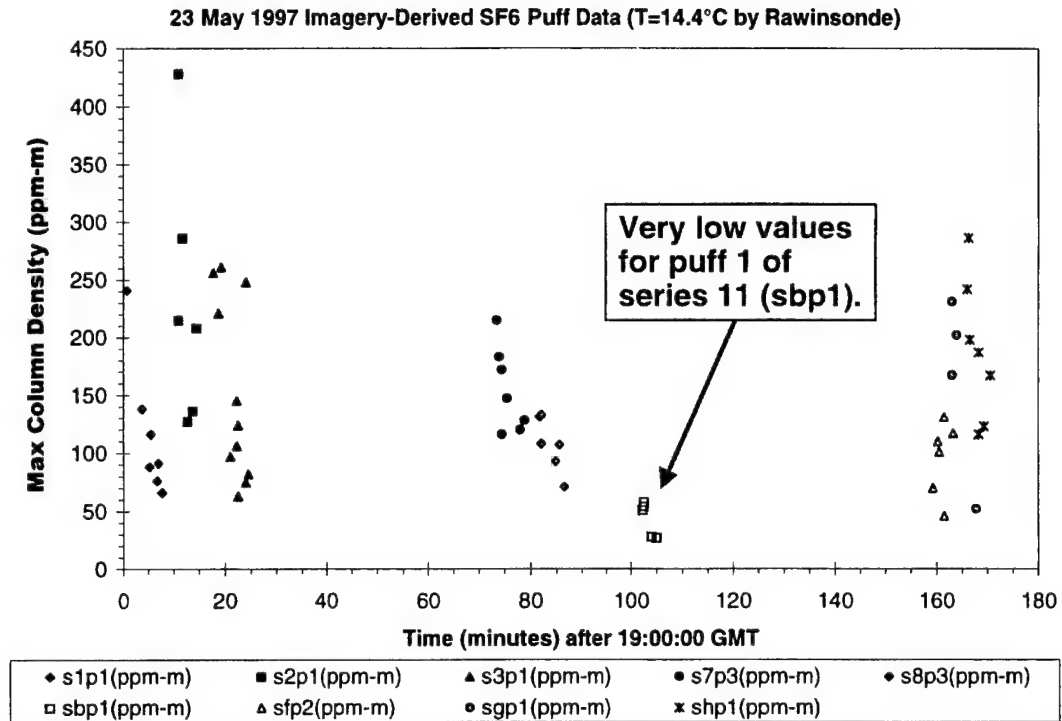
Figure D-12. Max column density versus GMT with puff labels (23 May 1997).

23 May 1997 Imagery-Derived Puff Data (T=14.4°C by Rawinsonde)

Area per Raw Pixel <= 50 m^2, Max Column Density between 60-200 ppm-m

$$y = -11.466x + 167.05$$
$$R^2 = 0.4317$$
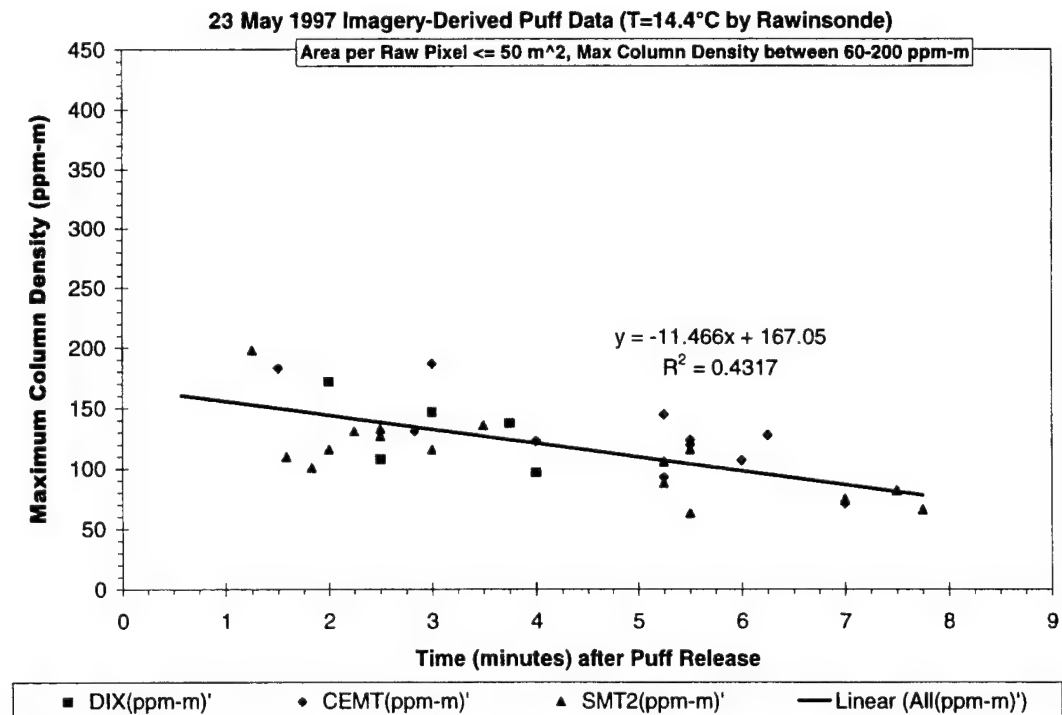
Figure D-13. Max column density versus time after release with site labels (23 May 1997).

plots, it is apparent that the column densities are consistently low for series B puff 1 (sbp1). There is also a systematic bias associated with the imagery from CEMT camera site, which yielded higher column densities than imagery from the other sites.

Figure D-12 also reveals that the maximum imagery-derived column densities are consistently low for sbp1. Due to the large scatter in the data, the smooth decay curves revealed in Figure D-2 for the 21 May data are not apparent in Figure D-12 for the 23 May data.

Figure D-13 includes data from all perspectives (i.e., alongwind, crosswind, and other tilt axes), after filtering the data. The filters were area per pixel (APP $\leq$ 50 m^2 per pixel) and maximum imagery-derived column density (Max CD between 60 and 200 ppm-m). The APP filter removes data that have poor resolution, long slant range, shallow elevation angles, and higher average background radiance. The maximum column density filter removed two sets of data: (1) the sbp1 data (CD < 60) and (2) the highest values for the column density (CD > 200ppm-m). It is apparent from Figure D-13 that there is much less scatter in the filtered data. These data document a decrease in maximum column density as the puff dilutes (i.e., with the passage of time).

Figures D-14 through D-17 are plots of the imagery-derived mass against time. In Figure D-14, the time is in minutes after 19:00:00 GMT (i.e., the release of the first puff on 23 May 1997). In Figures D-15 through D-17, the time is in minutes after the release of each puff.
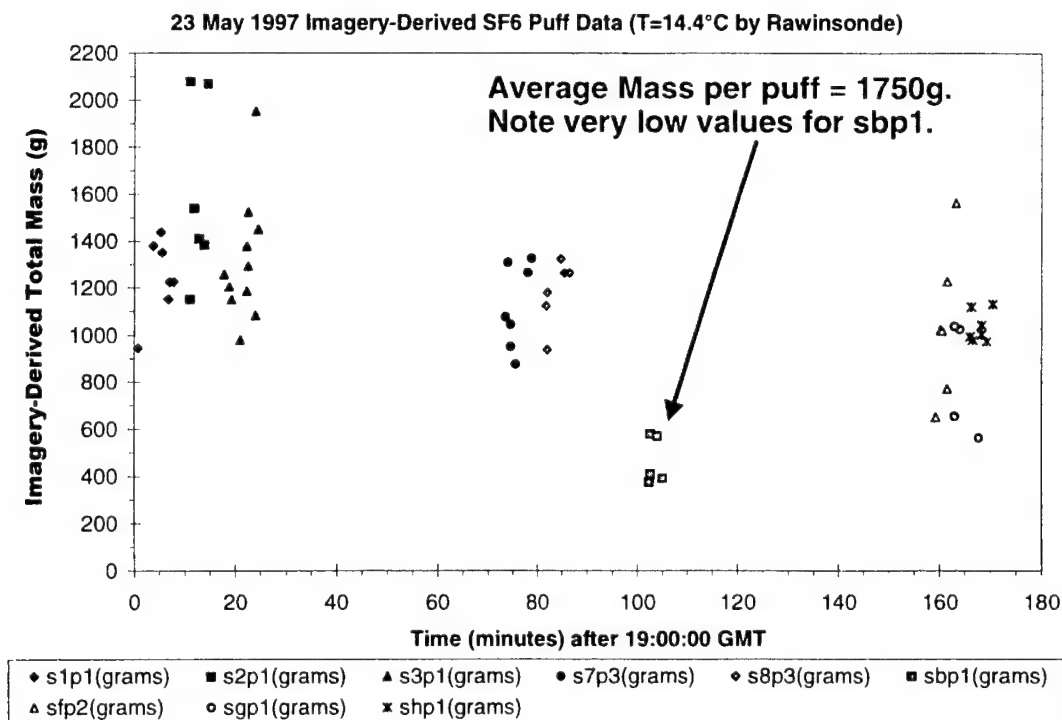
Figure D-14. Estimated mass versus GMT with puff labels (23 May 1997).

23 May 1997 Imagery-Derived SF6 Puff Data (T=14.4°C by Rawinsonde)
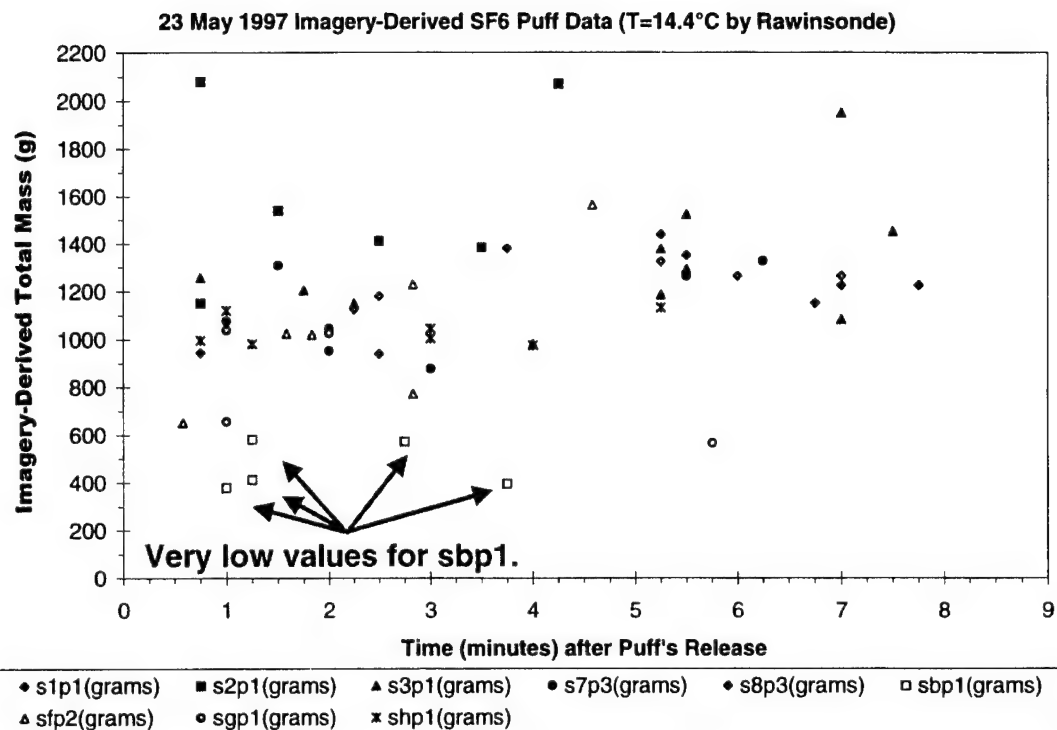
Figure D-15. Estimated mass versus time after release with puff labels (23 May 1997)

23 May 1997 Imagery-Derived Puff Mass (T=14.4°C by Rawinsonde)
Total Mass per Puff ~ 1750 Grams
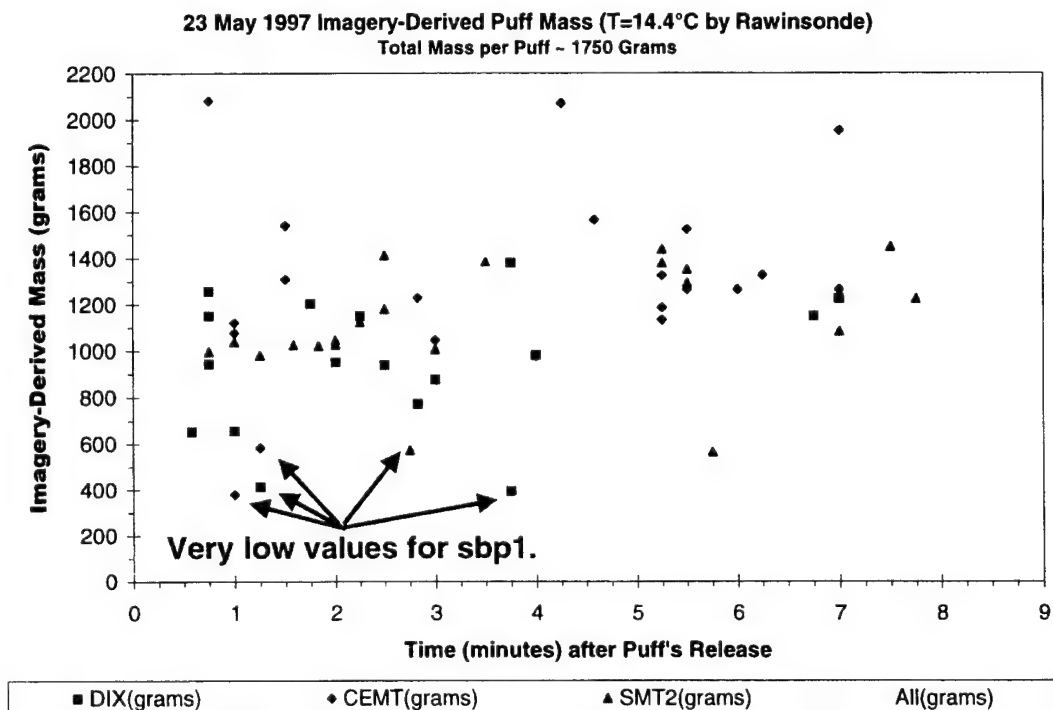
Figure D-16. Estimated mass versus time after release with site labels (23 May 1997)

23 May 1997 Imagery-Derived Puff Mass (T=14.4°C by Rawinsonde)
Total Mass per Puff ~ 1750 Grams

Area per Raw Pixel <= 50 m^2, Max Column Density between 60-200 ppm-m

$y = 48.179x + 996.81$
$R^2 = 0.2656$

Imagery-Derived Mass (grams)

Time (minutes) after Puff's Release

■ DIX(grams)'   ◆ CEMT(grams)'   ▲ SMT2(grams)'   ——Linear (All(grams)')
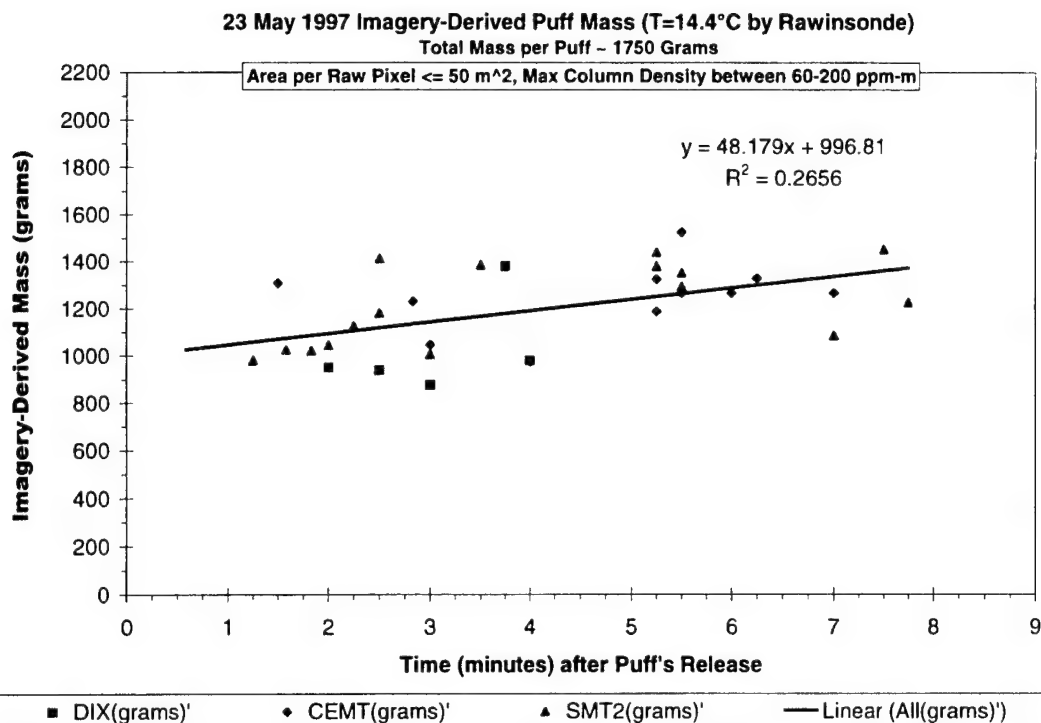
Figure D-17.   Filtered estimates of mass versus time after release with site labels and trend line (23 May 1997).

Figure D-14 documents that the mass estimates are typically low (i.e., less than the nominal puff mass of 1750 g). The results for sbp1 are consistently even lower than for the other puffs. The highest mass estimates are actually overestimates (i.e., greater than the nominal 1750 g). Most of the data fall between 800 and 1600 g, which represents 50% to 90% of the actual mass per puff (i.e., 1750 g). On 23 May, the amount of tracer in each puff is twice (10-s puffs) as much as on 21 May (5-s puffs). The sky was cloudy, foggy, or hazy throughout 23 May 1997. Considering the poor quality of the imagery and the higher column densities, the mass estimates are surprisingly good.

The same data are plotted in Figures D-15 and D-16, using different labels for the data points (i.e., puff number and site number, respectively). Figure D-15 reveals that the sbp1 results are consistently lower than the other puffs. This is not unexpected since the maximum column densities were also lower for this puff. Figure D-16 reveals that the overestimates of mass are all derived from CEMT site, while Figure D-15 documents that two out of three of these overestimated data points are for s2p1.

Figure D-17 includes filtered data labeled by camera site. The filters were area per pixel (APP ≤ 50 m² per pixel) and maximum imagery-derived column density (Max CD between 60 and 200 ppm-m). The APP filter removed data that had poor resolution, long slant range, shallow elevation angle, and higher average background radiance. The maximum column density filter removed two sets of data: (1) the sbp1 data (CD < 60) and (2) the highest values for the column density (CD > 200ppm-m). It is apparent from Figure D-17 that there is much less scatter in the filtered data. These data document

an improvement in the accuracy of the mass estimates as the puff dilutes with the passage of time. This observation is consistent with greater errors in the estimates at high column densities, which corresponds to concentrated puffs. The underestimation of mass at high CD is apparently not due to the poor edge detection. One would not expect the estimates to improve with dilution if the errors were dominated by poor edge detection, which would worsen with dilution.

Figures D-18 through D-20 are plots of imagery-derived mass against the imagery-derived maximum column density. Figures D-18 and D-19 are similar plots but use different labels for the plotted points (i.e., puff number and perspective, respectively). Figure D-18 includes all perspectives, while Figure d-19 includes only along- and crosswind data. As with the earlier plots, the sbp1 results are consistently lower than the other puffs, and there are a few points that are aberrantly high. In contrast to the differences between along- and crosswind data illustrated in Figure D-4 (21 May data), Figure D-19 documents similar results for along- and crosswind data. We infer from this result that the dominant cause of poor imagery was randomized on 23 May 1997 and systematic on 21 May 1997. The clear skies on 21 May meant that the quality of the imagery was determined by the relative position of the camera to the puff. Under those conditions APP is linked to SR and EL, which determine the average BR. Therefore, the quality of the alongwind data, derived with a smaller APP, was better than crosswind data, derived with a larger APP. The partially cloudy and foggy sky on 23 May meant that the puff randomly moved into and out of obscuring features. Under those conditions, APP is not linked to the quality of the imagery, and there is no systematic bias.
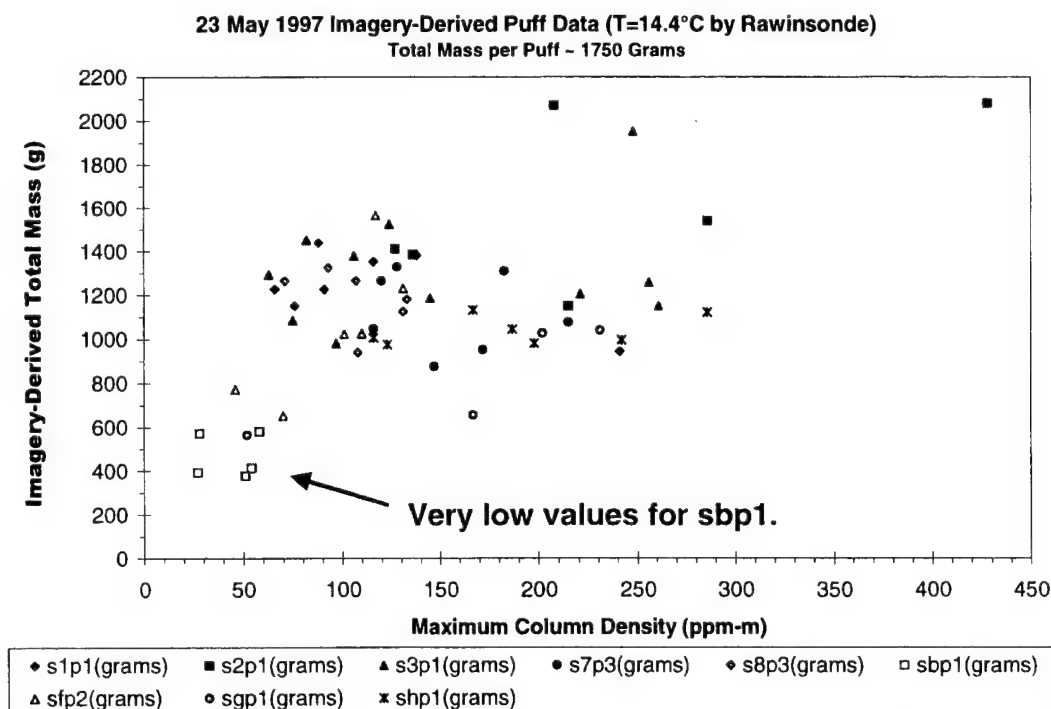
Figure D-18. Estimated mass versus column density with puff labels (23 May 1997).
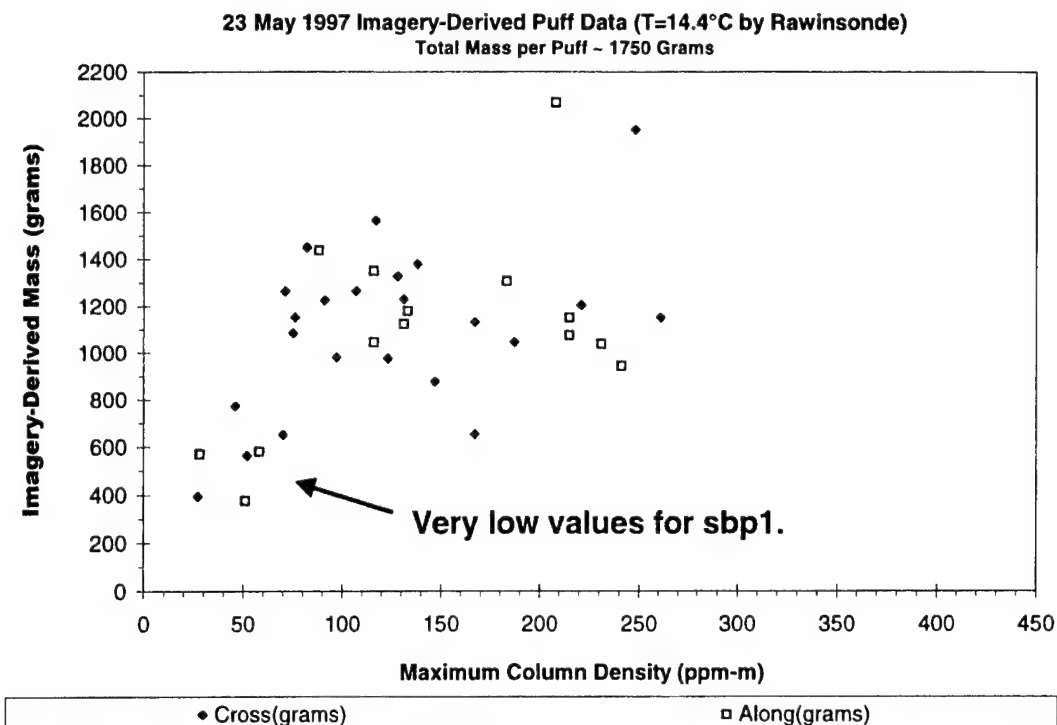
Figure D-19. Estimated mass versus max column density with tilt axis labels (23 May 1997).
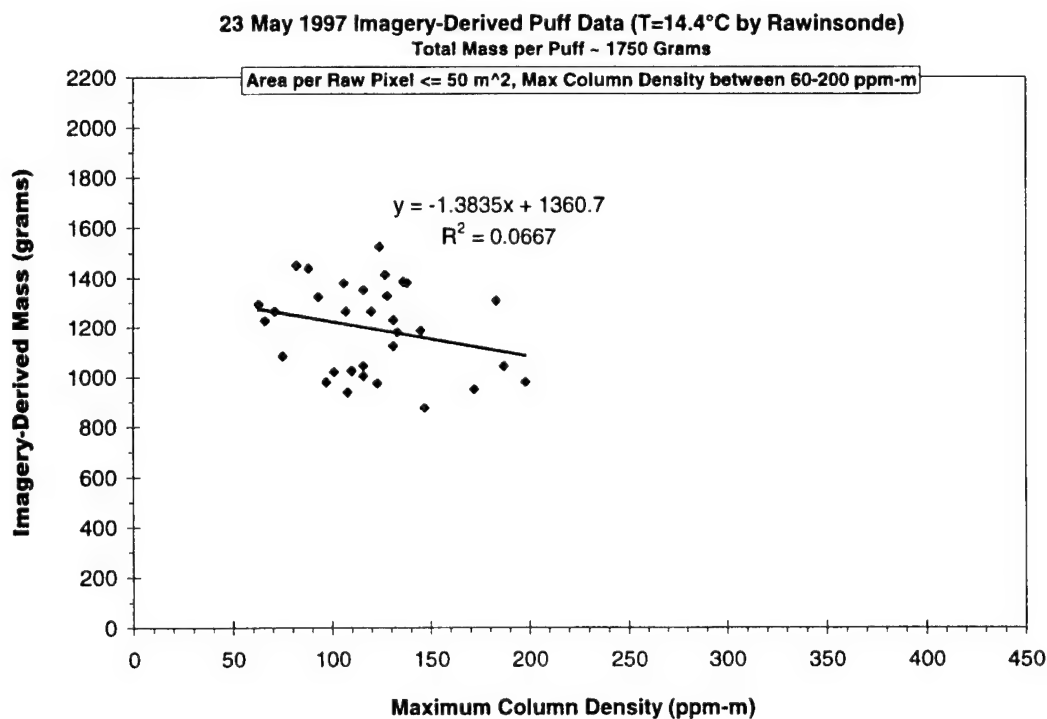
Figure D-20. Filtered estimates of mass versus max column density (23 May 1997).

Figure D-20 is a plot of estimated mass against maximum column density, after filtering the results. The filters were area per pixel (APP ≤ 50 m^2 per pixel) and maximum imagery-derived column density (Max CD between 60 and 200 ppm-m). The APP filter removed data that had poor resolution, long slant range, shallow elevation angles, and higher average background radiance. The maximum column density filter removed two sets of data: (1) the data for puff sbp1 (CD < 60) and (2) the most concentrated puffs (i.e., highest values for the column density, CD > 200ppm-m). Based upon Figure D-5 (21 May data), one expects a decrease in apparent mass with increasing column density. Unfortunately, the scattered data in Figure D-20 do not reveal any trend over their relatively short extent. It is noteworthy, that the filter values were much lower (20 m^2 per pixel and 100 ppm-m) for the 21st than for the 23rd (50 m^2 per pixel and 200 ppm-m). Therefore, the data plotted in Figure D-5 for 21 May are much higher average quality than the data plotted in Figure D-20 for 23 May. As discussed previously, the APP value is not linked to the presence or absence of interfering features (i.e., clouds, fog, or aircraft contrails) that dominated the errors for the 23 May data. Therefore, the poor quality of the 23 May mass estimates is consistent with the less than optimal release geometry (larger values of APP) and with the partially cloudy sky on 23 May.

Figures D-21 through D-23 are plots of the imagery-derived mass against area per pixel (APP). The field of view (FOV) of the scanners remained constant, but the APP, SR, EL, and average BR all systematically changed as the puff moved relative to the camera site. Since the APP is linked to SR, EL, and average BR, Figures D-21 through D-23 should document sensitivity to all of these linked variables. Unfortunately, random obscuration of the puff by fog and clouds further reduced the image quality on 23 May. This random reduction in image quality is, of course, not linked to APP and, therefore, complicates any trends that might have been revealed by these figures.

23 May 1997 Imagery-Derived Puff Data (T=14.4°C by Rawinsonde)
Total Mass per Puff ~ 1750 Grams
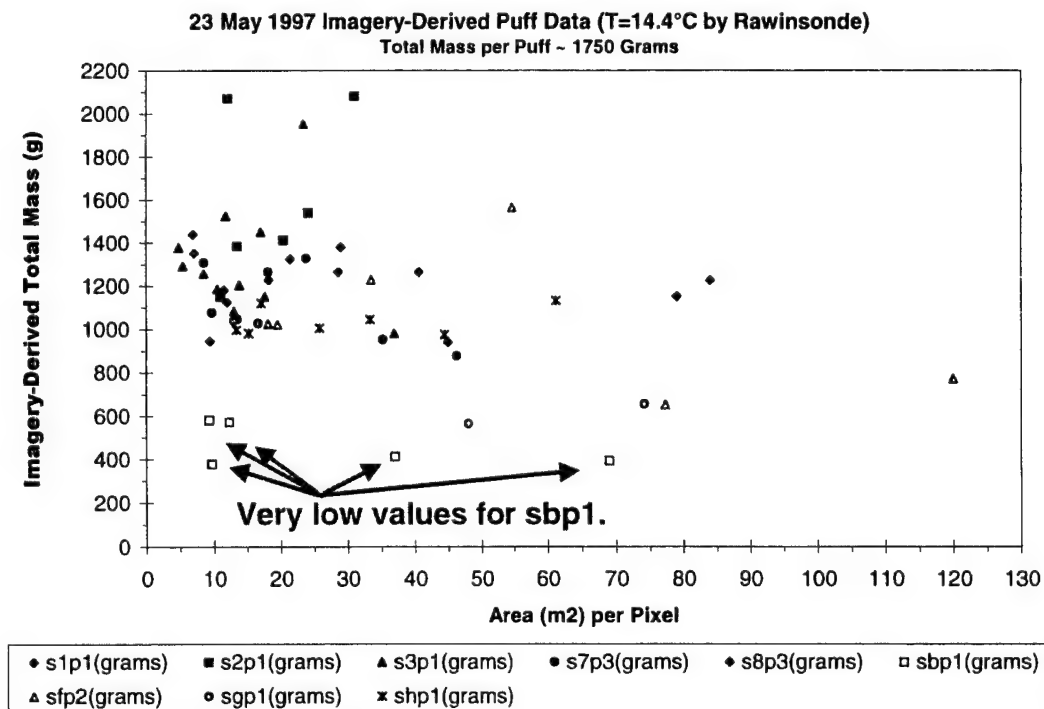
Figure D-21. Estimated mass versus APP with puff labels (23 May 1997).

23 May 1997 Imagery-Derived Puff Data (T=14.4°C by Rawinsonde)
Total Mass per Puff ~ 1750 Grams

$y = 1362.4x^{-0.0893}$
$R^2 = 0.0369$

Very low values for sbp1.

Area (m²) per Pixel

♦ Cross(grams)   □ Along(grams)   —— Power (Both(grams))
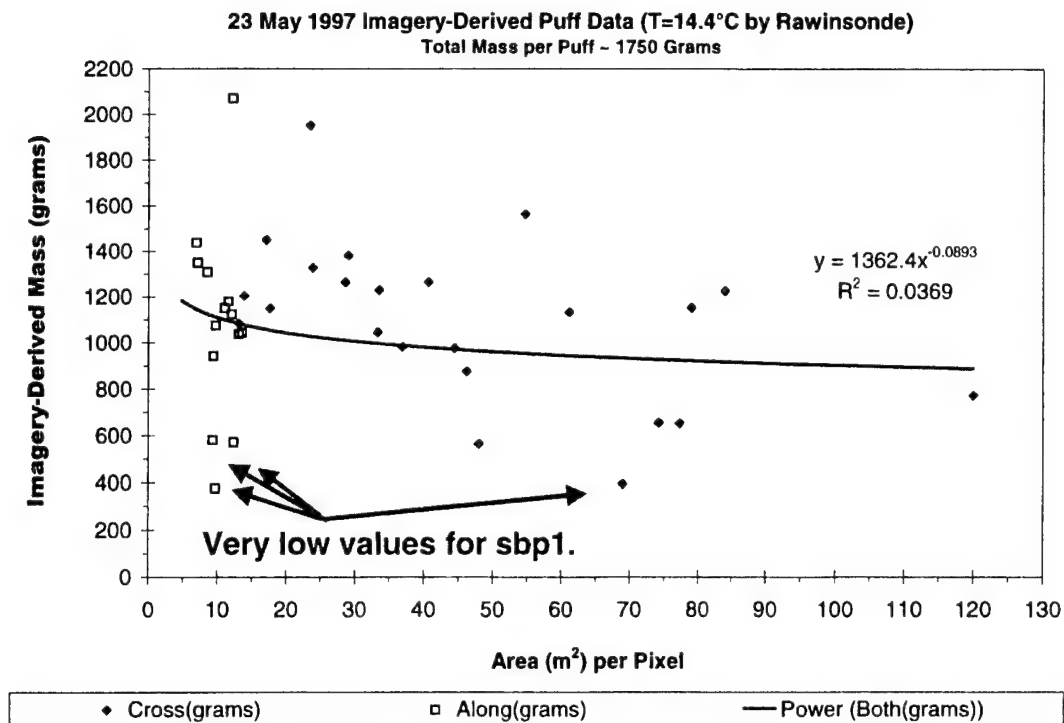
Figure D-22. Estimated mass versus APP with tilt axis labels (23 May 1997).

23 May 1997 Imagery-Derived Puff Data (T=14.4°C by Rawinsonde)
Total Mass per Puff ~1750 Grams

Area per Raw Pixel <= 50 m^2, Max Column Density between 60-200 ppm-m

$y = -7.8971x + 1364.7$
$R^2 = 0.2925$

Area (m²) per Pixel
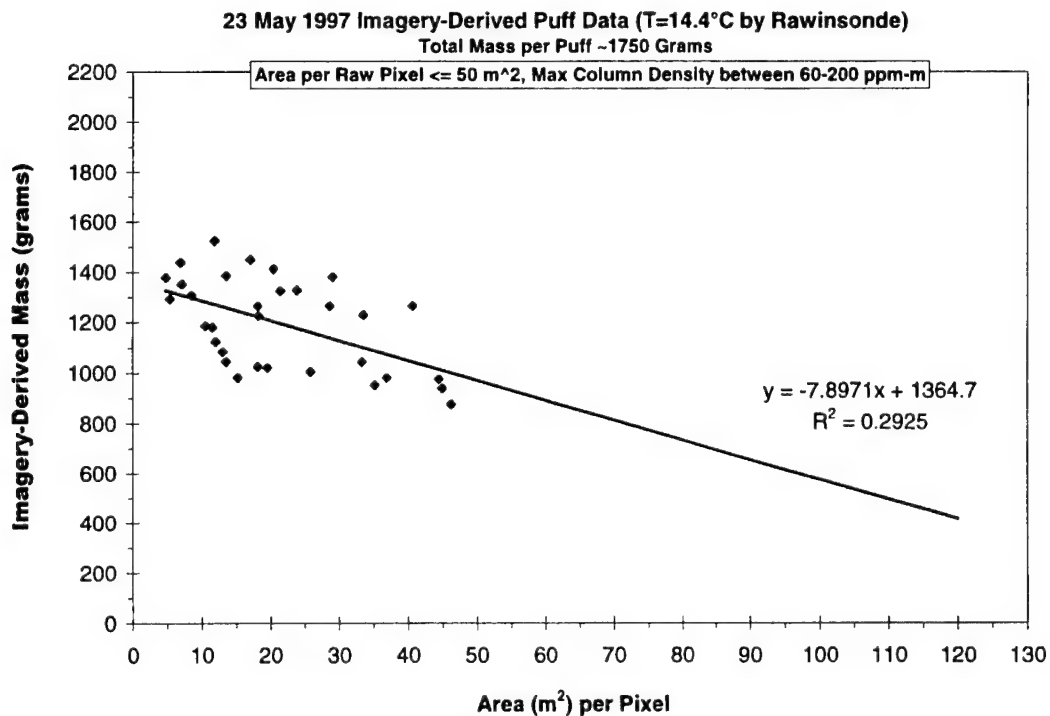
Figure D-23. Filtered estimates of mass versus APP with trend line.

94

Figures D-21 and D-22 are similar plots of estimated mass against APP, except for the data labels (i.e., puff number and perspective, respectively). Figure D-21 includes data from all perspectives, while Figure D-22 only includes along- and crosswind data. As with the earlier plots, the results for puff sbp1 are aberrantly low, and there are a few points that are higher than the nominal puff mass (i.e. 1750 g). Figure D-22 reveals that most of the alongwind data are derived from higher quality imagery (i.e., lower APP) than the crosswind data. This is reasonable since the alongwind data is obtained from a crosswind perspective, while the crosswind data is obtained from an alongwind perspective. The crosswind perspective is obtained when the puff is closest to each camera, while the alongwind perspective requires greater distances for the release geometry used during MVP #4. Although a low value of APP documents better resolution, shorter SR, steeper EL, and lower average background radiance, it is not linked to the actual image contrast, which was determined by fog and cloud cover on 23 May 1997. Therefore, unlike the differences revealed in Figure D-7 (21 May data), Figure D-22 reveals equivalent scatter in the results for the along- and crosswind data on 23 May. We infer from this result that the image quality was dominated by random obscuration by fogs and clouds on 23 May and, therefore, was not linked to the APP parameter.

Figure D-23 is a plot of estimated mass against APP, after filtering by area per pixel (APP ≤ 50 m2 per pixel) and maximum column density (CD ≤ 200 ppm-m). These values for the filters are the same as used previously for Figure D-17 and Figure D-20. The trend line reveals that the estimates of mass improve slightly as the APP decreases. This result illustrates that the PLMMASS estimates are most accurate when one has high quality imagery. A low value of APP documents better resolution as well as shorter slant range, steeper elevation, and better contrast (i.e., lower average background radiance). Therefore, the image quality is better in all systematic respects. However, APP is not linked to the actual image contrast which was determined by fog and cloud cover on 23 May 1997.

Appendix E-Imagery-Derived Characteristics for S1P1

This appendix includes a detailed analysis of the imagery-derived characteristics for the first puff of series 1 (S1P1) from 21 May 1997. These imagery-derived results illustrate the precision and accuracy of the various analysis schemes. Appendices F and G provide two other examples (i.e., S1P2 and S2P1, respectively) from 21 May 1997. These three cases illustrate that there can be significant quantifiable differences in the release geometry and the dispersion characteristics for puffs separated by relatively small distances or times.

This appendix illustrates various analysis schemes. The results support the contention that the most accurate method of estimating the puff's size uses the puff's angular extent measured within each image. The puff's extent is measured within each image as pixels that are converted to angles using the known field of view (FOV) of each camera. The angular extent is converted to physical extent by knowing the slant range between the camera and the "best" value of the puff's position. The "best" position comes from linear regressive fits to PLMTRACK MID data. The fitted data include the "best" available perspectives from all pair-wise combinations of the available imagery. As described in Appendix A, various angles provide the basis for filtering the data for specific perspectives and for better accuracy. Appendix C documented that the expansion rates measured by the "best" method are insensitive to the resolution, slant range, elevation, and background radiance over their operational ranges. Appendix D discussed the quality of the imagery and documented that the observed puff extent included the bulk of the tracer. This appendix compares the various methods and documents the puff characteristics that can be derived from quantitative analysis of multi-site calibrated imagery.

PLMTRACK-Derived Position, Bearing and Speed

PLMTRACK analysis provides the vertices of a polygon about the extent of the puff. Each pair-wise combination of camera sites yields another set of vertices and another polygon. Appendix A described the PLMTRACK-derived rays and vertices. The most accurate PLMTRACK-derived output is the middle of the puff. Appendix B illustrated that PLMTRACK's accuracy is comparable to the GPS when applied to tracking the blimp. For four camera sites, the pair-wise PLMTRACK analysis provides six measurements of the middle of the puff for every set of simultaneous images. The plots in this section document puff characteristics derived solely from the PLMTRACK-derived middle of the puff.

Figure E-1 is a plot of the imagery-derived trajectory of puff S1P1 from 21 May 1997. This Cartesian plot uses distance from the camera site 1 (NASA) as position 0,0. MID (PT) is the middle of the puff and is a direct output from each pair-wise application of PLMTRACK (PT). It is apparent from this plot that the puff went over the VHF camera site. The heading of the plot documents that the data is derived from pair-wise analysis using multiple perspectives (i.e., various pairings of sites). Appendix A defined the variable Ac2c1n. The best positional accuracy occurs when the camera pair view the puff with perspectives that are normal to each other (i.e., |Ac2c1n| = 0°). As indicated in

the heading, the data included in Figure E-1 meet the requirement that the two cameras were within 40° of having normal perspectives of the puff (i.e., |Ac2c1n| ≤ 40°). The heading also indicates that the source position (i.e., the earliest imagery-derived position) was measured by imagery from sites 1 (NASA) and 3 (MOTU). These early images of the puff were collected 0.25 min after the imagery-derived start of the release. The imagery-derived times are accurate to the nearest 0.25 min, which is the data rate for the IR scanner.

Figure E-1 provides the formula and correlation coefficient for the linear regressive fit to the puff's middle (MID) data. The slope (−1.2549) is easily converted to puff bearing (i.e., 90 − ATAN(−1.2549) = 141.45° clockwise of north). The data fall along a straight line, which is confirmed by a correlation coefficient of 1 (i.e., the best possible value). This plot documents a puff bearing toward the southeast but contains no time information (speed).

Figure E-2 presents both bearing and speed for the puff's middle (MID). Figure E-2 documents puff bearing derived by a second method. The instantaneous bearing (Asm) is the angle (A) from the source (s) position to the current middle (m) of the puff at each instant in time. As defined earlier, the source is the earliest measured position of the puff. For a constant bearing and no scatter, one expects a horizontal line when plotting Asm against time. In Figure E-2, the plot documents that this is the case for the PLMTRACK-derived data. Likewise the intercept (142.49°) of the plot of instantaneous bearing against time (i.e., Figure E-2) is equivalent to the average bearing (141.45°) derived by the fit to the Cartesian plot in Figure E-1. The tables in this report list the bearing derived from the linear regressive fit to the Cartesian data (i.e., Figure E-1) since it is less sensitive than the instantaneous bearing to errors in the source position.

21 MAY 1997 SF6 Puff 1 from Series 1 Tracked by Various Pairings of Sites

|Ac2c1n| <= 40   Source = Puff @ 0.25 min by Sites 1 and 3   Trends Derived from PLMTRACK MID

$y = -1.2549x - 332.65$
$R^2 = 1$
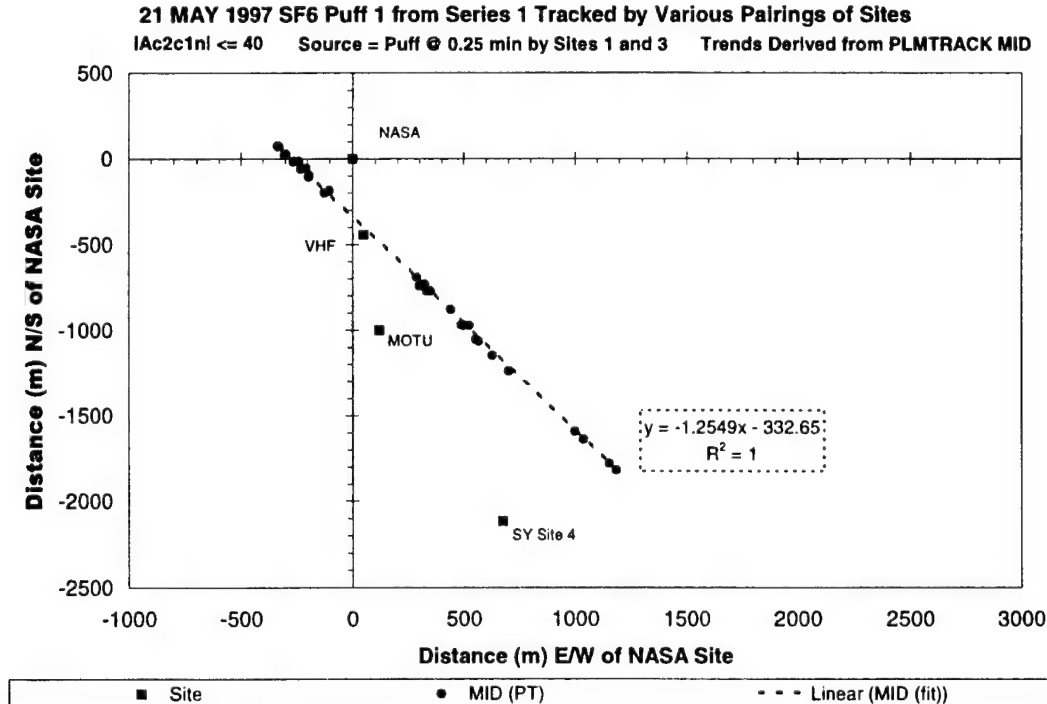
Figure E-1. Cartesian plot documenting the bearing of puff S1P1.

21 MAY 1997 SF6 Puff 1 from Series 1 Tracked by Various Pairings of Sites

|Ac2c1n| <= 40   Source = Puff @ 0.25 min by Sites 1 and 3   Limit to dtsm(min) > 0.5

y = 231.08x - 0.0116
$R^2 = 1$

y = 231.08x - 6.1491
$R^2 = 0.9999$

y = -0.1027x + 142.49

Legend: ▲ Asm   ● Lsm (PT)   □ Lsm (fit)   —— Linear (Asm)   - - - Linear (Lsm (PT))   – – – Linear (Lsm (fit))
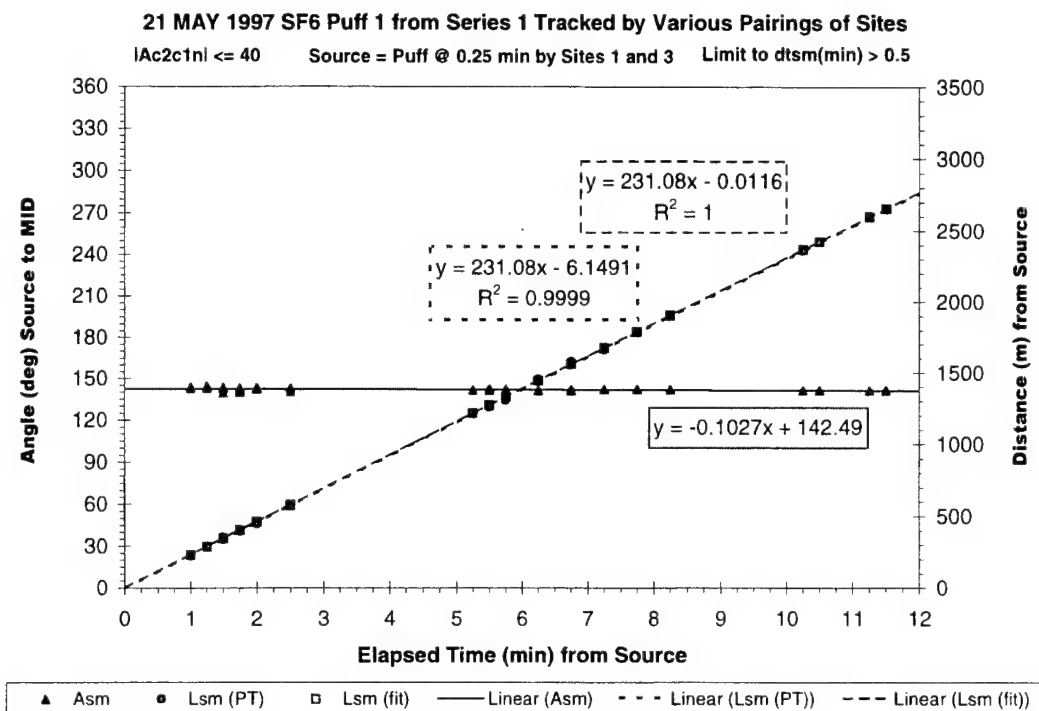
Figure E-2. Plot documenting the bearing and speed for puff S1P1.

Figure E-2 also includes a plot of horizontal distance (Lsm) between the source (s) and the middle (m) of the puff against time. The figure includes two values for Lsm. Lsm (PT) is derived from PLMTRACK output. Lsm (fit) is the value calculated from the formula for the puff's position as a function of time. Therefore Lsm (fit) is the "best" position used in our puff extent calculations. The fact that both values fall on the same curve shows that the fit is accurate. The slope of the plot of Lsm against time is the average puff speed (i.e., 231 m/min = 3.85 m/s).

Figure E-3 illustrates instantaneous speed data derived by two additional methods. Speed is the change in distance with time. In Figure E-2, all values of distance (Lsm) are plotted against time to determine the "average speed." Figure E-3 documents a different estimate of speed for every imagery-derived point. Figure E-3 uses the notation dLsm/dtSM(m/s) for a speed derived for each data point by dividing the differential distance from the source (dLsm) by the elapsed time from the source (dtSM). Since this approach uses the source position, the errors should decrease as the distance and time increase. Ideally, the "cumulative instantaneous speed" derived from this method should approach the "average speed" obtained by the method documented by Figure E-2. This appears to be the case.

Figure E-3 uses the notation dL/dt(m/s){15 s} for an instantaneous speed derived from the distance traveled every 15 s (dt). This method should reveal the scatter in the data over time since it calculates the speed as the distance traveled (dL) between points separated by 15 s (dt). The scatter in these data should reveal any variation in the precision of the data with time. As expected Figure E-3 documents greater scatter in the "instantaneous 15-s differential speed" than in the "instantaneous cumulative speed."
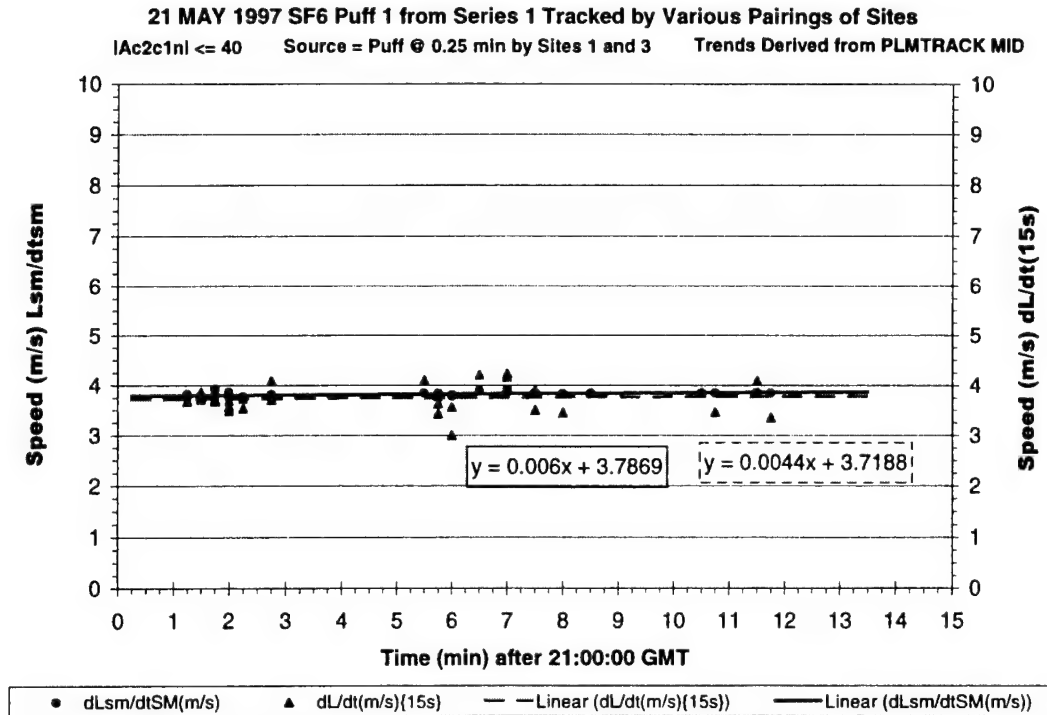
Figure E-3. Plot containing instantaneous and cumulative speeds for puff S1P1.

Comparison of the speeds reported in Figure E-2 (3.85 m/s) and Figure E-3 (3.79 m/s and 3.72 m/s intercepts) reveals that the PLMTRACK analysis provides fairly accurate estimates of speed using any of these methods. The "instantaneous cumulative speed" (dLsm/dtSM(m/s)) will approach the "average speed" at longer times since the percentage errors decrease as the time and distance increase. On the other hand, it should be equal to the "instantaneous 15-s differential speed" only at early times. These observations are consistent with the plotted trends.

Figure E-4 is a plot of the PLMTRACK-derived height of the puff's middle (MID) against time. The data in this plot passed through a couple of additional criteria (i.e., filters). The puff had to be at least 15 pixels in diameter. For any pair of cameras, at least one camera had to have a shallow elevation angle to the puff (i.e., ELmid ≤ 20°). Puff height is difficult to measure if both cameras are viewing the puff from below (i.e., steep EL). As with the previous plots, the data included in Figure E-4 meet the requirement that the two cameras were within 40° of having normal perspectives of the puff (i.e., lAc2c1nl ≤40°). As documented by Appendix B, the PLMTRACK results (30 m) can be more accurate than regular GPS (250 m) for vertical position. Based upon the 30-m accuracy for PLMTRACK, Figure E-4 documents a negligible change in height with time for the S1P1 data.

Puff Dimensions and Expansion Rates

This section of the appendix presents data that illustrate various ways to measure the dimensions of the puff. All of the methods discussed in this appendix use PLMTRACK to measure the position of the puff's middle (MID). The "best" method fits PLMTRACK-derived trends to obtain the formula

100

21 MAY 1997 SF6 Puff 1 from Series 1 Tracked by Various Pairings of Sites
|Ac2c1n| <= 40   Minimum Number of Pixels for Feature >=15   At least one site had ELmid <= 20

$y = -1.3453x + 792.81$

Trends Derived from PLMTRACK MID

■ MID (PT)   - - - Linear (MID (fit))
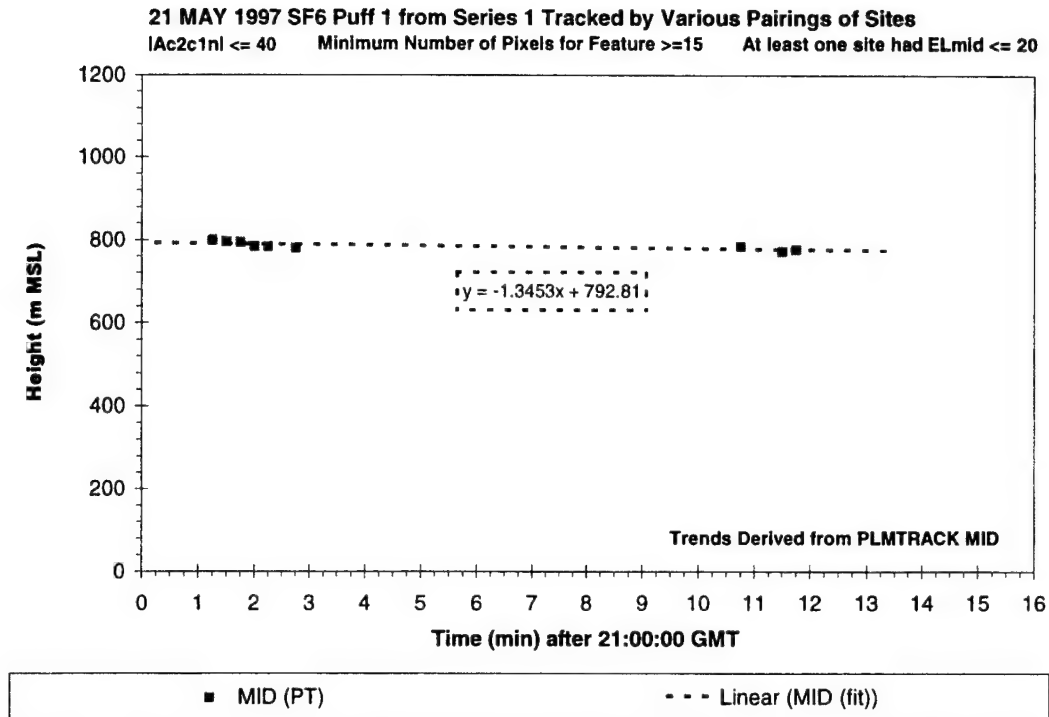
Figure E-4. Plot documenting negligible change in height with time for puff S1P1.

that describes the puff's position as a function of time. Then one can convert the angular extent of the puff in each image to physical extent from that perspective. The angular extent can be directly measured as the number of pixels occupied by the puff within the known FOV of the camera. Other, less accurate, methods use the individual PLMTRACK results to map the extent of the puff. The data included in this appendix illustrate that the PLMTRACK vertices can underestimate the extent of the puff. In spite of such systematic bias in puff dimensions, even the worse methods provided approximately the same expansion rates as the "best" method.

We tried two methods that use the PLMTRACK vertices from each pairing of cameras to measure the extent of the puff. In one approach, the analyst used PLMTRACK to triangulate the ends of the puff along a specific axis (i.e., along- or crosswind). The other approach calculated the extent from the eleven PLMTRACK vertices derived from each pair of cameras. The errors in these approaches resulted from the two factors: (1) calibration errors and (2) poor perspective.

Appendix B documented that the PLMTRACK data can be as accurate as regular GPS for horizontal position, which corresponds to 100 m for the 2-sigma value. Unfortunately, the magnitude of these errors is comparable to the initial size of the puffs. Since the PLMTRACK offsets (i.e., systematic errors) are often similar for the two ends of the puff, one can get fairly accurate extent for the puff by tracking the two ends. However, the analyst cannot always correctly identify the two ends since the perspective is constantly changing. Therefore, attempts to PLMTRACK the ends of the puff rely heavily upon the operator's bias (i.e., correction for perspective). From certain perspectives, the PLMTRACK offsets can be significantly different for the two ends of the puff. This can lead to larger systematic errors in the puff's dimensions during portions of its trajectory.

101

Appendix A illustrated that the PLMTRACK pair-wise analysis reports the nearest approach for various rays from two cameras' perspectives. The polygon formed by these vertices should contain the puff. The data in this appendix illustrate that the PLMTRACK polygon accurately mapped the puff's alongwind dimensions. However, the crosswind data in this appendix illustrate that the puff's dimensions are systematically underestimated by the PLMTRACK polygon when compared to the "best" method. The underestimation could result from calibration errors in either camera's pointing angles and from poor perspective for certain rays. When the rays are nearly parallel, small errors in the pointing angles result in large offsets (i.e., errors) in the nearest approach of the rays. As discussed in appendix A, the PLMTRACK-derived middle (MID) of the puff is included in the trend plots only when there is good perspective (i.e., data meets filter conditions). However, the various filters ensure good perspective only for the middle rays. Hence, there are much larger errors for some of the other rays (i.e., the other vertices of the polygon).

The discussions for the crosswind and alongwind analyses are in separate sections for S1P1. This should make comparisons easier. The analyses document the extent and expansion of the puff in several ways to illustrate the consistency of the results. In a third section, summary plots emphasize other axes and the sensitivity of the expansion rate to two experimental variables.

Crosswind Measurements

Figures E-5 and E-6 are plots of data derived from crosswind "end" measurements. When viewing the puff from the alongwind perspective (either from up- or downwind), the left and right ends of the

21 May 1997 SF6 Puff 1 from Series 1 Tracked by Various Pairings of Sites

PLMTRACK Line Method Applied to Crosswind End Measurements

$y = -1.2073x - 244.85$
$R^2 = 0.9997$

$y = -1.2769x - 385.53$
$R^2 = 1$
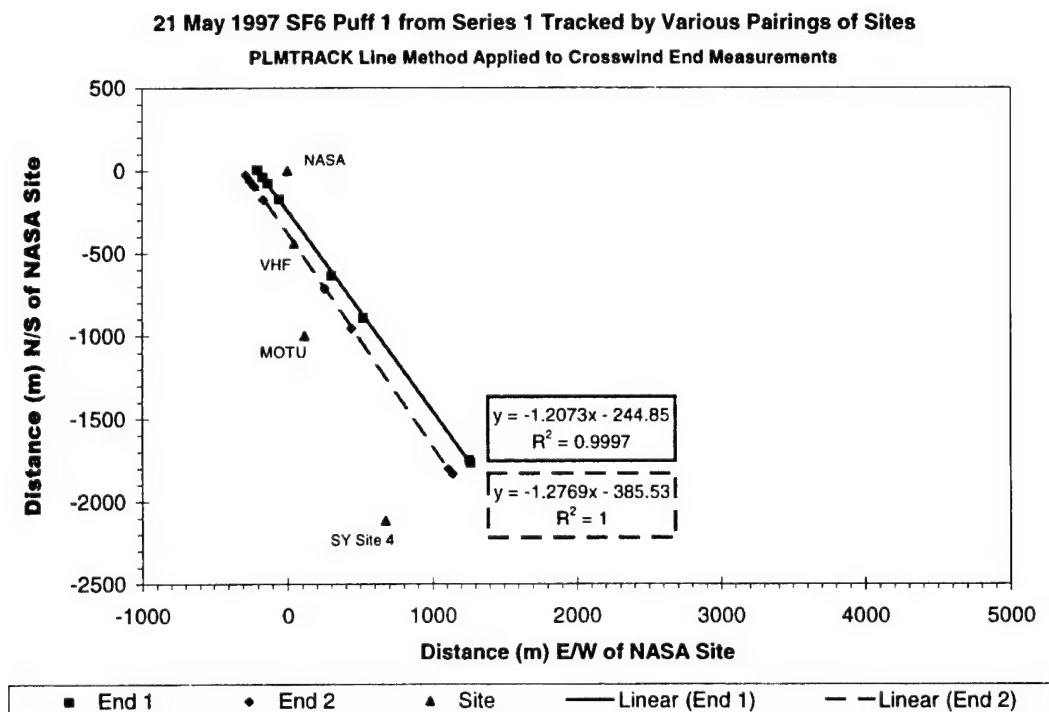
Figure E-5. Cartesian plot of the PLMTRACK-derived crosswind ends of the puff.

21 May 1997 SF6 Puff 1 from Series 1 Tracked by Various Pairings of Sites
PLMTRACK Line Method Applied to Crosswind End Measurements

232.13-231.42 = 0.7 m/min

$y = 231.42x - 16.046$
$R^2 = 0.9991$

$y = 232.13x - 19.866$
$R^2 = 0.9997$
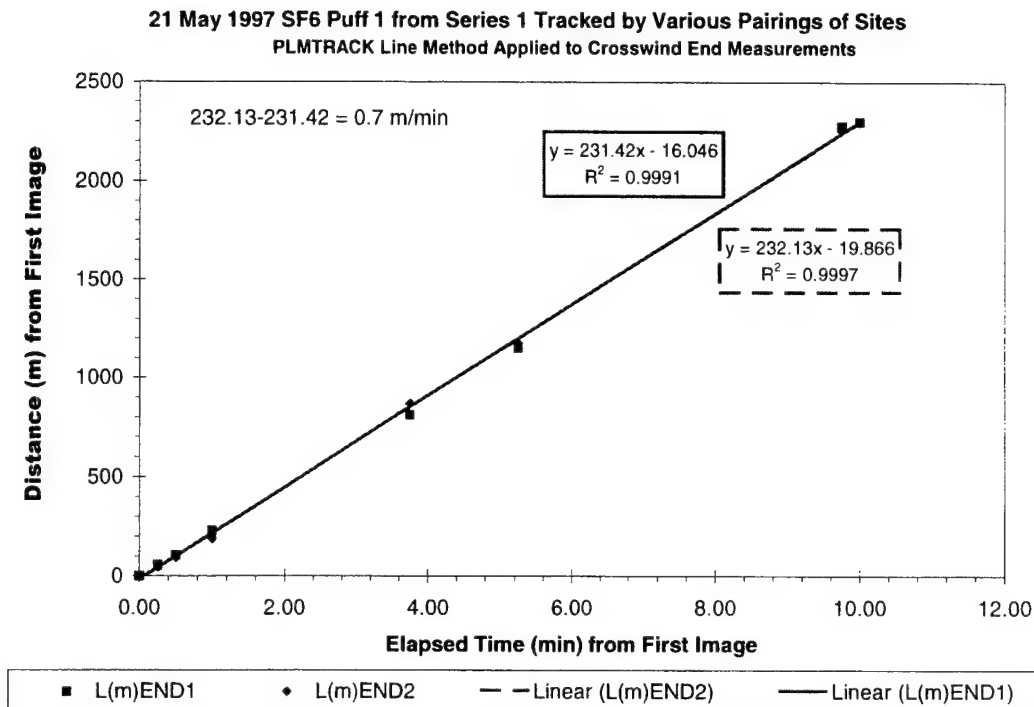
Figure E-6. Distance versus time (speed) plots for the crosswind ends of the puff.

puff within the image should correspond to the crosswind ends. The analyst used the best pair of images and PLMTRACK to triangulate the position of these ends. The best pair of sites would include one image from a camera with alongwind perspective and the other image from a camera with crosswind perspective. This end-triangulation analysis requires the analyst to point at the same end of the puff in the images from two sites. In spite of this difficulty, the results in Figures E-5 and E-6 document that the analyst was fairly successful. Figure E-5 is a Cartesian plot and documents that the crosswind ends traveled diverging trajectories as the puff moved from the source to the southeast of NASA site. Figure E-6 is a plot of distance versus time and documents that the two crosswind ends moved at the same speed. Since one expects the crosswind ends to move at the same speed away from the source and to diverge as the puff disperses, these plots illustrate reasonable results.

Figure E-7 is a plot of the PLMTRACK-derived crosswind diameter against time. Figures E-8 through E-10 illustrate large variations in experimental parameters during the movement of the puff. Appendix A illustrated the various dimensions and angles included in Figures E-7 through E-10. Figure E-8 documents different elevations to the middle of the puff from each site as well as trends as the puff moves. Figure E-9 documents that the camera site's perspective changes not only with respect to the puff's trajectory (i.e., Ac1n and Ac2n) but also with respect to the complimentary nature of the camera pair (i.e., Ac2c1n). Figure E-10 reports the camera locations relative to the puff's current position and average trajectory. Rather than reviewing the significance of the various angles (defined in Appendix A), these figures were intended to document the huge variations in perspective associated with the imagery-derived dataset. This variation in perspective can cause significant errors in the PLMTRACK polygon (i.e., PLMTRACK-derived extent). The figure headings

103

21 MAY 1997 SF6 Puff 1 from Series 1 Tracked by Various Pairings of Sites

Atilt = 90 +/- 10 |Ac2c1n| <= 40   For Dh_LR use: |Ac2c1n| <= 20   For Dhor(y), ELbot >= 70
Minimum Number of Raw Pixels for Feature >=18

$y = 9.6411x + 35.488$
$R^2 = 0.9736$

Derived from PLMTRACK Vertices

● DhC1_CER'	▲ DhC2_CER'	● DhC1_LRc2'
▲ DhC2_LRc1'	○ DhC1_NF'	△ DhC2_NF'
— —Linear (D (CER, LR, NF)')		
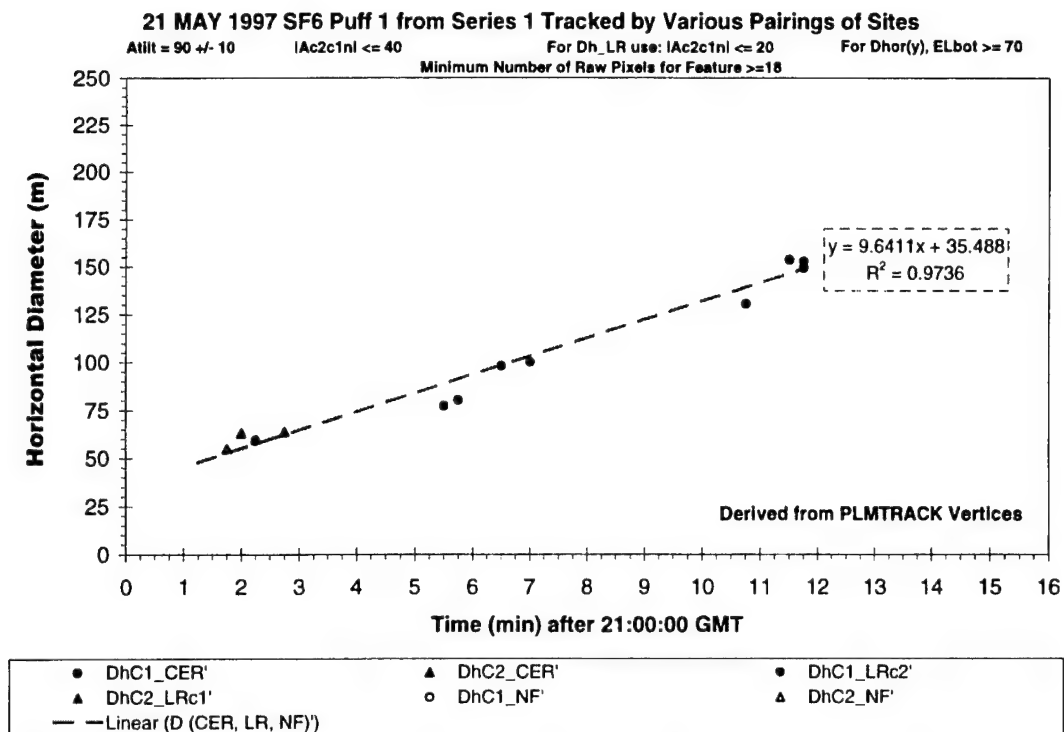
Figure E-7. PLMTRACK-derived crosswind extent versus time (expansion rate in m/min).

21 MAY 1997 SF6 Puff 1 from Series 1 Tracked by Various Pairings of Sites

|Ac2c1n| <= 40   Source = Puff @ 0.25 min by Sites 1 and 3   Trends Derived from PLMTRACK MID

| ● MID (C1) | △ MID (C2) |
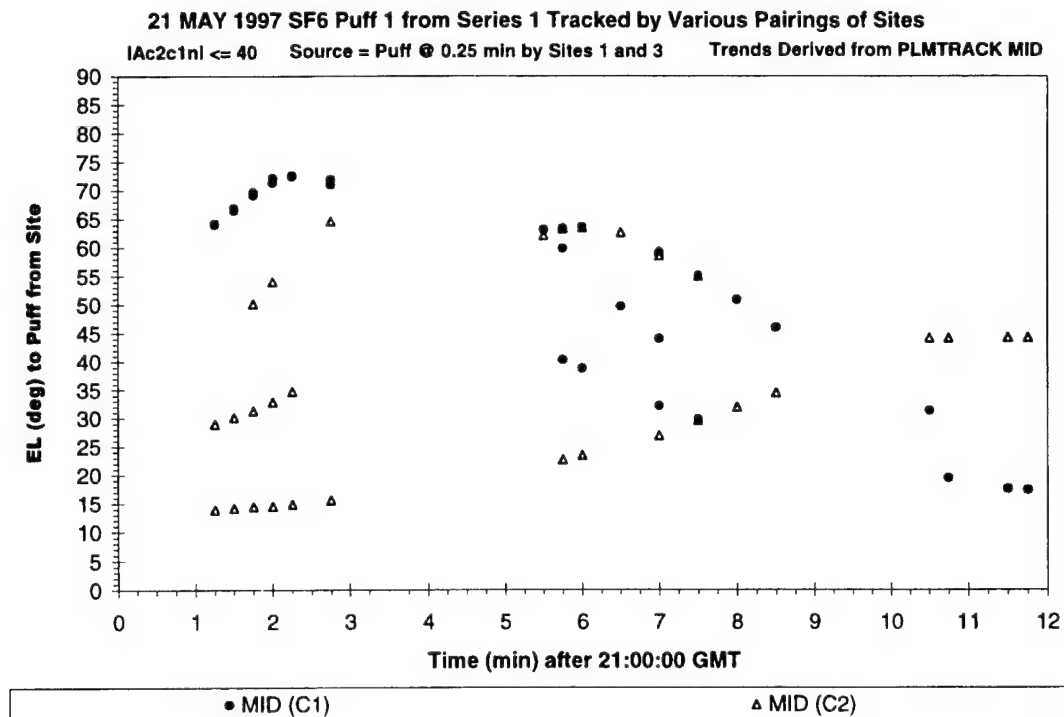
Figure E-8. Elevation angles to the puff plotted against time (data from all four sites).

104

21 MAY 1997 SF6 Puff 1 from Series 1 Tracked by Various Pairings of Sites

IAc2c1nI <= 40   Source = Puff @ 0.25 min by Sites 1 and 3   Trends Derived from PLMTRACK MID
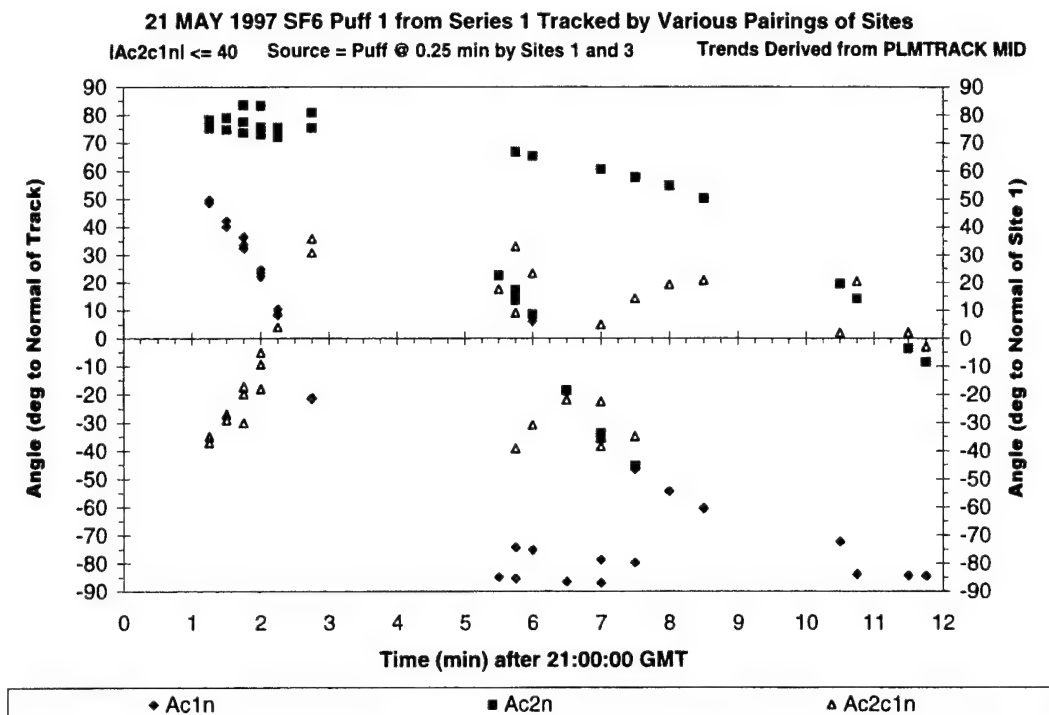
Figure E-9. Camera angles relative to each other versus time (data from all four sites).

21 MAY 1997 SF6 Puff 1 from Series 1 Tracked by Various Pairings of Sites

IAc2c1nI <= 40   Source = Puff @ 0.25 min by Sites 1 and 3 Trends Derived from PLMTRACK MID
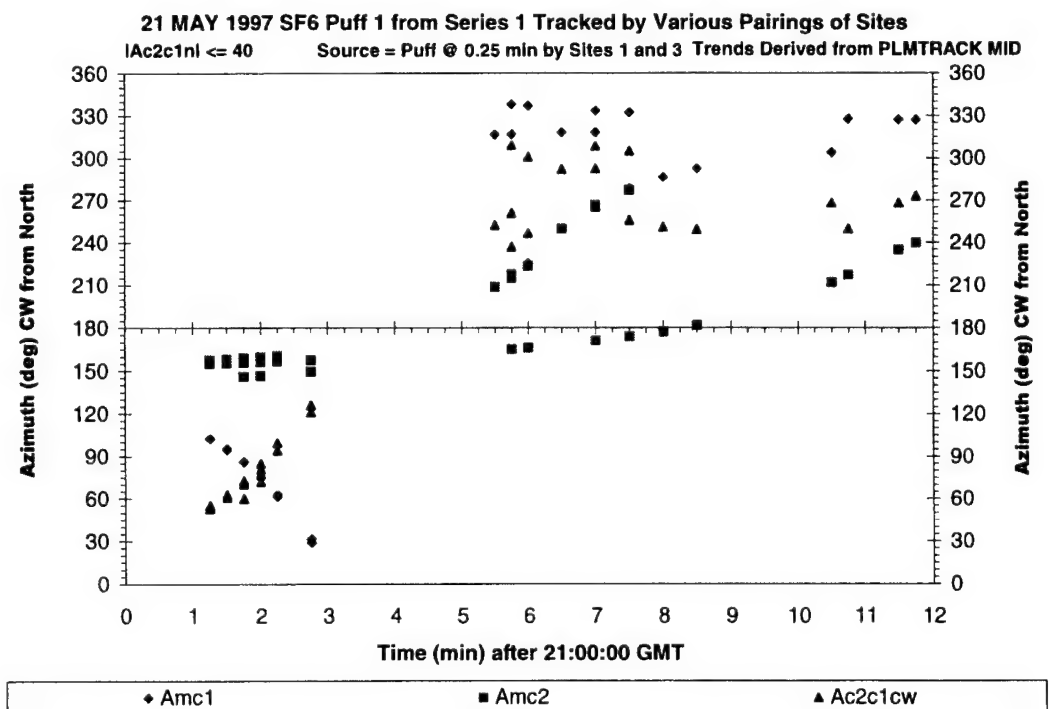
Figure E-10. Camera angles relative to puff middle versus time (data from all four sites).

105

document that the plotted data have been filtered for good perspective. After passing the filters (Atilt, Ac2c1n, ELbot, and pixel), it is apparent in Figure E-7 that all of the crosswind diameters fall on the same line. The slope (9.6m/min) of that line is the crosswind expansion rate. As mentioned in Appendix A, the apostrophe after a diameter's notation indicates that the diameter was derived from the PLMTRACK vertices (i.e., a polygon defined by one pair of camera sites).

Figures E-11 through E-13 document the puff's crosswind extent derived from the "best" method. As mentioned previously, the "best" method uses the fit-derived position of the puff to convert the angular extent within an image to physical extent (i.e., see appendix A). The angular extent is calculated directly from the puff's size in pixels and the FOV of that image. This method minimizes any errors associated with the PLMTRACK-derived polygon (i.e., Figure E-7). The fit-derived position is more accurate than any one PLMTRACK triangulation since it is based upon all six pair-wise combinations of all imagery after filtering for only the best perspectives.

Figure E-11 uses the same filters as used in Figure E-7. Although the slopes are similar, the puff dimensions are substantially smaller in Figure E-7 than in Figure E-11. The underestimation of the puff's diameter in Figure E-7 resulted from the conversion of the inaccurate PLMTRACK-derived polygon back to the puff's angular extent. Figures E-7 and E-11 contain approximately the same number of points only because we applied the same filters to the data. Since the "best" method does not rely directly on pair-wise analysis, Figures E-12 and E-13 document that the "best" method provides useful data from all imagery that can see the crosswind extent (i.e., Atilt = 90±10). Therefore, one is not concerned about the relative orientation of a second camera (i.e., no need to filter by Ac2c1n).
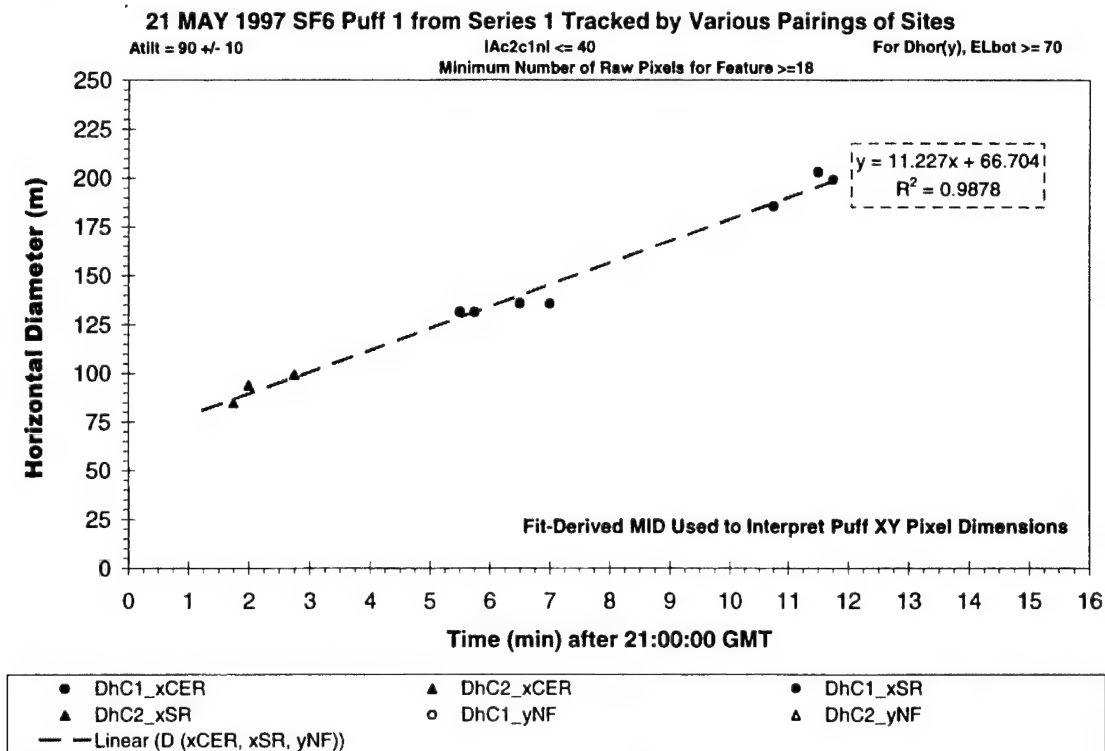
Figure E-11. Ac2c1n filtered "best" crosswind extent versus time (expansion rate in m/min).

106
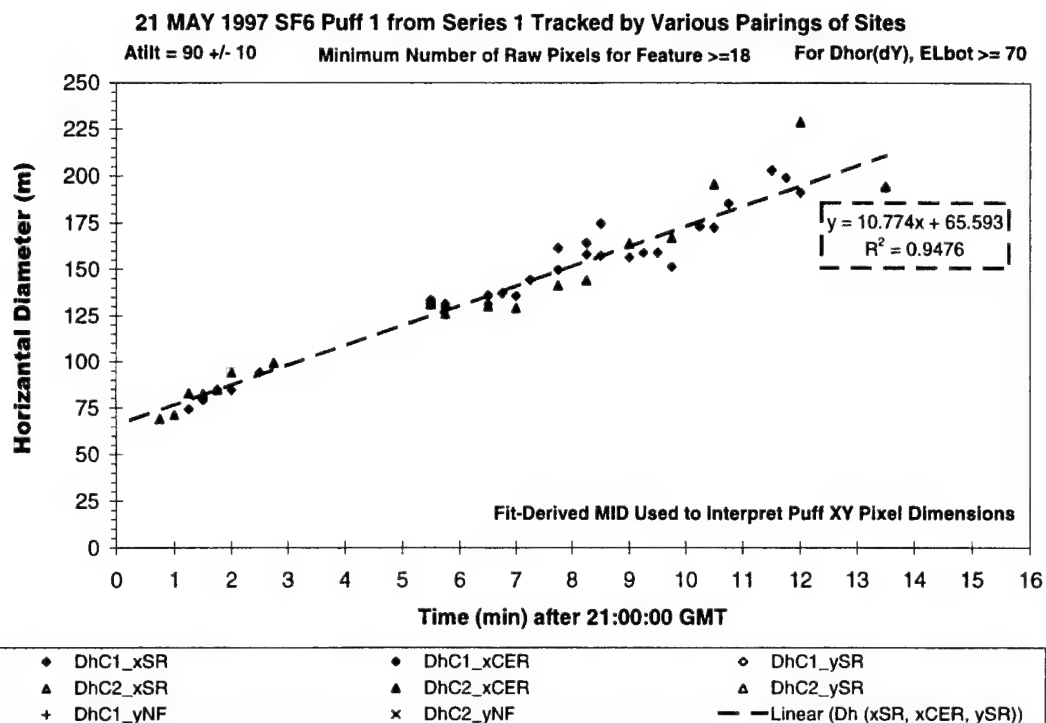
Figure E-12. "Best" crosswind extent versus time (expansion rate in m/min).
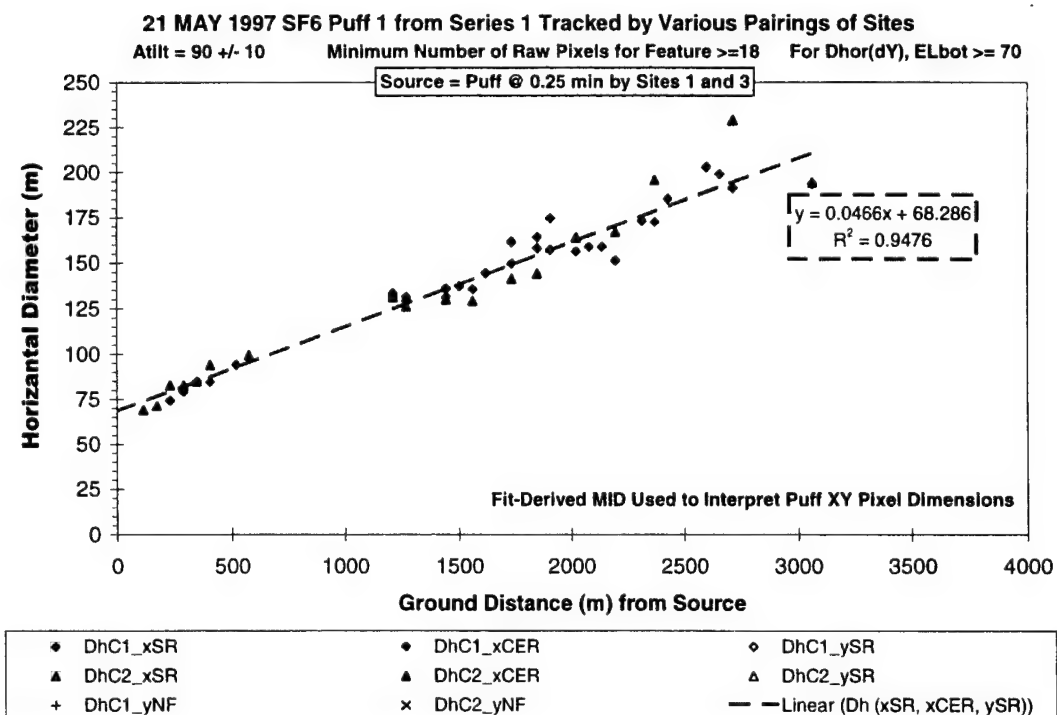
Figure E-13. "Best" crosswind extent versus distance (expansion rate in m/m).

Figures E-12 and E-13 plot the "best" diameters against time and distance, respectively. The slopes in Figure E-12 (10.8m/min) and Figure E-13 (0.047 m/m) are the expansion rates in m/min and m/m, respectively. The "best method" expansion rate (10.8m/min from Figure E-12) is 1.2m/min (13%) larger than the "PLMTRACK polygon" expansion rate (9.6m/min from Figure E-7).

Alongwind Measurements

Figures E-14 and E-15 are plots of data derived from alongwind "end" measurements. When viewing the puff from a crosswind perspective, the left and right ends of the puff within the image should correspond to the alongwind ends (i.e., up- and downwind ends). The analyst used the best pair of images and PLMTRACK to triangulate the position of these ends. The best pair of sites would include one image from a camera with crosswind perspective and the other image from a camera with an alongwind perspective. This end-triangulation analysis requires the analyst to point at the same end of the puff in the images from two sites. In spite of this difficulty, the results in Figures E-14 and E-15 document that the analyst was fairly successful. Figure E-14 documents as a Cartesian plot that the two ends traveled almost the same trajectories as the puff moved from the source to the southeast of NASA site. The alongwind ends should lie along the same vector (i.e., the wind bearing). Figure E-14 documents a 3° difference in bearing for the "alongwind" ends and, therefore, some error in the analyst's perspective or in the triangulation accuracy. Figure E-15 is a plot of distance versus time and documents that the two ends moved at different speeds. Since the puff is diverging as it moves along the wind bearing, the leading edge of the puff should move faster (average speed + dispersion) than the tailing end (average speed − dispersion). In Figure E-15, the difference in speed should be the expansion rate (i.e., 33 m/min).
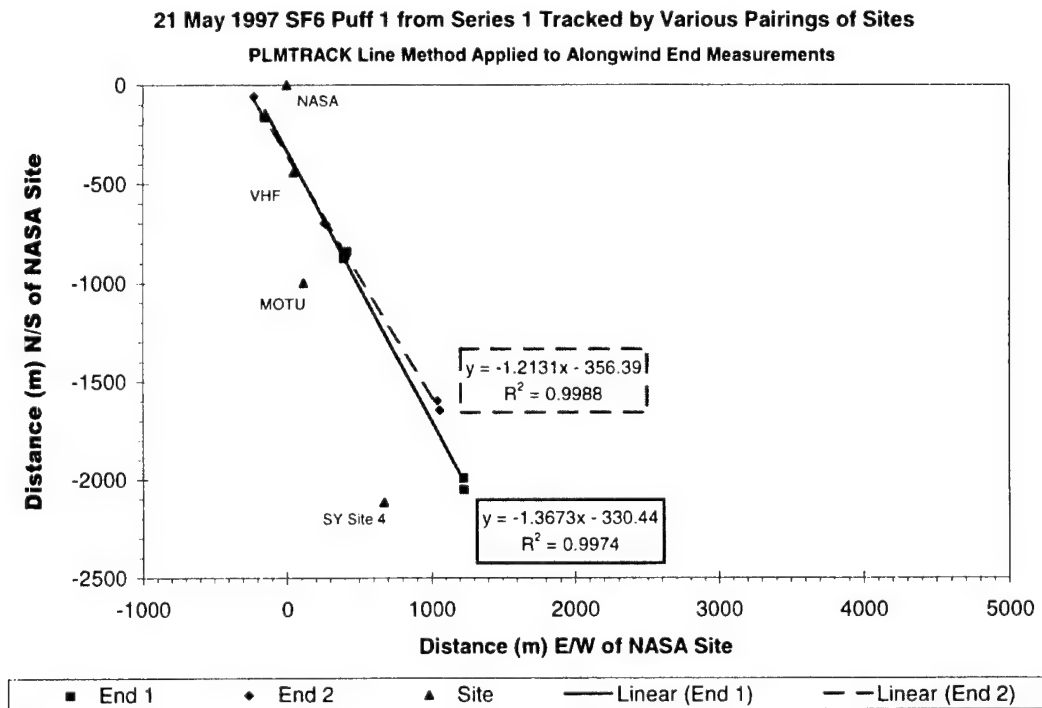
Figure E-14. Cartesian plot of the PLMTRACK-derived alongwind ends of the puff.

21 May 1997 SF6 Puff 1 from Series 1 Tracked by Various Pairings of Sites
PLMTRACK Line Method Applied to Alongwind End Measurements
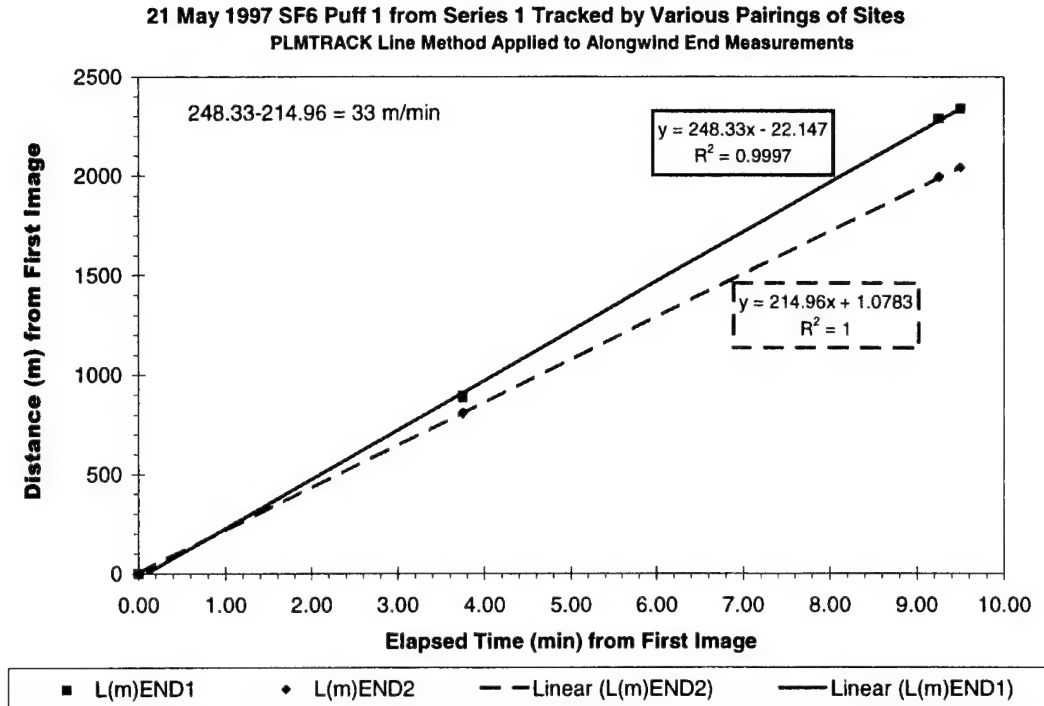
Figure E-15. Distance versus time (speed) plots for the alongwind ends of the puff.

Figures E-16 through E-19 are plots of the alongwind diameter against time or distance. The slope of these trends is the expansion rate of the puff. Appendix A illustrated the various dimensions and angles used in these figures and in their captions, legends, and headers. The crosswind section discussed the complexity of the imagery data and the need to filter the data for good accuracy and perspective. The figure headings document that the plotted data have been filtered for good perspective. After passing the filters (Atilt, Ac2c1n, ELbot, and pixel), Figure E-16 shows that the alongwind diameters are nicely fit by linear regression. The slope documents an expansion rate of 38 m/min, which is 5 m/min (15%) larger than the 33m/min value derived from the end-triangulation method illustrated in Figure E-15. As mentioned in Appendix A, the apostrophe after a diameter's notation indicates that the diameter was derived from the PLMTRACK vertices (i.e., a polygon defined by one pair of camera sites).

Figures E-17 through E-19 document the puff's alongwind extent derived from the "best" method. As mentioned previously, the "best" method uses the fit-derived position of the puff to convert the angular extent within an image to physical extent (i.e., see appendix A). The angular extent is calculated directly from the puff's size in pixels and the FOV of that image. This method minimizes any errors associated with the PLMTRACK-derived polygon (i.e., Figure E-16). The fit-derived position is more accurate than any one PLMTRACK triangulation since it is based upon all six pairwise combinations of all imagery after filtering for only the best perspectives.

Figure E-17 uses the same filters as used in Figure E-16. In these two plots, both the puff dimensions and the expansion rates (i.e., slopes) are similar in value. These results document that one can obtain an accurate PLMTRACK-derived polygon for favorable conditions. This was not the case
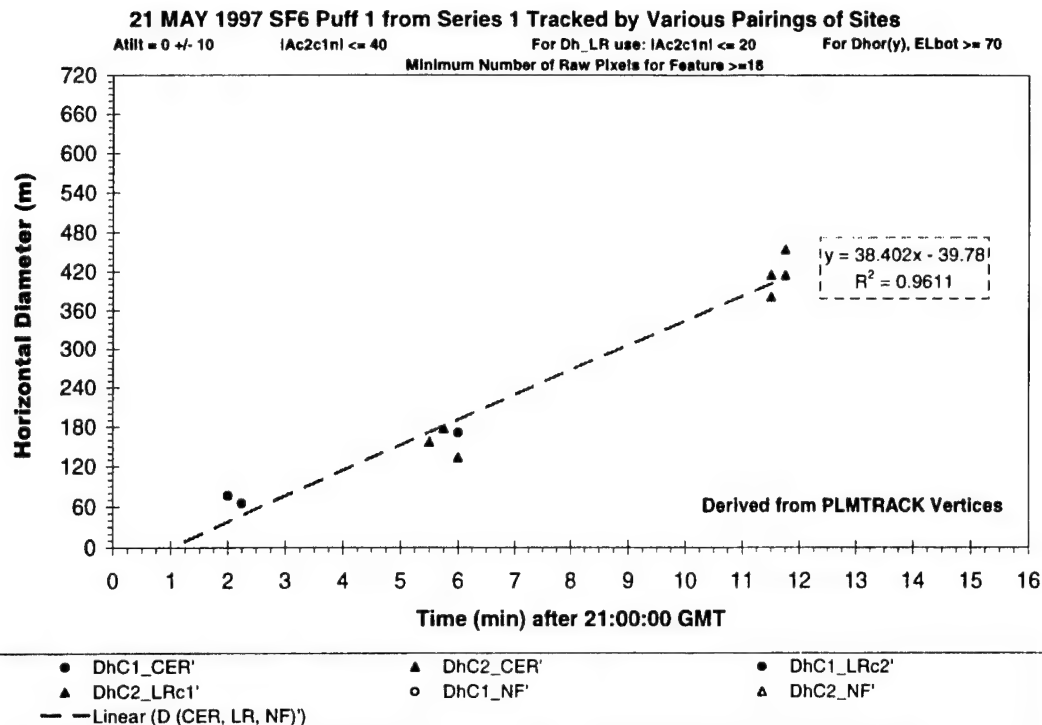
Figure E-16. PLMTRACK-derived alongwind extent versus time (expansion rate in m/min).
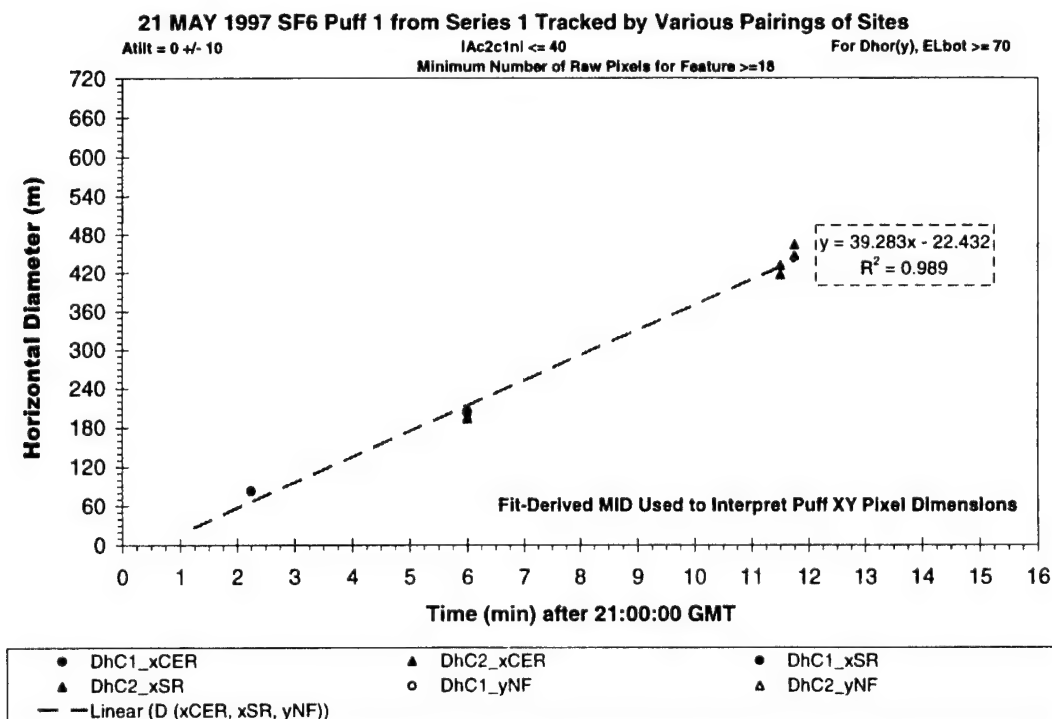
Figure E-17. Ac1c2n filtered "best" alongwind extent versus time (expansion rate in m/min).
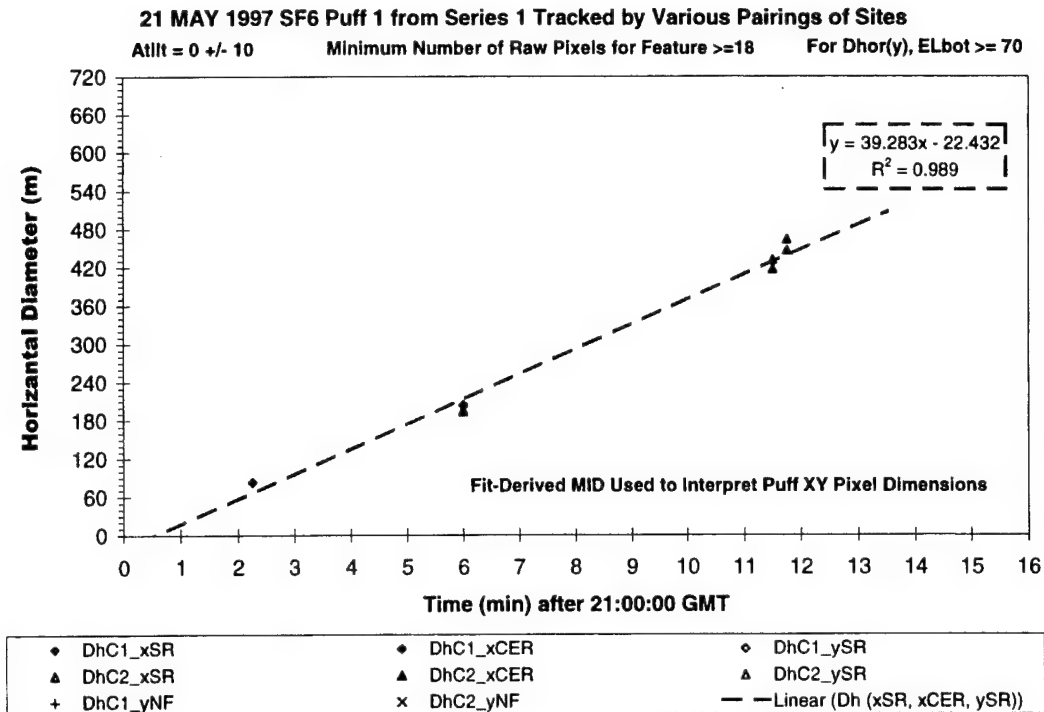
Figure E-18. "Best" alongwind extent versus time (expansion rate in m/min).
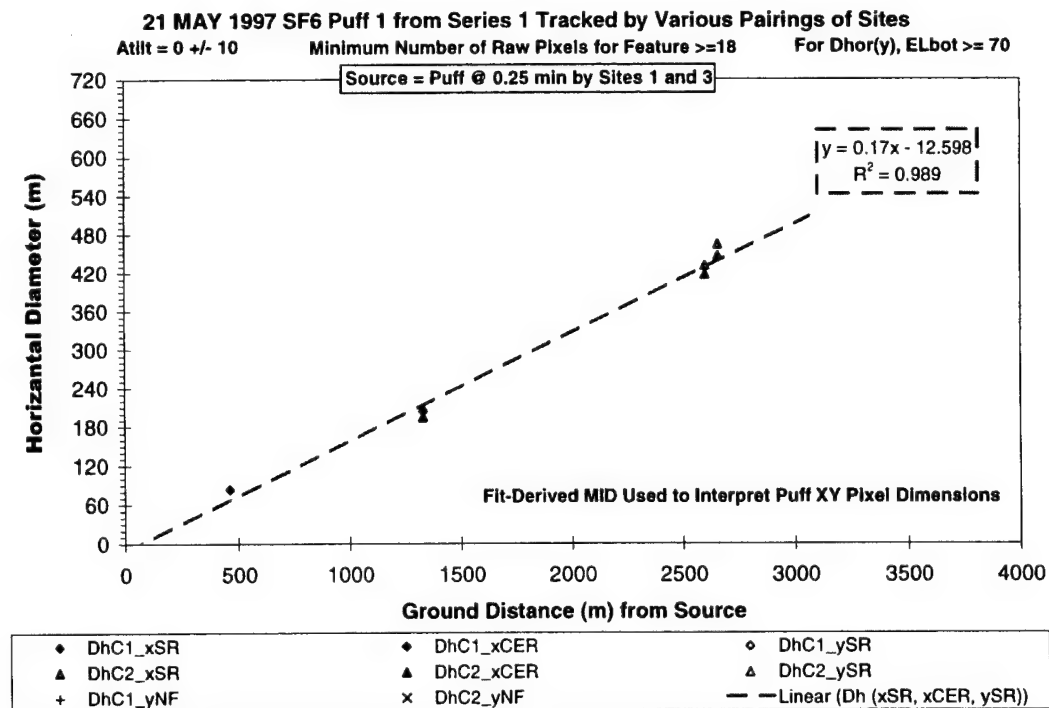
Figure E-19. "Best" alongwind extent versus distance (expansion rate in m/m).

111

for the crosswind data for S1P1 (i.e., the previous section of this appendix). Since the "best" method does not rely directly on pair-wise analysis, Figures E-18 and E-19 document results from all imagery that can see the crosswind extent (i.e., Atilt = 90±10). Since one is not concerned about the relative orientation of a second camera, there was no need to filter by Ac2c1n. Even though the Ac2c1n filter is not used in these plots, they contain the same number of data points as in Figure E-17 (i.e., filtered by Ac2c1n). Thus, the Ac2c1n filter did not eliminate any data.

The slopes in Figure E-18 (39 m/min) and Figure E-19 (0.17 m/m) are the "best method" values for the alongwind expansion rates in m/min and m/m, respectively. The "best method" result (39m/min) is 6 m/min (18%) greater that the expansion rate (33m/min) derived from the end-triangulation method (Figure E-15) and only 1m/min (3%) larger than the expansion rate (38m/min) derived from the PLMTRACK polygon method (Figure E-16).

Angular Trends and Sensitivity to Filters

The previous sections of this appendix reviewed the crosswind and alongwind data separately. This section provides summary plots that document angular trends in the dimension data as well as sensitivity of the expansion rates to experimental parameters.

Figure E-20 shows the puff's "best method" diameters derived from all available imagery plotted against time. The linear regressive lines are included to document the alongwind and crosswind trends. The diameters for other perspectives (i.e., tilt axes) fall between these two extremes.
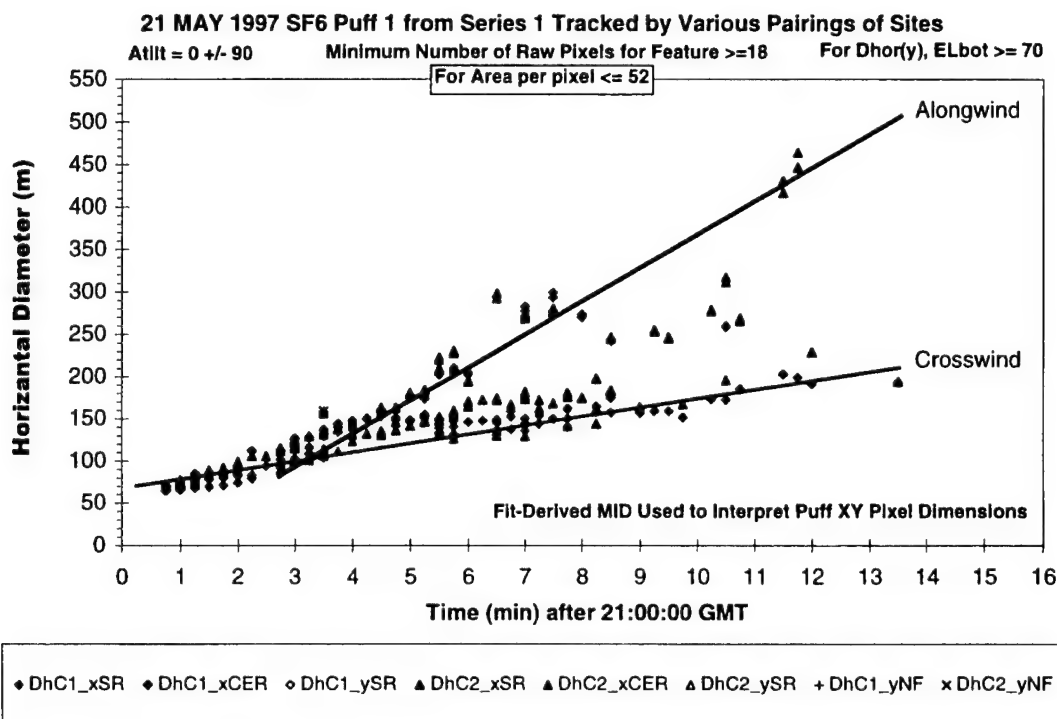
Figure E-20. Summary puff dimension plot showing all perspectives with regressive fits to the along- and crosswind trends.

Figure E-21 plots the PLMTRACK-derived horizontal expansion rate against tilt angle. The plotted diameters are from the PLMTRACK polygons. The plot reveals a relatively smooth transition from the fastest expansion rate in the alongwind axis (0° or 180°) to the slowest expansion rate in the crosswind axis (90°). The plot suggests a slight shifting of the minimum and maximum for the trend from the pure alongwind and crosswind axes. This apparent shift in the position of the maximum and minimum as well as the scatter in the data along the trend are probably due to the scatter in the data. In order to obtain enough data to fully characterize the trend, the filters were opened to include 10° of scatter about the tilt angle (i.e., Tilt Window ±10) and almost parallel perspectives (|Ac1c2n| < 80). In addition, the regressive fits were of limited accuracy (i.e., low correlation coefficients) for some perspectives due to the scatter and sparseness of the data.

Figures E-22 and E-23 show the effect of two filters on the alongwind and crosswind expansion rates. In these figures the along- and crosswind expansion rates are plotted against the value of pixel threshold and tilt window, respectively. Figure E-22 documents a constant value for both expansion rates as the threshold for the minimum number of pixels is raised from 0 to 40.

In contrast, Figure E-23 reveals that both expansion rates depend upon the tilt window. This dependence is consistent with the expansion rates' variation with tilt angle (i.e., Figure E-21). As the angular window for the tilt angle approaches 90°, all data plotted in Figure E-20 would be included in the fit. Therefore, the two curves in Figure E-23 should converge at a 90° window, but a regressive fit would no longer be appropriate. If there were not an angular dependence, the expansion rate would be the same for along- and crosswind perspectives, and there would be no sensitivity to the tilt window or tilt angle.
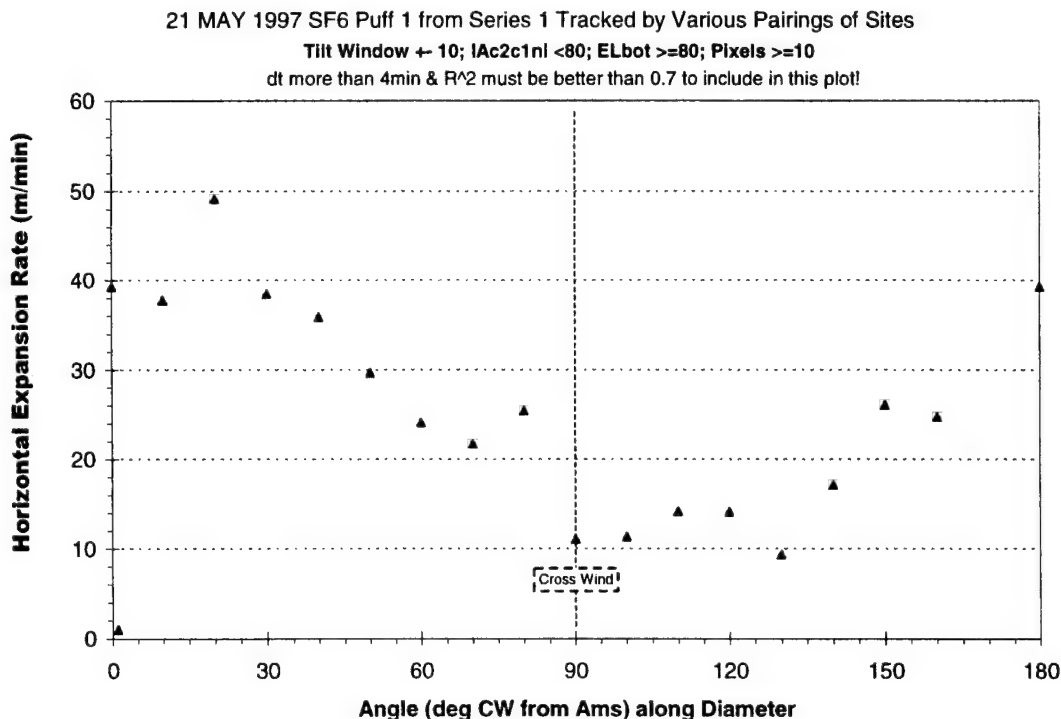
Figure E-21. Summary plot documenting the variation in expansion rate with perspective.
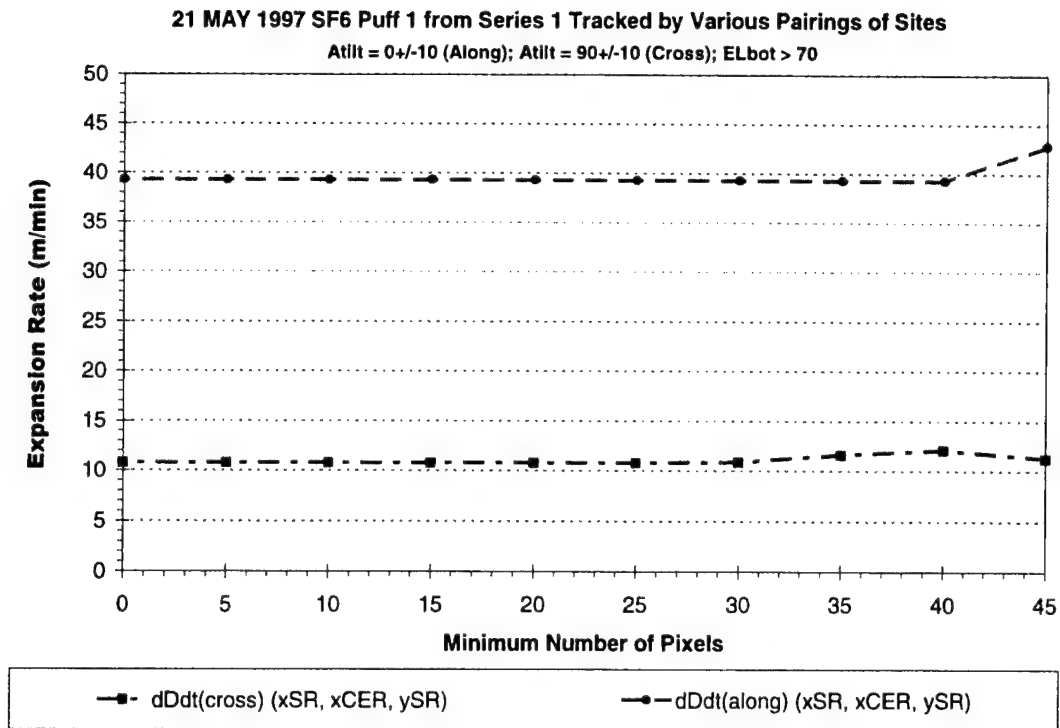
Figure E-22. Expansion rate sensitivity to puff size (in pixels) filtering.
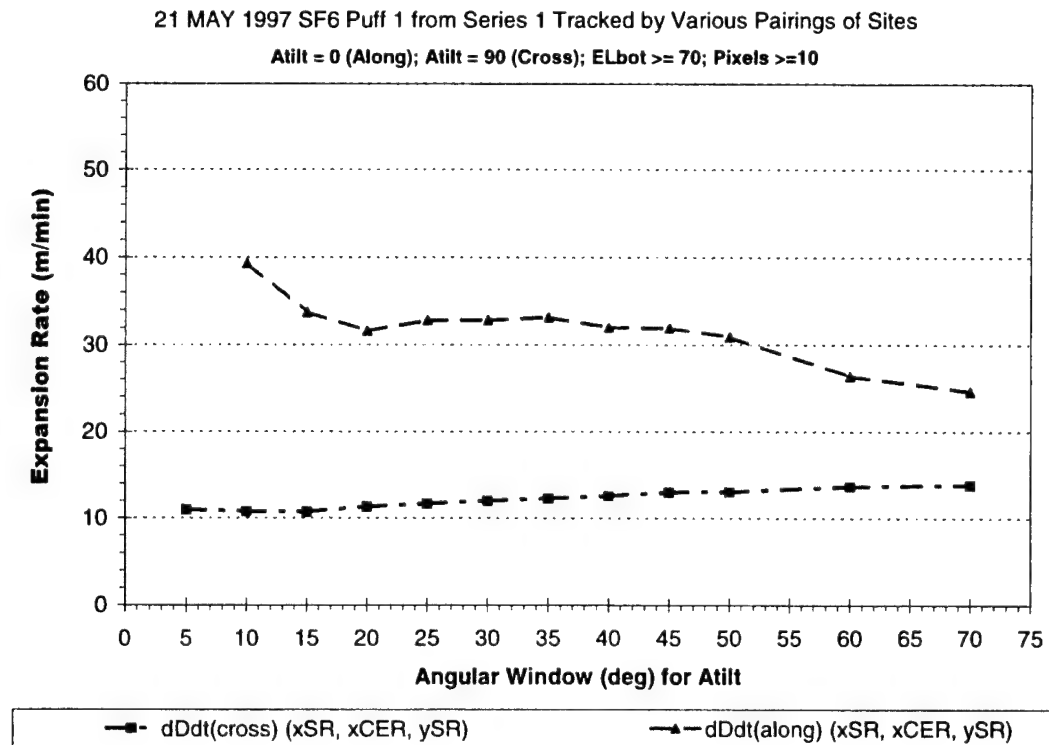
Figure E-23. Expansion rate sensitivity to the angular window about the perspective.

114

This appendix provided a detailed example of the puff analysis. The puff was series 1 puff 1 (S1P1) from 21 May 1997. Appendices F and G provide results for S1P2 and S2P1, respectively. Comparison reveals that S1P1 was dramatically different from the other puffs. In fact, the angular trends reversed. Therefore, in addition to illustrating the analysis schemes, these appendices illustrate that the dispersion rates are extremely sensitive both to release position and release time.

Appendix F-Imagery-Derived Characteristics for S1P2

This appendix includes a detailed analysis of the imagery-derived characteristics for the second puff of series 1 (S1P2) from 21 May 1997. These imagery-derived results illustrate the precision and accuracy of the various analysis schemes. Appendices E and G provide two other examples (i.e., S1P1 and S2P1, respectively) from 21 May 1997. These three cases illustrate that there can be significant quantifiable differences in the release geometry and the dispersion characteristics for puffs separated by relatively small distances or times.

This appendix illustrates various analysis schemes. The results support the contention that the most accurate method of estimating the puff's size uses the puff's angular extent measured within each image. The puff's extent is measured within each image as pixels that are converted to angles using the known field of view (FOV) of each camera. The angular extent is converted to physical extent by knowing the slant range between the camera and the "best" value of the puff's position. The "best" position comes from linear regressive fits to PLMTRACK MID data. The fitted data include the "best" available perspectives from all pair-wise combinations of the available imagery. As described in Appendix A, various angles provide the basis for filtering the data for specific perspectives and for better accuracy. Appendix C documented that the expansion rates measured by the "best" method are insensitive to the resolution, slant range, elevation, and background radiance over their operational ranges. Appendix D discussed the quality of the imagery and documented that the observed puff extent included the bulk of the tracer. This appendix compares the various methods and documents the puff characteristics that can be derived from quantitative analysis of multi-site calibrated imagery.

PLMTRACK-Derived Position, Bearing and Speed

PLMTRACK analysis provides the vertices of a polygon about the extent of the puff. Each pair-wise combination of camera sites yields another set of vertices and another polygon. Appendix A described the PLMTRACK-derived rays and vertices. The most accurate PLMTRACK-derived output is the middle of the puff. Appendix B illustrated that PLMTRACK's accuracy is comparable to the GPS when applied to tracking the blimp. For four camera sites, the pair-wise PLMTRACK analysis provides six measurements of the middle of the puff for every set of simultaneous images. The plots in this section document puff characteristics derived solely from the PLMTRACK-derived middle of the puff.

Figure F-1 is a plot of the imagery-derived trajectory of puff S1P2 from 21 May 1997. This Cartesian plot uses distance from camera site 1 (NASA) as position 0,0. MID (PT) is the middle of the puff and is a direct output from each pair-wise application of PLMTRACK (PT). It is apparent from this plot that the puff went over the VHF camera site. The heading of the plot documents that the data is derived from pair-wise analysis using multiple perspectives (i.e., various pairings of sites). Appendix A defined the variable Ac2c1n. The best positional accuracy occurs when the camera pair view the puff with perspectives that are normal to each other (i.e., |Ac2c1n| = 0°). As indicated in

the heading, the data included in Figure F-1 meet the requirement that the two cameras were within 65° of having normal perspectives of the puff (i.e., |Ac2c1n| ≤65°). The heading also indicates that the source position (i.e., the earliest imagery-derived position) was measured by imagery from sites 1 (NASA) and 2 (VHF). These source images were collected 0.25 min after the imagery-derived start of the release. The imagery-derived times are accurate to the nearest 0.25 min due to the data rate.

Figure F-1 provides the formula and correlation coefficient for the linear regressive fit to the puff's middle (MID) data. The slope (–1.6649) is easily converted to puff bearing (i.e., 90 – ATAN(– 1.6649) = 149.01° clockwise from north). The data fall along a straight line, which is confirmed by a correlation coefficient of 1 (i.e., the best possible value). This plot documents the bearing but contains no time information (speed).

Figure F-2 presents both bearing and speed for the puff's MID. Figure F-2 documents puff bearing derived by a second method. The instantaneous bearing (Asm) is the angle (A) from the source (s) position to the current middle (m) of the puff at each instant in time. As defined earlier, the source is the earliest measured position of the puff. For a constant bearing and no scatter, one expects a horizontal line when plotting Asm against time. In Figure F-2, the plot documents that this is the case for the PLMTRACK-derived data. Likewise the intercept (151.80°) of the plot of instantaneous bearing against time (i.e., Figure F-2) is equivalent to the average bearing (149.01°) derived by the fit to the Cartesian plot in Figure F-1. The tables in this report list the bearing derived from the linear regressive fit to the Cartesian data (i.e., Figure F-1) since it is less sensitive than the instantaneous bearing to errors in the source position.
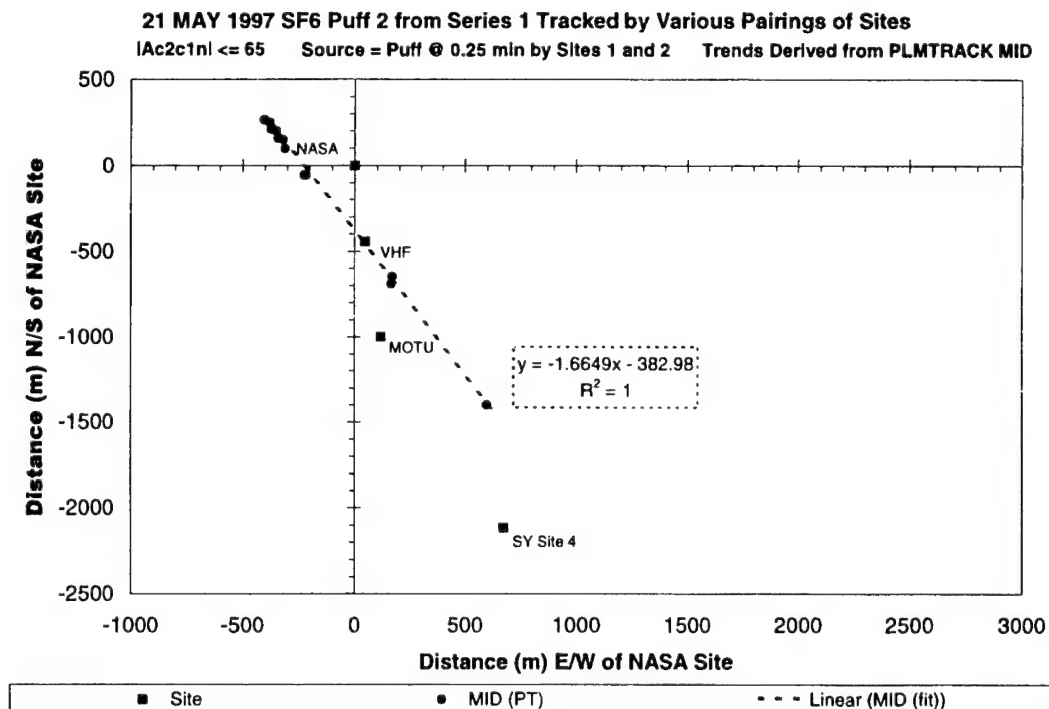
Figure F-1. Cartesian plot documenting the bearing of puff S1P2.

21 MAY 1997 SF6 Puff 2 from Series 1 Tracked by Various Pairings of Sites

|Ac2c1n| <= 65   Source = Puff @ 0.25 min by Sites 1 and 2   Limit to dtsm(min) > 0.5

$y = 241.45x - 0.0107$
$R^2 = 1$

$y = 241.44x - 23.054$
$R^2 = 0.9997$

$y = -0.3599x + 151.8$
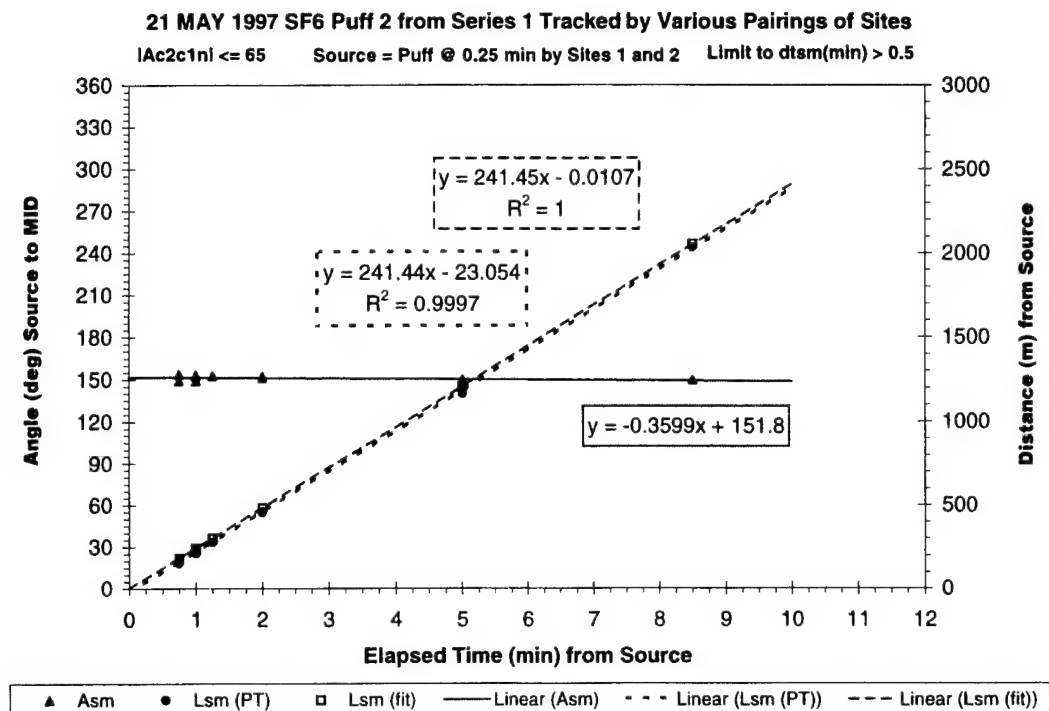
Figure F-2. Plot documenting the bearing and speed for puff S1P2.

Figure F-2 also includes a plot of horizontal distance (Lsm) between the source (s) and the middle (m) of the puff against time. The figure includes two values for Lsm. Lsm (PT) is derived from PLMTRACK output. Lsm (fit) is the value calculated from the formula for the puff's position as a function of time. Therefore, Lsm (fit) is the "best" position used in our puff extent calculations. The fact that both values fall on the same curve shows that the fit is accurate. The slope of the plot of Lsm against time is the average puff speed (i.e., 241 m/min = 4.0 m/s).

Figure F-3 illustrates instantaneous speed data derived by two additional methods. Speed is the change in distance with time. In Figure F-2, all values of distance (Lsm) are plotted against time to determine the "average speed." Figure F-3 documents a different estimate of speed for every imagery-derived point. Figure F-3 uses the notation dLsm/dtSM(m/s) for a speed derived for each data point by dividing the distance from the source (dLsm) by the elapsed time from the source (dtSM). Since this approach uses the source position, the errors should decrease as the distance and time increase. Ideally, the "cumulative instantaneous speed" derived from this method should approach the "average speed" obtained by the method used in Figure F-2. This appears to be the case.

Figure F-3 uses the notation dL/dt(m/s){15 s} for an instantaneous speed derived from the distance traveled every 15 s. This method calculates the speed as the distance traveled (dL) between points separated by 15 s (dt). The scatter in these data should reveal any variation in the precision of the data with time. As expected, Figure F-3 documents greater scatter in the "instantaneous 15-s differential speed" than in the "instantaneous cumulative speed."

119

21 MAY 1997 SF6 Puff 2 from Series 1 Tracked by Various Pairings of Sites

|Ac2c1n| <= 65   Source = Puff @ 0.25 min by Sites 1 and 2   Trends Derived from PLMTRACK MID

$y = 0.0668x + 3.527$ $y = 0.0317x + 3.7867$
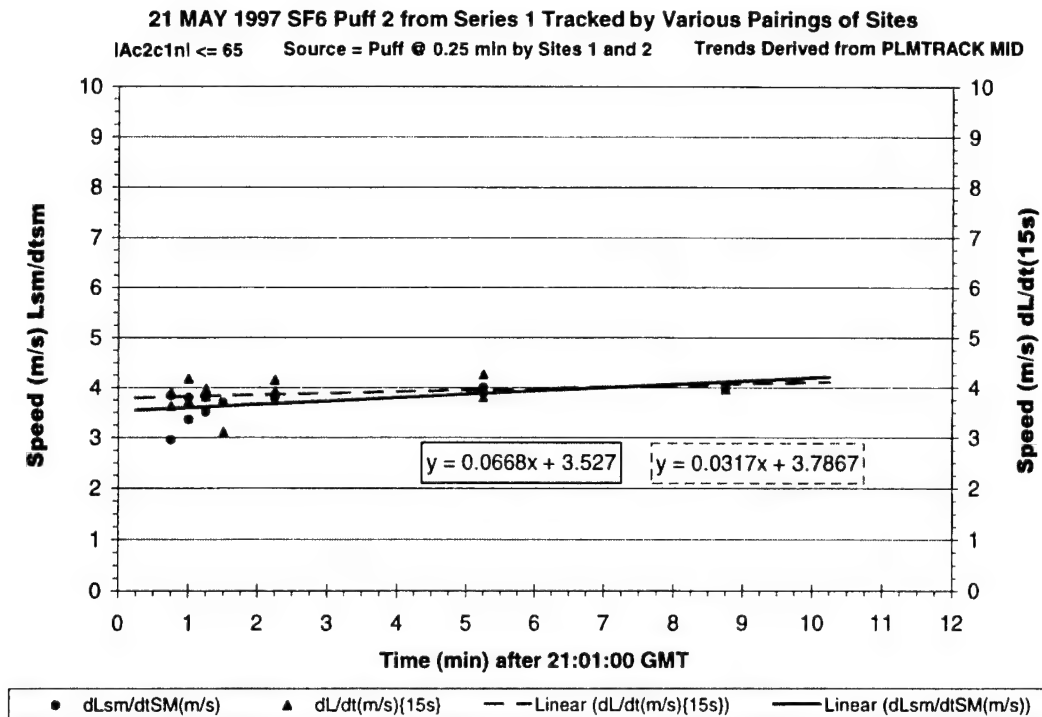
Figure F-3. Plot containing instantaneous and cumulative speeds for puff S1P2.

Comparison of the speeds reported in Figure F-2 (4.0 m/s) and Figure F-3 (3.5 m/s and 3.8 m/s inter-cepts) reveals that the PLMTRACK analysis provides fairly accurate estimates of speed using any of these methods. Appendix B documented that the PLMTRACK analysis was accurate to better than 100 m/s. The "instantaneous cumulative speed" (dLsm/dtSM(m/s)) will approach the "average speed" at longer times since the percentage errors decrease as the time and distance increase. On the other hand, it should be equal to the 15-s differential speed at early times. These observations are consistent with the plotted trends.

Figure F-4 is a plot of the PLMTRACK-derived height for the puff's middle (MID) against time. The data in this plot passed through a couple of additional criteria (i.e., filters). The puff had to be at least 15 pixels in diameter. For any pair of cameras, at least one camera had to have a shallow ele-vation angle to the puff (i.e., ELmid ≤ 25°). Puff height is difficult to measure if both cameras are viewing the puff from below (i.e., steep EL). As with the previous plots, the data included in Figure F-4 meet the requirement that the two cameras were within 65° of having normal perspectives of the puff (i.e., |Ac2c1n| ≤ 65°). As documented by Appendix B, the PLMTRACK results (30 m) can be more accurate than regular GPS (250 m) for vertical position. Based upon the 30-m accuracy for PLMTRACK, Figure F-4 documents a negligible change in height with time for the S1P2 data.

Puff Dimensions and Expansion Rates

This section of the appendix presents data that illustrate various ways to measure the dimensions of the puff. All of the methods discussed in this appendix use PLMTRACK to measure the position of the puff's middle (MID). The "best" methods fit PLMTRACK-derived trends to obtain the formula

120

21 MAY 1997 SF6 Puff 2 from Series 1 Tracked by Various Pairings of Sites
|Ac2c1n| <= 65   Minimum Number of Pixels for Feature >=15   At least one site had ELmid <= 25
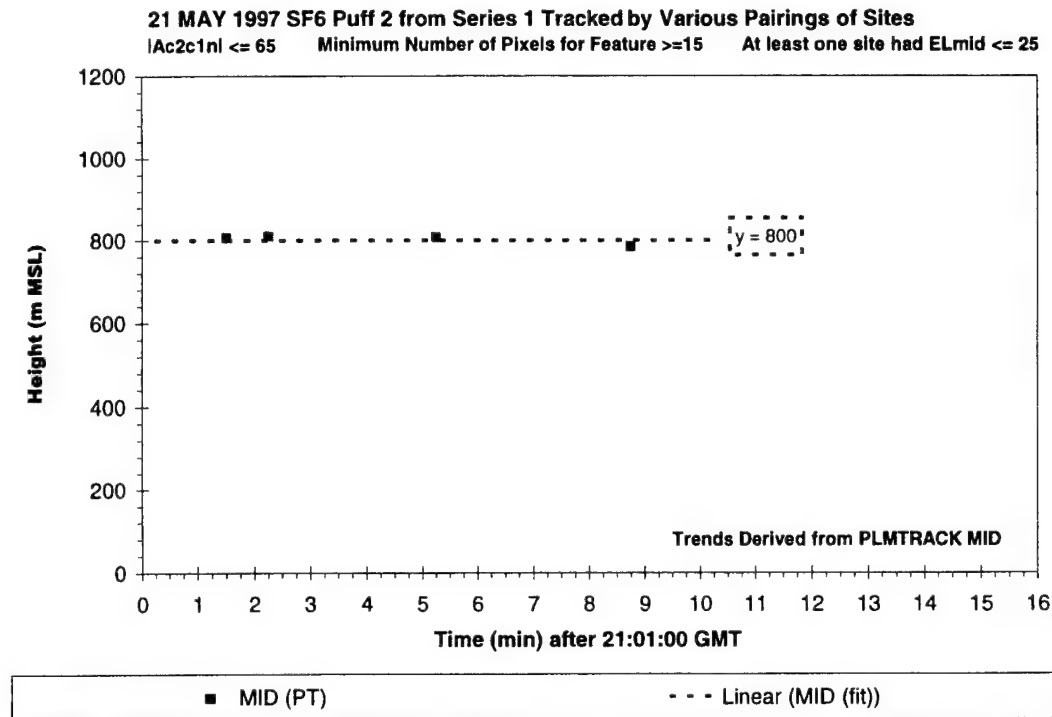
Figure F-4. Plot documenting negligible change in height with time for puff S1P2.

that describes the puff's position as a function of time. Then one can convert the angular extent of the cloud in each image to physical extent from that perspective. The angular extent is derived directly from the number of pixels occupied by the puff within the known FOV of the camera. Other, less accurate methods use the individual PLMTRACK results to map the extent of the puff. The data included in Appendix E illustrated that the PLMTRACK vertices accurately estimated the alongwind extent of puff S1P1 but underestimated its crosswind extent. In spite of such systematic bias, even the worse methods provided approximately the same expansion rates as the "best" method.

We tried two methods that use the PLMTRACK vertices from each pairing of cameras to measure the extent of the puff. In one approach, the analyst used PLMTRACK to triangulate the ends of the puff along a specific axis (i.e., along- or crosswind). The other approach calculated the extent from the eleven PLMTRACK vertices derived from each pair of cameras. The errors in these approaches resulted from the two factors: (1) calibration errors and (2) poor perspective.

Appendix B documented that the PLMTRACK data can be as accurate as regular GPS for horizontal position, which corresponds to 100 m for the 2-sigma value. Unfortunately, the magnitude of the errors is comparable to the initial size of the puffs. Since the PLMTRACK offsets (i.e., systematic errors) are often similar for the two ends of the puff, one can get fairly accurate extent for the puff by tracking the two ends. However, the analyst cannot always correctly identify the two ends since the perspective is constantly changing. Therefore, attempts to PLMTRACK the ends of the puff rely heavily upon the operator's bias (i.e., correction for perspective). From certain perspectives, the PLMTRACK offsets (errors) can be significantly different for the two ends of the puff. This can lead to larger systematic errors in the puff's dimensions during portions of its trajectory.

Appendix A illustrated that the PLMTRACK pair-wise analysis reports the nearest approach for various rays from each camera's perspective. The polygon formed by these vertices should map the extent of the puff. The alongwind data in Appendix E illustrated that the PLMTRACK polygon can accurately map the puff's extent (S1P1). However, the crosswind data in that appendix illustrated that the puff S1P1's dimensions are systematically underestimated by the PLMTRACK polygon when compared to the "best" method. The underestimation could result from calibration errors in either camera's pointing angles and from poor perspective for certain rays. When the rays are nearly parallel, small errors in the pointing angles result in large offsets (i.e., errors) in the nearest approach of the rays. As discussed in Appendix A, the PLMTRACK-derived middle of the puff is included in the trend plots only when there is good perspective (i.e., data meets filter conditions). However, the various filters ensure good perspective only for the middle rays. However, there are much larger errors for some of the other rays (i.e., the other vertices of the polygon).

The discussions for the crosswind analyses for S1P2 is in the following section. There are no useful alongwind data for S1P2. In a separate section, summary plots emphasize other axes and the sensitivity of the crosswind expansion rate to one experimental variable.

Crosswind Measurements

Figures F-5 and F-6 are plots of data derived from crosswind "end" measurements. When viewing the puff from the alongwind perspective (either from up- or downwind), the left and right ends of the puff within the image should correspond to the crosswind ends. The analyst used the best pair of images and PLMTRACK to triangulate the position of these ends. The best pair of sites would include one image from a camera with alongwind perspective and the other image from a camera

21 May 1997 SF6 Puff 2 from Series 1 Tracked by Various Pairings of Sites

PLMTRACK Line Method Applied to Crosswind (90 Tilt) End Measurements

$$y = -1.343x - 246.09$$
$$R^2 = 0.9993$$

$$y = -1.6525x - 424.02$$
$$R^2 = 0.9988$$

| ■ End 1 | ◆ End 2 | ▲ Site | ——Linear (End 1) | — —Linear (End 2) |
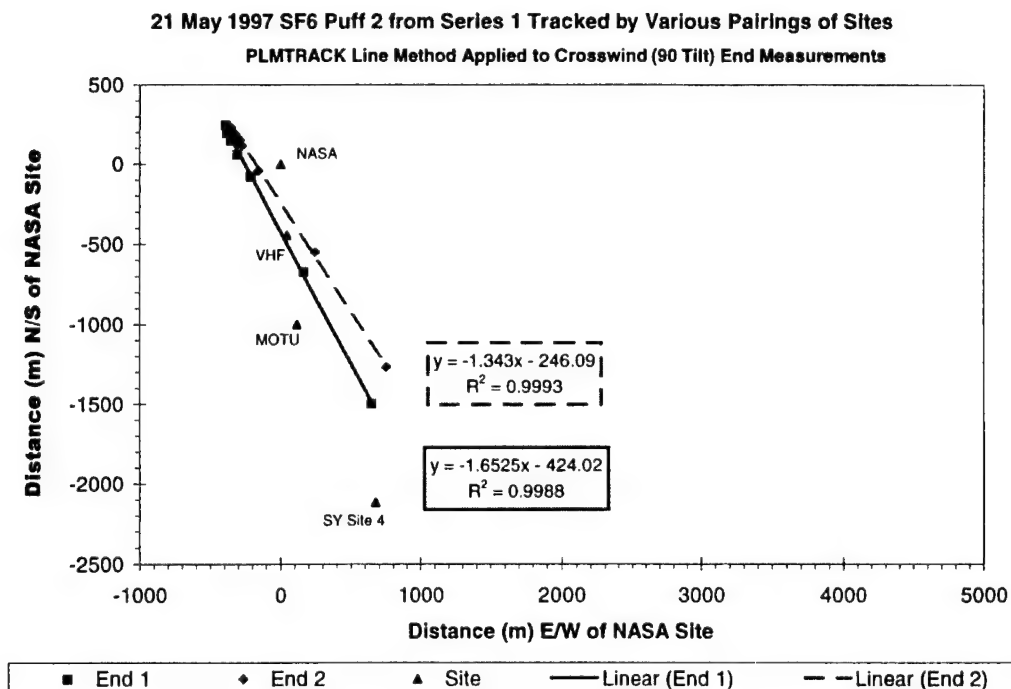
Figure F-5. Cartesian plot of the PLMTRACK-derived crosswind ends of the puff.

21 May 1997 SF6 Puff 2 from Series 1 Tracked by Various Pairings of Sites
PLMTRACK Line Method Applied to Crosswind (90 Tilt) End Measurements
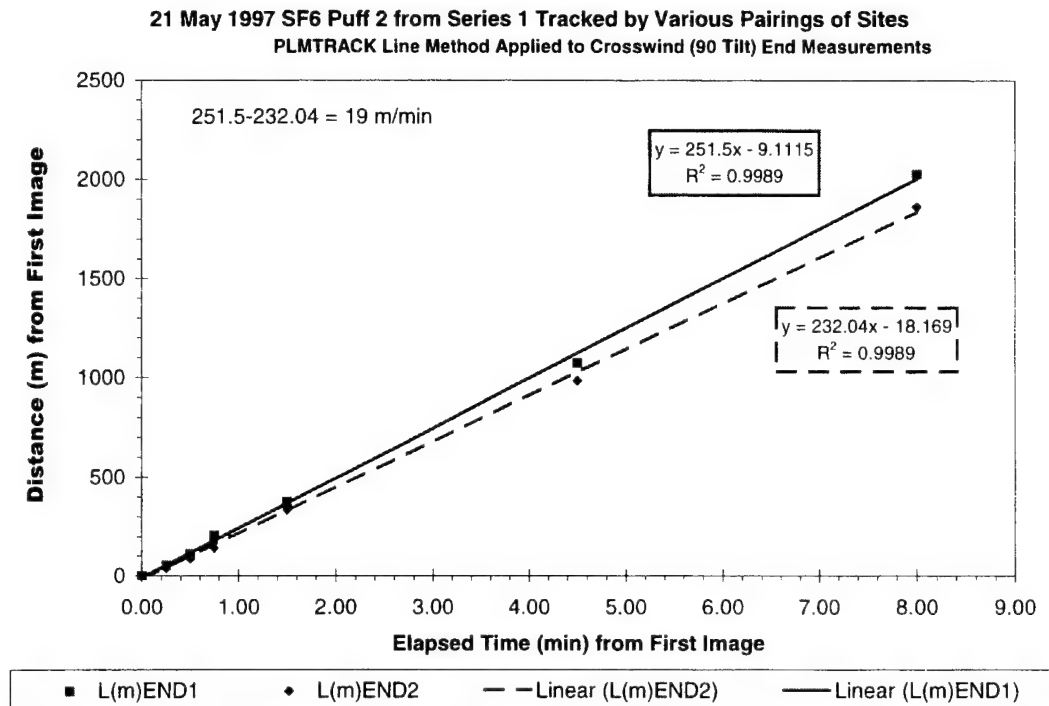
Figure F-6. Distance versus time (speed) plots for the crosswind ends of the puff.

with crosswind perspective. This end-triangulation analysis requires the analyst to point at the same end of the puff in the images from two sites. Because of this difficulty, the results in Figures F-5 and F-6 document marginal success for this approach. Figure F-5 is a Cartesian plot and documents that the two ends traveled diverging trajectories as the puff moved from the source to the southeast of NASA site. Figure F-6 is a plot of distance versus time and documents that the two ends moved at different speeds. Figure F-6 illustrates that it is difficult for the analyst to correctly identify the true crosswind ends. The crosswind ends should move at the same speed from the source. Instead there is a 19 m/min difference in speed for the two sides, which indicates a substantial bias in the analysts perspective.

Figures F-7 and F-8 document the puff's crosswind extent derived from the "best" method. As mentioned previously, the "best" method uses the fit-derived position of the puff to convert the angular extent within an image to physical extent (i.e., see Appendix A). The angular extent is calculated directly from the puff's size in pixels and the FOV of that image. This method minimizes any errors associated with the PLMTRACK-derived polygon. The fit-derived position is more accurate than any one PLMTRACK triangulation since it is based upon all six pair-wise combinations of all imagery after filtering for only the best perspectives.

The "best" method does not rely directly on pair-wise analysis. Therefore, Figure F-7 and F-8 include data from all imagery that can see the crosswind extent (i.e., Atilt = 90±10). This method of analysis is independent of the relative orientation of a second camera. Therefore, it was not necessary to filter these data by Ac2c1n. Figures F-7 and F-8 plot the "best method" diameters against
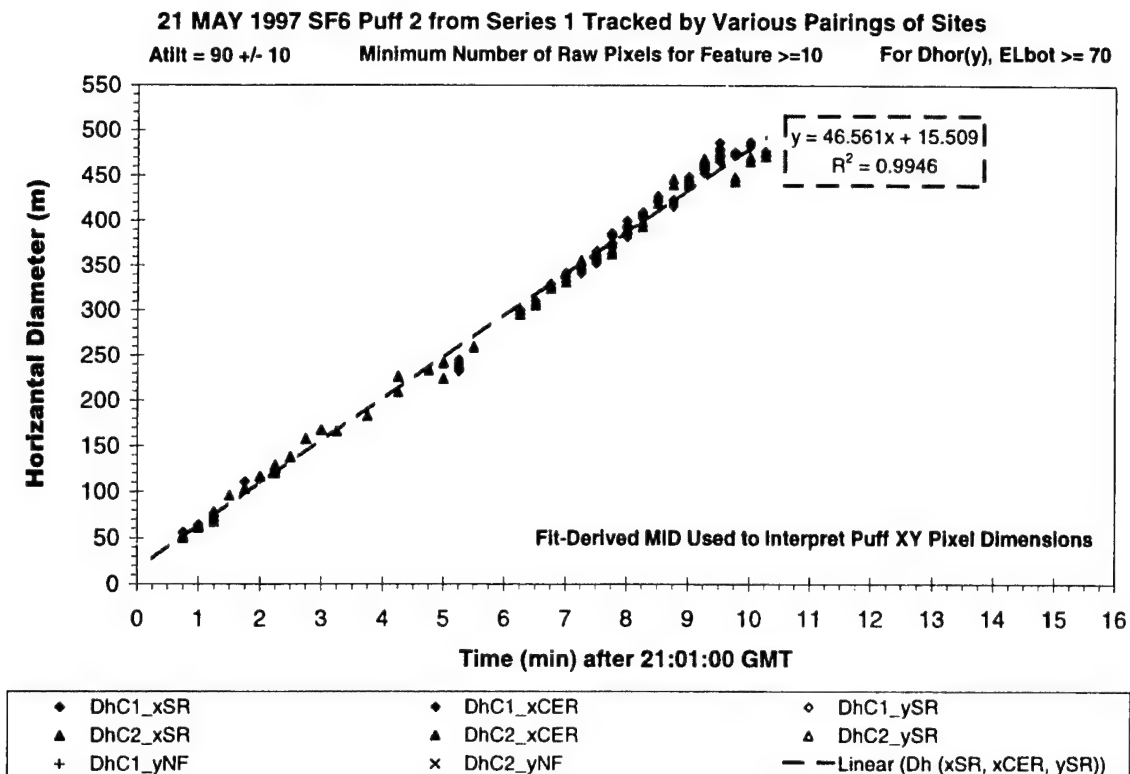
Figure F-7. "Best" crosswind extent versus time (expansion rate in m/min).
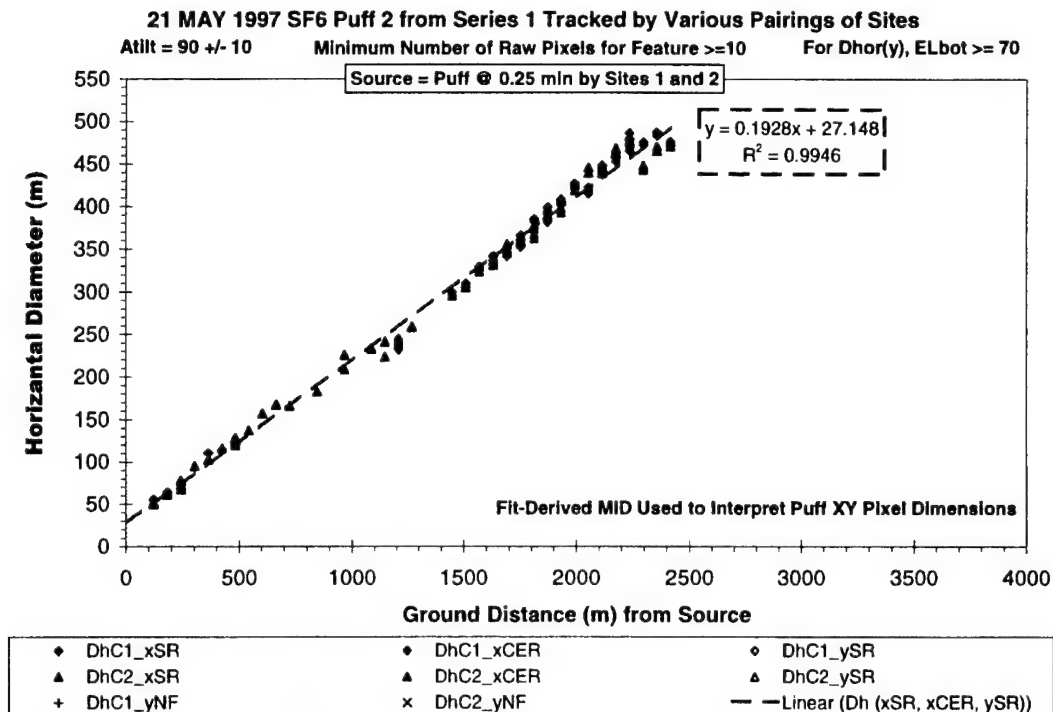
Figure F-8. "Best" crosswind extent versus distance (expansion rate in m/m).

time and distance, respectively. The slopes in Figure F-7 (47 m/min) and Figure F-8 (0.19 m/m) are the expansion rates in m/min and m/m, respectively.

Angular Trends and Sensitivity to Filters

The previous section of this appendix reviewed the crosswind expansion data. This section provides summary plots that document angular trends in the dimension data as well as sensitivity of the expansion rates to one experimental parameter.

Figure F-9 is a time plot of the puff's "best" diameters for all viewing perspectives. The linear regressive line documents the same crosswind trend as in Figure F-7. The diameters for other perspectives (i.e., axes) scatter about the crosswind trend since the only useful data was within a narrow window about the crosswind perspective.

Figure F-10 plots the PLMTRACK-derived horizontal expansion rate against tilt angle. The plotted diameters are from the PLMTRACK polygons. The plot reveals a relatively flat trend near the crosswind axis (90°). The plot suggests a maximum dimension along the crosswind axes (i.e., perpendicular to the puff's bearing). It is apparent from the plot that there were not enough data at other angles to fully characterize the angular dependence of the expansion rates for S1P2.

Figure F-11 shows the effect of one filter on the crosswind expansion rates. In this figure the crosswind expansion rate is plotted against the value of pixel threshold. Figure F-11 documents that the value of the expansion rate remains relatively constant as the threshold for the minimum number of pixels is raised from 0 to 25. Since the imagery-derived data only contains a limited angular perspective, we cannot document the sensitivity of the expansion rate upon the tilt window. See Appendices E and G for plots that document these trends for S1P1 and S2P1, respectively.
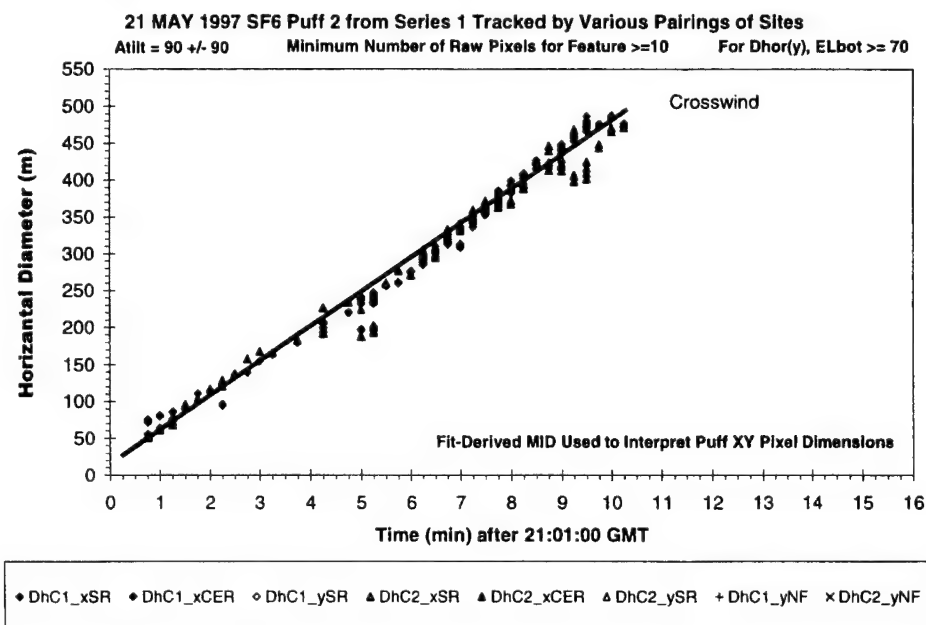
Figure F-9. Summary puff dimension plot showing all axes with regressive fits to the crosswind trend.

21 MAY 1997 SF6 Puff 2 from Series 1 Tracked by Various Pairings of Sites

Tilt Window +- 10; IAc2c1nI <65; ELbot >=70; Pixels >=15

dt more than 4min & R^2 must be better than 0.7 to include in this plot!
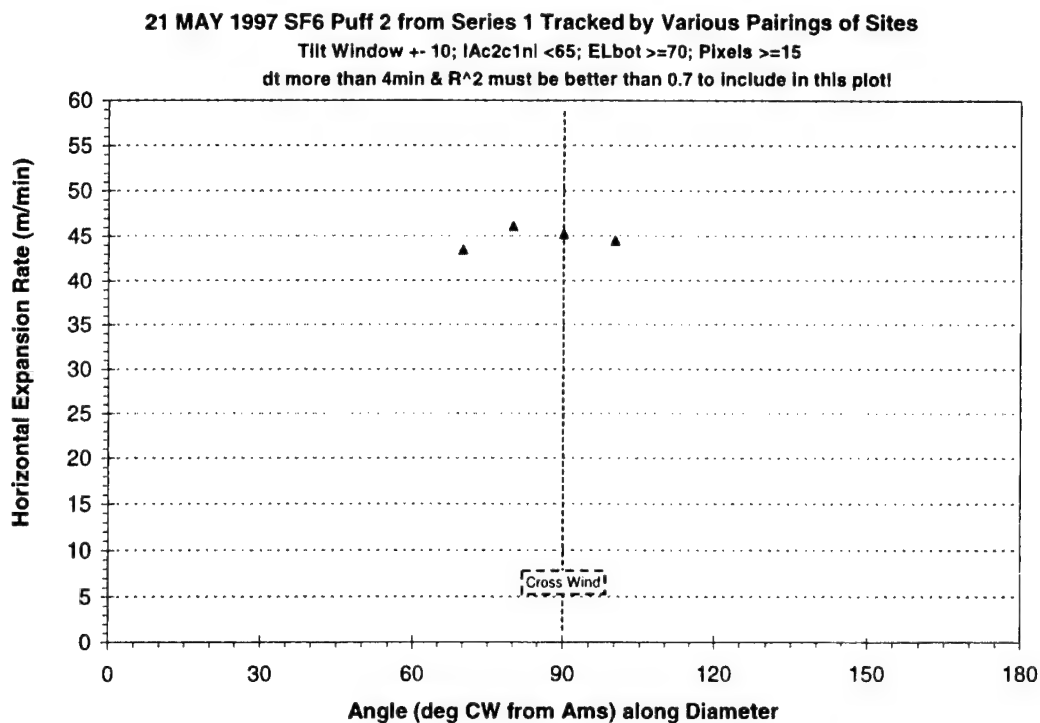
Figure F-10. Summary plot documenting the variation in expansion rate with perspective.

21 MAY 1997 SF6 Puff 2 from Series 1 Tracked by Various Pairings of Sites

Atilt = 0+/-10 (Along); Atilt = 90+/-10 (Cross); ELbot >= 70

—■- dDdt(cross) (xSR, xCER, ySR)   —●—dDdt(along) (xSR, xCER, ySR)
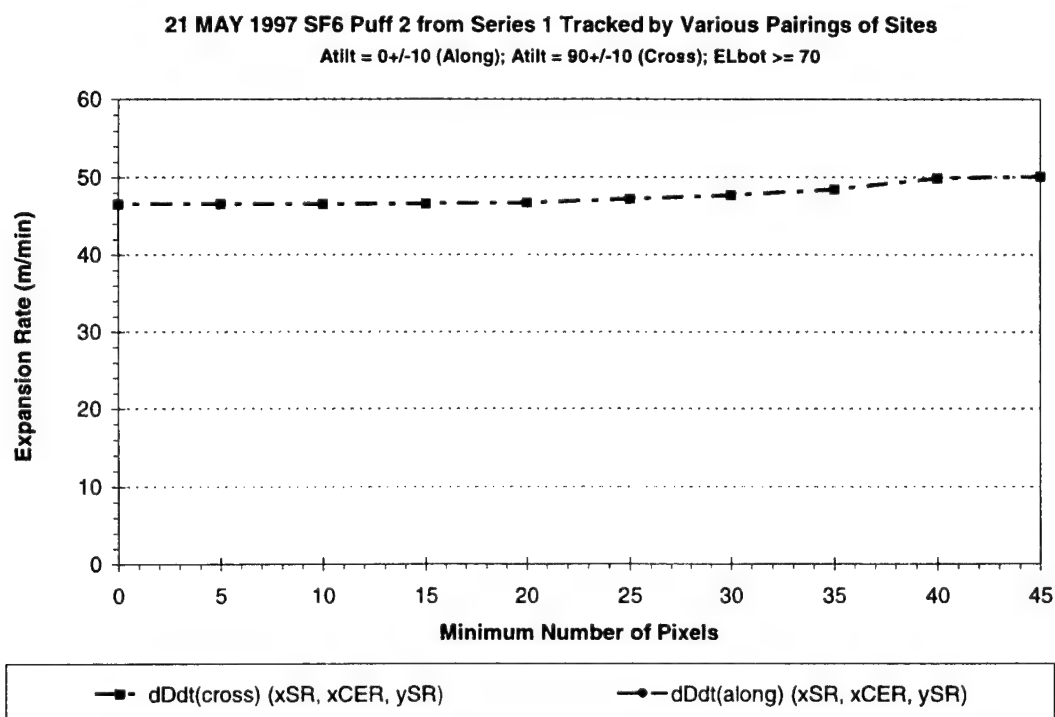
Figure F-11. Expansion rate sensitivity to puff size (in pixels) filtering.

126

Appendix G-Imagery-Derived Characteristics for S2P1

This appendix includes a detailed analysis of the imagery-derived characteristics for the first puff of series 2 (S2P1) from 21 May 1997. These imagery-derived results illustrate the precision and accuracy of the various analysis schemes. Appendices E and F provide two other examples (i.e., S1P1 and S1P2, respectively) from 21 May 1997. These three cases illustrate that there can be significant quantifiable differences in the release geometry and the dispersion characteristics for puffs separated by relatively small distances or times.

This appendix illustrates various analysis schemes. The results support the contention that the most accurate method of estimating the puff's size uses the puff's angular extent measured within each image. The puff's extent is measured within each image as pixels that are converted to angles using the known field of view (FOV) of each camera. The angular extent is converted to physical extent by knowing the slant range between the camera and the "best" value of the puff's position. The "best" position comes from linear regressive fits to PLMTRACK MID data. The fitted data include the "best" available perspectives from all pair-wise combinations of the available imagery. As described in Appendix A, various angles provide the basis for filtering the data for specific perspectives and for better accuracy. Appendix C documented that the expansion rates measured by the "best" method are insensitive to the resolution, slant range, elevation, and background radiance over their operational ranges. Appendix D discussed the quality of the imagery and documented that the observed puff extent included the bulk of the tracer. This appendix compares the various methods and documents the puff characteristics that can be derived from quantitative analysis of multi-site calibrated imagery.

PLMTRACK-Derived Position, Bearing and Speed

PLMTRACK analysis provides the vertices of a polygon about the extent of the puff. Each pair-wise combination of camera sites yields another set of vertices and another polygon. Appendix A described the PLMTRACK-derived rays and vertices. The most accurate PLMTRACK-derived output is the middle of the puff. Appendix B illustrated that PLMTRACK's accuracy is comparable to the GPS when applied to tracking the blimp. For four camera sites, the pair-wise PLMTRACK analysis provides six measurements of the middle of the puff for every set of simultaneous images. The plots in this section document puff characteristics derived solely from the PLMTRACK-derived middle of the puff.

Figure G-1 is a plot of the imagery-derived trajectory of puff S2P1 from 21 May 1997. This Cartesian plot uses distance from the camera site 1 (NASA) as position 0,0. MID (PT) is the middle of the puff and is a direct output from each pair-wise application of PLMTRACK (PT). It is apparent from this plot that the puff moved to the southeast along the row of cameras. The heading of the plot documents that the data is derived from pair-wise analysis using multiple perspectives (i.e., various pairings of sites). Appendix A defined the variable Ac2c1n. The best positional accuracy occurs when the camera pair view the puff with perspectives that are normal to each other (i.e., |Ac2c1n|
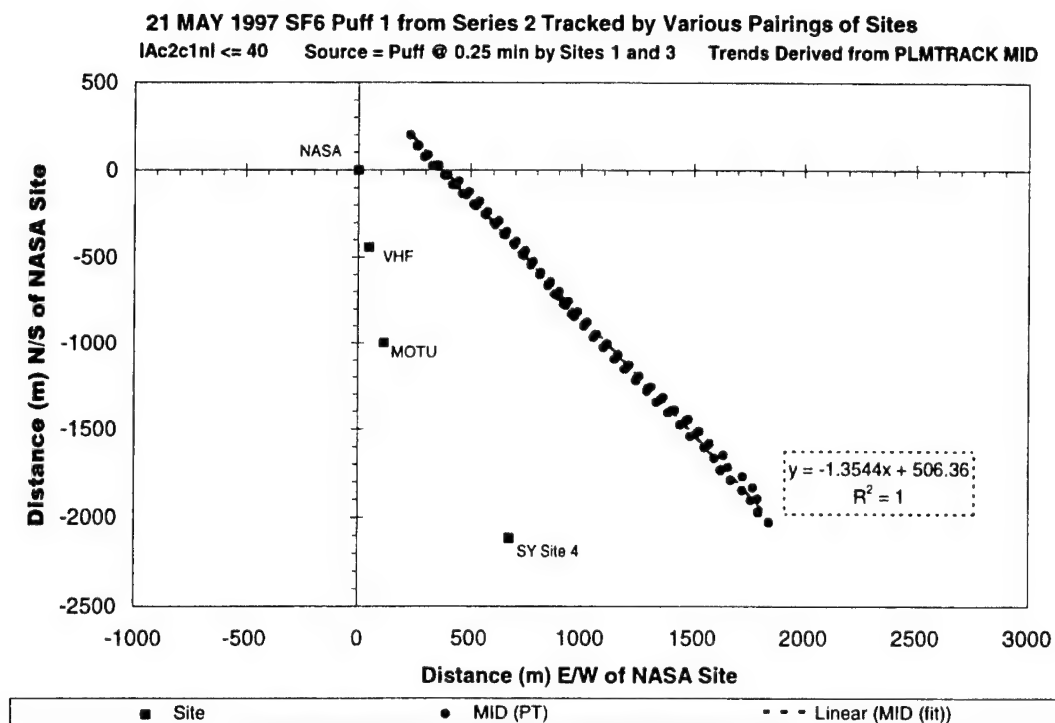
Figure G-1. Cartesian plot documenting the bearing of puff S2P1.

= 0°). As indicated in the heading, the data included in Figure G-1 meet the requirement that the two cameras were within 40° of having normal perspectives of the puff (i.e., |Ac2c1n| ± 40°). The heading also indicates that the source position (i.e., the earliest imagery-derived position) was measured by imagery from sites 1 (NASA) and 3 (MOTU). These source images were collected 0.25 min after the imagery-derived start of the release. The imagery-derived times are accurate to the nearest 0.25 min due to the data rate.

Figure G-1 provides the formula and correlation coefficient for the linear regressive fit to the puff's middle (MID) data. The slope (–1.3544) is easily converted to puff bearing (i.e., 90 – ATAN(–1.3544) = 143.56° clockwise of north). The data fall along a straight line, which is confirmed by a correlation coefficient of 1 (i.e. the best possible value). This plot documents a puff bearing toward the southeast but contains no time information (speed).

Figure G-2 presents both bearing and speed for the puff's middle (MID). Figure G-2 documents puff bearing derived by a second method. The instantaneous bearing (Asm) is the angle (A) from the source (s) position to the current middle (m) of the puff at each instant in time. As defined earlier, the source is the earliest measured position of the puff. For a constant bearing and no scatter, one expects a horizontal line when plotting Asm against time. In Figure G-2, the plot documents that this is the case for the PLMTRACK-derived data. Likewise the intercept (143.93°) of the plot of instantaneous bearing against time (i.e., Figure G-2) is equivalent to the average bearing (143.56°) derived by the fit to the Cartesian plot in Figure G-1. The tables in this report list the bearing derived from the linear regressive fit to the Cartesian data (i.e., Figure G-1) since it is less sensitive than the instantaneous bearing to errors in the source position.

128

21 MAY 1997 SF6 Puff 1 from Series 2 Tracked by Various Pairings of Sites

|Ac2c1n| <= 40   Source = Puff @ 0.25 min by Sites 1 and 3   Limit to dtsm(min) > 0.5

$y = 290x - 0.0074$
$R^2 = 1$

$y = 299.97x - 74.869$
$R^2 = 0.9989$

$y = -0.051x + 143.93$

▲ Asm   ● Lsm (PT)   □ Lsm (fit)   ——Linear (Asm)   - - - Linear (Lsm (PT))   – – – Linear (Lsm (fit))
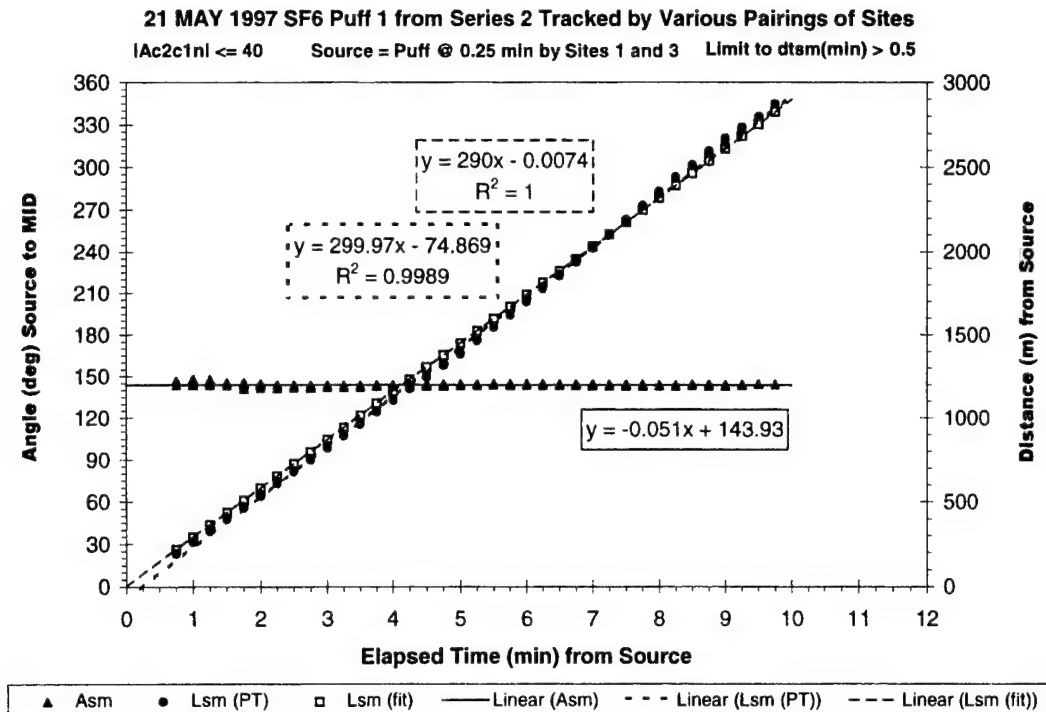
Figure G-2. Plot documenting the bearing and speed for puff S2P1.

Figure G-2 also includes a plot of horizontal distance (Lsm) between the source (s) and the middle (m) of the puff against time. The figure includes two values for Lsm. Lsm (PT) is derived from PLMTRACK output. Lsm (fit) is the value calculated from the formula for the puff's position as a function of time. Therefore Lsm (fit) is the "best" position used in our puff extent calculations. The plot documents the accuracy of the fit. The slope of the plot of Lsm against time is the average puff speed (i.e., 290–300 m/min = 4.8–5.0 m/s).

Figure G-3 illustrates instantaneous speed data derived by two additional methods. Speed is the change in distance with time. In Figure G-2, all values of distance (Lsm) are plotted against time to determine the "average speed." Figure G-3 documents a different estimate of speed for every imagery-derived point. Figure G-3 uses the notation dLsm/dtSM(m/s) for a speed derived for each data point by dividing the differential distance from the source (dLsm) by the elapsed time from the source (dtSM). Since this approach uses the source position, the errors should decrease as the distance and time increase. Ideally, the "cumulative instantaneous speed" derived from this method should approach the "average speed" obtained by the method documented by Figure G-2. After allowing for the scatter in the data, this appears to be the case.

Figure G-3 uses the notation dL/dt(m/s){15 s} for an instantaneous speed derived from the distance traveled every 15 s (dt). This method should reveal the scatter in the data over time since it calculates the speed as the distance traveled (dL) between points separated by 15 s (dt). The scatter in these data should reveal any variation in the precision of the data with time. As expected Figure G-3 documents greater scatter in the "instantaneous 15-s differential speed" than in the "instantaneous cumulative speed."

21 MAY 1997 SF6 Puff 1 from Series 2 Tracked by Various Pairings of Sites

|Ac2c1n| <= 40   Source = Puff @ 0.25 min by Sites 1 and 3   Trends Derived from PLMTRACK MID

$y = 0.0686x + 4.3084$

$y = 0.1007x + 4.4186$

Legend: ● dLsm/dtSM(m/s)   ▲ dL/dt(m/s){15s}   — —Linear (dL/dt(m/s){15s})   ——Linear (dLsm/dtSM(m/s))
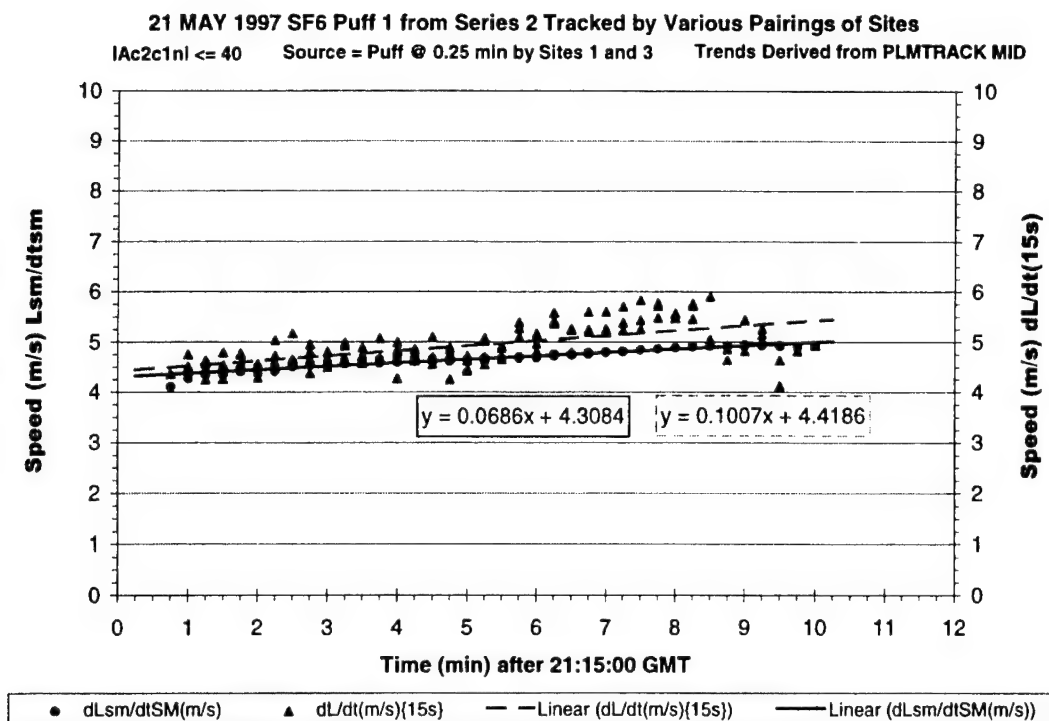
Figure G-3. Plot containing instantaneous and cumulative speeds for puff S2P1.

Comparison of the speeds reported in Figure G-2 (4.8–5.0 m/s) and Figure G-3 (4.3 m/s and 4.4 m/s intercepts) reveals that the PLMTRACK analysis provides fairly accurate (i.e., ±0.5 m/s) estimates of speed using any of these methods. The "instantaneous cumulative speed" (dLsm/dtSM(m/s)) will approach the "average speed" at longer times since the percentage errors decrease as the time and distance increase. On the other hand, it should be equal to the "instantaneous 15-s differential speed" only at early times. These observations are consistent with the plotted trends. Comparison of these data to those obtained for S1P1 (Appendix E) and S1P2 (Appendix F) documents larger random positional errors (i.e., scatter) for the S2P1 case. This is consistent with larger slant ranges for the S2P1 release.

Figure G-4 is a plot of the PLMTRACK-derived height of the puff's middle (MID) against time. The data in this plot passed through a couple of additional criteria (i.e., filters). The puff had to be at least 15 pixels in diameter. For any pair of cameras, at least one camera had to have a shallow elevation angle to the puff (i.e., ELmid ≤20°). Puff height is difficult to measure if both cameras are viewing the puff from below (i.e., steep EL). As with the previous plots, the data included in Figure G-4 meet the requirement that the two cameras were within 40° of having normal perspectives of the puff (i.e., |Ac2c1n| ≤40°). As documented by Appendix B, the PLMTRACK results (30 m) can be more accurate than regular GPS (250 m) for vertical position. Based upon the 30-m accuracy for PLMTRACK, Figure G-4 documents a negligible change in height with time for the S2P1 data.

21 MAY 1997 SF6 Puff 1 from Series 2 Tracked by Various Pairings of Sites
IAc2c1nI <= 40   Minimum Number of Pixels for Feature >=15   At least one site had ELmid <= 20
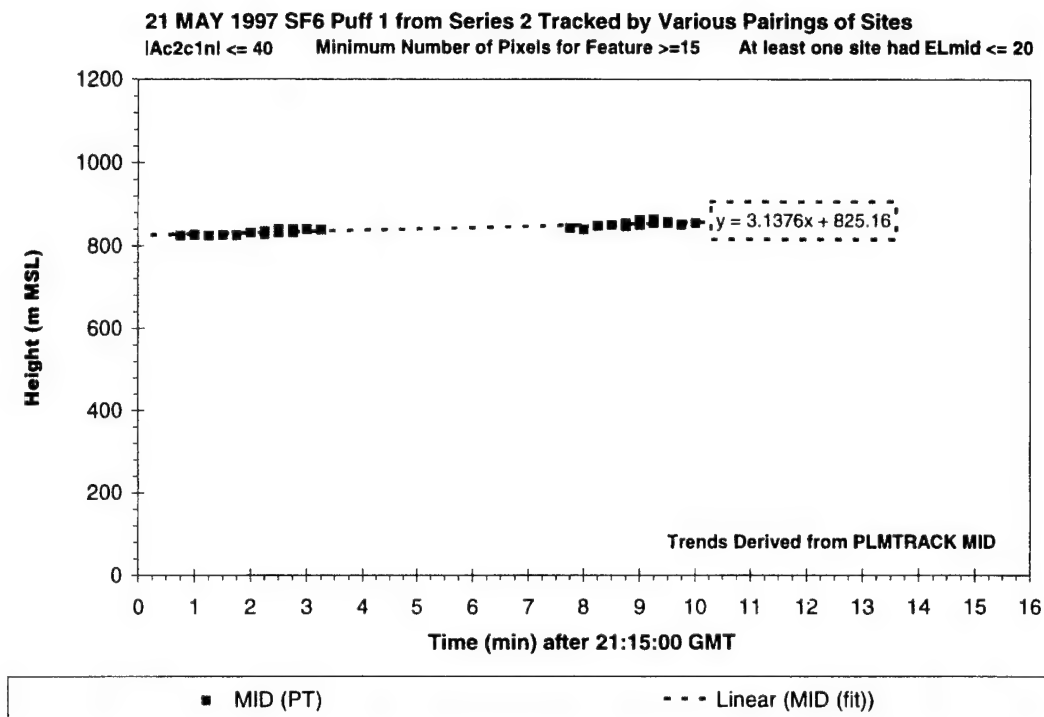
Figure G-4. Plot documenting negligible change in height with time for puff S2P1.

Puff Dimensions and Expansion Rates

This section of the appendix presents data that illustrate various ways to measure the dimensions of the puff. All of the methods discussed in this appendix use PLMTRACK to measure the position of the puff's middle (MID). The "best" methods fit PLMTRACK-derived trends to obtain the formula that describes the puff's position as a function of time. Then one can convert the angular extent of the cloud in each image to physical extent from that perspective. The angular extent is derived directly from the number of pixels occupied by the puff within the known FOV of the camera. Other, less accurate methods use the individual PLMTRACK results to map the extent of the puff. The data included in Appendix E illustrated that the PLMTRACK vertices can underestimate the extent of the puff. In spite of such systematic bias in puff dimensions, even the worst methods provided approximately the same expansion rates as the "best" method.

We tried two methods that use the PLMTRACK vertices from each pairing of cameras to measure the extent of the puff. In one approach, the analyst used PLMTRACK to triangulate the ends of the puff along a specific axis (i.e., along- or crosswind). The other approach calculated the extent from the eleven PLMTRACK vertices derived from each pair of cameras. The errors in these approaches resulted from the two factors: (1) calibration errors and (2) poor perspective.

Appendix B documented that the PLMTRACK data can be as accurate as regular GPS for horizontal position, which corresponds to 100 m for the 2-sigma value. Unfortunately, the magnitude of these errors is comparable to the initial size of the puffs. Since the PLMTRACK offsets (i.e., systematic errors) are often similar for the two ends of the puff, one can get fairly accurate extent for the puff by tracking the two ends. However, the analyst cannot always correctly identify the two ends since the

131

perspective is constantly changing. Therefore, attempts to PLMTRACK the ends of the puff rely heavily upon the operator's bias (i.e., correction for perspective). From certain perspectives, the PLMTRACK offsets can be significantly different for the two ends of the puff. This can lead to larger systematic errors in the puff's dimensions during portions of its trajectory.

Appendix A illustrated that the PLMTRACK pair-wise analysis reports the nearest approach for various rays from each camera's perspective. The polygon formed by these vertices should contain the puff. The alongwind data in Appendix E illustrated that the PLMTRACK polygon can accurately map the puff's extent. However, the crosswind data in that same appendix illustrated that the puff's dimensions are systematically underestimated by the PLMTRACK polygon. The underestimation could result from calibration errors in either camera's pointing angles and from poor perspective for certain rays. When the rays are nearly parallel, small errors in the pointing angles result in large offsets (i.e., errors) in the nearest approach of the rays. As discussed in Appendix A, the PLMTRACK-derived middle (MID) of the puff is included in the trend plots only when there is good perspective (i.e., data meets filter conditions). However, the various filters ensure good perspective only for the middle rays. Hence, there are much larger errors for some of the other rays (i.e., the other vertices of the polygon).

The discussions for the crosswind and alongwind analyses are in separate sections for S2P1. This should make comparisons easier. The analyses document the extent and expansion of the puff in several ways to illustrate the consistency of the results. In a third section, summary plots emphasize other axes and the sensitivity of the expansion rate to two experimental variables.

Crosswind Measurements

Figures G-5 and G-6 are plots of data derived from crosswind "end" measurements. When viewing the puff from the alongwind perspective (either from up- or downwind), the left and right ends of the puff within the image should correspond to the crosswind ends. The analyst used the best pair of images and PLMTRACK to triangulate the position of these ends. The best pair of sites would include one image from a camera with alongwind perspective and the other image from a camera with crosswind perspective. This end-triangulation analysis requires the analyst to point at the same end of the puff in the images from two sites. In spite of this difficulty, the results in Figures G-5 and G-6 document that the analyst was fairly successful. Figure G-5 is a Cartesian plot and documents that the crosswind ends traveled diverging trajectories as the puff moved from the source to the southeast of NASA site. Figure G-6 is a plot of distance versus time and documents that the two crosswind ends moved at different speeds. Since one expects the crosswind ends to move at the same speed away from the source and to diverge as the puff disperses, the 15 m/min difference in speed illustrates some bias in the analyst's perspective.

Figures G-7 and G-8 document the puff's crosswind extent derived from the "best" method. As mentioned previously, the "best" method uses the fit-derived position of the puff to convert the angular extent within an image to physical extent (i.e., see Appendix A). The angular extent is calculated directly from the puff's size in pixels and the FOV of that image. This method minimizes any errors associated with the PLMTRACK-derived polygon. The fit-derived position is more accurate than any one PLMTRACK triangulation since it is based upon all six pair-wise combinations of all imagery after filtering for only the best perspectives. Figures G-7 and G-8 plot the "best" dia-

132

21 May 1997 SF6 Puff 1 from Series 2 Tracked by Various Pairings of Sites

PLMTRACK Line Method Applied to Crosswind End Measurements
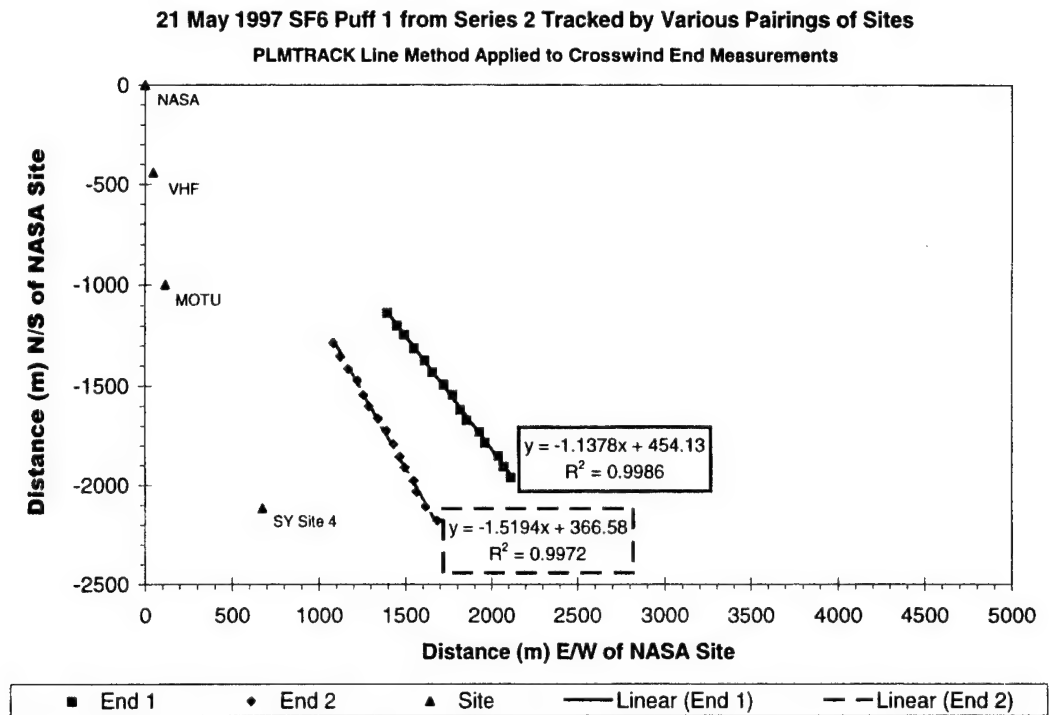
Figure G-5. Cartesian plot of the PLMTRACK-derived crosswind ends of the puff.

21 May 1997 SF6 Puff 1 from Series 2 Tracked by Various Pairings of Sites

PLMTRACK Line Method Applied to Crosswind End Measurements
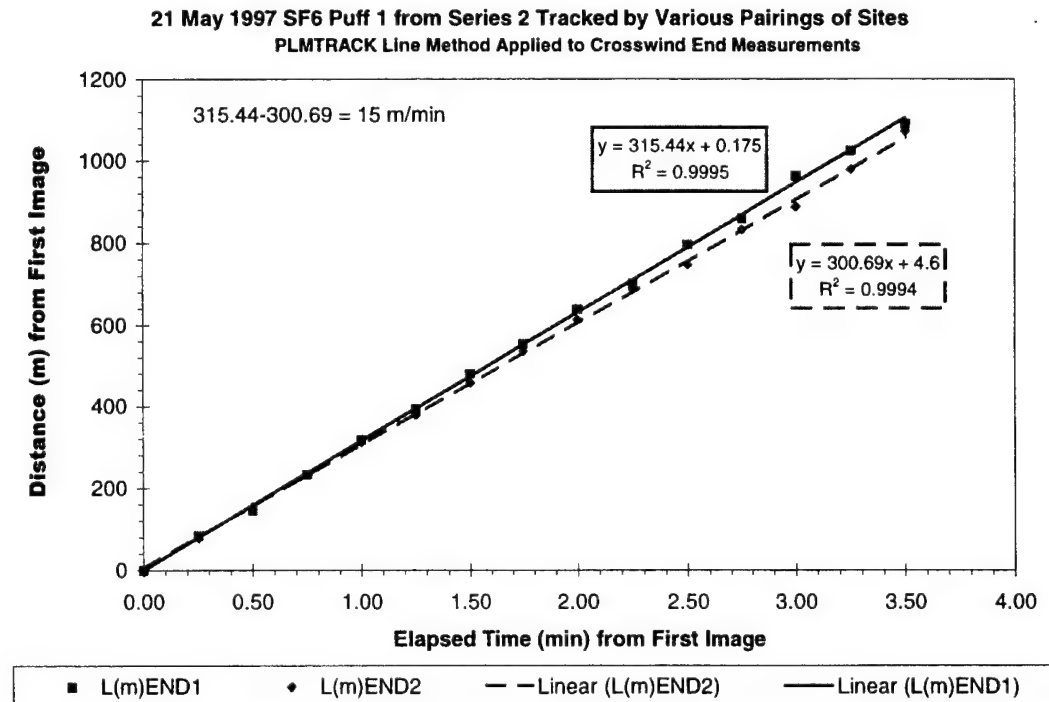
Figure G-6. Distance versus time (speed) plots for the crosswind ends of the puff.

21 MAY 1997 SF6 Puff 1 from Series 2 Tracked by Various Pairings of Sites

Atilt = 90 +/- 10   Minimum Number of Raw Pixels for Feature >=35   For Dhor(y), ELbot >= 61

$y = 34.492x + 117.74$
$R^2 = 0.9733$

Fit-Derived MID Used to Interpret Puff XY Pixel Dimensions

Horizantal Diameter (m)

Time (min) after 21:15:00 GMT

• DhC1_xSR	◆ DhC1_xCER	◦ DhC1_ySR
▲ DhC2_xSR	▲ DhC2_xCER	▵ DhC2_ySR
+ DhC1_yNF	× DhC2_yNF	— —Linear (Dh (xSR, xCER, ySR))
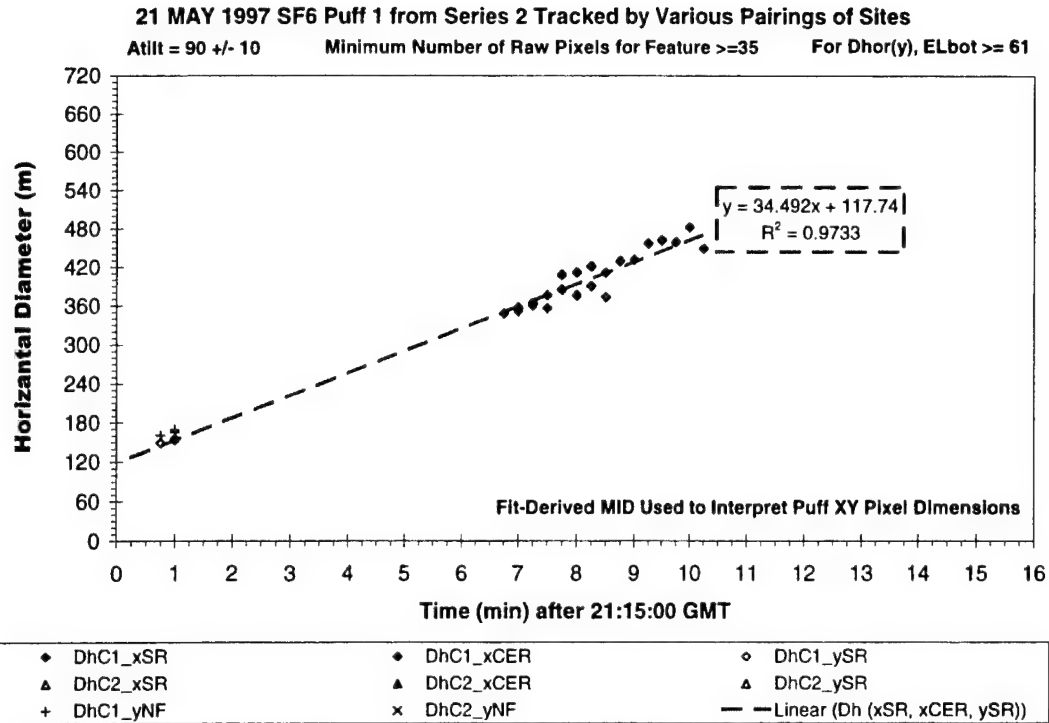
Figure G-7. "Best" crosswind extent versus time (expansion rate in m/min).

21 MAY 1997 SF6 Puff 1 from Series 2 Tracked by Various Pairings of Sites

Atilt = 90 +/- 10   Minimum Number of Raw Pixels for Feature >=35   For Dhor(y), ELbot >= 61

Source = Puff @ 0.25 min by Sites 1 and 3

$y = 0.1189x + 126.36$
$R^2 = 0.9733$

Fit-Derived MID Used to Interpret Puff XY Pixel Dimensions

Horizantal Diameter (m)

Ground Distance (m) from Source

• DhC1_xSR	◆ DhC1_xCER	◦ DhC1_ySR
▲ DhC2_xSR	▲ DhC2_xCER	▵ DhC2_ySR
+ DhC1_yNF	× DhC2_yNF	— —Linear (Dh (xSR, xCER, ySR))

Figure G-8. "Best" crosswind extent versus distance (expansion rate in m/m).

134

meters against time and distance, respectively. The slopes in Figure G-7 (34 m/min) and Figure G-8 (0.12 m/m) are the expansion rates in m/min and m/m, respectively.

Alongwind Measurements

Figures G-9 and G-10 are plots of data derived from alongwind "end" measurements. When viewing the puff from the crosswind perspective, the left and right ends of the puff should correspond to the alongwind ends. The analyst used the best pair of images and PLMTRACK to triangulate the position of these ends. The best pair of sites would include one image from a camera with crosswind perspective and the other image from a camera with an alongwind perspective. This end-triangulation analysis requires the analyst to point at the same end of the puff in the images from two sites. In spite of this difficulty, the results in Figures G-9 and G-10 document that the analyst was fairly successful. Figure G-9 documents as a Cartesian plot that the two ends traveled almost the same trajectories as the puff moved from the source to the southeast of NASA site. The alongwind ends should lie along the same vector (i.e., the wind bearing). Figure G-9 documents only a 1° difference in bearing for the "alongwind" ends and, therefore, some error in the analyst's perspective or in the triangulation accuracy. Figure G-10 is a plot of distance versus time and documents that the two ends moved at different speeds. Since the puff is diverging as it moves along the wind bearing, the leading edge of the puff should move faster (average speed + dispersion) than the tailing end (average speed – dispersion). In Figure G-10, the difference in speed should be the expansion rate (i.e., 9 m/min).
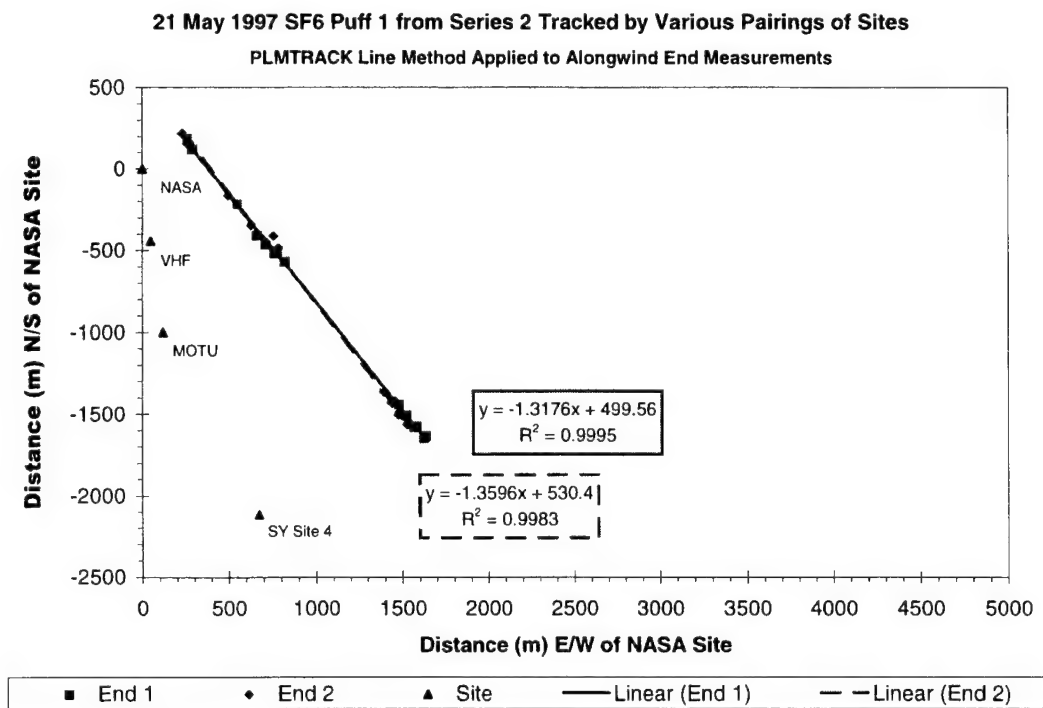
Figure G-9. Cartesian plot of the PLMTRACK-derived alongwind ends of the puff.

135

21 May 1997 SF6 Puff 1 from Series 2 Tracked by Various Pairings of Sites
PLMTRACK Line Method Applied to Alongwind End Measurements
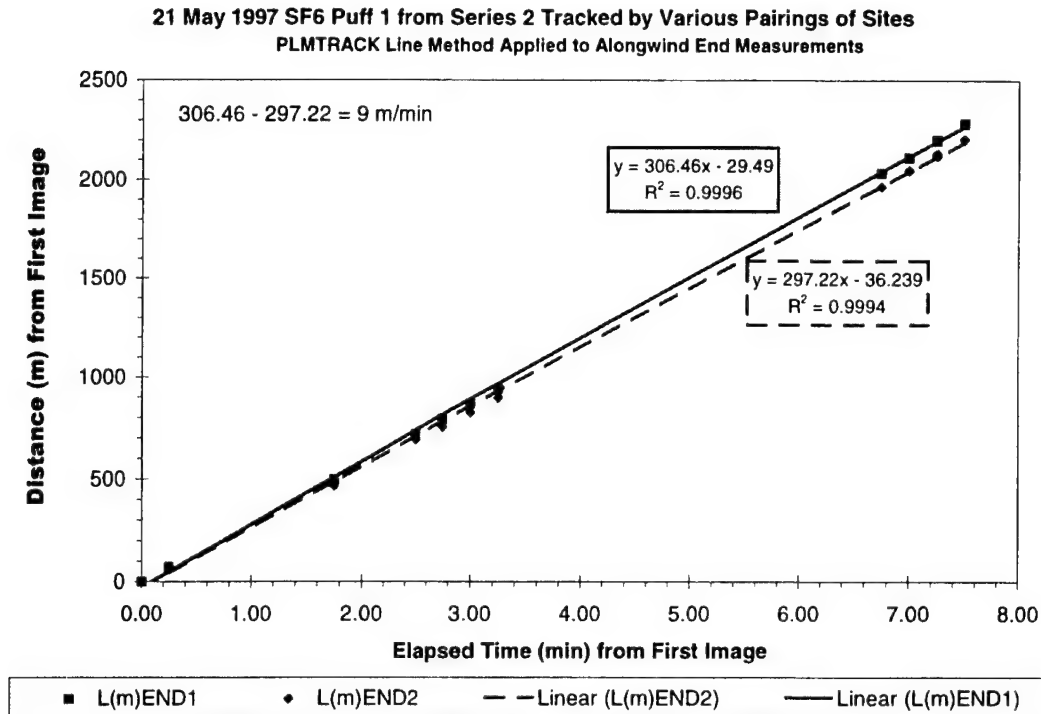
Figure G-10. Distance versus time (speed) plots for the alongwind ends of the puff.

Figures G-11 and G-12 document the puff's alongwind extent derived from the "best" method. As mentioned previously, the "best" method uses the fit-derived position of the puff to convert the angular extent within an image to physical extent (see Appendix A). The figure headings document that the plotted data have been filtered for good perspective. Since the "best" method does not rely directly on pair-wise analysis, Figures G-11 and G-12 document results from all imagery that can see the crosswind extent (i.e., Atilt = 90±10). The slopes in Figure G-11 (9.6 m/min) and Figure G-12 (0.033 m/m) are the expansion rates in m/min and m/m, respectively. The slope documents a "best method" expansion rate of 9.6m/min, which is 0.6m/min (7%) larger than the 9.0m/min value derived from the end-triangulation method illustrated in Figure G-10.

Angular Trends and Sensitivity to Filters

The previous sections of this appendix reviewed the crosswind and alongwind data separately. This section provides summary plots that document angular trends in the dimension data as well as sensitivity of the expansion rates to experimental parameters.

Figure G-13 shows the puff's "best" diameters derived from all available imagery plotted against time. The linear regressive lines are included to document the alongwind and crosswind trends. The diameters for other perspectives (i.e., axes) fall between these two extremes.

21 MAY 1997 SF6 Puff 1 from Series 2 Tracked by Various Pairings of Sites

Atilt = 0 +/- 10   Minimum Number of Raw Pixels for Feature >=35   For Dhor(y), ELbot >= 61

$y = 9.5762x + 82.456$
$R^2 = 0.8777$

Fit-Derived MID Used to Interpret Puff XY Pixel Dimensions

♦ DhC1_xSR	♦ DhC1_xCER	◊ DhC1_ySR
▲ DhC2_xSR	▲ DhC2_xCER	△ DhC2_ySR
+ DhC1_yNF	× DhC2_yNF	― ―Linear (Dh (xSR, xCER, ySR))
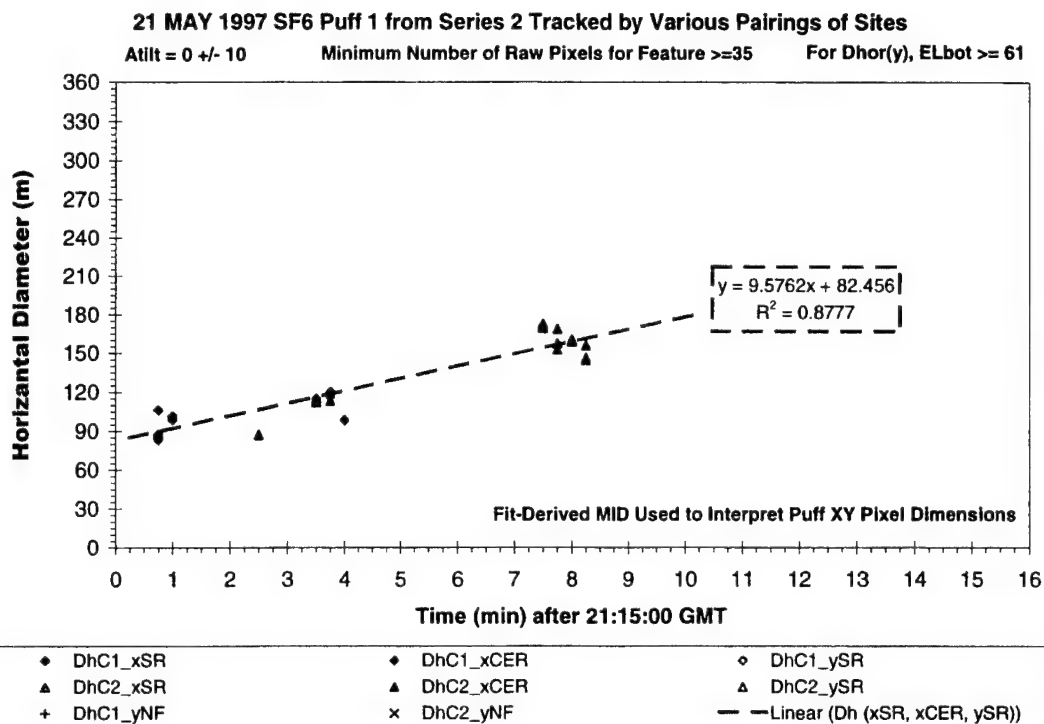
Figure G-11. "Best" alongwind extent versus time (expansion rate in m/min).

21 MAY 1997 SF6 Puff 1 from Series 2 Tracked by Various Pairings of Sites

Atilt = 0 +/- 10   Minimum Number of Raw Pixels for Feature >=35   For Dhor(y), ELbot >= 61

Source = Puff @ 0.25 min by Sites 1 and 3

$y = 0.033x + 84.851$
$R^2 = 0.8777$

Fit-Derived MID Used to Interpret Puff XY Pixel Dimensions

♦ DhC1_xSR	♦ DhC1_xCER	◊ DhC1_ySR
▲ DhC2_xSR	▲ DhC2_xCER	△ DhC2_ySR
+ DhC1_yNF	× DhC2_yNF	― ―Linear (Dh (xSR, xCER, ySR))
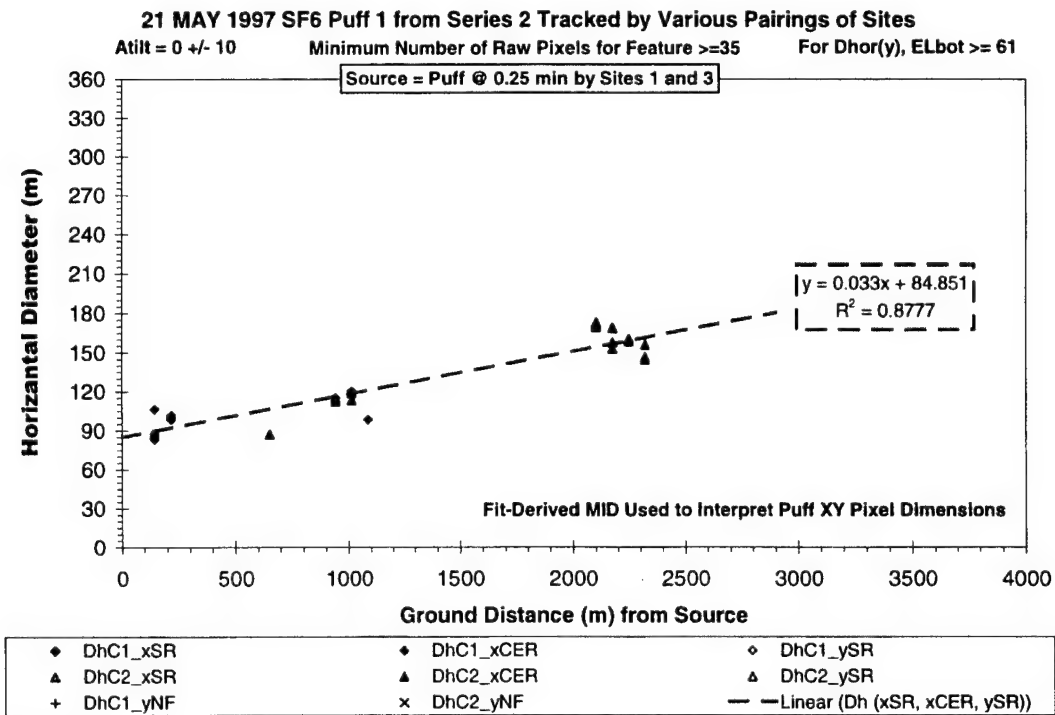
Figure G-12. "Best" alongwind extent versus distance (expansion rate in m/m).

137
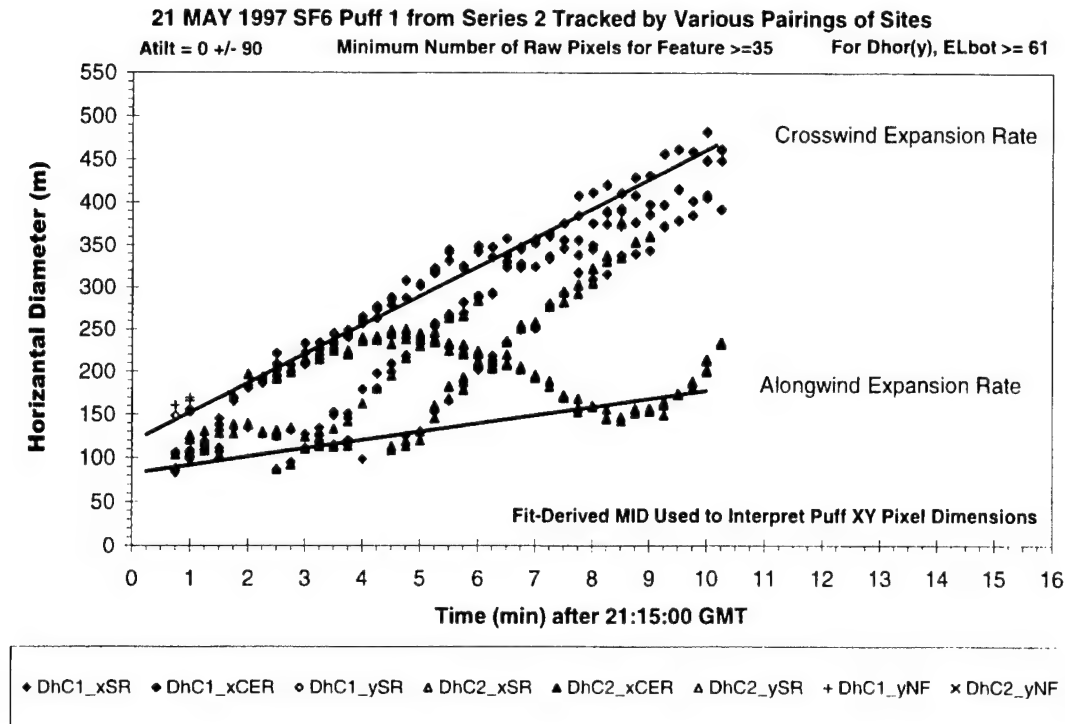
Figure G-13. Summary puff dimension plot showing all perspectives with regressive fits to the along- and crosswind trends.

Figure G-14 plots the PLMTRACK-derived horizontal expansion rate against tilt angle. The plotted diameters are from the PLMTRACK polygons. The plot reveals a relatively smooth transition from the slowest expansion rate in the alongwind axis (0° or 180°) to the fastest expansion rate in the crosswind axis (90°). This is the opposite of the trend observed for S1P1 (Appendix E). The plot suggests a slight shifting of the minimum and maximum for the trend from the pure alongwind and crosswind axes. This apparent shift in the position of the maximum and minimum as well as the scatter in the data along the trend is probably due to the scatter in the data. In order to obtain enough data to fully characterize the trend, the filters were opened to include 10° of scatter about the tilt angle (i.e., Tilt Window ±10) and fairly diverse perspectives ($|Ac1c2n| < 60$). In addition, the regressive fits were of limited accuracy (i.e., low correlation coefficients) for some perspectives due to the scatter and sparseness of the data.

Figures G-15 and G-16 show the effect of two filters on the alongwind and crosswind expansion rates. In these figures the along- and crosswind expansion rates are plotted against the value of pixel threshold and tilt window, respectively. Figure G-15 documents a constant value for both expansion rates as the threshold for the minimum number of pixels is raised from 0 to 30. In contrast, Figure G-16 reveals a dependence of both expansion rates on the tilt window. This sensitivity is consistent with the expansion rates' sensitivity to tilt angle (i.e., Figure G-14). As the angular window for the tilt angle approaches 90°, the fit would include all of the data plotted in Figure G-13. Therefore, the two curves in Figure G-16 should converge at a 90° window, but a regressive fit would no longer be appropriate. If there were not an angular dependence, the expansion rate would be the same for along- and crosswind perspectives, and there would be no sensitivity to the tilt window or tilt angle.

138

21 MAY 1997 SF6 Puff 1 from Series 2 Tracked by Various Pairings of Sites

Tilt Window +- 10; |Ac2c1n| <60; ELbot >=61; Pixels >=10

dt more than 4min & R^2 must be better than 0.7 to include in this plot!
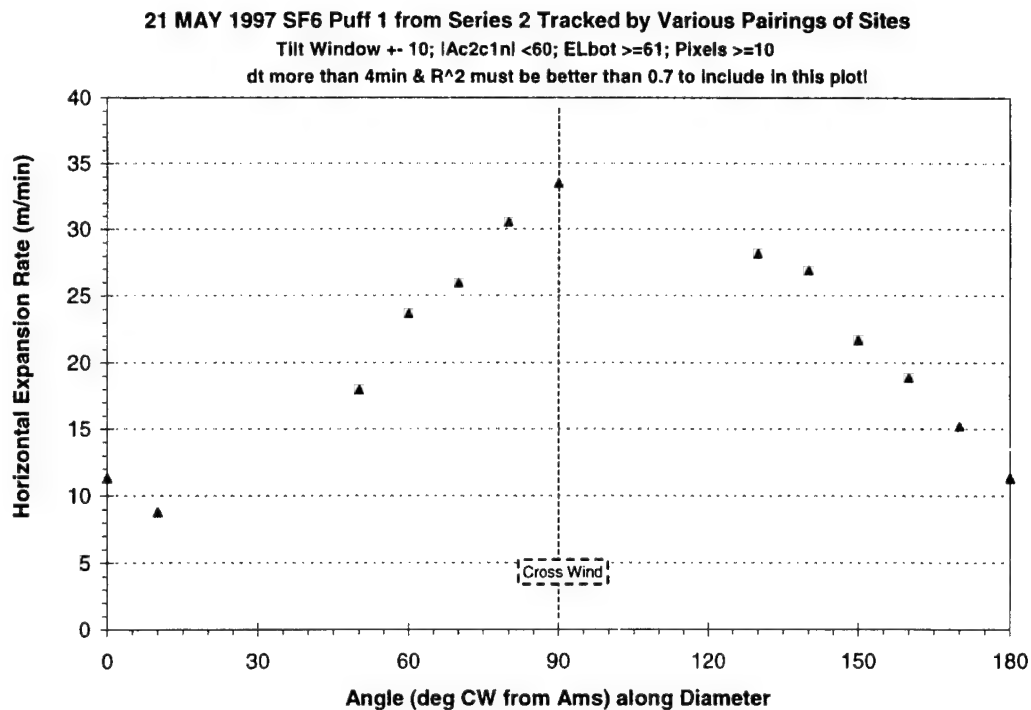
Figure G-14. Summary plot documenting the variation in expansion rate with perspective.

21 MAY 1997 SF6 Puff 1 from Series 2 Tracked by Various Pairings of Sites

Atilt = 0+/-10 (Along); Atilt = 90+/-10 (Cross); ELbot > 61

—■- dDdt(cross) (xSR, xCER, ySR)   —●—dDdt(along) (xSR, xCER, ySR)
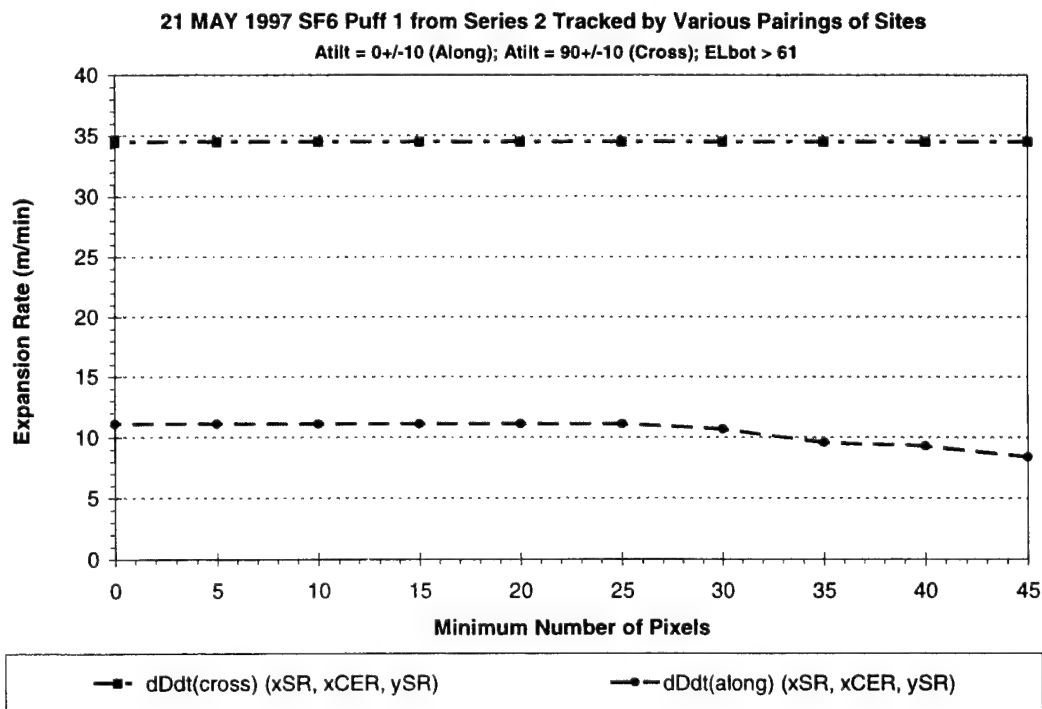
Figure G-15. Expansion rate sensitivity to puff size (in pixels) filtering

139

21 MAY 1997 SF6 Puff 1 from Series 2 Tracked by Various Pairings of Sites

Atilt = 0 (Along); Atilt = 90 (Cross); ELbot >= 61; Pixels >=10

Legend: dDdt(cross) (xSR, xCER, ySR) — dDdt(along) (xSR, xCER, ySR)
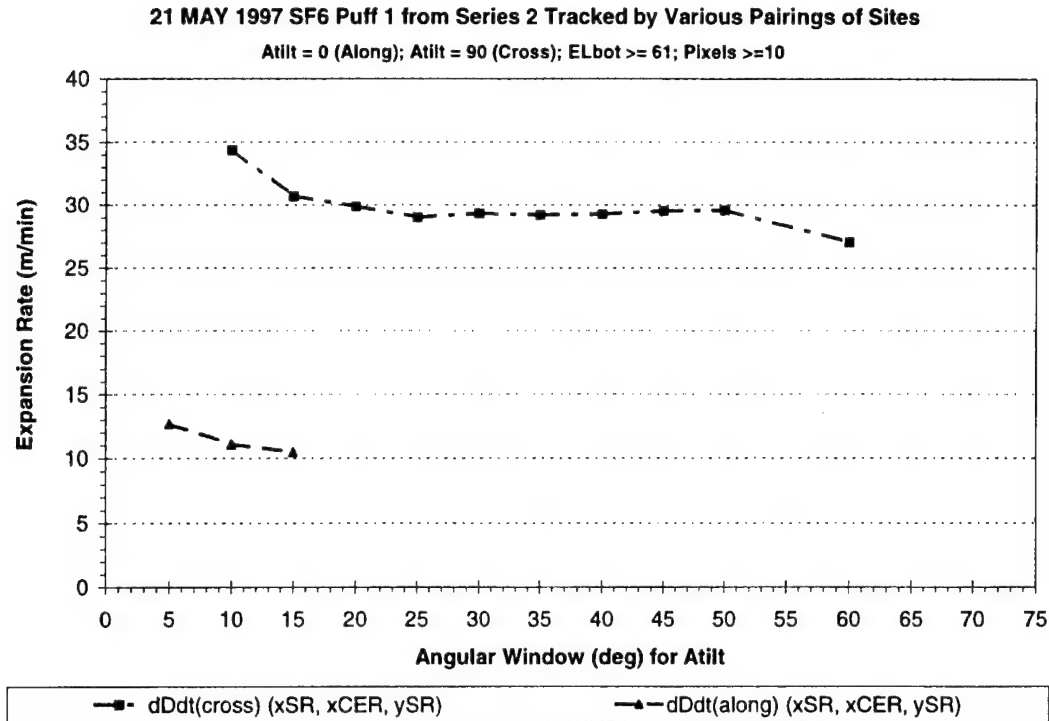
Figure G-16. Expansion rate sensitivity to the angular window about the perspective.

Both the along- and crosswind curves are incomplete in Figure G-16 because the dimension data fell on a line for relatively narrow windows about the tilt angle. We did not fit the data to a line when there was not a linear trend.

This appendix provided a detailed example of the puff analysis. The puff was series 2 puff 1 (S2P1) from 21 May 1997. Appendices E and F provide results for S1P1 and S1P2, respectively. Comparison reveals that S1P1 was dramatically different from the other puffs. In fact, the angular trends are reversed for S1P1 (Appendix E, Figure E-21) and for S2P1 (this appendix, Figure G-14). Therefore, in addition to illustrating the analysis schemes, these appendices illustrate that the dispersion rates are extremely sensitive both to release position and release time.

Appendix H-Imagery-Derived Expansion Rates for 21 May Puffs

"Best" Estimates of Puff Dimensions for 21 May 1997 Tracer Releases

The data plotted in this appendix are the "best" imagery-derived estimates of each puff's dimensions for the 21 May 1997 tracer releases. The first step of the analysis involved the use of PLMTRACK to measure the position of the puff's middle (MID). After combining all available data, the analysis generated the "best" formula for the puff's position as a function of time. This fit-derived position is more accurate than any one PLMTRACK triangulation since it is based upon all six pair-wise combinations of all imagery after filtering for the best perspectives. This "best" fit formula allows the conversion of the puff's angular extent in any single image to physical extent from that perspective. The angular extent is merely the proportion of FOV occupied by the puff. This "best" method minimizes any errors associated with the PLMTRACK-derived polygon (see Appendices A, E, F, and G). It also allows processing of individual images, separately.

Each plot's headings document the experimental variables that served as filters for those data. The filtering not only improved accuracy but also specified perspective (i.e., dispersion axis). Appendix A illustrated the various angles and diameters associated with these analyses and the filtering of the data. Appendix C documented that the expansion rates measured by the "best" method are insensitive to the resolution, slant range, elevation, and background radiance over their operational ranges. Appendix D documented that the observed extent included the bulk of the tracer gas. Appendices E, F, and G provided more detailed analysis for three puffs.

Puff Dimensions and Expansion Rates for 21 May 1997 Tracer Releases

This appendix presents the imagery-derived dimension and expansion rate data for the 21 May 1997 tracer puffs. Each puff's diameter is plotted against time after release and distance from the source. The slopes of these two plots are the expansion rates in m/min and m/m, respectively. As discussed in the body of the report, a tilt angle of 0° (or 180°) corresponds to alongwind dispersion, while a tilt angle of 90° corresponds to crosswind dispersion. These plots document the quantity and quality of the data used to measure the expansion rates. These along- and crosswind expansion rates were included in Table 4 and several figures in the body of this report.

There are several plots for each puff. The first figure of each series is a plot of the puff's diameter against time after its release. The data in this summary plot include all perspectives (i.e., all tilt angles). This plot also includes the linear regressive trend lines for selected axes (i.e., perspectives). These lines provide the analyst with a frame of reference for comparing the combined data (i.e., summary plot) to the filtered data. Subsequent plots include only the filtered data associated with each trend line (i.e., a specific axis). The headings for each figure document that the plotted data have been filtered to provide better accuracy and a specific perspective. Since the "best" method does not rely directly on pair-wise analysis, these plots document results from every image that saw the puff's extent from the specified perspective (Atilt ± Window). The diameter along the specified

axis is plotted against distance from the source or elapsed travel time from the source. The formula for the linear regressive fit reveals the expansion rate (i.e., slope in m/m) for the specified perspective (Atilt ± Window).

These data document that the puff's diameters typically fell between the extremes defined by the along- and crosswind expansion rates. This should be the case if the puff's major or minor axes were aligned with the direction of maximum dispersion. The results suggest that the maximum expansion rates were always parallel or normal to the puff bearing (i.e., wind direction). This is consistent with the results presented in Appendices F and H. There are gaps in the along- or crosswind trends at times when the fixed sites did not provide the desired perspective and when the puff overfilled the FOV. See the body of this report for further discussion of these results.

Figure H-1. Summary dimension plot showing all perspectives of S1P1 on 21 May 1997.

Figure H-2. Crosswind extent (Atilt = 90±10) versus distance for S1P1 on 21 May 1997.

143

21 MAY 1997 SF6 Puff 1 from Series 1 Tracked by Various Pairings of Sites

Atilt = 0 +/- 10   Minimum Number of Raw Pixels for Feature >=18   For Dhor(y), ELbot >= 70

Source = Puff @ 0.25 min by Sites 1 and 3

$y = 0.17x - 12.598$
$R^2 = 0.989$

Fit-Derived MID Used to Interpret Puff XY Pixel Dimensions

Horizantal Diameter (m) vs Ground Distance (m) from Source

◆	DhC1_xSR	◆	DhC1_xCER	○	DhC1_ySR
▲	DhC2_xSR	▲	DhC2_xCER	△	DhC2_ySR
+	DhC1_yNF	×	DhC2_yNF	— —	Linear (Dh (xSR, xCER, ySR))

Figure H-3. Alongwind extent (Atilt = 0±10) versus distance for S1P1 on 21 May 1997.

21 MAY 1997 SF6 Puff 2 from Series 1 Tracked by Various Pairings of Sites

Atilt = 90 +/- 90   Minimum Number of Raw Pixels for Feature >=10   For Dhor(y), ELbot >= 70

Crosswind

No Alongwind Perspective

Fit-Derived MID Used to Interpret Puff XY Pixel Dimensions

Horizantal Diameter (m) vs Time (min) after 21:01:00 GMT

◆ DhC1_xSR ◆ DhC1_xCER ◇ DhC1_ySR ▲ DhC2_xSR ▲ DhC2_xCER △ DhC2_ySR + DhC1_yNF × DhC2_yNF

Figure H-4. Summary dimension plot showing all perspectives of S1P2 on 21 May 1997.

144

21 MAY 1997 SF6 Puff 2 from Series 1 Tracked by Various Pairings of Sites

Atilt = 90 +/- 10   Minimum Number of Raw Pixels for Feature >=10   For Dhor(y), ELbot >= 70

Source = Puff @ 0.25 min by Sites 1 and 2

$y = 0.1928x + 27.148$
$R^2 = 0.9946$

Fit-Derived MID Used to Interpret Puff XY Pixel Dimensions

◆ DhC1_xSR	● DhC1_xCER	○ DhC1_ySR
▲ DhC2_xSR	▲ DhC2_xCER	△ DhC2_ySR
+ DhC1_yNF	× DhC2_yNF	— —Linear (Dh (xSR, xCER, ySR))

Figure H-5. Crosswind extent (Atilt = 90±10) versus distance for S1P2 on 21 May 1997.

21 MAY 1997 SF6 Puff 1 from Series 2 Tracked by Various Pairings of Sites

Atilt = 0 +/- 90   Minimum Number of Raw Pixels for Feature >=35   For Dhor(y), ELbot >= 61

Crosswind Expansion Rate

Alongwind Expansion Rate

Fit-Derived MID Used to Interpret Puff XY Pixel Dimensions

◆ DhC1_xSR   ◆ DhC1_xCER   ○ DhC1_ySR   ▲ DhC2_xSR   ▲ DhC2_xCER   △ DhC2_ySR   + DhC1_yNF   × DhC2_yNF

Figure H-6. Summary dimension plot showing all perspectives of S2P1 on 21 May 1997.

145

Figure H-7. Crosswind extent (Atilt = 90±10) versus distance for S2P1 on 21 May 1997.
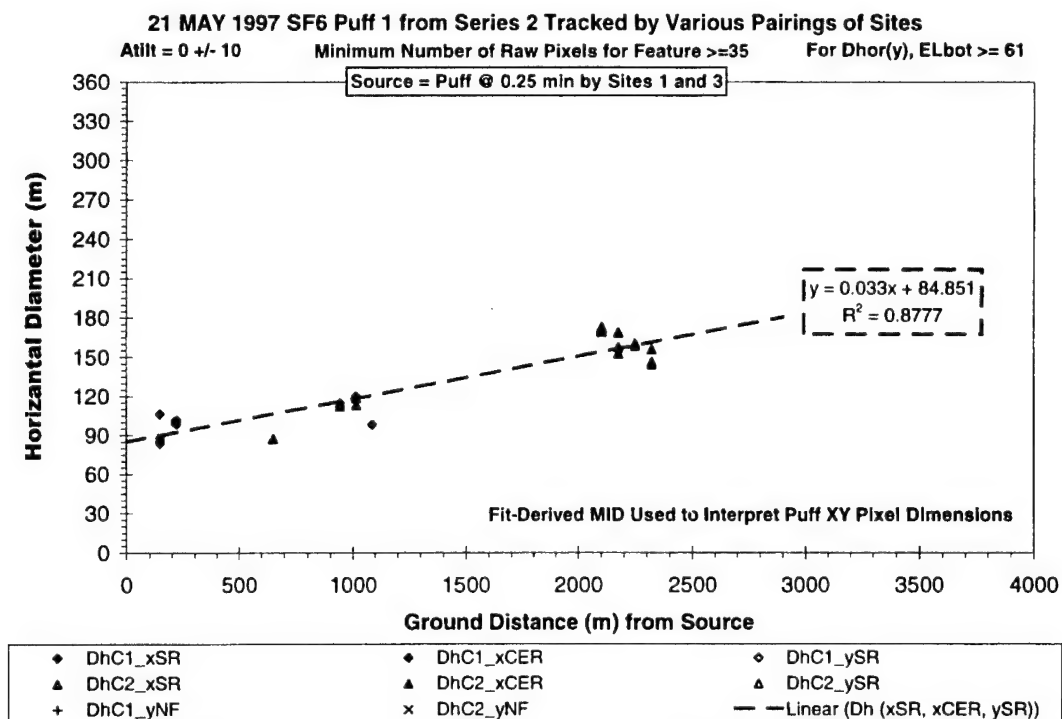
Figure H-8. Alongwind extent (Atilt = 0±10) versus distance for S2P1 on 21 May 1997.
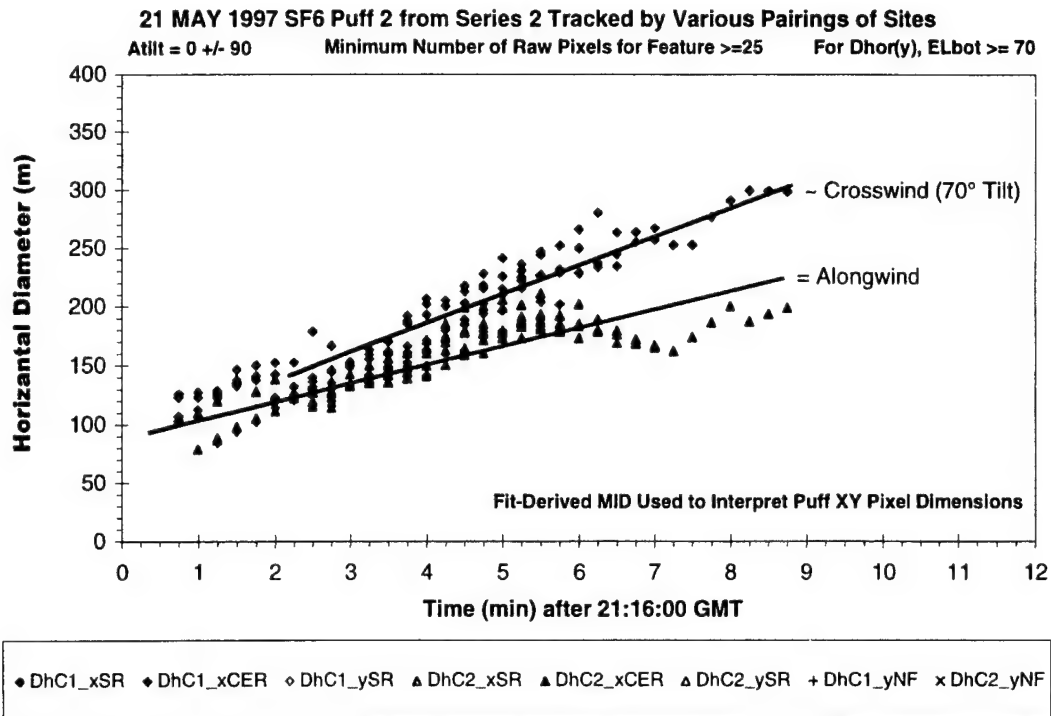
Figure H-9. Summary dimension plot showing all perspectives of S2P2 on 21 May 1997.
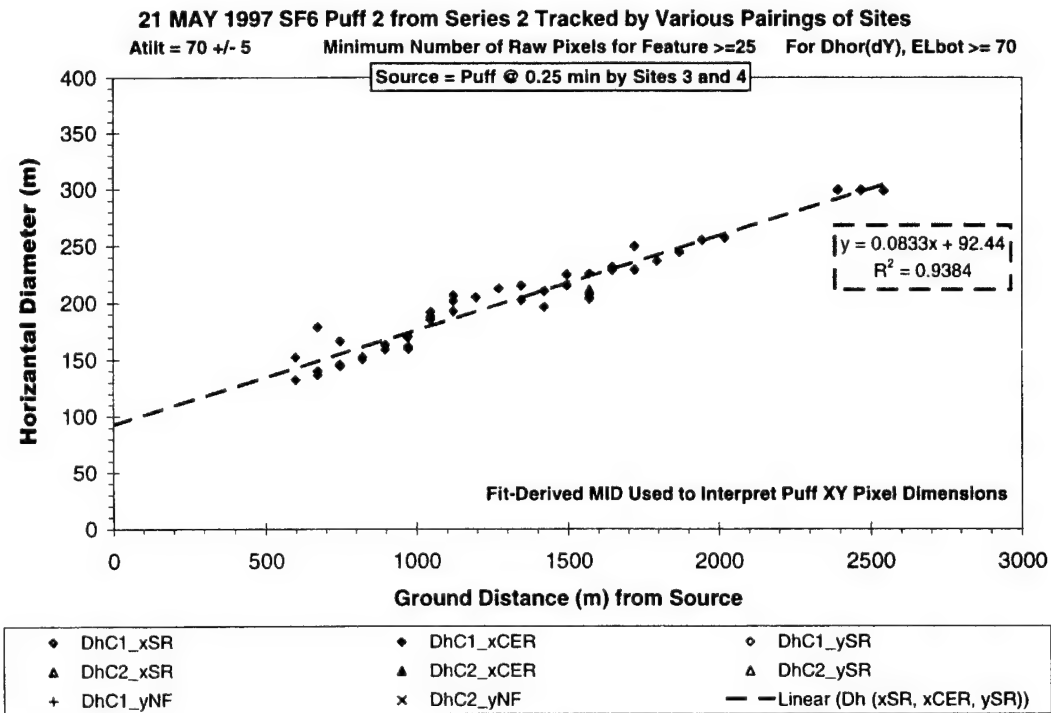
Figure H-10. Crosswind extent (Atilt = 70±5) versus distance for S2P2 on 21 May 1997.

147
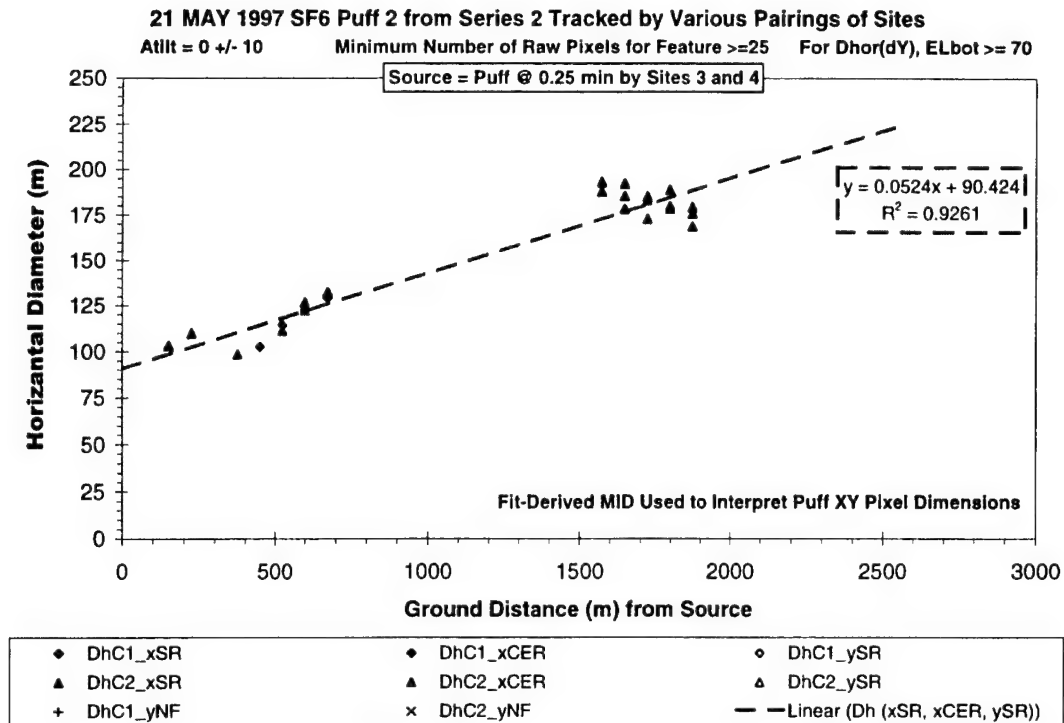
Figure H-11. Alongwind extent (Atilt = 0±10) versus distance for S2P2 on 21 May 1997.
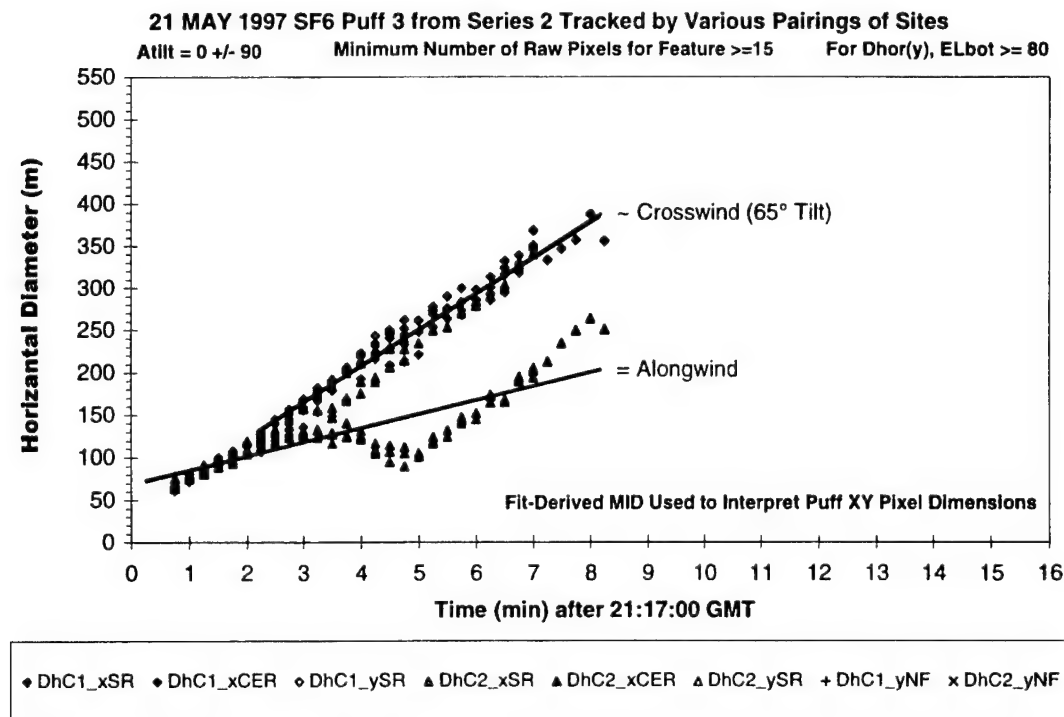
Figure H-12. Summary dimension plot showing all perspectives of S2P3 on 21 May 1997.
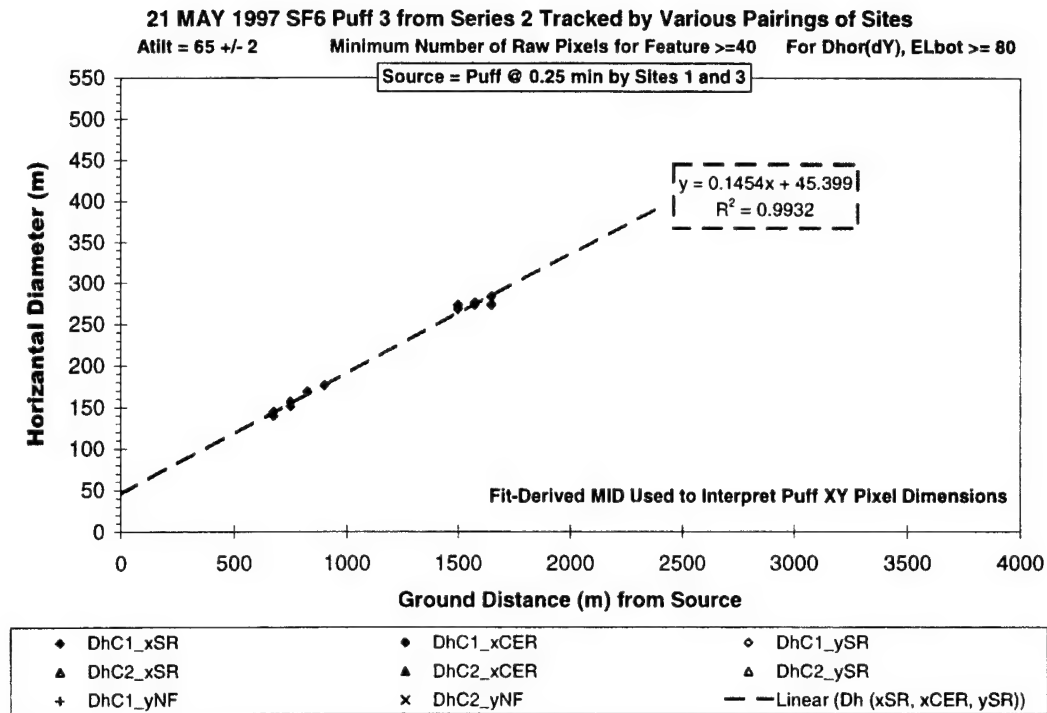
Figure H-13. Cross-diagonal extent (Atilt=65±2) versus distance for S2P3 on 21 May 1997.
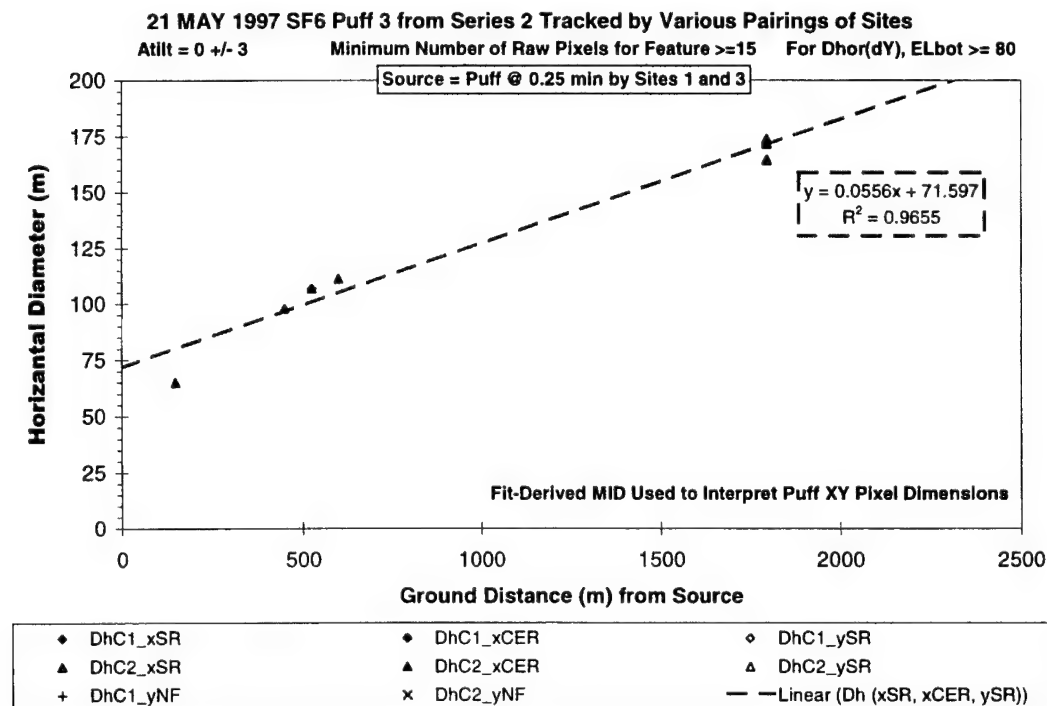
Figure H-14. Alongwind extent (Atilt = 0±3) versus distance for S2P3 on 21 May 1997.
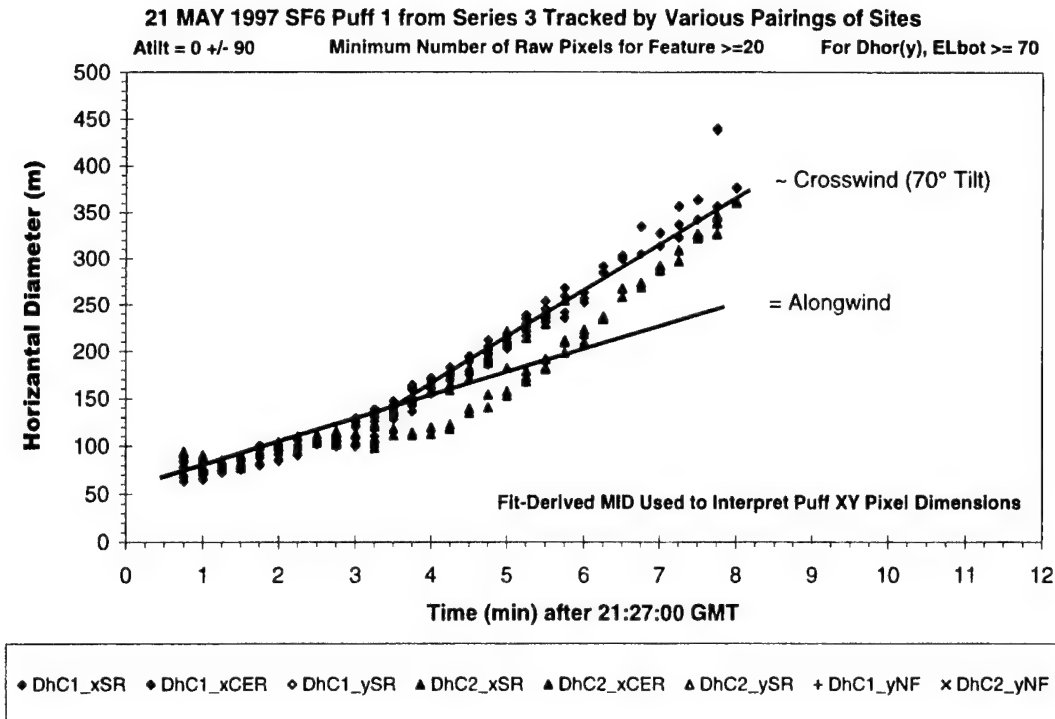
Figure H-15. Summary dimension plot showing all perspectives of S3P1 on 21 May 1997.
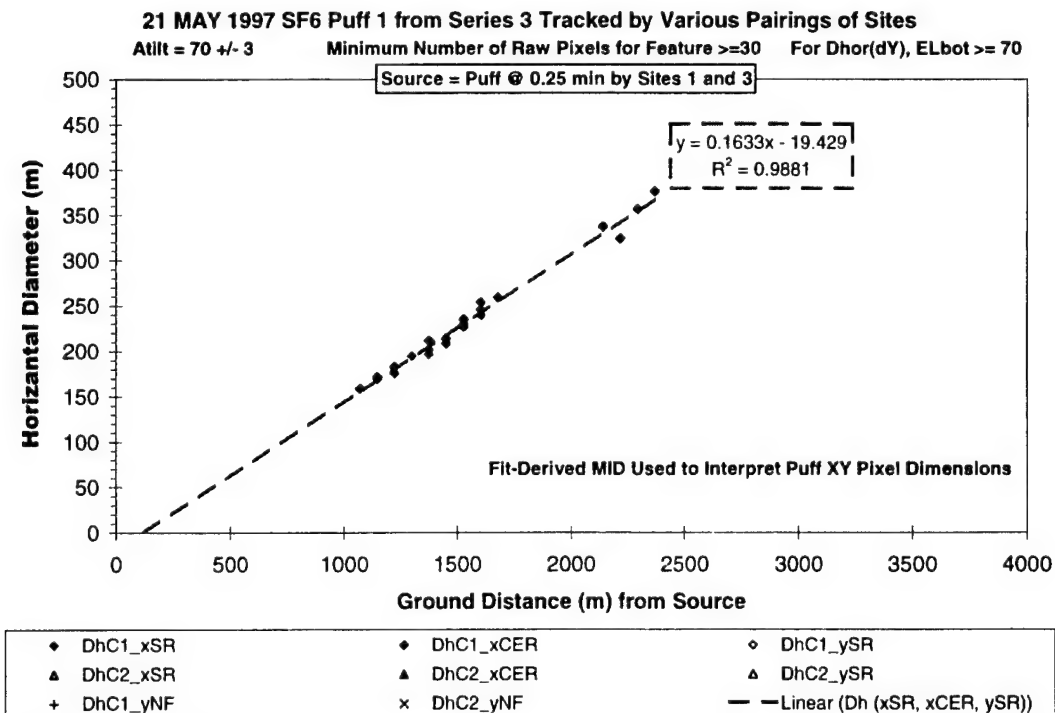
Figure H-16. Crosswind extent (Atilt = 70±3) versus distance for S3P1 on 21 May 1997.
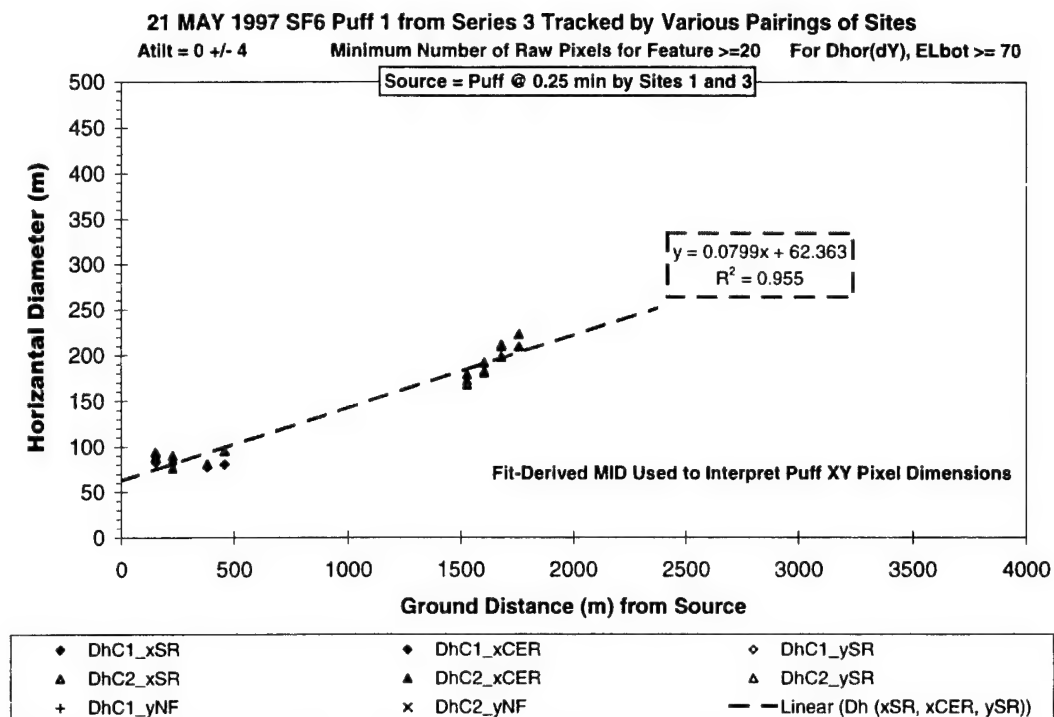
Figure H-17. Alongwind extent (Atilt = 0±4) versus distance for S3P1 on 21 May 1997.
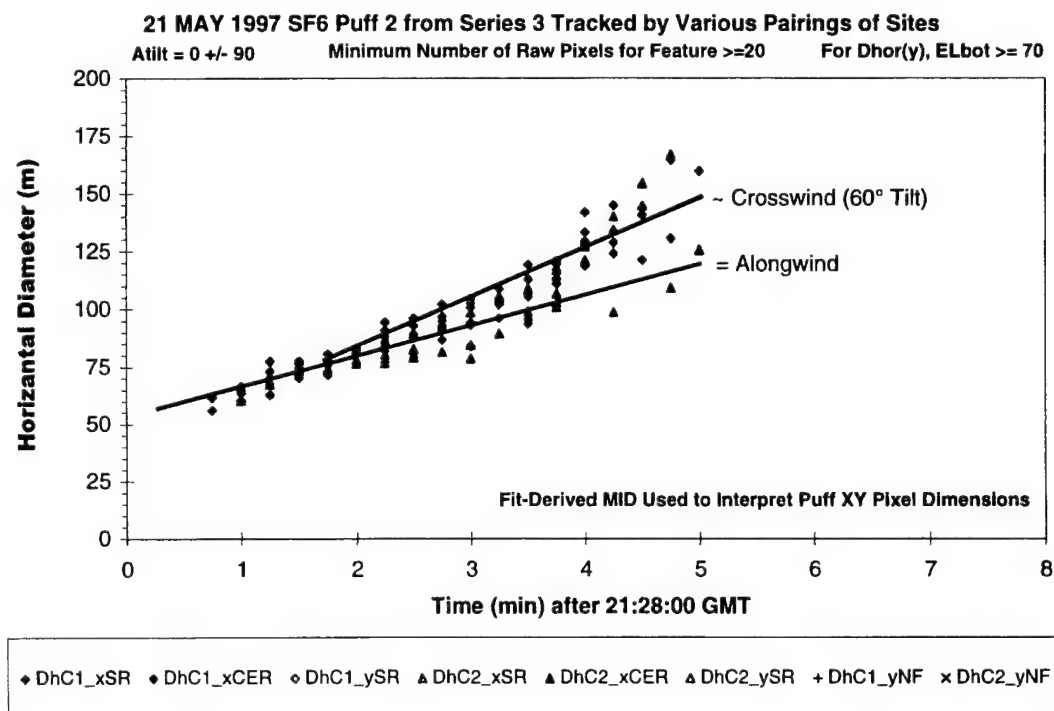
Figure H-18. Summary dimension plot showing all perspectives of S3P2 on 21 May 1997.

151
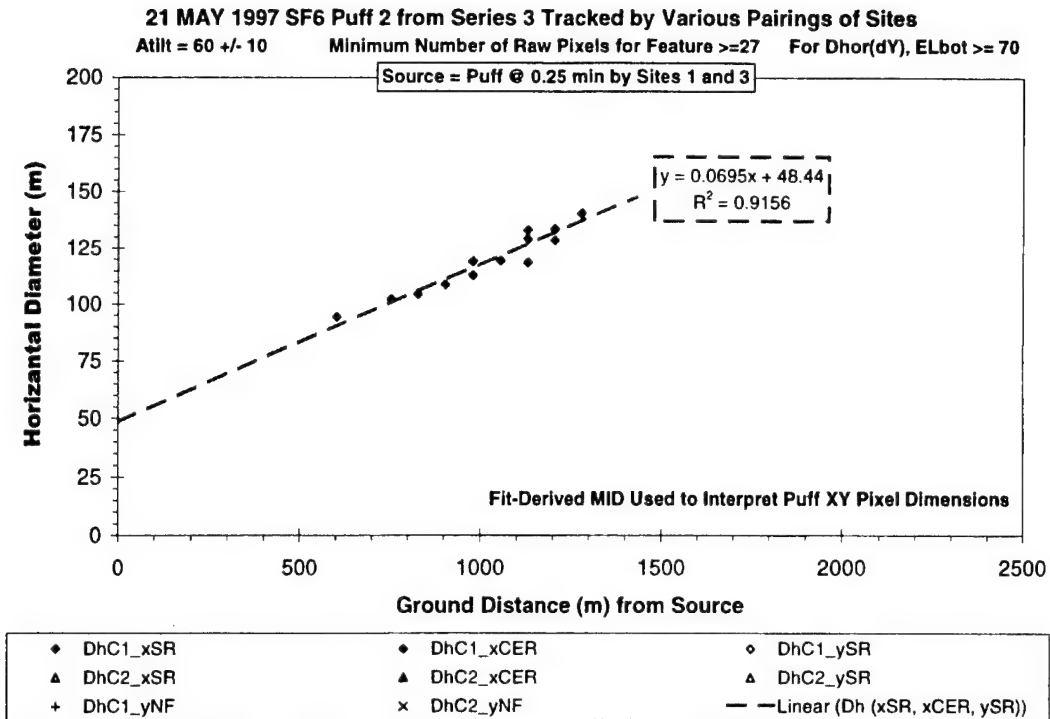
Figure H-19. Cross-diagonal extent (Atilt=60±10) versus distance for S3P2 on 21 May 1997.
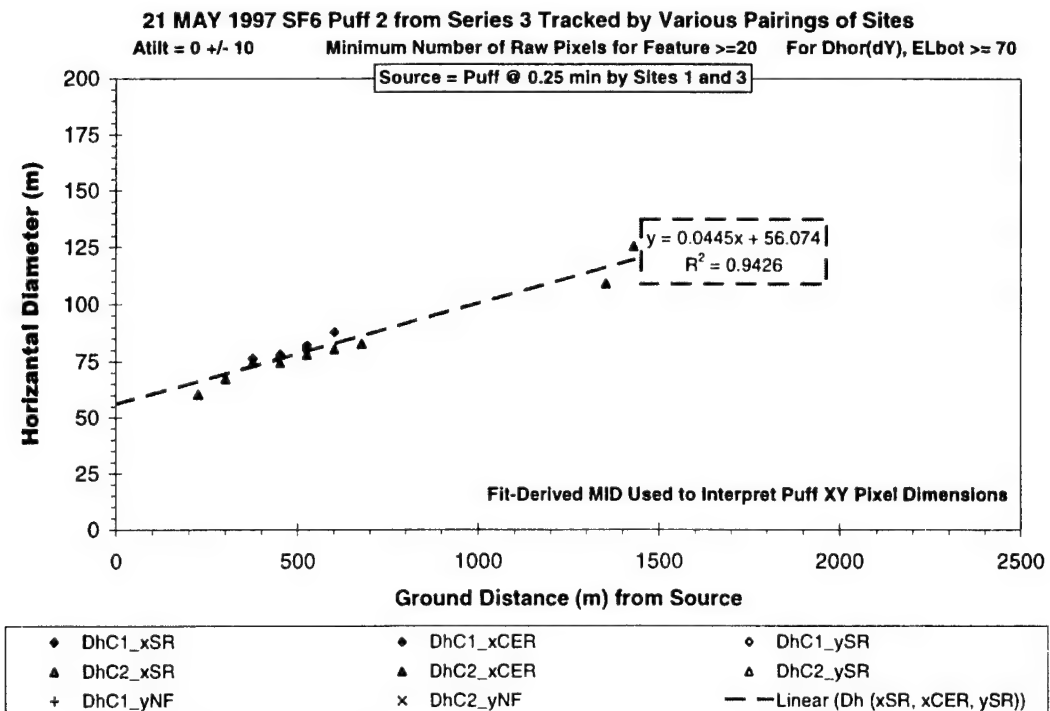
Figure H-20. Alongwind extent (Atilt = 0±10) versus distance for S3P2 on 21 May 1997.

152
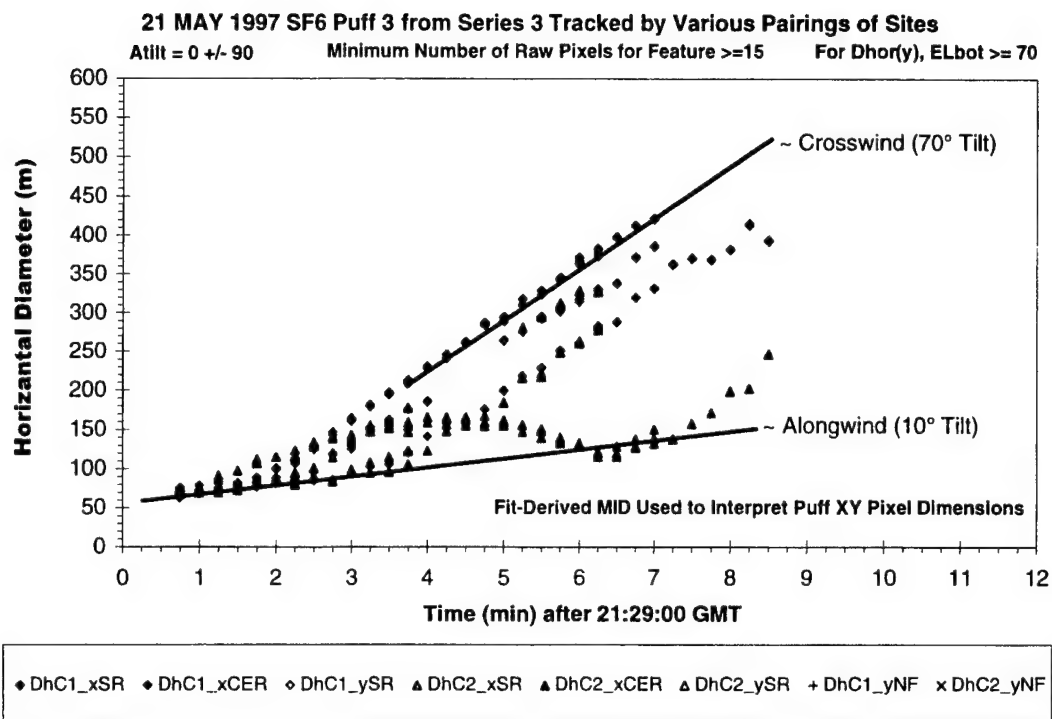
Figure H-21. Summary dimension plot showing all perspectives of S3P3 on 21 May 1997.
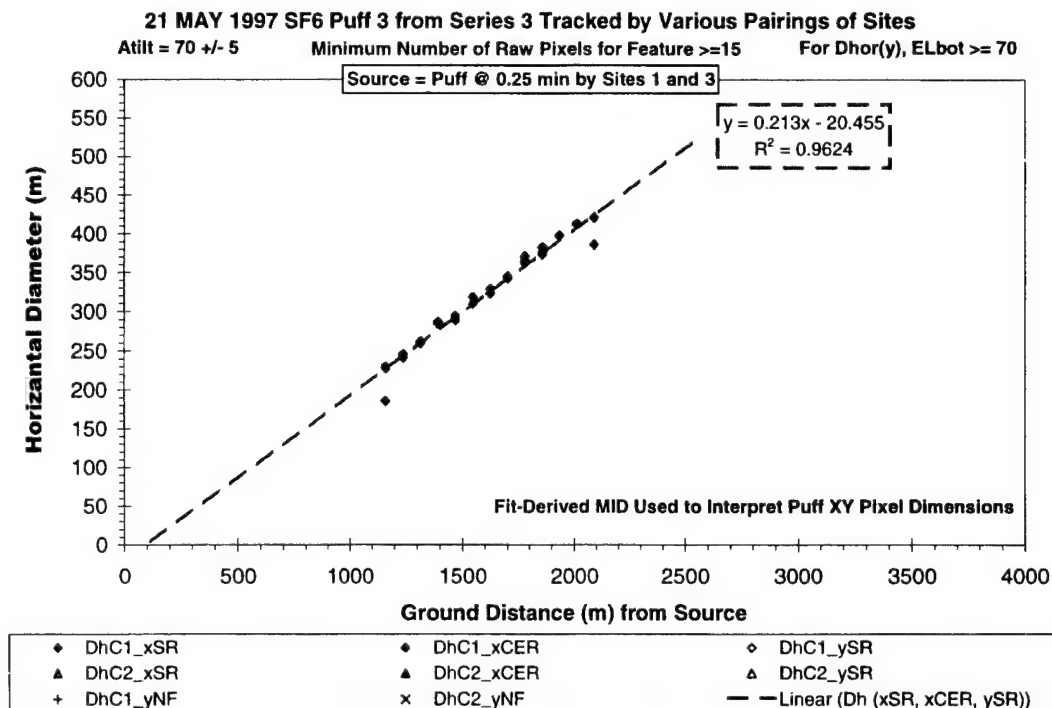
Figure H-22. ~ Crosswind extent (Atilt = 70±5) versus distance for S3P3 on 21 May 1997.

153
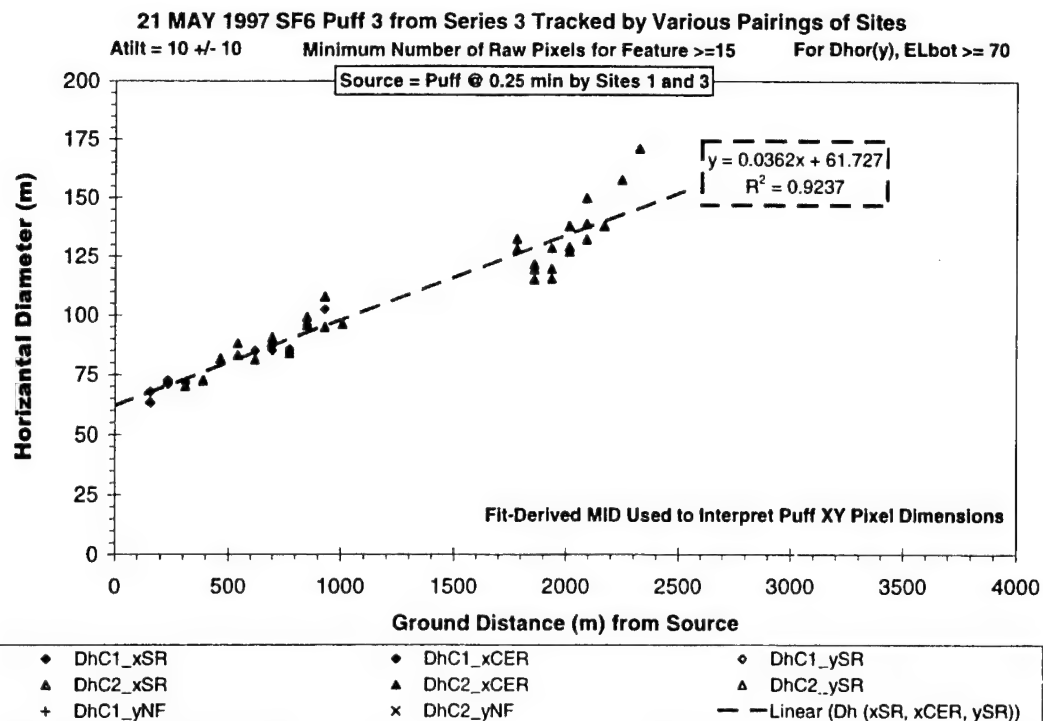
Figure H-23. ~ Alongwind extent (Atilt = 10±10) versus distance for S3P3 on 21 May 1997.
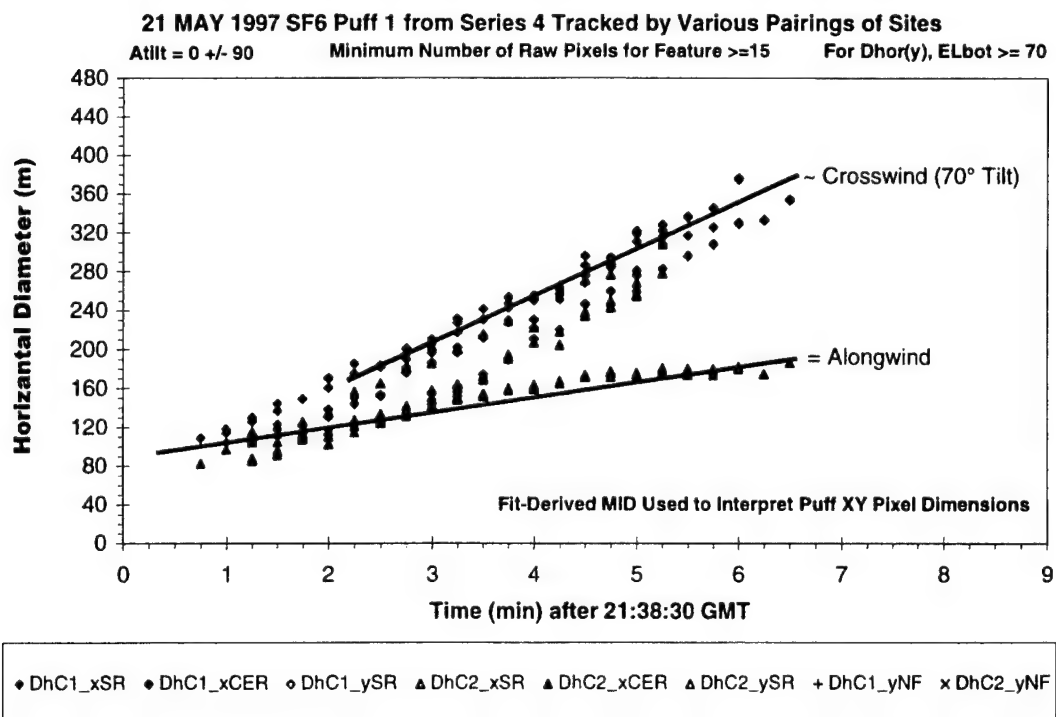
Figure H-24. Summary dimension plot showing all perspectives of S4P1 on 21 May 1997.
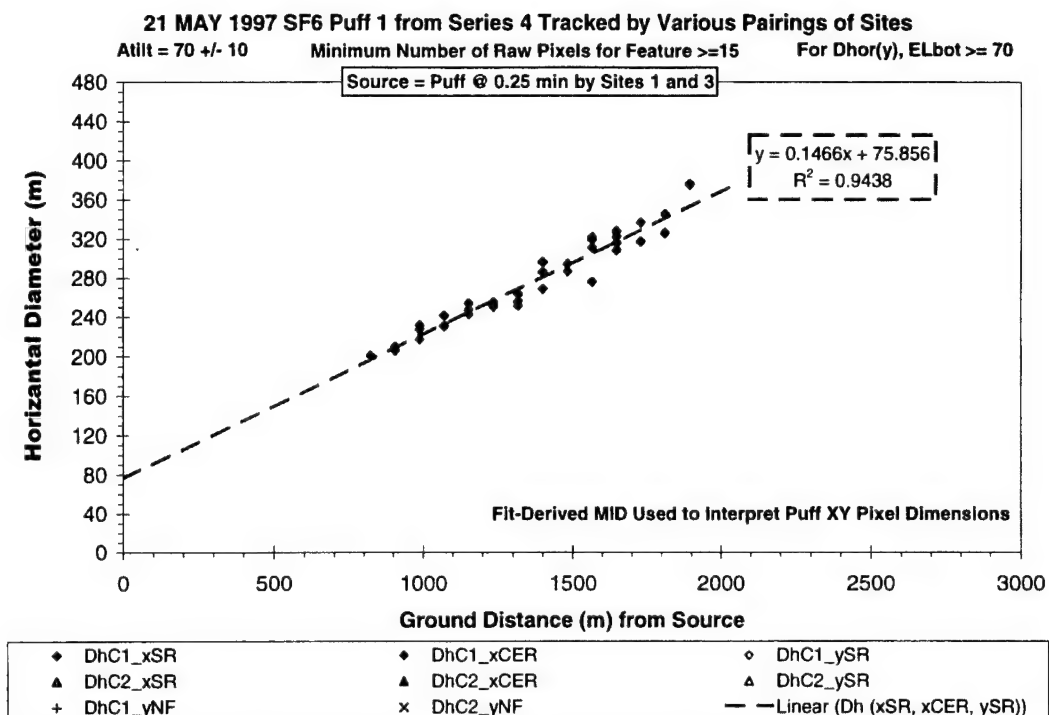
Figure H-25. ~ Crosswind extent (Atilt = 70±10) versus distance for S4P1 on 21 May 1997.
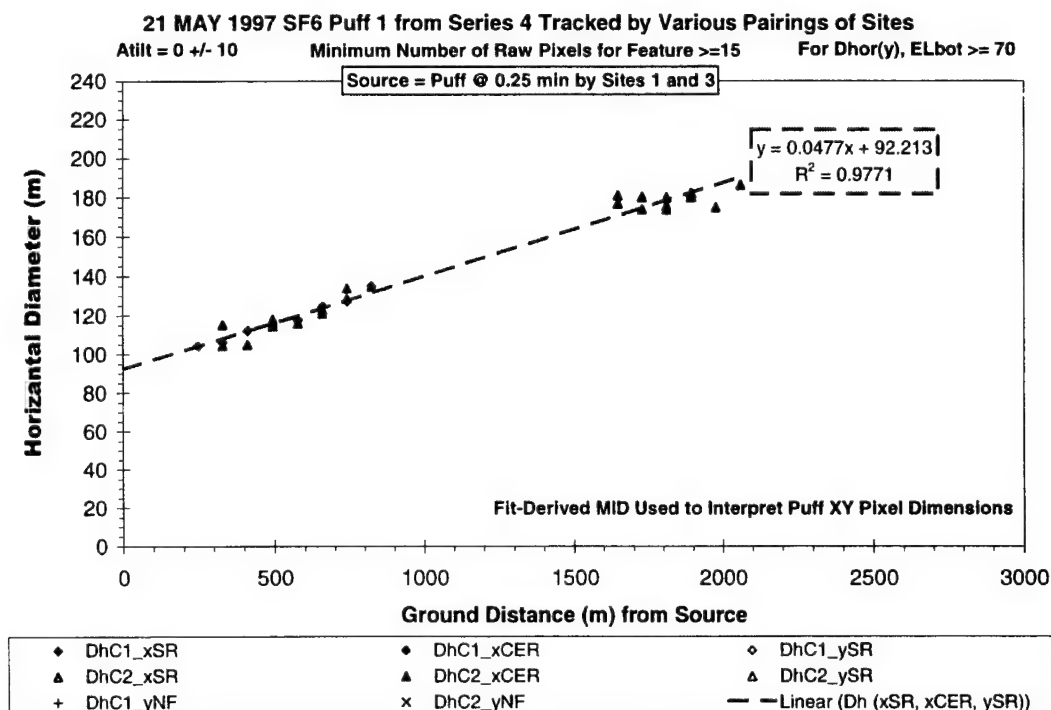
Figure H-26. Alongwind extent (Atilt = 0±10) versus distance for S4P1 on 21 May 1997.
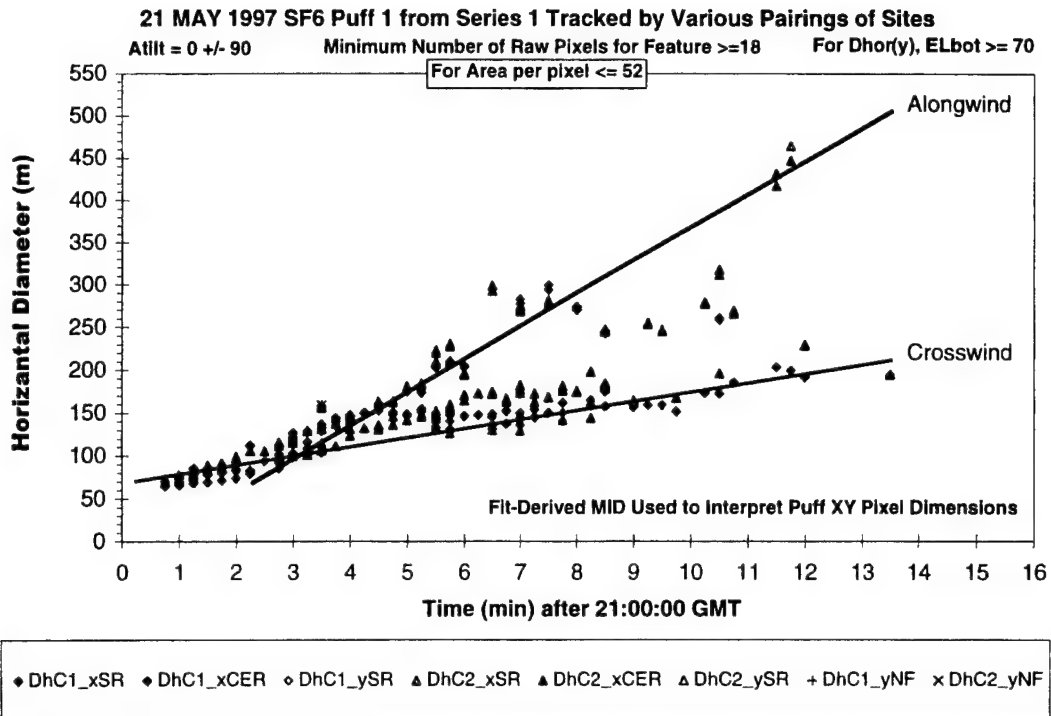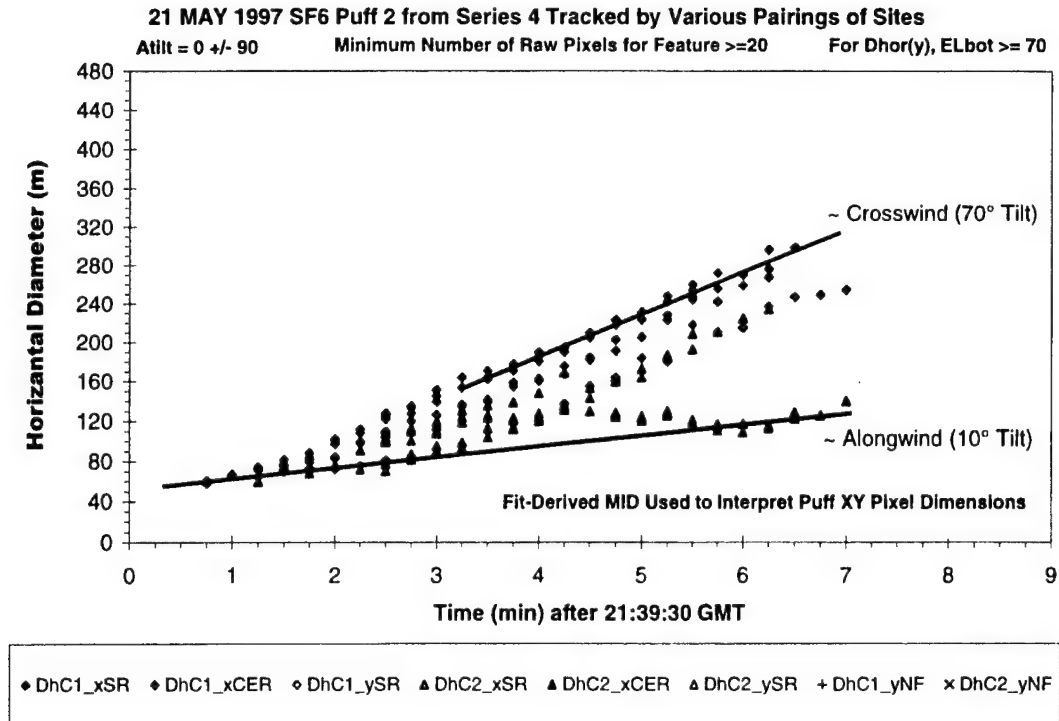
Figure H-27. Summary dimension plot showing all perspectives of S4P2 on 21 May 1997.
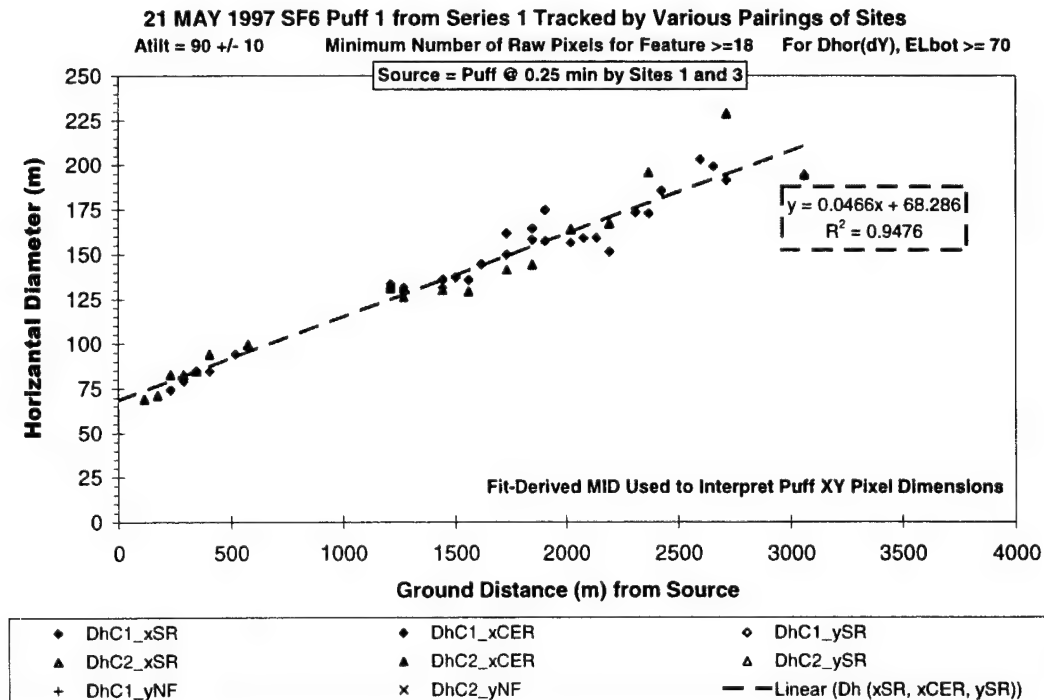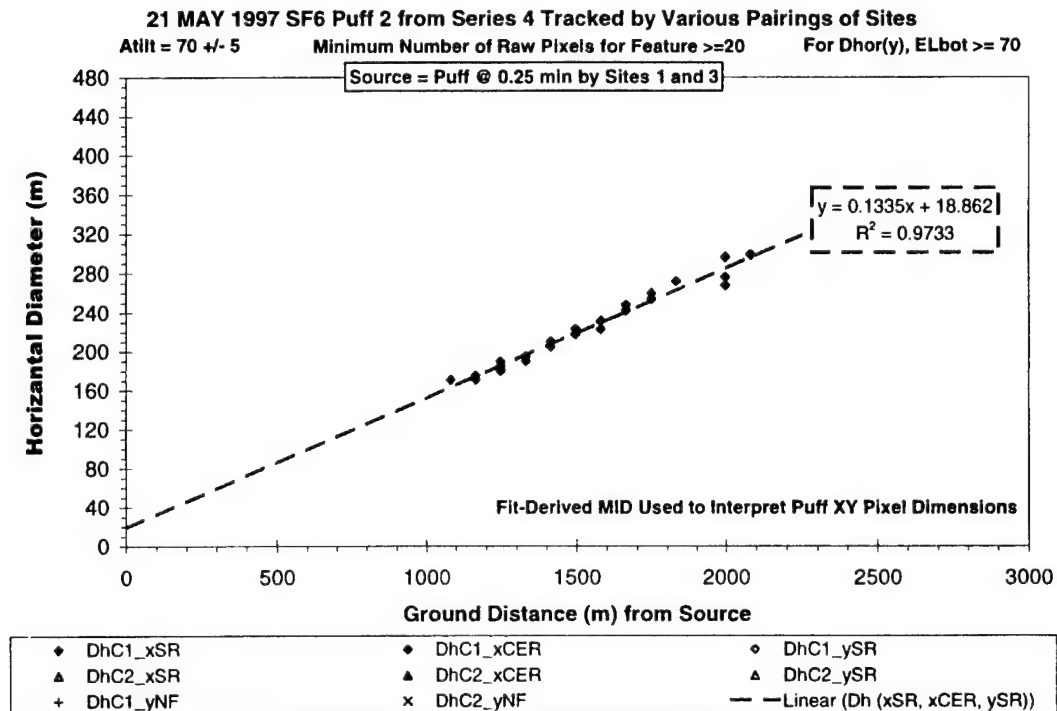

Figure H-28. Crosswind extent (Atilt = 70±5) versus distance for S4P2 on 21 May 1997.

156
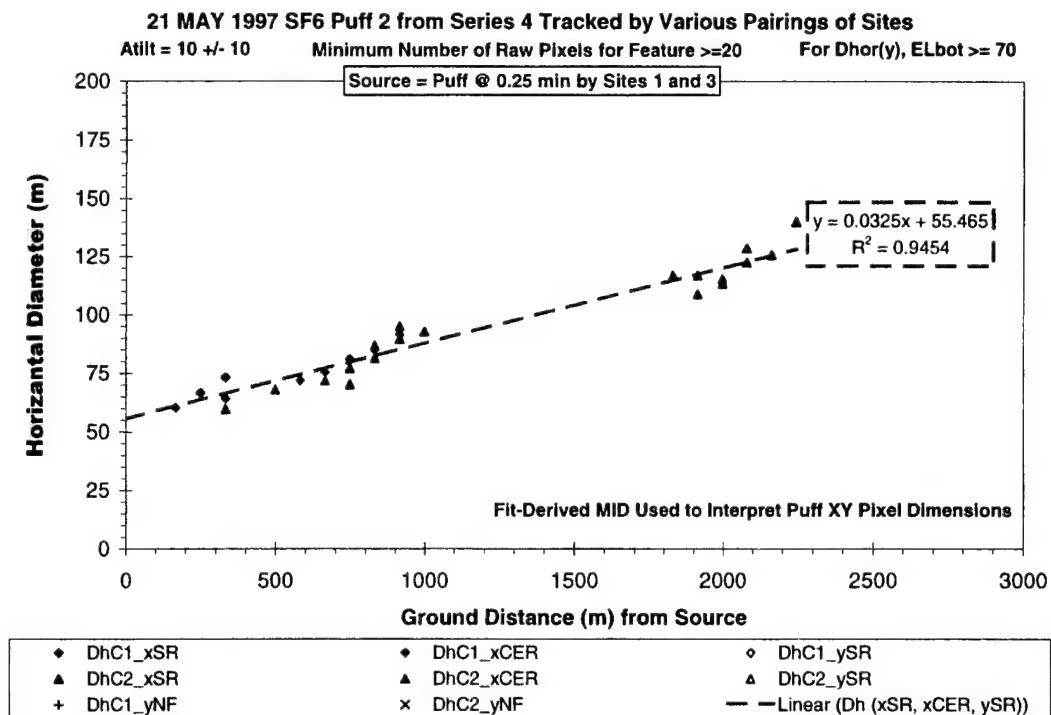
Figure H-29. ~ Alongwind extent (Atilt = 10±10) versus distance for S4P2 on 21 May 1997.
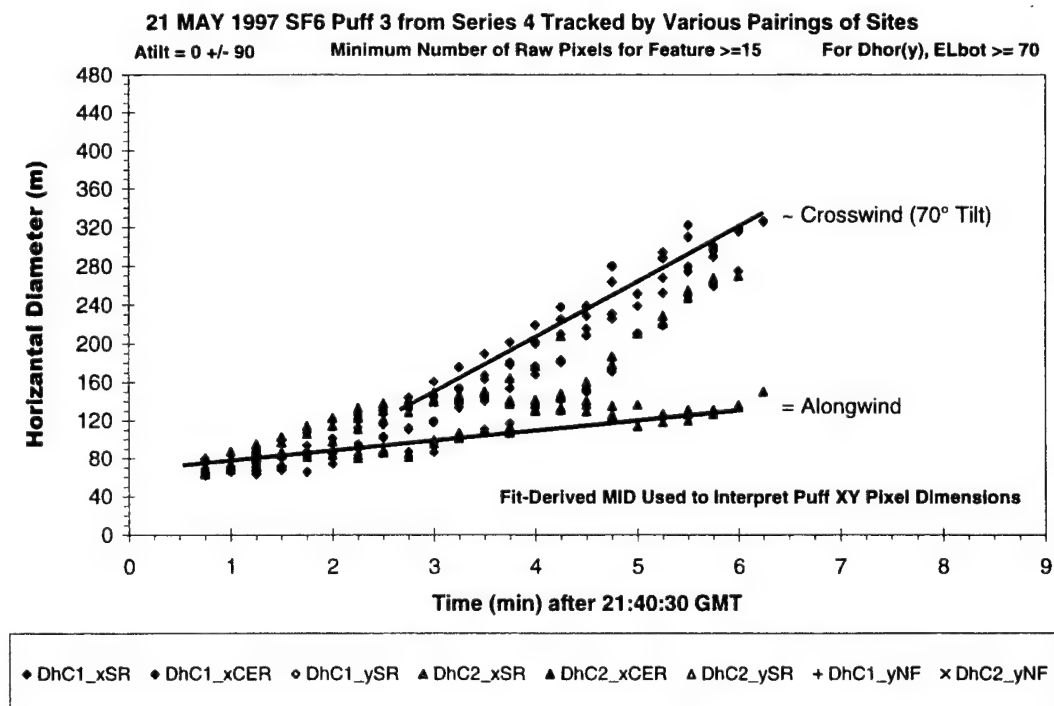
Figure H-30. Summary dimension plot showing all perspectives of S4P3 on 21 May 1997.

157

21 MAY 1997 SF6 Puff 3 from Series 4 Tracked by Various Pairings of Sites

Atilt = 70 +/- 10   Minimum Number of Raw Pixels for Feature >=15   For Dhor(y), ELbot >= 70

Source = Puff @ 0.25 min by Sites 1 and 2

$y = 0.1758x - 12.094$
$R^2 = 0.9465$

Fit-Derived MID Used to Interpret Puff XY Pixel Dimensions

Y-axis: Horizantal Diameter (m) — 0 to 480
X-axis: Ground Distance (m) from Source — 0 to 3000

♦ DhC1_xSR	◆ DhC1_xCER	◇ DhC1_ySR
▲ DhC2_xSR	▲ DhC2_xCER	△ DhC2_ySR
+ DhC1_yNF	× DhC2_yNF	— —Linear (Dh (xSR, xCER, ySR))

Figure H-31. Crosswind extent (Atilt = 70±10) versus distance for S4P3 on 21 May 1997.

21 MAY 1997 SF6 Puff 3 from Series 4 Tracked by Various Pairings of Sites

Atilt = 0 +/- 5   Minimum Number of Raw Pixels for Feature >=20   For Dhor(y), ELbot >= 70

Source = Puff @ 0.25 min by Sites 1 and 2

$y = 0.033x + 69.056$
$R^2 = 0.9743$

Fit-Derived MID Used to Interpret Puff XY Pixel Dimensions

Y-axis: Horizantal Diameter (m) — 0 to 200
X-axis: Ground Distance (m) from Source — 0 to 3000

♦ DhC1_xSR	◆ DhC1_xCER	◇ DhC1_ySR
▲ DhC2_xSR	▲ DhC2_xCER	△ DhC2_ySR
+ DhC1_yNF	× DhC2_yNF	— —Linear (Dh (xSR, xCER, ySR))

Figure H-32. Alongwind extent (Atilt = 0±5) versus distance for S4P3 on 21 May 1997.

158
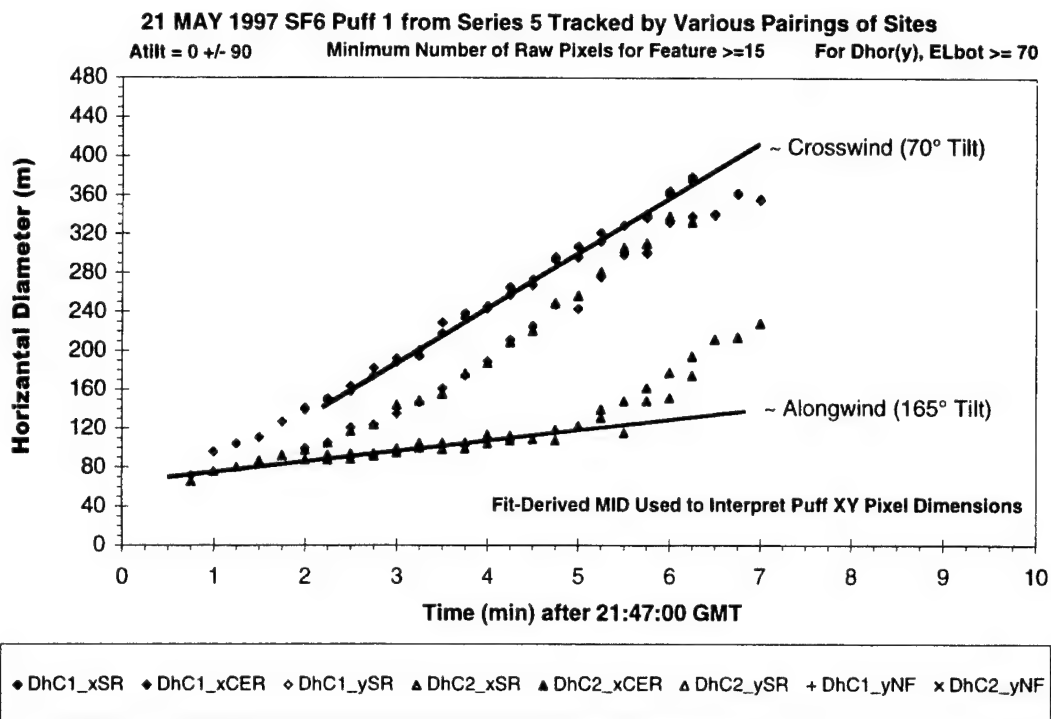
Figure H-33. Summary dimension plot showing all perspectives of S5P1 on 21 May 1997.
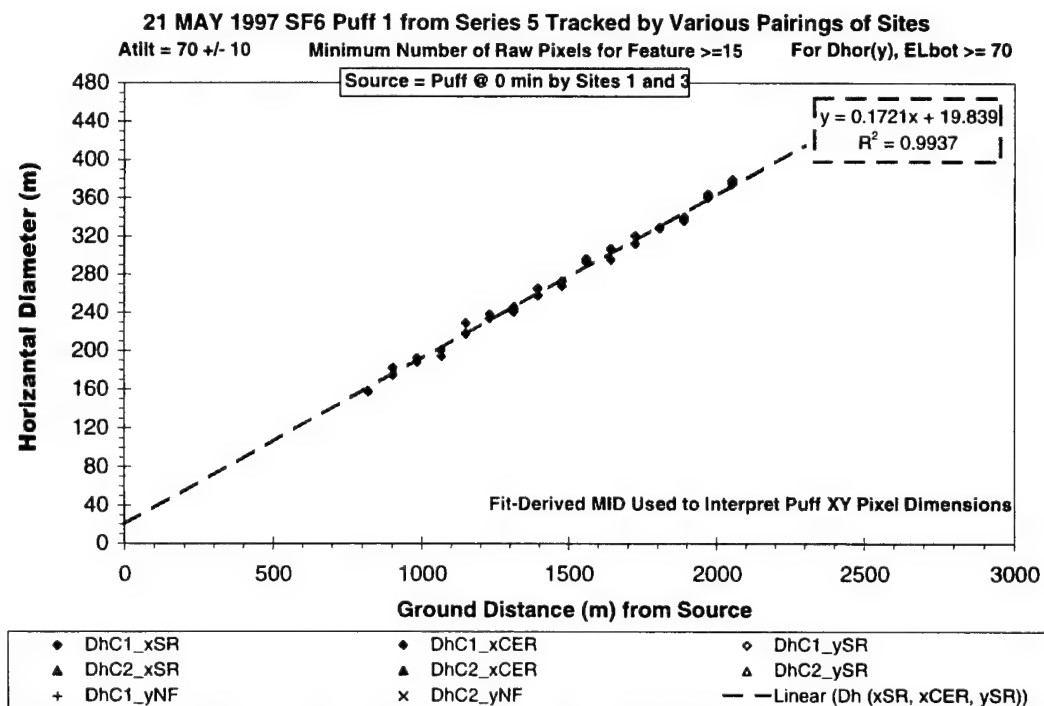
Figure H-34. Crosswind extent (Atilt = 70±10) versus distance for S5P1 on 21 May 1997.
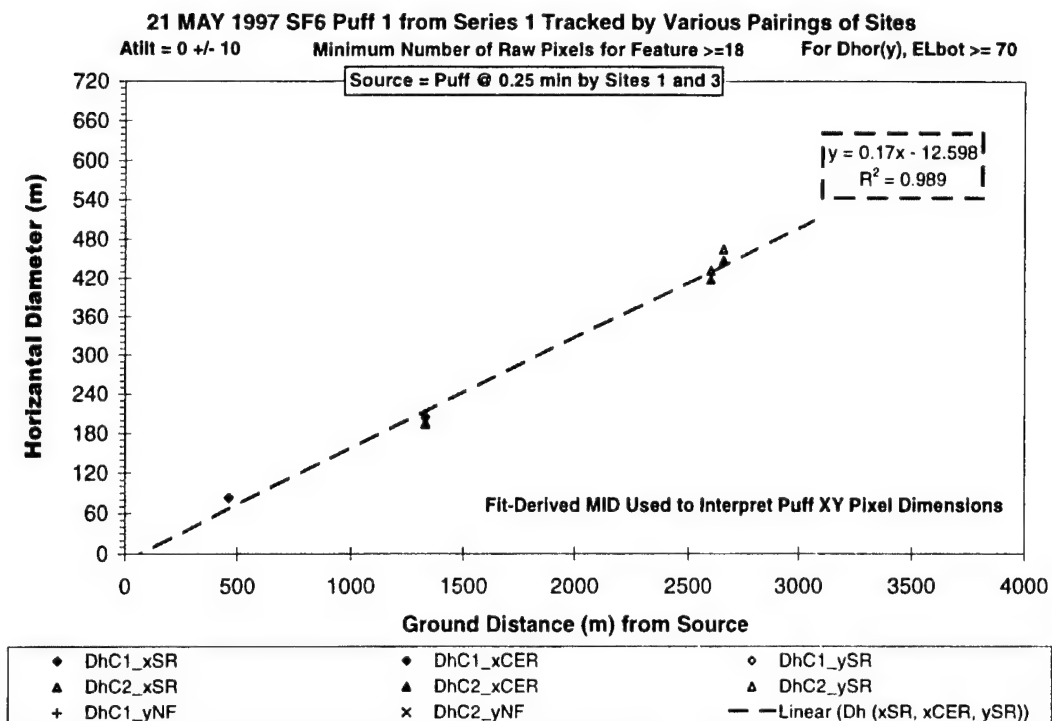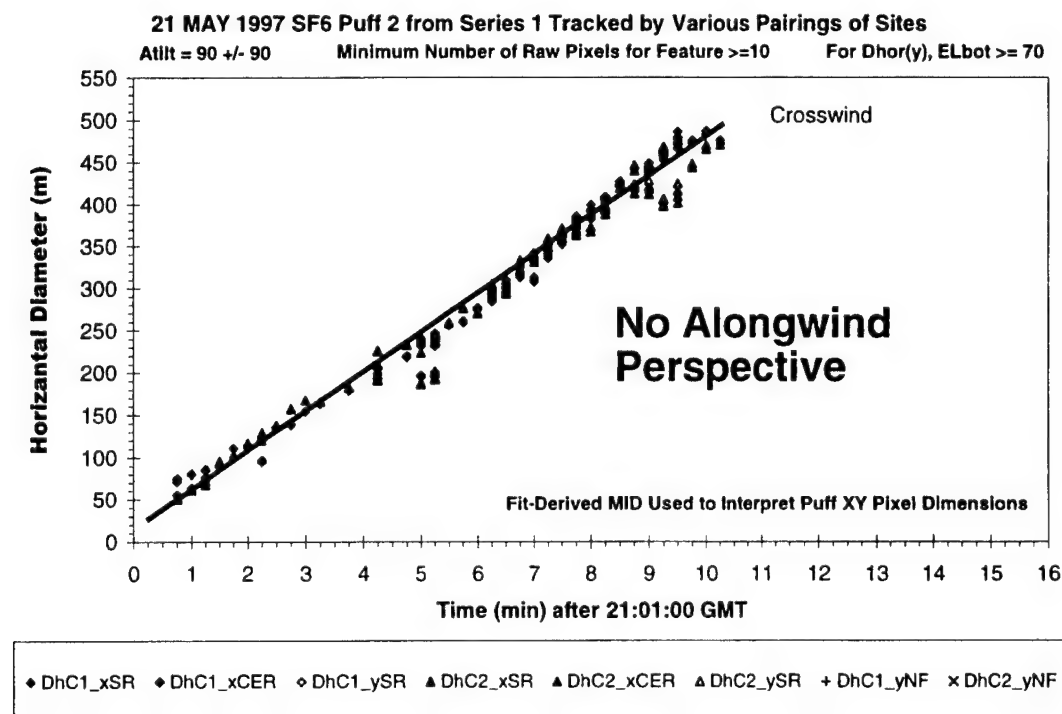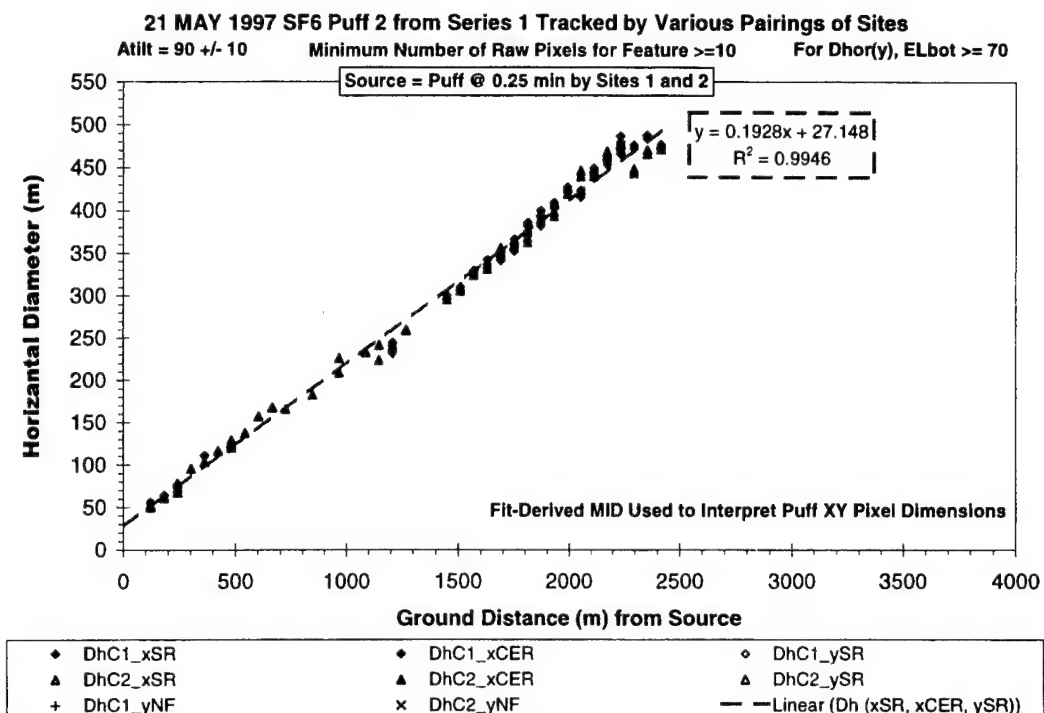
159
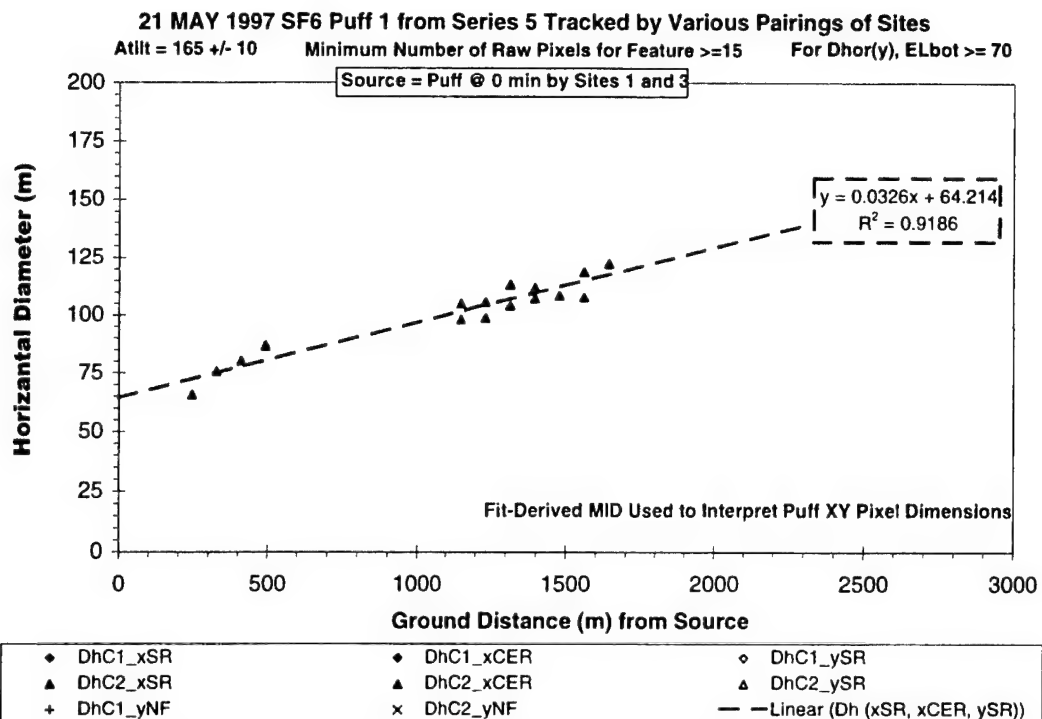
Figure H-35. Alongwind extent (Atilt=165±10) versus distance for S5P1 on 21 May 1997.
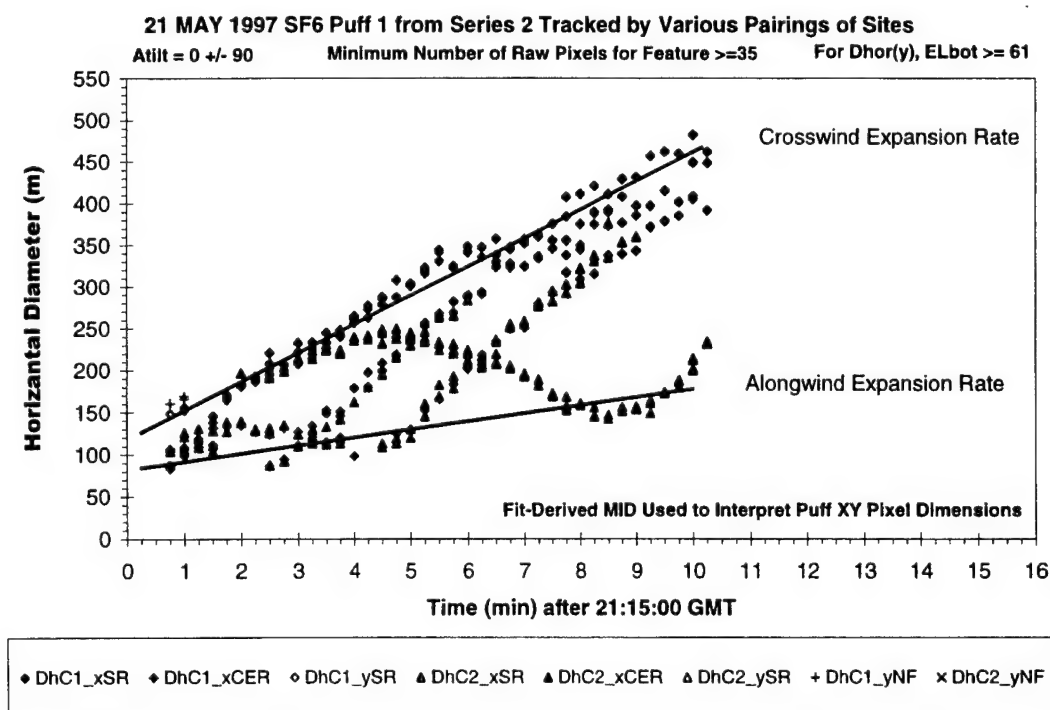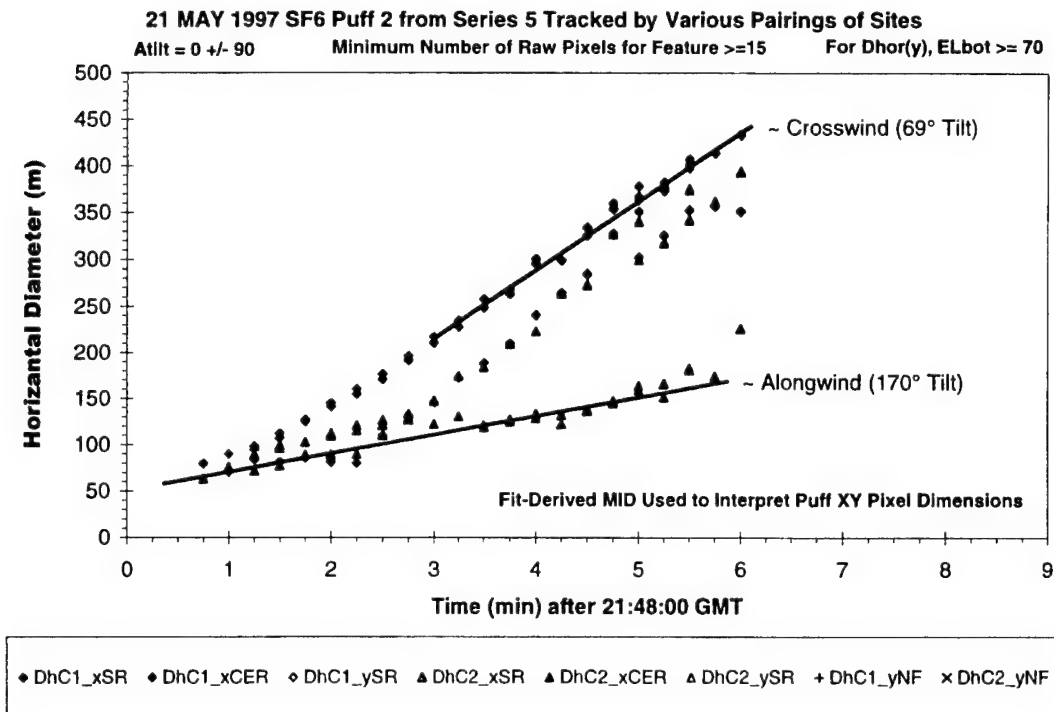

Figure H-36. Summary dimension plot showing all perspectives of S5P2 on 21 May 1997.
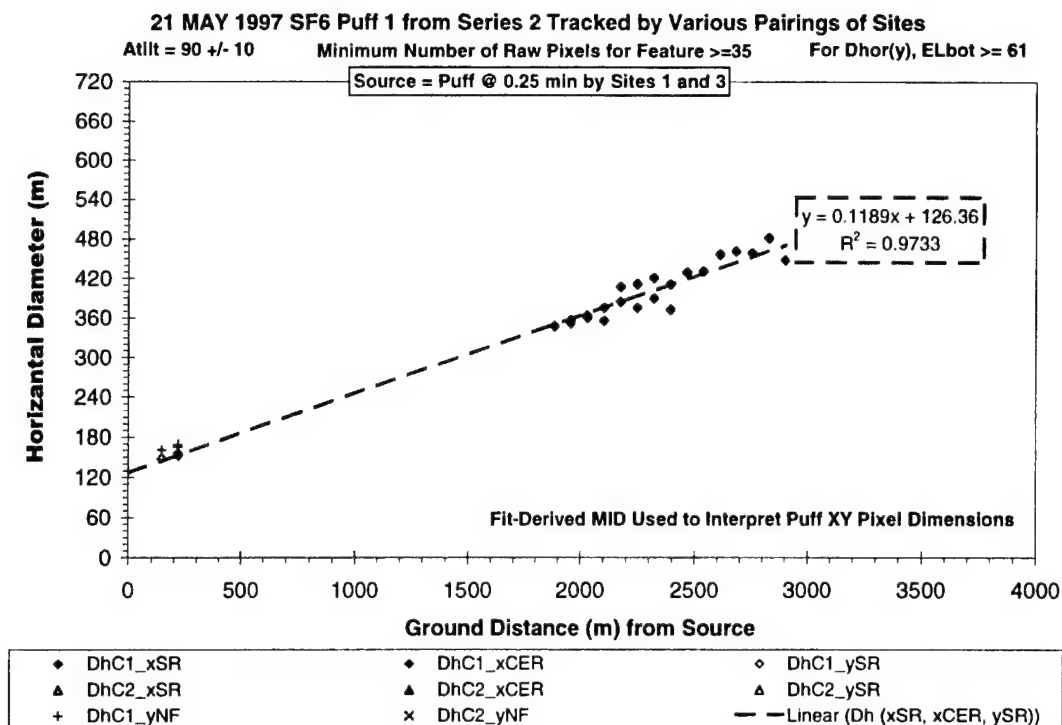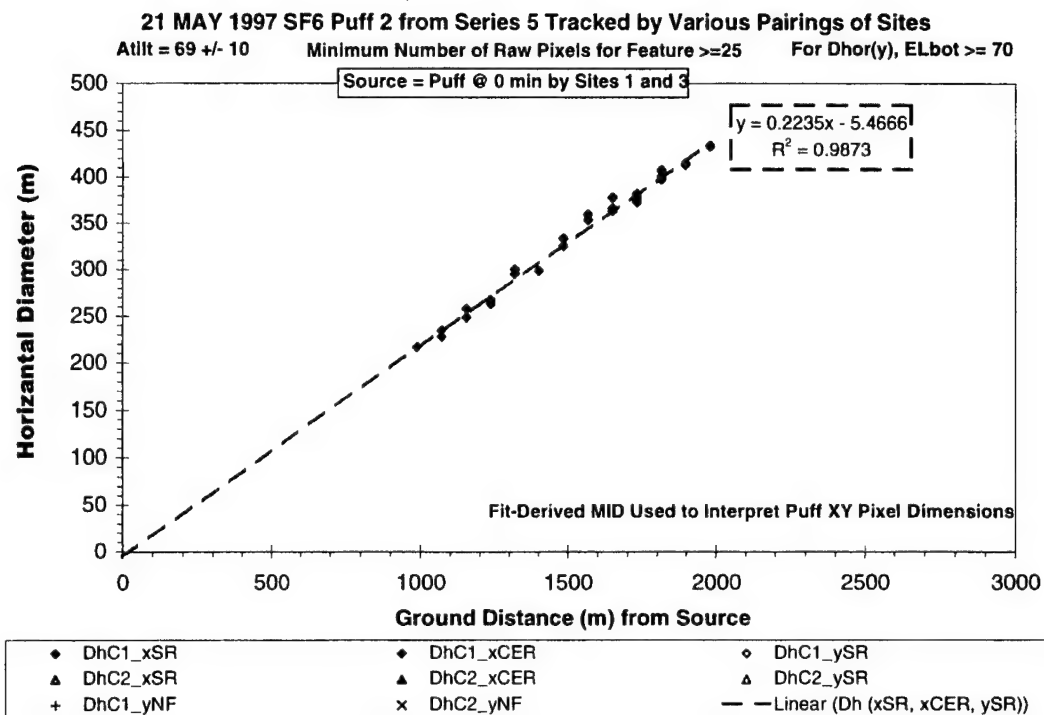
Figure H-37. Crosswind extent (Atilt = 69±10) versus distance for S5P2 on 21 May 1997.
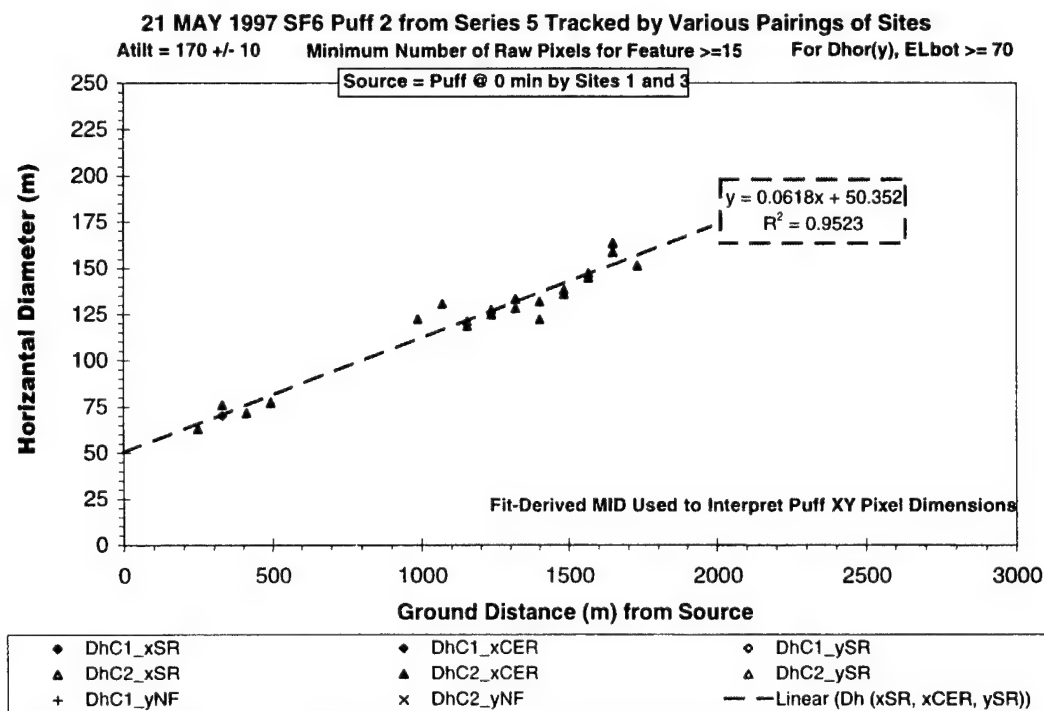
Figure H-38. Alongwind extent (Atilt=170±10) versus distance for S5P2 on 21 May 1997.

161

Figure H-39. Summary dimension plot showing all perspectives of S5P3 on 21 May 1997.
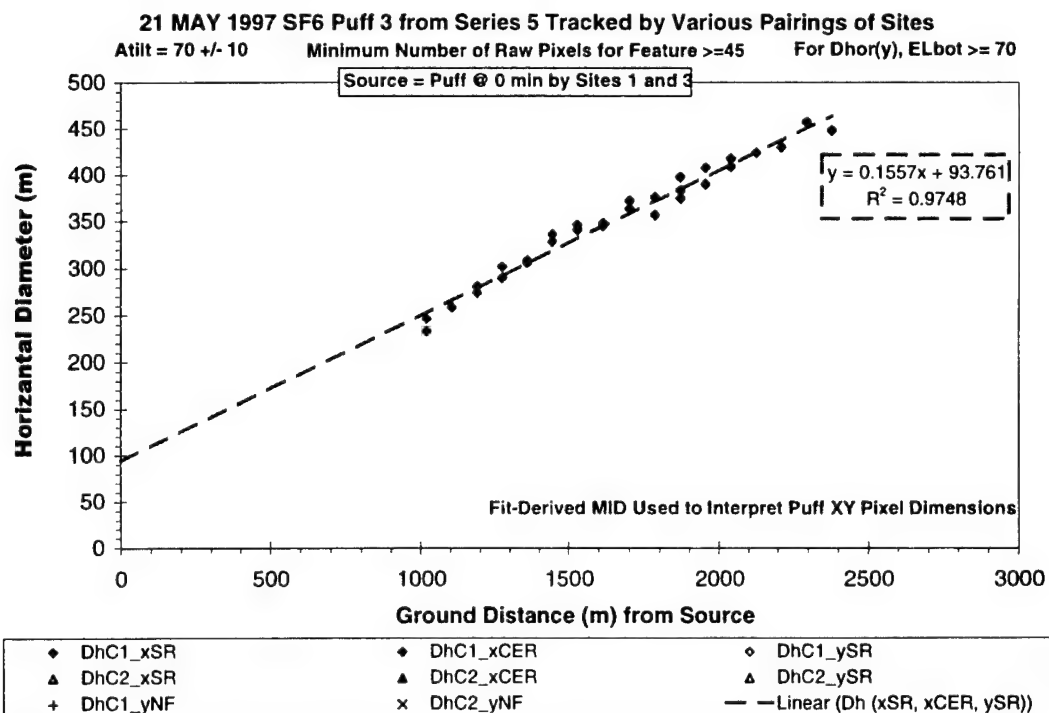
Figure H-40. Crosswind extent (Atilt=70±10) versus distance for S5P3 on 21 May 1997.

162
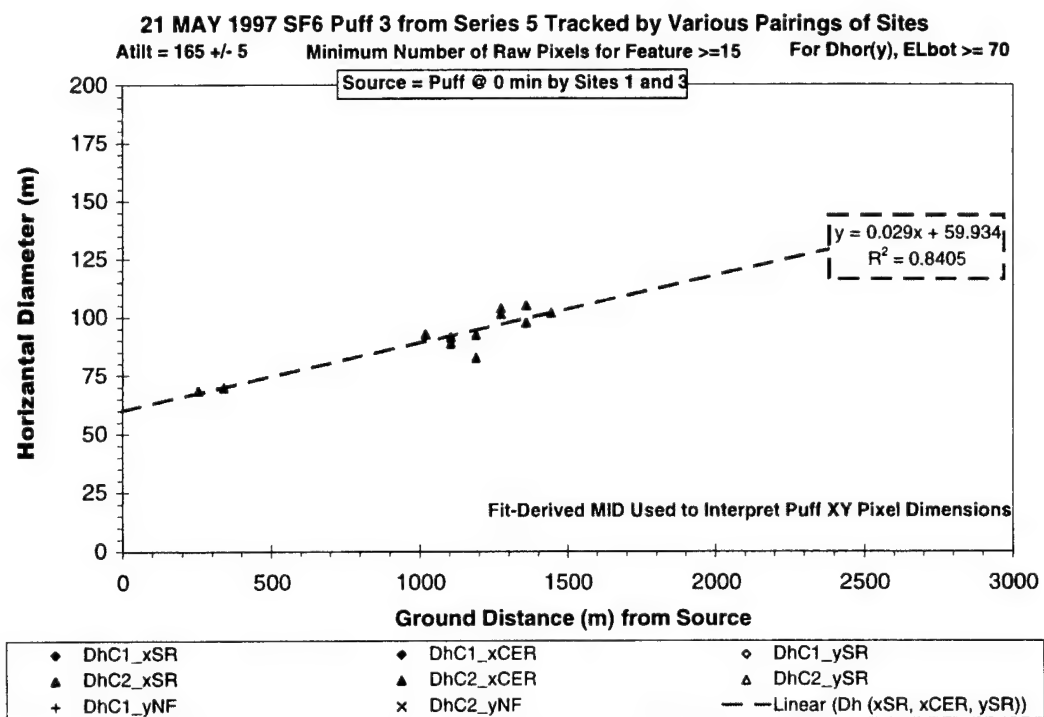
Figure H-41. Alongwind extent (Atilt=165±5) versus distance for S5P3 on 21 May 1997.

Appendix I-Imagery-Derived Expansion Rates for 23 May Puffs

"Best" Estimates of Puff Dimensions for 23 May 1997

The data plotted in this appendix are the "best" imagery-derived estimates of each puff's dimensions for the 23 May 1997 tracer releases. The first step of the analysis involved the use of PLMTRACK to measure the position of the puff's middle (MID). After combining all available data, the analysis generated the "best" formula for the puff's position as a function of time. This fit-derived position is more accurate than any one PLMTRACK triangulation since it is based upon all six pair-wise combinations of all imagery after filtering for only the best perspectives. This "best" fit formula allows the conversion of the puff's angular extent in any image to physical extent from that perspective. The angular extent is merely the proportion of FOV occupied by the puff. This "best" method minimizes any errors associated with the PLMTRACK-derived polygon (see Appendices A, E, F, and G). It also allows the direct processing of each image separately.

The plot headings document the experimental variables that served as filters for the data. The filtering not only improved accuracy but also specified perspective (i.e., dispersion axis). Appendix A illustrated the various angles and diameters associated with the analysis. Appendices E, F, and G provided examples (i.e., S1P1, S1P2 and S2P1, respectively) of the detailed analysis of the 21 May imagery. Those three cases illustrated significant differences in the dispersion characteristics for puffs separated by relatively small distances or times. Appendix C documented that the expansion rates measured by the "best" method are insensitive to the resolution, slant range, elevation, and background radiance over their operational ranges. Appendix D documented marginal contrast for series B, F, and G on 23 May. Appendix D also documented that the observed extent contained the bulk of the tracer gas.

Puff Dimensions and Expansion Rates for 23 May 1997 Tracer Releases

This appendix presents the imagery-derived dimension and expansion rate data for the 23 May 1997 tracer puffs. Each puff's diameter is plotted against time after release and distance from the source. The slopes of these plots are the expansion rates in m/min and m/m, respectively. As discussed in the body of the report, a tilt angle of $0°$ (or $180°$) corresponds to alongwind dispersion, while a tilt angle of $90°$ corresponds to crosswind dispersion. The along- and crosswind expansion rates were included in Table 5, Table 6, and in several figures in the body of this report.

This appendix also includes expansion rate plots for other tilt axes referred to as follows:

- alongwind $0°$ or $180°$ Tilt (dimension aligned with puff's bearing)
- along-diagonal   dimension is between alongwind and a diagonal
- – diagonal $45°$ Tilt (left end of dimension, as seen from source, is closer to source and halfway between alongwind and crosswind)
- cross-diagonal   dimension is between crosswind and a diagonal

165

- crosswind   90° Tilt (dimension perpendicular to puff's bearing)
- + diagonal   135° Tilt (left end of dimension, as seen from source, is farther from source and halfway between alongwind and crosswind)

There are several plots for each puff. The first plot of each series is of the puff's diameter against time after its' release. The data in this summary plot include all perspectives (i.e., all tilt angles). This plot also includes the linear regressive trend lines for selected axes (i.e., perspectives). The slopes of these lines would be the expansion rates in m/min. These lines provide the analyst with a frame of reference for comparing the combined data (i.e., summary plot) to the filtered data. Subsequent plots include only the filtered data associated with each trend line (i.e., a specific axis). The headings for each figure document that the plotted data have been filtered to provide better accuracy and a specific perspective. Since the "best" method does not rely directly on pair-wise analysis, these plots document results from every image that saw the puff's extent from the specified perspective (Atilt ± Window). The diameter along the specified axis is plotted against distance from the source (i.e., initial imagery-derived position of the puff). The formula for the linear regressive fit reveals the expansion rate (i.e., slope in m/m) for the specified perspective (Atilt ± Window).

These data document that the puffs' diameters did not always fall between extremes defined by the along- and crosswind perspectives. This should be the case if the puff's major or minor dispersion axes align with the wind bearing. Instead, the data document that the maximum dispersion occasionally occurred along a diagonal axis (i.e., neither along- nor crosswind). The correlation coefficients document that the expansion rate data are nicely fit by linear regression.

There were several factors that complicated these experiments. As mentioned in the body of this report and in Appendix D, the sky was cloudy on 23 May 1997. Coastal fog and range restrictions further complicated the release geometry. The complicated backgrounds resulted in reduced signal-to-noise ratio. The combination of poor contrast and releases near the third camera site resulted in more-limited viewing perspectives on 23 May than on 21 May 1997. In addition, the puffs on the 23rd were twice as long (i.e., 10-s releases) as the puffs on the 21st (i.e., 5-s releases).

The intent of longer tracer releases was to compensate for the reduced contrast. The imagery documented that the airship was not always heading into the wind during the release. Hence, the release did not always align the long axis of the puff with the wind bearing. This initial tilt of the puff may have complicated the expansion rate measurements since one axis was initially much longer than the other. As illustrated by the plots within this appendix, the initial puff dimensions could differ by a factor of 2 along the various tilt axes. To compensate for the short track that spanned only two imagery sites, the tilt window was opened to obtain enough data to reveal a trend. The combination of poor contrast, poor perspective, and longer puffs reduced the quality (i.e., increased the scatter) of the data for 23 May 1997. In spite of these complications, the 23 May 1997 imagery-derived expansion rates spanned a similar range of values to the expansion rates measured on 21 May 1997.

Differences Between the 21 May and the 23 May 1997 Tracer Releases

There were several differences in the results for 23 May and 21 May 1997. Table 4 in the body of this report documented that all but one puff had a greater crosswind than alongwind expansion rate on 21 May 1997. In contrast, the results in this appendix document that the orientation of the maxi-

mum expansion rate seemed almost randomized on 23 May 1997. Although the range of values was comparable on 23 May (0.00 to 0.16 m/m) and on 21 May (0.02 to 0.22 m/m), the expansion rates were typically lower on 23 May than on 21 May 1997.

The 23 May releases occurred under cloud cover, while the 21 May releases were under clear sky. Both releases occurred over rough terrain. However, one might expect a more complicated windfield for the 21 May releases. On a sunny day above Santa Ynez ridge, an inland sea breeze and hillside thermals would have contributed to the prevailing wind flow patterns. The sea breeze and the hillside thermals are both driven by solar heating of the land. The sea breeze would head east from the ocean up Lompoc valley. The hillside thermals would head south and southeast up the hills from Lompoc valley. It is likely that wind shear may account for the large crosswind dispersion rates observed on 21 May 1997. For the 23 May releases, both the sea breeze and the hillside thermals would head up hill (east) from the coast. However, the heavy cloud cover would have minimized these solar-driven winds. The release location combined with cloud cover might have produced less turbulence for the 23 May releases.
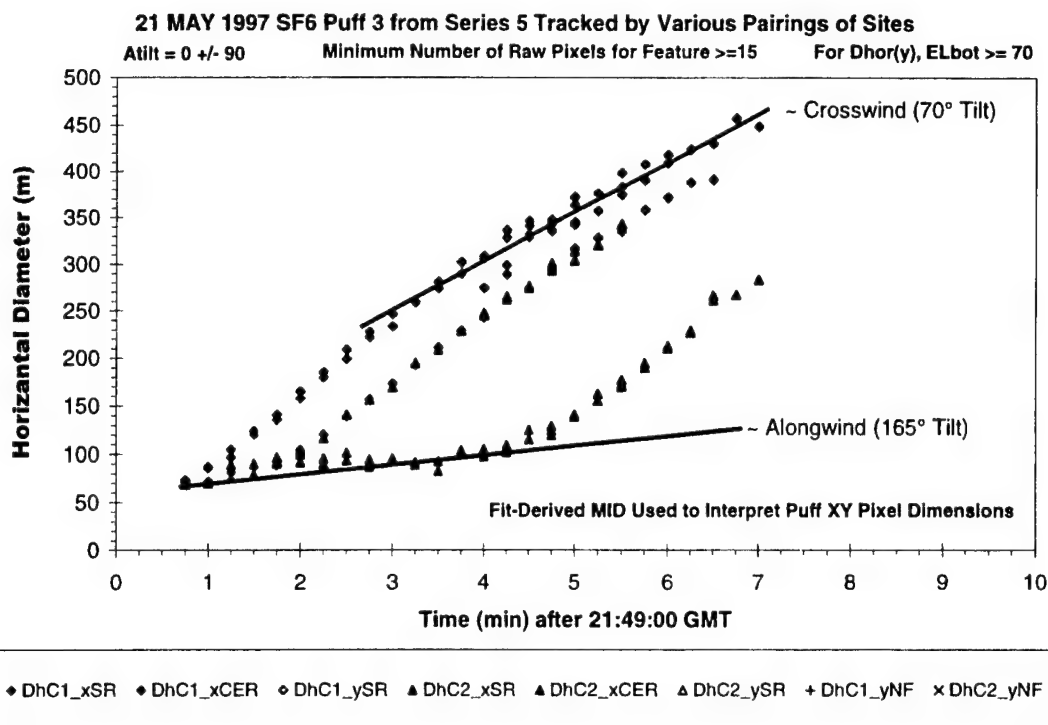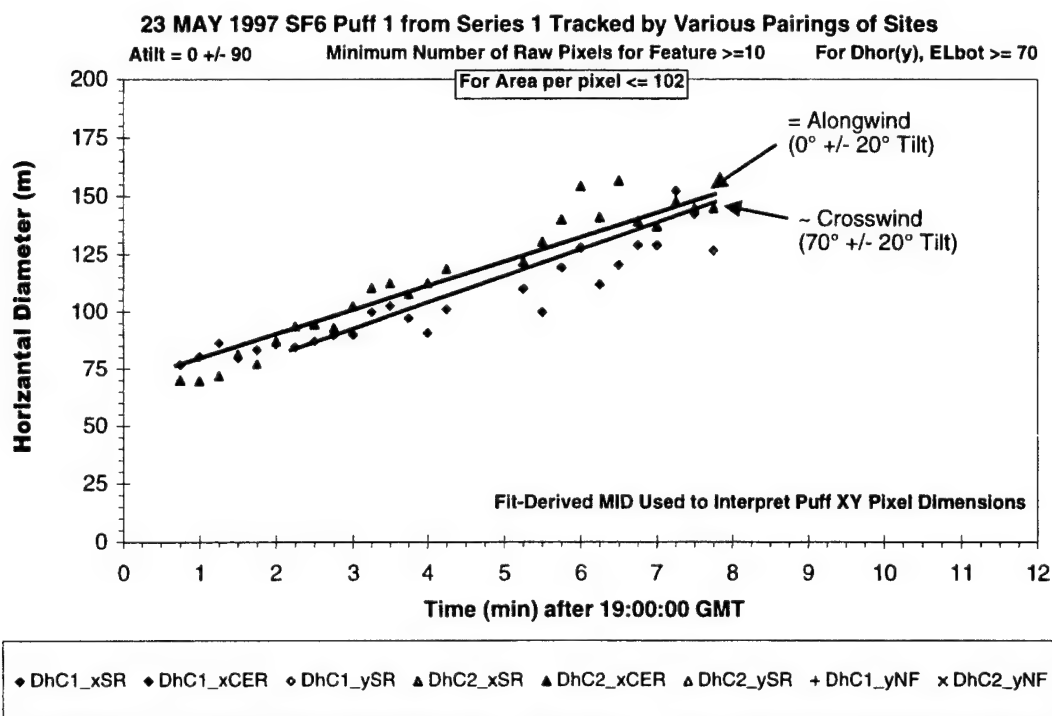

Figure I-1. Summary dimension plot showing all perspectives of S1P1 (23 May 1997).
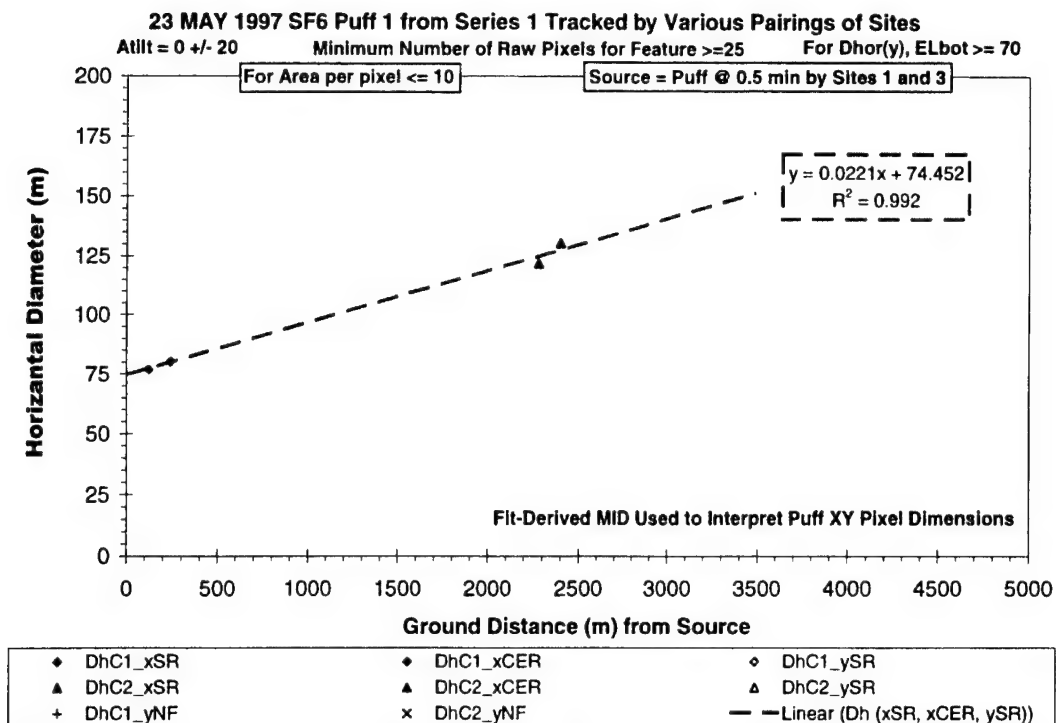
Figure I-2. Alongwind extent (Atilt = 0±20) versus distance for S1P1 (23 May 1997).
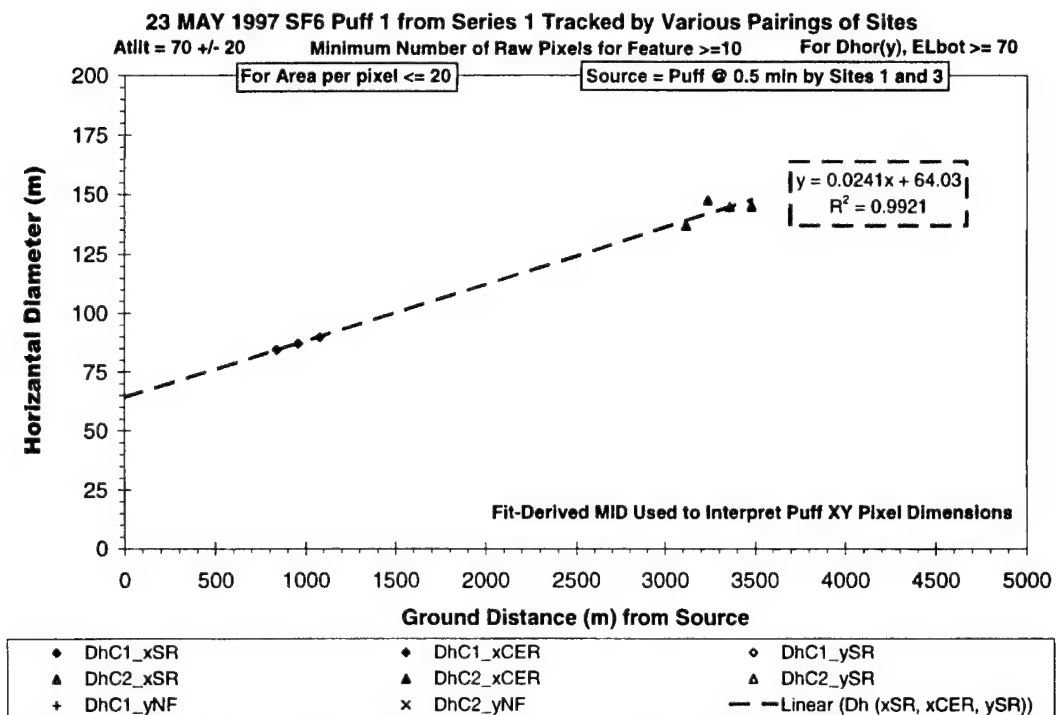
Figure I-3. Crosswind extent (Atilt = 70±20) versus distance for S1P1 (23 May 1997).

168
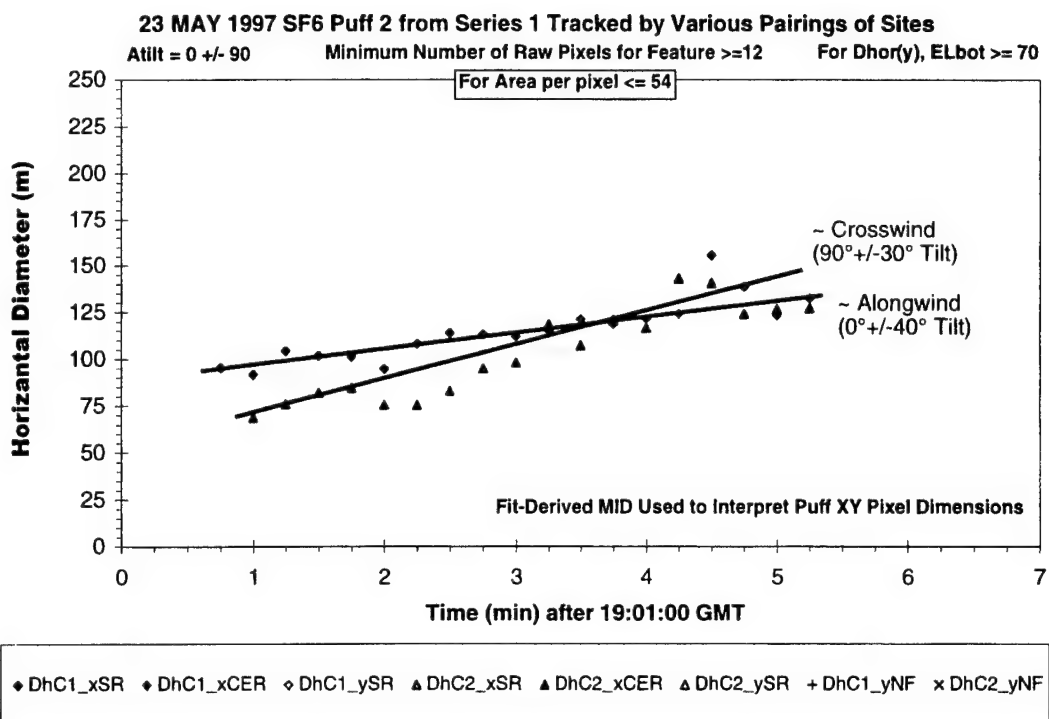
Figure I-4. Summary dimension plot showing all perspectives of S1P2 (23 May 1997).
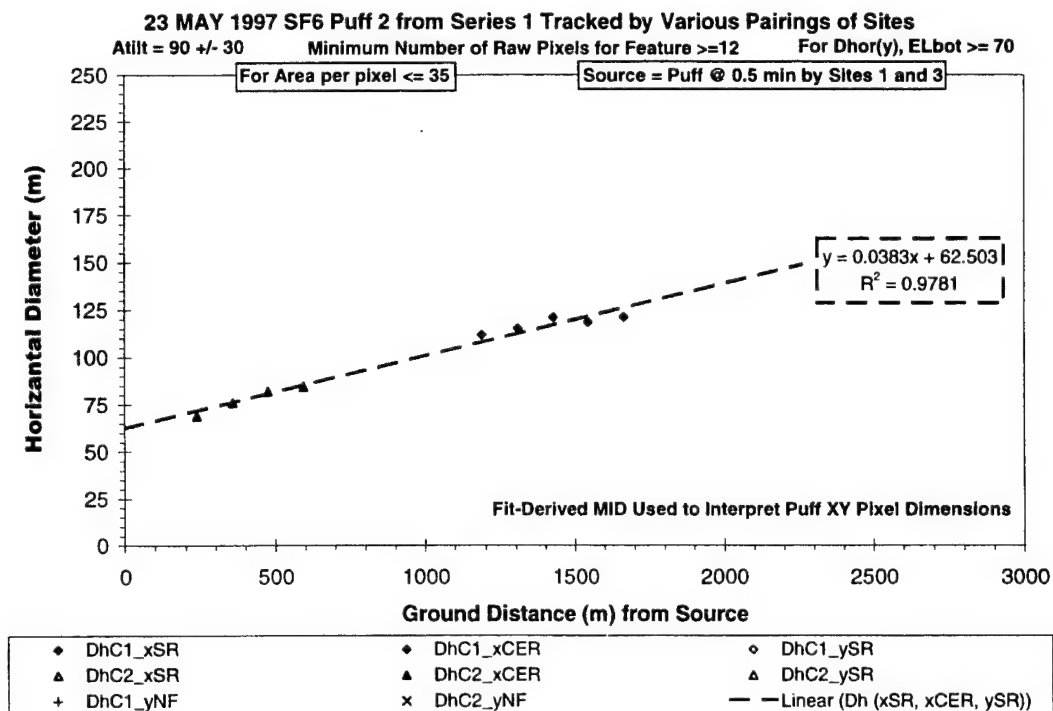
Figure I-5. Crosswind extent (Atilt = 90±30) versus distance for S1P2 (23 May 1997).

169
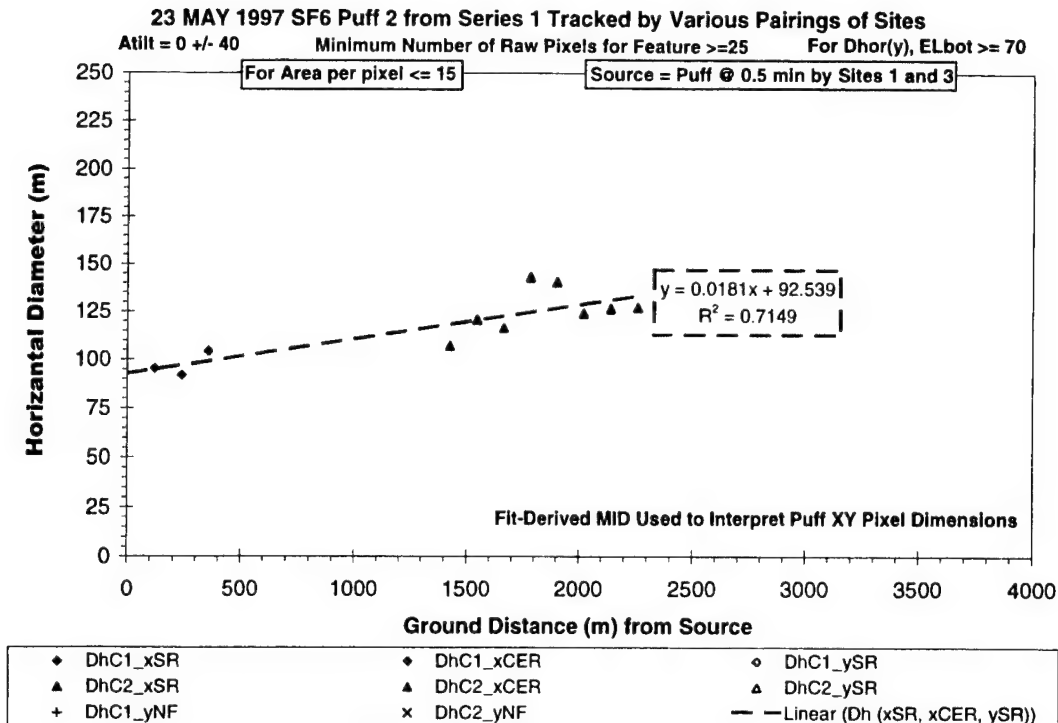
Figure I-6. Alongwind extent (Atilt = 0±40) versus distance for S1P2 (23 May 1997).
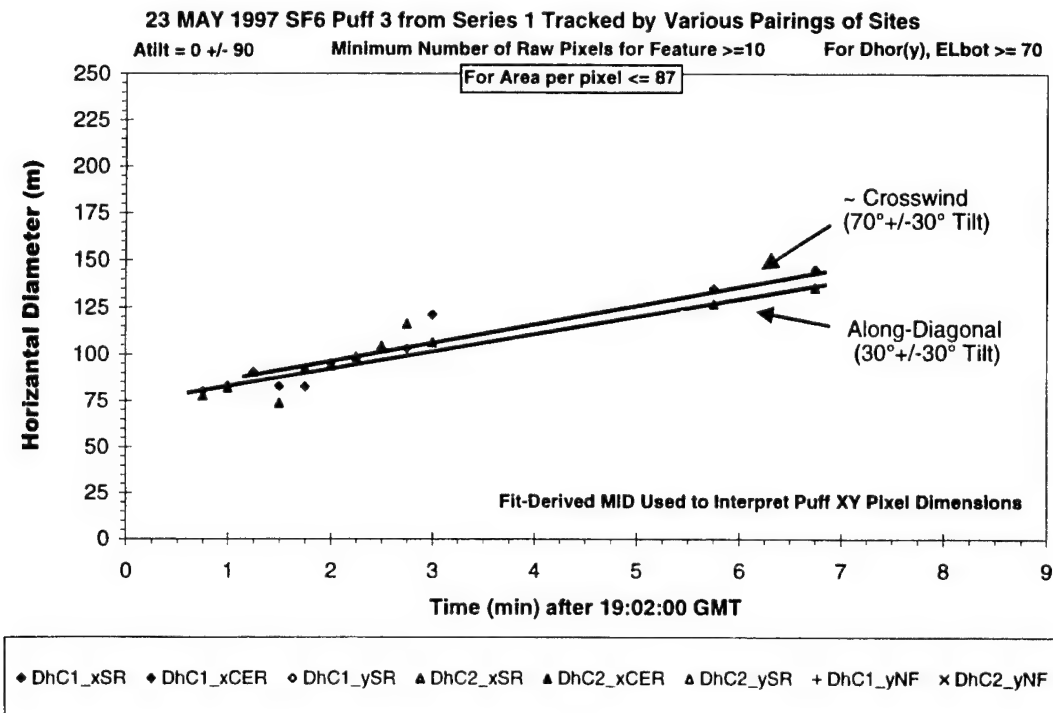
Figure I-7. Summary dimension plot showing all perspectives of S1P3 (23 May 1997).

23 MAY 1997 SF6 Puff 3 from Series 1 Tracked by Various Pairings of Sites

Atilt = 70 +/- 30   Minimum Number of Raw Pixels for Feature >=10   For Dhor(y), ELbot >= 70
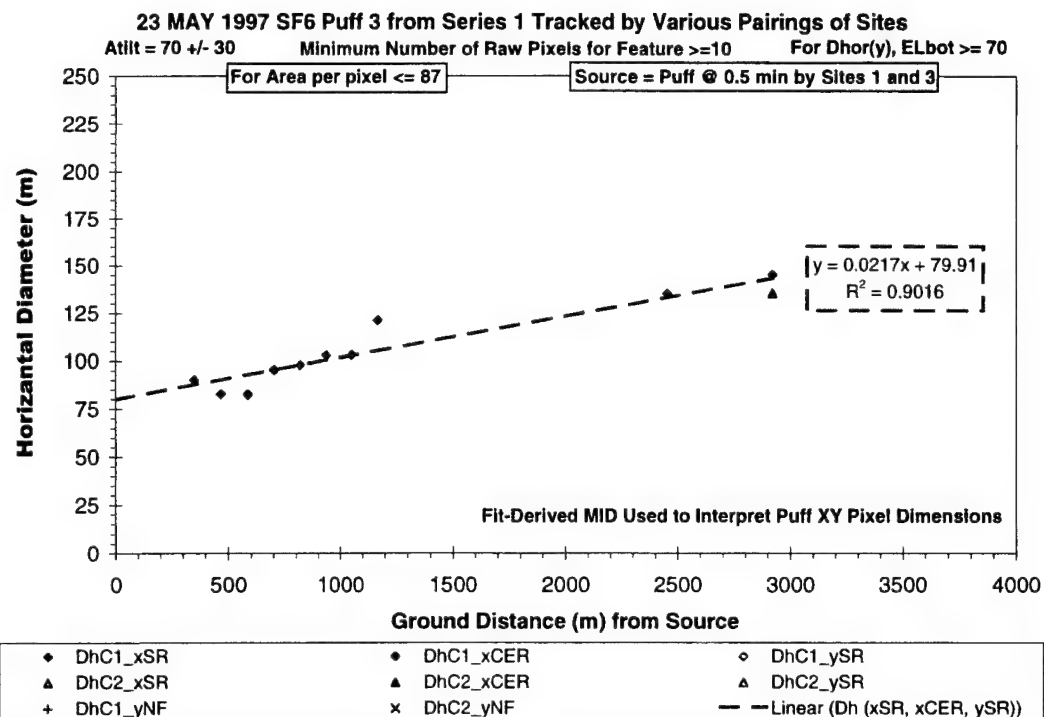
Figure I-8. Crosswind extent (Atilt = 70±30) versus distance for S1P3 (23 May 1997).

23 MAY 1997 SF6 Puff 3 from Series 1 Tracked by Various Pairings of Sites

Atilt = 30 +/- 30   Minimum Number of Raw Pixels for Feature >=15   For Dhor(y), ELbot >= 70
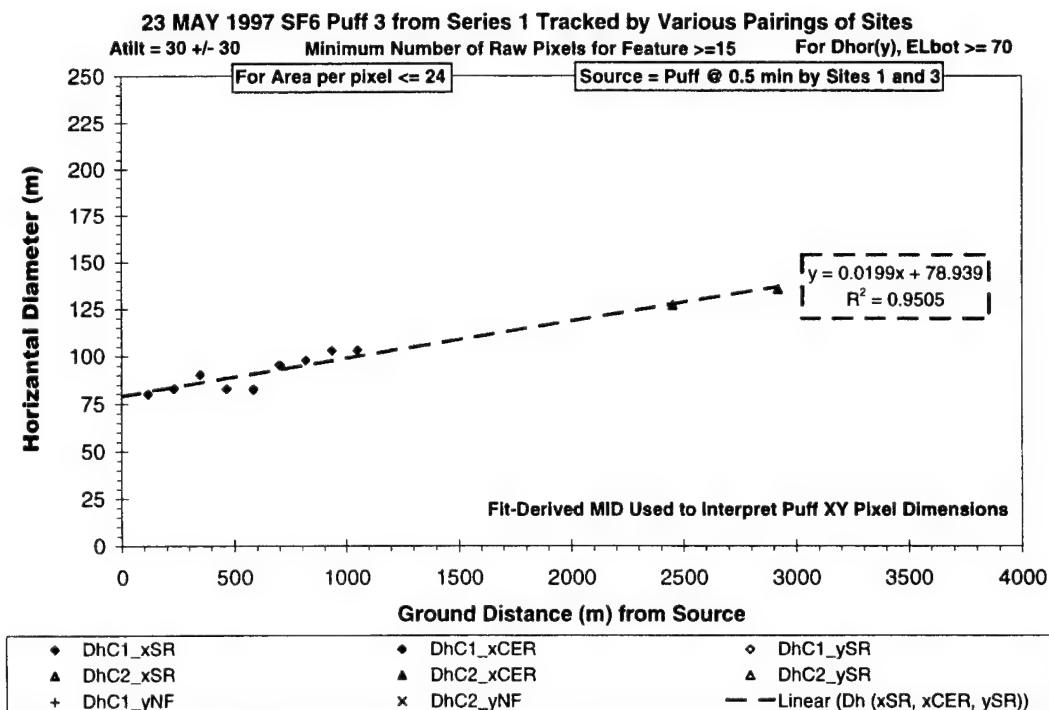
Figure I-9. Along-Diagonal extent (Atilt = 30±30) versus distance for S1P3 (23 May 1997).

171
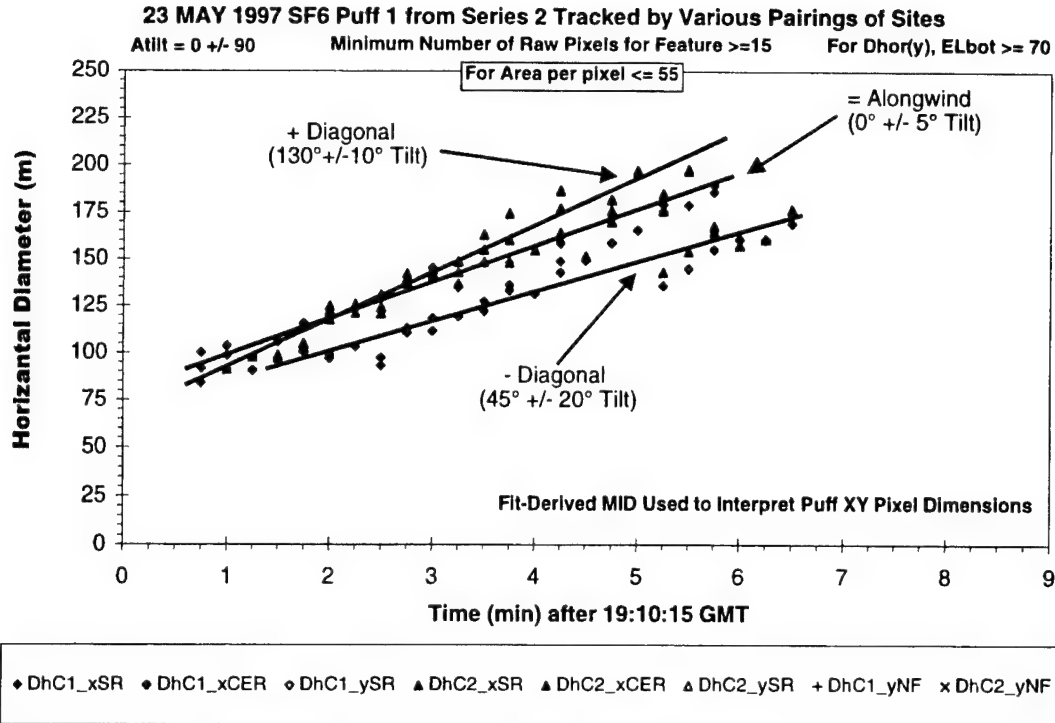
Figure I-10. Summary dimension plot showing all perspectives of S2P1 (23 May 1997).
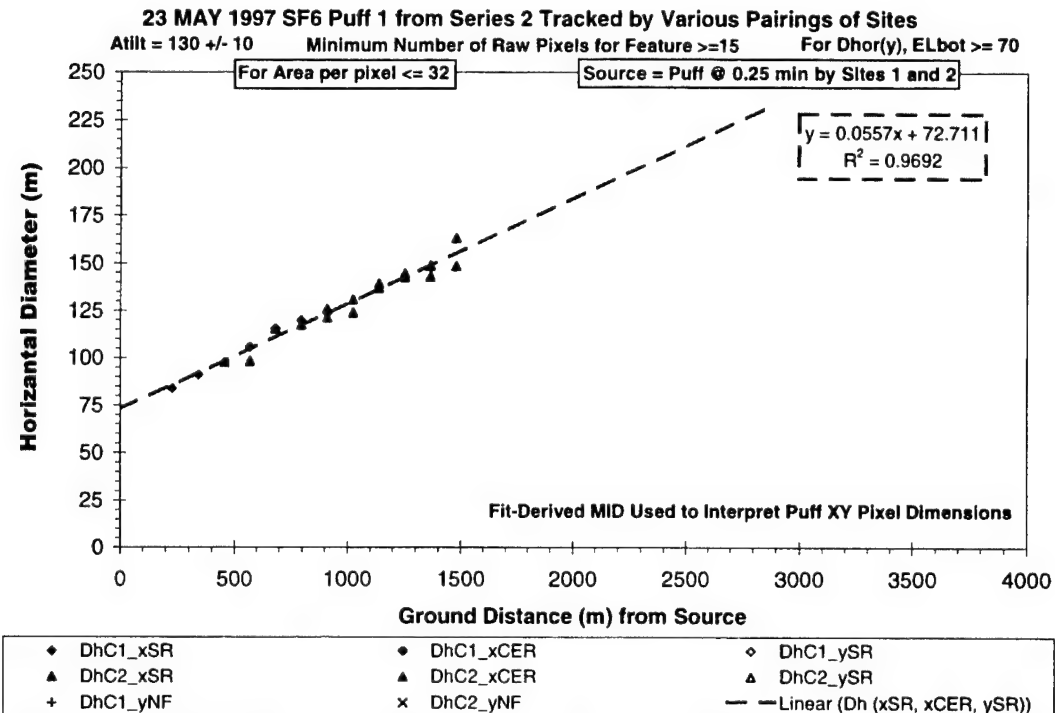
Figure I-11. + Diagonal extent (Atilt = 130±10) versus distance for S2P1 (23 May 1997).

Figure I-12. Alongwind extent (Atilt = 0±5) versus distance for S2P1 (23 May 1997).

Figure I-13. - Diagonal extent (Atilt = 45±20) versus distance for S2P1 (23 May 1997).

Figure I-14. Summary dimension plot showing all perspectives of S2P2 (23 May 1997).

Figure I-15. Alongwind extent (Atilt = 0±20) versus distance for S2P2 (23 May 1997).

23 MAY 1997 SF6 Puff 2 from Series 2 Tracked by Various Pairings of Sites

Atilt = 90 +/- 30   Minimum Number of Raw Pixels for Feature >=10   For Dhor(y), ELbot >= 70

For Area per pixel <= 55   Source = Puff @ 0.5 min by Sites 1 and 2

$y = 0.0292x + 76.149$
$R^2 = 0.923$

Fit-Derived MID Used to Interpret Puff XY Pixel Dimensions

♦ DhC1_xSR	● DhC1_xCER	◇ DhC1_ySR
▲ DhC2_xSR	▲ DhC2_xCER	△ DhC2_ySR
+ DhC1_yNF	× DhC2_yNF	— —Linear (Dh (xSR, xCER, ySR))

Figure I-16. Crosswind extent (Atilt = 90±30) versus distance for S2P2 (23 May 1997).

23 MAY 1997 SF6 Puff 3 from Series 2 Tracked by Various Pairings of Sites

Atilt = 0 +/- 90   Minimum Number of Raw Pixels for Feature >=20   For Dhor(y), ELbot >= 70

For Area per pixel <= 42

Along-Diagonal
(30° +/- 30° Tilt)

Cross-Diagonal
(60° +/- 15° Tilt)

Fit-Derived MID Used to Interpret Puff XY Pixel Dimensions

♦ DhC1_xSR ♦ DhC1_xCER ◇ DhC1_ySR ▲ DhC2_xSR ▲ DhC2_xCER △ DhC2_ySR + DhC1_yNF × DhC2_yNF

Figure I-17. Summary dimension plot showing all perspectives of S2P3 (23 May 1997).

Figure I-18. Along-Diagonal extent (Atilt = 30±30) versus distance for S2P3 (23 May 1997).
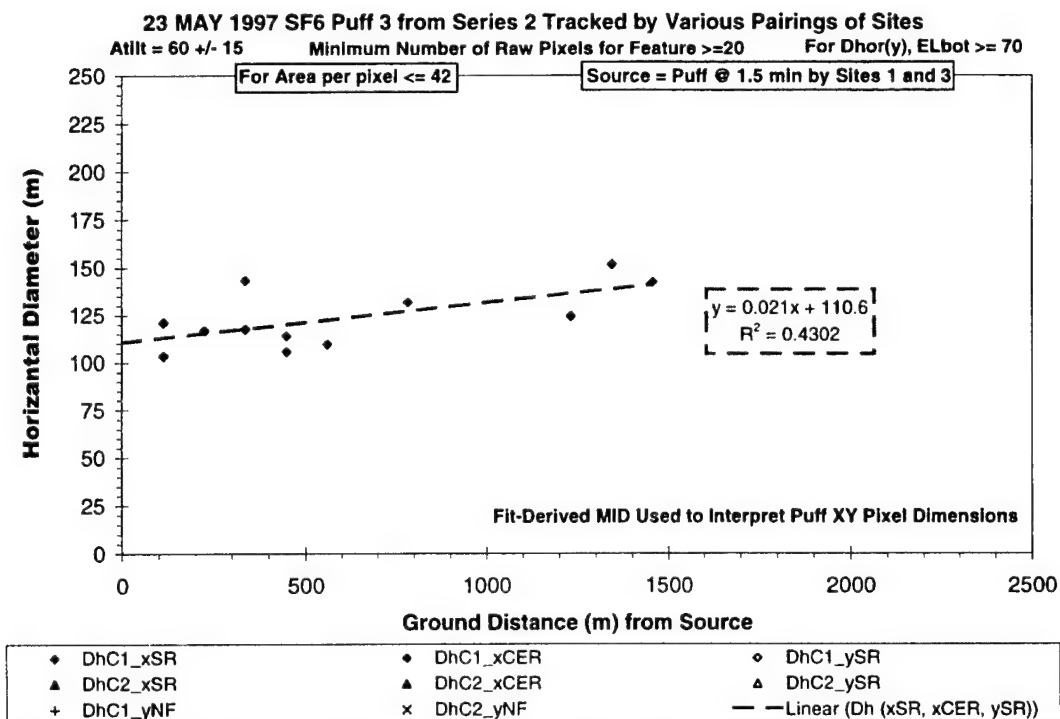
Figure I-19. Cross-Diagonal extent (Atilt = 60±15) versus distance for S2P3 (23 May 1997).

176

Figure I-20. Summary dimension plot showing all perspectives of S3P1 (23 May 1997).

Figure I-21. + Diagonal extent (Atilt = 130±30) versus distance for S3P1 (23 May 1997).

Figure I-22. - Diagonal extent (Atilt = 40±10) versus distance for S3P1 (23 May 1997).
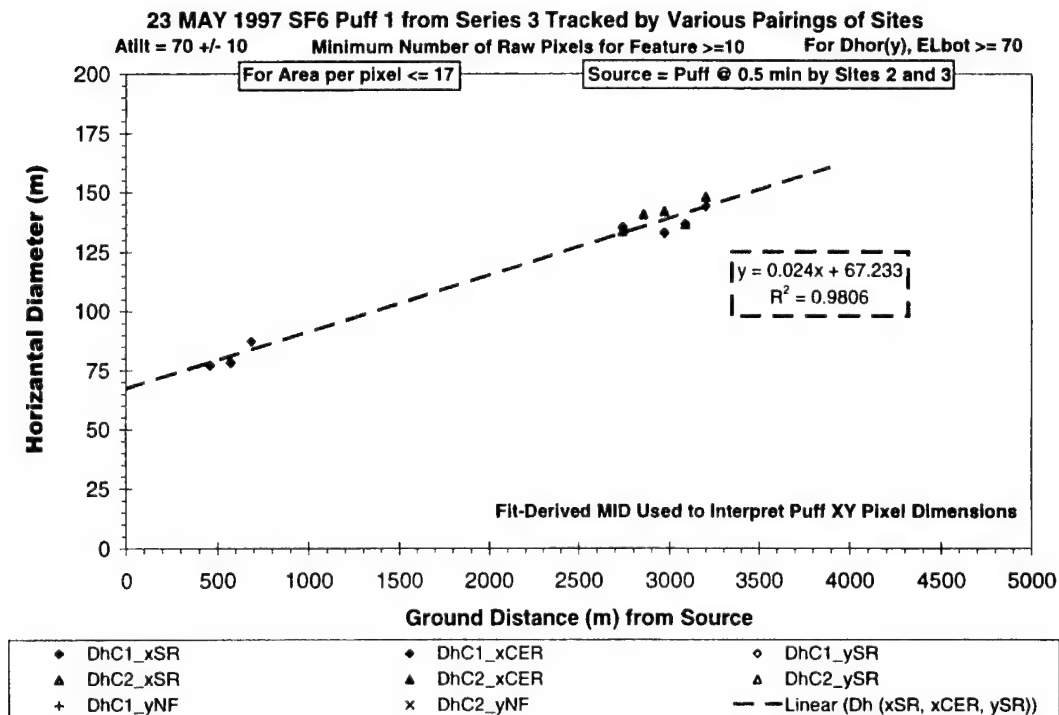
Figure I-23. Crosswind extent (Atilt = 70±10) versus distance for S3P1 (23 May 1997).
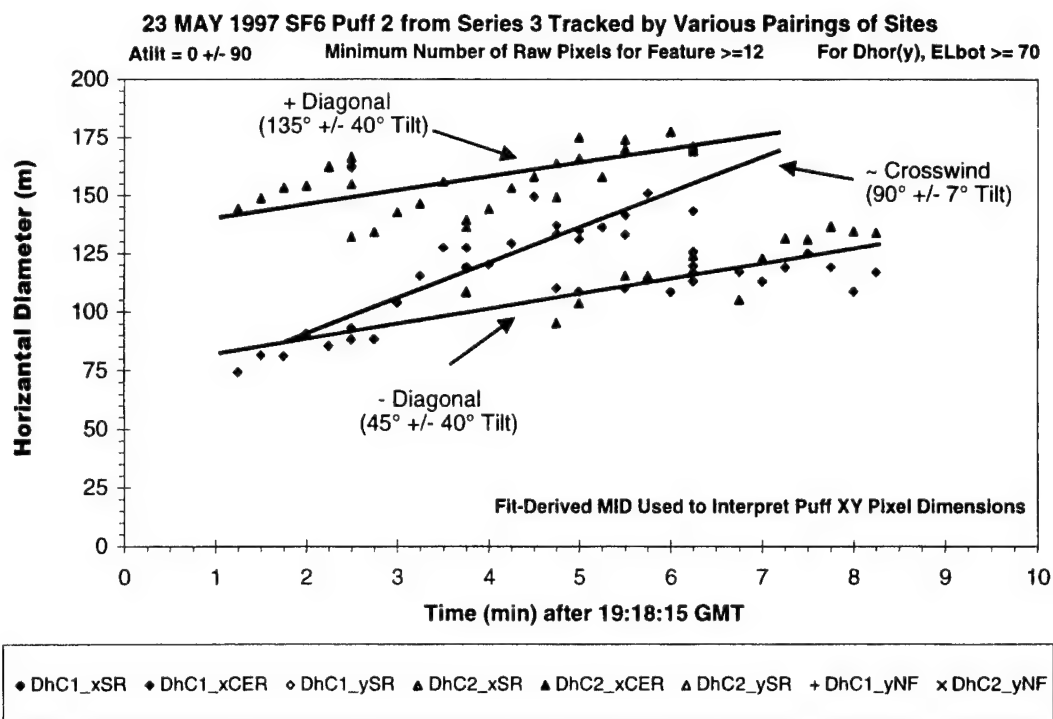
Figure I-24. Summary dimension plot showing all perspectives of S3P2 (23 May 1997).
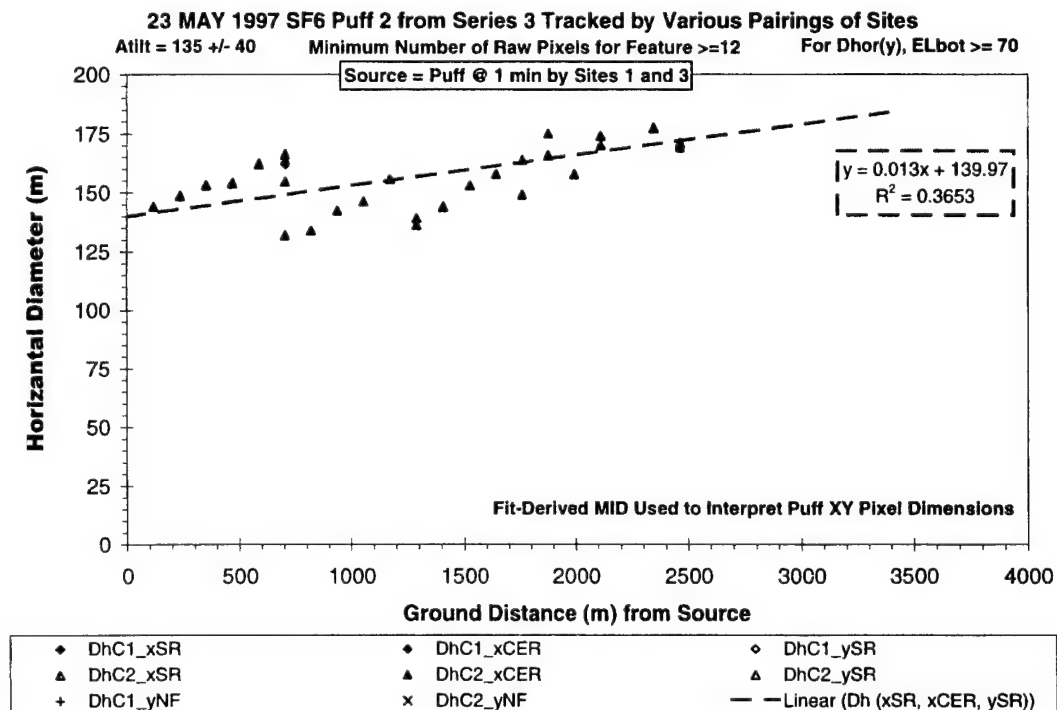
Figure I-25. + Diagonal extent (Atilt = 135±40) versus distance for S3P2 (23 May 1997).

23 MAY 1997 SF6 Puff 2 from Series 3 Tracked by Various Pairings of Sites

Atilt = 90 +/- 7   Minimum Number of Raw Pixels for Feature >=12   For Dhor(y), ELbot >= 70

Source = Puff @ 1 min by Sites 1 and 3

$y = 0.0327x + 74.8$
$R^2 = 0.826$

Fit-Derived MID Used to Interpret Puff XY Pixel Dimensions

Horizantal Diameter (m)

Ground Distance (m) from Source

♦ DhC1_xSR	♦ DhC1_xCER	◊ DhC1_ySR
▲ DhC2_xSR	▲ DhC2_xCER	△ DhC2_ySR
+ DhC1_yNF	✕ DhC2_yNF	— —Linear (Dh (xSR, xCER, ySR))

Figure I-26. Crosswind extent (Atilt = 90±7) versus distance for S3P2 (23 May 1997).

23 MAY 1997 SF6 Puff 2 from Series 3 Tracked by Various Pairings of Sites

Atilt = 45 +/- 40   Minimum Number of Raw Pixels for Feature >=12   For Dhor(y), ELbot >= 70

Source = Puff @ 1 min by Sites 1 and 3

$y = 0.0139x + 81.593$
$R^2 = 0.7646$

Fit-Derived MID Used to Interpret Puff XY Pixel Dimensions

Horizantal Diameter (m)

Ground Distance (m) from Source

♦ DhC1_xSR	♦ DhC1_xCER	◊ DhC1_ySR
▲ DhC2_xSR	▲ DhC2_xCER	△ DhC2_ySR
+ DhC1_yNF	✕ DhC2_yNF	— —Linear (Dh (xSR, xCER, ySR))

Figure I-27. - Diagonal extent (Atilt = 45±40) versus distance for S3P2 (23 May 1997).

180

23 MAY 1997 SF6 Puff 3 from Series 3 Tracked by Various Pairings of Sites

Atilt = 0 +/- 90   Minimum Number of Raw Pixels for Feature >=10   For Dhor(y), ELbot >= 70

For Area per pixel <= 91

= Crosswind
(90° +/- 10° Tilt)

Cross-Diagonal
(110° +/- 10° Tilt)

Fit-Derived MID Used to Interpret Puff XY Pixel Dimensions

Horizantal Diameter (m)

Time (min) after 19:19:15 GMT

♦ DhC1_xSR   ♦ DhC1_xCER   ◇ DhC1_ySR   ▲ DhC2_xSR   ▲ DhC2_xCER   △ DhC2_ySR   + DhC1_yNF   × DhC2_yNF

Figure I-28. Summary dimension plot showing all perspectives of S3P3 (23 May 1997).

23 MAY 1997 SF6 Puff 3 from Series 3 Tracked by Various Pairings of Sites

Atilt = 90 +/- 10   Minimum Number of Raw Pixels for Feature >=12   For Dhor(y), ELbot >= 70

For Area per pixel <= 91   Source = Puff @ 0 min by Sites 1 and 4

$y = 0.0467x + 32.457$
$R^2 = 0.9754$

Fit-Derived MID Used to Interpret Puff XY Pixel Dimensions

Horizantal Diameter (m)

Ground Distance (m) from Source

♦	DhC1_xSR	♦	DhC1_xCER	◇	DhC1_ySR
▲	DhC2_xSR	▲	DhC2_xCER	△	DhC2_ySR
+	DhC1_yNF	×	DhC2_yNF	— —	Linear (Dh (xSR, xCER, ySR))

Figure I-29. Crosswind extent (Atilt = 90±10) versus distance for S3P3 (23 May 1997).

23 MAY 1997 SF6 Puff 3 from Series 3 Tracked by Various Pairings of Sites

Atilt = 110 +/- 10   Minimum Number of Raw Pixels for Feature >=10   For Dhor(y), ELbot >= 70

For Area per pixel <= 50   Source = Puff @ 0 min by Sites 1 and 4

y = 0.0456x + 4.3979
R² = 0.9121

Fit-Derived MID Used to Interpret Puff XY Pixel Dimensions

♦ DhC1_xSR	● DhC1_xCER	○ DhC1_ySR
▲ DhC2_xSR	▲ DhC2_xCER	△ DhC2_ySR
+ DhC1_yNF	× DhC2_yNF	— Linear (Dh (xSR, xCER, ySR))

Figure I-30. Cross-Diagonal extent (Atilt= 110±10) versus distance for S3P3 (23 May 1997).

23 MAY 1997 SF6 Puff 1 from Series 7 Tracked by Various Pairings of Sites

Atilt = 0 +/- 90   Minimum Number of Raw Pixels for Feature >=15   For Dhor(y), ELbot >= 70

~ Alongwind (10° +/- 10° Tilt)

~ Crosswind (110° +/- 10° Tilt)

Fit-Derived MID Used to Interpret Puff XY Pixel Dimensions

♦ DhC1_xSR ♦ DhC1_xCER ◊ DhC1_ySR ▲ DhC2_xSR ▲ DhC2_xCER △ DhC2_ySR + DhC1_yNF × DhC2_yNF

Figure I-31. Summary dimension plot showing all perspectives of S7P1 (23 May 1997).

182

23 MAY 1997 SF6 Puff 1 from Series 7 Tracked by Various Pairings of Sites

Atilt = 10 +/- 10   Minimum Number of Raw Pixels for Feature >=15   For Dhor(y), ELbot >= 70

Source = Puff @ 0.25 min by Sites 1 and 3

$y = 0.0586x + 84.2$
$R^2 = 0.9753$

Fit-Derived MID Used to Interpret Puff XY Pixel Dimensions

Horizantal Diameter (m) vs **Ground Distance (m) from Source**

◆ DhC1_xSR	◆ DhC1_xCER	◇ DhC1_ySR
▲ DhC2_xSR	▲ DhC2_xCER	△ DhC2_ySR
+ DhC1_yNF	× DhC2_yNF	— —Linear (Dh (xSR, xCER, ySR))

Figure I-32. Alongwind extent (Atilt = 10±10) versus distance for S7P1 (23 May 1997).

23 MAY 1997 SF6 Puff 1 from Series 7 Tracked by Various Pairings of Sites

Atilt = 110 +/- 10   Minimum Number of Raw Pixels for Feature >=15   For Dhor(y), ELbot >= 70

Source = Puff @ 0.25 min by Sites 1 and 3

$y = 0.0181x + 97.987$
$R^2 = 0.7206$

Fit-Derived MID Used to Interpret Puff XY Pixel Dimensions

Horizantal Diameter (m) vs **Ground Distance (m) from Source**

◆ DhC1_xSR	◆ DhC1_xCER	◇ DhC1_ySR
▲ DhC2_xSR	▲ DhC2_xCER	△ DhC2_ySR
+ DhC1_yNF	× DhC2_yNF	— —Linear (Dh (xSR, xCER, ySR))

Figure I-33. Crosswind extent (Atilt= 110±10) versus distance for S7P1 (23 May 1997).

183

23 MAY 1997 SF6 Puff 2 from Series 7 Tracked by Various Pairings of Sites

Atilt = 0 +/- 90   Minimum Number of Raw Pixels for Feature >=10   For Dhor(y), ELbot >= 70

~ Alongwind
(10° +/- 10° Tilt)

Cross-Diagonal
(120° +/- 10° Tilt)

Fit-Derived MID Used to Interpret Puff XY Pixel Dimensions

Horizantal Diameter (m)

Time (min) after 20:11:45 GMT

◆ DhC1_xSR   ◆ DhC1_xCER   ◇ DhC1_ySR   ▲ DhC2_xSR   ▲ DhC2_xCER   △ DhC2_ySR   + DhC1_yNF   × DhC2_yNF

Figure I-34. Summary dimension plot showing all perspectives of S7P2 (23 May 1997).

23 MAY 1997 SF6 Puff 2 from Series 7 Tracked by Various Pairings of Sites

Atilt = 10 +/- 10   Minimum Number of Raw Pixels for Feature >=10   For Dhor(y), ELbot >= 70

Source = Puff @ 0.25 min by Sites 1 and 3

$y = 0.0478x + 67.417$
$R^2 = 0.9007$

Fit-Derived MID Used to Interpret Puff XY Pixel Dimensions

Horizantal Diameter (m)

Ground Distance (m) from Source

◆	DhC1_xSR	●	DhC1_xCER	◇	DhC1_ySR
▲	DhC2_xSR	▲	DhC2_xCER	△	DhC2_ySR
+	DhC1_yNF	×	DhC2_yNF	— —Linear (Dh (xSR, xCER, ySR))	

Figure I-35. Alongwind extent (Atilt = 10±10) versus distance for S7P2 (23 May 1997).

184

23 MAY 1997 SF6 Puff 2 from Series 7 Tracked by Various Pairings of Sites

Atilt = 120 +/- 10   Minimum Number of Raw Pixels for Feature >=10   For Dhor(y), ELbot >= 70

Source = Puff @ 0.25 min by Sites 1 and 3

$y = 0.0199x + 70.649$
$R^2 = 0.7395$

Fit-Derived MID Used to Interpret Puff XY Pixel Dimensions

◆ DhC1_xSR	◆ DhC1_xCER	◇ DhC1_ySR
▲ DhC2_xSR	▲ DhC2_xCER	△ DhC2_ySR
+ DhC1_yNF	✕ DhC2_yNF	— —Linear (Dh (xSR, xCER, ySR))

Figure I-36. Cross-Diagonal extent (Atilt= 120±10) versus distance for S7P2 (23 May 1997).

23 MAY 1997 SF6 Puff 3 from Series 7 Tracked by Various Pairings of Sites

Atilt = 0 +/- 90   Minimum Number of Raw Pixels for Feature >=10   For Dhor(y), ELbot >= 70

For Area per pixel <= 80

Along-Diagonal
(30° +/- 10° Tilt)

~ Crosswind
(110° +/- 15° Tilt)

Fit-Derived MID Used to Interpret Puff XY Pixel Dimensions

◆ DhC1_xSR   ◆ DhC1_xCER   ◇ DhC1_ySR   ▲ DhC2_xSR   ▲ DhC2_xCER   △ DhC2_ySR   + DhC1_yNF   ✕ DhC2_yNF

Figure I-37. Summary dimension plot showing all perspectives of S7P3 (23 May 1997).

185

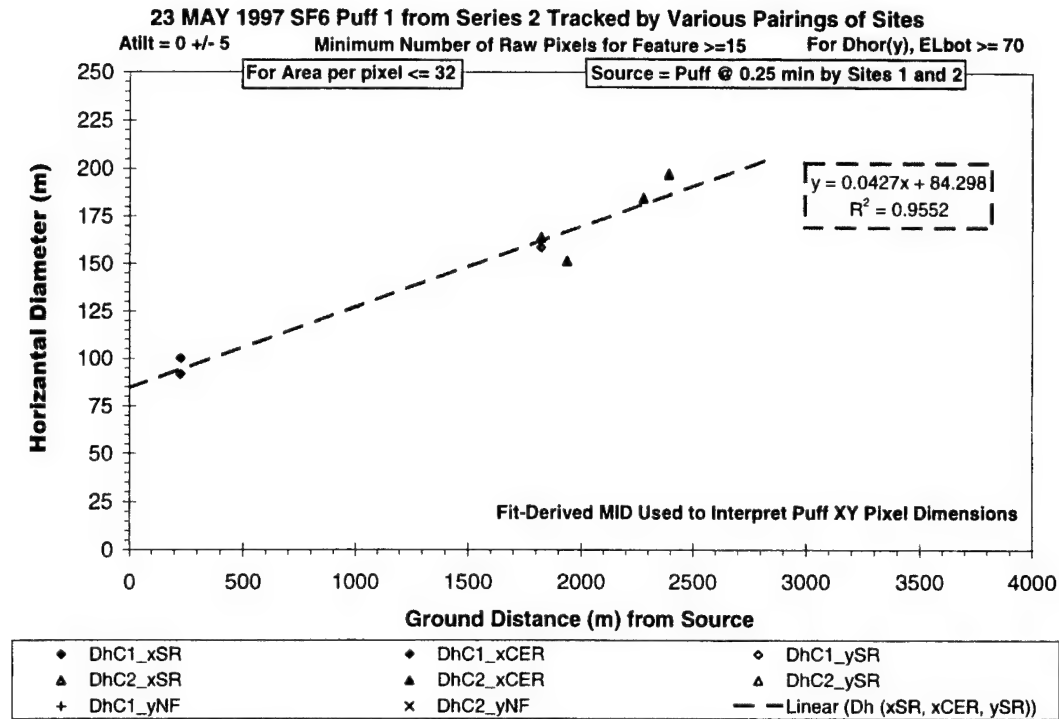Figure I-38. Along-diagonal extent (Atilt = 30±10) versus distance for S7P3 (23 May 1997).

Figure I-39. Crosswind extent (Atilt= 110±15) versus distance for S7P3 (23 May 1997).
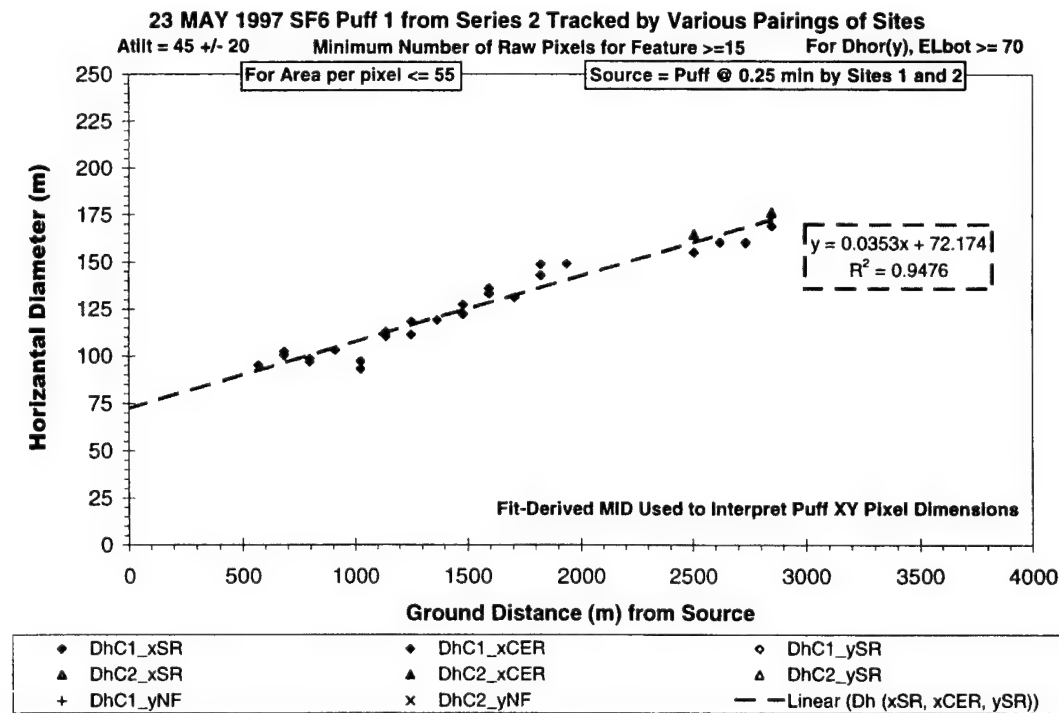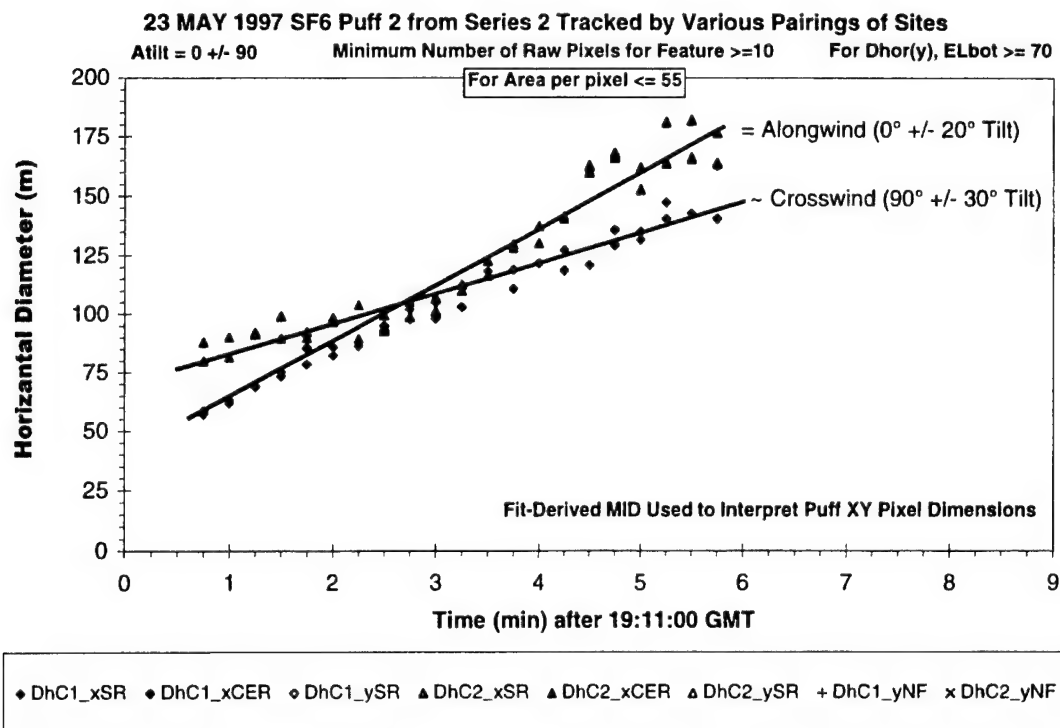
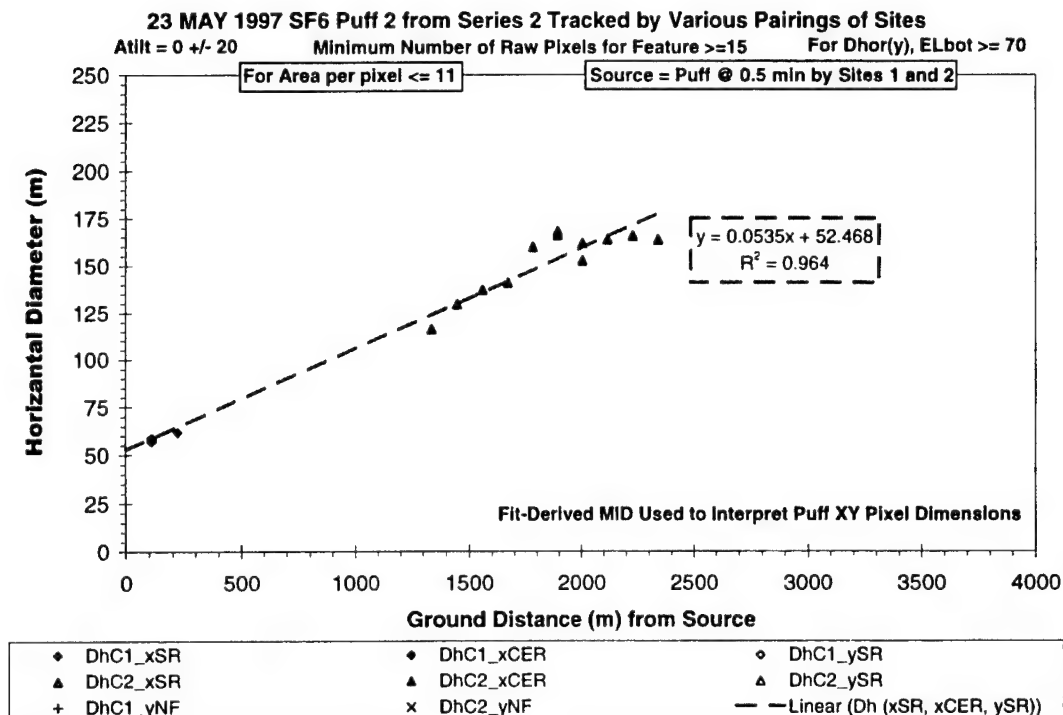Figure I-40. Summary dimension plot showing all perspectives of S8P1 (23 May 1997).

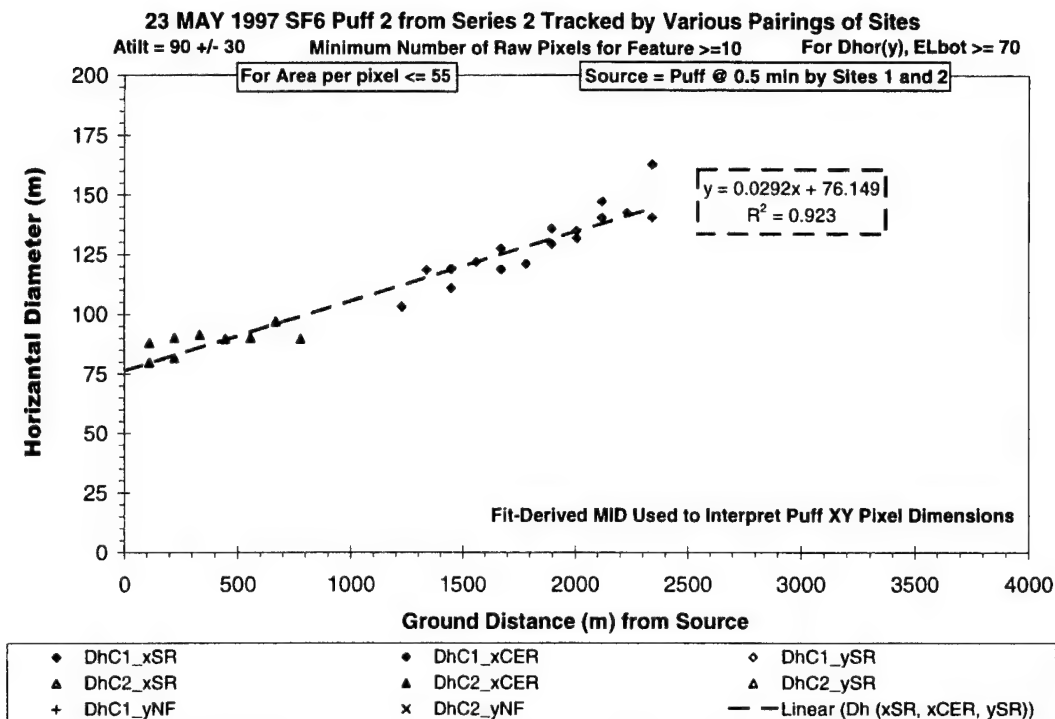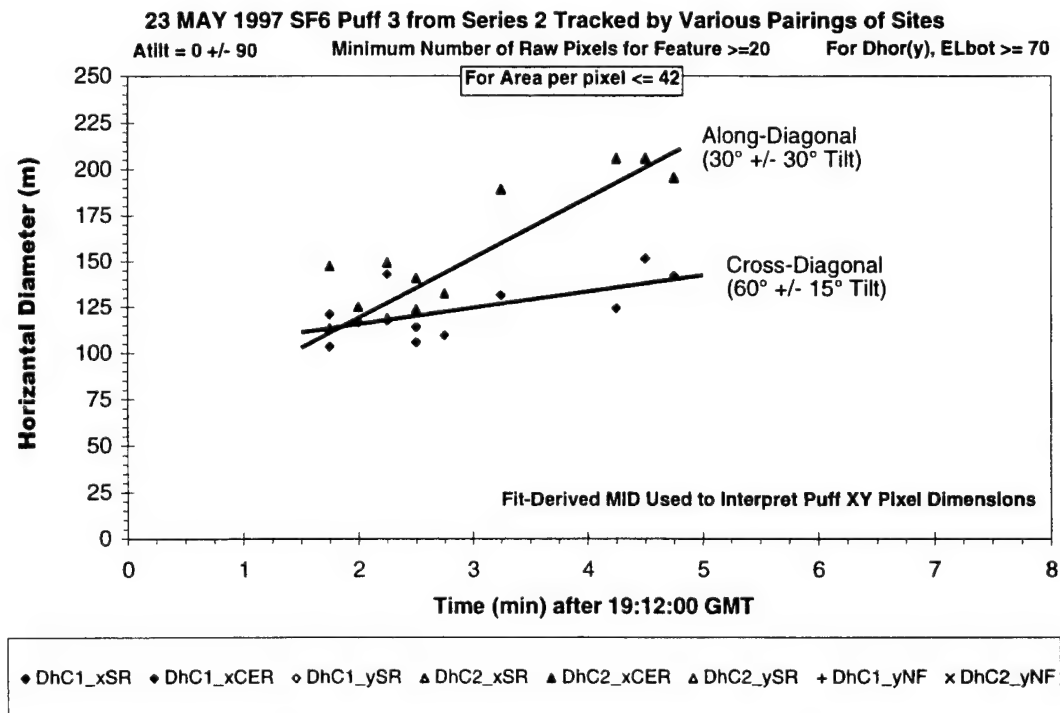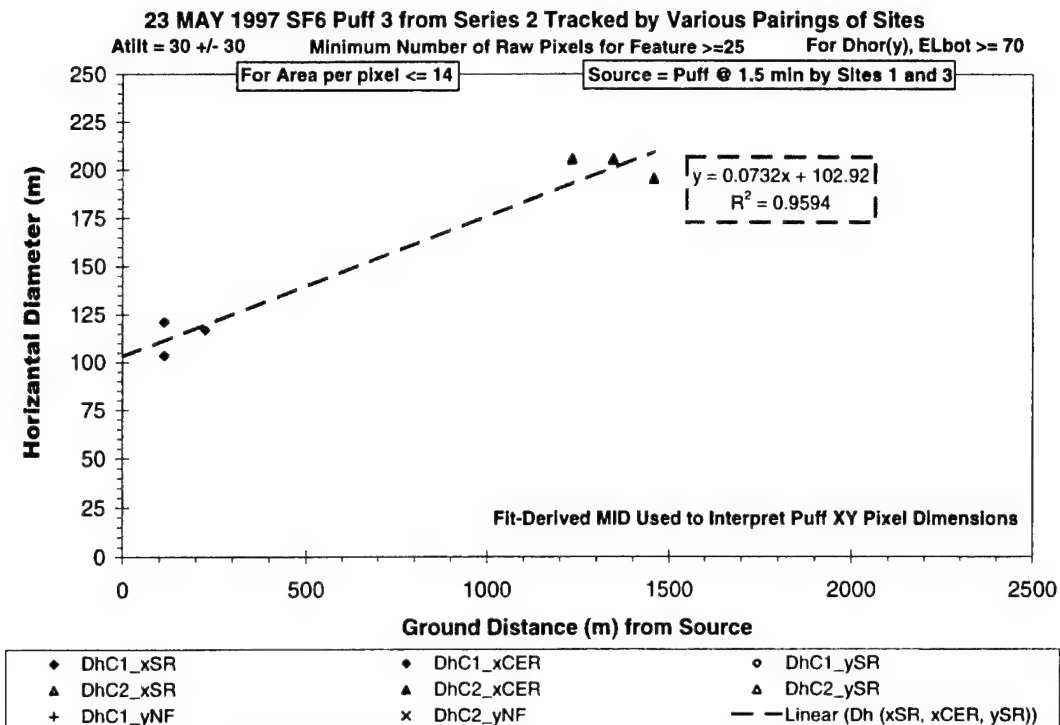Figure I-41. Alongwind extent (Atilt= 0±8) versus distance for S8P1 (23 May 1997).

187

23 MAY 1997 SF6 Puff 1 from Series 8 Tracked by Various Pairings of Sites

Atilt = 110 +/- 15   Minimum Number of Raw Pixels for Feature >=10   For Dhor(y), ELbot >= 70

Source = Puff @ 0.5 min by Sites 1 and 3

$y = 0.0507x + 84.533$
$R^2 = 0.8823$

Fit-Derived MID Used to Interpret Puff XY Pixel Dimensions

◆ DhC1_xSR	◆ DhC1_xCER	◇ DhC1_ySR
▲ DhC2_xSR	▲ DhC2_xCER	△ DhC2_ySR
+ DhC1_yNF	× DhC2_yNF	— —Linear (Dh (xSR, xCER, ySR))
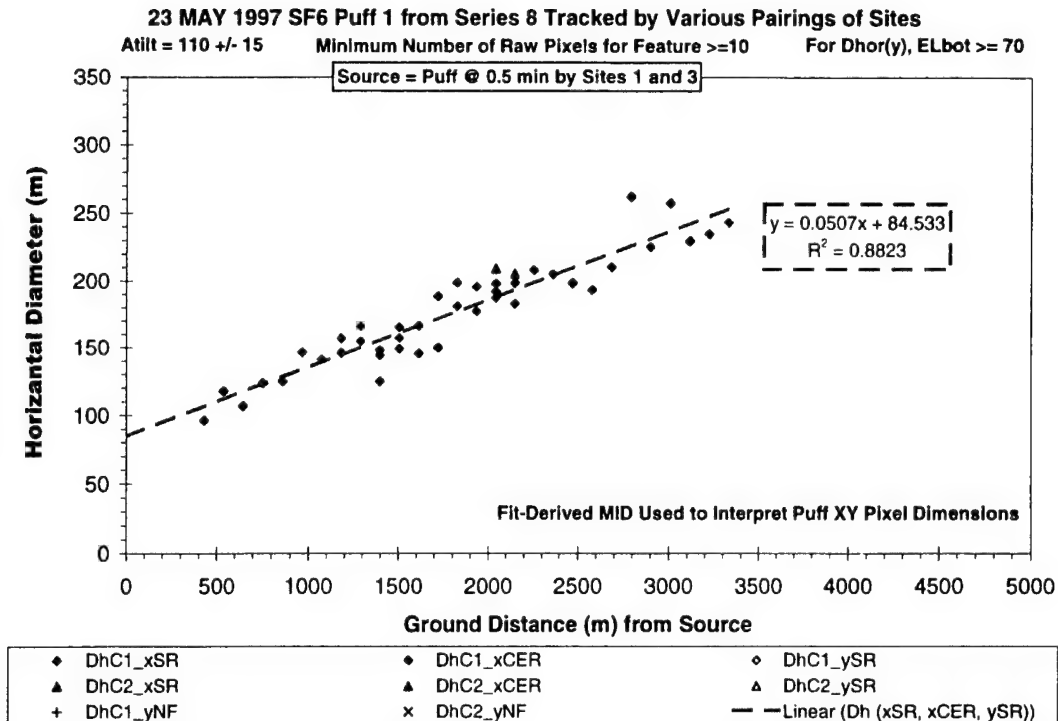
Figure I-42. + Crosswind extent (Atilt= 110±15) versus distance for S8P1 (23 May 1997).

23 MAY 1997 SF6 Puff 2 from Series 8 Tracked by Various Pairings of Sites

Atilt = 0 +/- 90   Minimum Number of Raw Pixels for Feature >=15   For Dhor(y), ELbot >= 70

= Alongwind
(0° +/- 5° Tilt)

Cross-Diagonal
(120°+/-10° Tilt)

- Diagonal
(45° +/- 5° Tilt)

Fit-Derived MID Used to Interpret Puff XY Pixel Dimensions

◆ DhC1_xSR   ◆ DhC1_xCER   ◇ DhC1_ySR   ▲ DhC2_xSR   ▲ DhC2_xCER   △ DhC2_ySR   + DhC1_yNF   × DhC2_yNF
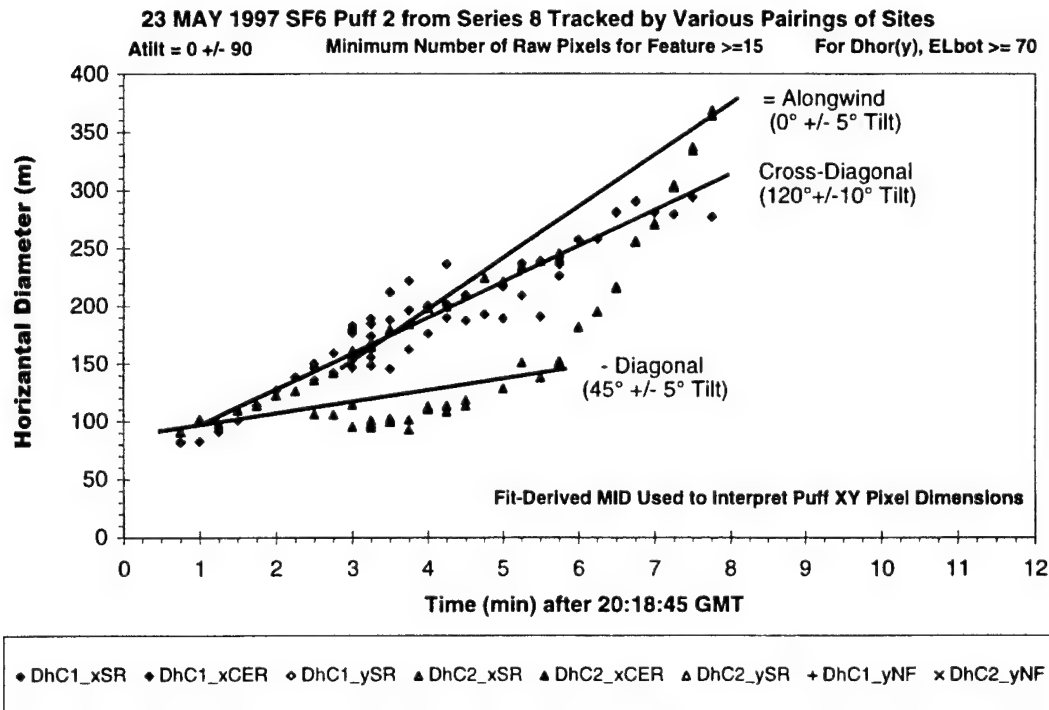
Figure I-43. Summary dimension plot showing all perspectives of S8P2 (23 May 1997).

188
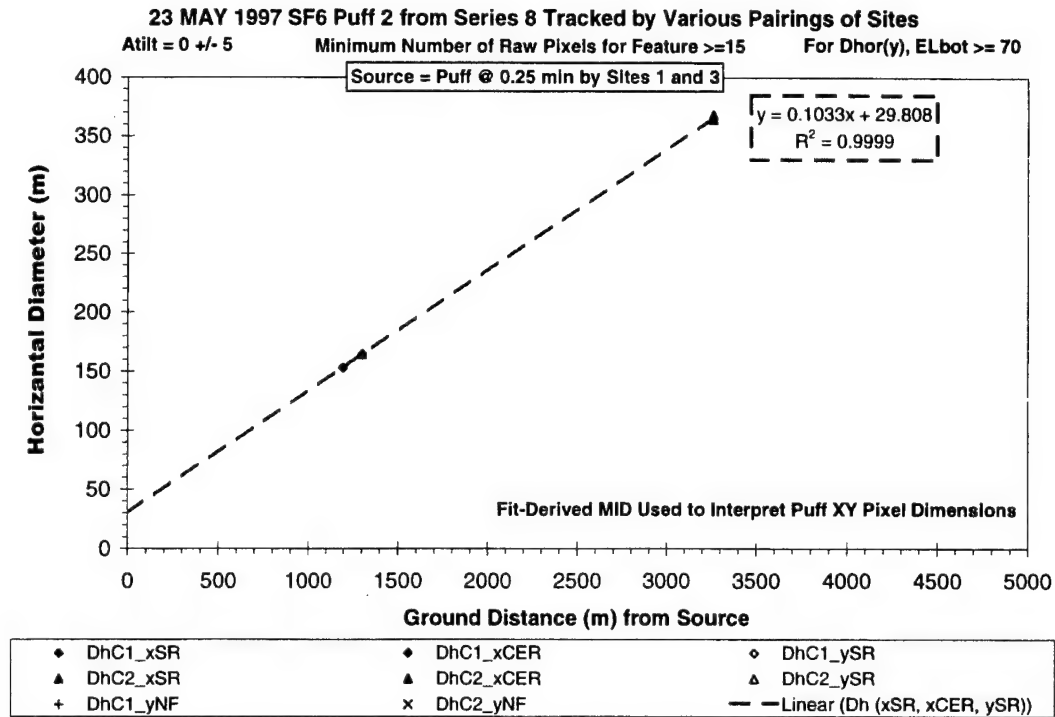
Figure I-44. Alongwind extent (Atilt= 0±5) versus distance for S8P2 (23 May 1997).
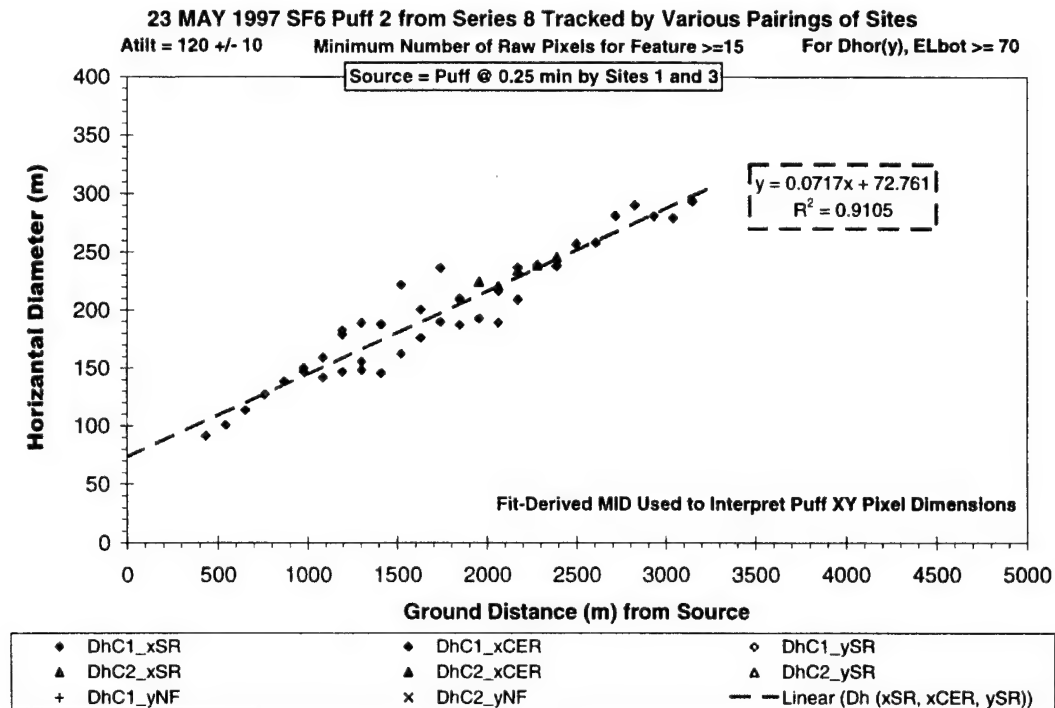
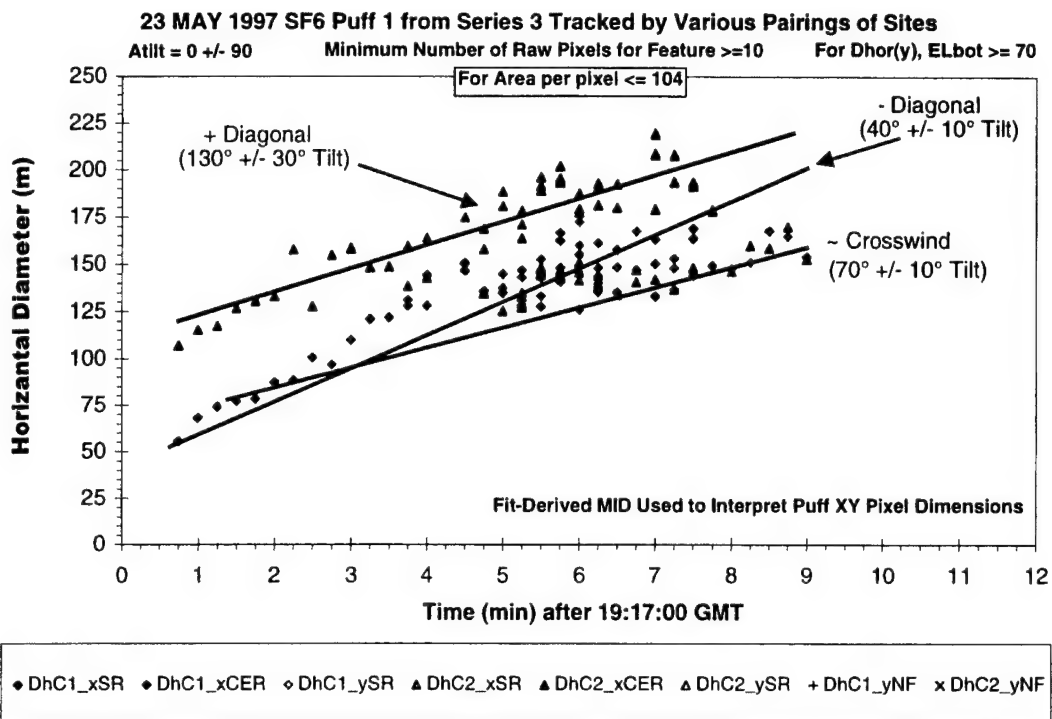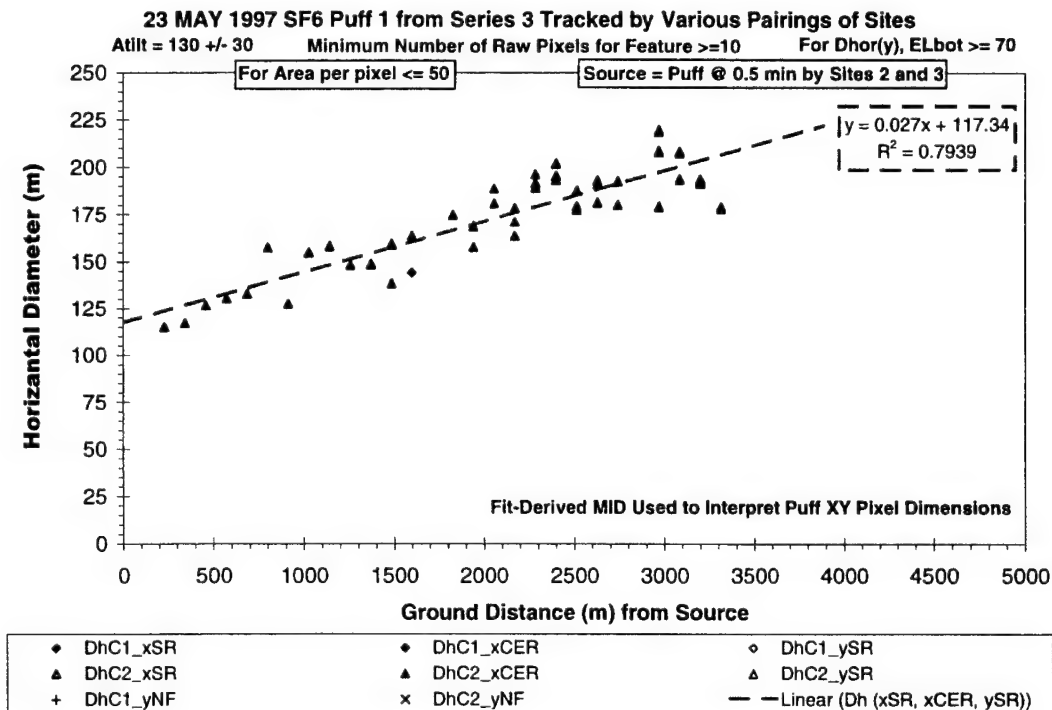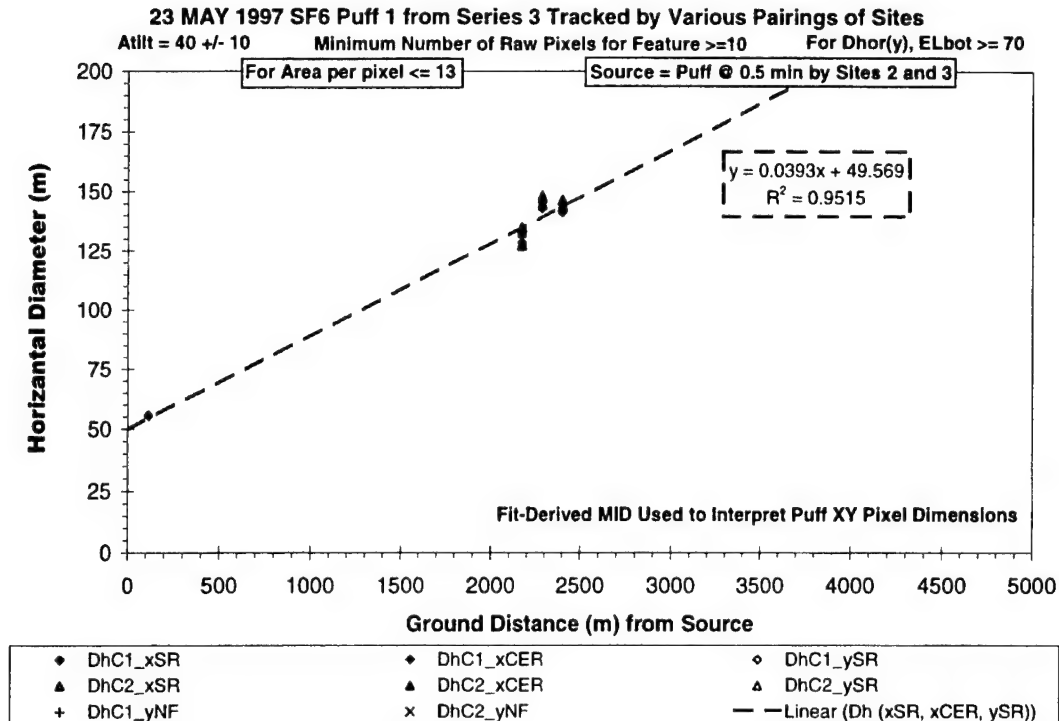Figure I-45. Cross-Diagonal extent (Atilt= 120±10) versus distance for S8P2 (23 May 1997).

189

23 MAY 1997 SF6 Puff 2 from Series 8 Tracked by Various Pairings of Sites

Atilt = 45 +/- 5   Minimum Number of Raw Pixels for Feature >=15   For Dhor(y), ELbot >= 70

Source = Puff @ 0.25 min by Sites 1 and 3

$y = 0.0237x + 89.549$
$R^2 = 0.9121$

Fit-Derived MID Used to Interpret Puff XY Pixel Dimensions

Horizantal Diameter (m)

Ground Distance (m) from Source

	DhC1_xSR		DhC1_xCER		DhC1_ySR
	DhC2_xSR		DhC2_xCER		DhC2_ySR
	DhC1_yNF		DhC2_yNF		Linear (Dh (xSR, xCER, ySR))
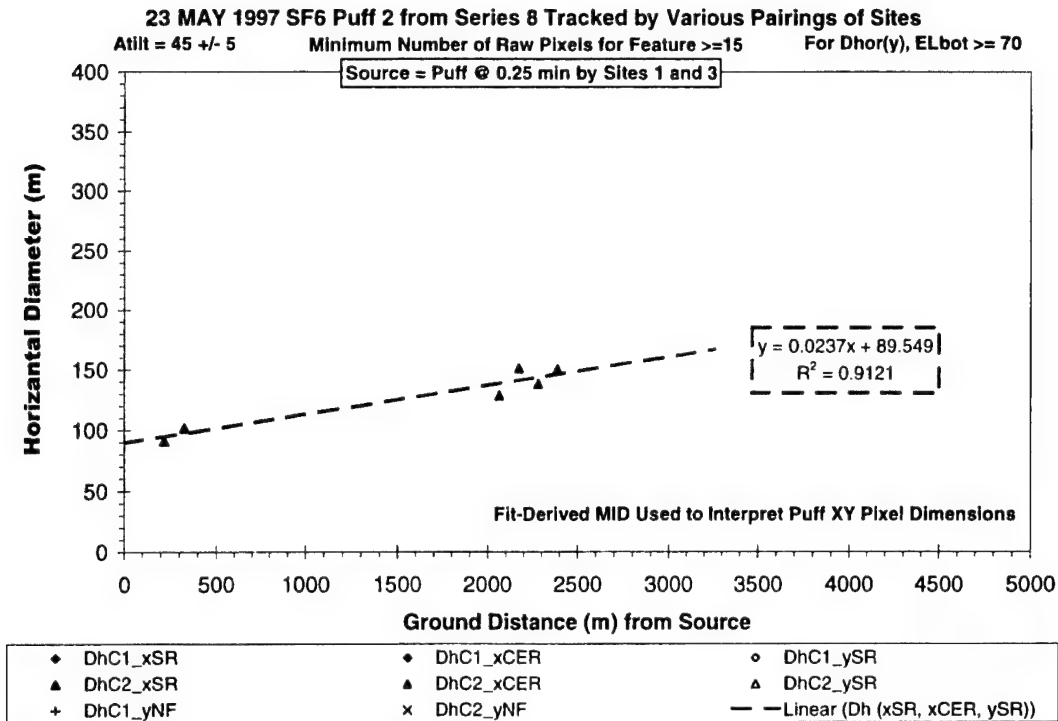
Figure I-46. - Diagonal extent (Atilt= 45±5) versus distance for S8P2 (23 May 1997).

23 MAY 1997 SF6 Puff 3 from Series 8 Tracked by Various Pairings of Sites

Atilt = 0 +/- 90   Minimum Number of Raw Pixels for Feature >=20   For Dhor(y), ELbot >= 70

For Area per pixel <= 82

~ Crosswind
(110° +/- 15° Tilt)

~ Alongwind
(15° +/- 5° Tilt)

- Diagonal
(45° +/- 5° Tilt)

Fit-Derived MID Used to Interpret Puff XY Pixel Dimensions

Horizantal Diameter (m)

Time (min) after 20:19:30 GMT

DhC1_xSR   DhC1_xCER   DhC1_ySR   DhC2_xSR   DhC2_xCER   DhC2_ySR   + DhC1_yNF   x DhC2_yNF

Figure I-47. Summary dimension plot showing all perspectives of S8P3 (23 May 1997).

190

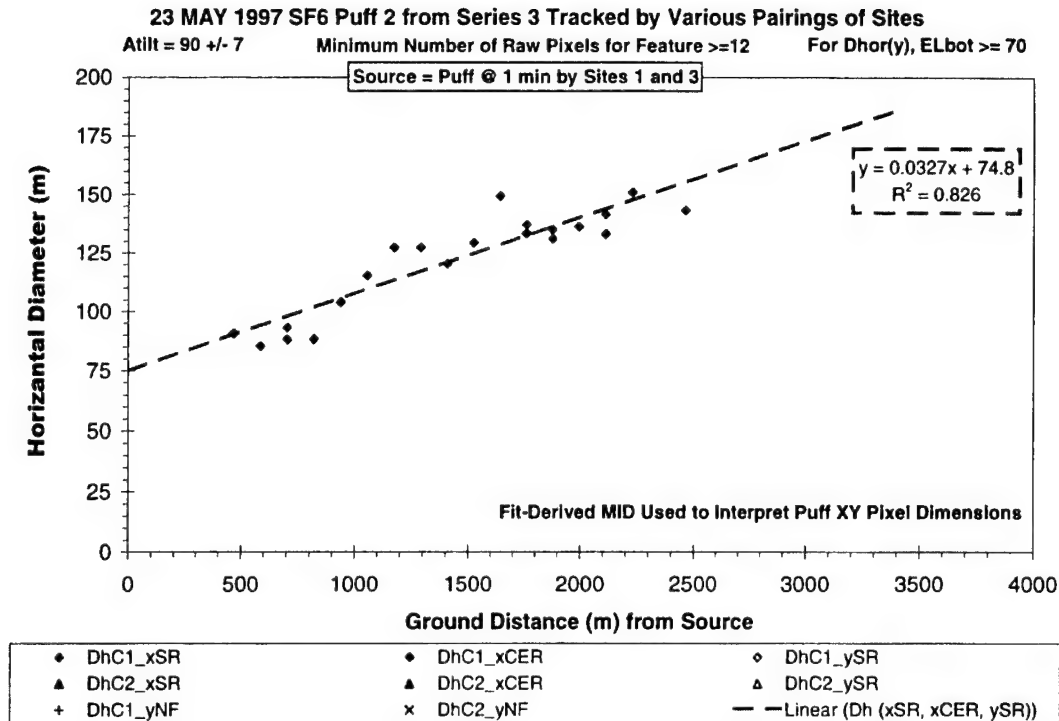Figure I-48. Crosswind extent (Atilt= 110±15) versus distance for S8P3 (23 May 1997).

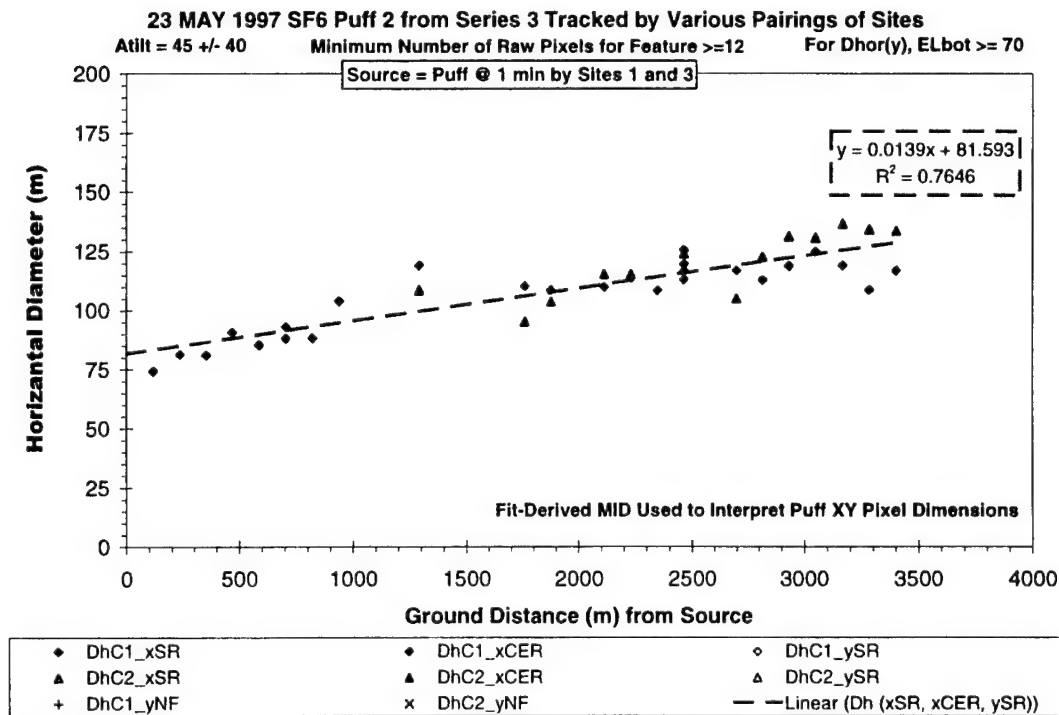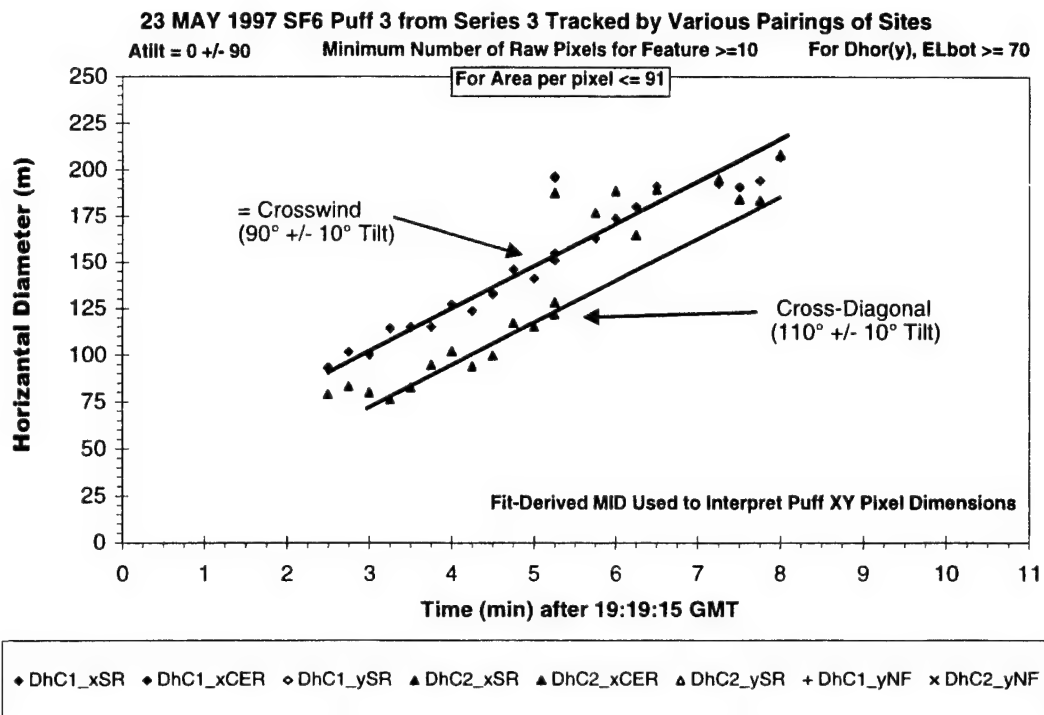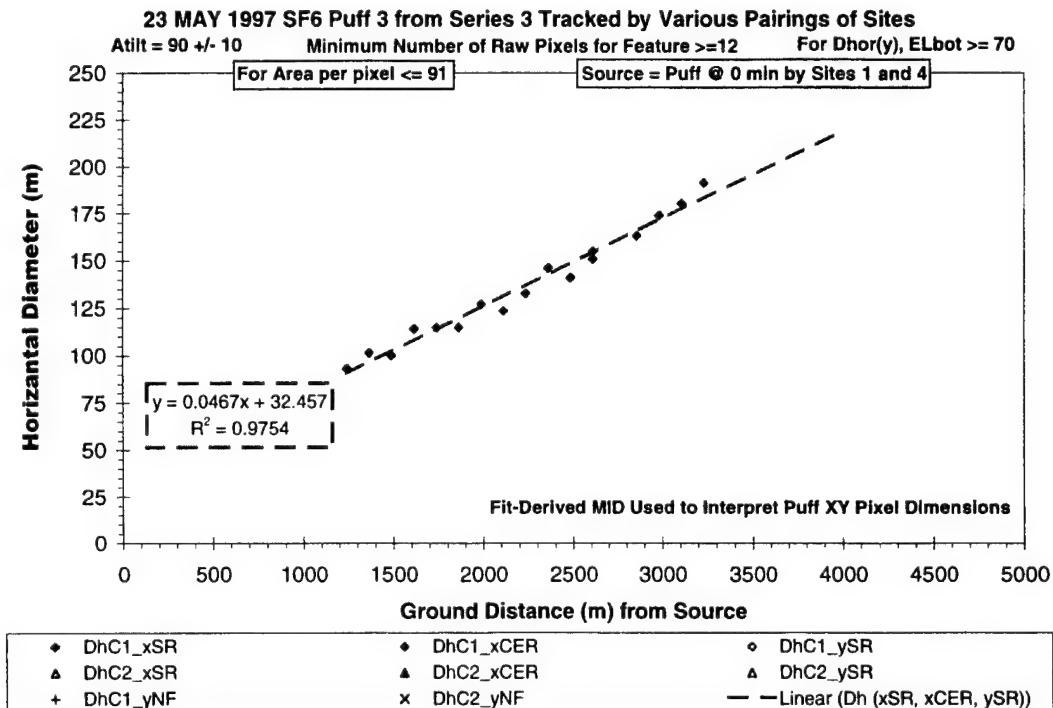Figure I-49. Alongwind extent (Atilt= 15±5) versus distance for S8P3 (23 May 1997).

191

23 MAY 1997 SF6 Puff 3 from Series 8 Tracked by Various Pairings of Sites

Atilt = 45 +/- 5   Minimum Number of Raw Pixels for Feature >=20   For Dhor(y), ELbot >= 70

For Area per pixel <= 82   Source = Puff @ 0.5 min by Sites 1 and 3

$y = 0.0109x + 90.319$
$R^2 = 0.6264$

Fit-Derived MID Used to Interpret Puff XY Pixel Dimensions

Horizantal Diameter (m)

Ground Distance (m) from Source

◆ DhC1_xSR	● DhC1_xCER	○ DhC1_ySR
▲ DhC2_xSR	▲ DhC2_xCER	△ DhC2_ySR
+ DhC1_yNF	✕ DhC2_yNF	─ ─ Linear (Dh (xSR, xCER, ySR))

Figure I-50. - Diagonal extent (Atilt= 45±5) versus distance for S8P3 (23 May 1997).

23 MAY 1997 SF6 Puff 1 from Series B Tracked by Various Pairings of Sites

Atilt = 0 +/- 90   Minimum Number of Raw Pixels for Feature >=10   For Dhor(y), ELbot >= 70

For Area per pixel <= 85

~ Alongwind
(20° +/- 30° Tilt)

Cross-Diagonal
(120° +/- 20° Tilt)

Fit-Derived MID Used to Interpret Puff XY Pixel Dimensions

Horizantal Diameter (m)

Time (min) after 20:41:15 GMT

| ◆DhC1_xSR | ◆DhC1_xCER | ◇DhC1_ySR | ▲DhC2_xSR | ▲DhC2_xCER | △DhC2_ySR | +DhC1_yNF | ✕DhC2_yNF |

Figure I-51. Summary dimension plot showing all perspectives of SBP1 (23 May 1997).

192

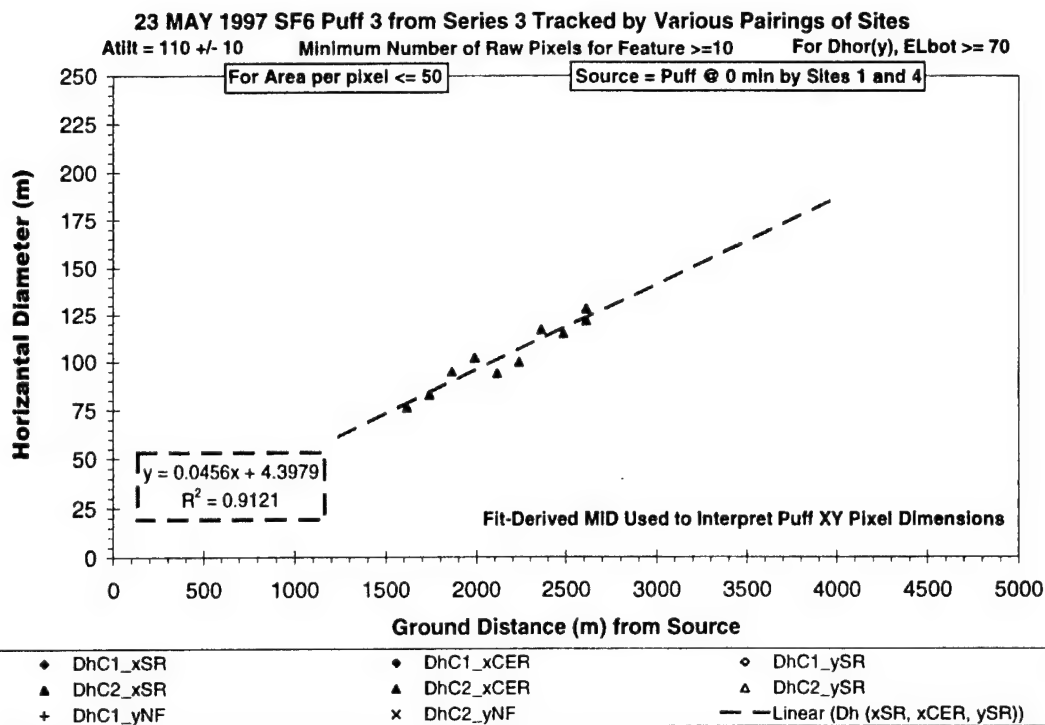Figure I-52. Alongwind extent (Atilt = 20±30) versus distance for SBP1 (23 May 1997).

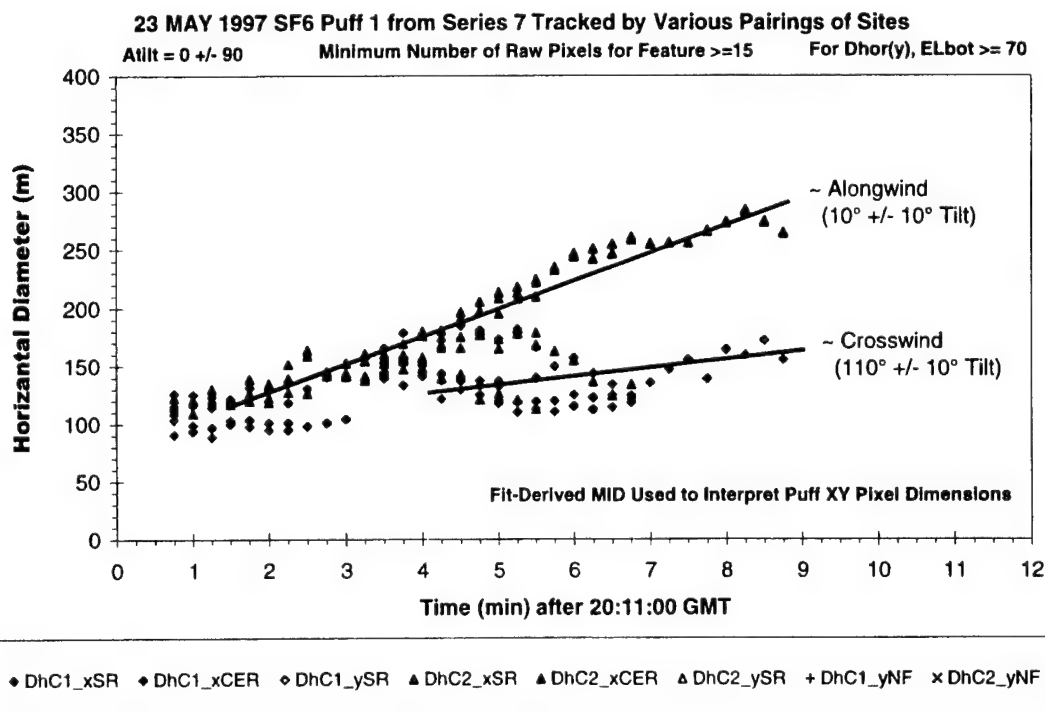Figure I-53. Cross-Diagonal extent (Atilt= 120±20) versus distance for SBP1 (23 May 1997).

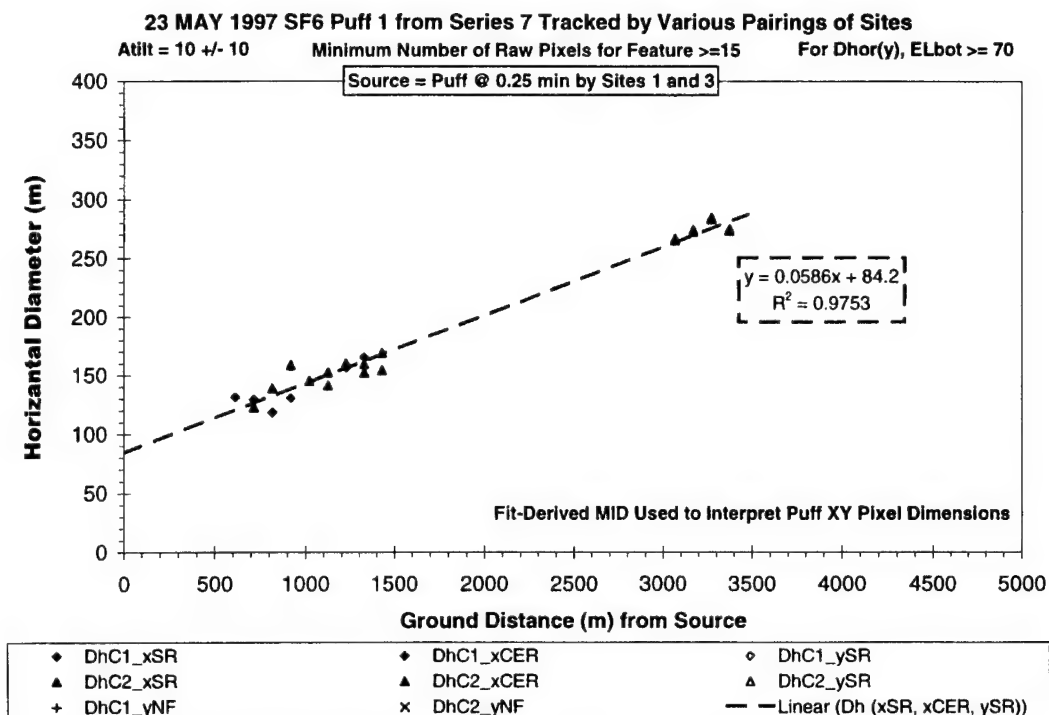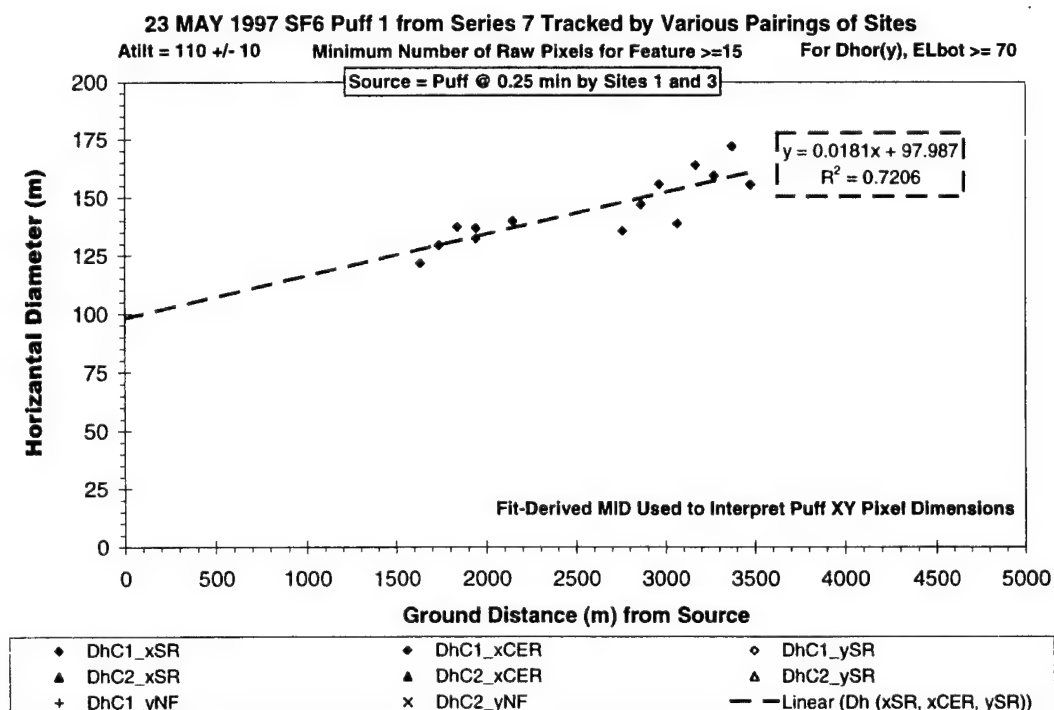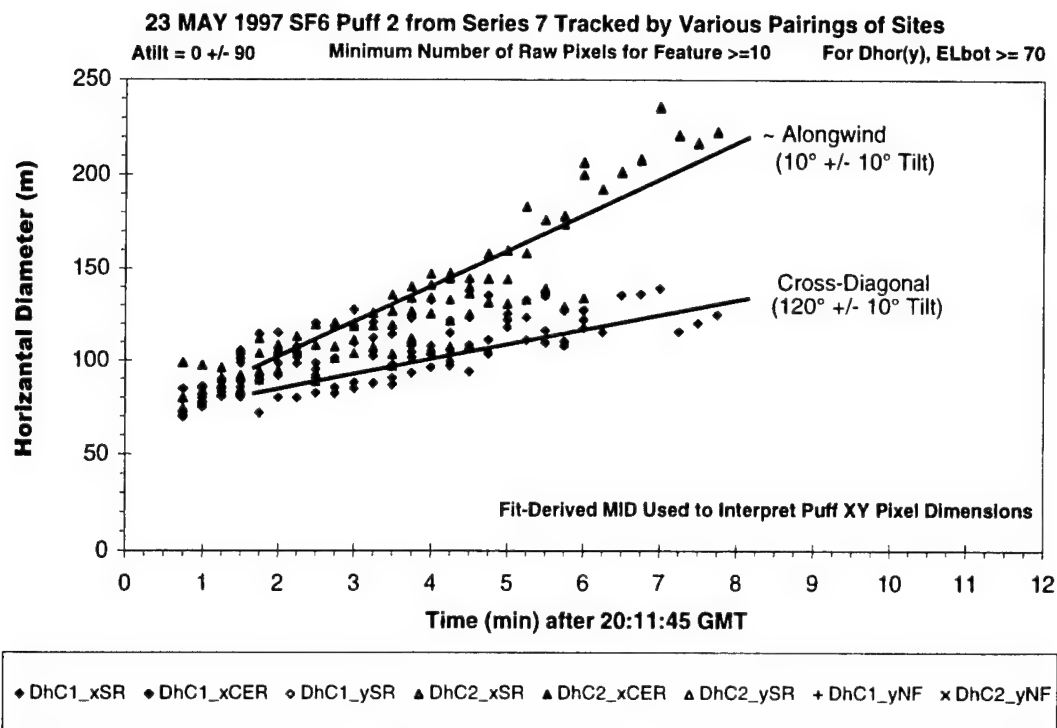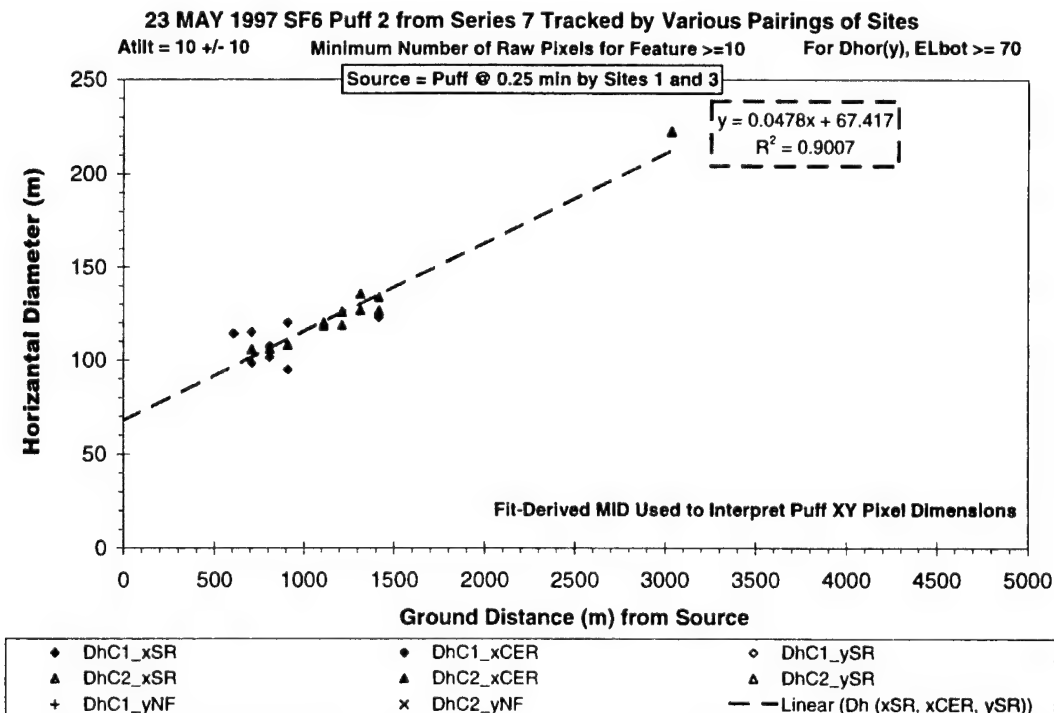Figure I-54. Summary dimension plot showing all perspectives of SBP2 (23 May 1997).

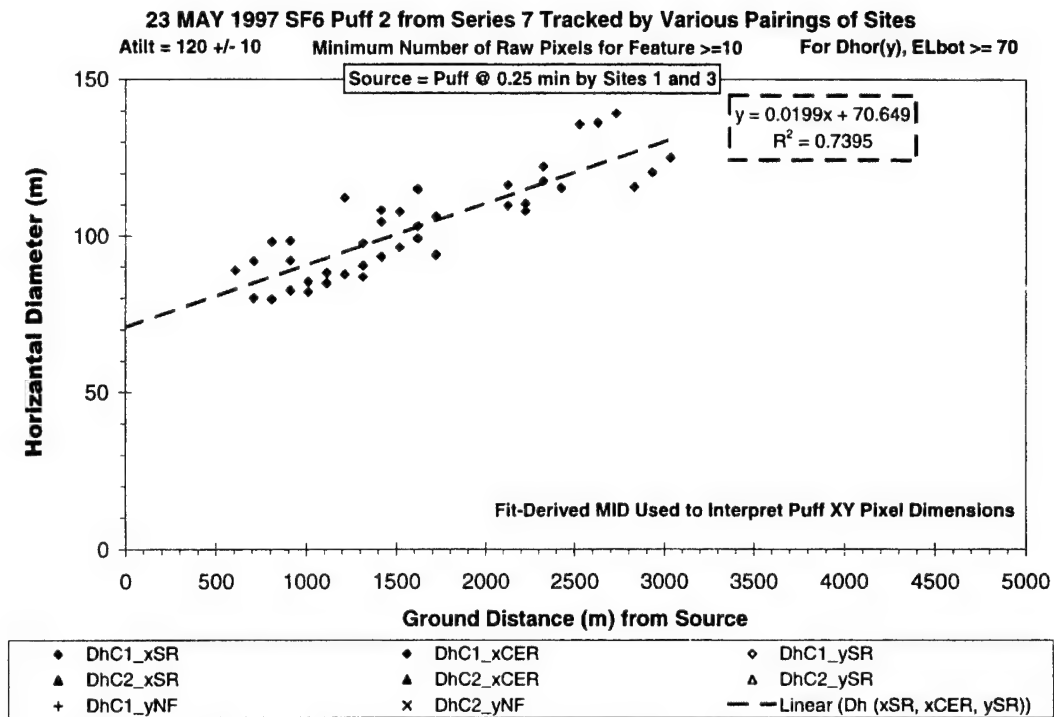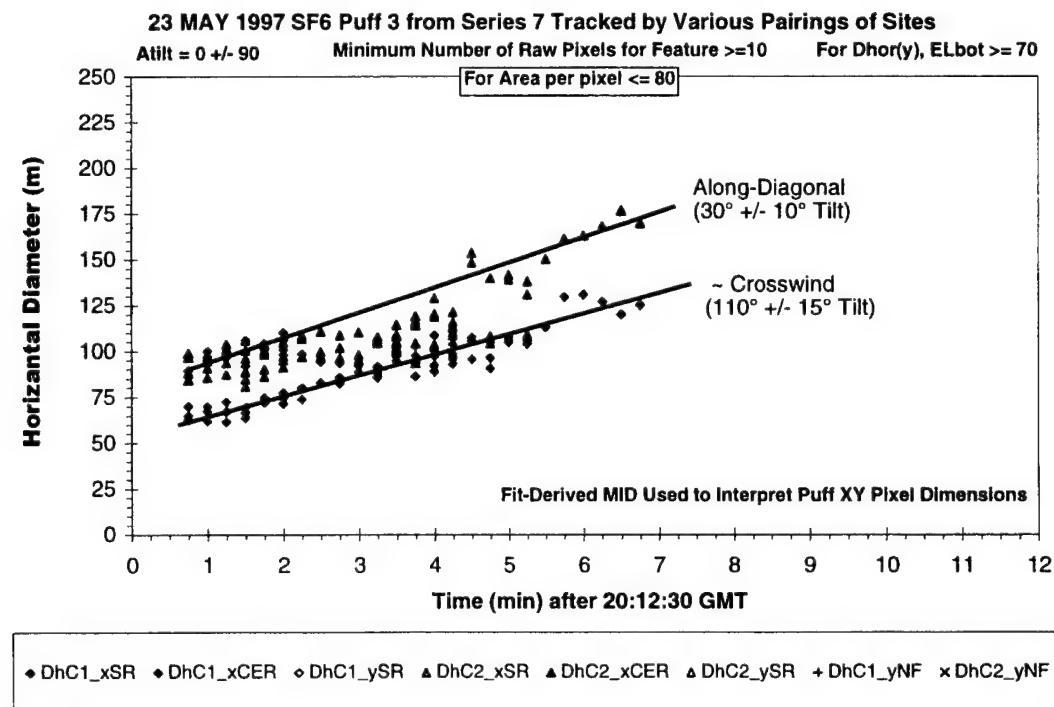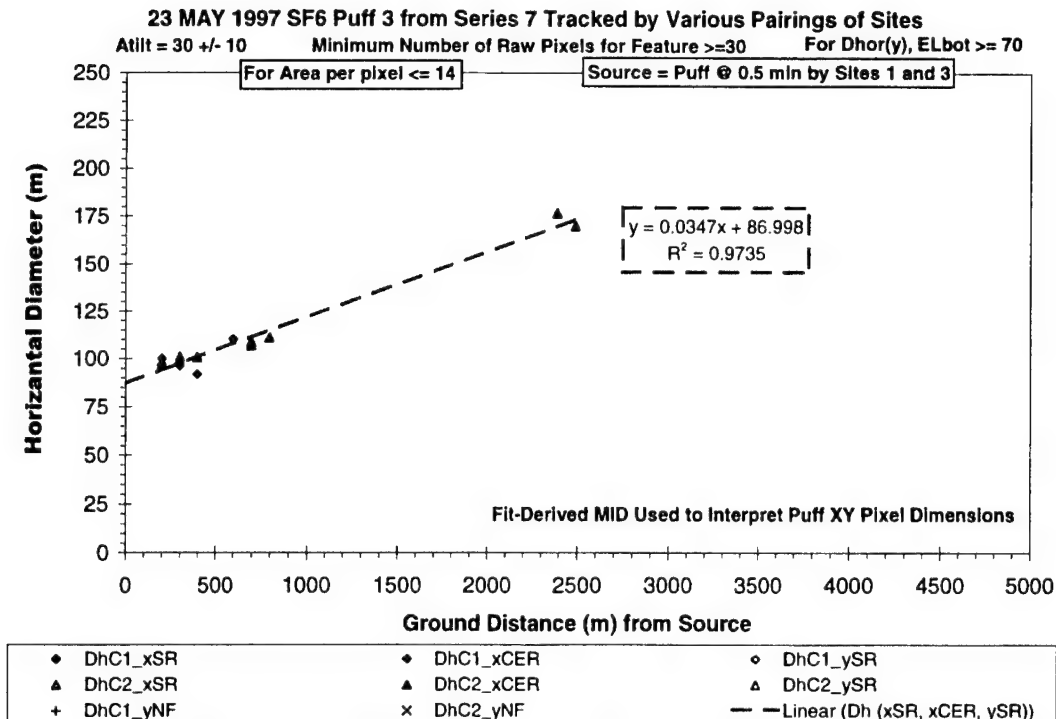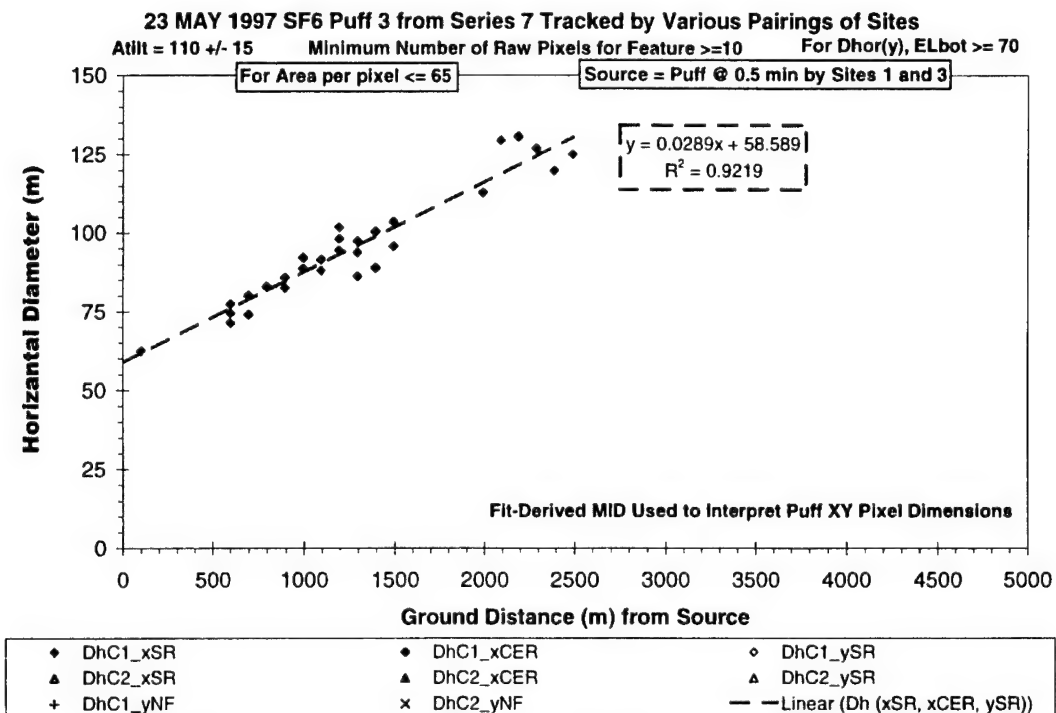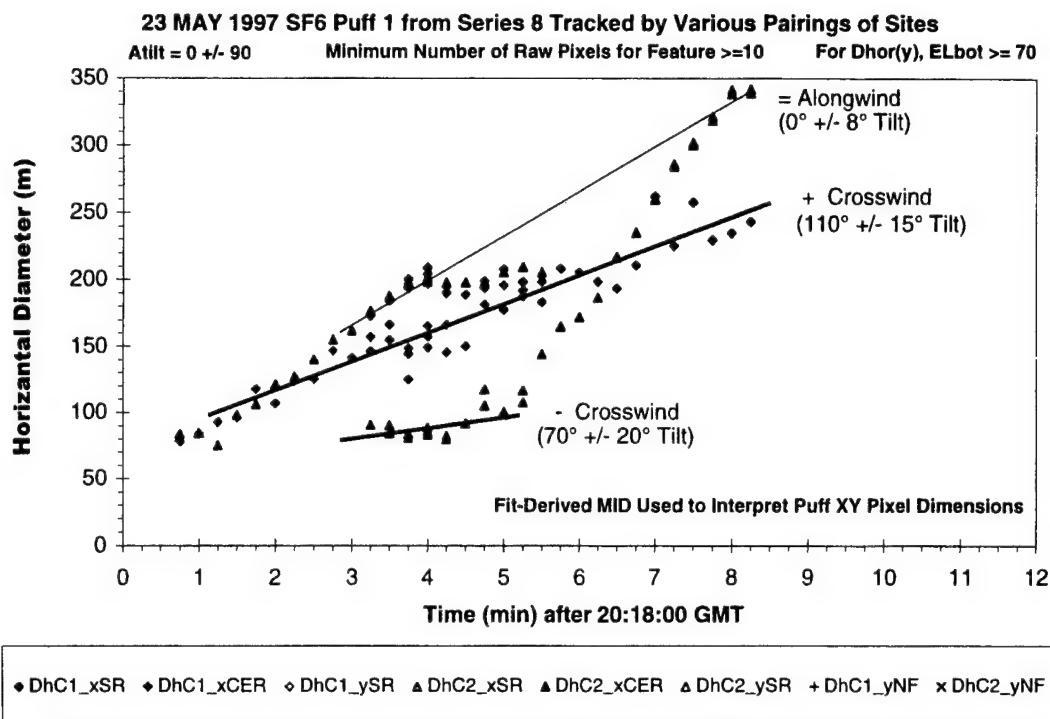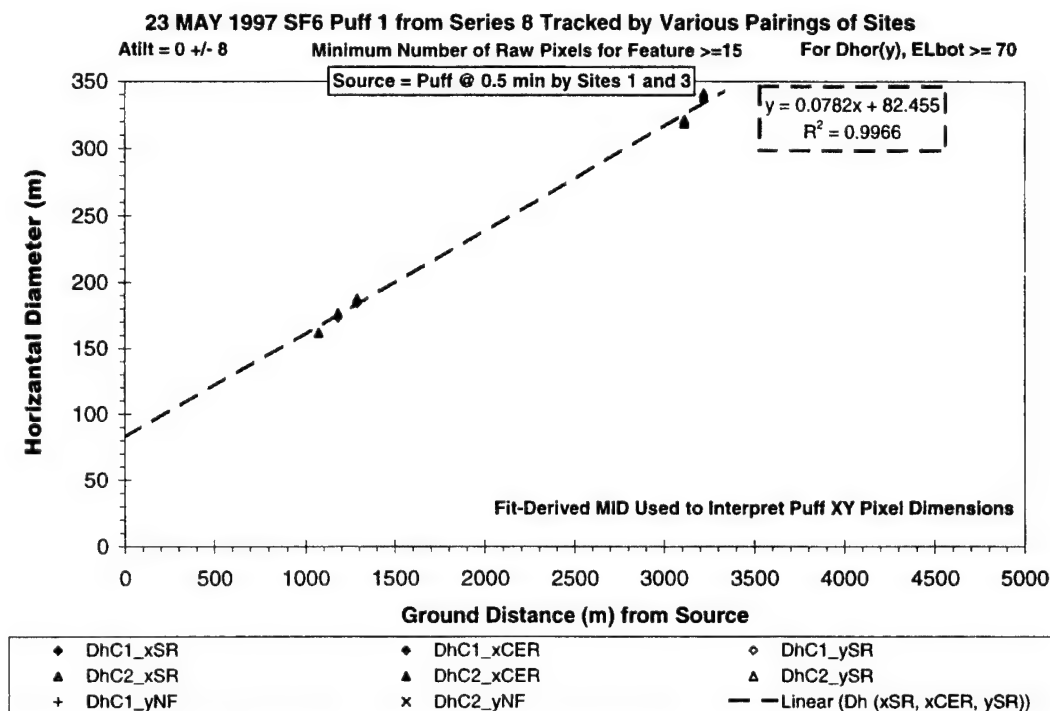Figure I-55. Alongwind extent (Atilt = 0±15) versus distance for SBP2 (23 May 1997).

194

23 MAY 1997 SF6 Puff 2 from Series B Tracked by Various Pairings of Sites

Atilt = 120 +/- 20   Minimum Number of Raw Pixels for Feature >=10   For Dhor(y), ELbot >= 70

For Area per pixel <= 65   Source = Puff @ 0.5 min by Sites 1 and 3

$y = 0.0052x + 114.25$
$R^2 = 0.1042$

Fit-Derived MID Used to Interpret Puff XY Pixel Dimensions

Horizantal Diameter (m)

Ground Distance (m) from Source

◆ DhC1_xSR	◆ DhC1_xCER	◇ DhC1_ySR
▲ DhC2_xSR	▲ DhC2_xCER	△ DhC2_ySR
+ DhC1_yNF	× DhC2_yNF	− −Linear (Dh (xSR, xCER, ySR))

Figure I-56. Cross-Diagonal extent (Atilt= 120±20) versus distance for SBP2 (23 May 1997).

23 MAY 1997 SF6 Puff 1 from Series F Tracked by Various Pairings of Sites

Atilt = 0 +/- 90   Minimum Number of Raw Pixels for Feature >=10   For Dhor(y), ELbot >= 70

+ Diagonal
(135 +/- 20 Tilt)

~ Crosswind
(110 +/- 10 Tilt)

- Diagonal
(45 +/- 20 Tilt)

Fit-Derived MID Used to Interpret Puff XY Pixel Dimensions

Horizantal Diameter (m)

Time (min) after 21:38:00 GMT

◆ DhC1_xSR   ◆ DhC1_xCER   ◇ DhC1_ySR   ▲ DhC2_xSR   ▲ DhC2_xCER   △ DhC2_ySR   + DhC1_yNF   × DhC2_yNF

Figure I-57. Summary dimension plot showing all perspectives of SFP1 (23 May 1997).

23 MAY 1997 SF6 Puff 1 from Series F Tracked by Various Pairings of Sites

Atilt = 135 +/- 20   Minimum Number of Raw Pixels for Feature >=10   For Dhor(y), ELbot >= 70

Source = Puff @ 0.25 min by Sites 2 and 4

$y = 0.0066x + 121.32$
$R^2 = 0.0418$

Fit-Derived MID Used to Interpret Puff XY Pixel Dimensions

◆	DhC1_xSR	◆	DhC1_xCER	○	DhC1_ySR
▲	DhC2_xSR	▲	DhC2_xCER	△	DhC2_ySR
+	DhC1_yNF	×	DhC2_yNF	— —Linear (Dh (xSR, xCER, ySR))

Figure I-58. + Diagonal extent (Atilt = 135±20) versus distance for SFP1 (23 May 1997).

23 MAY 1997 SF6 Puff 1 from Series F Tracked by Various Pairings of Sites

Atilt = 110 +/- 10   Minimum Number of Raw Pixels for Feature >=10   For Dhor(y), ELbot >= 70

Source = Puff @ 0.25 min by Sites 2 and 4

$y = 0.0058x + 118.22$
$R^2 = 0.0444$

Fit-Derived MID Used to Interpret Puff XY Pixel Dimensions

◆	DhC1_xSR	◆	DhC1_xCER	○	DhC1_ySR
▲	DhC2_xSR	▲	DhC2_xCER	△	DhC2_ySR
+	DhC1_yNF	×	DhC2_yNF	— —Linear (Dh (xSR, xCER, ySR))

Figure I-59. Crosswind extent (Atilt = 110±10) versus distance for SFP1 (23 May 1997).

196

23 MAY 1997 SF6 Puff 1 from Series F Tracked by Various Pairings of Sites

Atilt = 45 +/- 20   Minimum Number of Raw Pixels for Feature >=10   For Dhor(y), ELbot >= 70

Source = Puff @ 0.25 min by Sites 2 and 4

$y = 0.0338x + 67.67$
$R^2 = 0.7689$

Fit-Derived MID Used to Interpret Puff XY Pixel Dimensions

Horizantal Diameter (m)

Ground Distance (m) from Source

● DhC1_xSR	● DhC1_xCER	◇ DhC1_ySR
▲ DhC2_xSR	▲ DhC2_xCER	△ DhC2_ySR
+ DhC1_yNF	× DhC2_yNF	— —Linear (Dh (xSR, xCER, ySR))

Figure I-60. - Diagonal extent (Atilt = 45±20) versus distance for SFP1 (23 May 1997).

23 MAY 1997 SF6 Puff 2 from Series F Tracked by Various Pairings of Sites

Atilt = 0 +/- 90   Minimum Number of Raw Pixels for Feature >=9   For Dhor(y), ELbot >= 70

For Area per pixel <= 120

Horizantal Diameter (m)

+ Diagonal
(135 +/- 30 Tilt)

~ Alongwind
(170 +/- 30 Tilt)

~ Crosswind
(110 +/- 10 Tilt)

- Diagonal
(50 +/- 10 Tilt)

Fit-Derived MID Used to Interpret Puff XY Pixel Dimensions

Time (min) after 21:38:40 GMT

◆ DhC1_xSR	◆ DhC1_xCER	◇ DhC1_ySR	▲ DhC2_xSR	▲ DhC2_xCER	△ DhC2_ySR	+ DhC1_yNF	× DhC2_yNF

Figure I-61. Summary dimension plot showing all perspectives of SFP2 (23 May 1997).

197

Figure I-62. + Diagonal extent (Atilt = 135±30) versus distance for SFP2 (23 May 1997).

Figure I-63. Alongwind extent (Atilt = 170±30) versus distance for SFP2 (23 May 1997).

Figure I-64. Crosswind extent (Atilt = 110±10) versus distance for SFP2 (23 May 1997).

Figure I-65. - Diagonal extent (Atilt = 50±10) versus distance for SFP2 (23 May 1997).
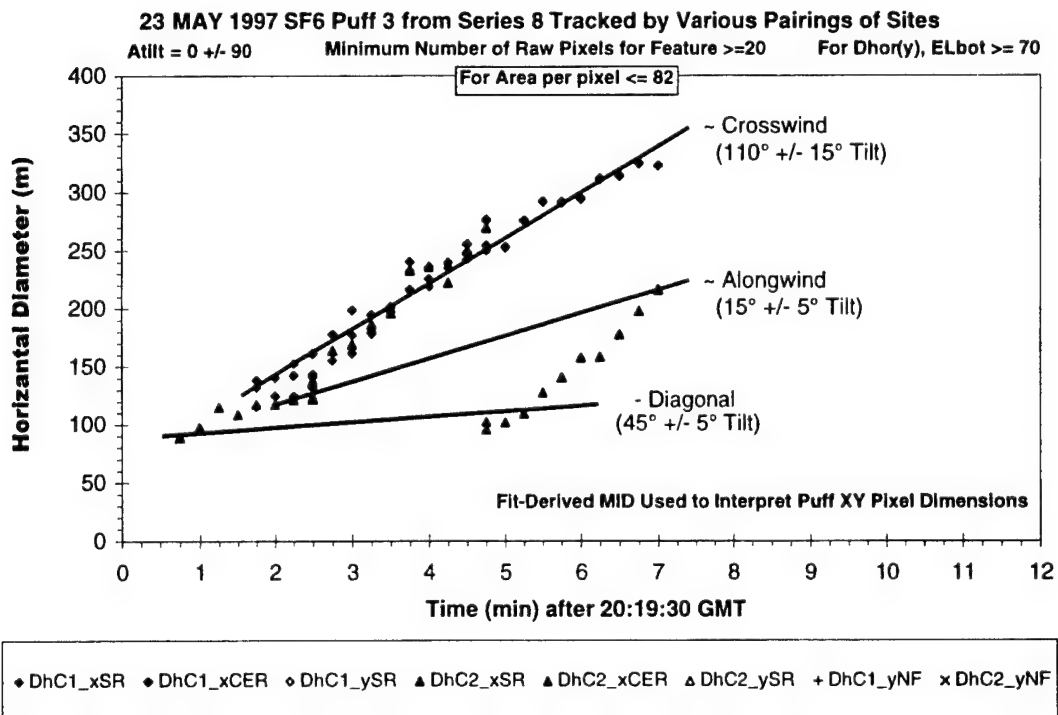
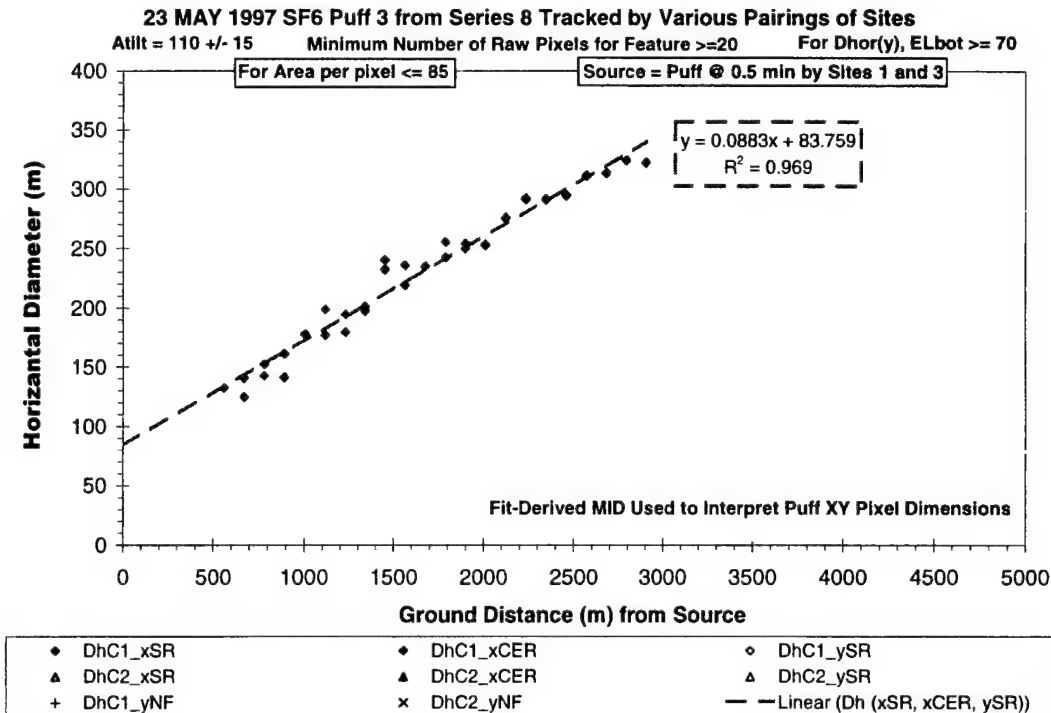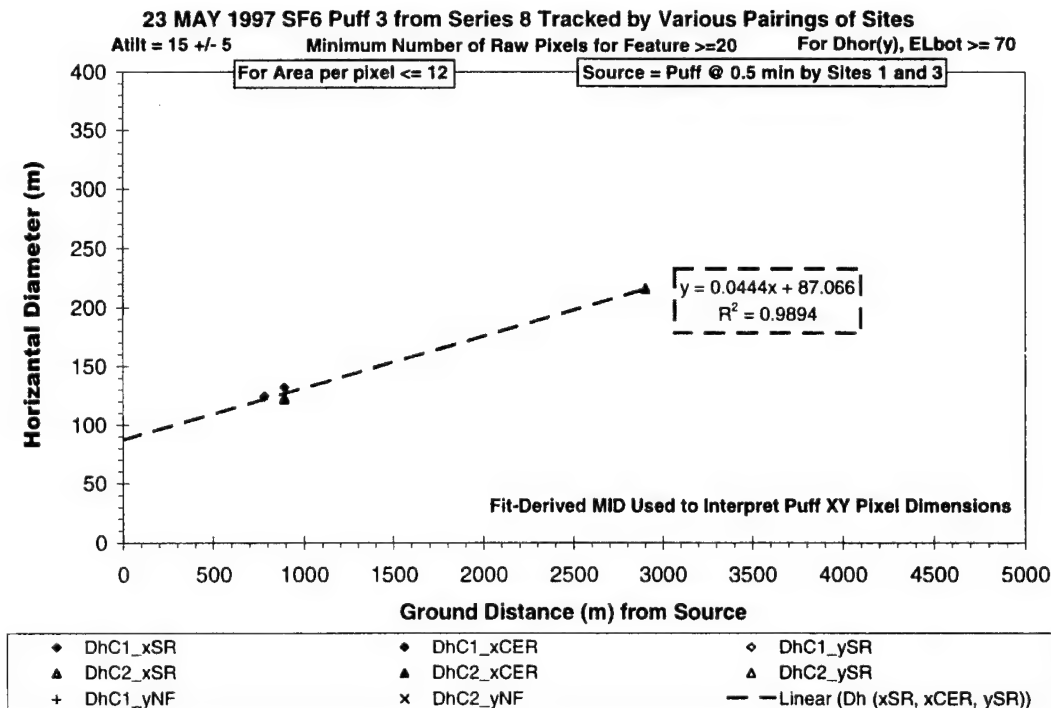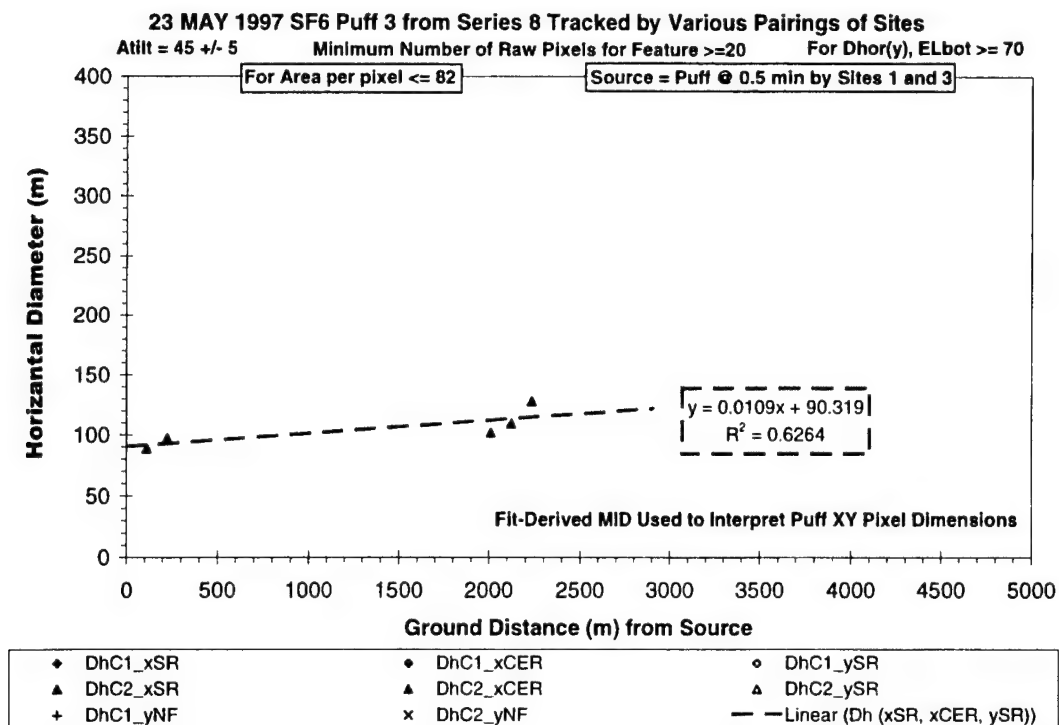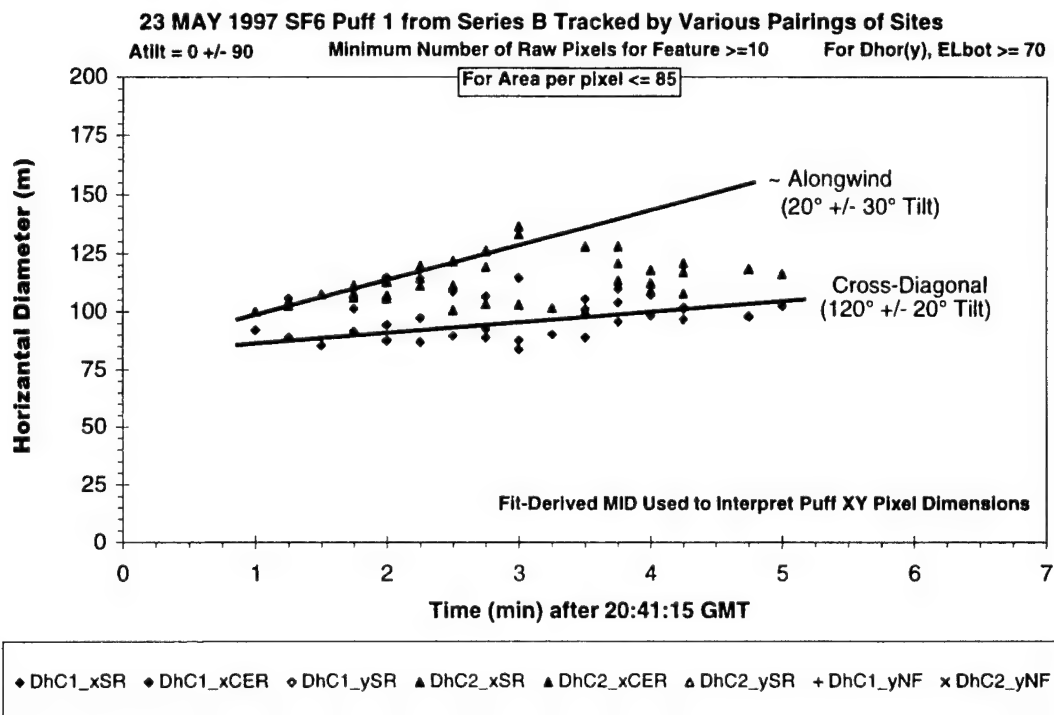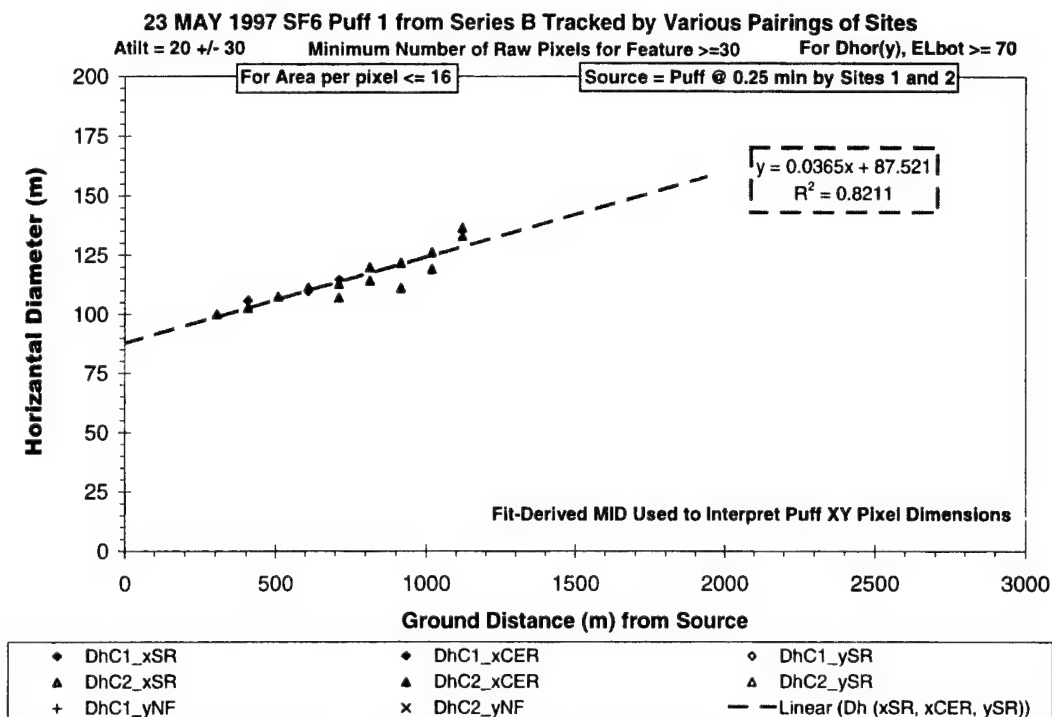Figure I-66. Summary dimension plot showing all perspectives of SFP3 (23 May 1997).

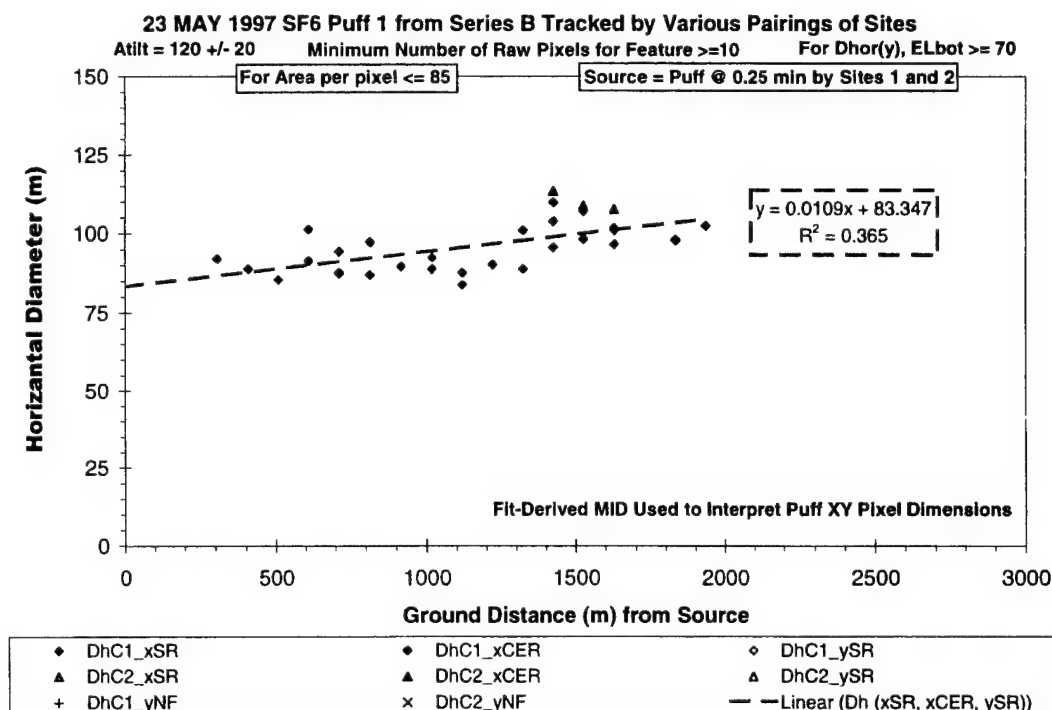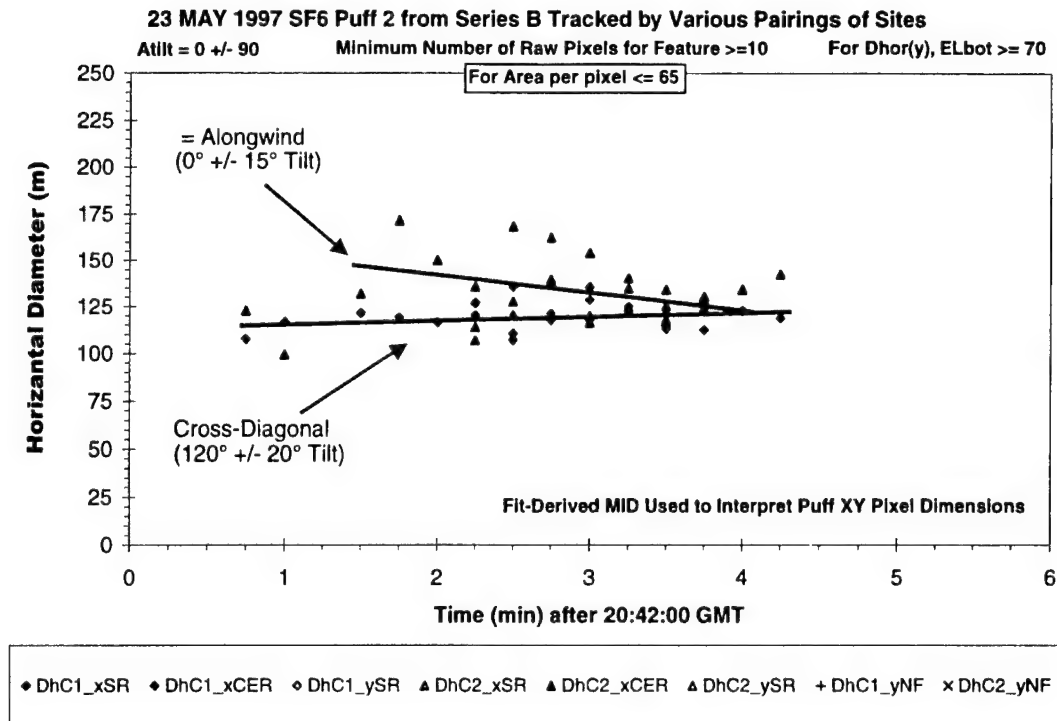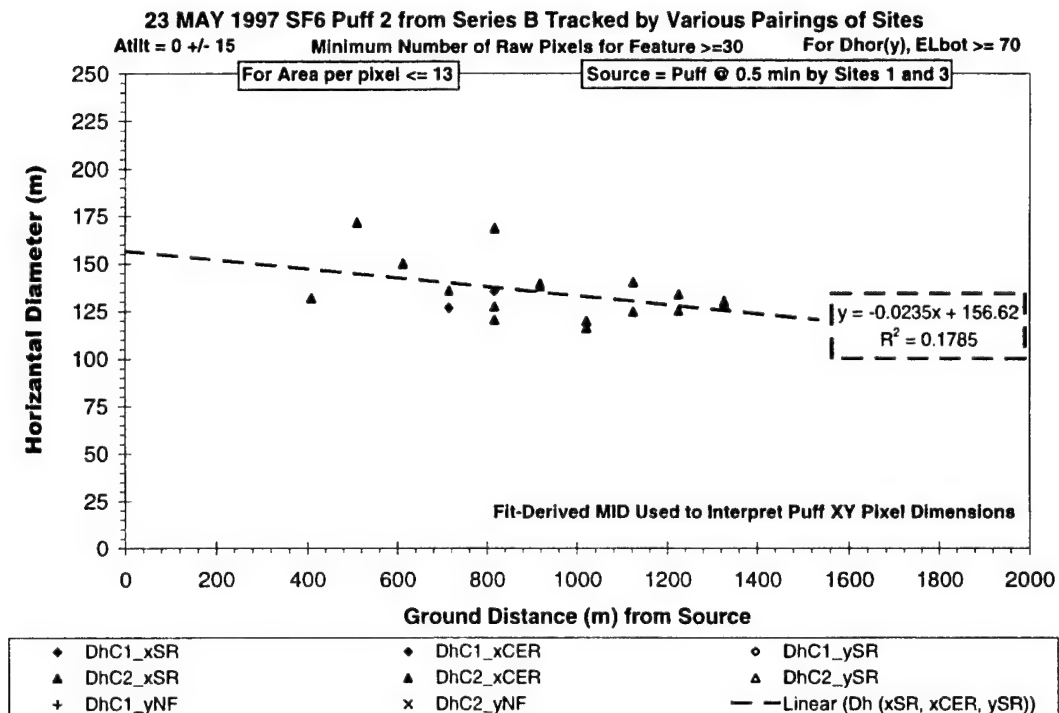Figure I-67. Alongwind extent (Atilt = 0±20) versus distance for SFP3 (23 May 1997).
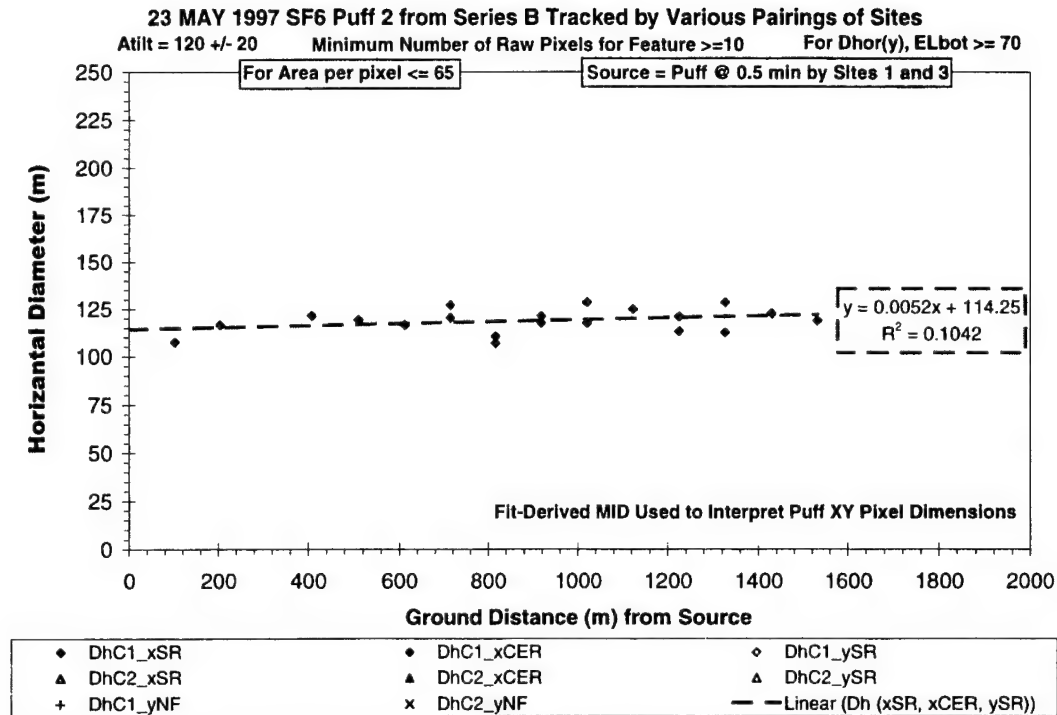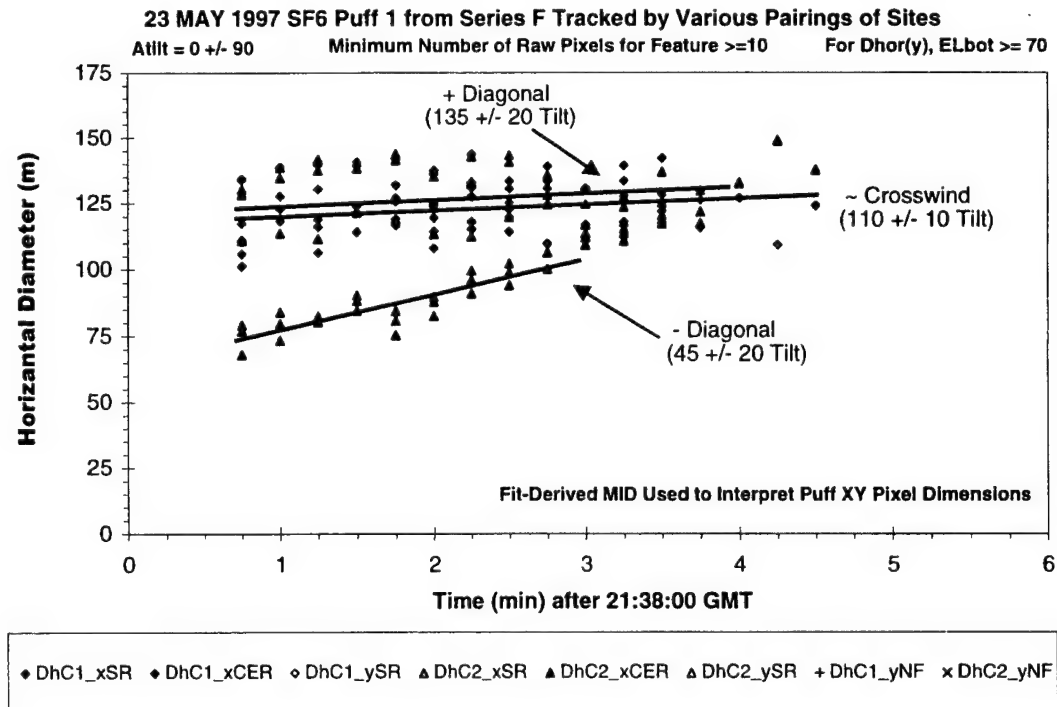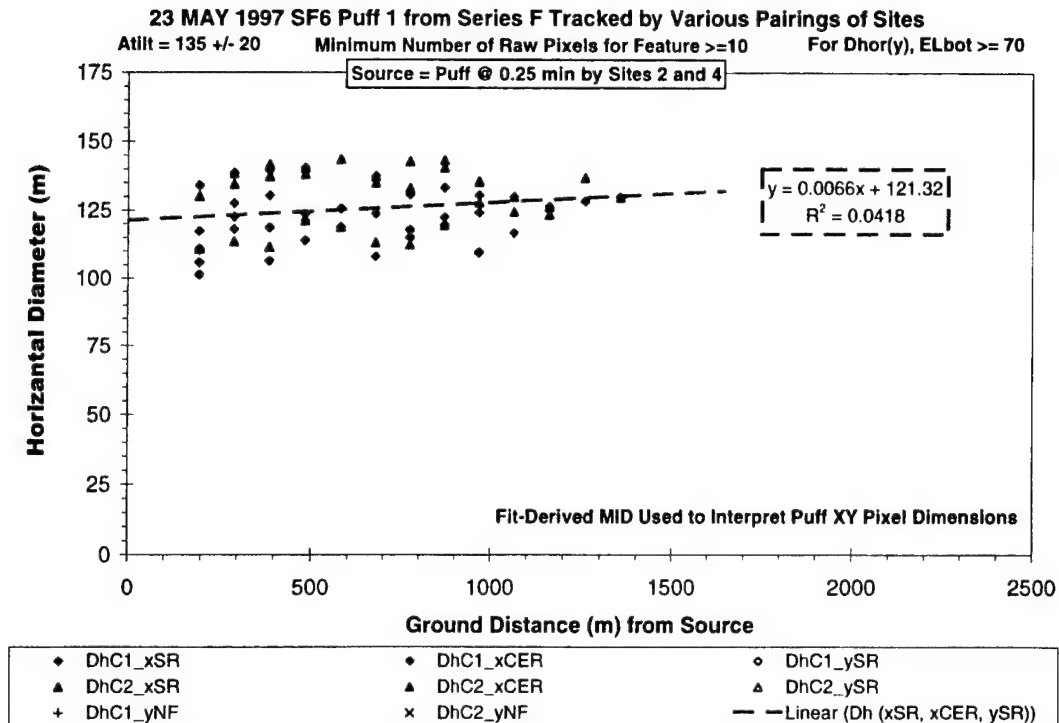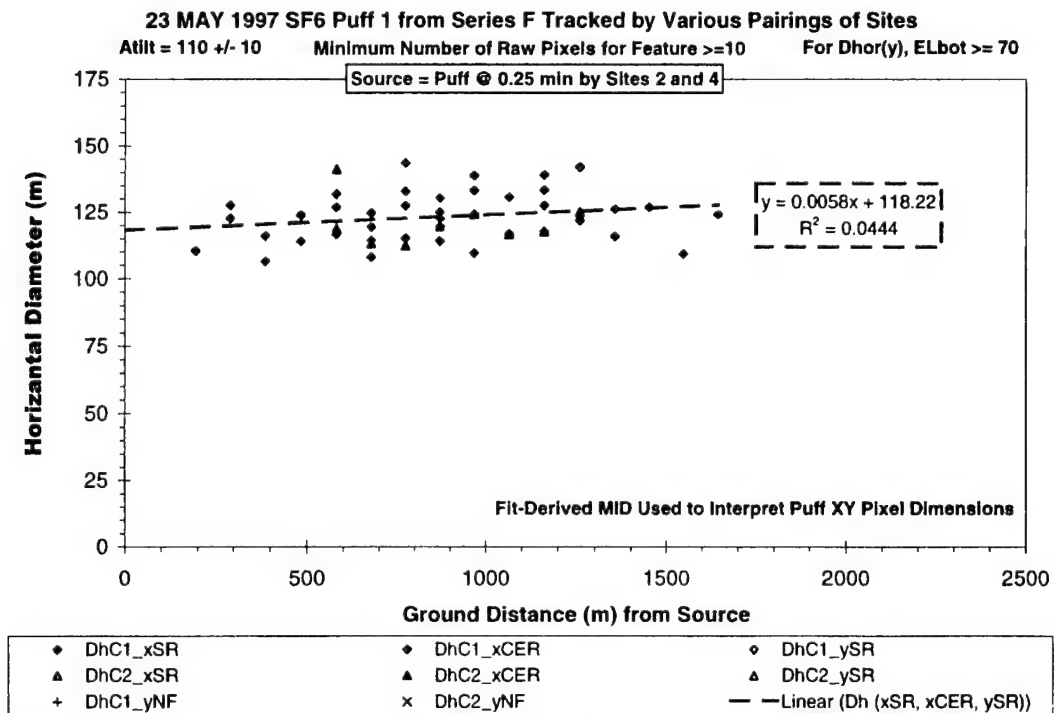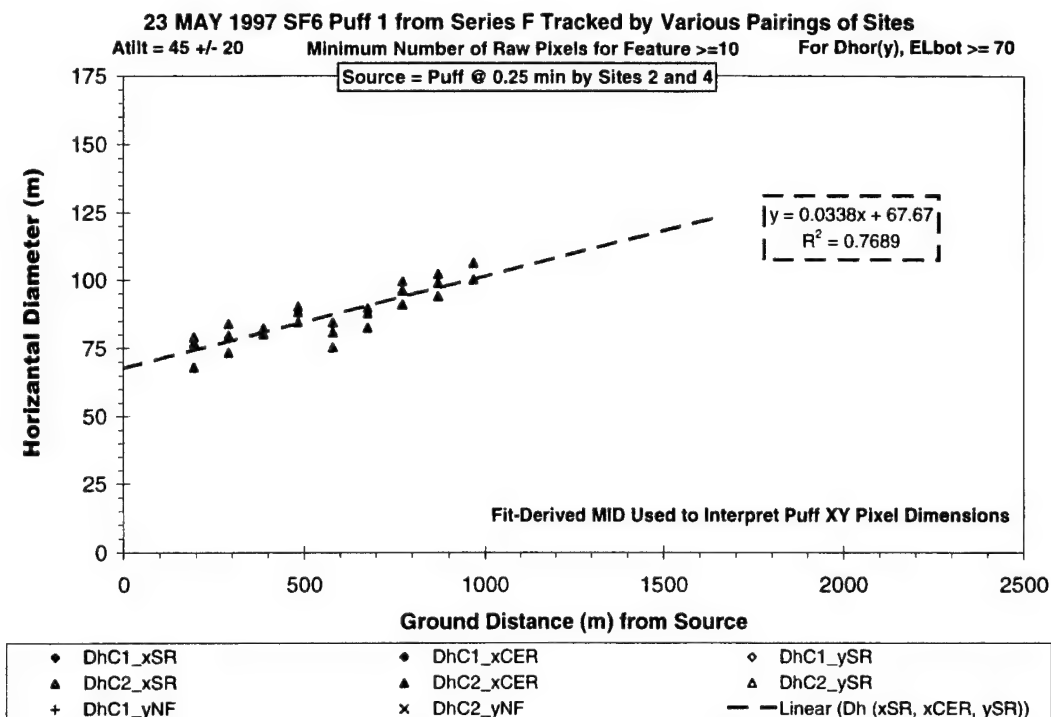
200

23 MAY 1997 SF6 Puff 3 from Series F Tracked by Various Pairings of Sites

Atilt = 135 +/- 10   Minimum Number of Raw Pixels for Feature >=10   For Dhor(y), ELbot >= 70

For Area per pixel <= 110   Source = Puff @ 0.5 min by Sites 1 and 2

y = 0.0069x + 98.308
R² = 0.0458

Fit-Derived MID Used to Interpret Puff XY Pixel Dimensions

●	DhC1_xSR	●	DhC1_xCER	◇	DhC1_ySR
▲	DhC2_xSR	▲	DhC2_xCER	△	DhC2_ySR
+	DhC1_yNF	×	DhC2_yNF	— —	Linear (Dh (xSR, xCER, ySR))

Figure I-68. + Diagonal extent (Atilt = 135±10) versus distance for SFP3 (23 May 1997).

23 MAY 1997 SF6 Puff 3 from Series F Tracked by Various Pairings of Sites

Atilt = 115 +/- 10   Minimum Number of Raw Pixels for Feature >=10   For Dhor(y), ELbot >= 70

For Area per pixel <= 110   Source = Puff @ 0.5 min by Sites 1 and 2

y = 0.001x + 97.319
R² = 0.0019

Fit-Derived MID Used to Interpret Puff XY Pixel Dimensions

●	DhC1_xSR	●	DhC1_xCER	◇	DhC1_ySR
▲	DhC2_xSR	▲	DhC2_xCER	△	DhC2_ySR
+	DhC1_yNF	×	DhC2_yNF	— —	Linear (Dh (xSR, xCER, ySR))

Figure I-69. Crosswind extent (Atilt = 115±10) versus distance for SFP3 (23 May 1997).

23 MAY 1997 SF6 Puff 3 from Series F Tracked by Various Pairings of Sites

Atilt = 50 +/- 10   Minimum Number of Raw Pixels for Feature >=15   For Dhor(y), ELbot >= 70

For Area per pixel <= 25   Source = Puff @ 0.5 min by Sites 1 and 2

$y = 0.0411x + 79.278$
$R^2 = 0.8279$

Fit-Derived MID Used to Interpret Puff XY Pixel Dimensions

Horizantal Diameter (m)

Ground Distance (m) from Source

◆ DhC1_xSR	◆ DhC1_xCER	○ DhC1_ySR
▲ DhC2_xSR	▲ DhC2_xCER	△ DhC2_ySR
+ DhC1_yNF	× DhC2_yNF	— — Linear (Dh (xSR, xCER, ySR))

Figure I-70. - Diagonal extent (Atilt = 50±10) versus distance for SFP3 (23 May 1997).

23 MAY 1997 SF6 Puff 1 from Series G Tracked by Various Pairings of Sites

Atilt = 0 +/- 90   Minimum Number of Raw Pixels for Feature >=8   For Dhor(y), ELbot >= 70

For Area per pixel <= 110

+ Diagonal
(135 +/- 10 Tilt)

~ Crosswind
(110+/-10 Tilt)

~ Alongwind
(0+/-40 Tilt)

- Diagonal
(45 +/- 20 Tilt)

Fit-Derived MID Used to Interpret Puff XY Pixel Dimensions

Horizantal Diameter (m)

Time (min) after 21:42:00 GMT

◆ DhC1_xSR ◆ DhC1_xCER ◇ DhC1_ySR ▲ DhC2_xSR ▲ DhC2_xCER △ DhC2_ySR + DhC1_yNF × DhC2_yNF
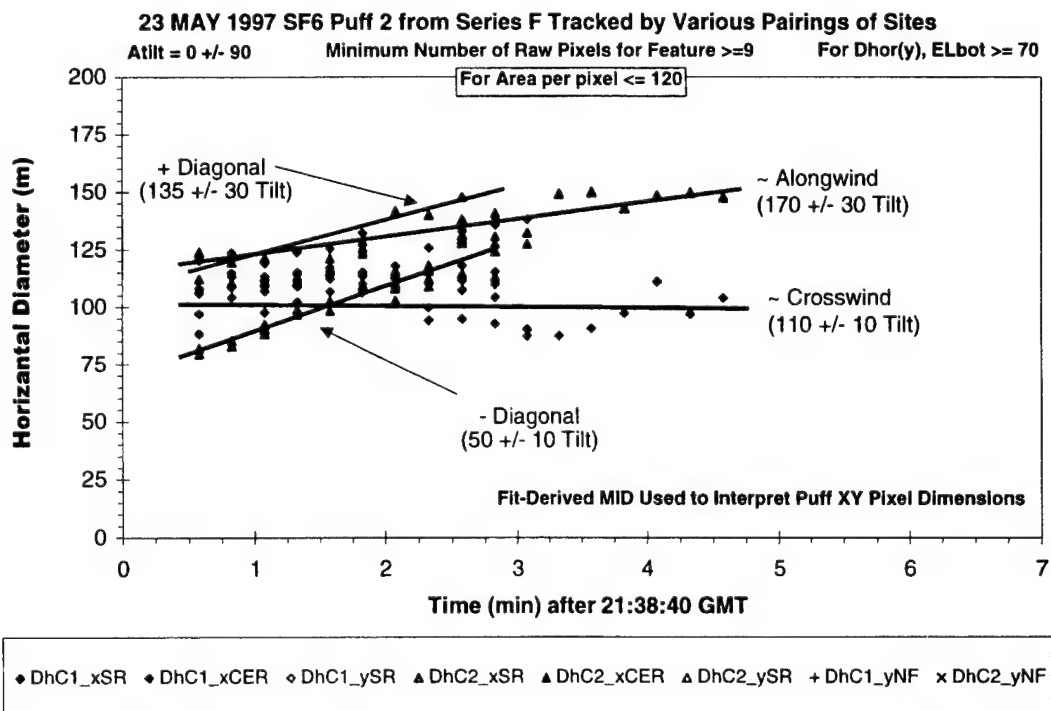
Figure I-71. Summary dimension plot showing all perspectives of SGP1 (23 May 1997).
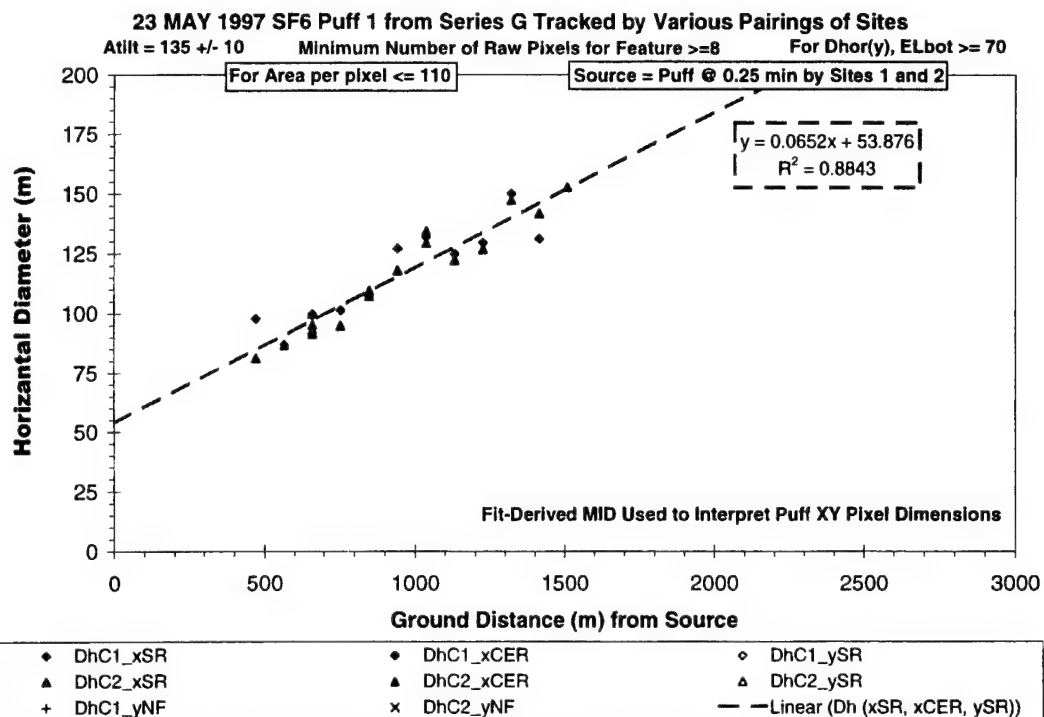
Figure I-72. + Diagonal extent (Atilt = 135±10) versus distance for SGP1 (23 May 1997).
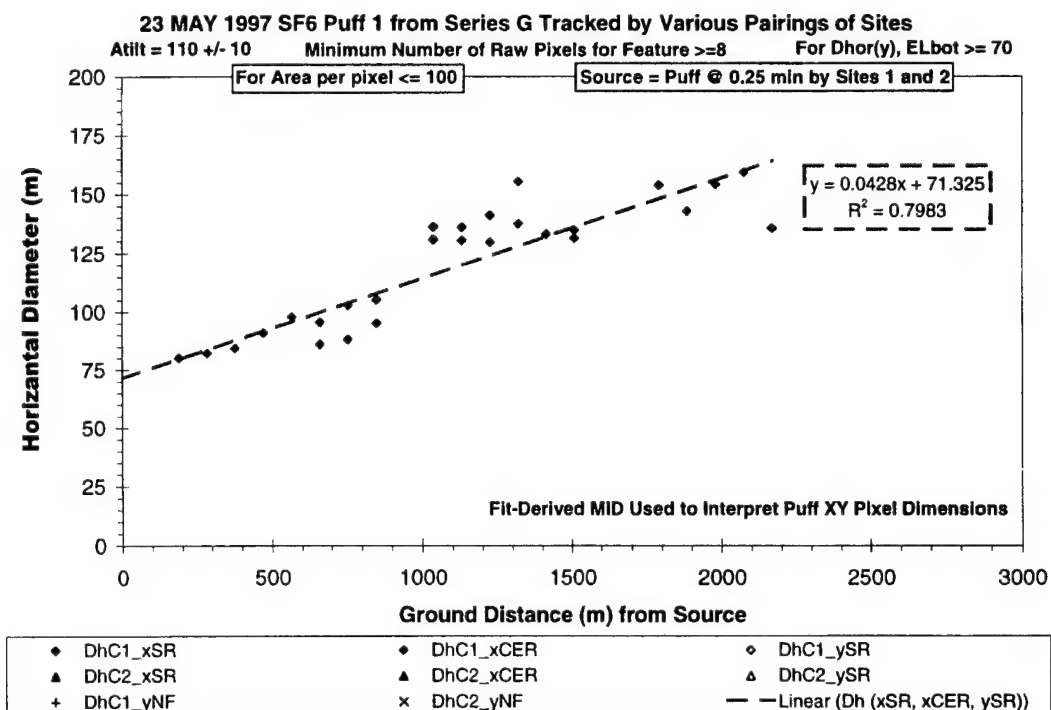
Figure I-73. Crosswind extent (Atilt = 110±10) versus distance for SGP1 (23 May 1997).
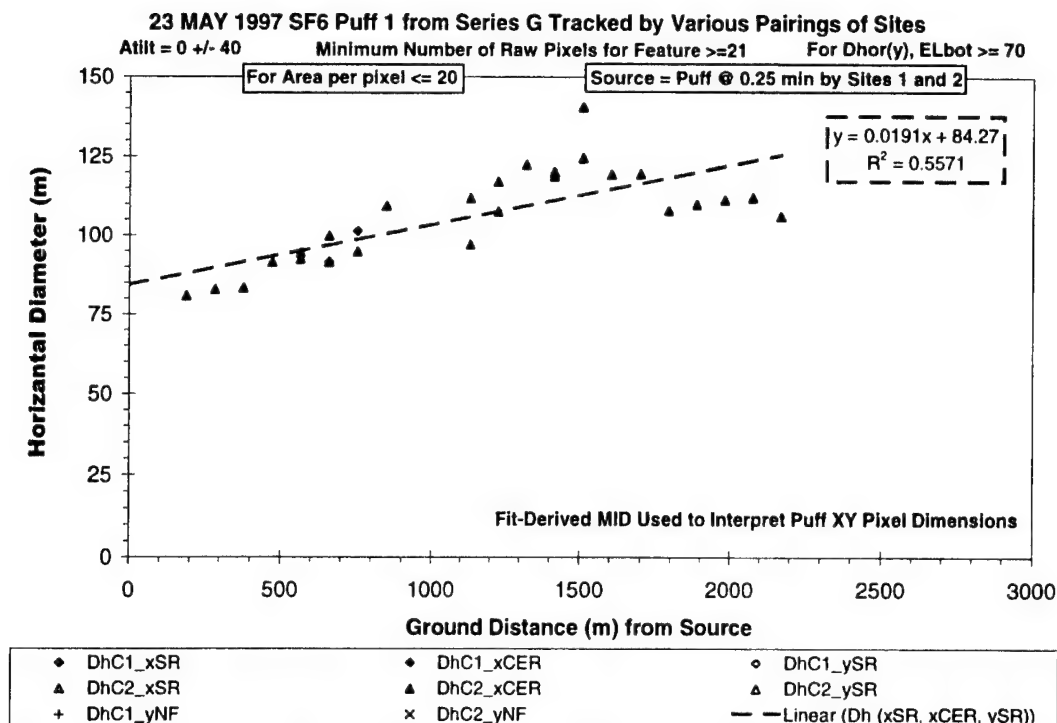
Figure I-74. Alongwind extent (Atilt = 0±40) versus distance for SGP1 (23 May 1997).
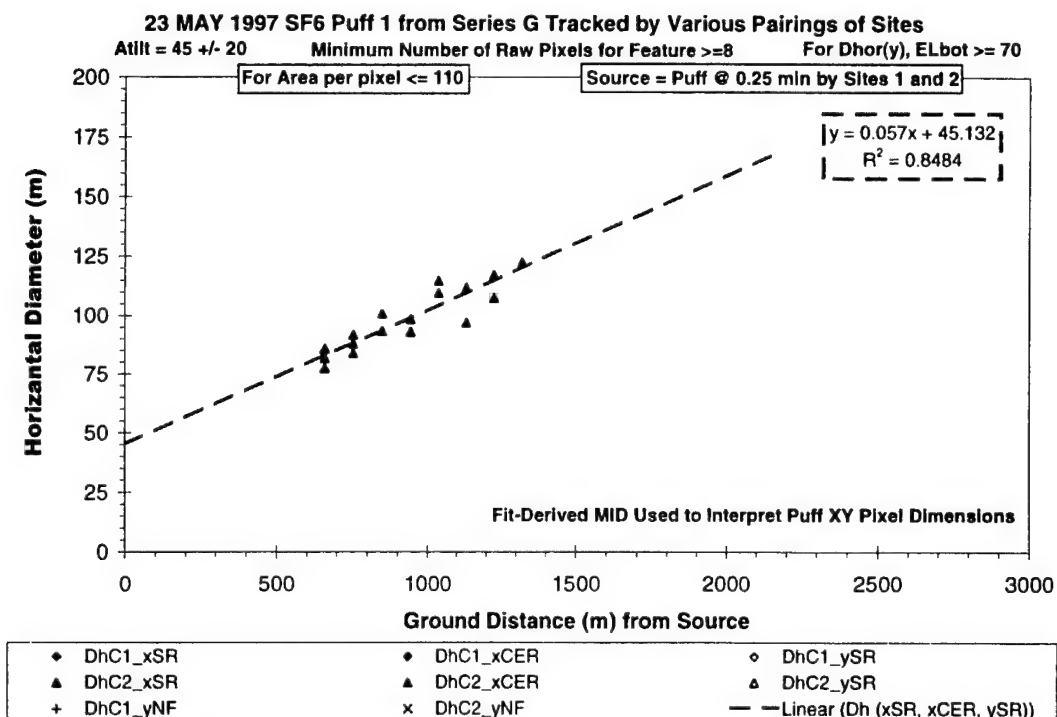
Figure I-75. - Diagonal extent (Atilt = 45±20) versus distance for SGP1 (23 May 1997).

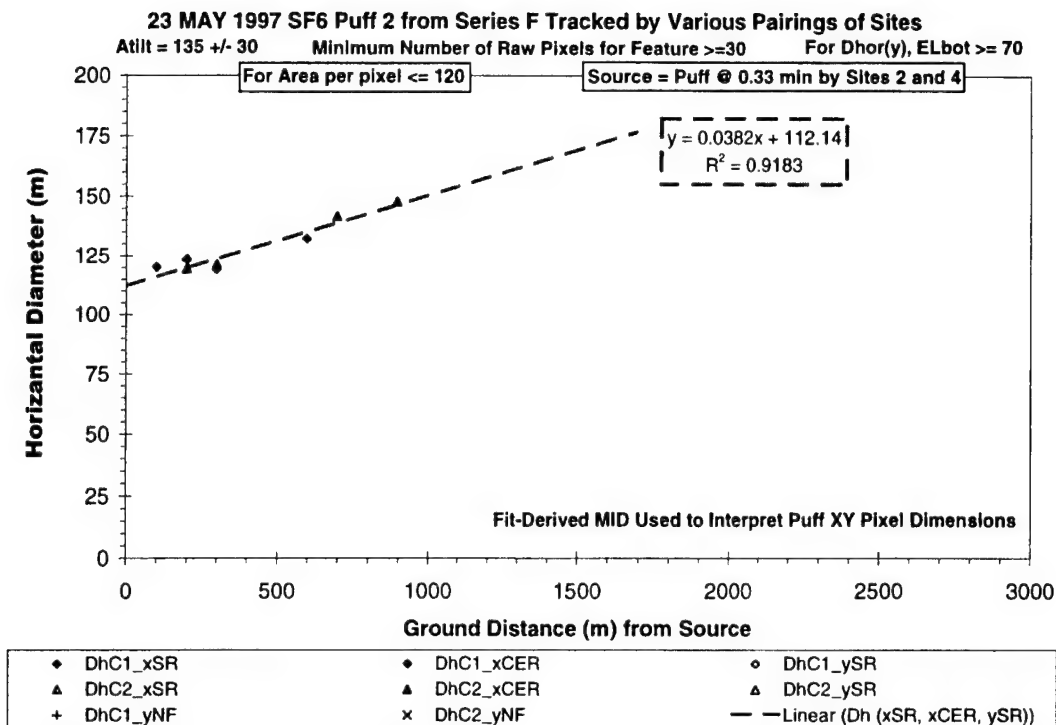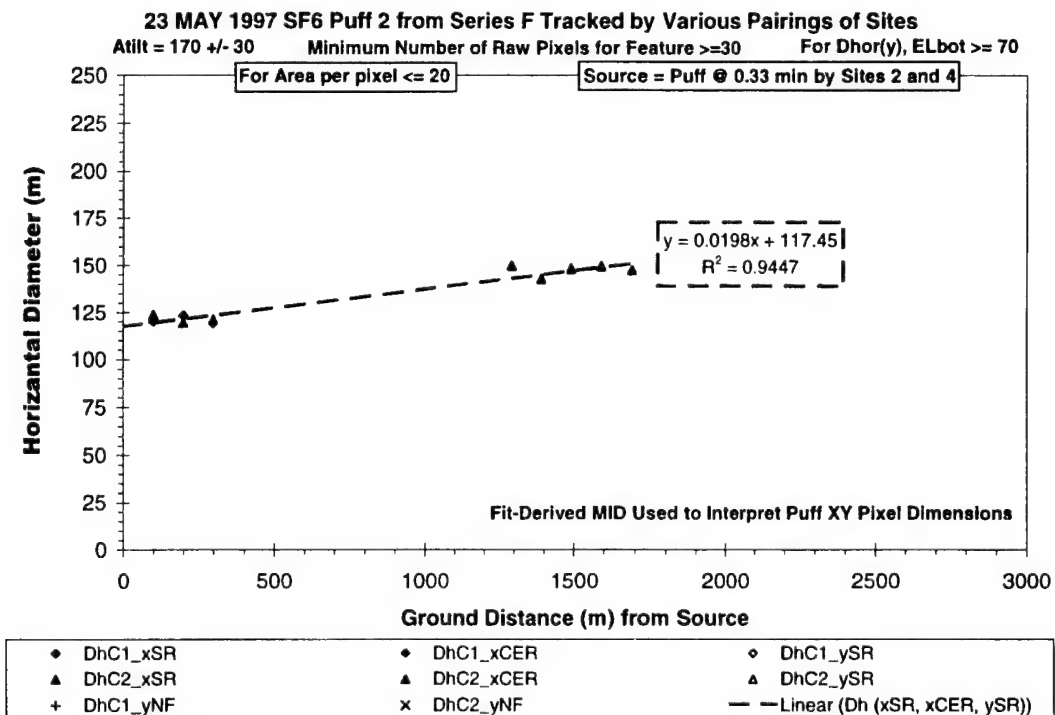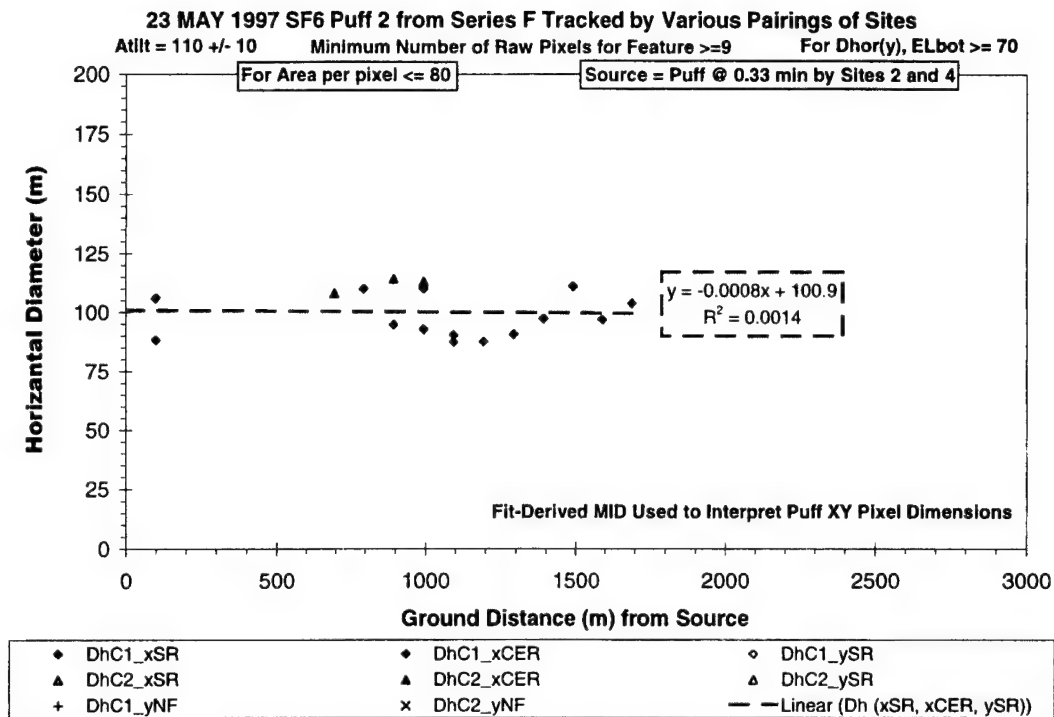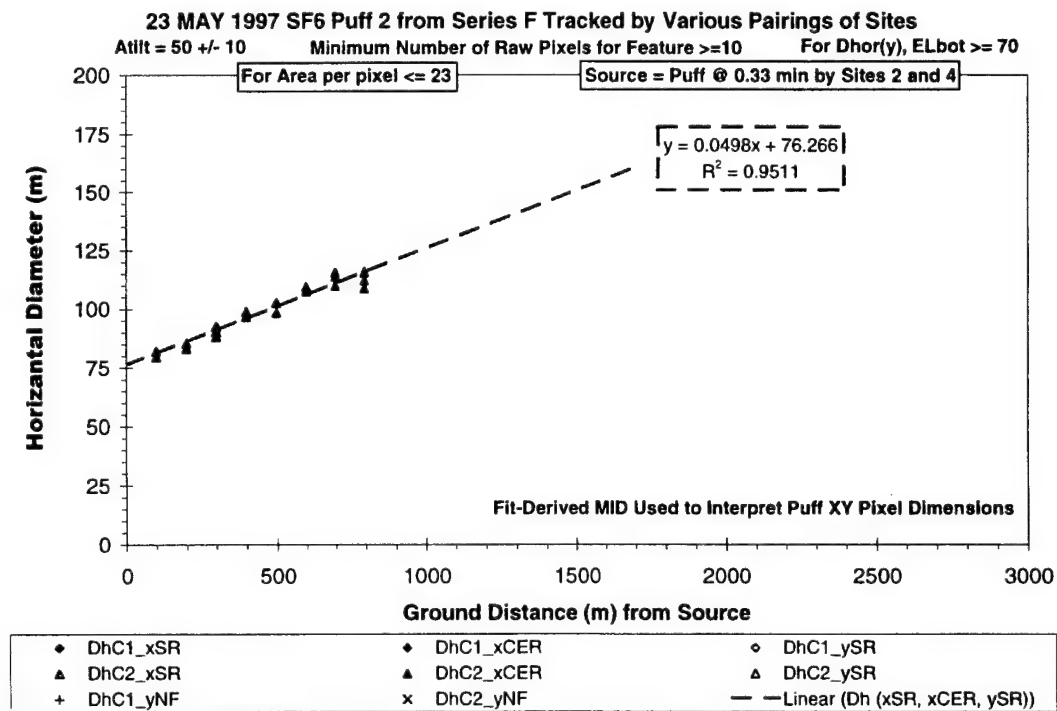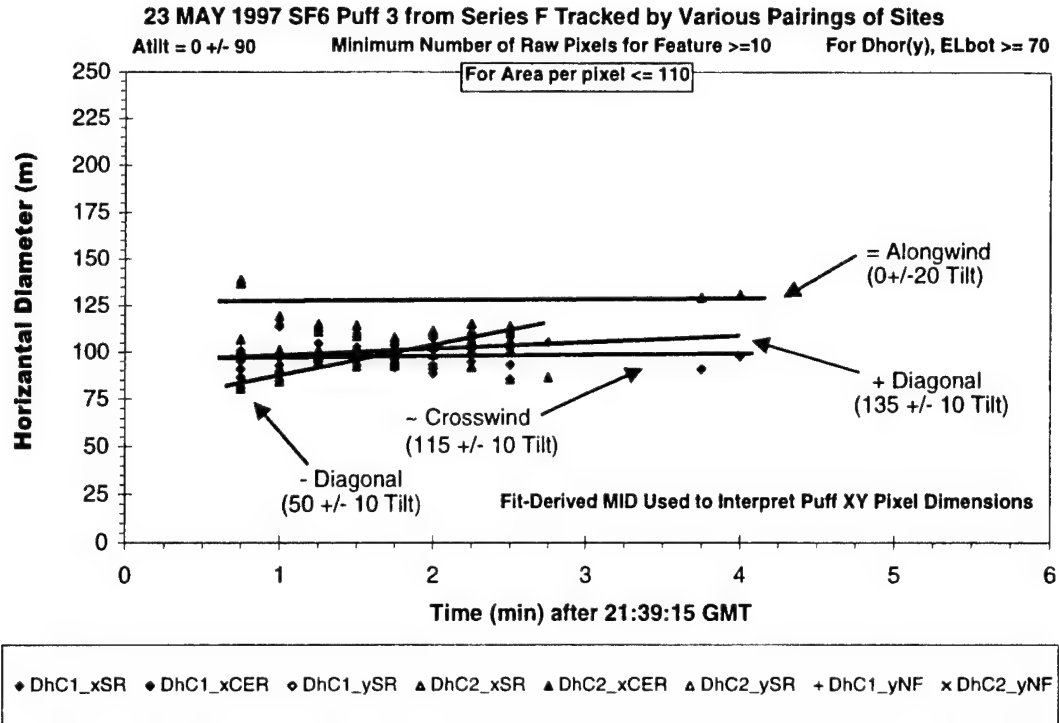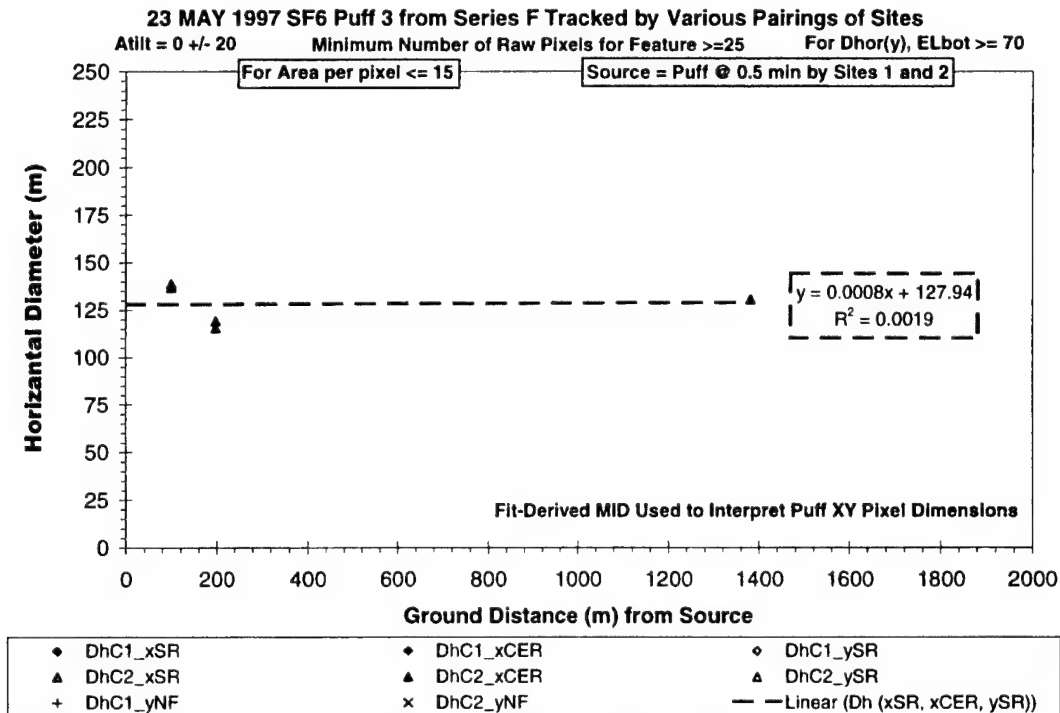Figure I-76. Summary dimension plot showing all perspectives of SGP2 (23 May 1997).

Figure I-77. - Diagonal extent (Atilt = 45±20) versus distance for SGP2 (23 May 1997).
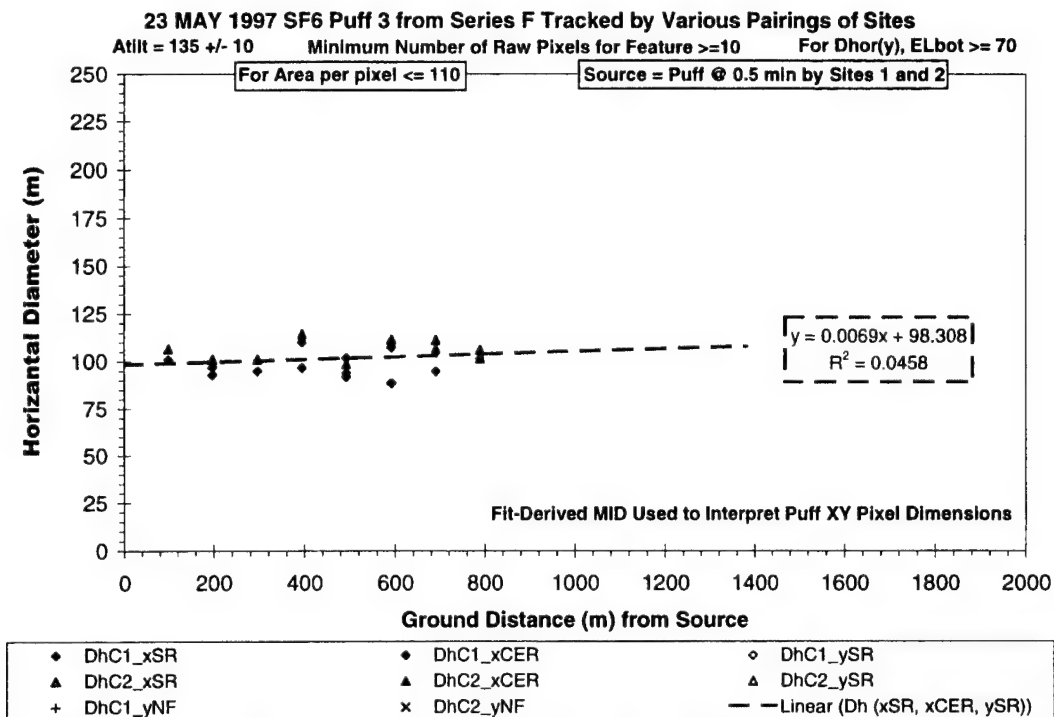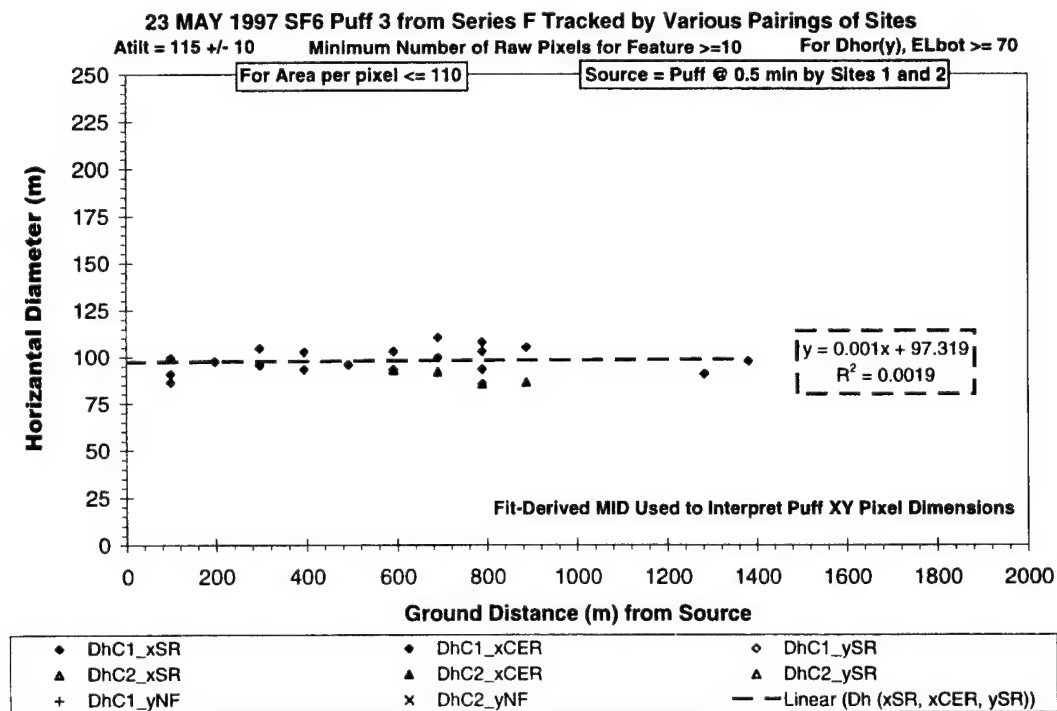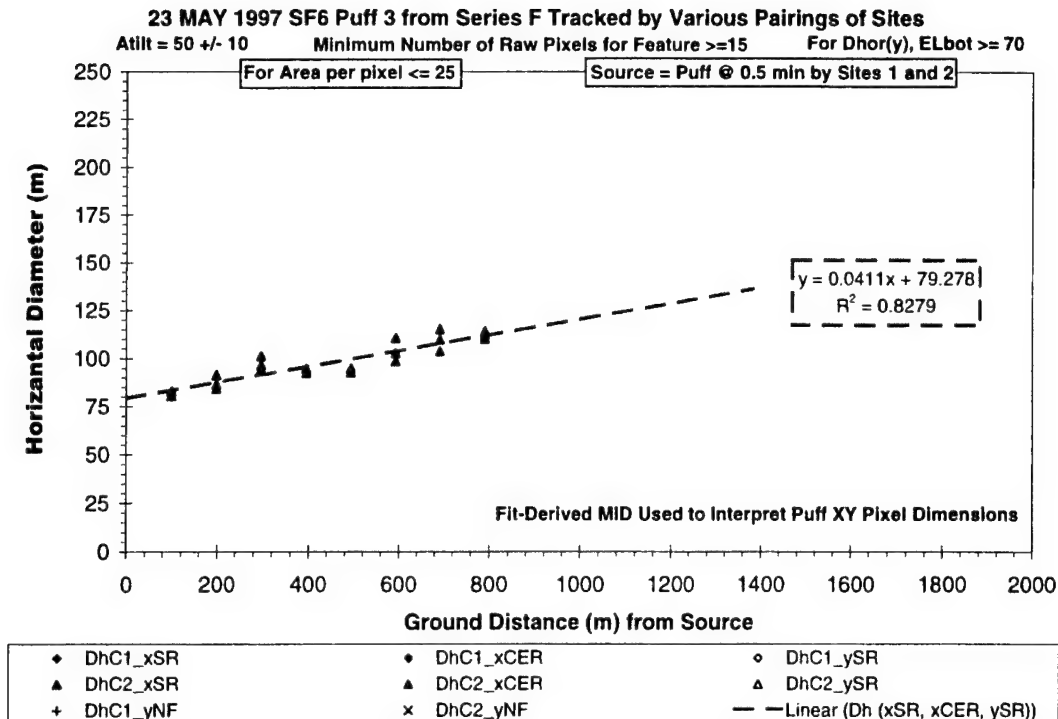
205

23 MAY 1997 SF6 Puff 2 from Series G Tracked by Various Pairings of Sites

Atilt = 0 +/- 25   Minimum Number of Raw Pixels for Feature >=20   For Dhor(y), ELbot >= 70

Figure I-78. Alongwind extent (Atilt = 0±25) versus distance for SGP2 (23 May 1997).

23 MAY 1997 SF6 Puff 2 from Series G Tracked by Various Pairings of Sites

Atilt = 135 +/- 20   Minimum Number of Raw Pixels for Feature >=10   For Dhor(y), ELbot >= 70

Figure I-79. + Diagonal extent (Atilt = 135±20) versus distance for SGP2 (23 May 1997).

23 MAY 1997 SF6 Puff 2 from Series G Tracked by Various Pairings of Sites

Atilt = 110 +/- 20   Minimum Number of Raw Pixels for Feature >=20   For Dhor(y), ELbot >= 70

For Area per pixel <= 45   Source = Puff @ 0.5 min by Sites 1 and 3

$y = 0.0324x + 79.815$
$R^2 = 0.8383$

Fit-Derived MID Used to Interpret Puff XY Pixel Dimensions

Horizantal Diameter (m)

Ground Distance (m) from Source

◆ DhC1_xSR	◆ DhC1_xCER	◇ DhC1_ySR
▲ DhC2_xSR	▲ DhC2_xCER	△ DhC2_ySR
+ DhC1_yNF	× DhC2_yNF	— — Linear (Dh (xSR, xCER, ySR))

Figure I-80. Crosswind extent (Atilt = 110±20) versus distance for SGP2 (23 May 1997).

23 MAY 1997 SF6 Puff 3 from Series G Tracked by Various Pairings of Sites

Atilt = 0 +/- 90   Minimum Number of Raw Pixels for Feature >=12   For Dhor(y), ELbot >= 70

For Area per pixel <= 94

Along-Diagonal
(30° +/- 20° Tilt)

+ Diagonal
(135° +/- 10° Tilt)

~ Crosswind
(110° +/- 20° Tilt)

- Diagonal
(45° +/- 15° Tilt)

Fit-Derived MID Used to Interpret Puff XY Pixel Dimensions

Horizantal Diameter (m)

Time (min) after 21:43:15 GMT

◆ DhC1_xSR ◆ DhC1_xCER ◇ DhC1_ySR ▲ DhC2_xSR ▲ DhC2_xCER △ DhC2_ySR + DhC1_yNF × DhC2_yNF

Figure I-81. Summary dimension plot showing all perspectives of SGP3 (23 May 1997).

23 MAY 1997 SF6 Puff 3 from Series G Tracked by Various Pairings of Sites

Atilt = 30 +/- 20   Minimum Number of Raw Pixels for Feature >=25   For Dhor(y), ELbot >= 70

For Area per pixel <= 14   Source = Puff @ 0.5 min by Sites 1 and 2

y = 0.1225x + 72.804
R² = 0.885

Fit-Derived MID Used to Interpret Puff XY Pixel Dimensions

Horizantal Diameter (m) — Ground Distance (m) from Source

	DhC1_xSR		DhC1_xCER		DhC1_ySR
▲	DhC2_xSR	▲	DhC2_xCER	△	DhC2_ySR
+	DhC1_yNF	×	DhC2_yNF	— —	Linear (Dh (xSR, xCER, ySR))

Figure I-82. Along-Diagonal extent (Atilt= 30±20) versus distance for SGP3 (23 May 1997).

23 MAY 1997 SF6 Puff 3 from Series G Tracked by Various Pairings of Sites

Atilt = 135 +/- 10   Minimum Number of Raw Pixels for Feature >=20   For Dhor(y), ELbot >= 70

For Area per pixel <= 30   Source = Puff @ 0.5 min by Sites 1 and 2

y = 0.0633x + 78.944
R² = 0.943

Fit-Derived MID Used to Interpret Puff XY Pixel Dimensions

Horizantal Diameter (m) — Ground Distance (m) from Source

	DhC1_xSR		DhC1_xCER		DhC1_ySR
▲	DhC2_xSR	▲	DhC2_xCER	△	DhC2_ySR
+	DhC1_yNF	×	DhC2_yNF	— —	Linear (Dh (xSR, xCER, ySR))

Figure I-83. + Diagonal extent (Atilt = 135±10) versus distance for SGP3 (23 May 1997).

208

Figure I-84. Crosswind extent (Atilt = 110±20) versus distance for SGP3 (23 May 1997).

Figure I-85. - Diagonal extent (Atilt = 45±15) versus distance for SGP3 (23 May 1997).
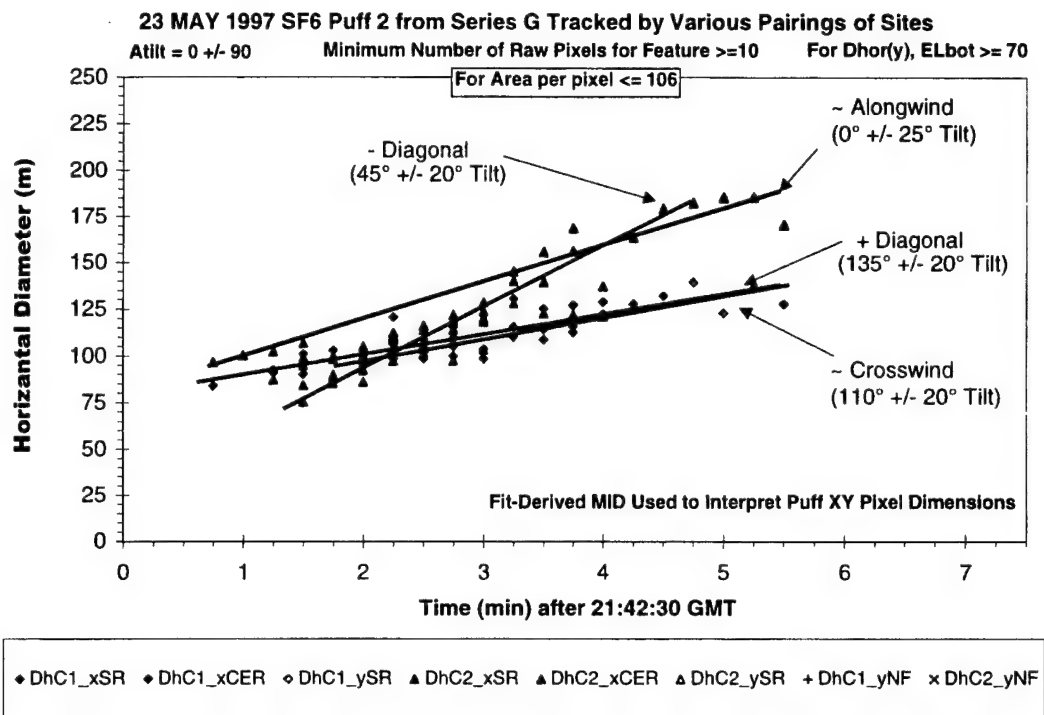
209

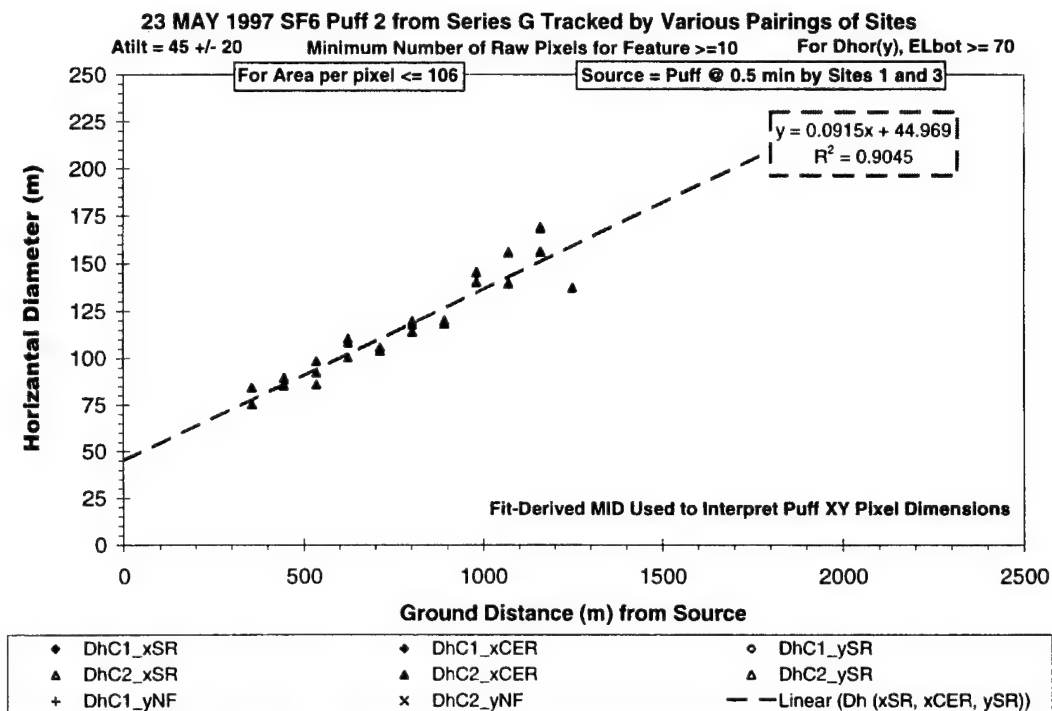Figure I-86. Summary dimension plot showing all perspectives of SHP1 (23 May 1997).

Figure I-87. + Diagonal extent (Atilt = 135±10) versus distance for SHP1 (23 May 1997).
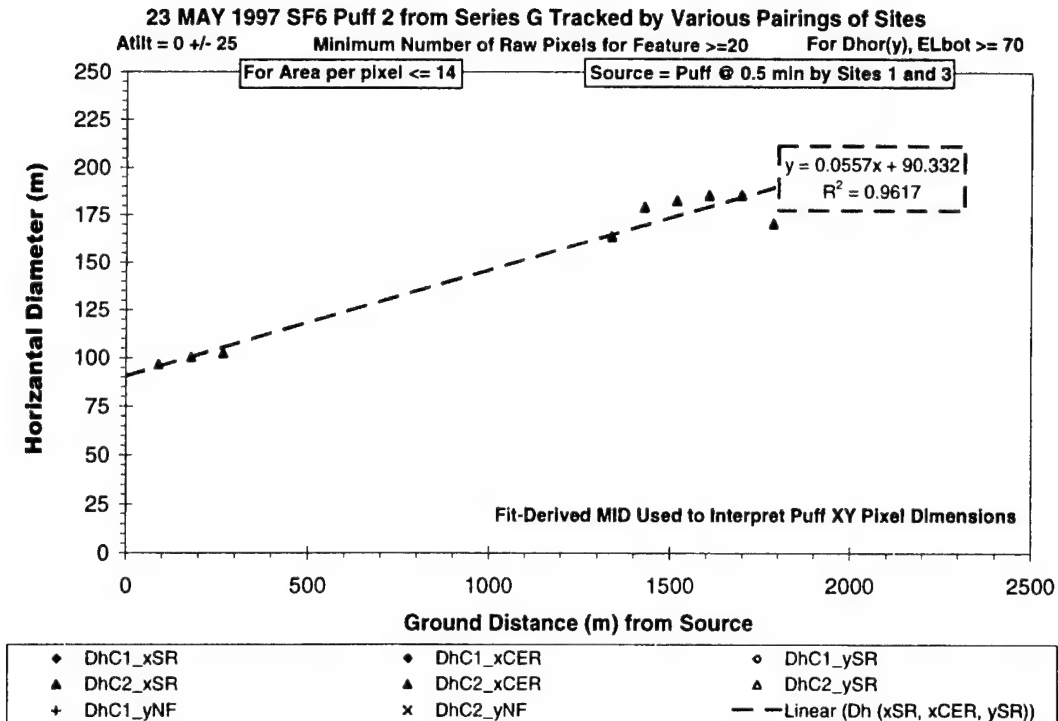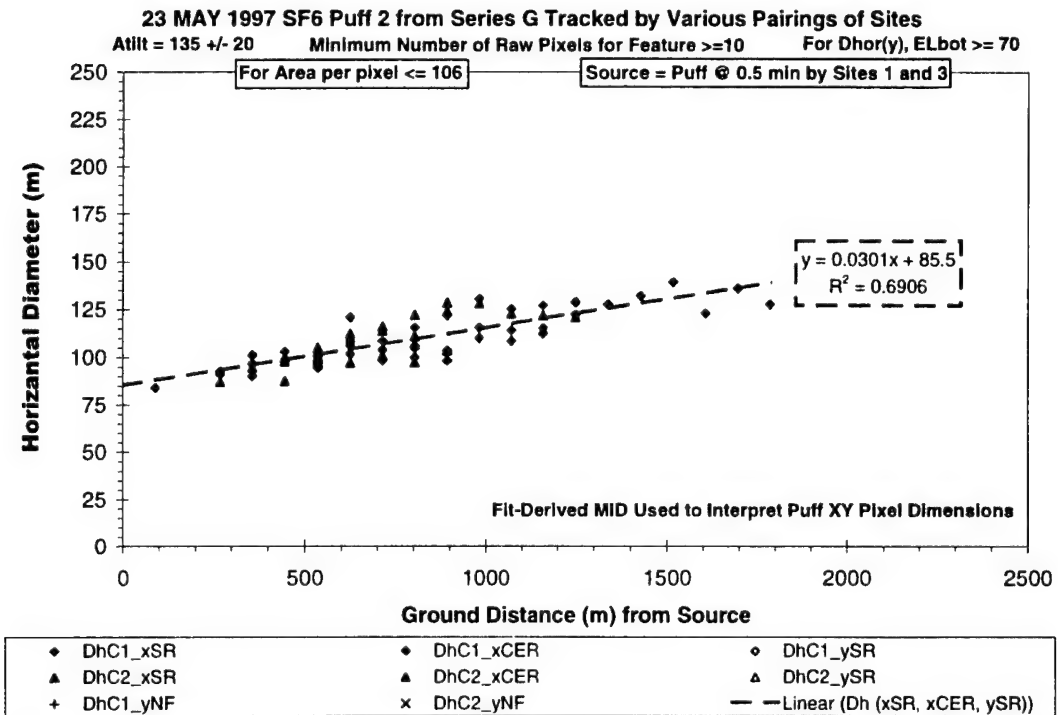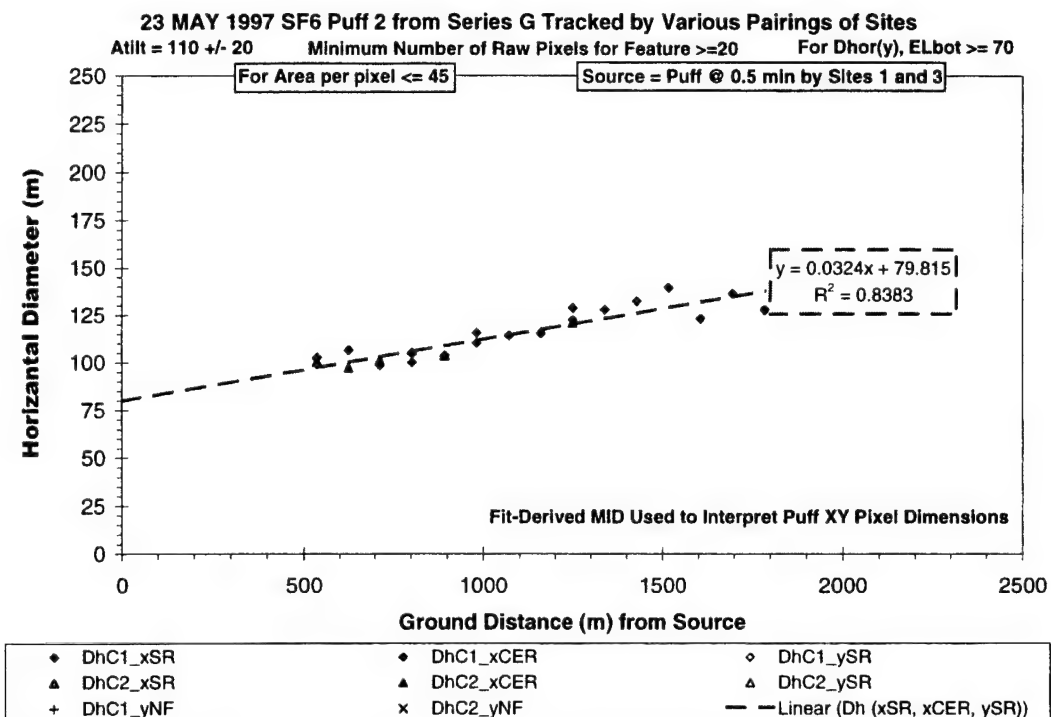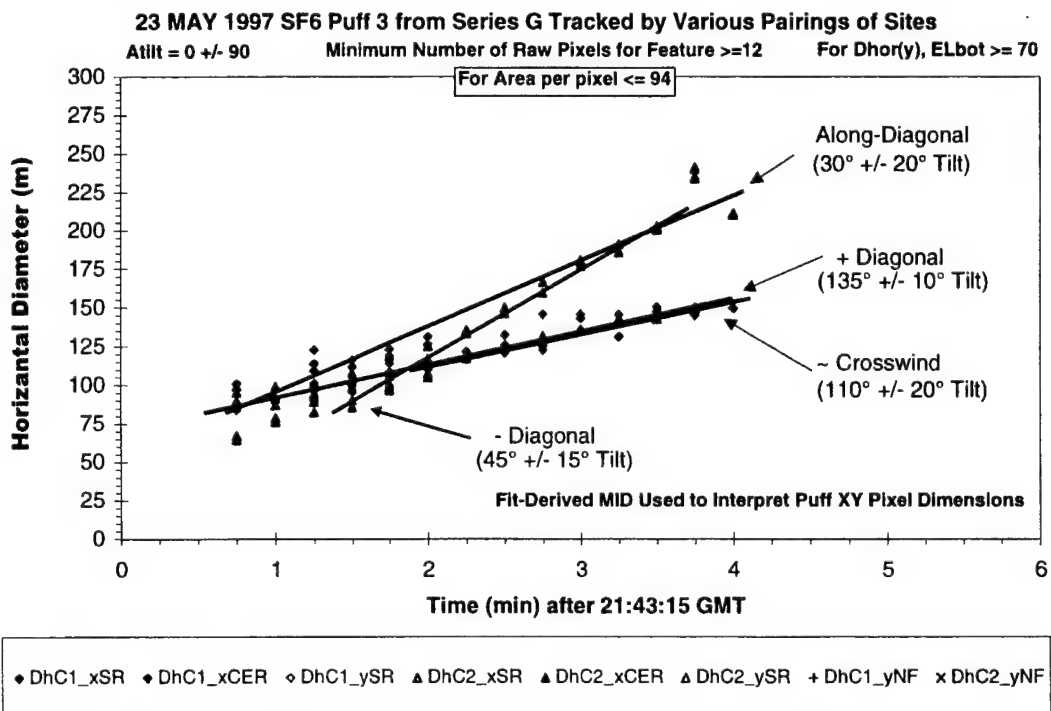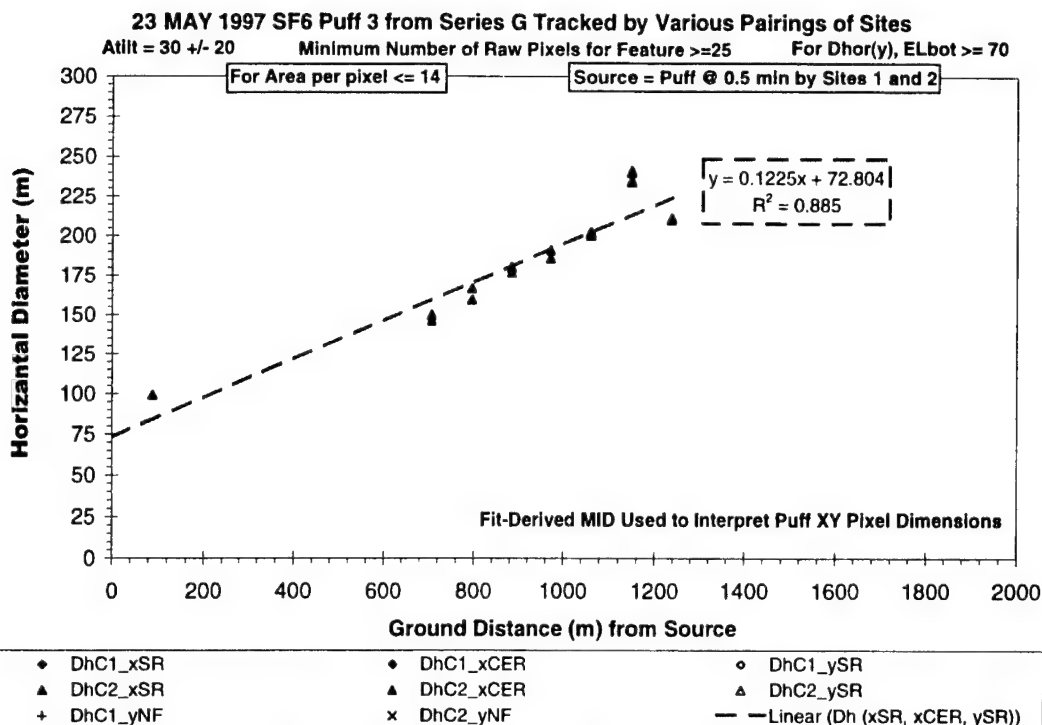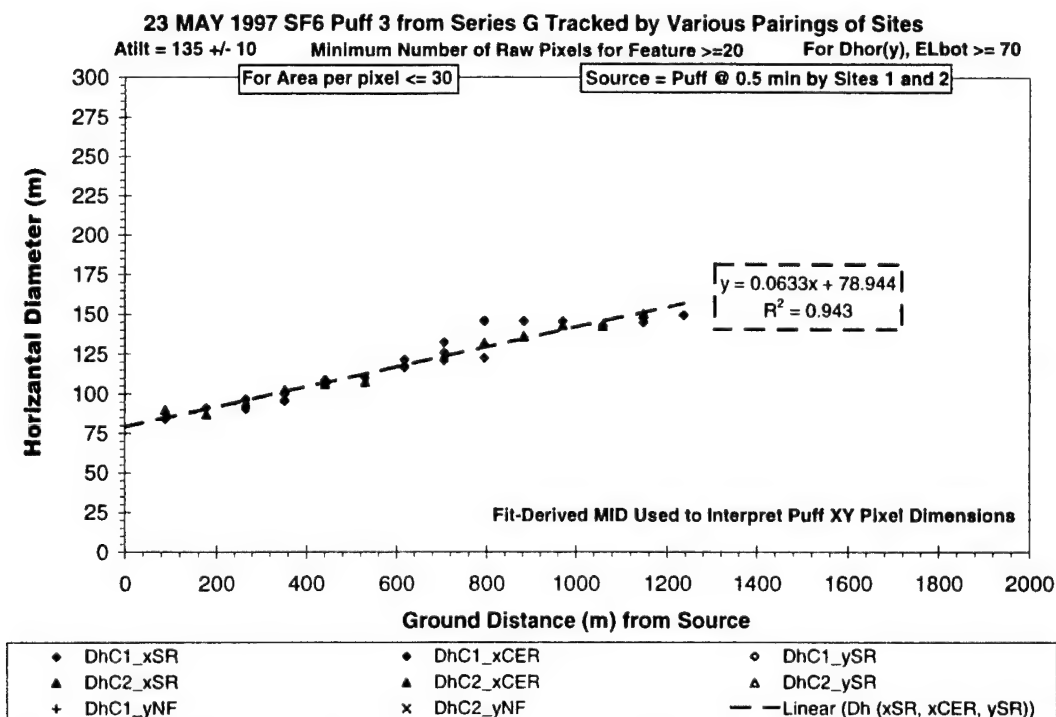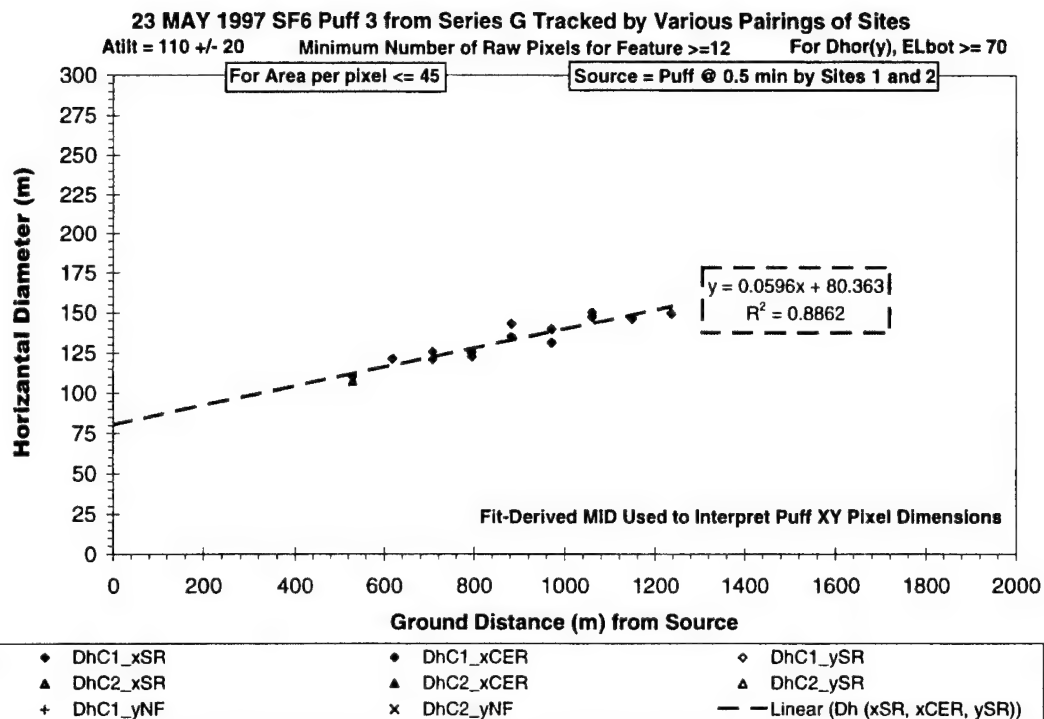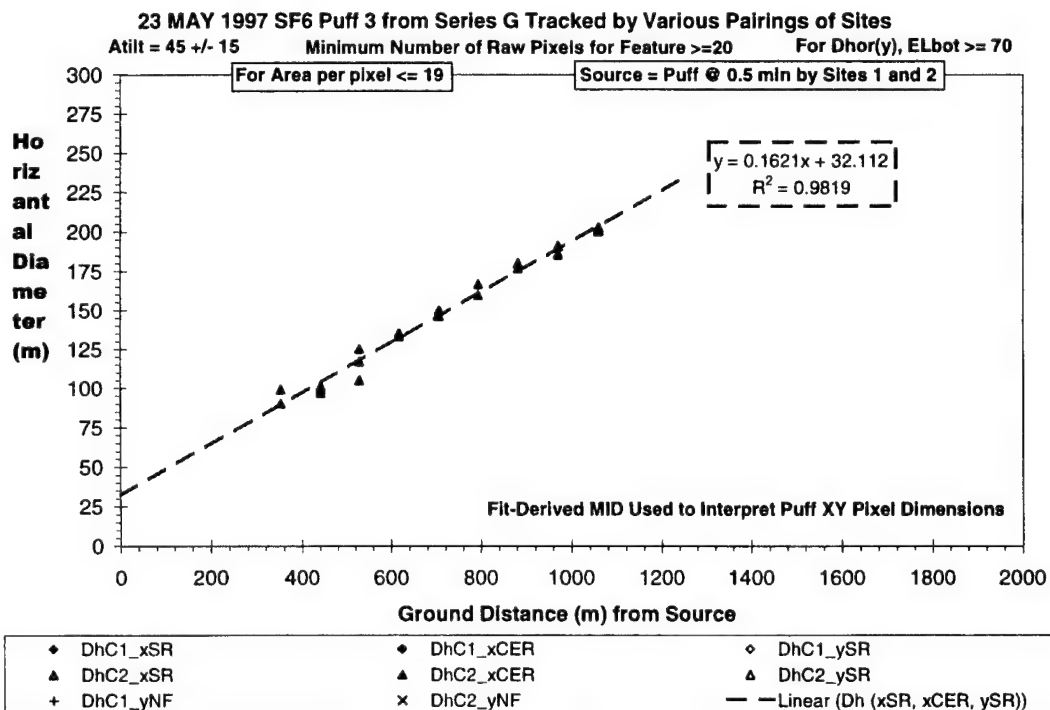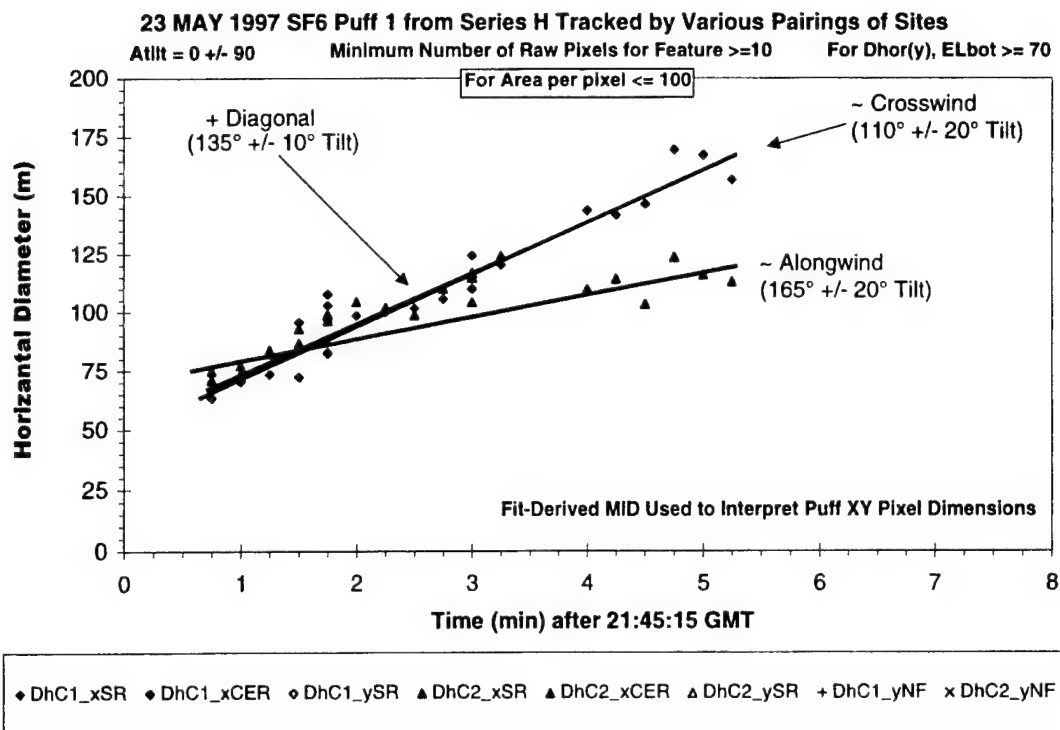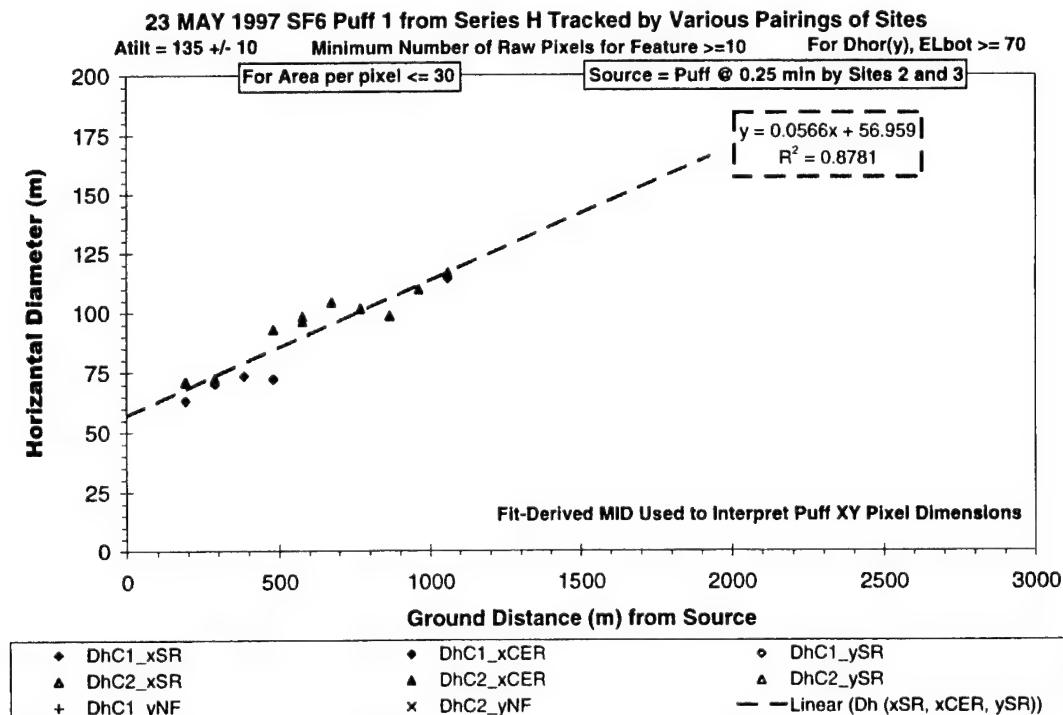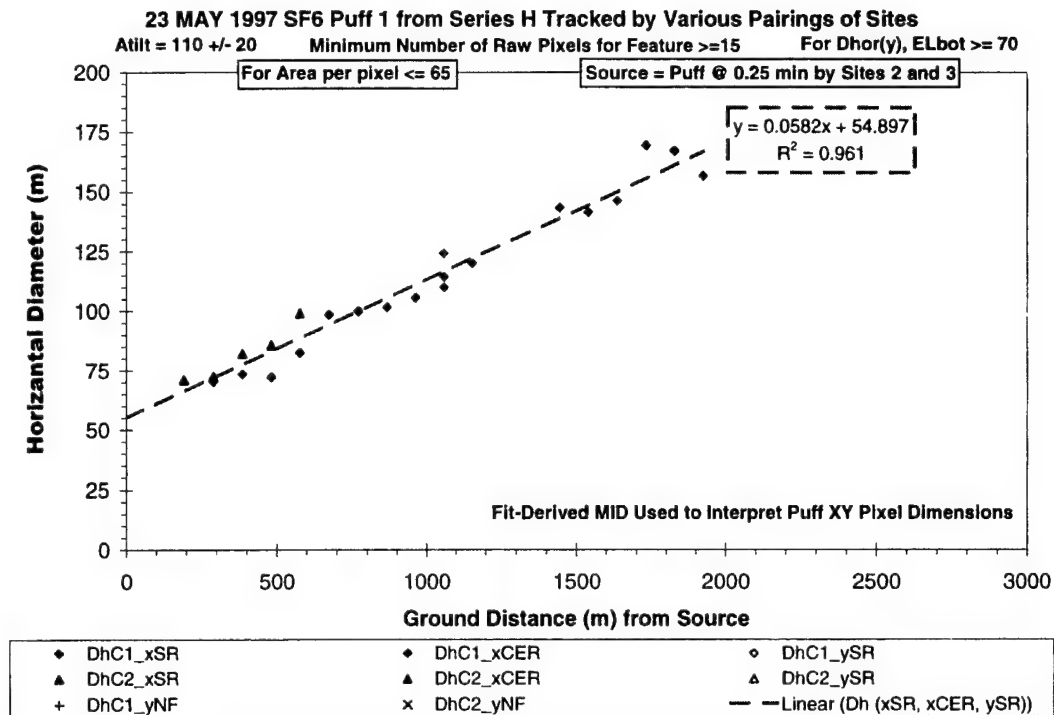
23 MAY 1997 SF6 Puff 1 from Series H Tracked by Various Pairings of Sites

Atilt = 110 +/- 20   Minimum Number of Raw Pixels for Feature >=15   For Dhor(y), ELbot >= 70

For Area per pixel <= 65   Source = Puff @ 0.25 min by Sites 2 and 3

$y = 0.0582x + 54.897$
$R^2 = 0.961$

Fit-Derived MID Used to Interpret Puff XY Pixel Dimensions

◆ DhC1_xSR	◆ DhC1_xCER	○ DhC1_ySR
▲ DhC2_xSR	▲ DhC2_xCER	△ DhC2_ySR
+ DhC1_yNF	✕ DhC2_yNF	— —Linear (Dh (xSR, xCER, ySR))

Figure I-88. Crosswind extent (Atilt = 110±20) versus distance for SHP1 (23 May 1997).

23 MAY 1997 SF6 Puff 1 from Series H Tracked by Various Pairings of Sites

Atilt = 165 +/- 20   Minimum Number of Raw Pixels for Feature >=10   For Dhor(y), ELbot >= 70

For Area per pixel <= 17   Source = Puff @ 0.25 min by Sites 2 and 3

$y = 0.0245x + 71.476$
$R^2 = 0.9291$

Fit-Derived MID Used to Interpret Puff XY Pixel Dimensions

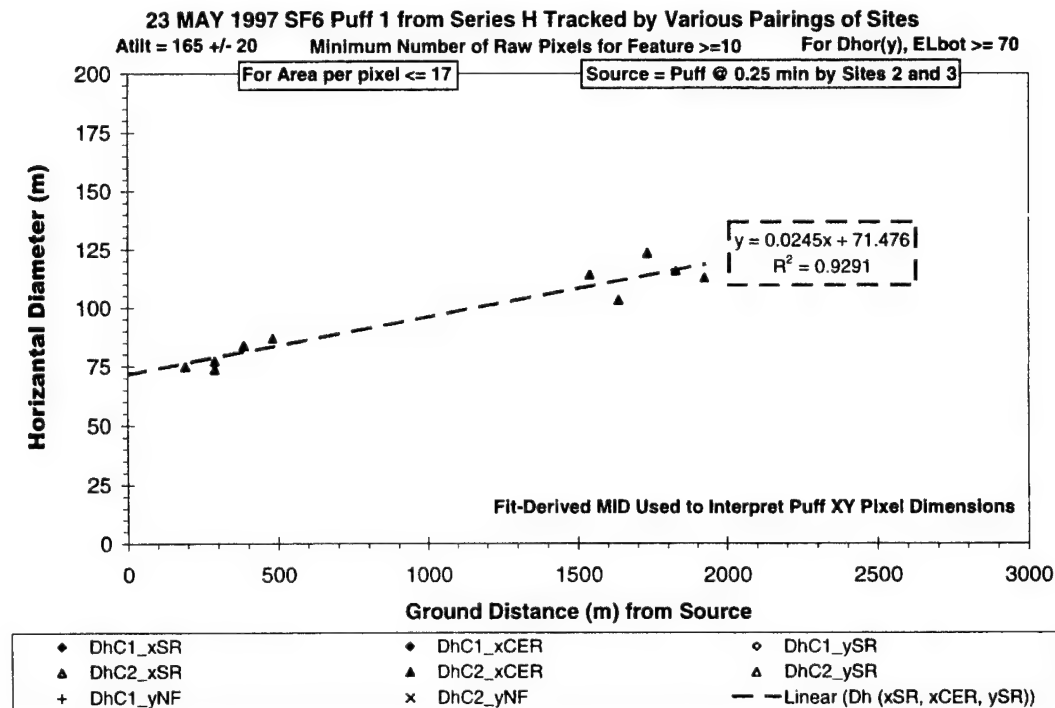| ◆ DhC1_xSR | ◆ DhC1_xCER | ○ DhC1_ySR |
| ▲ DhC2_xSR | ▲ DhC2_xCER | △ DhC2_ySR |
| + DhC1_yNF | ✕ DhC2_yNF | — —Linear (Dh (xSR, xCER, ySR)) |

Figure I-89. Alongwind extent (Atilt = 165±20) versus distance for SHP1 (23 May 1997).
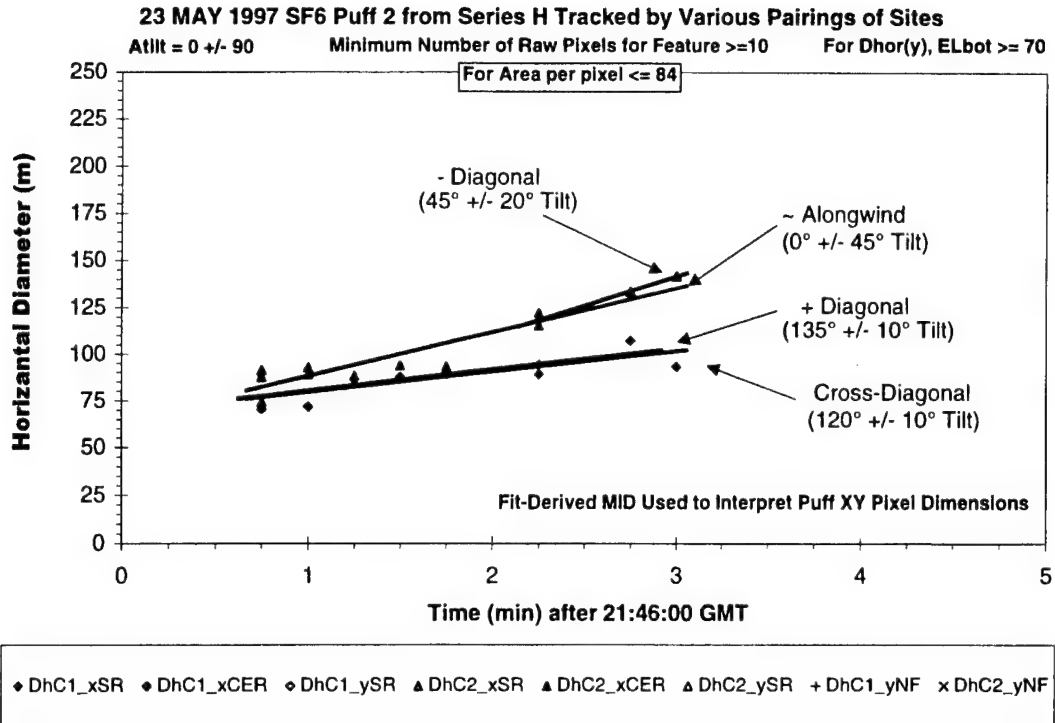
211

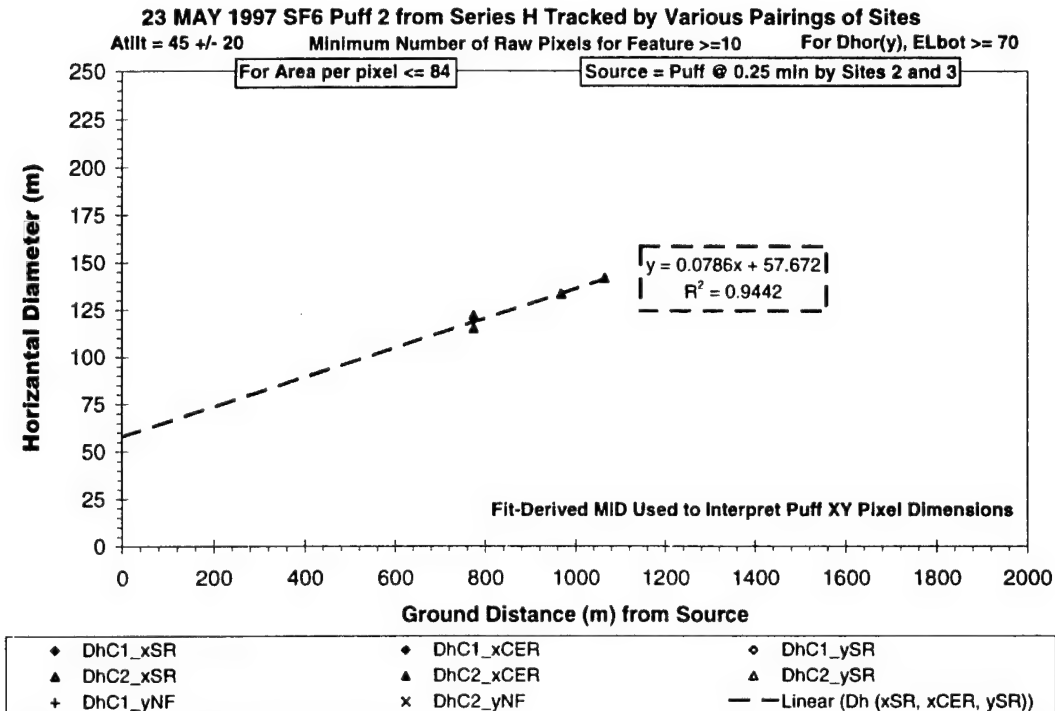Figure I-90. Summary dimension plot showing all perspectives of SHP2 (23 May 1997).

Figure I-91. - Diagonal extent (Atilt = 45±20) versus distance for SHP2 (23 May 1997).
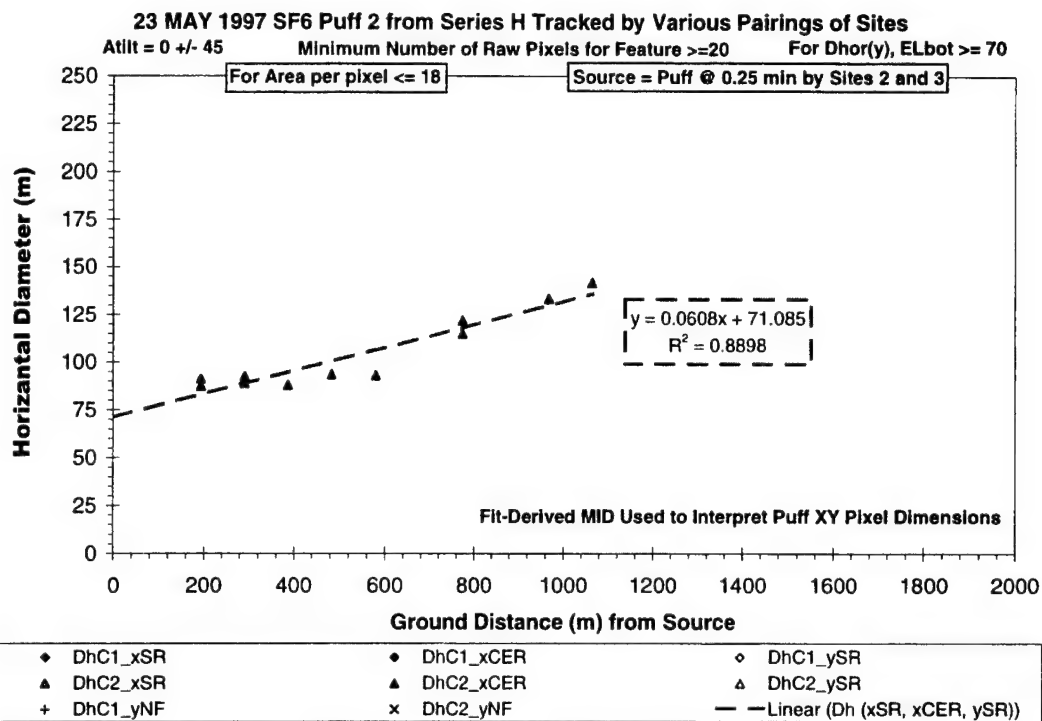
212

23 MAY 1997 SF6 Puff 2 from Series H Tracked by Various Pairings of Sites

Atilt = 0 +/- 45   Minimum Number of Raw Pixels for Feature >=20   For Dhor(y), ELbot >= 70

For Area per pixel <= 18   Source = Puff @ 0.25 min by Sites 2 and 3

$$y = 0.0608x + 71.085$$
$$R^2 = 0.8898$$

Fit-Derived MID Used to Interpret Puff XY Pixel Dimensions

Horizantal Diameter (m) vs **Ground Distance (m) from Source**

◆ DhC1_xSR	● DhC1_xCER	◇ DhC1_ySR
▲ DhC2_xSR	▲ DhC2_xCER	△ DhC2_ySR
+ DhC1_yNF	× DhC2_yNF	— —Linear (Dh (xSR, xCER, ySR))

Figure I-92. Alongwind extent (Atilt = 0±45) versus distance for SHP2 (23 May 1997).

23 MAY 1997 SF6 Puff 2 from Series H Tracked by Various Pairings of Sites

Atilt = 135 +/- 10   Minimum Number of Raw Pixels for Feature >=10   For Dhor(y), ELbot >= 70

For Area per pixel <= 30   Source = Puff @ 0.25 min by Sites 2 and 3

$$y = 0.0319x + 69.851$$
$$R^2 = 0.7005$$

Fit-Derived MID Used to Interpret Puff XY Pixel Dimensions

Horizantal Diameter (m) vs **Ground Distance (m) from Source**

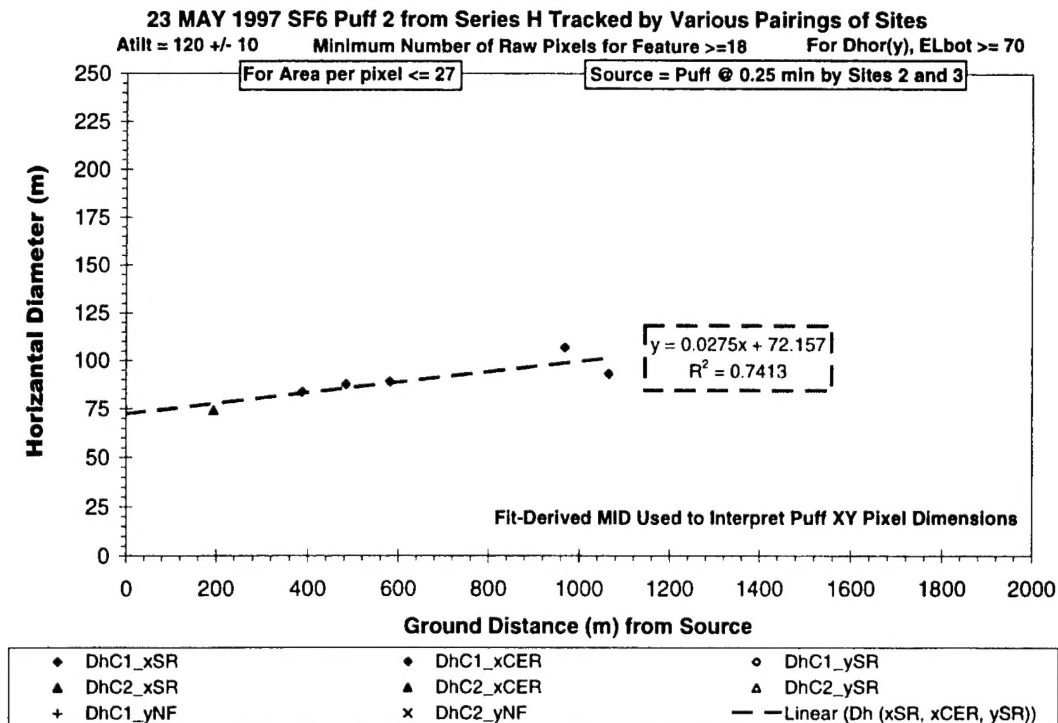| ◆ DhC1_xSR | ● DhC1_xCER | ◇ DhC1_ySR |
| ▲ DhC2_xSR | ▲ DhC2_xCER | △ DhC2_ySR |
| + DhC1_yNF | × DhC2_yNF | — —Linear (Dh (xSR, xCER, ySR)) |

Figure I-93. + Diagonal extent (Atilt = 135±10) versus distance for SHP2 (23 May 1997).

213

23 MAY 1997 SF6 Puff 2 from Series H Tracked by Various Pairings of Sites

Atilt = 120 +/- 10   Minimum Number of Raw Pixels for Feature >=18   For Dhor(y), ELbot >= 70

Figure I-94. Cross-Diagonal extent (Atilt= 120±10) versus distance for SHP2 (23 May 1997).

23 MAY 1997 SF6 Puff 3 from Series H Tracked by Various Pairings of Sites

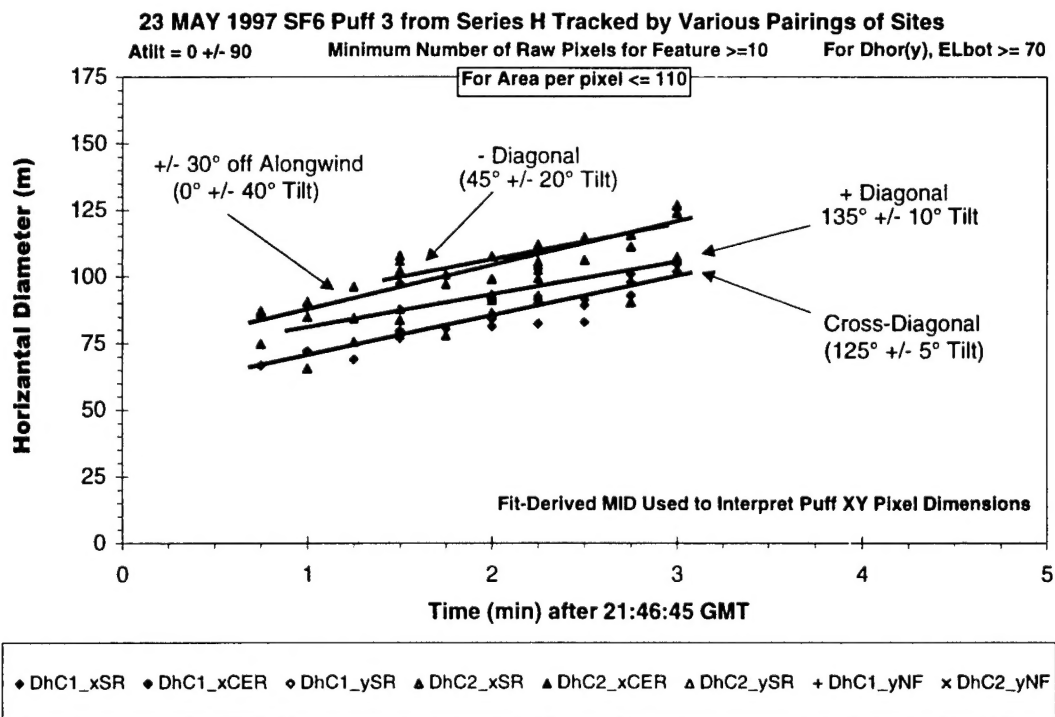Atilt = 0 +/- 90   Minimum Number of Raw Pixels for Feature >=10   For Dhor(y), ELbot >= 70

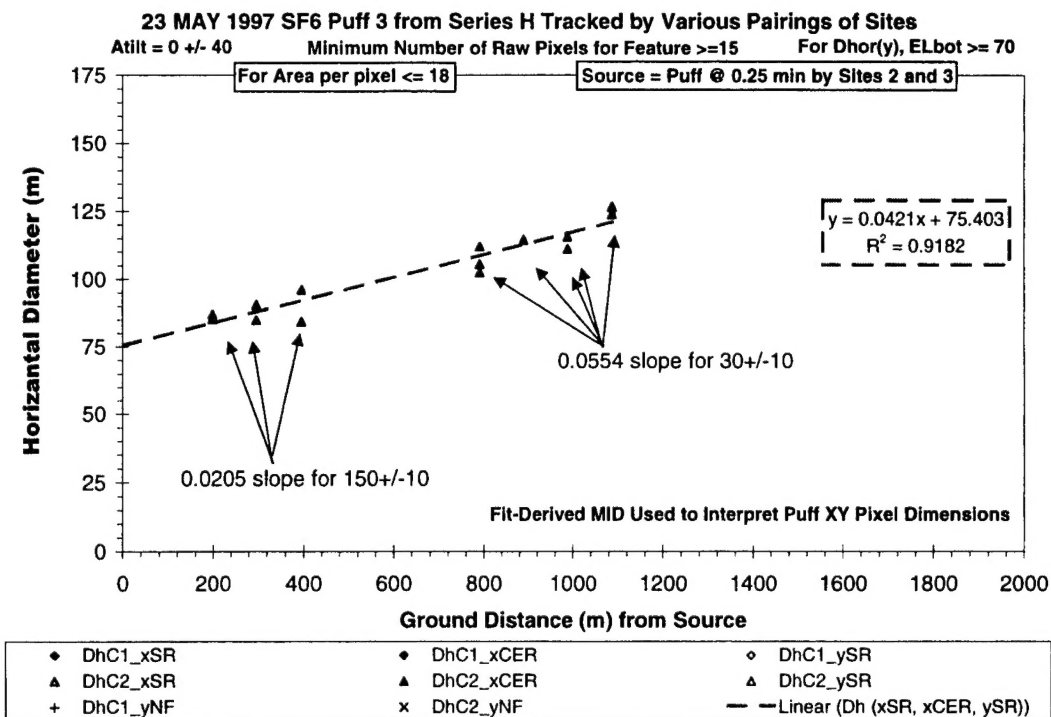Figure I-95. Summary dimension plot showing all perspectives of SHP3 (23 May 1997).

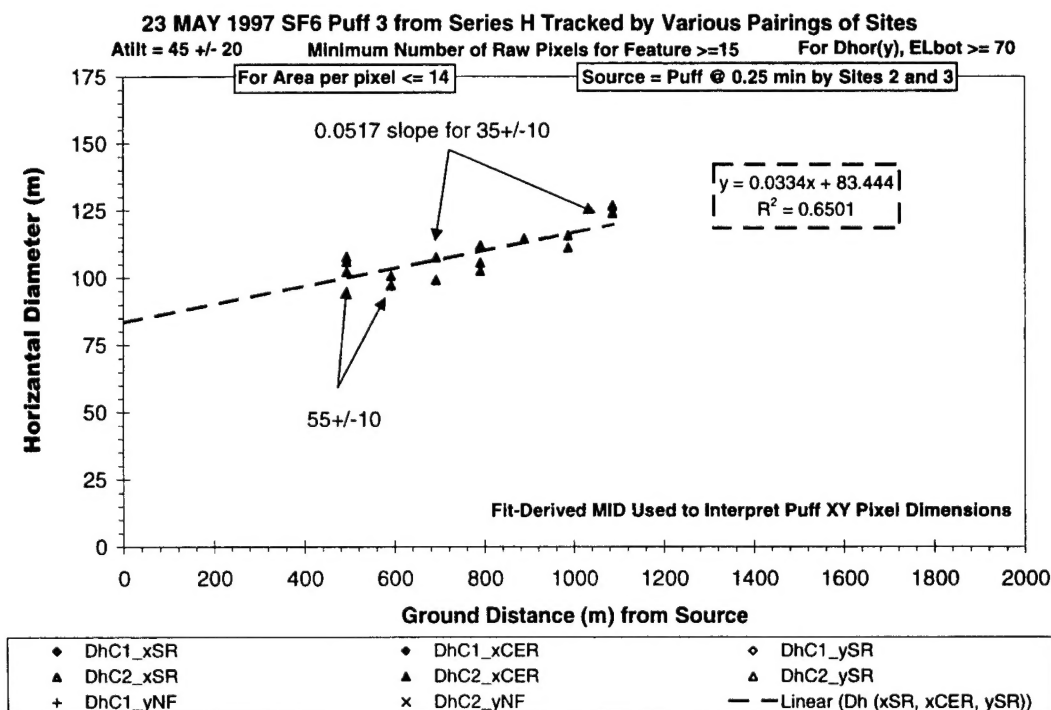Figure I-96. Along-diagonal extent (Atilt = 0±40) versus distance for SHP3 (23 May 1997).

Figure I-97. - Diagonal extent (Atilt = 45±20) versus distance for SHP3 (23 May 1997).
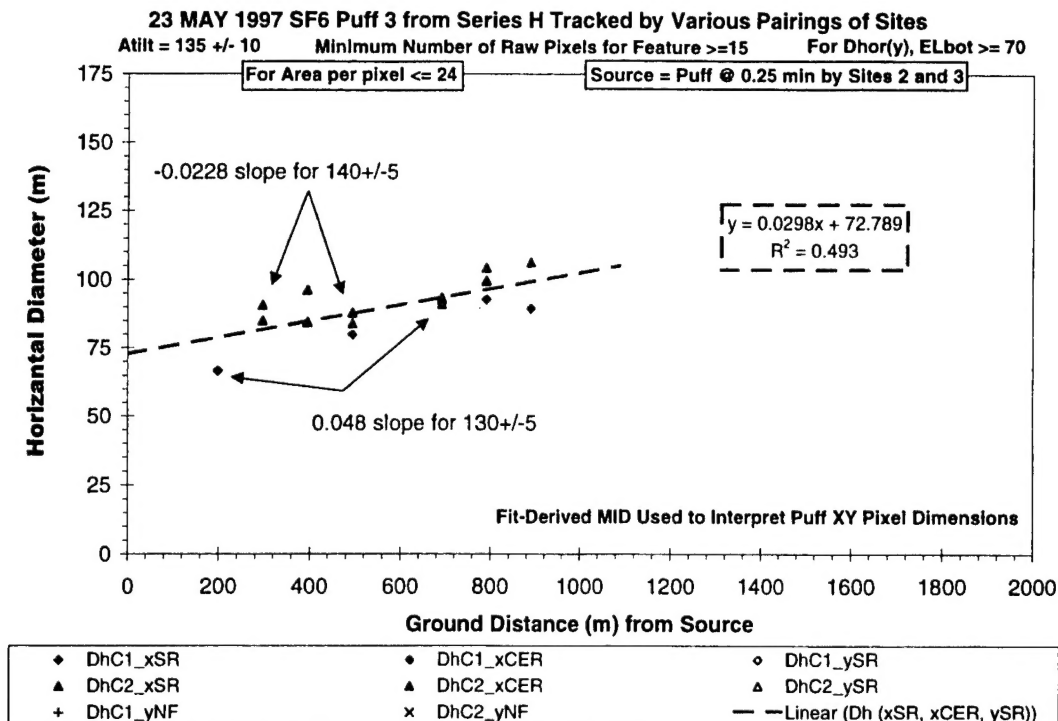
215

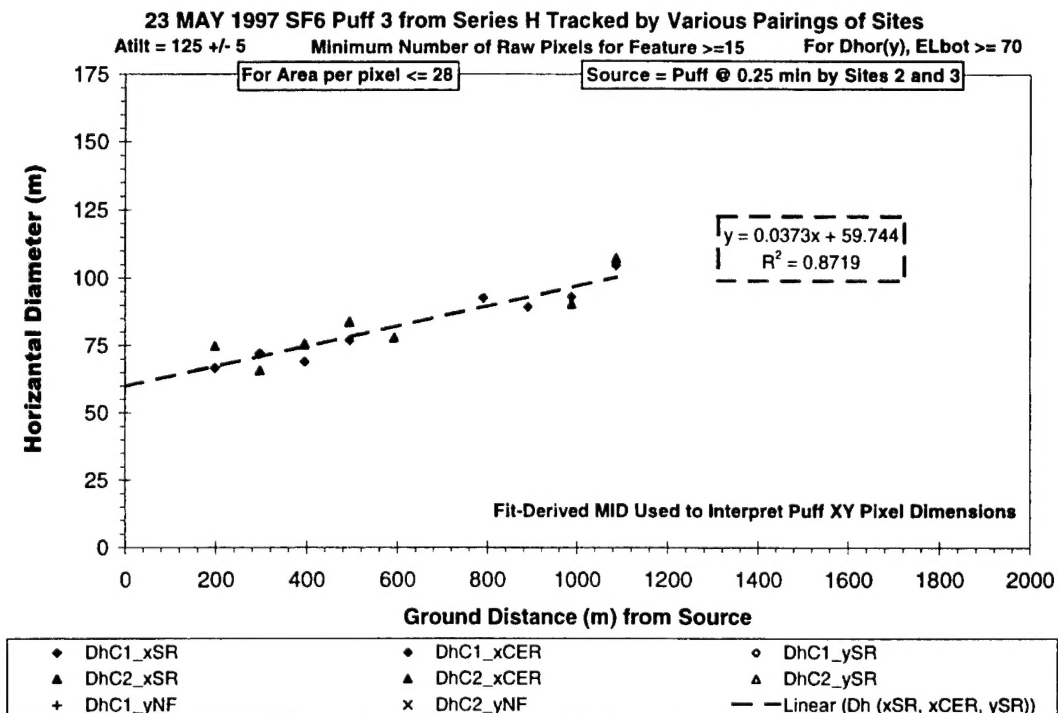Figure I-98. + Diagonal extent (Atilt = 135±10) versus distance for SHP3 (23 May 1997).

Figure I-99. Cross-Diagonal extent (Atilt= 125 +/- 5) versus distance for SHP3 (23 May 1997).

LABORATORY OPERATIONS

The Aerospace Corporation functions as an "architect-engineer" for national security programs, specializing in advanced military space systems. The Corporation's Laboratory Operations supports the effective and timely development and operation of national security systems through scientific research and the application of advanced technology. Vital to the success of the Corporation is the technical staff's wide-ranging expertise and its ability to stay abreast of new technological developments and program support issues associated with rapidly evolving space systems. Contributing capabilities are provided by these individual organizations:

Electronics and Photonics Laboratory: Microelectronics, VLSI reliability, failure analysis, solid-state device physics, compound semiconductors, radiation effects, infrared and CCD detector devices, data storage and display technologies; lasers and electro-optics, solid state laser design, micro-optics, optical communications, and fiber optic sensors; atomic frequency standards, applied laser spectroscopy, laser chemistry, atmospheric propagation and beam control, LIDAR/LADAR remote sensing; solar cell and array testing and evaluation, battery electrochemistry, battery testing and evaluation.

Space Materials Laboratory: Evaluation and characterizations of new materials and processing techniques: metals, alloys, ceramics, polymers, thin films, and composites; development of advanced deposition processes; nondestructive evaluation, component failure analysis and reliability; structural mechanics, fracture mechanics, and stress corrosion; analysis and evaluation of materials at cryogenic and elevated temperatures; launch vehicle fluid mechanics, heat transfer and flight dynamics; aerothermodynamics; chemical and electric propulsion; environmental chemistry; combustion processes; space environment effects on materials, hardening and vulnerability assessment; contamination, thermal and structural control; lubrication and surface phenomena.

Space Science Application Laboratory: Magnetospheric, auroral and cosmic ray physics, wave-particle interactions, magnetospheric plasma waves; atmospheric and ionospheric physics, density and composition of the upper atmosphere, remote sensing using atmospheric radiation; solar physics, infrared astronomy, infrared signature analysis; infrared surveillance, imaging, remote sensing, and hyperspectral imaging; effects of solar activity, magnetic storms and nuclear explosions on the Earth's atmosphere, ionosphere and magnetosphere; effects of electromagnetic and particulate radiations on space systems; space instrumentation, design fabrication and test; environmental chemistry, trace detection; atmospheric chemical reactions, atmospheric optics, light scattering, state-specific chemical reactions and radiative signatures of missile plumes.

Center for Microtechnology: Microelectromechanical systems (MEMS) for space applications; assessment of microtechnology space applications; laser micromachining; laser-surface physical and chemical interactions; micropropulsion; micro- and nanosatellite mission analysis; intelligent microinstruments for monitoring space and launch system environments.

Office of Spectral Applications: Multispectral and hyperspectral sensor development; data analysis and algorithm development; applications of multispectral and hyperspectral imagery to defense, civil space, commercial, and environmental missions.